



Eidgenössische Technische Hochschule Zürich
Swiss Federal Institute of Technology Zurich

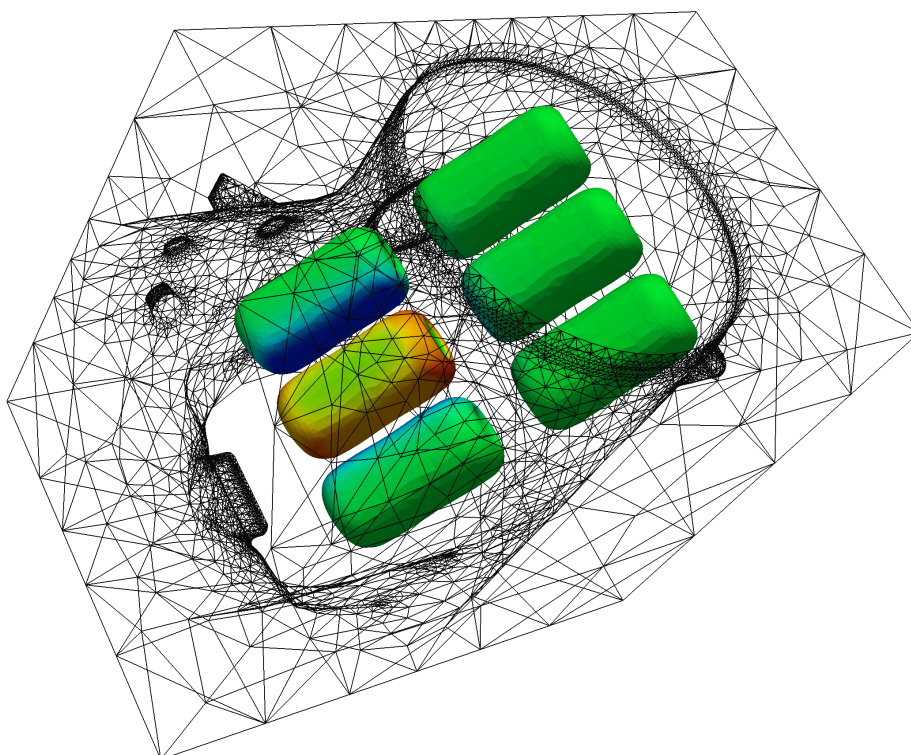
SCEE2012

Scientific Computing in Electrical Engineering

September 11-14, 2012

hosted by ETH Zurich and ABB Corporate Research, Switzerland

Conference Program and Book of Abstracts



BOSCH

Invented for life

This conference program was sponsored by Robert Bosch GmbH

Cover image: electric field strength on the surface of electrodes, geometry data from ABB Switzerland, computations carried out by Lars Kielhorn, SAM, ETH Zürich, using the BETL boundary element library, see www.sam.math.ethz.ch/betl.

Main Sponsors



Eidgenössische Technische Hochschule Zürich
Swiss Federal Institute of Technology Zurich

Sponsors



SWISS NATIONAL SCIENCE FOUNDATION



BOSCH

Invented for life



Stadt Zürich

DMATH

Department of Mathematics

Fred Tischer Fond

Table of Contents

Instructions for speakers and for poster presenters	1
General information	2
Maps of locations	3-6
Schedule of the week	7
Sessions and Schedule Tuesday	8-9
Sessions and Schedule Wednesday	10-11
Sessions and Schedule Thursday	12-13
Sessions and Schedule Friday	14-15
List of Contributors (chronologically)	17-18
Abstracts of Talks (chronologically)	23 - 114
Abstracts of Posters (alphabetically)	117 - 212
List of Participants	213 - 215
Local Organizers and Programme Committee	217 - 218
Notes	

Instructions for Speakers (SCEE 2012)

- If possible speakers should bring their presentations in electronic form (PDF or PowerPoint) on an USB memory stick and give it to SCEE 2012 staff no later than 15 Minutes before the start of the session. File names should start with the speaker's last name.
- In exceptional cases speakers may use their own laptops. It is their responsibility to make sure that the projection works. To that end they are strongly encouraged to test the setup during the break before their session.
- SCEE addresses a broad audience with diverse backgrounds and speakers should take this into account as well as the focus of the conference on computational aspects.

Instructions for Poster Presenters:

Day & Time	Session type	Location
Tuesday, 14:50 - 16:20	regular session	ETH, Zurich
Wednesday, 14:50 - 16:20	regular session	ETH, Zurich
Wednesday, 14:50 - 16:20	Young Scientist Award session	ETH, Zurich
Thursday, 12:30 - 13:30	Industry Poster session	ABB, Baden

Location ETH Zurich: Main Building, E-Floor

Format: Maximum size is A0

When: Please look at "List of Contributors" in "Conference Program and Book of Abstracts", where you can find your personal session day.

Procedure

- All posters can be attached to vacant poster walls already on Tuesday morning in the ETH Main Hall.
- For all who participate in the Young Scientist Award, please use poster walls that are especially marked for that (label with "Young Scientist Award")
- The posters should be removed on Friday at 12:00 at the latest
- During your poster session you are expected to stand next to your poster during the entire session ready to answer questions. ¹

Industry Poster Session

For all those who present their poster on Thursday, please do not forget to bring it to ABB in Baden.

¹Short leaves are permitted.

General information

- *WLAN*

You will have WLAN access at the ETH conference venue. Detailed information will be handed out at the registration desk.

WLAN access on Thursday at ABB Baden: Access information is available in the Bardeen seminar room.

- *Lunch at the ETH-Mensa*

For the Mensa, please take the lift to the level B and follow the signs.

- *Conference Dinner*

Conference badges are considered as 'Conference Dinner' vouchers (Thursday).

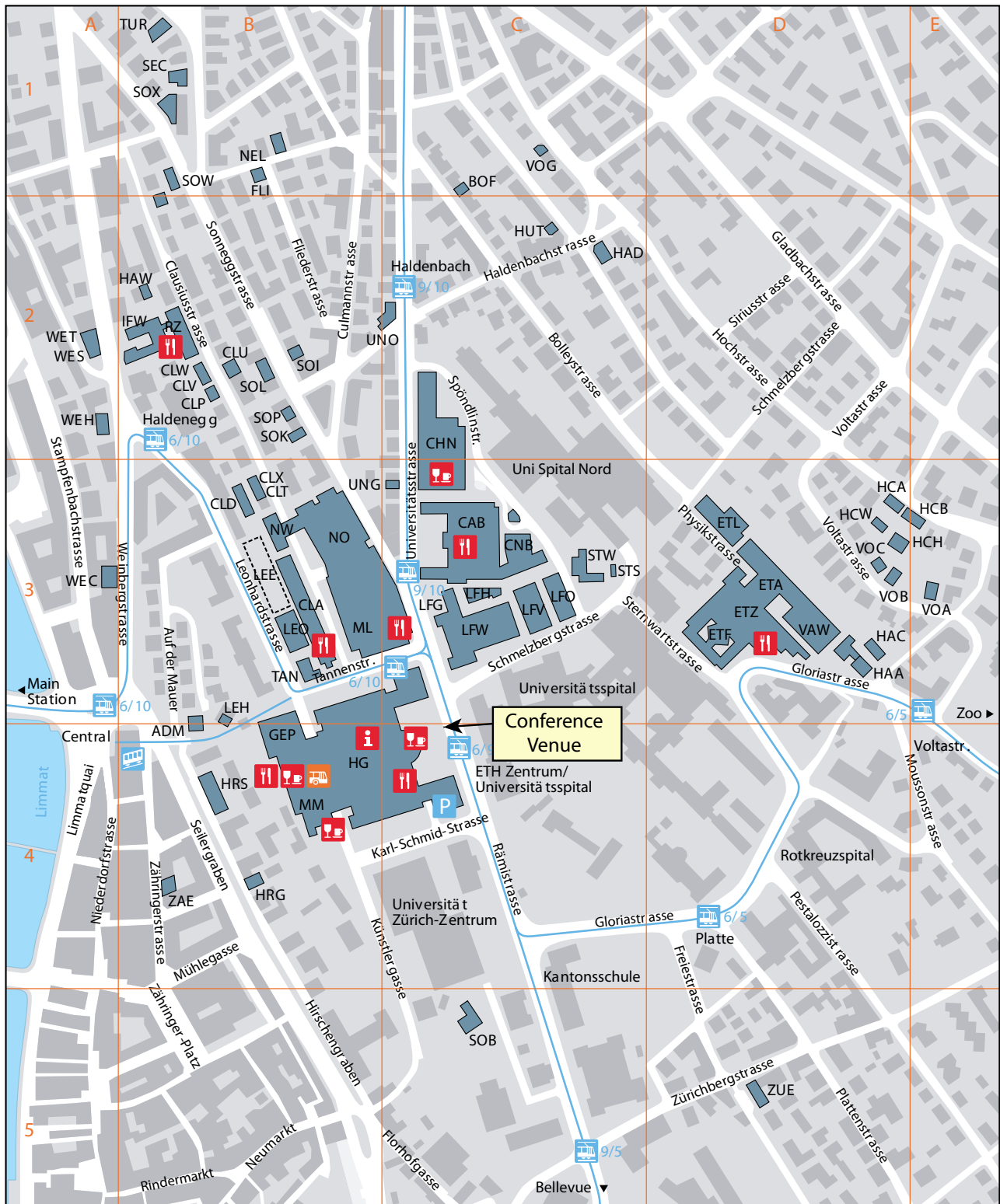
- *Industry day participants*







Badges and conference dinner vouchers for visitors of only the industry day can be picked up at the ABB registration desk on Thursday (Mrs. Weber).

- *Lunch and Industry Poster session at ABB*

At ABB Baden-Dättwil we will first have Lunch in the "Gartenhaus" from 12:00 - 12:30. Afterwards coffee will be served together with the poster session in the "Foyer" from 12:30 - 13:30.

ETH Zurich - Conference Venue



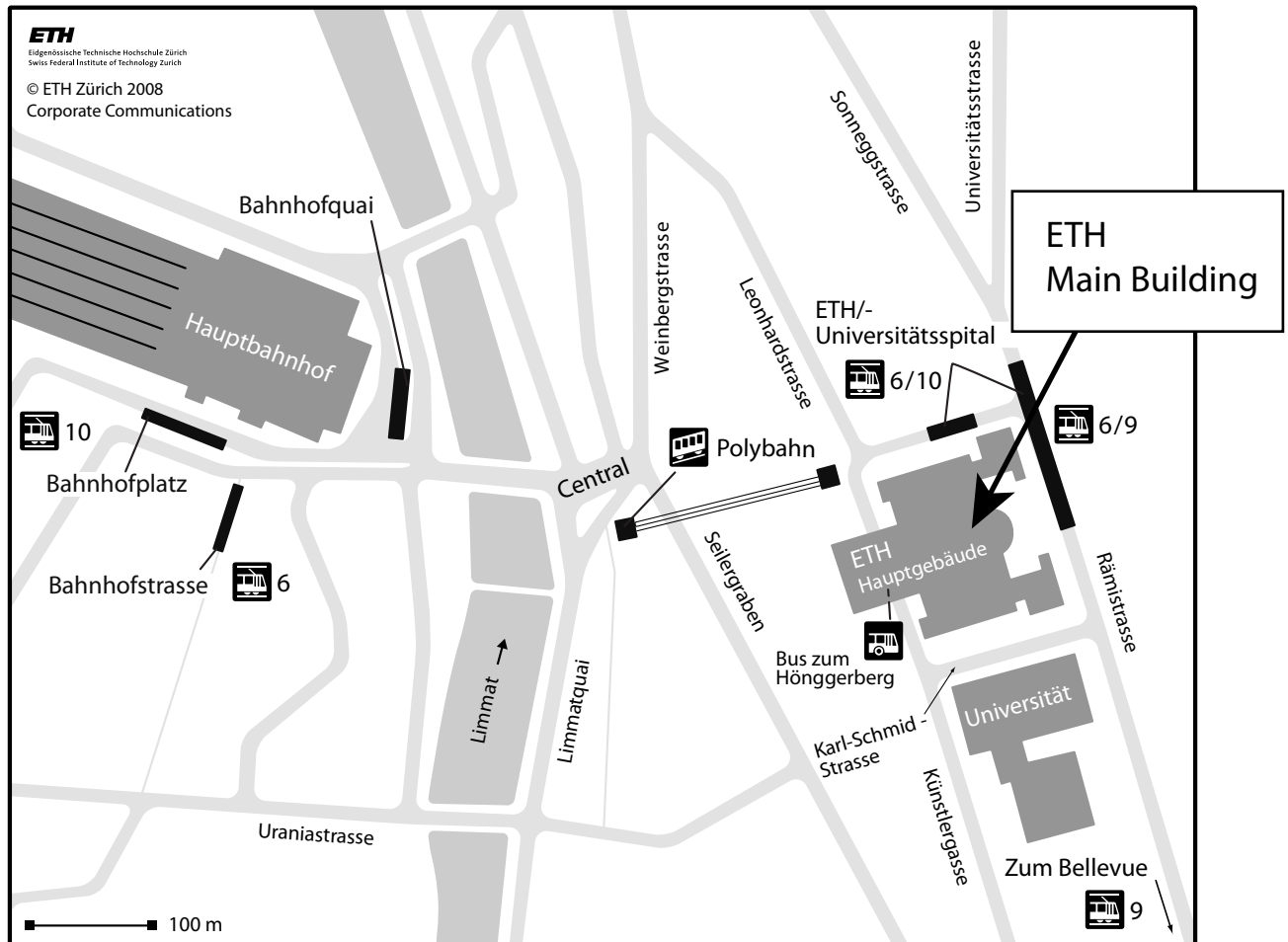
- | | | | |
|---|---------------------------------|---|---|
|  | Tram stop |  | Canteen |
|  | Cable Car "Polybahn" |  | Cafeteria |
|  | ETH-shuttle "Science City Link" |  | Information desk (phone +41 44 632 25 50) |

Publisher: ETH Zürich, Corporate Communications, May 2011

Map: Institute of Cartography of ETH Zurich, edited by Immobilien,
Stab Portfoliomanagement, and Corporate Communications

ETH Zurich

From Zurich main station to ETH Main Building



Location of bus stop on Thursday, 13 September Departure 8:00

For underground bus stop on Thu, 8.00 please enter the underpass, then follow street for approx. 30 meters

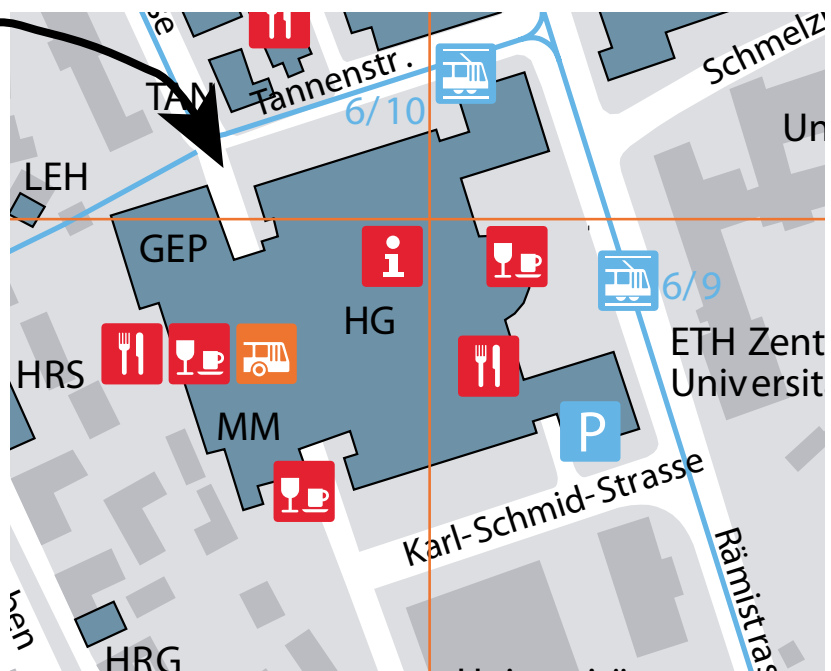
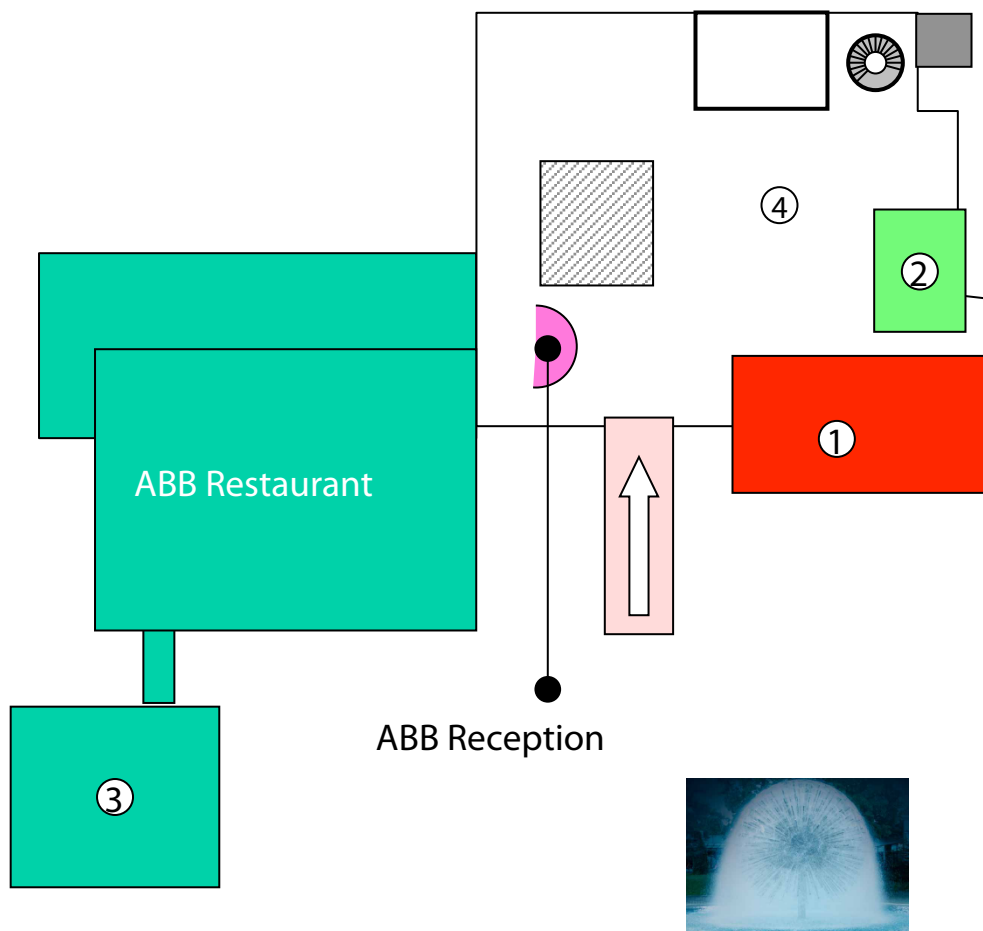


ABB Corporate Research Dättwil



- 1 Euler Auditorium (Plenary Sessions)
- 2 Bardeen Seminar (WLAN)
- 3 Gartenhaus (Lunch)
- 4 Foyer (Coffee + Posters)

Address

ABB Schweiz AG, Corporate Research
Segelhofstrasse 1k
CH-5405 Baden-Dättwil

Schloss Wildegg
Effingerweg 5
CH-5103 Schloss Wildegg

Schedule

11 - 14 September 2012

	Tuesday	Wednesday	Thursday <i>Industry Day at ABB</i>	Friday
08:00 - 08:45	<i>Registration</i>		<i>Bus transfer to Dättwil</i>	
08:45 - 09:00	<i>Opening</i>			
09:00 - 09:40	Andreas Klöckner	Alper Demir	Welcome	Sascha Schnepf
09:40 - 10:00	Stefan Kurz	Kai Bittner	Didier Cottet	Nicolay Komarevskiy
10:00 - 10:20	Timo Hülsmann	Timo Rahkonen	Thorsten Steinmetz	Mark Blome
10:20 - 10:50	<i>Coffee break</i>	<i>Coffee break</i>	<i>Coffee break</i> 10:20 - 10:40	<i>Coffee break</i>
10:50 - 11:10	Irene Hiltunen	Oratio Muscato	10:40 - 12:00	Aram Markosyan
11:10 - 11:30	Matteo Porro	Vito Dario Camiola	Utz Wever	Davide Cagnoni
11:30 - 11:50	Bastian Bandlow	Evelyn Knapp	Sebastian Schöps	Christof Kaufmann
11:50 - 12:10	Aytac Alparslan	Carlo de Falco	Maximilian Wiesmüller	11:50 - 12:30 Giuseppe Nicosia
12:10 - 13:30	<i>Lunch break</i>	<i>Lunch break</i>	<i>Lunch 12:00 - 12:30</i> <i>Industry Poster Session</i> 12:30 - 13:30	12:30 - 12:45
13:30 - 14:10	Olivier Le Maître	Karl Meerbergen	13:30 - 14:30	<i>Closing</i>
14:10 - 14:30	E. Jan W. ter Maten	Judith Schneider	Lab Visit	
14:30 - 14:50	Michaela Mehlin	Lihong Feng		
14:50 - 16:20	<i>Coffee break + Poster Session</i>	<i>Coffee break + Poster Sessions (regular + Award)</i>	14:30 - 15:50	13:00
16:20 - 16:40	Jian Cui	Ulrich Matthes	Lin Zschiedrich	Lunch
16:40 - 17:00	Kersten Schmidt	Nicodemus Banagaaya	Lucas Kostetzer	
17:00 - 17:20	Alberto Paganini	André Bodendiek	Mustafa Boyvat	
17:20 - 17:40	Nils Lavesson	Martin Hess	16:00	Departure
19:00	<i>Workshop Apéro</i>		<i>Excursion + Conference Dinner</i>	

Locations:

- Bus to Baden/Dättwil:* ETH Polyterrasse, see also map at page 4
- Registration:* ETH Main Building, F floor, "Uhrenhalle"
- Workshop Apéro:* Dozentenfoyer, Main Building, J floor (lift east)
- Oral Presentations:* Main Building, F floor, F5
- Poster Presentations:* Main Building, E floor, Main Hall
- Coffee breaks:* Main Building, E floor, Main Hall
- Lunch:* ETH Mensa, Main Building, B-Floor

Sessions for Tuesday:

CE: Computational Electromagnetics

Chairman: Pascal Leuchtmann
Ursula van Rienen

MM: Mathematical and Computational Methods

Chairman: Ralf Hiptmair
Michael Günther

Poster Session:

Chairman: Wil Schilders

Contributors of Poster Session (see P.115/116):

Daniele Altomonte
Oana Antonescu
Matthias Bollhöfer
Angelo Brambilla
Beatrice Bugert
Ignasi Colominas
Luca Di Rienzo
Thomas Flisgen
Antti Hannukainen
Magnus Herberthson
Michael Kolmbauer

Fritz Kretzschmar
Bastiaan Michielsen
Andrey Pethukov
Adina Racasan
Andreas Rathsfeld
Santi Rizzo
Nunzio Salerno
Eike Scholz
Murat Simsek
Andreas Stock

Tuesday, September 11

Invited talks
Contributed talks

Chair				page
CE	09:00 - 09:40	A. Klöckner	Transformational programming for time- and frequency-domain EM simulation	23
	09:40 - 10:00	St. Kurz	Improved electromagnetic modelling and simulation of axial flux machines	25
	10:00 - 10:20	T. Hülsmann	Computation of optimal model parameters of an extended Brauer model for ferromagnetic material behaviour	27
P. Leuchtman U. van Rienen	10:20 - 10:50 <i>Coffee break (sponsored by Maschinenfabrik Reinhausen)</i>			
	10:50 - 11:10	I. Hiltunen	Broad band surface impedance boundary conditions for higher order time domain discontinuous Galerkin method	29
	11:10 - 11:30	M. Porro	Bulk and interface balance equations for organic solar cell	31
	11:30 - 11:50	N. Bandlow	Electromagnetic eigenmode characterization by sensitivity analysis simulation	33
	11:50 - 12:10	A. Alparslan	Analysis of photonic structures in layered geometries by MMP	35
12:10 - 13:30		Lunch		
MM	13:30 - 14:10	O. LeMaître	Stochastic spectral methods for uncertainty propagation in numerical models	37
	14:10 - 14:30	E. ter Maten	Robust time-domain source stepping for DC-solution of circuit equations	39
	14:30 - 14:50	M. Mehlin	High-order local time-stepping with explicit Runge-Kutta methods	41
R. Hiptmair M. Günther	14:50 - 16:20 <i>Coffee break (sponsored by Maschinenfabrik Reinhausen) + Poster Session</i>			
	16:20 - 16:40	J. Cui	Body-fitting meshes for the discontinuous Galerkin methods	43
	16:40 - 17:00	K. Schmidt	Robust transmission conditions of high order for thin conducting sheets	45
	17:00 - 17:20	A. Paganini	Efficient convolution based impedance boundary conditions	47
	17:20 - 17:40	N. Lavesson	Modeling of streamers in transformer oil using OpenFOAM	49
19:00		Workshop Apéro in the Dozentenfoyer		

Sessions for Wednesday:

CS: Circuit and Device Modelling & Simulation

Chairman: *Georg Denk*
Vittorio Romano

MOR: Model Order Reduction

Chairman: *Gabriela Ciuprina*
Jan ter Maten

Poster Session:

CS/MOR + Young Scientist Award

Chairman: *Georg Denk*

Contributors of Poster Session (see P.115/116):

Regular Poster Session

Gabriela Ciuprina
Selçuk Emiroglu
Claudia Hebedean
Van Hai Jorks
Umesh Kumar
Giovanni Mascali
Claudia Pacurar
Ihsan Pehlivan
Timo Rakhonen
Yilmaz Uyaroglu

Young Scientist Award

Daniele Altomonte
Oana Antonescu
Nicodemus Banagaaya
Beatrice Bugert
Davide Cagnoni
Vito Dario Camiola
Jian Cui
Selçuk Emiroglu
Thomas Flisgen
Claudia Hebedean
Irene Hiltunen
Timo Hülsmann
Van Hai Jorks
Evelyne Knapp
Michael Kolmbauer
Nikolay Komarevskiy
Fritz Kretzschmar
Umesh Kumar
Aram Markosyan
Andrey Petukhov
Matteo Porro
Judith Schneider
Elke Scholz
Murat Simsek
Andreas Stock
Maximilian Wiesmüller

Wednesday, September 12

Invited talks
Contributed talks

Chair				page
CS	09:00 - 09:40	A. Demir	Phase models and phase computations for oscillators	53
	09:40 - 10:00	K. Bittner	Optimal frequency sweep method in multi-rate circuit simulation	55
	10:00 - 10:20	T. Rahkonen	Polynomial fitting of nonlinear sources with correlating inputs	57
G. Denk V. Romano	10:20 - 10:50	<i>Coffee break (sponsored by CADFEM (Suisse) AG)</i>		
	10:50 - 11:10	O. Muscato	Heat generation in silicon nanometric semiconductor devices	59
	11:10 - 11:30	V.D. Camiola	Simulation of a double-gate MOSFET by a non parabolic energy-transport subband model based on MEP including crystal heating	61
	11:30 - 11:50	E. Knapp	Electrical modelling of large-area organic light-emitting devices	63
	11:50 - 12:10	C. de Falco	Numerical estimation of the impact of Energetic disorder on the low-frequency CV characteristics of organic MOS structures	65
12:10 - 13:30				<i>Lunch</i>
MOR	13:30 - 14:10	K. Meerbergen	Model order reduction for PDE constrained optimization in vibrations	67
	14:10 - 14:30	J. Schneider	Stochastic collocation methods and model reduction for Maxwell's equations	69
	14:30 - 14:50	L. Feng	Automatic model order reduction by moment-matching according to an efficient output error bound	71
G. Ciuprina J. ter Maten	14:50 - 16:20	<i>Coffee break (sponsored by CADFEM) + Poster Session + Young Scientist Award</i>		
	16:20 - 16:40	U. Matthes	Reduced order modeling of ODE-PDE networks	73
	16:40 - 17:00	N. Banagaaya	Index-aware model Order Reduction: LTI DAEs in electric networks	75
	17:00 - 17:20	A. Bodendiek	Adaptive-order rational Arnoldi method for Maxwell's equations	77
	17:20 - 17:40	M. Hess	Reduced basis modeling for time-harmonic Maxwell's equations	79

Sessions for Thursday:

I1: Industry Session 1

Chairman: Jörg Ostrowski

I2: Industry Session 2

Chairman: Andreas Blaszczyk

I3: Industry Session 4

Chairman: Bastiaan Michielsen

Industry Poster Session (12:30 - 13:30)
--

Chairman: Andreas Blaszczyk

Contributors of Poster Session (see P.115/116)

Giuseppe Ali

Andreas Blaszczyk

Marcos Bockholt

Thomas Christen

Yaser A Khalifa

Industry Day
Thursday, September 13
Location: ABB Baden-Dättwil

Invited talks
Contributed talks

Chair	08:00		Departure: Bus transfer to Dättwil (start ETH Polyterrasse)	
I1	09:00 - 09:20		Welcome by Research Director ABB Switzerland	
J. Ostrowski	09:20 - 09:50	D. Cottet	Electromagnetic simulations in power electronic converter design	83
	09:50 - 10:20	T. Steinmetz	Numerical simulations for power and distribution transformers	85
10:20 - 10:40 <i>Coffee break</i>				
I2 A. Blaszczyk	10:40 - 11:20	U. Wever	Uncertainty quantification from an industrial perspective	87
	11:20 - 11:40	S. Schöps	Uncertainty quantification of inrush currents in electric machines with respect to measured material data	89
	11:40 - 12:00	M. Wiesmüller	Dielectric breakdown simulations of an on-load tap-changer in a transformer considering the Influence of tap leads and windings	91
12:00 - 12:30 <i>Lunch</i>				
12:30 - 13:30 <i>Industry Poster Session</i>				
I3 B. Michielsen	13:30 - 14:30		Lab Visit	
	14:30 - 15:10	L. Zschiedrich	Nonlocal hydrodynamic Drude model of nano-plasmonic optical devices	93
	15:10 - 15:30	L. Kostetzer	Model order reduction for efficient battery electro-thermal simulation	95
	15:30 - 15:50	M. Boyvat	Metamaterial design for magnetic field shielding	97
	16:00		Excursion + Conference Dinner	

Program Excursion:

16:00 - 16:15 *Meeting time at bus stop*
16:30 *Departure: bus transfer from Dättwil to Schloss Wildegg*
17:00 - 19:30 *Apéro + Introduction history of the Schloss Wildegg (18:00-18:20)*
19:30 - 22:30 *Conference Dinner + "Young Scientist Award"*
22:30 - 22:45 *Meeting time at bus stop*
23:00 *Departure: bus transfer from Schloss Wildegg to Zurich*

Sessions for Friday:

CP: Coupled Problems

Chairman: *Andreas Blaszczyk*
Bastiaan Michielsen

Friday, September 14

Invited talks
Contributed talks

Chair				page
CP	09:00 - 09:40	S. Schnepf	The discontinuous Galerkin method on dynamical hp-meshes	101
	09:40 - 10:00	N. Komarevskiy	Optimal design of reflecting photonic structures for space applications	103
	10:00 - 10:20	M. Blome	Back-reflector optimization in thin-film silicon solar cells using 3D finite element simulations	105
A. Blaszczyk B. Michielsen	10:20 - 10:50	<i>Coffee break</i>		
	10:50 - 11:10	A. Markosyan	Derivation and test of high order fluid model for streamer discharges	107
	11:10 - 11:30	D. Cagnoni	Electro-hydrodynamic numerical modelling of corona discharge	109
	11:30 - 11:50	Ch. Kaufmann	Efficient simulation of frequency-transient mixed co-simulation of coupled heat-electromagnetic problems	111
	11:50 - 12:30	G. Nicosia	Designing high performance electronic devices, circuits and systems	113
	12:30 : 12:45		Closing	

13:00

Lunch and Departure

List of Contributors

page abstract/poster	Contributors	Presentation
117	Ali, Giuseppe	<i>POSTER SESSION</i> , Thursday
35	Alparslan, Aytac	Tuesday, 11:50
119	Altomonte, Daniele	<i>POSTER SESSION</i> , Tuesday, <i>AWARD SESS.</i> , Wednesday
121	Antonescu, Oana	<i>POSTER SESSION</i> , Tuesday, <i>AWARD SESS.</i> , Wednesday
75, 123	Banagaaya, Nicodemus	Wednesday, 16:40 + <i>AWARD SESSION</i> , Wednesday
33	Bandlow, Bastian	Tuesday, 11:30
55	Bittner, Kai	Wednesday, 09:40
125	Blaszczyk, Andreas	<i>POSTER SESSION</i> , Thursday
105	Blome, Mark	Friday, 10:00
127	Bockholt, Marcos	<i>POSTER SESSION</i> , Thursday
77	Bodendiek, André	Wednesday, 17:00
129	Bollhöfer, Matthias	<i>POSTER SESSION</i> , Tuesday
97	Boyvat, Mustafa	Thursday, 14:30
131	Brambilla, Angelo	<i>POSTER SESSION</i> , Tuesday
135	Bugert, Beatrice	<i>POSTER SESSION</i> , Tuesday, <i>AWARD SESS.</i> , Wednesday
109	Cagnoni, Davide	Friday, 11:10 + <i>AWARD SESSION</i> , Wednesday
61, 139	Camiola, Vito Dario	Wednesday, 11:10 + <i>AWARD SESSION</i> , Wednesday
141	Christen, Thomas	<i>POSTER SESSION</i> , Thursday
143	Ciuprina, Gabriela	<i>POSTER SESSION</i> , Wednesday
145	Colominas, Ignasi	<i>POSTER SESSION</i> , Tuesday
83	Cottet, Didier	Thursday, 09:40
147	Cui, Jian	Tuesday, 16:20 + <i>AWARD SESSION</i> , Wednesday
65	De Falco, Carlo	Wednesday, 11:50
53	Demir, Alper	Wednesday, 09:00
149	Di Rienzo, Luca	<i>POSTER SESSION</i> , Tuesday
151	Emiroglu, Selçuk	<i>POSTER SESSION/AWARD SESSION</i> , Wednesday
71	Feng, Lihong	Wednesday, 14:30
153	Flisgen, Thomas	<i>POSTER SESSION</i> , Tuesday, <i>AWARD SESS.</i> , Wednesday
155	Hannukainen, Antti	<i>POSTER SESSION</i> , Tuesday
157	Hebedean, Claudia	<i>POSTER SESSION/AWARD SESSION</i> , Wednesday
159	Herberthson, Magnus	<i>POSTER SESSION</i> , Tuesday
79	Hess, Martin	Wednesday, 17:20
29, 161	Hiltunen, Irene	Tuesday, 10:50 + <i>AWARD SESSION</i> , Wednesday
27, 163	Hülsman, Timo	Tuesday, 10:00 + <i>AWARD SESSION</i> , Wednesday
165	Jorks, Van Hai	<i>POSTER SESSION/AWARD SESSION</i> , Wednesday
111	Kaufmann, Christof	Friday, 11:30
23	Klößner, Andreas	Tuesday, 09:00

63, 167	Knapp, Evelyne	Wednesday, 11:30 + <i>AWARD SESSION</i> , Wednesday
169	Kolmbauer, Michael	<i>POSTER SESSION</i> , Tuesday, <i>AWARD SESS.</i> , Wednesday
103, 171	Komarevskiy, Nikolay	Friday, 09:40 + <i>AWARD SESSION</i> , Wednesday
95	Kostetzer, Lucas	Thursday, 14:30
173	Kretzschmar, Fritz	<i>POSTER SESSION</i> , Tuesday, <i>AWARD SESS.</i> , Wednesday
175	Kumar, Umesh	<i>POSTER SESSION/AWARD SESSION</i> , Wednesday
25	Kurz, Stefan	Tuesday, 09:40
49	Lavesson, Nils	Tuesday, 17:20
37	Le Maître, Olivier	Tuesday, 13:30
107, 177	Markosyan, Aram	Friday, 10:50 + <i>AWARD SESSION</i> , Wednesday
179	Mascali, Giovanni	<i>POSTER SESSION</i> , Wednesday
73	Matthes, Ulrich	Wednesday, 16:20
67	Meerbergen, Karl	Wednesday, 13:30
41	Mehlin, Michaela	Tuesday, 14:30
181	Michielsen, Baastian	<i>POSTER SESSION</i> , Tuesday
59	Muscato, Orazio	Wednesday, 10:50
113	Nicosia, Giuseppe	Friday, 11:50
183	Pacurar, Claudia	<i>POSTER SESSION</i> , Wednesday
47	Paganini, Alberto	Tuesday, 17:00
185	Pehlivan, Ihsan	<i>POSTER SESSION</i> , Wednesday
187	Petukhov, Andrey	<i>POSTER SESSION</i> , Tuesday, <i>AWARD SESS.</i> , Wednesday
31, 189	Porro, Matteo	Tuesday, 11:10 + <i>AWARD SESSION</i> , Wednesday
191	Racasan, Adina	<i>POSTER SESSION</i> , Tuesday
57, 193	Rahkonen, Timo	Wednesday, 10:00 + <i>POSTER SESSION</i> , Wednesday
195	Rathsfeld, Andreas	<i>POSTER SESSION</i> , Tuesday
197	Rizzo, Santi	<i>POSTER SESSION</i> , Tuesday
199	Salerno, Nunzio	<i>POSTER SESSION</i> , Tuesday
45	Schmidt, Kersten	Tuesday, 16:40
69, 201	Schneider, Judith	Wednesday, 14:10 + <i>AWARD SESSION</i> , Wednesday
203	Scholz, Eike	<i>POSTER SESSION</i> , Tuesday, <i>AWARD SESS.</i> , Wednesday
101	Schnepp, Sascha	Friday, 09:00
89	Schöps, Sebastian	Thursday, 10:40
205	Simsek, Murat	<i>POSTER SESSION</i> , Tuesday, <i>AWARD SESS.</i> , Wednesday
85	Steinmetz, Thorsten	Thursday, 10:00
207	Stock, Andreas	<i>POSTER SESSION</i> , Tuesday, <i>AWARD SESS.</i> , Wednesday
39	ter Maten, Jan	Tuesday, 14:10
209	Uyaroglu, Yilmaz	<i>POSTER SESSION</i> , Wednesday
87	Wever, Utz	Thursday, 10:40
91, 211	Wiesmüller, Maximilian	Thursday, 10:40 + <i>AWARD SESSION</i> , Wednesday
93	Zschiedrich, Lin	Thursday, 14:30

Abstracts for Talks

Tuesday, September 11

Transformational Programming for time- and frequency-domain EM simulation

Andreas Klöckner¹

Courant Institute of Mathematical Sciences, 251 Mercer St, New York, NYU kloeckner@cims.nyu.edu

Summary. Detailed, high-fidelity electromagnetic simulations entail a significant computational cost, and this cost may be managed by efficient use of modern computational resources. Modern many-core architectures pose a challenge by being both more diverse and more complicated than conventional computers. This contribution presents strategies and software packages based on run-time code generation that help deal with this emerging complexity. We demonstrate their use and effectiveness by applications to discontinuous Galerkin time-domain and integral-equation-based frequency-domain EM simulations.

1 Introduction

Graphics processing units (GPUs) and many-core machines have enjoyed tremendous impact in recent years, because their use has brought about significant cost reductions for a number of numerical methods. Yet, gains from the use of many-core machines have not been uniformly distributed across methods. Further, adoption of these machines, despite their advantages, has been far from universal. These two facts hint at underlying issues that must be resolved before the promise of these recent hardware advances is realized.

The first issue is that the choice of computational method has thus far often been made in complete ignorance of machine concerns. Examples of this are methods that may satisfy some theoretical optimality criterion, but which are outrun in practice by methods that make some concessions to the hardware and are slightly suboptimal in theory. The consequence of this is that computational methods and their implementation have merged into one joint design space that cannot easily be split into separate concerns.

The second issue is that this new hardware requires specialist knowledge to program. Not only must the programmer be aware of the sometimes intricate semantics of parallel programming models—she must also understand the performance implications of each of the (often many) semantically equivalent ways of expressing a single computation. And even if the programmer possesses some intuition on hardware response to different coding techniques, any given computational task may still require trying numerous approaches to achieve good machine utilization. Worse, this procedure has some likelihood of needing to be repeated when new generations of the same hardware,

or *especially* when a different vendor's hardware is to be used. All this translates to extra cost, leading many potential users to forgo the potential execution time gains of many-core implementation.

2 Transformational programming

Unlocking the benefit of GPUs for a majority of users is a thorny problem, to which many solutions have been proposed—too many to even begin to provide a concise overview in this setting. In 2009, we pioneered one very simple starting strategy that has enjoyed a measure of success in the marketplace, in the form of our packages *PyCUDA* and *PyOpenCL*, whose use will be briefly discussed. A cornerstone of this strategy was to enable run-time code generation ('RTCG') [1]. RTCG allows the user to apply more intelligence than customarily supplied by compilers to process and reason about the source code that carries out a desired computation. The basic flow of information in this setting is illustrated in Fig. 1. In other words, our tool provided, in some sense, the smallest possible stepping stone for the creation of additional tools.

Our current work reapplies this recipe of *creating the smallest possible tool* at the next higher level of abstraction, within the field of code generation. We start from the assumption that a computational task is given as a mathematical statement in index-based form, such as

$$c[i, j] = \text{sum}(k, a[i, k] * b[k, j]).$$

Further, a set of bounds on the loop variables (i , j , and k in this case) is given as an intersection of affine constraints, in the notation of the *isl* integer set library [4]:

$$[n] \rightarrow \{[i, j, k]: 0 \leq i, j, k < n\},$$

where we note that n , the matrix size, enters as a run-time-variable parameter. Starting from this mathematical statement of the desired operation (along with declarations specifying data storage formats and types), the user may then issue *transformations* that make the generated code more suitable for a certain piece of target hardware by better respecting granularities such as machine vector widths and appropriate sizing of prefetch buffers. Importantly, each

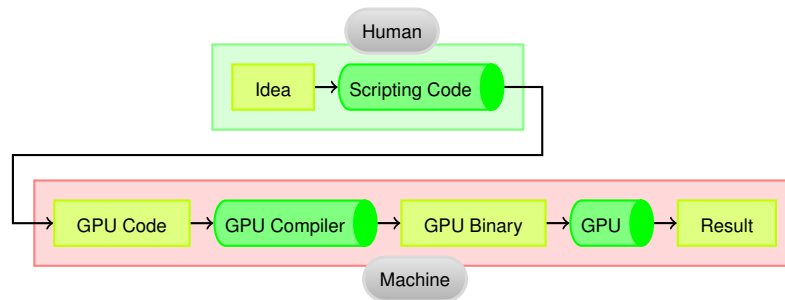


Fig. 1. Operating principle of GPU run-time code generation.

such transformation is guaranteed to preserve the operational semantics meaning of the original, untransformed kernel—but, given the right transformations, may execute far faster on a given piece of hardware. Available transformations include strip-mining, loop unrolling, parallelization, prefetching, cache management, and many more.

Like our previous tools, this code generator, called ‘*loo.py*’, cannot solve *all* problems encountered in making GPU programming accessible. Nonetheless, we claim that what it provides is useful:

- *Increase the trial rate of an expert programmer.* Manually carrying out the transformations allowed by the tool is a tedious, error-prone task. Finding and correcting these errors takes time that can be put to better use.
- *Provide a stepping stone on which more tools can be built.* Loo.py is deterministic and does not attempt to guess or be intelligent on the user’s behalf. Tools with such intelligence can be built *on top of* loo.py with relative ease.
- *Facilitate performance portability.* Since loo.py clearly distinguishes the description of the desired computation from the transformations achieving hardware specialization, this latter part may be changed or adapted to new hardware *without* having to revisit the basic computational goal.
- *Channel thought through language design.* The tool enforces a clear separation between mathematical and implementation concerns, even if both influence each other in a conceptually more abstract design space.

In proposing this tool, we have built upon experience gained from earlier work [2] on the type of transformations necessary in GPU programming. In the next section, we discuss how loo.py conceptually and factually supersedes this research.

While loo.py bears some similarity to prior efforts in transformational programming (e.g. CUDA-CHILL [3]), it is novel because, first, it is *not* a source-to-source translator, but instead views transformations as first-class objects in its language, and second, it integrates into an existing ecosystem of GPU scripting tools centered on PyOpenCL.

3 Evaluation and Conclusions

We evaluate our tool by applying it to time-domain EM simulations using discontinuous Galerkin methods as well as to singular quadrature tasks originating from electromagnetic problems in the frequency-domain, demonstrating the effectiveness of the language exposed along with its applicability to real-world tasks in electromagnetic simulation. We further show performance results supporting the notion that high-performance codes on a broad variety of hardware can be reached by the provided transformations.

In providing loo.py, we hope to build a bridge between computer science innovation in tool building, and application scientist needs. We hope that the tool may provide a basis for innovation and discussion in methods for producing both prototype- and production-grade EM solvers with the least possible effort.

Acknowledgement. The author’s research was partially funded by AFOSR under contract number FA9550-07-1-0422, through the AFOSR/NSSEFF Program Award FA9550-10-1-0180 and also under contract DEFG0288ER25053 by the Department of Energy. Loo.py is joint work with Tim Warburton. Time-domain EM is joint work with Jan Hesthaven and Tim Warburton. Frequency-domain EM is joint work with Leslie Greengard and his group.

References

1. A. Klöckner, N. Pinto, Y. Lee, B. Catanzaro, P. Ivanov, and A. Fasih. PyCUDA and PyOpenCL: A Scripting-Based Approach to GPU Run-Time Code Generation. *Parallel Computing*, 38(3):157–174, 2012.
2. A. Klöckner, T. Warburton, J. Bridge, and J.S. Hesthaven. Nodal discontinuous Galerkin methods on graphics processors. *J. Comp. Phys.*, 228:7863–7882, 2009.
3. G. Rudy, M. Khan, M. Hall, C. Chen, and J. Chame. A programming language interface to describe transformations and code generation. *Languages and Compilers for Parallel Computing*, pages 136–150, 2011.
4. S. Verdoolaege. isl: An integer set library for the polyhedral model. In Komei Fukuda, Joris Hoeven, Michael Joswig, and Nobuki Takayama, editors, *Mathematical Software – ICMS 2010*, volume 6327 of *Lecture Notes in Computer Science*, pages 299–302. Springer Berlin / Heidelberg, 2010.

Improved Electromagnetic Modelling and Simulation of Axial Flux Machines

Ossi Niemimäki and Stefan Kurz

Tampere University of Technology, Electromagnetics, P.O. Box 692, FI-33101 Tampere, Finland
 {ossi.niemimaki, stefan.kurz}@tut.fi

Summary. Axial-field permanent magnet synchronous machines can be tackled by means of the so-called quasi 3D approach, where the 3D problem is reduced to a family of decoupled 2D problems. This approach is placed in proper mathematical context and the modelling error is discussed. The resulting 2D problems are cast into standard radial flux topology.

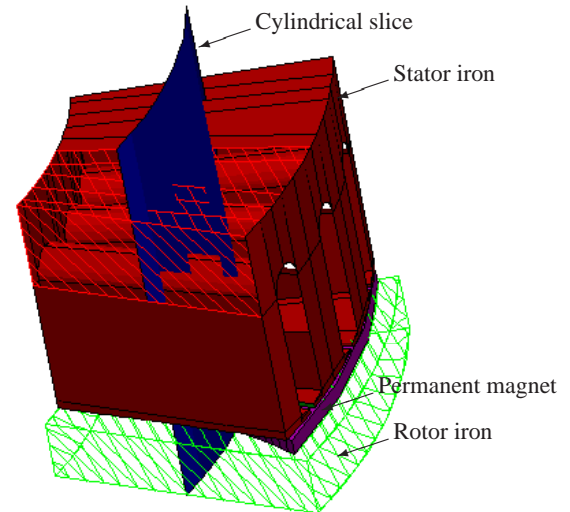
1 Introduction

Axial-field permanent magnet synchronous machines enjoy increasing importance. In particular, their flat and compact shape renders them attractive for several applications, for instance in electric vehicles, elevator drives, or wind generators. However, when it comes to electromagnetic modelling and simulation, there is much less literature and tools available compared to the standard radial flux topology. Since full transient 3D Finite Element simulations are still at the feasibility limit, the so called *quasi 3D approach* is often reported in literature, both for numerical [3] and analytical [1, 2, 4, 5] modelling.

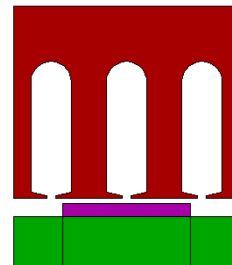
The machine geometry is represented by a number of cylindrical slices, compare Fig. 1(a). Each slice is then unrolled, which yields the flat geometry depicted in Fig. 1(b), which we will call *translational model*. Eventually, the slice might be distorted into the segment shown in Fig. 1(c), which we will call *rotational model*. The latter corresponds with the symmetry cell in the cross section of a standard radial flux permanent magnet synchronous machine, and can therefore be computed by well-established methods.

2 Mathematical Modelling

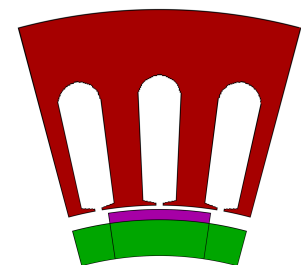
In references [1] – [5] it is usually taken for granted that the magnetic flux in the machine has no radial component. It is then claimed that each translational or rotational model can be analyzed separately, based on a single component magnetic vector potential. The torque of the machine is obtained by adding up the contributions of the individual slices. We will put this approach into proper mathematical context. For the purpose of this paper we restrict ourselves to a magnetostatic model for each time step.



(a) 3D model of a symmetry cell cut by a cylindrical slice.



(b) Unrolling the slice yields the 2D *translational model*.



(c) The 2D *rotational model* is obtained by distortion.

Fig. 1. Geometry of an axial flux machine. Stator coils are omitted. Images (a) and (b) are taken from [4, Fig. 1], reprint with kind permission.

The magnetostatic field in the 3D model is governed by $\text{curl} \mu^{-1} \text{curl} \mathbf{A} = \mathbf{J}$, where μ is the magnetic permeability, in general dependent on the field, \mathbf{A} is the magnetic vector potential, $\mathbf{B} = \text{curl} \mathbf{A}$, and \mathbf{J} is the total current density, where $\text{div} \mathbf{J} = 0$ holds. \mathbf{J} takes into account both the stator currents as well as the permanent magnets, in terms of magnetization currents. We introduce cylindrical coordinates (r, φ, z) , compare Fig. 3, left. The vector potential can be gauged such that $A_z = 0$ holds, without loss of generality. We introduce the second order differential operators

$$\begin{aligned}\Delta_{\varphi z} &= \partial_{\varphi} \mu^{-1} \frac{1}{r^2} \partial_{\varphi} + \partial_z \mu^{-1} \partial_z, \\ \Delta_{rz} &= \partial_r \mu^{-1} \frac{1}{r} \partial_r r + \partial_z \mu^{-1} \partial_z.\end{aligned}$$

In the chosen gauge, the double curl equation reads

$$\begin{bmatrix} \Delta_{\varphi z} & -\partial_{\varphi} \mu^{-1} \frac{1}{r^2} \partial_r r \\ -\partial_r \mu^{-1} \frac{1}{r} \partial_{\varphi} & \Delta_{rz} \end{bmatrix} \begin{bmatrix} A_r \\ A_{\varphi} \end{bmatrix} = - \begin{bmatrix} J_r \\ J_{\varphi} \end{bmatrix}. \quad (1)$$

This system can be interpreted as a family of problems defined on cylinders $r = \text{const.}$ in terms of a radial potential A_r , plus a family of problems defined on half-planes $\varphi = \text{const.}$ in terms of an azimuthal potential A_{φ} . Both families are coupled via off-diagonal terms. It can be shown that if and only if $B_r = 0$ holds, the field can be described in terms of A_r alone. In practice, in axial flux machines $B_r \approx 0$ holds, so the first family dominates over the second.

This motivates working with the modelling assumption $B_r = 0$, that is, $A_{\varphi} = 0$. In this case, the first equation of (1) reduces to $\Delta_{\varphi z} A_r = -J_r$, which can be solved on each cylinder $r = \text{const.}$ separately. The second equation gives rise to a residual

$$\mathcal{R} = \partial_r \mu^{-1} \frac{1}{r} \partial_{\varphi} A_r - J_{\varphi} = -\partial_r H_z - J_{\varphi},$$

where $\mathbf{H} = \mu^{-1} \mathbf{B}$ holds. The residual gives an indication for the error introduced by the modelling assumption $B_r = 0$. For an interpretation see Fig. 2.

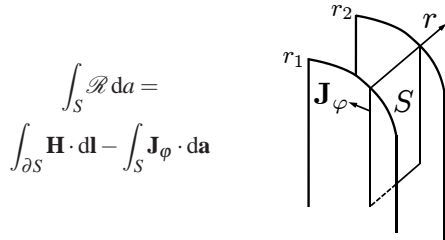


Fig. 2. The residual may be integrated over rectangle S . A non-zero residual indicates failure to fulfill Ampère's law in zr -planes.

For fixed radius r , introduce a new coordinate $\ell = r\varphi$. In coordinates (ℓ, z) the equation to be solved for A_r reads $(\partial_{\ell} \mu^{-1} \partial_{\ell} + \partial_z \mu^{-1} \partial_z) A_r = -J_r$, the governing equation for the translational model, Fig. 1(b).

From a practical point of view, existing software for the numerical analysis of standard radial flux machines should be employed. To that end, a transformation is required that maps lines $\ell = \text{const.}$ to radial half-lines, while lines $z = \text{const.}$ shall be mapped to concentric circles. We pick the conformal map $\mathcal{Z} = c \exp(\mathcal{W}/r) : \mathcal{W} = \ell + iz \mapsto \mathcal{Z} = x + iy = \rho \exp(i\varphi)$, for fixed $c, r \in \mathbb{R}$. The transformation is depicted in Fig. 3.

Let $A_z(x, y) = A_r(\ell, z)$, $J_z(x, y) = J_r(\ell, z)$, which yields $(\partial_x \mu^{-1} \partial_x + \partial_y \mu^{-1} \partial_y) A_z = -h^2 J_z$, with the con-

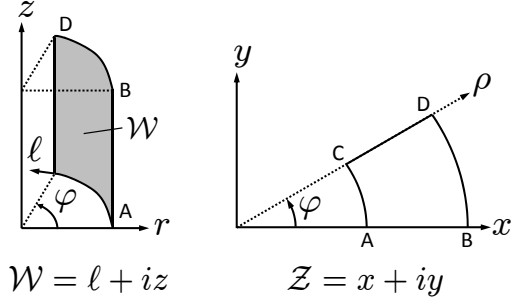


Fig. 3. The conformal map $\mathcal{Z} = c \exp(\mathcal{W}/r)$ relates the rotational to the translational model, for fixed $c, r \in \mathbb{R}$.

formal factor $h = r/\rho$. This is the usual magneto-static 2D vector potential formulation, the governing equation of the rotational model, Fig. 1(c). The Laplace operator is invariant under conformal transformation, while the current density has to be scaled by h^2 . The rotational model can therefore be solved efficiently with commercially available software, for each cylindrical slice $r = \text{const.}$ that is contained in the discretization. Relevant postprocessing quantities like the torque of the machine can be computed once the solutions for the slices are available.

An example for this approach will be given in the full paper.

Acknowledgement. Financial support by KONE is acknowledged.

References

1. Jaouad Azzouzi, Georges Barakat, and Brayima Dakyo. Quasi-3-D analytical modeling of the magnetic field of an axial flux permanent-magnet synchronous machine. *IEEE Transactions on Energy Conversion*, 20(4):746–752, December 2005.
2. Jang-Young Choi, Sung-Ho Lee, Kyoung-Jin Ko, and Seok-Myeong Jang. Improved analytical model for electromagnetic analysis of axial flux machines with double-sided permanent magnet rotor and coreless stator windings. *IEEE Transactions on Magnetics*, 47(10):2760–2763, October 2011.
3. G. Cvetkovski, L. Petkovska, and S. Gair. Torque analysis of axial field synchronous PM motor for EV. In *SPEEDAM 2006. International Symposium on Power Electronics, Electrical Drives, Automation and Motion*, pages 214–217, Taormina, May 2006.
4. Asko Parviainen, Markku Niemelä, and Juha Pyrhönen. Modeling of axial flux permanent-magnet machines. *IEEE Transactions on Industry Applications*, 40(5):1333–1340, 2004.
5. Peter Vrtič, Peter Pišek, Tine Marčič, Miralem Hadžiselimović, and Bojan Štumberger. Analytical analysis of magnetic field and back electromotive force calculation of an axial-flux permanent magnet synchronous generator with coreless stator. *IEEE Transactions on Magnetics*, 44(11):4333–4336, November 2008.

Computation of Optimal Model Parameters of an Extended Brauer Model for Ferromagnetic Material Behaviour

Timo Hülsmann¹, Andreas Bartel¹, Sebastian Schöps¹, and Herbert De Gersem²

¹ Bergische Universität Wuppertal {huelmann, bartel, schoeps}@math.uni-wuppertal.de,

² Katholieke Universiteit Leuven Herbert.DeGersem@kuleuven-kulak.be

Summary. Simulation of low-frequency magnetic fields in electric machines demands for implicit time integration. For the nonlinear reluctivity of the ferromagnetic yoke, a smooth material curve is needed to avoid convergence problems in Newton's method. In this paper the Brauer model is extended to fit the material behavior at low fields more accurately and to guarantee physically correctness for high fields. Furthermore, a procedure to obtain optimal parameters is developed and discussed using a numerical example.

1 Introduction

Typically Finite Element (FE) based simulations of eddy currents use the magnetic vector potential \mathbf{A} and the curl-curl equation

$$\sigma \frac{d\mathbf{A}}{dt} + \nabla \times (\nu \nabla \times \mathbf{A}) = \mathbf{J}_s, \quad (1)$$

with conductivity σ , reluctivity ν and source current density \mathbf{J}_s . For iron parts the material relation $\mathbf{H}(\mathbf{B}) = \nu \mathbf{B}$ becomes nonlinear, where $\mathbf{B} = \nabla \times \mathbf{A}$ is the magnetic flux density and \mathbf{H} the magnetic field strength. We neglect anisotropy and hysteresis. Hence, we can apply $H = \nu B$ in terms of $H := \|\mathbf{H}\|_2$ and $B := \|\mathbf{B}\|_2$. Typical models are spline interpolations of measurements, [3], and Brauer's model, [1]:

$$H_{br}(B) = \nu_{br}(B^2)B = (k_1 e^{k_2 B^2} + k_3)B.$$

Both allow a simple calculation of the reluctivity $\nu = \nu(B^2)$ and its derivative $\frac{d}{dB^2} \nu$, needed in the computation of material matrices occurring in the space discretization of (1), see e.g. [2]. Brauer's model is well understood, e.g., a sensitivity analysis shows that currents and fluxes through machines are most sensitive w.r.t. to perturbations in k_2 followed by k_1 and k_3 . The model is sufficiently accurate for medium fields but the behavior for low fields (Rayleigh region) and high fields (full saturation, i.e., $\frac{dH}{dB} = \nu_0$ as for vacuum) cannot be represented accurately.

2 Extended Brauer model

For high fields the material behaves like vacuum

$$H_{sat}(B) = \nu_0(B - B_s) + H_s.$$

For low fields the dependence of B on H is quadratic:

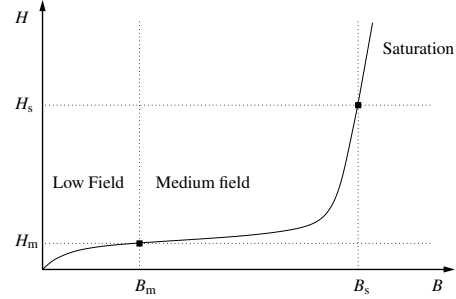


Fig. 1. Regions of the $H(B)$ -curve.

$$H_{ray}(B) = \sqrt{\frac{1}{4\alpha^2 \nu_{init}^2} + \frac{B}{\alpha}} - \frac{1}{2\alpha \nu_{init}}$$

with initial reluctivity ν_{init} and Rayleigh constant α . In combination we obtain a $H(B)$ -curve as shown in Fig. 1, with interface points (B_m, H_m) and (B_s, H_s) .

Let us determine the coefficients of an extended Brauer model s.t. the global model is continuous differentiable. The classical model does not simply allow to replace low field and high field parts. A shift of the Brauer model enables to fulfill the continuity and differentiability conditions at B_m :

$$H_{ebr}(B) = (k_1(e^{k_2(B-B_m)^2} - 1) + \nu_{d,m})(B - B_m) + H_m$$

with $\nu_{d,m} := \frac{dH}{dB} H_{ray}(B_m)$ the differential reluctivity at the end of the Rayleigh region. We define the function

$$H(B) := \begin{cases} H_{ray}(B) & \text{if } 0 \leq B < B_m, \\ H_{ebr}(B) & \text{if } B_m \leq B < B_s, \\ H_{sat}(B) & \text{if } B_s \leq B. \end{cases} \quad (2)$$

To fix the model parameters k_1 and k_2 , we use the continuity conditions $H_{ebr}(B_s) = H_s$ and $\frac{dH}{dB} H_{ebr}(B_s) = \nu_0$, and solve each equation for k_1 :

$$k_1 = \frac{\frac{H_s - H_m}{B_s - B_m} - \nu_{d,m}}{e^{k_2(B_s - B_m)^2} - 1}, \quad (3)$$

$$k_1 = \frac{\nu_0 - \nu_{d,m}}{(2k_2(B_s - B_m)^2 + 1)e^{k_2(B_s - B_m)^2} - 1}. \quad (4)$$

From (3) and (4) we find a nonlinear equation for $k_2 > 0$, which is solvable under the conditions $\nu_0 > \nu_{d,m}$

$$0 < \frac{\frac{H_s - H_m}{B_s - B_m} - \nu_{d,m}}{\nu_0 - \nu_{d,m}} < \frac{1}{3}$$

and $B_s > B_m > 0$, $H_s > H_m > 0$, $\nu_0 > \nu_{d,m}$.

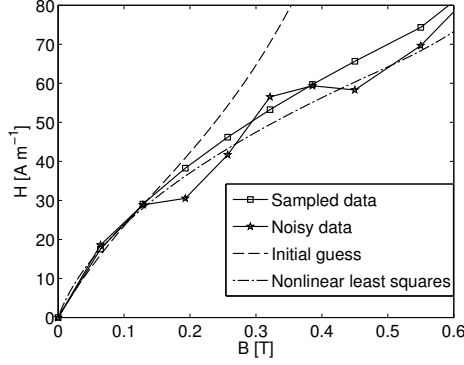


Fig. 2. Low field region.

The Rayleigh constant can be obtained by $\alpha := (B_m/H_m - 1/v_{\text{init}})/H_m$. Therefore the model (2) can be fixed from the data $\mathbf{p} := (v_{\text{init}}, B_m, H_m, B_s, H_s)$.

3 Optimal Model Parameters

Let us consider measurement points (B_j, H_j) , $j = 1, \dots, N$, of a ferromagnetic material. We assume monotonicity of the data and a distinctive Rayleigh region.

To find optimal model parameters we solve a nonlinear least squares (NLS) problem, i.e.,

$$\min_{\mathbf{p}} \sum_{j=1}^N \frac{(H(B_j; \mathbf{p}) - H_j)^2}{H_j^2}. \quad (5)$$

Proper initial guesses are important because of the nonliterary. A procedure for this purpose is given by:

- The fraction of first non-zero measurement points approximates v_{init} . Then find index r that minimizes $(H_{r+1} - H_r)/(B_{r+1} - B_r)$. (B_r, H_r) . It is an approximation to (B_m, H_m) . Compute α and $v_{d,m}$.
- Approximate the beginning of the saturation region with the last measurement points. Solve (3) and (4) for k_1 and k_2 by replacing v_0 with the secant slope v_N of the last two measurement points.
- If $v_N \approx v_0$, use the last point as approximation of (B_s, H_s) . Otherwise solve $\frac{dH}{dB} H_{\text{ebr}}(B_s) = v_0$ for B_s and compute $H_s = H_{\text{ebr}}(B_s)$.
- Solve the NLS problem (5).

4 Example

For validation we created test data from (2) using $v_{\text{init}} = 400 \text{ mH}^{-1}$, $(B_m, H_m) = (0.5 \text{ T}, 70 \text{ A m}^{-1})$ and $(B_s, H_s) = (2 \text{ T}, 100 \text{ kA m}^{-1})$. We sample the first two regions with 8 equidistant points. We incorporate Gaussian measurement noise by $\tilde{H}_i = \max(0, H_i \cdot (1 + \sigma X_i))$, where $X_i \sim \mathcal{N}(0, 1)$ and $\sigma = 0.1$. Fig. 2 and 3 show the fitted results. The proposed initial guess is sufficient to achieve convergence of the NLS problem. We obtain a curve close to the original curve.

The extended Brauer model is tested in a 2-D FE simulation of a transformer at no-load. Simulation results with the extended Brauer model with parameters

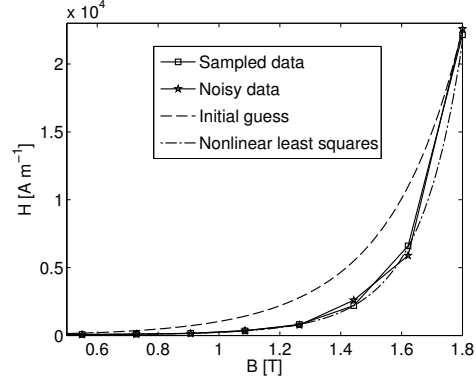


Fig. 3. Medium field region.

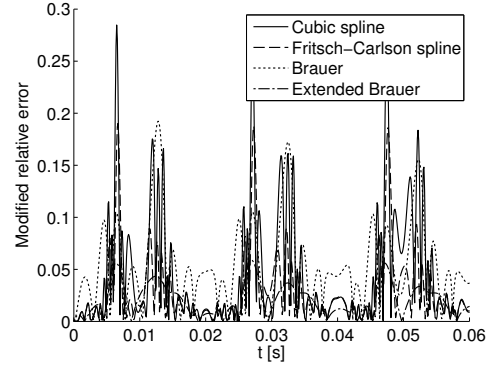


Fig. 4. Errors $|i - \hat{i}|/(|i| + 0.1)$ of no-load current. The current peaks are at 0.01, 0.03 and 0.05.

from above are used as a reference. For the spline interpolation (cubic and Fritsch-Carlson spline) we smoothened the noisy samples in the Rayleigh region with a moving average filter. Errors of the no-load current i through the device are depicted in Fig. 4.

The original Brauer model is the computationally least expensive but yields large errors in comparison to the reference solution. It cannot match the shape of the material curve for low and high fields. Spline interpolated measurements yield medium errors but need a high number of Newton steps to converge, cf. [4]. The extended Brauer model is only slightly more expensive than the original Brauer model but is the most accurate also in Fig. 4. It also recovers the reference curve.

References

- J. R. Brauer. Simple Equations for the Magnetization and Reluctivity Curves of Steel. *IEEE Trans. Magn.*, 11(1):81, 1975.
- H. De Gersem, I. Munteanu, and T. Weiland. Construction of Differential Material Matrices for the Orthogonal Finite-Integration Technique With Nonlinear Materials. *IEEE Trans. Magn.*, 44(6):710–713, 2008.
- B. Heise. Analysis of a fully discrete finite element method for a nonlinear magnetic field problem. *SIAM J. Num. Ana.*, 31(3):745–759, 1994.
- H. Vande Sande, F. Henrotte, and K. Hameyer. The Newton-Raphson method for solving non-linear and anisotropic time-harmonic problems. *COMPEL*, 23(4):950–958, 2004.

Broad Band Surface Impedance Boundary Conditions for Higher Order Time Domain Discontinuous Galerkin Method

Irene Hiltunen^{1,2}, Erion Gjonaj², and Thomas Weiland²

¹Graduate School of Computational Engineering, Technische Universität Darmstadt, Dolivostr. 8, D-64293 Darmstadt

²Institut für Theorie Elektromagnetische Felder, Technische Universität Darmstadt, Schloßgartenstr. 8, D-64289 Darmstadt
hiltunen@temf.tu-darmstadt.de, gjonaj@temf.tu-darmstadt.de,
weiland@temf.tu-darmstadt.de

Summary. An implementation of the broad band Surface Impedance Boundary Condition (SIBC) for the high order Discontinuous Galerkin (DG) method in the time domain is presented. In order to treat the frequency dependent impedance function a set of auxiliary differential equations is introduced. The effect of the DG approximation order on the accuracy will be studied, and the results will be compared with the conventional time domain Finite Element Method.

1 Introduction

Time domain modeling is very attractive for wide band electromagnetic problems, since it allows to compute for a large range of frequencies in a single simulation. However, when the frequency band of interest is wide, the dispersive nature of material parameters, i.e. their variation with respect to frequency, needs to be considered. In order to model dispersive electromagnetic materials in time domain simulations, one generally needs to evaluate one or more convolution integrals. Clearly a direct computation of convolution terms is too expensive for every practical computation. For this purpose, several numerically efficient approaches have been proposed. One approach is a recursive convolution [7]. Another technique which is particularly suited for explicit time domain simulations is the Auxiliary Differential Equation (ADE) method. In the following, ADE is applied in the context of SIBC for arbitrary frequency dependent electric conductivities. Finite Difference Time Domain method (FDTD) [11] is widely used for time domain simulations. It leads to explicit time stepping and it is straightforward to implement. However, FDTD has a two important disadvantages: First, the method loses substantial accuracy at curved geometrical boundaries. Second, FDTD is at most 2nd order accurate, thus, it suffers under large numerical dispersion errors at high frequencies. Finite Element Method (FEM) [12] is very accurate as far as the modeling of arbitrary geometries is concerned. However, the time domain FEM leads to implicit time stepping [5], and is therefore numerically extremely expensive. The Time Domain Discontinuous Galerkin Method (DG) [3] combines the advantages of the

mentioned methods: it is free of numerical dispersion, modeling of arbitrary geometries is straightforward, and due to the global discontinuity of the basis functions, the resulting time stepping scheme is explicit. However, due to the discontinuity of basis functions at cell interfaces, unphysical spurious modes will occur. A possible cure to the problem of spurious modes is the application of various penalization methods as proposed, e.g., in [3], [1].

In this study, we will describe the implementation of a wide band SIBC for higher order DG by means of the ADE method. Furthermore, the effect of discretization order, rational approximation order for the impedance function as well as the impact of penalization on the accuracy of DG simulations with SIBC will be investigated.

2 DG Method

In this study, we will consider the Maxwellian initial value problem. The three-dimensional computational domain Ω is discretized into N non-overlapping elements, and on the boundary $\partial\Omega$, the SIBC is applied. Within an element, the electric field \mathbf{E} and the magnetic flux density \mathbf{B} are approximated by a linear combination of vectorial basis functions ϕ_E and ϕ_B , respectively. As both of the basis functions, ϕ_E and ϕ_B , are defined cell-wise without global continuity, in the DG method, a numerical flux approach is applied in order to impose the necessary continuity at the interfaces between mesh cells in the weak sense. A detailed description of the method as well as of the approximation functions, ϕ_E and ϕ_B , used in the present implementation is given in [1].

3 The SIBC Approach

Modeling of media with large but finite electrical conductivities typically leads to very dense meshes and thus to small time steps as required for stability in explicit time domain simulations. Therefore, it is desirable to exclude the lossy media from the computational domain. This can be done by introducing at the boundary surface of the conductive do-

main impedance-like conditions, which provide a relationship between the tangential electric field to the tangential magnetic field components. The classical SIBC was introduced by Leontovich (cf. [10]). It assumes the lossy surface to be planar and ignores the tangential variation of the field quantities. The error of the Leontovich SIBC is order of $O(\delta^2)$, where δ is skin depth, which makes it especially suitable for high frequencies. [4]. The second order SIBC [6] takes into account also the curvature of the surface. It is, furthermore, possible to construct higher order, thus, more accurate SIBC by taking into account, in addition, the tangential variation of the field components along the lossy surface [8]. When the thickness of the conductive medium is of the order of skin depth, the electromagnetic fields on the different sides of lossy medium interact with each other. Also this type of problems can be modeled by means of SIBC, using e.g. Sarto's [9] approach.

4 Approximation of Impedance Function

In order to transform the dispersive impedance function into the time domain, it is first approximated in the frequency domain as a series of rational functions [2]. The rational approximation for the tangential magnetic field can be written as:

$$Y(\omega)\mathbf{E}_t \approx Y_0\mathbf{E}_t + \sum_{i=1}^P \frac{Y_i\mathbf{E}_t}{j\omega - \omega_i}, \quad (1)$$

where \mathbf{E}_t is tangential electric field on the surface, P is the order of the rational approximation, Y_0 free space admittance, Y_i and ω_i are approximation parameters. Let us rewrite the rational approximation given in (1) as $Y(\omega)\mathbf{E}_t \approx \mathbf{Y}_0 + \sum_{i=1}^P \mathbf{Y}_i$. The the SIBC condition transforms in the time domain to

$$\mathbf{Y}_0 = Y_0\mathbf{E}_t \quad \text{and} \quad \frac{d}{dt}\mathbf{Y}_i - \omega_i\mathbf{Y}_i = Y_i\mathbf{E}_t. \quad (2)$$

Equation (2) represent the auxiliary differential equations of the ADE method which need to be solved for in the time domain together with the full set of Maxwell's equations.

5 System of Equations

The system of discrete equations to be solved in the time domain can be written as:

$$\begin{cases} \mathbf{C}_E\mathbf{e} + \frac{d}{dt}\mathbf{M}_\mu\mathbf{h} = 0 \\ \mathbf{C}_H\mathbf{h} - \frac{d}{dt}\mathbf{M}_\epsilon\mathbf{e} = \mathbf{C}_Y\sum_{i=0}^P \mathbf{Y}_i \\ \mathbf{Y}_0 = Y_0\mathbf{e}_t \\ \frac{d}{dt}\mathbf{Y}_i - \omega_i\mathbf{Y}_i = Y_i\mathbf{e} \quad \text{for } i = 1 \dots P, \end{cases} \quad (3)$$

where \mathbf{C}_E and \mathbf{C}_B are curl-matrices obtained by high order DG discretization, \mathbf{C}_Y is so called "admittance flux" matrix, and \mathbf{M}_μ and \mathbf{M}_ϵ are block-diagonal

mass matrices. In the full paper, the numerical accuracy and efficiency of this approach with respect to discretization order for different rational function approximations (1) will be discussed.

6 Summary

Dispersive SIBC will be implemented for time domain DG method in order to model a wide frequency band at a single simulation. The frequency dependent conductivity of lossy surfaces is considered in time domain by auxiliary differential equations. We will study the accuracy of the solution for different DG discretization orders and impedance function approximations, and compare our results with the standard SIBC-FDTD method.

Acknowledgement. This work is supported by the Graduate School of Computational Engineering at Technische Universität Darmstadt.

References

1. E. Gjonaj and T. Weiland. A projection penalization approach for the high-order dg-fem in the time domain. *Radio Science*, 46(10), 2011.
2. B. Gustavsen and A. Semlyen. Rational approximation of frequency domain responses by vector fitting. *Power Delivery, IEEE Transactions on*, 14(3):1052–1061, jul 1999.
3. J.S. Hesthaven and T. Warburton. *Nodal Discontinuous Galerkin Methods: Algorithms, Analysis, and Applications*. Springer Verlag, New York., 2008.
4. N. Ida, Lemenach Y., and Henneron T. High order surface impedance boundary conditions with the a- ϕ formulation. *Facta Univ. Ser.: Elec. Energ.*, 24(2):147–155, Aug. 2011.
5. J.M. Jin. *The Finite Element Method in Electromagnetics*. New York: John Wiley & Sons, 1993.
6. K.M. Mitzner. An integral equation approach to scattering from a body of finite conductivity. *Radio Science*, 2(12):1459–1470, 1967.
7. K.S. Oh and J.E. Schutt-Aine. An efficient implementation of surface impedance boundary conditions for the finite-difference time-domain method. *Antennas and Propagation, IEEE Transactions on*, 43(7):660–666, jul 1995.
8. S.M. Rytov. Calcul du skin-effet par la methode des perturbations. *Journal of Physics*, II(3), 1940.
9. M.S. Sarto. A new model for the fdtd analysis of the shielding performances of thin composite structures. *Electromagnetic Compatibility, IEEE Transactions on*, 41(4):298–306, nov 1999.
10. T. Senior. Impedance boundary conditions for imperfectly conducting surfaces. *Applied Scientific Research, Section B*, 8:418–436, 1960. 10.1007/BF02920074.
11. K. Yee. Numerical solution of initial boundary value problems involving maxwell's equations in isotropic media. *Antennas and Propagation, IEEE Transactions on*, 14(3):302–307, 1966.
12. O.C. Zienkiewicz. *The Finite Element Method*. London; New York : McGraw-Hill, 1977.

Bulk and Interface Balance Equations for Organic Solar Cell Simulation

Matteo Porro^{1,2}, Carlo de Falco^{1,3}, Riccardo Sacco¹, and Maurizio Verri¹

¹ Dipartimento di Matematica “F. Brioschi”, Politecnico di Milano, Piazza L. da Vinci 32, 20133 Milano, Italy

² Center for Nano Science and Technology @PoliMi, Istituto Italiano di Tecnologia, via Pascoli 70/3, 20133 Milano, Italy

³ MOX Modeling and Scientific Computing

matteo.porro@mail.polimi.it, carlo.defalco@polimi.it, riccardo.sacco@polimi.it, maurizio.verri@polimi.it

Summary. In this communication, we present a computational model for heterojunction Organic Solar Cells (OSCs) consisting of a system of semilinear PDEs and ODEs. The mathematical model is discussed, focusing on the transmission conditions at material interfaces, together with the numerical method used for its solution. Steady-state and transient simulations are performed on realistic devices with various interface morphologies.

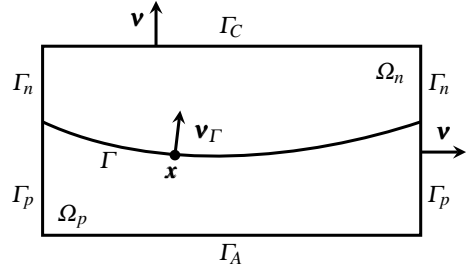


Fig. 1. OSC cell geometry.

1 Introduction and Motivation

In the design of efficient OSCs the impact of material interface morphology on performance is currently considered to be of paramount importance. For this reason, material scientists are putting much of their research effort into techniques for controlling interfaces down to the nanoscale, for example by studying materials that have the ability to self-assemble into ordered nanostructures during the deposition process. For the same reason, computational models that allow to estimate device performance carefully accounting for the material interface geometry and the phenomena occurring on it are in high demand. Previous approaches in this direction can be found in [1] (for biplanar devices) and [7]. In this communication we present our work aimed at extending the model of [1] to treat arbitrary multidimensional morphologies.

2 Mathematical Model

Let Ω be an open subset of \mathbb{R}^d , $d = 1, 2, 3$, representing the geometrical model of an OSC and \mathbf{v} be the unit outward normal vector over the boundary $\partial\Omega$. The device structure is divided into two open disjoint subregions, Ω_n (acceptor) and Ω_p (donor), separated by a regular surface Γ on which \mathbf{v}_Γ is the unit normal vector oriented from Ω_p into Ω_n . The cell electrodes, cathode and anode, are denoted as Γ_C and Γ_A , respectively (see Fig. 1 for the 2D case). Let e, n and p denote the volumetric densities of excitons, electrons and holes in the cell, respectively, P be the areal density of polaron pairs and ϕ be the electric potential. For any function $f : \Omega \rightarrow \mathbb{R}$, let $\llbracket f \rrbracket := f_n - f_p$, f_n and f_p being the traces of f on Γ from Ω_n and Ω_p ,

respectively. Excitation phenomena occurring in the bulk are described by the parabolic problem:

$$\begin{cases} \frac{\partial e}{\partial t} - \nabla \cdot (D_e \nabla e) = Q - \frac{e}{\tau_e} & \text{in } \Omega \setminus \Gamma, \\ \llbracket e \rrbracket = 0, & \text{on } \Gamma, \\ \llbracket -\mathbf{v}_\Gamma \cdot D_e \nabla e \rrbracket = \eta k_{\text{rec}} P - \frac{2H}{\tau_{\text{diss}}} e & \text{on } \Gamma, \\ e = 0 & \text{on } \Gamma_C \cup \Gamma_A, \\ e(\mathbf{x}, 0) = 0, & \forall \mathbf{x} \in \Omega. \end{cases} \quad (1a)$$

Dissociation/recombination of excitons, electrons and holes into polaron pairs at the material interface is described by the ODE:

$$\begin{cases} \frac{\partial P}{\partial t} = \frac{2H}{\tau_{\text{diss}}} e + 2H\gamma n p - (k_{\text{diss}} + k_{\text{rec}}) P & \text{on } \Gamma, \\ P(\mathbf{x}, 0) = 0, & \forall \mathbf{x} \in \Gamma. \end{cases} \quad (1b)$$

Transport of photogenerated electrons in the acceptor domain Ω_n is described by the parabolic problem:

$$\begin{cases} \frac{\partial n}{\partial t} + \nabla \cdot \mathbf{J}_n = 0 & \text{in } \Omega_n, \\ \mathbf{J}_n = -D_n \nabla n + \mu_n n \nabla \phi & \text{in } \Omega_n, \\ -\mathbf{v}_\Gamma \cdot \mathbf{J}_n = -k_{\text{diss}} P + 2H\gamma n p & \text{on } \Gamma, \\ -\kappa_n \mathbf{v} \cdot \mathbf{J}_n + \alpha_n n = \beta_n & \text{on } \Gamma_C, \\ n(\mathbf{x}, 0) = 0, & \forall \mathbf{x} \in \Omega. \end{cases} \quad (1c)$$

A parabolic problem completely similar to (1c) describes hole transport in the donor domain Ω_p . The dependence of the electric potential and field on the space charge density in the cell is described by the Poisson equation:

$$\begin{cases} \nabla \cdot (-\epsilon \nabla \phi) = -qn & \text{in } \Omega_n, \\ \nabla \cdot (-\epsilon \nabla \phi) = +qp & \text{in } \Omega_p, \\ \llbracket \phi \rrbracket = \llbracket -\mathbf{v}_\Gamma \cdot \epsilon \nabla \phi \rrbracket = 0 & \text{on } \Gamma, \\ \phi = 0 & \text{on } \Gamma_C, \\ \phi = V_{\text{appl}} + V_{\text{bi}} & \text{on } \Gamma_A. \end{cases} \quad (1d)$$

A list of the model parameters with their corresponding physical meaning is reported in Table 1. The PDE/ODE model (1) has been introduced in [2] and represents a multi-dimensional generalization of the 1D formulation proposed in [1]. System (1) is completed by periodic boundary conditions on $\Gamma_n \cup \Gamma_p$. We notice that the dissociation and recombination processes occurring at the donor-acceptor interface Γ are dealt with by the nonlinear transmission conditions (1a)₃ and (1c)₂, whose dependence on the local electric field magnitude and orientation is contained in the polaron dissociation rate constant k_{diss} [2].

Table 1. Model parameters.

Symbol	Parameter
μ_i, D_i	Mobility and diffusivity of species i , $i = e, n, p$
Q	Exciton generation rate
$\tau_e, \tau_{\text{diss}}$	Exciton decay and dissociation times
$k_{\text{rec}}, k_{\text{diss}}$	Polaron recombination and dissociation rates
γ	Electron-hole recombination rate constant
η	Singlet exciton fraction
H	Active layer thickness

3 Algorithms and Simulation Results

System linearization (by a quasi-Newton method) and approximation are carried out by adapting the approach used in [3]. Time advancing is treated using Rothe's method and adaptive BDF formulas, while the exponentially fitted Galerkin finite element method studied in [5] is used for spatial discretization. The interface conditions at the donor-acceptor interface are taken care of by means of the substructuring techniques described in [6].

Model (1) is here validated in both stationary and transient regimes. In a first set of simulations, we study the finger-shaped heterostructure considered in [7]. Fig. 2 shows the output current-voltage characteristics predicted by our model, which is in excellent agreement with that computed in [7]. In a second set

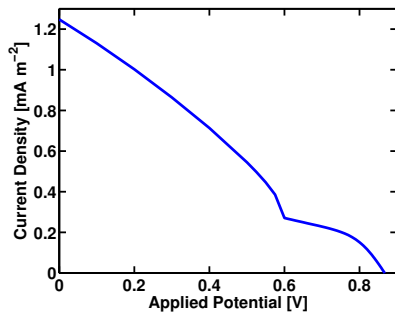


Fig. 2. Current-voltage characteristics for the finger-shaped heterostructure investigated in [7].

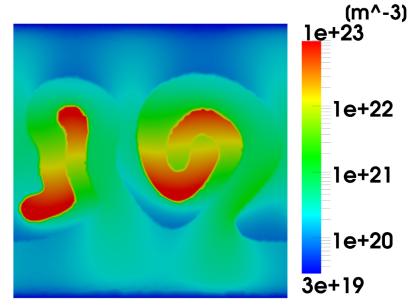


Fig. 3. Free carrier densities for a device with complex morphology

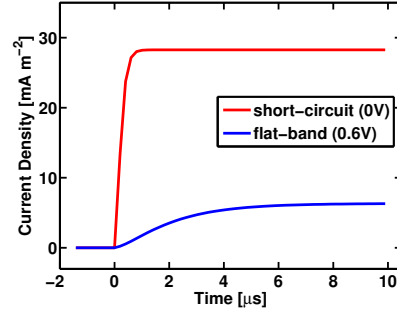


Fig. 4. Contact current density transient at two different voltage regimes.

of simulations, we test the ability of the model to describe the behaviour of a cell characterized by a complex interface morphology. Fig. 3 shows the free carrier densities computed for a “curly-shaped” geometry at short circuit working conditions. In a third set of simulations, we test the model in the time-dependent case. Fig. 4 shows the cell current response under two different biasing conditions for a planar device geometry similar to that studied in [1]. Ongoing activity is devoted to the investigation of the working principles of the light-harvesting device described in [4].

References

1. J.A. Barker, C.M. Ramsdale, and N.C. Greenham. Modeling the current-voltage characteristics of bilayer polymer photovoltaic devices. *Phys. Rev. B*, 67:075205, 2003.
2. C. de Falco, M. Porro, R. Sacco, and M. Verri. Multiscale modeling and simulation of organic solar cells. Under review, 2012.
3. C. de Falco, R. Sacco, and M. Verri. Analytical and numerical study of photocurrent transients in organic polymer solar cells. *Comput. Meth. Appl. Mech. Engrg.*, 199(25-28):1722 – 1732, 2010.
4. M. Garbugli, M. Porro, V. Roiati, A. Rizzo, G. Gigli, A. Petrozza, and G. Lanzani. Light energy harvesting with nano-dipoles. *Nanoscale*, 4:1728–1733, 2012.
5. E. Gatti, S. Micheletti, and R. Sacco. A new Galerkin framework for the drift-diffusion equation in semiconductors. *East-West J. Numer. Math.*, 6:101–136, 1998.
6. T.J.R. Hughes, G. Engel, L. Mazzei, and M.G. Larson. The continuous Galerkin method is locally conservative. *J. Comp. Phys.*, 163:467–488, 2000.
7. J. Williams and A.B. Walker. Two-dimensional simulations of bulk heterojunction solar cell characteristics. *Nanotechnology*, 19:424011, 2008.

Electromagnetic Eigenmode Characterization by Sensitivity Analysis

Bastian Bandlow and Rolf Schuhmann

FG Theoretische Elektrotechnik, EN 2, Technische Universität Berlin, Einsteinufer 17, D-10587 Berlin, Germany
bandlow@tet.tu-berlin.de, schuhmann@tet.tu-berlin.de

Summary. Computational models of resonant electromagnetic structures which are bounded by perfectly matched layers have an eigenvalue spectrum which is spoiled by eigenmodes which reside within these layers. In the context of the finite integration technique we apply a computational inexpensive sensitivity analysis in order to identify those undesired eigenmodes.

1 Motivation

The computation of electrodynamic eigenmodes of radiating structures is a challenging task, since the transition to free-space at the boundaries has to be modeled. An established technique to model that transition is the use of a *perfectly matched layer* (PML) [5]. The PML causes the eigenvalue problem of Maxwell's equations to become complex for structures of any material. Moreover, the PML consists of artificial materials whose parameters can be large in magnitude, which causes some eigenmodes to be *trapped* within the PML. In this contribution we show an computationally efficient analysis which is based on the eigenvalues' sensitivity that is able to decide whether a specific eigenmode is bound to the PML or the structure. The approach follows an adjoint technique which is known since quite some time [2, 3]. Recent advances considering the sensitivity analysis of waveguide models has been shown in [1].

2 Computational Approach

The discrete Maxwell's eigenvalue problem is set up in the framework of the finite integration technique (FIT) [4]. The Maxwell grid equations can be written down in frequency domain, neglecting currents and charges, for dispersive materials as

$$\mathbf{C}\hat{\mathbf{e}} = -s\mathbf{M}_\mu(s)\hat{\mathbf{h}}, \quad \mathbf{C}^T\hat{\mathbf{h}} = s\mathbf{M}_\epsilon(s)\hat{\mathbf{e}}, \quad (1)$$

where $\mathbf{C} \in \mathbb{R}^{N \times N}$ is the topological curl-operator consisting of entries with $\{-1; 0; 1\}$ and $s = i\omega = 2\pi if$ is the frequency. The constitutive relations read

$$\hat{\mathbf{d}} = \mathbf{M}_\epsilon(s)\hat{\mathbf{e}} \quad \text{and} \quad \hat{\mathbf{b}} = \mathbf{M}_\mu(s)\hat{\mathbf{h}}. \quad (2)$$

An absorbing boundary condition based on complex metric stretching perfectly matched layer (PML) [5]

can be introduced in FIT in a straight-forward manner. Since the PML is only in the continuous case *perfectly matched* a remaining reflection error is introduced that can be controlled by the number and the step width of the absorbing layers. The introduction of dielectric and magnetic losses in the PML cause the diagonal material matrices \mathbf{M}_μ and \mathbf{M}_ϵ to become complex. The actual frequency dependency of the components of the material matrices on the PML parameters reads exemplarily for the permeability

$$\mu^{-1}(s) = \frac{1 + \frac{\sigma_\mu}{s}}{1 + \frac{\sigma_{\mu 1}}{s} + \frac{\sigma_{\mu 2}}{s^2}} \mu_0^{-1}. \quad (3)$$

In frequency domain we solve the curl-curl eigenmode equation for complex resonance frequencies $-s^2$ and grid-voltages $\hat{\mathbf{e}}$, which are derived from (1) as

$$\mathbf{A}(s)\hat{\mathbf{e}} = -s^2\hat{\mathbf{e}}, \quad \mathbf{A}(s) = \mathbf{M}_\epsilon^{-1}(s)\mathbf{C}^T\mathbf{M}_\mu^{-1}(s)\mathbf{C}. \quad (4)$$

At this point the eigenvalue problem (4) has a polynomial-type nonlinearity. Since the PML is designed to operate quite well over a certain frequency range, the frequency dependent material matrices are evaluated at the estimation frequency s_{est} , in order to linearize the eigenvalue problem (4). Yet, the system matrix $\mathbf{A}(s)$ remains complex with eigenvalues $-s^2$. The solution can be computationally expensive, but yields the modal field distributions as well as their resonance frequency and quality factors $Q = \Im\{s\}/2\Re\{s\}$. Moreover, the spectrum is spoiled by undesired modes, which are trapped within the PML and occur at similar frequencies like the desired modes.

3 Eigenvalue Sensitivity Analysis

We start with a complex eigenvalue problem of the type $\mathbf{A}\mathbf{x} = \lambda\mathbf{x}$ and its derivative

$$(\mathbf{A}' - \lambda'\mathbf{I})\mathbf{x} + (\mathbf{A} - \lambda\mathbf{I})\mathbf{x}' = 0. \quad (5)$$

The primed quantities denote derivations with respect to the design parameter p e.g. $\mathbf{A}' := \partial\mathbf{A}/\partial p$. Following the standard perturbation theory [2] the multiplication from the left with the corresponding left eigenvector \mathbf{y}^H and substitution of $\mathbf{y}^H\mathbf{A} = \lambda\mathbf{y}^H$ (the definition of the left eigenvalue problem) finally yields the derivative of the eigenvalue

$$\lambda' = \frac{\mathbf{y}^H \mathbf{A}' \mathbf{x}}{\mathbf{y}^H \mathbf{x}}, \quad (6)$$

which could be further simplified, if the left and right eigenvectors were orthonormalized. The left eigenvectors \mathbf{y}^H of a matrix eigenvalue problem $\mathbf{y}^H \mathbf{A} = \lambda \mathbf{y}^H$ can be computed as the right eigenvectors of the matrix' adjoint $\mathbf{A}^H \mathbf{y} = \lambda^* \mathbf{y}$, where $*$ denotes the complex conjugate.

4 Application to an Example in the FIT

The FIT system matrix \mathbf{A} from (4) can be made complex-symmetric by a similarity transform with $\mathbf{M}_{\varepsilon^{-1/2}}$. The adjoint of the complex-symmetrized matrix satisfies

$$\mathbf{A}_{sym}^H = \mathbf{A}_{sym}^*, \quad (7)$$

which is simply the complex-conjugate matrix. Eigenvectors of \mathbf{A}^H are identified as the dielectric grid fluxes $\hat{\mathbf{d}}^*$. However, instead of solving the eigenvalue problem itself we can get the dielectric grid fluxes simply from the matrix-vector multiplication given in the material relation (2).

Figure 1a shows the structure for our numerical tests, which consists of a small dielectric slab having $\varepsilon_r = 5$ in a parallel-plate waveguide. An undesired as well as an desired eigenmode are included in Fig. 1b and 1c respectively. The lateral boundaries are modeled by a PML.

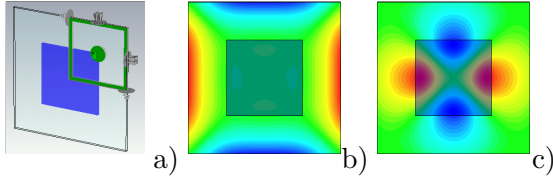


Fig. 1. a) Model of dielectric square having $\varepsilon_r = 5$. b) Undesired eigenmode at 13.76 GHz. c) Structure eigenmode at 12.82 GHz.

In Fig. 2 the loci of eigenvalues are plotted for different values of the linearization parameter s_{est} . It turns out that eigenvalues which are weakly dependent on s_{est} are those of structure eigenmodes (\circ). For sensitivity analysis the frequency dependent system matrix is derived by s_{est} .

Figure 3 shows the magnitude $|\lambda'|$ obtained by (6). Again small values belong to eigenmodes whose field distribution (cf. Fig. 1c) is primarily concentrated within the structure (\circ). Eigenmodes whose field distribution is contained within the PML show a magnitude of $|\lambda'|$ which is larger than zero. The absolute limits for decisions on $|\lambda'|$ are the topic for further investigations.

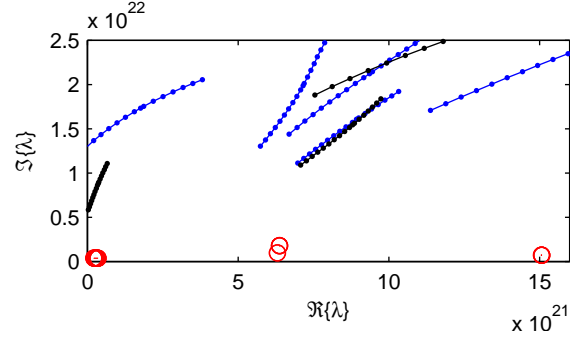


Fig. 2. Loci of eigenvalues λ for linearization parameters $s_{est} \in [2\pi i \cdot 8 \text{ GHz}, 2\pi i \cdot 16 \text{ GHz}]$. Neglectable deviations of the data sets indicate eigenfrequencies with a field distribution within structure and low PML dependency (\circ).

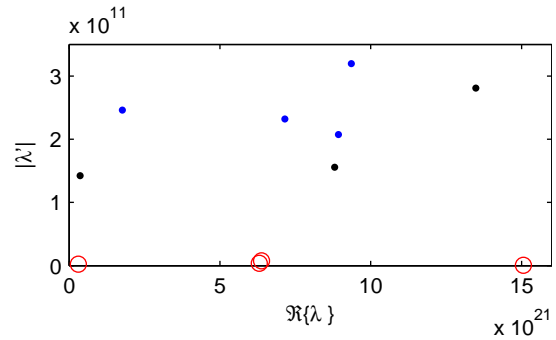


Fig. 3. Magnitude of the derivative $|\lambda'|$ over $\Re\{\lambda\}$, linearized at $s_{est} = 2\pi i \cdot 12.83 \text{ GHz}$. Small values indicate eigenmodes that are bound to the dielectric substructure (\circ).

5 Conclusion

We present a methodology which is able to decide which eigenmode belongs originally to the computational model and which is introduced by the perfectly matched layers absorbing boundary condition.

References

1. N. B. Burschäpers, S. Fiege, R. Schuhmann, and A. Walther. Sensitivity analysis of waveguide eigenvalue problems. *Advances in Radio Science*, 9:85–89, 2011.
2. R.B. Nelson. Simplified calculation of eigenvector derivatives. *AIAA Journal*, 14(9):1201–1205, 1976.
3. N.K. Nikolova, J.W. Bandler, and M.H. Bakr. Adjoint techniques for sensitivity analysis in high-frequency structure cad. *Microwave Theory and Techniques, IEEE Transactions on*, 52(1):403 – 419, jan. 2004.
4. T. Weiland. Eine Methode zur Lösung der Maxwellschen Gleichungen für sechskomponentige Felder auf diskreter Basis. *Archiv für Elektronik und Übertragungstechnik*, 31:116–120, 1977.
5. L. Zhao and A.C. Cangellaris. GT-PML: generalized theory of perfectly matched layers and its application to the reflectionless truncation of finite-difference time-domain grids. *Microwave Theory and Techniques, IEEE Transactions on*, 44(12):2555 –2563, Dec 1996.

Analysis of photonic structures in layered geometries by MMP

Aytac Alparslan¹ and Christian Hafner¹

IFH, ETH Zurich, Switzerland aytaca@ifh.ee.ethz.ch, christian.hafner@ifh.ee.ethz.ch

Summary. In this work, a numerical analysis method is introduced by combining the Multiple Multipole Program (MMP) and layered geometry Green's functions. By the method, several difficulties in the analysis of photonic structures in layered geometries are eliminated and an efficient simulation tool is obtained that can analyze both 2D and 3D geometries.

1 Introduction

The advancements in the fabrication process of photonic structures, made various nano devices quite popular, including photonic crystals, chemical and bio sensors, optical antennas and waveguides [1]. Mostly, these photonic devices are fabricated in a multilayered structure. In the numerical analysis of such structures, the layers are often ignored for the sake of simplicity of simulations, which can cause substantial inaccuracies in the results. Especially for structures that support Surface Plasmon Polariton (SPP) or guided wave modes, the errors become so high that the computations become useless. In order to understand the physical phenomena related to layered geometries and to improve the efficiency of the devices, a numerical analysis tool that takes the layered geometries into account efficiently is needed. In this paper, a candidate for such a numerical tool is introduced by combining MMP and layered media Green's functions.

2 The Method

Since the main idea of the method introduced, is to combine MMP and layered media Green's functions, both of them will be discussed briefly below.

2.1 MMP

MMP is one of the most reliable and efficient computational tools for the analysis of plasmonic structures in frequency domain [2]. It is a semi-analytical, boundary discretization method that uses various analytic solutions of the Maxwell equations or so called expansions (e.g. plane waves, cylindrical waves, spherical waves, etc.) in order to approximate the fields scattered by the objects. In the MMP analysis, the electromagnetic field in domain i (F^i) can be written as a superposition of the fields generated by the expansions as:

$$F^i = \sum_{n=1}^{N_i} A_n^i E_n^i + \text{error} \quad (1)$$

where E_n^i is the field generated by expansion n and A_n^i is the corresponding complex amplitude. The amplitudes are computed in such a way that the weighted residuals are minimized on the interfaces between different domains.

2.2 Layered media Green's functions

The Green's function describes the field generated by an infinitesimal source at a certain location. In free space, the Green's function can be represented by closed form formulations (1D (an infinitely large plane is the source): plane wave, 2D (an infinitely long line is the source): cylindrical monopole waves, 3D (a point is the source): spherical dipole waves), which makes it easy and fast to use them as expansions in methods such as MMP or Method of Moments (MoM). In the case of a layered geometry, the Green's functions can only be obtained by summing up all the plane waves that are generated at the location of the point source, for which the continuity conditions between different layers are fulfilled analytically. Since the spectrum of a point source is continuous (i.e. all the propagating and evanescent plane waves should be taken into account), the summation leads to an integral (Sommerfeld integral) with infinite bounds as follows (when the layers are stacked in y -direction and $e^{-i\omega t}$ is used):

$$G(x, y, z) = \frac{1}{2\pi} \int_{-\infty}^{\infty} \int_{-\infty}^{\infty} dk_z dk_x e^{ik_z z} e^{ik_x x} \tilde{G}(k_x, k_z) \quad (2)$$

where $G(x, y, z)$ and $\tilde{G}(k_x, k_z)$ are the spatial and spectral domain Green's functions for the given field component, respectively. In this calculation, the reflection and the transmission relations for the given plane wave is contained in the spectral domain Green's function [3]. In general, the integrands of (2) are oscillatory and slowly decaying which makes the integration numerically expensive. This burden can be handled by using series acceleration techniques. In this work, the Aitken series and weighted averages methods are used in order to decrease the time needed for the integrations [4].

Equation (2) is the most general form of the Sommerfeld integral, which provides the Green's function

in 3D. One can obtain the Green's function in 2D by (2), e.g., by taking the k_z value as a constant for a line source in z-direction. It is also possible to obtain the Green's function of a complex origin source which generates beams by changing the integration paths, so that the integrands stay stable. This kind of expansions can be used to decrease the total number of expansions, especially for long structures compared to the wavelength.

By using layered media Green's functions as an expansion set in MMP, one can decrease the complexity of the problems, since the continuity conditions on the layered geometry is fulfilled analytically [5]. In the next section, numerical examples will follow, demonstrating the efficiency of the method.

3 Numerical Examples

As the first example, a 2D triangle scatterer is placed in a four layered geometry. The result of the simulation, and the problem specifications are given in Fig. 1. For this simulation, a total of 76 expansions (38 for the field inside the scatterer (free space monopoles) and 38 for the field outside the scatterer (layered expansions)) are used, which makes the maximum relative error on the interface of the scatterer $\sim 0.1\%$. For this problem, since the incident field does not propagate in z-direction ($k_{z,inc} = 0$), the layered expansions are obtained by (2) with $k_z = 0$.

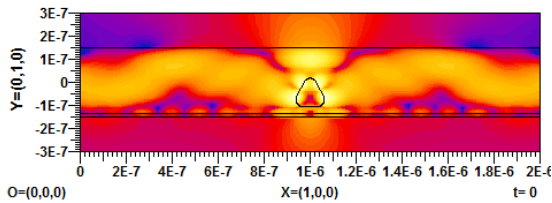


Fig. 1. Scattered field, magnitude of H_z component in logarithmic scale. Incident field: H_z polarized plane wave impinging normally on top of the structure with $\lambda_0 = 600nm$. Layer-1(lowermost layer) and Layer-4(uppermost layer) are free-space, Layer-2: Ag ($\epsilon_{r2} = -15.91 + i0.43$) $d_2 = 15nm$, Layer-3: dielectric material ($\epsilon_{r3} = 9.0$) $d_3 = 285nm$. The scatterer is Ag elevated $50nm$ from the boundary between layers 2 and 3. The side lengths of the scatterer are 160 , $160\sqrt{5}$ and $160\sqrt{5}nm$ with the rounding radius of $30nm$.

For the second example, an Ag sphere in a dielectric slab sitting above an Ag substrate is analyzed. For this simulation, 73 expansions (1 for the field inside the sphere (free-space multipole with max. order and degree of 5) and 72 for the field outside the sphere (layered expansions)) are used resulting in a maximum relative error of $\sim 0.1\%$. The result and the problem specifications are given in Fig. 2.

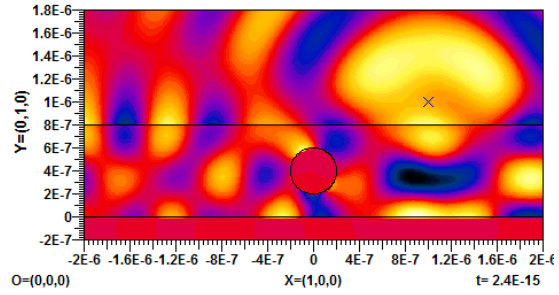


Fig. 2. Total field, E_y component at an instance of time on XY -plane ($z = 0$). Incident field: Vertical electrical dipole at $(1, 1, 1)\mu m$ $\lambda_0 = 750nm$. Layer-1(lowermost layer): Ag ($\epsilon_{Ag} = -26.73 + i0.33$), Layer-2: dielectric material ($\epsilon_{r2} = 9.0$) $d_2 = 800nm$ and Layer-3(uppermost layer) is free-space. The scatterer is an Ag sphere with $r = 200nm$ located at the center of Layer-2.

4 Conclusion

In this paper a numerical tool is introduced by combining layered media Green's functions and MMP. As a result, an efficient tool is obtained that can solve the scattering problems in 2D and 3D geometries.

Acknowledgement. This work is supported by Swiss National Science Foundation under Project 200021 – 119813/1.

References

1. P. Bharadwaj B. Deutsch and L. Novotny. Optical antennas. *Adv. Opt. Photon.*, 1(3):438–483, 2009.
2. Ch. Hafner. *Generalized multipole technique for computational electromagnetics*. Artech House Antenna library. Artech House, Boston, MA, 1990.
3. N. Kinayman and M. I. Aksun. *Modern Microwave Circuits*. Artech House, 2005.
4. K. A. Michalski. Extrapolation methods for sommerfeld integral tails. *Antennas and Propagation, IEEE Transactions on*, 46(10):1405–1418, Oct 1998.
5. A. Alparslan and Ch. Hafner. Using layered geometry green's functions in the multiple multipole program. *J. Comput. Theor. Nanosci.*, 8(8):1600–1608, Aug. 2011.

Stochastic Spectral Methods for Uncertainty Propagation in Numerical Models

Olivier P. Le Maître¹

LIMSI-CNRS, BP 133, F-91403 Orsay cedex, France olm@limsi.fr

Summary. This talk reviews the stochastic spectral methods for the propagation of parametric uncertainties in a numerical model. The alternative non-intrusive and Galerkin methods for the definition of the spectral expansion of an uncertain model output are introduced, and associated computational strategies are discussed. Examples are shown to highlight the interest of these methods and recent developments.

1 Content

The constant development of numerical methods and computational resources allow the simulation of more and more complex systems with ever increasing accuracy. As a result, numerical simulations are today widely used, in both academia and industry, to study phenomena and systems that would be hardly, or costly, investigated by means of experimental approaches. However, modeling improvements often raise the necessity to provide a more complete and accurate information regarding the input-data of the simulation (boundary and initial conditions, geometry, external forcing, material properties, model constants, ...). In many situations, the information needed is unfortunately subjected to uncertainty, either because of an inherent variability of the system studied or due to issues in identifying the values of the parameters involved in the model. Therefore, it is critical to assess the impact of such model input uncertainties on the numerical predictions.

Classically, the propagation of uncertainties in a numerical model is treated in a probabilistic framework, where the input-data are regarded as random quantities with prescribed probability law, leading to the problem of characterizing the random model output or solution. This can be achieved for instance by means of simulation approaches (*e.g.* Monte Carlo methods), where one samples the input to generate a sample set of output that serves subsequent analysis (moments estimation, reconstruction of probability density functions, sensitivity analysis, ...). Such approaches are robust and present the advantage of reusing deterministic simulation tools, but they can be computationally very expensive when the resolution of the model is costly.

In this talk, I will review stochastic spectral methods [1], where the uncertain model solution is seen

as a functional of the random input. Owing to the introduction of a suitable functional basis spanning the random input space, the objective is then to approximate the model output as convergent Fourier-like series. Compared to the simulation approaches, stochastic spectral methods aim at exploiting the (usually) smooth dependence of the model solution with respect to the input, in order to reduce the computational complexity (spectral convergence rate), while the functional representation greatly facilitates the analysis of the solution's variance to separate for instance the respective impact of different source of uncertainty. The determination of the series amounts to the computation of a set of deterministic coefficients representing the coordinates of the random solution in the stochastic basis. Two classes of methods can be used for the computation of these coefficients. Non-intrusive (NI) methods use a sample set of deterministic simulations to compute the coefficients, by solving a problem that depends on the selected definition of the sought approximation (projection, interpolation, least square residual or Bayesian inference). Alternative to the NI methods, the stochastic Galerkin methods uses the random model equations to reformulate a problem for the series coefficients of its solution, with possibly the need for a significant adaptation of the solvers.

Examples of applications will be shown, for linear and nonlinear models, highlighting recent advances in stochastic spectral methods (in particular reduced basis methods and stochastic adaptivity) which aim at improving computational efficiency.

Acknowledgement. This work is supported by the French National Research Agency (ANR), grant ANR-2010-Blan-0904.

References

1. O. Le Maître and O. Knio. *Spectral Methods for Uncertainty Quantification, with applications to computational fluid dynamics*. Springer, Scientific Computation series, New York, 2010.

Robust time-domain source stepping for DC-solution of circuit equations

E. Jan W. ter Maten^{1,2}, Theo G.J. Beelen³, Alex de Vries⁴, and Maikel van Beurden³

¹ Eindhoven University of Technology, Dept. Mathematics and Computer Science, CASA, P.O. Box 513, 5600 MB Eindhoven, the Netherlands, E.J.W.ter.Maten@tue.nl

² Chair of Applied Mathematics / Numerical Analysis, Fachbereich C, Bergische Universität Wuppertal, Gaußstraße 20, D-42119 Wuppertal, Germany, Jan.ter.Maten@math.uni-wuppertal.de

³ NXP Semiconductors, High Tech Campus 46, 5656 AE Eindhoven, the Netherlands, {Theo.G.J.Beelen, Maikel.van.Beurden}@nxp.com

⁴ NewHer Systems, Steenovenweg 5, 5708 HN Helmond, the Netherlands, AlexdeVries@gmail.com

Summary. Most analyses of circuit equations start with solving the steady-state (DC) solution. In several cases this can be very hard. We present a novel time domain source stepping procedure to obtain a DC solution of circuit equations. The source stepping procedure is automatically adaptive. Controlled sources can be elegantly dealt with. The method can easily be combined with existing pseudo-transient procedures. The method is robust and efficient.

1 Introduction

The circuit equations can be written as [5, 10]

$$\frac{d}{dt}\mathbf{q}(\mathbf{x}) + \mathbf{j}(\mathbf{x}) + \mathbf{s}(t, \mathbf{x}) = 0 \quad (1)$$

Here $\mathbf{s}(t, \mathbf{x})$ represents the specifications of the sources. The unknown $\mathbf{x} = \mathbf{x}(t)$ consists of nodal voltages and of currents through voltage defined elements. We assume that $\mathbf{q}(0) = 0$, and $\mathbf{j}(0) = 0$.

The steady state solution, which is called DC-solution (Direct Current solution), \mathbf{x}_{DC} , satisfies

$$\mathbf{j}(\mathbf{x}_{DC}) + \mathbf{s}(0, \mathbf{x}_{DC}) = 0. \quad (2)$$

Usually, and already hinted by setting $t = 0$ in (2), the DC-solution provides the initial value for the transient problem (1). In general, the problem (2) is non-linear. How to solve this problem is the subject of this note. The importance of the DC-problem lies in the fact that the DC-solution is crucial as starting solution for a number of next analyses (transient analysis, AC analysis, Harmonic Balance analysis, Periodic Steady-State analysis). In general, (1) forms a system of Differential-Algebraic Equations (DAEs). With $\mathcal{C} = \left. \frac{\partial \mathbf{q}(\mathbf{x})}{\partial \mathbf{x}} \right|_{\mathbf{x}=\mathbf{x}_{DC}}$ and $\mathcal{G} = \left. \frac{\partial \mathbf{j}(\mathbf{x})}{\partial \mathbf{x}} \right|_{\mathbf{x}=\mathbf{x}_{DC}}$. We assume that $\lambda \mathcal{C} + \mathcal{G}$ is non-singular for λ in some neighbourhood of 0 (may be excluding $\lambda = 0$). To solve the equations Newton's method, or variants, may be applied [3, 5, 8], which can be combined with g_{\min} -stepping, in which linear conductors g are placed parallel to the non-linear part inside each transistor (device). Iteratively $g \downarrow g_{\min}$, after which the Newton counter is increased.

Another approach is Pseudo-Transient [2]. In Pseudo-Transient (PT) one can use relaxed tolerances for the Newton process and for the time step control procedure. Also this can be combined with g_{\min} -stepping during each time step. In PT one has to provide a non-trivial initial solution. A new procedure is described in the next section. Other methods are: temperature stepping, source stepping (the sources are iteratively increased to their final value), homotopy methods, or optimization [1, 4, 7, 9–12].

2 Time-domain Source Stepping

Usually, in Source Stepping one introduces a parameter λ and considers the problem

$$\mathbf{j}(\mathbf{x}(\lambda)) + \lambda \mathbf{s}(0, \mathbf{x}(\lambda)) = 0. \quad (3)$$

In this case it is assumed that for $\lambda = 0$ the problem (3) is easily solved so that in the end the original problem is solved. The same parameter λ is applied to all sources s in the circuit. In general, for each value of λ a nonlinear problem has to be solved.

We introduce a time-domain variant (SSPT) that offers an automatic continuation process, based on PT and adapting the transient stepsize and the λ stepsize at the same time.

We define a time $t = T$ at which we want to have solved the original DC-problem. We also introduce a time $T_\alpha = \alpha T$ (by default $\alpha = 0.5$) at which ordinary PT will start simulation using the sources as in the original DC-problem, i.e. using $\lambda = 1$ and where PT integrates from T_α to T' , where $T' \leq T$ is the point where all transient effects have become negligible (see also Fig. 1).

On the interval $[0, T_\alpha]$, a special PT integration is performed with the function $\lambda(t) = t/T_\alpha$. Hence, at each time step, also the actual applied source values change. The interval $[0, T_\alpha]$ is the switch-on interval, the interval $[T_\alpha, T]$ is the interval to damp-out transient effects. On both intervals PT uses an automatic time step determination procedure. On the interval $[T_\alpha, T]$ an ordinary PT procedure is executed. Hence,

if, at some time point, the Newton iterative process does not converge, a re-integration will be done with a smaller stepsize. Recursion in controlled sources asks

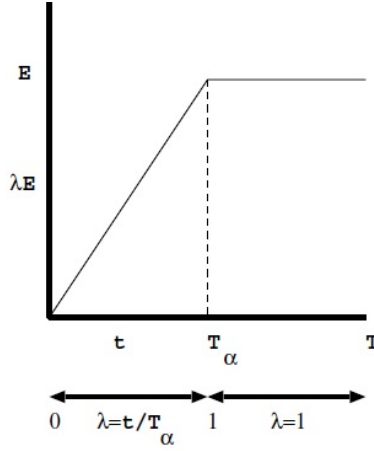


Fig. 1. On $[0, T_\alpha]$ a time-dependent voltage source $\lambda(t)E$ is used where $\lambda(t) = t/T_\alpha$. On $[T_\alpha, T]$ we have $\lambda \equiv 1$.

for a modification in (3). An expression for a controlled voltage source $E_1(0, 1)$ may look like

$$V(E_1) = 5 + 4I(E_1) + [6V(R_1) + 7I(E_2) + 12]^2 \quad (4)$$

It is controlled by the controlling "ev's" (electrical variables) $I(E_1)$, $V(R_1)$, and $I(E_2)$. We write the expression for the applied value $V(E_1)$ as

$$V(E_1) = \psi(\text{ev}_1, \text{ev}_2, \dots, \text{ev}_n) \quad (5)$$

As value during the source stepping at time t on $[0, T_\alpha]$ we propose to take

$$V(E_1) = \tilde{\psi}(\text{ev}_1, \dots, \text{ev}_n), \text{ where} \quad (6)$$

$$\tilde{\psi}(\text{ev}_1, \dots, \text{ev}_n) = \psi(\text{ev}_1, \dots, \text{ev}_n) + (\lambda(t) - 1)\psi(0, \dots, 0). \quad (7)$$

Note that in (4), $\psi(0, \dots, 0) = 149$. This value has to be calculated once. When in (4) E_2 is a controlled voltage source too, contributions to the Jacobian matrix are calculated by $\frac{\partial \tilde{\psi}}{\partial \mathbf{x}} = \frac{\partial \tilde{\psi}}{\partial \text{ev}_i} \frac{\partial \text{ev}_i}{\partial \mathbf{x}}$, which gives recursion. Note that λ does not occur in the matrix. Clearly, for $\lambda = 0$ the applied voltage is zero (assuming starting from the zero solution, which implies that all ev's are zero), which makes the zero solution the exact solution. When $\lambda = 1$ the original voltage expression is used. Since our equations (1) are DAEs we remark that for all t the generated solution is consistent for the problem at hand. Because of the switch-on and the damp-out phase the process mimics a real physical process.

3 Results

We tested the SSPT on a set of difficult problems where parameters were swept (temperature, and statis-

tics). The SSPT was always convergent (without needing g_{\min} -iteration). It was 1-13 times faster than Newton-Raphson (that sometimes needed internal g_{\min} -iteration). Normal PT was less robust than SSPT. Further improvements in the time-domain integrations, after starting with a proper \mathbf{x}_{DC} , have been tuned to fault analysis [6].

References

1. E.L. Allgower, K. Georg. Numerical path following. In: P.G. Ciarlet, J.L. Lions (Eds.), *Handbook of Numerical Analysis*, Vol. 5, Elsevier BV, North-Holland, 3-207, 1997.
2. T.S. Coffey, C.T. Kelley, D.E. Keyes. Pseudotransient continuation and differential-algebraic equations. *SIAM J. Sci. Comput.*, 25-2:553-569, 2003.
3. P. Deuffhard. *Newton methods for nonlinear problems - Affine invariance and adaptive algorithms*. Springer-Verlag, Berlin, 2004.
4. A. Dyess, E. Chan, H. Hofmann, W. Horia, L. Trajkovic. Simple implementations of homotopy algorithms for finding DC solutions of nonlinear circuits. *Proc. ISCAS 1999 Vol. VI*, 290-293, 1999.
5. M. Günther, U. Feldmann, J. ter Maten. Modelling and discretization of circuit problems. In: W.H.A. Schilders, E.J.W. ter Maten (eds.), *Handbook of Numerical Analysis, Vol. XIII, Special Volume on Numerical methods in electromagnetics*, Elsevier BV, North-Holland, 523-659, 2005.
6. H. Hashempour, J. Dohmen, B. Tasić, B. Kruseman, C. Hora, M. van Beurden, Y. Xing. Test time reduction in analogue/mixed-signal devices by defect oriented testing: An industrial example. *Proc. DATE 2010*, 371-376, 2010.
7. M. Honkala, J. Roos, V. Karanko. On nonlinear iteration methods for DC analysis of industrial circuits. In: A. Di Bucchianico, R.M.M. Mattheij, M.A. Peletier (Eds.), *Progress in industrial mathematics at ECMI 2004*, Springer-Verlag, Berlin, 144-148, 2006.
8. C.T. Kelley. *Iterative methods for linear and nonlinear equations*. SIAM - Society for Industrial and Applied Mathematics, Philadelphia, 1995.
9. W. Mathis, L. Trajkovic, M. Koch, U. Feldmann: Parameter embedding methods for finding DC operating points of transistor circuits. *Proc. NDES-1995, Dublin*, 147-150, 1995.
10. J. Ogródkzi. *Circuit simulation methods and algorithms*. CRC Press, Boca Raton, FL, USA, 1994.
11. L. Trajkovic, E. Fung, S. Sanders. HomSPICE: Simulator with homotopy algorithms for finding DC and steady-state solutions of nonlinear circuits. *Proc. ISCAS 1998 Vol. 6*, 227-231, 1998.
12. L.T. Watson, R.C. Melville, A.P. Morgan, H.F. Walker. HOMPAC90: A suite of Fortran 90 codes for globally convergent homotopy algorithms. *ACM Trans. on Math. Software*, 23-4:514-549, 1997.

High-Order Local Time-Stepping with Explicit Runge-Kutta Methods

Marcus J. Grote¹, Michaela Mehlin¹, and Teodora Mitkova²

¹ Institute of Mathematics, University of Basel, Rheinsprung 21, CH-4051 Basel marcus.grote@unibas.ch,
michaela.mehlin@unibas.ch

² Department of Mathematics, University of Fribourg, Chemin du Musée 23, CH-1700 Fribourg
teodora.mitkova@unifr.ch

Summary. We propose explicit local time-stepping (LTS) schemes of high accuracy based either on classical or low-storage Runge-Kutta schemes for time dependent Maxwell's equations. By using smaller time steps precisely where smaller elements in the mesh are located, these methods overcome the bottleneck caused by local mesh refinement in explicit time integrators.

1 FE Discretizations of Maxwell's Equations

The evolution of a time-dependent electromagnetic field $\mathbf{E}(\mathbf{x}, t)$, $\mathbf{H}(\mathbf{x}, t)$ propagating through a linear isotropic medium is governed by Maxwell's equations:

$$\varepsilon \mathbf{E}_t = \nabla \times \mathbf{H} - \sigma \mathbf{E} + \mathbf{j}, \quad (1)$$

$$\mu \mathbf{H}_t = \nabla \times \mathbf{E}. \quad (2)$$

Here the coefficients μ , ε and σ denote the relative magnetic permeability, the relative electric permittivity and the conductivity of the medium, respectively. The source term \mathbf{j} corresponds to the applied current density.

We discretize (1)-(2) in space by using standard edge finite elements (FE) with mass lumping [6] or a discontinuous Galerkin (DG) FE discretization [4, 5], while leaving time continuous. Either discretization leads to a system of ordinary differential equations with an essentially diagonal mass matrix. Thus, when combined with explicit time integration, the resulting fully discrete scheme of (1)-(2) will be truly explicit.

2 Runge-Kutta based LTS

Locally refined meshes impose severe stability constraints on explicit time-stepping methods for the numerical solution of (1)-(2). Local time-stepping methods overcome that bottleneck by using smaller time-steps precisely where the smallest elements in the mesh are located. In [1, 2], explicit second-order LTS integrators for transient wave motion were developed, which are based on the standard leap-frog scheme. In the absence of damping, i.e. $\sigma = 0$, these time-stepping schemes, when combined with the modified equation approach, yield methods of arbitrarily

high (even) order. By blending the leap-frog and the Crank-Nicolson methods, a second-order LTS scheme was also derived there for (damped) electromagnetic waves in conducting media, i.e. $\sigma > 0$, yet this approach cannot be readily extended beyond order two. To achieve arbitrarily high accuracy in the presence of damping, while remaining fully explicit, explicit LTS methods for the scalar damped wave equation based on Adams-Bashforth multi-step schemes were derived in [3].

Here we propose explicit LTS methods of high accuracy based either on explicit classical or low-storage Runge-Kutta (RK) schemes. In contrast to Adams-Bashforth methods, RK methods are one-step methods; hence, they do not require a starting procedure and easily accommodate adaptive time-step selection. Although, RK methods do require several further evaluations per time-step, that additional work is compensated by a less stringent CFL stability restriction.

Clearly, the idea of using different time-steps for different components in the context of ordinary differential equations is not new [7]. However, RK methods achieve higher accuracy not by extrapolating farther from the (known) past but instead by including further intermediate stages from the current time-step. Thus, for the numerical solution of partial differential equations, the derivation of high-order local time-stepping methods that are based on RK schemes, is generally more difficult.

3 Numerical Experiments

To illustrate the versatility of our approach, we consider the scalar damped wave equation

$$u_{tt} + \sigma u_t - \nabla \cdot (c^2 \nabla u) = f \quad \text{in } \Omega \times (0, T), \quad (3)$$

in a rectangular domain of size $[0, 2] \times [0, 1]$ with two rectangular barriers inside forming a narrow gap. Here $f(x, t)$ is a (known) source term, whereas the damping coefficient $\sigma(x) \geq 0$ and the speed of propagation $c(x) > 0$ are piecewise smooth. We use continuous P^2 elements on a triangular mesh, which is highly refined in the vicinity of the gap, as shown in Fig. 1. For the time discretization, we choose an LTS

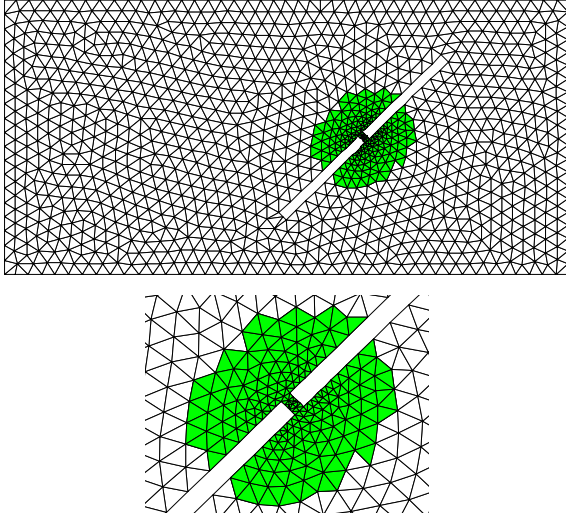


Fig. 1. The initial triangular mesh (left); zoom on the “fine” mesh indicated by the darker (green) triangles (right).

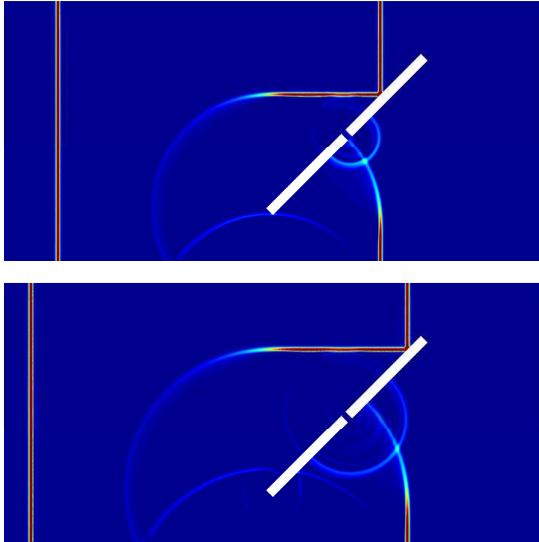


Fig. 2. The solution at times $t=0.6$ and 0.7 .

method based on an explicit third-order low-storage Runge-Kutta scheme. Since the typical mesh size inside the refined region is about $p = 7$ times smaller than that in the surrounding coarser region, we take p local time steps of size $\Delta\tau = \Delta t/p$ for every time step Δt . Thus, the numerical method is third-order accurate both in space and time with respect to the L^2 -norm. In Fig. 2, a Gaussian pulse initiates two plane waves, which propagate horizontally in opposite directions. As the right-moving wave impinges upon the obstacle, a small fraction of the wave penetrates the gap and generates multiple circular waves on both sides of the obstacle, which further interact with the wave field.

References

1. J. Diaz and M.J. Grote. Energy conserving explicit local time-stepping for second-order wave equations. *SIAM Journal on Scientific Computing*, 31 (2009), 1985-2014.
2. M.J. Grote and T. Mitkova. Explicit local time-stepping for Maxwell’s equations. *Journal of Computational and Applied Mathematics*, 234 (2010), 3283-3302.
3. M.J. Grote and T. Mitkova. High-order explicit local time-stepping methods for damped wave equations. *Preprint arXiv: 1109.4480v1*, 2011.
4. M.J. Grote, A. Schneebeli and D. Schötzau. Interior penalty discontinuous Galerkin method for Maxwell’s equations: Energy norm error estimates. *Journal of Computational and Applied Mathematics*, 204 (2007), 375-386.
5. J.S. Hesthaven and T. Warburton. *Nodal Discontinuous Galerkin Methods*. Springer, 2008.
6. P. Monk. *Finite Element Methods for Maxwell’s Equations*. OUP New York, 2003.
7. J.R. Rice. Split Runge-Kutta methods for simultaneous equations. *J. of Res. Nat. Bureau of Standards-B*, 64B (1960), 151-170.

Body-fitting meshes for the Discontinuous Galerkin Method

J. Cui¹, S. M. Schnepf¹, and T. Weiland^{1,2}

¹ Graduate School of Computational Engineering, Technische Universitaet Darmstadt, Dolivostrasse 15, 64293 Darmstadt, Germany, cui@gsc.tu-darmstadt.de, schnepf@gsc.tu-darmstadt.de

² Institut fuer Theorie Elektromagnetischer Felder, Technische Universitaet Darmstadt, Schlossgartenstrasse 8, 64289 Darmstadt, Germany, thomas.weiland@temf.tu-darmstadt.de

Summary. A mesh scheme is developed to deal with curved boundaries of the geometry using quadrilateral elements for the Discontinuous Galerkin Method (DGM). To achieve this, we first generate the inner part of the mesh in a structured manner and connect it to the curved boundary with a so-called buffer layer. Elements in the buffer layer employ a high order mapping to fit the boundary. We demonstrate high order convergence rates with an electromagnetic problem in a cylindrical cavity. Furthermore, we show that the frequency spectrum, which is extracted from the time-domain signal is clean, i.e., no spurious modes are observed in any of the examples considered.

1 Introduction

The DGM is a high order numerical method. In order to maintain its high order accuracy in the presence of curved objects, boundaries (surfaces) of the geometries have to be described with high order accuracy as well. The study in [1] shows that meaningful high order accurate results can be obtained only if the curved boundaries are considered with high order geometric approximations. In [2] problems in a cylindrical cavity are solved by pushing the straight edges of elements onto the exact circular boundary.

Both implementations [1, 2] employ triangular meshes for the DGM and achieve high order convergence. We propose an alternative mesh scheme based on Cartesian grids. It generates quadrilateral meshes in a simple process for both, exact geometries and objects represented by Non-Uniform Rational B-Splines (NURBS). The scheme enjoys many advantages due to the ability of applying tensor product bases within quadrilateral elements (see e.g. [3, 4]).

2 Body-fitting mesh scheme

We generate a set of buffer elements in the gap between the exact curved boundary and the interior structured mesh as demonstrated in Fig. 1. Figure 2 (left) shows that if no buffer layer is applied, degenerated elements (marked with arrows) are likely to occur, which is guaranteed not to happen with the insertion of a buffer layer [5] (right). Figure 3 gives an example, where a

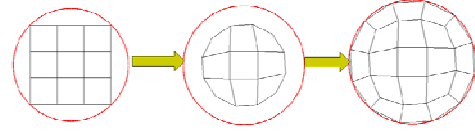


Fig. 1: Buffer layer mesh scheme based on a 3-by-3 regular mesh.

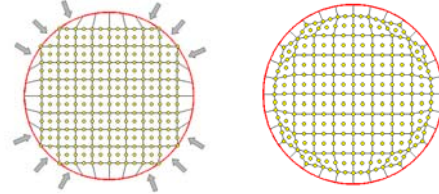


Fig. 2: Curved elements of 2nd order without (left) and with (right) buffer layer scheme based on a 9-by-9 regular mesh.

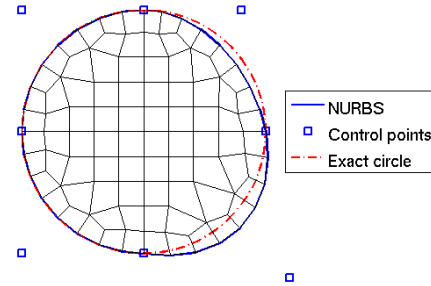


Fig. 3: Buffer layer mesh with NURBS. The approximation can be exact for both a circle (left half) and an arbitrary curve (right half) using control points.

mesh is generated fitting a geometry described by NURBS. For performing the local element deformation in the buffer layer we apply Transfinite Interpolation (TFI) [6].

3 Solving electromagnetic problems

We consider transverse magnetic (TM) problems in a two-dimensional circular domain Ω with the boundary $\partial\Omega$. The Maxwell's equations read as follows:

$$\mu \frac{\partial H_x}{\partial t} = -\frac{\partial E_z}{\partial y}, \quad \mu \frac{\partial H_y}{\partial t} = \frac{\partial E_z}{\partial x}, \quad (1)$$

$$\varepsilon \frac{\partial E_z}{\partial t} = \frac{\partial H_y}{\partial x} - \frac{\partial H_x}{\partial y}, \quad (2)$$

where H_x and H_y are the x- and y-components of the magnetic field vector, and E_z the z-component of the electric field vector. The parameters ε and μ are the electric permittivity and the magnetic permeability, respectively.

In this DGM approach, Legendre polynomials are applied as basis functions and the explicit leap-frog scheme is used for the time discretization [4]. The TM31 mode in a cylindrical cavity is chosen for a convergence study. The errors are measured in the L^2 norm at the end of one periodic oscillation.

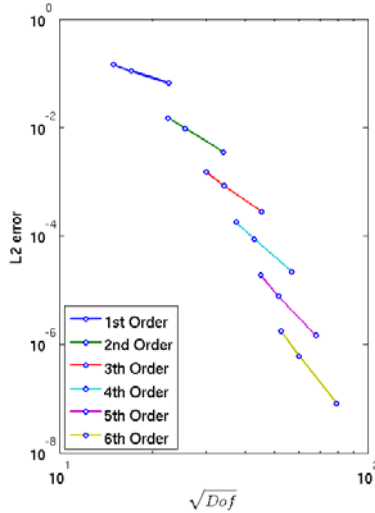


Fig. 4: For a resonant mode in the cylindrical cavity, DGM with upwind flux shows $(p+1)$ convergence using body-fitting meshes.

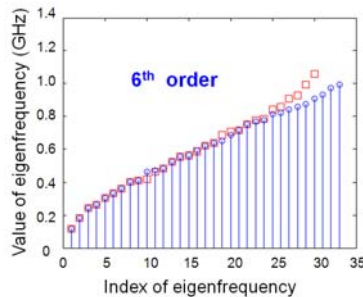


Fig. 5: Analytical values (red squares) and captured numerical eigen-modes (blue stems)

Figure 4 shows that the optimal convergence of $(p+1)$ is achieved where p is the polynomial order. We also extracted eigenfrequencies via a Fourier Transform. The results in Fig. 5 were obtained using central fluxes and 32 elements of 6th order. The eigenfrequencies obtained from the time-domain solution agree with the analytical ones for frequencies up to 0.8 GHz. Above this frequency the spatial resolution is insufficient leading to errors.

4 Conclusions

A body-fitting mesh scheme employing high order curved elements with the DG method is proposed. High order convergence rates in the presence of curved objects are observed. Furthermore, we extracted frequency spectra from simulations of a cylindrical cavity and found the agreement between the numerical results and the respective analytical solutions, i.e., clean spectra are obtained.

Acknowledgement. The work of J. Cui and S. M. Schnepf is supported by the 'Initiative for Excellence' of the German Federal and State Governments and the Graduate School of Computational Engineering at Technische Universitaet Darmstadt.

References

1. F. Bassi and S. Rebay, "High-Order Accurate Discontinuous Finite Element Solution of the 2D Euler Equations* 1", *J. Comput. Phys.* 138(2), 251–285, 1997.
2. J. S. Hesthaven and T. Warburton, *Nodal discontinuous Galerkin methods: algorithms, analysis, and applications*. Springer Verlag, 2007.
3. D. Wirasaet, S. Tanaka, E. J. Kubatko, J. J. Westerink, and C. Dawson, "A performance comparison of nodal discontinuous Galerkin methods on triangles and quadrilaterals", *Int. J. Numer. Math. Fl.* 64(10–12), 1336–1362, 2010.
4. Schnepf and Weiland, "Efficient Large Scale Electromagnetics Simulations Using Dynamically Adapted Meshes with the Discontinuous Galerkin Method", *J. Comput. Appl. Math. (Article in Press)*, 2011
5. S. J. Owen and J. F. Shepherd, "Embedding Features in a Cartesian Grid", *Proceedings of the 18th International Meshing Roundtable*, pp. 117–138, 2009.
6. W. J. Gordon and C. A. Hall, "Transfinite element methods: blending-function interpolation over arbitrary curved element domains", *Numerische Mathematik*, 21(2), 109–129, 1973.

Robust transmission conditions of high order for thin conducting sheets

Kersten Schmidt¹ and Alexey Chernov²

¹ TU Berlin, DFG research center MATHEON, 10623 Berlin, Germany kersten.schmidt@math.tu-berlin.de

² Hausdorff Center for Mathematics, University of Bonn, 53115 Bonn, Germany chernov@hcm.uni-bonn.de

Summary. Resolving thin conducting sheets for shielding or even skin layers inside by the mesh of numerical methods like the finite element method (FEM) can be avoided by using impedance transmission conditions (ITCs). Those ITCs shall provide an accurate approximation for small sheet thicknesses d , where the accuracy is best possible independent of the conductivity or the frequency being small or large – this we will call *robustness*. We investigate the accuracy and robustness of popular [1, 2] and recently developed ITCs [4], and propose robust ITCs which are accurate up to $O(d^2)$.

1 Introduction

Thin conducting sheets for the protection of electronic devices exhibit large ratios of characteristic lengths which require a small mesh size when using finite difference or finite element schemes. Besides this issue of computational cost due to the small geometry detail, many commercial mesh generators get difficulties with anisotropic geometrical features.

The shielding behaviour can be modelled alternatively by replacing the thin sheet by an interface on which *impedance transmission conditions* are set.

We consider the time-harmonic eddy current model (convention $\exp(-i\omega t)$, $\omega > 0$) in two dimensions

$$\mathbf{curl}_{2D} e(\mathbf{x}) = i\omega\mu_0 \mathbf{h}(\mathbf{x}), \quad (1)$$

$$\mathbf{curl}_{2D} \mathbf{h}(\mathbf{x}) = \sigma e(\mathbf{x}) + j_0(\mathbf{x}) \quad (2)$$

where e and \mathbf{h} are the out-of-plane electric and in-plane magnetic fields, σ is the conductivity of the thin sheet of thickness d and zero elsewhere, and j_0 is the out-of-plane imposed current which is outside the conductor. We have used the 2D rotation operators $\mathbf{curl}_{2D} = (\partial_y, -\partial_x)^\top$ and $\mathbf{curl}_{2D} = (-\partial_y, \partial_x)$. The skin depth inside the conductor is $\delta = \sqrt{2/\omega\mu_0\sigma}$.

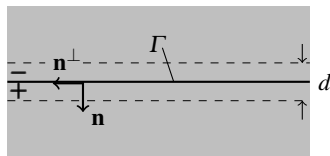


Fig. 1. Impedance transmission conditions are set on the mid-line Γ of the sheet and shall approximate the exact field outside the area the sheet was originally located.

2 Thin sheet and limit conditions

2.1 Thin sheet transmission conditions

With $\beta = i\omega\mu_0$ and $\gamma = \sqrt{-i\omega\mu_0\sigma}$ the impedance transmission conditions by Krähenbühl and Muller [1] and Mayergoyz and Bedrosian [2] are given by

$$\begin{aligned} e_{\text{KM}}^+ - e_{\text{KM}}^- &= \frac{\beta}{\gamma} \tanh\left(\frac{\gamma d}{2}\right) (\mathbf{h}_{\text{KM}}^+ \cdot \mathbf{n} + \mathbf{h}_{\text{KM}}^- \cdot \mathbf{n}), \\ \mathbf{h}_{\text{KM}}^+ \cdot \mathbf{n}^\perp - \mathbf{h}_{\text{KM}}^- \cdot \mathbf{n}^\perp &= \frac{\gamma}{\beta} \tanh\left(\frac{\gamma d}{2}\right) (e_{\text{KM}}^+ + e_{\text{KM}}^-) \end{aligned} \quad (3)$$

which are set on the mid-line Γ of the thin sheet. Here, the subscript KM denotes the approximative electric and magnetic field, the superscript \pm denotes the values on the two sides of the sheet, and $\mathbf{n} = (n_1, n_2)^\top$ and $\mathbf{n}^\perp = (n_2, -n_1)^\top$ are the normalised normal and tangential vectors on Γ like shown in Fig. 1.

2.2 The limit of vanishing thickness

Impedance transmission conditions are developed for thin sheets and their accuracy shall be larger the thinner the sheet. We observe three different limits for vanishing sheet thickness ($d \rightarrow 0$):

1. The conductivity σ is remained or is increased less than $1/d$. Then, we have twofold continuity

$$\begin{aligned} e_0^+ - e_0^- &= 0, \\ \mathbf{h}_0^+ \cdot \mathbf{n}^\perp - \mathbf{h}_0^- \cdot \mathbf{n}^\perp &= 0. \end{aligned} \quad (4)$$

The limit corresponds to the low-frequency eddy current limit $\delta \rightarrow \infty$.

2. The conductivity σ increases like $1/d$, where we get the non-trivial limit conditions [3]

$$\begin{aligned} e_1^+ - e_1^- &= 0, \\ \mathbf{h}_1^+ \cdot \mathbf{n}^\perp - \mathbf{h}_1^- \cdot \mathbf{n}^\perp &= \frac{\sigma d}{2} (e_1^+ + e_1^-). \end{aligned} \quad (5)$$

3. The conductivity σ increases more than $1/d$, e. g., like $1/d^2$. Then, the electric field on both sides get zero in the limit $d \rightarrow 0$,

$$e_2^+ = e_2^- = 0, \quad (6)$$

equivalently to the high-frequency limit $\delta \rightarrow 0$.

Here, the respective subscripts 0, 1 and 2 correspond to the scaling $\sigma \sim 1/d^\alpha$ with $\alpha = 0, 1, 2$.

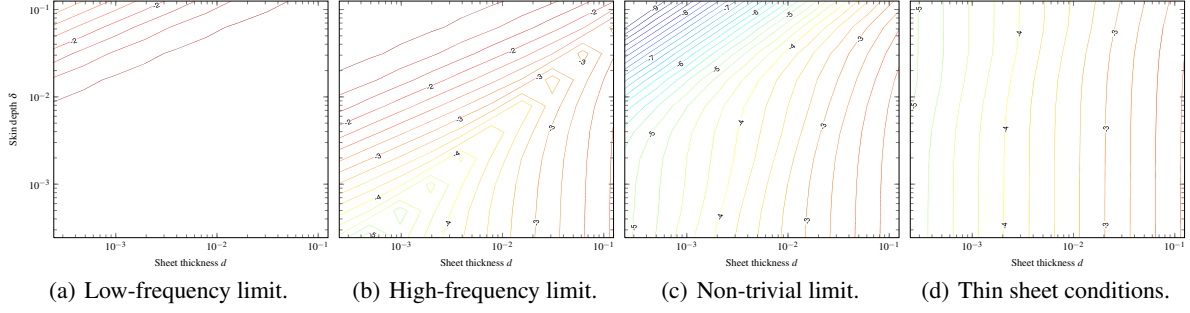


Fig. 2. The modelling error when using (a) the low-frequency limit, (b) the high-frequency limit, (c) the non-trivial limit, and (d) the thin sheet conditions (3) to approximate the shielding of conducting sheets of different thicknesses d and different frequencies or skin depth δ . The shown error is the one of the magnetic field outside the thin sheet.

2.3 Discussion

We investigated the thin sheet conditions and the limit conditions with high-order finite elements for a straight thin sheet in a rectangular box (with periodic boundary conditions) and two circular live wires with opposite current direction. The original thin sheet conditions (3) turn out to be robust with respect to the skin depth or frequency, see Fig. 2(d), which is obvious as they transform into (4) for low frequencies and into (6) for high frequencies, cf. [1].

The low-frequency limit conditions (4) achieve only some accuracy if the sheet thickness is more than one or two orders smaller than the skin depth. The high-frequency limit conditions (6) entail some accuracy if the skin depth is at least at the order of the sheet thickness.

The non-trivial limit conditions (5) are again robust and their accuracy is comparable to the one of the original thin sheet conditions for large skin depths / thickness ratios and much better if the skin depth gets relatively small, see Fig. 2(c). This observation is remarkable as the expression of (5) is much simpler than the one of (3).

3 High order transmission conditions

In order to improve the accuracy we have studied an asymptotic expansion for $d \rightarrow 0$ where – motivated by the non-trivial limit conditions – the conductivity is once scaled like $1/d$ (case $\alpha = 1$) and – motivated by asymptotically constant skin depth – the conductivity is once scaled like $1/d^2$ (case $\alpha = 2$).

3.1 Conductivity scaled like $1/d$

The first order ITCs related to $\alpha = 1$ are given by [4]

$$\begin{aligned} e_{1,1}^+ - e_{1,1}^- &= 0, \\ \mathbf{h}_{1,1}^+ \cdot \mathbf{n}^\perp - \mathbf{h}_{1,1}^- \cdot \mathbf{n}^\perp &= \frac{\sigma d}{2} (1 + \frac{1}{6} i \omega \mu_0 \sigma d^2) (e_{1,1}^+ + e_{1,1}^-). \end{aligned}$$

The second and third ITCs involve curvature terms and second order tangential derivatives, see [4].

3.2 Conductivity scaled like $1/d^2$

The first order ITCs related to $\alpha = 2$ are given by

$$\begin{aligned} e_{2,1}^+ - e_{2,1}^- &= \frac{\beta d}{2} \left(1 - \frac{\tanh(\frac{\gamma d}{2})}{\frac{\gamma d}{2}} \right) (\mathbf{h}_{2,1}^+ \cdot \mathbf{n} + \mathbf{h}_{2,1}^- \cdot \mathbf{n}), \\ \mathbf{h}_{2,1}^+ \cdot \mathbf{n}^\perp - \mathbf{h}_{2,1}^- \cdot \mathbf{n}^\perp &= \frac{\gamma}{\beta} \frac{\sinh(\frac{\gamma d}{2})}{\cosh(\frac{\gamma d}{2}) - \frac{\gamma d}{2} \sinh(\frac{\gamma d}{2})} (e_{2,1}^+ + e_{2,1}^-). \end{aligned}$$

Additional terms will be present for curved sheets.

3.3 Discussion

Both proposed ITCs are robust and get improved accuracy in comparison to the non-trivial limit and the original thin sheet conditions. The accuracy for both ITCs is asymptotically like $O(d^2)$. Especially, the $\alpha = 2$ -ITCs achieve accurate results even for larger sheet thicknesses. Since their expression has the same form as the original thin sheet conditions (3) they are preferable – for low and for high frequencies.

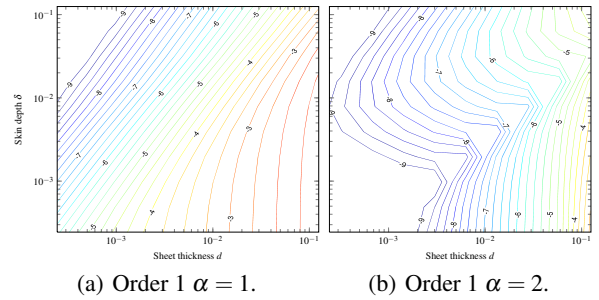


Fig. 3. Error of the impedance models of order 1 derived by asymptotic expansion for the scaling $\sigma \sim 1/d^\alpha$, $\alpha = 0, 1$.

References

1. L. Krähenbühl and D. Müller. *IEEE Trans. Magn.*, 29:1450–1455, 1993.
2. I.D. Mayergoyz and G. Bedrosian. *IEEE Trans. Magn.*, 31(3):1319–1324, 1995.
3. K. Schmidt and S. Tordeux. *Z. Angew. Math. Phys.*, 61(4):603–626, 2010.
4. K. Schmidt and S. Tordeux. *ESAIM: M2AN*, 45(6):1115–1140, 2011.

Efficient Convolution Based Impedance Boundary Conditions

Alberto Paganini¹

ETHZ, Rämistrasse 101, 8092 Zürich, Switzerland.

Summary. When formulating impedance boundary conditions in time domain, the Dirichlet-to-Neumann map of the interior of a good conductor involves convolutions. A. Schädle, M. López-Fernández and C. Lubich have developed a fast and memory efficient algorithm based on Runge-Kutta methods for computing convolutions when only the Laplace transform of the kernel is known. We investigate the coupling of FCQ with FEM for solving parabolic PDE with impedance boundary conditions involving convolutions.

1 Introduction

Alternating electromagnetic fields decay exponentially when penetrating a good conductor (skin effect). Therefore, a reasonable approximation of the electromagnetic Dirichlet-to-Neumann map of the interior of a good conductor is provided by the impedance boundary conditions

$$(\mathbf{curl} \mathcal{L}(\mathbf{E})(s)) \times \mathbf{n} = \frac{\sqrt{2\mu\sigma s}}{(1-i)\sqrt{i}} \gamma_D \mathcal{L}(\mathbf{E})(s), \quad (1)$$

where $\mathcal{L}(\mathbf{E})(s)$ denotes the temporal Laplace transform of the electric field, s is a complex variable and γ_D is the tangential Dirichlet trace operator. The conductivity σ and permeability μ are known material parameters.

The relationship (1) is valid in the Laplace domain only. When formulating impedance boundary conditions in the time domain, we encounter temporal convolutions of the form

$$\mathbf{curl} \mathbf{E}(\mathbf{x}, t) \times \mathbf{n} = \int_{t_0}^t k(\mu, \sigma, \tau - t) \gamma_D \mathbf{E}(\mathbf{x}, \tau) d\tau. \quad (2)$$

2 Fast Convolution Quadrature

C. Lubich and A. Ostermann first introduced the Runge-Kutta convolution quadrature in [1]. Their algorithm requires only the knowledge of the Laplace transform K of the possibly weakly singular kernel and experiences excellent stability properties and high order of convergence.

Subsequently in [2] A. Schädle, M. López-Fernández and C. Lubich rearranged the computations and combined the convolution quadrature with the exponentially convergent approximation of the convolution

weights along hyperbolae. They obtained a fast and memory efficient algorithm which virtually shares the convergence and stability properties of the convolution quadrature. Table 1 compares the complexity of a naive implementation of the convolution quadrature with the reduced complexity of the FCQ.

Table 1. Complexity of Convolution Quadrature and FCQ, n indicates the number of timesteps.

	CQ	FCQ
multiplications	$\mathcal{O}(n^2)$	$\mathcal{O}(n \log n)$
evaluations of K	$\mathcal{O}(n)$	$\mathcal{O}(\log n)$
active memory	$\mathcal{O}(n)$	$\mathcal{O}(\log n)$

3 FEM-FCQ Coupling

We have investigated the coupling of the FEM and the FCQ for solving the exterior eddy current problem. The algorithm benefits from the computational efficiency of the FCQ and seems to inherit the good convergence and stability properties which both the FEM and the FCQ supply.

For example we have combined the linear Lagrangian FEM on a triangular mesh with nodal basis functions with the RadauIIA based FCQ for solving the eddy current problem, after assuming a translation symmetry of the model and the TE-mode. We have observed that both the maximal order of convergence in space of FEM and the maximal order of convergence in time of FCQ have been achieved.

References

1. Ch. Lubich and A. Ostermann. Runge-Kutta methods for parabolic equations and convolution quadrature. *Math. Comp.*, 60(201):105–131, 1993.
2. Achim Schädle, María López-Fernández, and Christian Lubich. Fast and oblivious convolution quadrature. *SIAM J. Sci. Comput.*, 28(2):421–438 (electronic), 2006.

Modeling of Streamers in Transformer Oil using OpenFOAM

Nils Lavesson¹, Jonathan Fors^{2,1}, and Ola Widlund¹

¹ ABB Corporate Research, Forskargränd 7, SE-72178 Västerås, Sweden nils.lavesson@se.abb.com,
ola.widlund@se.abb.com

² Linköping University, SE-58183 Linköping, Sweden jonathan@modulus.se

Summary. Streamers occur prior to breakdown in electrical insulation and understanding streamers is important in order to optimize insulation design. In earlier works a model that describes streamers in transformer oil has been developed and implemented in a finite element simulation tool. In this paper the consequences of changing simulation method to the finite volume method is investigated and the simulation is extended from 2D axial symmetry to 3D.

1 Introduction

When electricity is transmitted over large distances in a power grid high voltages are required to limit the ohmic losses. High voltage puts a number of demands on electrical equipment in particular the electric insulation. For power transformers the insulation systems usually consists of mineral oil and high density cellulose. The primary mode of failure is an electric arc through the oil, which normally destroys the transformer.

Before an electric arc is formed a pre-breakdown event called a streamer occurs. The streamer is an ionizing wave traveling rapidly through the oil. The wave starts when the oil gets highly stress causing excessive build up of charge, which in turn affects the electric field leading to a high electric field region nearby. The strong electric field causes additional ionization and the wave propagates.

2 The Streamer Model

Researchers at Massachusetts Institute of Technology (MIT) have together with ABB Corporate Research developed a model for describing streamers in transformer oil [2–5]. The model consists of ion and electron transport equations coupled with Poisson's equation. The ions and electrons are produced through a field dependent ionization term based on the Zener model for electron tunneling.

3 Numerical Methods

The streamer simulations at MIT have been done using Comsol Multiphysics, which is a computational

tool based on the finite element method (FEM). Although Comsol is a powerful tool with a large number of applications, it has its limitations when computing convectively dominated flow, which is the main part of the streamer model. To be able to run the simulation various artificial diffusion techniques needs to be applied to stabilize the solutions.

A preferred method for convection dominated problems is the finite volume method (FVM). When implementing the MIT model in FVM OpenFOAM was chosen due to its flexibility and open structure. Moving to FVM also make the simulations more efficient, which allows larger problems to be treated.

4 Results

The MIT model was implemented in OpenFOAM at ABB and has been tested as part of the master thesis by Jonathan Fors [1]. The geometry simulated is a needle-sphere geometry, which is a standard geometry for testing the breakdown strength of insulating liquids.

The new solver is checked against a selection of MIT results [2]. These test cases are all 2D axisymmetric and include different model parameters and voltages. Most cases give quite similar results, but some differences are seen which are attributed to more stable numerics in the OpenFOAM solver.

The new solver has also been applied to a 3D version of the same needle-sphere geometry. The heavy computational load means that techniques for efficient meshing need to be used.

References

1. J. Fors. Modeling of streamers in transformer oil. Master's thesis, Linköping University, Linköping, Sweden, 2012. In preparation.
2. J.G. Hwang. *Elucidating the mechanisms behind pre-breakdown phenomena in transformer oil systems*. PhD thesis, Massachusetts Institute of Technology, Cambridge, MA, USA, 2010.
3. J.G. Hwang, M. Zahn, L.A.A. Pettersson, O. Hjortstam, and Rongsheng Liu. Modeling streamers in transformer oil: The transitional fast 3rd mode streamer. In *Properties and Applications of Dielectric Materials*, ICPADM, pages 573–578, 2009.

4. F. O'Sullivan. *A model for the initiation and propagation of electrical streamers in transformer oil and transformer oil based nanofluids*. PhD thesis, Massachusetts Institute of Technology, Cambridge, MA, USA, 2007.
5. F. O'Sullivan, J.G. Hwang, M. Zahn, O. Hjortstam, L. Pettersson, Rongsheng Liu, and P. Biller. A model for the initiation and propagation of positive streamers in transformer oil. In *Electrical Insulation*, ISEI, pages 210–214, 2008.

Wednesday, September 12

Phase Models and Phase Computations for Oscillators

Alper Demir and Önder Şuvak

Koç University, Istanbul, Turkey aldemir@ku.edu.tr, osuvak@ku.edu.tr

Summary. Oscillators have been a research focus in many disciplines such as electronics and biology. The time keeping capability of oscillators is best described by the scalar quantity called *phase*. Phase computations and equations describing phase dynamics have been useful in understanding oscillator behavior and designing oscillators least affected by disturbances such as noise. In this talk, we present a unified review of phase models for oscillators assimilating the work that has been done in electronics and biology for the last seven decades.

Oscillatory behavior is seen in physical and man-made systems, where their time keeping ability is important. Oscillators are particularly encountered in or introduced into biological and electronic systems where the adverse effects of disturbances such as noise degrade their time keeping and synchronization capability.

The dynamical behavior of oscillators is best described and analyzed in terms of the scalar quantity, *phase*. Of the pertaining notions in the literature, the most straightforward phase definition is obtained when a planar oscillator is expressed in polar coordinates, with amplitude and polar angle as the state variables. The usefulness of the polar angle as phase does not generalize to higher dimensional oscillators. In the general case, it is our conviction that the most rigorous and precise definition of phase is the one based on the so-called *isochrons* of an oscillator [1–4]. The notion of isochrons was first proposed by Arthur Winfree [1, 3] in 1974, who has also coined the term. It was later revealed that isochrons are intimately related to the notion of asymptotic phase in the theory of differential equations [5, 6]. The isochron theoretic phase of a free-running oscillator is simply time itself. Such an unperturbed oscillator serves as a perfect time keeper if it is in the process of converging to a limit cycle, even when it has not yet settled to a periodic steady-state solution. Perturbations make the actual phase deviate from time, due to the degrading impact of disturbances on the time keeping ability.

Phase is a quantity that compactly describes the dynamical behavior of an oscillator. One is then interested in computing the phase of a perturbed oscillator. If this can be done in a semi or fully analytical manner for a practical oscillator, one can draw conclusions and obtain useful characterizations in assessing

the time keeping performance. Indeed, we observe in the literature that, in various disciplines, researchers have derived *phase equations* that compactly describe the dynamics of weakly perturbed oscillators [2, 7]. It appears that a phase equation for oscillators has first been derived by Malkin [8] in his work on the reduction of weakly perturbed oscillators to their phase models [2], and the same equation has been subsequently reinvented by various other researchers in several disciplines [1, 7, 9]. This phase equation has been used in mathematical biology to study circadian rhythms and coupled oscillators in models of neurological systems [1, 2, 10], and in electronics for the analysis of phase noise and timing jitter in oscillators [7, 11, 12]. The acclaimed phase equation is a nonlinear but *scalar* differential equation. As such, it is the ultimate *reduced-order* model for a complex nonlinear dynamical system. Its scalar nature and the specific form of the nonlinearity in this equation makes it possible in some cases to solve, or characterize the solutions of, this equation in (semi) analytical form, e.g., in the investigation of synchronization of coupled oscillators [2, 9] and in characterizing phase noise in electronic oscillators with stochastic perturbations as models of electronic noise sources [7, 13].

In this talk, we present a unified review of phase models for autonomous oscillators assimilating the work that has been done on oscillator analysis in both electronics and mathematical biology during the past seventy years. We first review the notion of isochrons, which forms the basis for the generalized phase notion for an oscillator. We then present an overview of techniques for computing local approximations for the isochrons of an oscillator [4, 14]. Next, we describe phase models and phase computation schemes based on local approximations of isochrons, for continuous periodic (single-frequency) oscillators [15], continuous quasi-periodic (multi-frequency) oscillators [16], as well as for discrete molecular oscillators [17, 18].

Acknowledgement. This work was financially supported by the Scientific and Technological Research Council of Turkey (TÜBİTAK).

References

1. Arthur T. Winfree. *The Geometry of Biological Time*. Springer, 2001.
2. E.M. Izhikevich. *Dynamical Systems in Neuroscience: The Geometry of Excitability and Bursting*. Chapter 10. MIT Press, 2007.
3. K. Josic, E. T. Shea-Brown, and J. Moehlis. Isochron. *Scholarpedia*, 1(8):1361, 2006.
4. O. Suvak and A. Demir. Quadratic approximations for the isochrons of oscillators: A general theory, advanced numerical methods and accurate phase computations. *IEEE Transactions On Computer-Aided Design of Integrated Circuits and Systems*, 29(8):1215–1228, August 2010.
5. M. Farkas. *Periodic Motions*. Springer-Verlag, 1994.
6. A. Demir. Fully nonlinear oscillator noise analysis: An oscillator with no asymptotic phase. *International Journal of Circuit Theory and Applications*, pages 175–203, March-April 2007.
7. A. Demir, A. Mehrotra, and J. Roychowdhury. Phase noise in oscillators: A unifying theory and numerical methods for characterisation. *IEEE Transactions on Circuits and Systems-I: Fundamental Theory and Applications*, 47(5):655–674, May 2000.
8. I.G. Malkin. *Methods of Poincare and Liapunov in the theory of non-linear oscillations*. Gostexizdat, Moscow, 1949.
9. Y. Kuramoto. *Chemical Oscillations, Waves, and Turbulence*. Springer-Verlag, New York, 1984.
10. Eric Brown, Jeff Moehlis, and Philip Holmes. On the phase reduction and response dynamics of neural oscillator populations. *Neural Comput*, 16(4):673–715, Apr 2004.
11. F. X. Kaertner. Analysis of white and $f^{-\alpha}$ noise in oscillators. *International Journal of Circuit Theory and Applications*, 18:485–519, 1990.
12. T. Djurhuus, V. Krozer, J. Vidkjær, and T.K. Johansen. Oscillator phase noise: A geometrical approach. *Circuits and Systems I: Regular Papers, IEEE Transactions on*, 56(7):1373–1382, 2009.
13. A. Demir. Phase noise and timing jitter in oscillators with colored noise sources. *IEEE Transactions on Circuits and Systems-I: Fundamental Theory and Applications*, 49(12):1782–1791, December 2002.
14. O. Suvak and A. Demir. Computing quadratic approximations for the isochrons of oscillators: A general theory and advanced numerical methods. In *IEEE/ACM International Conference on Computer-Aided Design*, November 2009.
15. O. Suvak and A. Demir. On phase models for oscillators. *IEEE Transactions On Computer-Aided Design of Integrated Circuits and Systems*, 30(7):972–985, July 2011.
16. A. Demir, C. Gu, and J. Roychowdhury. Phase equations for quasi-periodic oscillators. In *IEEE/ACM International Conference on Computer-Aided Design*, November 2010.
17. O. Suvak and A. Demir. Phase models and computations for molecular oscillators. In *8th International Workshop on Computational Systems Biology (WCSB 2011)*, June 2011.
18. O. Suvak and A. Demir. Phase models and phase computations for discrete molecular oscillators. *EURASIP Journal on Bioinformatics and Systems Biology*, July 2012.

Optimal frequency sweep method in multi-rate circuit simulation

Kai Bittner¹ and Hans-Georg Brachtendorf¹

University of Applied Sciences Upper Austria, Softwarepark 11, 4232 Hagenberg, Austria
Kai.Bittner@fh-hagenberg.at, Hans-Georg.Brachtendorf@fh-hagenberg.at

Summary. We present a new approach for the computation of a not a-priori known, time-varying frequencies in a multi-rate circuit simulation. Typical examples are the start-up simulation of oscillators, or circuits with frequency modulation. The method is based on the optimization of the smoothness of the multi-rate solution, which is in turn essential for the efficiency of the computation.

1 Introduction

Widely separated time-scales occur in many radio-frequency (RF) circuits such as mixers, oscillators, PLLs, etc., making the analysis with standard numerical methods difficult and costly. Low frequency or baseband signals and high frequency carrier signals often occur in the same circuit, enforcing very small time-steps over a long time-period for the numerical solution, which results in prohibitively long run-times.

A method to circumvent this bottleneck is to reformulate the ordinary circuit DAEs as a system of partial DAEs (multi-rate PDAE). The method was first presented in [5] for the computation of steady states. The technique was adapted to the transient simulation of driven circuits with a-priori known frequencies in [7,9]. A generalization for circuits with a-priori unknown or time-varying frequencies was developed in [3,4,6].

Here, we present a new approach for the computation of a not a-priori known, time-varying frequency, which is driven by the requirement to have a smooth multi-rate solution, crucial for the efficiency of the computation.

2 The multi-rate circuit simulation problem

We consider circuit equations in the charge/flux oriented modified nodal analysis (MNA) formulation, which yields a mathematical model in the form of a system of differential-algebraic equations (DAEs):

$$\frac{d}{dt}q(x(t)) + g(x(t)) = s(t). \quad (1)$$

To separate different time scales the problem is reformulated as a multi-rate PDAE, i.e.,

$$\left(\frac{\partial}{\partial \tau} + \omega(\tau) \frac{\partial}{\partial t}\right)q(\hat{x}(\tau, t)) + g(\hat{x}(\tau, t)) = \hat{s}(\tau, t). \quad (2)$$

If the new source term is chosen, such that $s_\theta(t) = \hat{s}(t, \Omega_\theta(t))$, where $\Omega_\theta(t) = \theta + \int_0^t \omega(s) ds$, then a solution \hat{x} of (2) determines a family $\{x_\theta : \theta \in \mathbb{R}\}$ of solutions for

$$\frac{d}{dt}q(x(t)) + g(x(t)) = s_\theta(t), \quad (3)$$

by $x_\theta(t) = \hat{x}(t, \Omega_\theta(t))$.

Although the formulation (2) is valid for any circuit, it offers a more efficient solution only for certain types of problems. This is the case if $\hat{x}(\tau, t)$ is periodic in t and smooth with respect to τ . In the sequel we will consider (2) with periodicity conditions in t , i.e., $\hat{x}(\tau, t) = \hat{x}(\tau, t + P)$ and suitable initial conditions $\hat{x}(0, t) = X_0(t)$. Here P is an arbitrary but fixed period length.

3 Meaning and suitable choice of $\omega(\tau)$

Note that $\omega(\tau)$ can, with a corresponding choice of $\hat{s}(\tau, t)$, be chosen arbitrarily. This freedom may be used to facilitate an efficient numerical solution of (2). The smoothness of $\hat{x}(\tau, t)$ is essential for the efficiency of classical solvers. Therefore, we require

$$\int_{\tau_1}^{\tau_2} \int_0^P \left| \frac{\partial}{\partial \tau} \hat{x}(\tau, t) \right|^2 dt d\tau \rightarrow \min. \quad (4)$$

in order to determine $\omega(\tau)$. For frequency modulated oscillations one obtains indeed the instantaneous frequency as $\frac{\omega(t)}{P}$, while $\hat{x}(\tau, t)$ is constant with respect to τ . For some examples a (nearly) optimal $\omega(t)$ might be known in advance, while in other case (e.g. start-up of an oscillator) it might be necessary to determine $\omega(t)$ during the simulation, by enforcing the smoothness condition (4).

4 Discretization

We discretize (2) with respect to τ by a Rothe method using a linear multi step method (e.g. Gear's BDF or the trapezoidal rule). This results in a periodic boundary value problem in t of the form

$$\begin{aligned}\omega_k \frac{d}{dt} q_k(X_k(t)) + f_k(X_k, t) &= 0, \\ X_k(t) &= X_k(t + P),\end{aligned}\quad (5)$$

where $X_k(t)$ is the approximation of $\hat{x}(\tau_k, t)$ for the k -th time step τ_k , while ω_k is an approximation of $\omega(\tau_k)$. An optimal ω_k is determined with the condition

$$\int_0^P |X_k(t) - X_{k-1}(t)|^2 dt \rightarrow \min, \quad (6)$$

which is a good approximation of condition (4).

The periodic problem (5) can be solved by a collocation or Galerkin method, where $X_k(t)$ is expanded in a periodic basis $\{\phi_k\}$ (as a Fourier, B-spline, or wavelet basis) and tested at collocation points or integrated against test functions, respectively. This leads to a nonlinear system of equations for the coefficients $c_{k,\ell}$ of the basis expansion $X_k(t) = \sum_{\ell} c_{k,\ell} \phi_{\ell}(t)$. Here, the condition (6) is replaced by the condition

$$\sum_{\ell} \|c_{k,\ell} - c_{k-1,\ell}\|_2^2 \rightarrow \min. \quad (7)$$

5 Example: A Phase Locked Loop

The method has been tested our method on several circuits. To solve the periodic problem we have used an adaptive spline wavelet method described in [1, 2]. We show results from the multi-rate simulation of a Phase Locked Loop (PLL) with a frequency modulated input signal. Both the frequency parameter $\omega(\tau)$ (Fig. 1) determined by our method, and the control signal of the oscillator (Fig. 2) reflect perfectly the instantaneous frequency. The feedback signal in Fig. 3 shows that the computed $\omega(\tau)$ leads indeed to optimal smoothness.

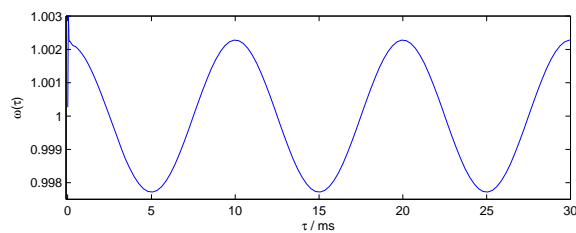


Fig. 1. Plot of simulated $\omega(\tau)$.

Acknowledgement. This work was funded partly by the Austrian Science Fund (FWF): P22549-N18, and the project ARTEMOS No. 270683-2, by the FFG Austria and the ENIAC Joint Undertaking.

References

1. K. Bittner and E. Dautbegovic. Adaptive wavelet-based method for simulation of electronic circuits. In *Scientific*

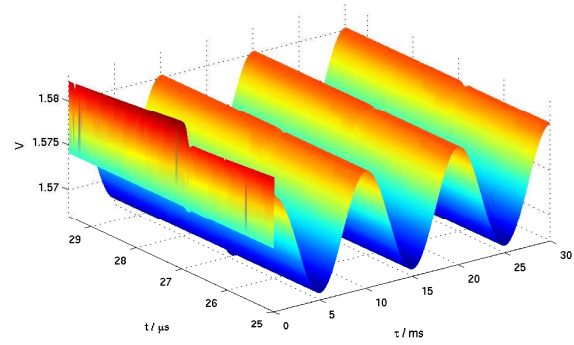


Fig. 2. Control signal for the oscillator in the PLL (multi-rate).

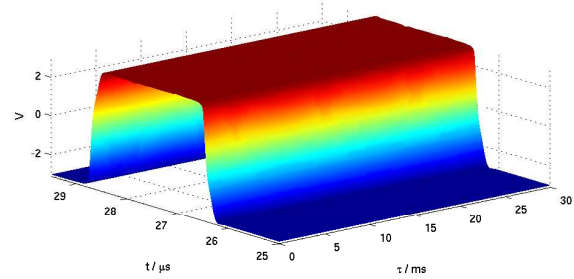


Fig. 3. Feedback signal of the PLL (multi-rate).

Computing in Electrical Engineering 2010, Mathematics in Industry. Springer, Berlin Heidelberg, 321–329.

2. K. Bittner and E. Dautbegovic. Wavelets algorithm for circuit simulation. In *Progress in Industrial Mathematics at ECMI 2010*, Mathematics in Industry. Springer, Berlin Heidelberg, to appear.
3. H. G. Brachtendorf. On the relation of certain classes of ordinary differential algebraic equations with partial differential algebraic equations. Technical Report 1131G0-971114-19TM, Bell-Laboratories, 1997.
4. H. G. Brachtendorf. Theorie und Analyse von autonomen und quasiperiodisch angeregten elektrischen Netzwerken. Eine algorithmisch orientierte Betrachtung. Universität Bremen, 2001. Habilitationsschrift.
5. H. G. Brachtendorf, G. Welsch, R. Laur, and A. Bunsen-Gerstner. Numerical steady state analysis of electronic circuits driven by multi-tone signals. *Electronic Engineering*, 79(2):103–112, 1996.
6. S. Houben. Simulating multi-tone free-running oscillators with optimal sweep following. In *Scientific computing in Electrical Engineering*, volume 4 of *Mathematics in Industry*, pages 240–247. Springer, 2004.
7. E. Ngoya and R. Larchevêque. Envelope transient analysis: A new method for the transient and steady state analysis of microwave communication circuit and systems. In *Proc. IEEE MTT-S Int. Microwave Symp.*, pages 1365–1368, San Francisco, 1996.
8. R. Pulch and M. Günther. A method of characteristics for solving multirate partial differential equations in radio frequency application. *Appl. Numer. Math.*, 42:399–409, 2002.
9. J. Roychowdhury. Efficient methods for simulating highly nonlinear multi-rate circuits. In *Proc. IEEE Design Automation Conf.*, pages 269–274, 1997.

Polynomial Fitting of Nonlinear Sources with Correlating Inputs

Janne P. Aikio¹, Timo Rahkonen¹, Ville Karanko²

¹ Department of Electrical Engineering, Electronics Laboratory, P.O. Box 4500 90014 University of Oulu, Finland

² AWR-APLAC Corporation, Lars Sonckin kaari 10, FI-02600 Espoo, Finland.

Summary. This paper proposes methods to improve the LSE polynomial fitting of bivariate nonlinear VCCS sources for distortion contribution analysis. The main problem in fitting is usually the fact that the input signals correlate strongly. It is shown that the correlation can be reduced by perturbing the input signals, which highly improves the quality of the fit. The ways to recognize a bad fit are discussed and the comparison between general, Chebychev and perturbed polynomial is performed.

1 Introduction

Volterra analysis is a powerful tool for finding the contributions of nonlinear distortion [1],[2]. However, it relies on the use of polynomial models that are usually not available. Volterra models are mostly built using high-order derivatives of the I-V and Q-V functions, but a polynomial model fitted using existing DC or AC I-V data is certain to converge over the data range. However, the fitting suffers from ill-conditioning resulting in non-physical coefficients. This paper illustrates heuristic methods how to recognise a bad fit, and ways to prevent it. We will propose a method that guarantees a physically meaningful fitted polynomial models are that converge over a the required signal range.

Here we utilize the frequency domain polynomial fitting [3] using large-signal voltage and current spectra of each nonlinear VCCS obtained from HB simulation. Hence, we can monitor the quality of the fitting of each VCCS individually and improve the fitting of those sources that suffer from a bad fit. The I_{DS} - V_{GS} - V_{DS} current source of a MOS transistor [4] is used as an example. Its frequency domain polynomial can be written as

$$\begin{aligned} I_{DS}(f) = & K_{00} + K_{10} \cdot V_{10}(f) + K_{20} \cdot V_{20}(f) \\ & + K_{30} \cdot V_{30}(f) + K_{40} \cdot V_{40}(f) + K_{50} \cdot V_{50}(f) \\ & + K_{01} \cdot V_{01}(f) + K_{02} \cdot V_{02}(f) + K_{03} \cdot V_{03}(f) \\ & + K_{11} \cdot V_{11}(f) + K_{21} \cdot V_{21}(f) + K_{12} \cdot V_{12}(f) \end{aligned} \quad (1)$$

where $V_{ij}(f)$ means the spectrum of a product term $v_{GS}^{i} v_{DS}^j$ - e.g. $V_{30}(f)$ are obtained by convolving $V_{10}(f)$ twice with itself. Controlling voltages V_{GS} and V_{DS} often correlate rather strongly, and this easily causes excessively strong V_{DS} -related product terms in the polynomial on lines 3 and 4 in (1).

2 Ways to Recognize a Bad Fit

The LSE fitting [5] tries to match the output current spectrum as accurately as possible, which is relatively easy to achieve. However, the model may still show excessive curvature outside the data range and does not make sense physically. In order to monitor the quality of the fit, we can calculate the estimated variance for fitted parameters [5]. This easily calculated numerical measure shows if the result is uncertain and has a risk. The condition number cond calculated from the singular values of the model matrix M in $y_{\text{est}} = Mc$, $c = (M^T M)^{-1} M^T y$ gives similar indication [5]. If $\text{cond}(M)$ is high, the model functions in M most probably correlate. Visually the quality of the fit can be illustrated by the model's capability to imitate the I-V shape of the original transistor. In Fig. 1 the I-V-curves of the original model are plotted on top of a narrow I_{DS} - V_{DS} swing (black) caused by the strongly correlating V_{GS} and V_{DS} . The general frequency domain polynomial (thick line) that is fitted using the narrow data range show excessive curvature outside the data trajectory, which implies that the model - though accurate - is non-physical.

3 Methods to Improve the Fitting

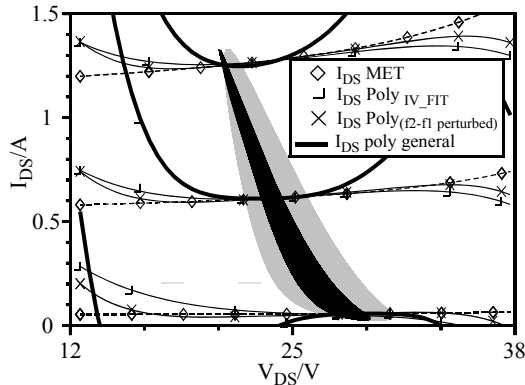
Several approaches have been proposed to guarantee that the fitted polynomial is physically meaningful. One is to reduce the order of the model (especially of V_{DS} -related terms). This helps, but also limits the usability of the model in highly nonlinear applications. Another method is to apply orthogonal series expansion like Chebychev series to reduce the correlation between odd and even degree terms. This works rather well with a multitone spectra, too: if the DC content is eliminated in the signals to be multiplied, the original frequency components will be attenuated in the resulting higher-order spectrum. The effect of this is shown in Fig. 2, in which the increase of $\text{cond}(M)$ between different order spectra $V_{ij}(f)$ is shown. It can be seen that condition number of the terms in Chebychev polynomial is indeed lower up to V_{50} but then increases above the general polynomial. In fact, a Chebychev polynomial can not break the correla-

Table 1: Coefficients and the reliability of general (C_1), Chebychev (C_2) and perturbed (C_3) polynomial.

Terms	DC	V ₁₀	V ₂₀	V ₃₀	V ₄₀	V ₅₀	V ₀₁	V ₀₂	V ₀₃	V ₁₁	V ₂₁	V ₁₂
C_1	0.33	1.29	1.78	0.35	-0.98	-0.25	2.3m	160u	20u	10.8m	8.9m	290u
C_1/sigma1	6310	2080	166	13	155	77	33	1.1	0.4	4.3	0.9	0.2
C_2	0.870	1.32	0.80	72.6m	-0.12	-15m	2.5m	80u	10u	10.8m	8.8m	290u
C_2/Sigma2	319	380	148	10.5	154	77	4.5	1.1	0.4	4.3	0.9	0.2
C_3	0.33	1.29	1.78	0.39	-0.99	-0.24	2.3m	140u	10u	10.5m	17m	640u
C_3/Sigma3	7640	3650	1300	97	174	140	60	18.6	2.8	82.4	17.4	6.9

tion between V_{GS} and V_{DS} , which is the main problem in the 2-D fitting. By fitting the V_{GS} and V_{DS} related polynomial terms in two phases (V_{GS} first, then V_{DS}), helps a little. One could also use the partial derivatives of I_{DS} to aid the fitting, as is often done in fitting DC models. However, that does not break the V_{GS} - V_{DS} correlation, either.

The obvious solution in breaking V_{GS} - V_{DS} correlation is to perturb either one of them [6]. This means that the data used for fitting is different from the one used for distortion contribution analysis, and we need to maintain the same peak amplitudes of the control signals. Also, two simulations are needed: one for fitting the models, and one for the real signals for the contribution analysis. This is implemented so that only the hard-to-fit I-V or Q-V sources are recognized, and fitted in a separate HB simulation loop where only that specific source is simulated and refitted. It can be seen in Fig. 2 that when a half the amplitude of the f_1 tone (900 mV $\angle 45^\circ$) is added to the f_2 - f_1 of V_{DS} , the cond(M) (especially cross-products) are highly reduced.

Fig. 1 I_{DS} - V_{DS} voltage swings with IV curves.

The IV-curves of this polynomial can be seen in Fig. 1 (X marker) and it behaves surprisingly well. The perturbation causes now wider data trajectory (grey) indicating lower correlation between V_{GS} and V_{DS} . With less correlating data it is possible to fit a frequency domain polynomial that is accurate and able to imitate the shape of the actual IV-curves. In fact, this polynomial is more accurate

than the IV-fitted polynomial(□ marker) based on the actual DC curves.

To observe the results further the Table 1 shows the coefficients of three different frequency domain polynomials and their reliability. The higher the reliability figure the smaller the deviation. It can be seen that the perturbation definitely increases the reliability of all terms, especially in the higher order terms and cross products.

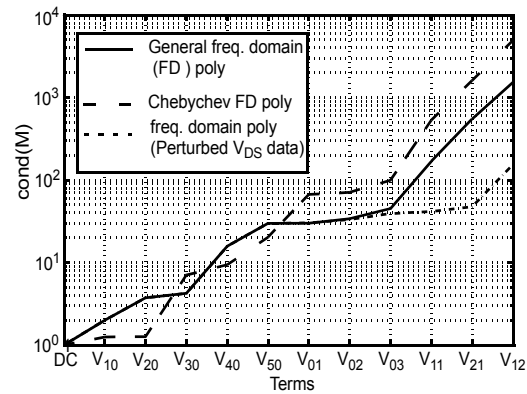


Fig. 2 Increase of the cond(M) term by term.

Acknowledgement. This work was supported by the Academy of Finland

References

- [1] P. Wambacq & W. M. C. Sansen. *Distortion Analysis of Analog Integrated Circuits*. Kluwer Academic Publisher, 1998
- [2] J. Vuolevi & T. Rahkonen, *Distortion in power amplifiers*. Artech House, 2003
- [3] J. P. Aikio, T. Rahkonen, "Detailed distortion analysis technique based on large-signal voltage and current spectra." *IEEE Trans. Microw. Theory Tech.*, vol 53, no. 10, pp. 3057-3066, Oct. 2005.
- [4] W. R. Curtice, J. A. Pla, D. Bridges, T. Liang, E. E. Shumate, "A new dynamic electro-thermal nonlinear model for silicon RF LDMOS FET's." *1999 IEEE MTT-S Int. Microwave Symp. Dig.*, vol. 2, pp. 419-422.
- [5] B. W. Rust, Fitting Nature's Basic Functions Part I: Polynomials and Linear Least Squares, *IEEE Computational Science and Engineering*, vol. 3, pp. 84 - 89, Sep/Oct. 2001
- [6] J. Pedro, J. Perez, "Accurate simulation of GaAs MESFET's intermodulation distortion using a new drain-source current model." *IEEE Trans. Microwave Theory and Tech.* Vol. 42, No. 1. 1994.

Heat generation in silicon nanometric semiconductor devices

Orazio Muscato and Vincenza Di Stefano

Dipartimento di Matematica e Informatica, Università di Catania, Viale A. Doria 6, 95125 Catania Italy
muscato@dmi.unict.it, vdistefano@dmi.unict.it

Summary. This paper is concerned with electron transport and heat generation in nanometric silicon semiconductor devices. An improved Monte Carlo method has been used, with the aim to reduce statistical fluctuations. Simulation results are presented for a 2D MOSFET device.

1 Introduction

In nano-devices the presence of very high and rapidly varying electric fields is the cause of thermal heating of the carriers and the crystal lattice. In fact, the external electric field transfers energy to the electrons and in turn to the lattice through the scattering mechanism. This self-heating process can influence significantly the electrical behaviour because the dissipated electrical energy causes a temperature rise in the device resulting in increased power dissipation. Power dissipation limits the performance of electronics from handheld devices ($\simeq 10^3$ W) to massive data centers ($\simeq 10^9$ W), all primarily based on silicon micro/nanotechnology [2].

In a diffusion-like regime, where the charge carriers are in thermal equilibrium with the lattice, there are small temperature gradients, and the device length is much larger than the phonon mean free path, the electro-thermal transport can be described accurately using the non isothermal drift-diffusion model [9]. Here the classical drift-diffusion equations are coupled with the Fourier law via the heat generation rate term

$$H_D = \mathbf{J} \cdot \mathbf{E} + (R - G)(E_G + 3k_B T) \quad (1)$$

where the cross product of the electric field (\mathbf{E}) and the current density (\mathbf{J}) represents the Joule heating, and the second term represents the heating rate due to the generation-recombination processes. But this field-dependent method does not give accurate for nanometric devices, where the regime is ballistic [2]. The mechanism through which lattice self-heating occurs is that of electron scattering with phonons, and therefore a model which deliberately incorporates all scattering events will also capture such energy dissipation details. The Monte Carlo method originally developed for studying hot electron effects, is also well-suited for computing a detailed picture of energy dissipation. In this case, the distribution of the heat generation rate is determined by counting the number of phonon emission and absorption events that re-

sult from electron-phonon scattering processes within the simulated region [3–5, 8]. This *counting estimator* writes

$$\langle H^C \rangle(x, y) = \frac{n}{N_p \Delta t} \sum_j \hbar \omega_j [C_j^+ - C_j^-] \quad (2)$$

where n is the electron density, N_p is the particle number in the (x,y)-cell, Δt is time interval in which the counting is made, $\hbar \omega_j$ the energy of the exchanged phonon, and C_j^+, C_j^- are the numbers of the j-th phonon emitted and absorbed respectively.

This counting method is a more fundamental approach, as it calculates power dissipation directly from the number of phonon emissions and absorptions. Furthermore, the method allows the investigation of the relative contribution of different phonon types to heat dissipation, which is not possible with most other methods. The main drawback of this method is the computational effort, because the estimator (2) is very noisy. In a recent paper [1], we have proposed a new estimator for the heat generation rate, which is based on the integrated probability scattering for the i-th phonon, i.e.

$$\lambda_i^\pm(\varepsilon, T_L) = \int w_i(\mathbf{k}, \mathbf{k}', T_L) d\mathbf{k}' \quad (3)$$

where ε the electron energy, T_L is the lattice temperature, w_i is the electron-phonon scattering rate, and + means emission of a phonon whereas - absorption of a phonon. The *integrated probability estimator* is

$$\langle H^F \rangle(x) = \frac{n}{N_p} \sum_{i=1}^{N_p} G(\varepsilon(\mathbf{k}_i)) \quad (4)$$

where

$$G(\varepsilon) = \sum_j \hbar \omega_j [\lambda_j^+(\varepsilon) - \lambda_j^-(\varepsilon)] \quad (5)$$

2 Simulation results

A npn silicon MOSFET is simulated via the Monte Carlo method to provide the heat generation rate. The MOSFET domain is 480 x 240 nm (see [6] for geometric details). The source/drain regions have a uniform n-type doping of 10^{18} cm^{-3} , the substrate a uniform p-type doping of 10^{14} cm^{-3} , and the gate oxide

is 40 nm thick with a gate length of 160 nm. The bias voltages applied are $V_s=0$, $V_g = 0.4$ V, $V_d = 1$ V. We have considered quasi-parabolic band approximation, scattering with acoustic phonons (in the elastic approximation) and optical phonons. The Monte Carlo device simulation is marched at a time step of 0.2 fs to steady state with 200,000 particles considered in the simulation. Once steady state is reached, statistics of electron-phonon scattering are collected over a time period of 5 ps. The results obtained by the integrated probability estimator (4) shown in the figure 1, have significantly lower fluctuations compared to those obtained by the counting estimator (2), plotted in the figure 2. Consequently a more efficient evaluation of the heat generation rate can be achieved using the new estimator (4). Moreover, the heat generation rate can

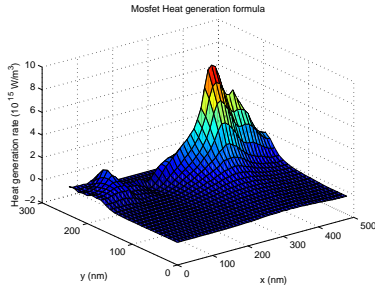


Fig. 1. Heat generation rate in the device obtained with the integrated probability estimator (4).

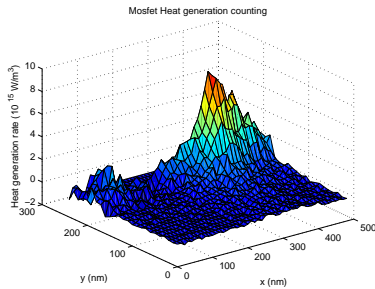


Fig. 2. Heat generation rate in the device obtained with the counting estimator (2).

be used to evaluate correctly the drain resistance in the device [7].

Acknowledgement. This work has been supported by Università degli Studi di Catania, by MIUR PRIN 2009 "Problemi Matematici delle Teorie Cinetiche e Applicazioni", and the CINECA Award N. HP10C3U0CA 2011 for the availability of high performance computing resources and support.

References

1. O. Muscato, V. Di Stefano, and W. Wagner. A variance-reduced electrothermal monte carlo method for semiconductor device simulation. *Computers and Mathematics with Applications*, to appear, 2012.
2. E. Pop. Energy dissipation and transport in nanoscale devices. *Nano Res.*, 3:147–169, 2010.
3. E. Pop, R. W. Dutton, and K. E. Goodson. Monte carlo simulation of joule heating in bulk and strained silicon. *Appl. Phys. Lett.*, 86:082101, 2005.
4. J. A. Rowlette and K. E. Goodson. Fully coupled nonequilibrium electron-phonon transport in nanometer-scale silicon fets. *IEEE Trans. Electron Dev.*, 55:220–232, 2008.
5. T. Sadi, R. Kelsall, and N. Pilgrim. Simulation of electron transport in ingaas/algaas hemts using an electrothermal monte carlo method. *IEEE Trans. Electron Dev.*, 53(8):1768–1774, 2006.
6. k. Tomizawa. *Numerical simulation of submicron semiconductor devices*. Artech, Boston, 1993.
7. Y.-T. Tsai and T.A. Grotjohn. Source and drain resistance studies of short-channel mesfets using two-dimensional device simulators. *IEEE Trans. Electron Dev.*, 37(3):775–780, 1990.
8. D. Vasileska, K. Raleva, and S. M. Goodnick. Modeling heating effects in nanoscale devices: The present and the future. *J. Comp. Electron.*, 7:66–93, 2008.
9. G.K. Wachutka. Rigorous thermodynamic treatment of heat generation and conduction in semiconductor device modeling. *IEEE Trans. CAD*, 9(11):1141–1149, 1990.

Simulation of a double-gate MOSFET by a non parabolic energy-transport subband model based on MEP including crystal heating

V. D. Camiola¹, G. Mascali², and V. Romano¹

¹ University of Catania, Italy camiola@dmi.unict.it, romano@dmi.unict.it

² University of Calabria, and INFN-Gruppo collegato di Cosenza, Italy mascali@unical.it

Summary. A nanoscale double-gate MOSFET is simulated by using a model based on the maximum entropy principle (MEP) by including the heating of the crystal lattice. The influence of this latter on the electrical performance of the device is discussed.

1 Mathematical model and simulations

The main aim of the paper is to simulate the nanoscale silicon double gate MOSFET (hereafter DG-MOSFET) reported in Fig. 1, by including also the crystal heating which can influence the electrical properties of the device and pose severe restrictions on its performance. In fact the phonons emitted by hot electrons create a phonon hot spot which increases the generated power density of the integrated circuits. This effect is becoming crucial by shrinking the dimension of the devices which is now below 100 nm, a length comparable with the wavelength of acoustic phonons [1, 2].

We consider a DG-MOSFET with length $L_x = 40$ nm, the width of the silicon layer $L_z = 8$ nm and the oxide thickness $t_{ox} = 1$ nm. The n^+ regions are 10 nm long. The doping in the n^+ regions is $N_D(x) = N_D^+ = 10^{20} \text{ cm}^{-3}$ and in the n region is $N_D(x) = N_D^- = 10^{15} \text{ cm}^{-3}$, with a regularization at the two junctions by a hyperbolic tangent profile.

Due to the symmetries and the dimensions of the device, the transport is, within a good approximation, one dimensional and along the longitudinal direction with respect the two oxide layers, while the electrons are quantized in the transversal direction. Six equivalent valleys are considered with a single effective mass $m^* = 0.32m_e$, m_e being the free electron mass.

Since the longitudinal length is of the order of a few tens of nanometers, the electrons as waves achieve equilibrium along the confining direction in a time which is much shorter than the typical transport time. Therefore we adopt a quasi-static description along the confining direction by a coupled Schrödinger-Poisson system which leads to a subband decomposition, while the transport along the longitudinal direction is described by a semiclassical Boltzmann equation for each subband.

Numerical integration of the Boltzmann-Schrödinger-Poisson system is very expensive from a computational point of view, for computer aided design (CAD) purposes (see references quoted in [3, 4]) In [3] we have formulated an energy transport model for the charge transport in the subbands by including the non parabolicity effects through the Kane dispersion relation. The model has been obtained, under a suitable diffusion scaling, from the Boltzmann equations by using the moment method and closing the moment equations with the Maximum Entropy Principle (MEP). Scatterings of electrons with acoustic and non polar optical phonons are taken into account. The parabolic subband case has been treated and simulated in [4].

The crystal heating is included adding a further equation for the lattice temperature T_L in the same spirit as in ref.s [5, 6]

$$\rho_{cV} \frac{\partial T_L}{\partial t} - \text{div} [K(T_L) \nabla T_L] = H, \quad (1)$$

with ρ and c_V silicon density and specific heat respectively. H is the phonon energy production given by

$$H = -(1 + P_S) n C_W + P_S \mathbf{J} \cdot \mathbf{E}, \quad (2)$$

where P_S plays the role of a thermopower coefficient, $n C_W$ is the electron energy production term with n electron density, and \mathbf{J} is the current. The electron density is related to the surface density in each subband by the relation

$$n = \sum_v \rho_v |\phi_v|^2$$

where ϕ_v are the envelope functions obtained solving the Schrödinger-Poisson system. In [5] a more general model for H has been proposed.

We stress that the lattice temperature enters into the electron-phonon scattering and in turn in the production terms of the balance equations for the electron variables. The main aim of the present paper is to address the importance of the crystal heating on the electric performance of the device.

A suitable modification of the numerical scheme for the MEP energy transport-Schrödinger-Poisson

system developed in [4] is proposed which includes also the discretization of the lattice temperature balance equation via an ADI approach. Since the characteristic time of the crystal temperature is about one or two orders of magnitude longer than that of electrons, a multirate time step method is employed as in [6].

In the figures we report some preliminary results. It is possible to see a tremendous raise of the crystal energy $k_B T_L$, which at room temperature is about 0.0259 eV, near the drain where the electron energy has its maximum values due to the high electric field present there. It is likely that the lattice temperature reaches the silicon melting temperature. This poses severe restrictions on the source/drain and source/gate voltages with stringent design constraints.

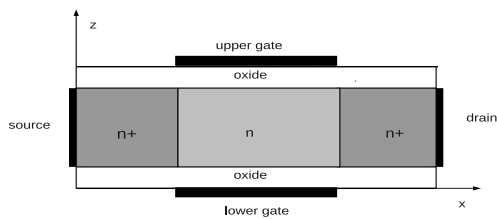


Fig. 1. Schematics representation of the simulated DG-MOSFET

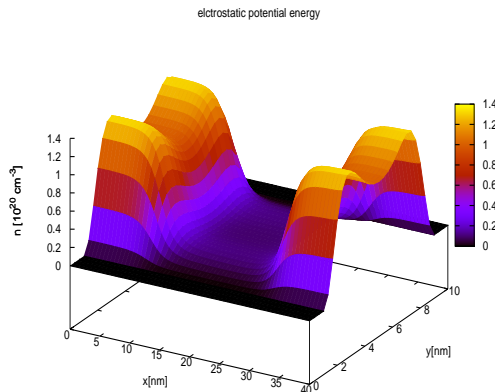


Fig. 2. Electron density when the applied potential between source and drain is $V_{SD} = 0.1$ V and source and gate are equipotential

Acknowledgement. V.D.C. and V. R. acknowledge the financial support by the P.R.I.N. project 2010 Kinetic and macroscopic models for particle transport in gases and semiconductors: analytical and computational aspects and by P.R.A. University of Catania. G. M. acknowledges the financial support by P.R.A., University of Calabria.

References

1. S. Sinha and K.E. Goodson. Thermal conduction in sub-100 nm transistors. *Microelectronics Journal*, 37: 1148–

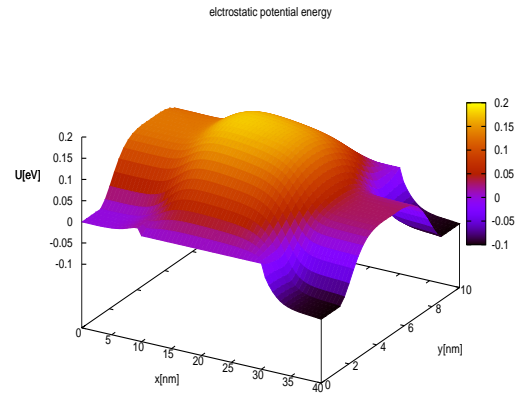


Fig. 3. Electrostatic energy when the applied potential between source and drain is $V_{SD} = 0.1$ V and source and gate are equipotential

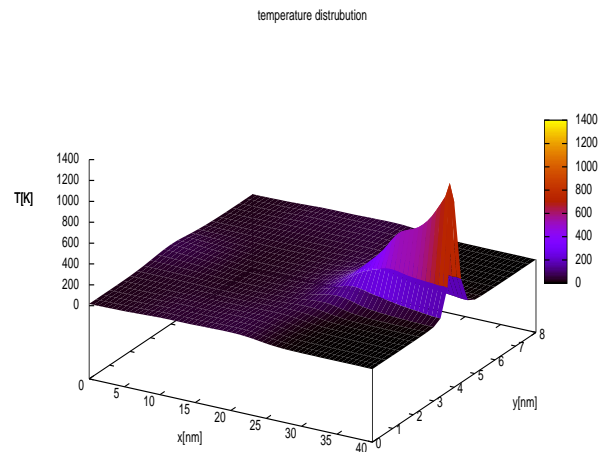


Fig. 4. Electrostatic energy when the applied potential between source and drain is $V_{SD} = 0.1$ V and source and gate are equipotential

- 1157, 2006.
2. J. A. Rowlette and K. E. Goodson. Fully coupled nonequilibrium electron-phonon transport in nanometer-scale silicon FETs *IEEE trans. on electron device*, 55: 220–232, 2008
3. G. Mascali and V. Romano. A non parabolic hydrodynamical subband model for semiconductors based on the maximum entropy principle. *Mathematical and Computer Modelling*, 55:1003–1020, 2012.
4. V.D. Camiola, G. Mascali and V. Romano. Numerical simulation of a double-gate MOSFET with a subband model for semiconductors based on the maximum entropy principle. *Continuum Mech. Thermodyn.*, 2012 (available online).
5. V. Romano and M. Zwierz. Electron-phonon hydrodynamical model for semiconductors. *Z. Angew. Math. Phys.*, 61:1111–1131, 2010.
6. V. Romano and A. Rusakov, 2d numerical simulations of an electronphonon hydrodynamical model based on the maximum entropy principle. *Comput. Methods Appl. Mech. Engrg.*, 199: 274–2751, 2010.

Electrical Modelling of Large-area Organic Light-emitting Devices

Evelyne Knapp and Beat Ruhstaller

Institute of Computational Physics, Zurich University of Applied Sciences, Wildbachstr. 21, 8401 Winterthur, Switzerland
evelyne.knapp@zhaw.ch, beat.ruhstaller@zhaw.ch

Summary. Systematic improvement of the performance and lifetime of organic light-emitting devices (OLEDs) are facilitated by electrical characterization through experiments and simulations. We model charge transport in organic disordered materials with the aid of a numerical 1D model for different experimental setups such as current-voltage curves, current transients and electrical impedance spectroscopy. For large-area OLEDs we couple the anode and cathode with the 1D model leading to an efficient 1+2D approach.

1 Introduction

Although the commercial success of organic light-emitting devices (OLEDs) in displays and lighting proceeds rapidly, further research is necessary to improve the efficiency and lifetime. Numerical simulations help to reduce the number of prototype iterations. Electrical characterization of devices and materials is crucial as it sheds light on the physical models of charge carrier transport in disordered, organic semiconductors. Charge transport and recombination models have been introduced several years ago for organic LEDs [1–5]. However, organic semiconductors differ considerably from their inorganic counterparts, not only by low carrier mobilities and long recombination times but also by the disorder. Taking the disordered nature of organic materials into account leads to a description in terms of a Gaussian density of states (DOS) which affects the mobility of charge carriers and the diffusion coefficient. The Gaussian DOS enhances the nonlinearities and the coupling between the equations. These circumstances prevent the use of classical drift-diffusion solvers. With the aid of a one-dimensional numerical OLED model we are able to simulate different operating conditions such as current-voltage curves [6], dark-injection measurements and impedance spectroscopy. We conduct steady-state, transient and small-signal analysis for the 1D OLED model and compare them with experiments. For lighting applications OLED panels are used that need to be as homogeneous as possible. To take this requirement into account we couple the 1D model to two 2D domains.

2 Physical Model

The drift-diffusion model (1) and (2) with the organic model ingredients (such as a Gaussian density of states and the use of the Fermi-Dirac statistics) are discretized with the finite volume method, the current expression (3) with the Scharfetter-Gummel discretization [7]. The resulting system of discretized equations is then solved in a coupled manner with Newton's algorithm for the transient as well as the steady-state case [8].

$$\nabla \cdot (\epsilon \nabla \psi) = q(n_f + n_t - p_f - p_t), \quad (1)$$

$$\begin{aligned} \nabla \cdot J_n - q \left(\frac{\partial n}{\partial t} \right) &= qR(n_f, p_f), \\ \nabla \cdot J_p + q \left(\frac{\partial p}{\partial t} \right) &= -qR(n_f, p_f), \end{aligned} \quad (2)$$

$$\begin{aligned} J_n &= -qn_f\mu_n\nabla\psi + qD_n\nabla n_f, \\ J_p &= -qp_f\mu_p\nabla\psi - qD_p\nabla p_f. \end{aligned} \quad (3)$$

For the small-signal analysis, the steady-state voltage V_0 is modulated with a sinusoidal voltage with the amplitude V^{ac} and with the angular frequency ω : $V = V_0 + V^{ac}e^{i\omega t}$. The potential ψ and the charge densities p and n can be expanded into a steady-state and harmonic term, e.g. $\psi(x, t) = \psi_0(x) + \psi^{ac}(x)e^{i\omega t}$ where the ac components are complex-valued. To solve the small-signal equations, the solution of the dc problem for $V = V_0$ is required. After inserting the expansions into the linearized drift-diffusion model we obtain a linear system of equations for the unknown ac components and thus for the ac current J^{ac} . From the complex admittance $Y = J^{ac}/V^{ac}$, the small-signal capacitance C and conductance G can be obtained. Charge traps originate in impurities or material degradation and affect the transport. In Fig. 1 we show the effect of different charge trap types on the normalized capacitance at different frequencies. Fast traps are in quasi-equilibrium with free carriers, the transit time is longer than the trapping time whereas for slow traps the transit time is shorter than the trapping time. Slow traps enhance the capacitance at low frequencies while fast traps follow the dynamics of the trap-free case [9]. Similarly, charge traps affect current transients and current-voltage curves.

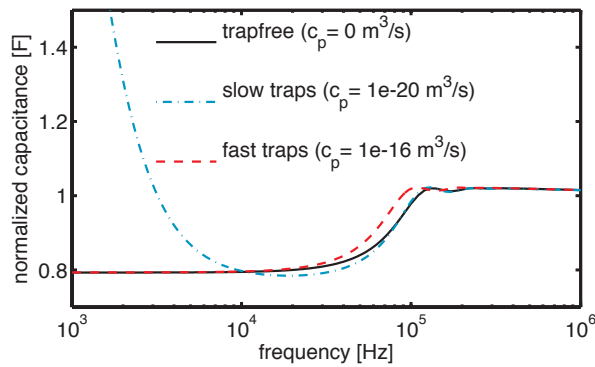


Fig. 1. Normalized capacitance of different trap types at various frequencies.

3 2+1D Approach for Large-area OLEDs

Aiming for a fast PC model for large-area OLEDs we have to take into account that realistic OLED structures consist of transparent anodes with a relatively low electrical conductivity. This affects the homogeneity of the OLED. Metal grid structures are applied to large-area OLEDs to improve the situation. To quantify the potential and temperature drop in large-area OLEDs we extend the 1D modelling of the organic material to higher dimensions. The 2+1D approach captures the important features of the transport process, and accounts for the high aspect ratio between the in-plane and the through-plane dimensions of OLEDs. In comparison to full 3D models, the 2+1D approach requires a reduced number of degrees of freedom, but still provides the lateral potential and temperature distribution. We make use of our in-house FEM tool (SESES) that allows the nonlinear coupling of 2D domains with the aid of the 1D model as shown in Fig. 2. The connection between the anode and cathode can either be:

- a parameterized experimental curve
- an analytical formula
- or a numerical model.

In Fig. 2 we show an OLED panel before optimizing the metal grid layout. No metal structure is present to improve the homogeneity of the OLED.

4 Conclusions

In this paper, we present a 1D model for organic LEDs that is applied to different operating conditions such as steady-state, transient and ac response. We investigate different charge trap types and their influence on the frequency-dependent capacitance. Further, we propose a 2+1D modeling approach for large-area OLEDs.

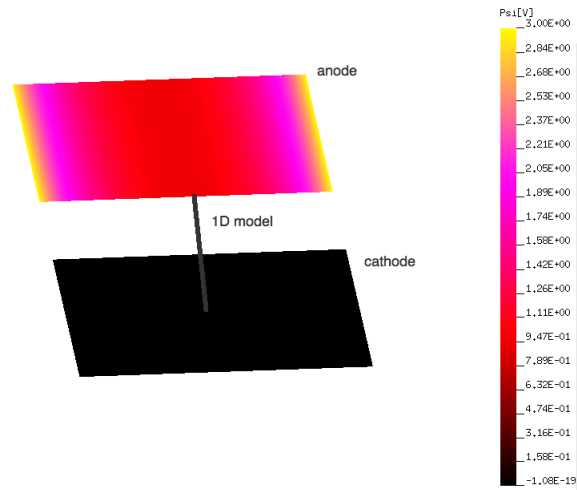


Fig. 2. Coupling of the 1D and 2D domains in an organic LED model. We display the potential drop before a metal grid structure is added.

Acknowledgement. We acknowledge financial support from the European Communitys Seventh Framework program under grant agreement no. 213708 (AEVIOM.eu) and NMP4-SL-2011-295368 (im3oled.eu).

References

1. J.C. Scott and G.G. Malliaras. Charge injection and recombination at the metalorganic interface. *Chem. Phys. Lett.*, 299:115, 1999.
2. B.K. Crone, P.S. Davids, I.H. Campbell, D.L. Smith. Device model investigation of bilayer organic light emitting diodes. *J. Appl. Phys.*, 87(4):1974, 2000.
3. P.W.M. Blom, M.J.M. de Jong, J.J.M. Vleggaar. Electron and hole transport in poly(p-phenylene vinylene) devices. *Appl. Phys. Lett.*, 68(23):3308, 1996.
4. B. Ruhstaller, S.A. Carter, S. Barth, H. Riel, W. Riess, J.C. Scott. Transient and steady-state behavior of space charges in multilayer organic light-emitting diodes. *J. Appl. Phys.*, 89(8):4575, 2001.
5. B. Ruhstaller, T. Beierlein, H. Riel, S. Karg, J.C. Scott, W. Riess. Simulating electronic and optical processes in multilayer organic light-emitting devices. *IEEE J. Sel. Top. Quantum Electron.*, 9(3):723, 2003.
6. S.L.M. van Mensfoort, S.I.E. Vulto, R.A.J. Janssen, R. Coehoorn. Hole transport in polyfluorenebased sandwich-type devices: quantitative analysis of the role of energetic disorder. *Phys. Rev. B*, 78(8):085208, 2008.
7. D.L. Scharfetter and H.K. Gummel. Large-signal analysis of a silicon read diode oscillator. *IEEE Trans. Electr. Dev.*, 16(28):64, 1969.
8. E. Knapp, R. Häusermann, H. Schwarzenbach, B. Ruhstaller. Numerical simulation of charge transport in disordered organic semiconductor devices. *J. Appl. Phys.*, 99(9):093304, 2011.
9. E. Knapp and B. Ruhstaller. Numerical impedance analysis for organic semiconductors with exponential density of localized states. *Appl. Phys. Lett.*, 108(5):054504, 2010.

Numerical Estimation of the Impact of Energetic Disorder on the Low-Frequency CV Characteristics of Organic MOS Structures

C. de Falco¹, F. Maddalena², and D. Natali³

¹ MOX-Modeling and Scientific Computing, Dipartimento di Matematica, Politecnico di Milano, P.zza L. da Vinci 32, 20133 Milano, Italy carlo.defalco@polimi.it

² Center for Nano Science and Technology of IIT@PoliMI, Istituto Italiano di Tecnologia, Via Pascoli 70/3 20133 francesco.maddalena@iit.it

³ Dipartimento di Elettronica e Informazione, Politecnico di Milano, P.zza L. da Vinci 32, 20133 Milano, Italy, and Center for Nano Science and Technology of IIT@PoliMI, Istituto Italiano di Tecnologia, Via Pascoli 70/3 20133 dario.natali@polimi.it

Summary. We propose a numerical model for estimating the low frequency Capacitance-Voltage (CV) characteristics of organic MOS structures and we use it to study the dependence of CV curves on the DOS. Preliminary results seem to suggest that low frequency CV measurements could be a viable means to estimate the DOS width of a material independently of its transport properties.

1 Introduction

Conjugated polymers are attracting increasing interest as viable semiconducting materials for various applications such as Organic Solar Cells (OSCs) [4], Field Effect Transistors (FETs) [7], Organic Light-Emitting Diodes (OLEDs) [5], photodetectors [1]. For this reason, much effort has recently gone in developing numerical tools for the simulation of this new class of devices [3, 8]. In particular regarding charge transport it must be reminded that organic semiconductors are generally amorphous and as such are to be modelled as disordered systems with localized states whose distribution is assumed to be in the simplest case a Gaussian with variance centered at the Lowest Unoccupied Molecular Orbital (LUMO) for electrons and centered at the Highest Occupied Molecular Orbital (HOMO) for holes. Charge carrier mobilities are modeled assuming that transport occurs as a hopping process (a thermally activated tunnelling) between localized sites and the variance of the Density of states appears as a parameter in the models. A method for determining the value of for a given material independently of its transport properties would greatly improve the predictive ability of numerical simulations. In this communication, we propose a numerical model for estimating the low frequency Capacitance-Voltage (CV) characteristics of organic MOS structures and we use it to study the dependence of CV curves on the DOS. In addition to the Gaussian DOS, we explore the effect on CV of more elaborate DOS models, such as two Gaussian distributions or a space-dependent distribution given by a Gaussian with an exponential tail

close to the insulator interfaces which fades into a Gaussian towards the bulk, simulating the effect of disordered electric dipoles within the insulator. Preliminary results seem to suggest that low frequency CV measurements could be a viable means to estimate the DOS width of a material independently of its transport properties.

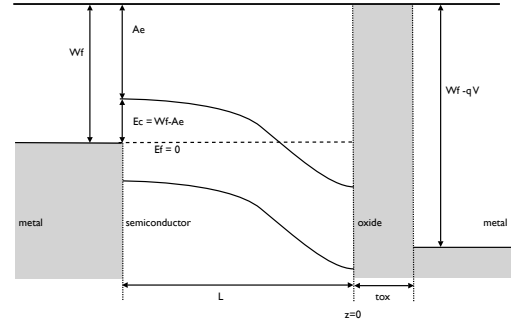


Fig. 1. Device geometry and relevant energetic levels involved with a positive voltage applied at the gate contact. Solid lines in the semiconductor refer to the LUMO and HOMO levels.

2 Model

A schematic representation of the device we consider is given in Fig. 1 together with the relevant energetic levels involved. It consists of a slab of thickness t_{ox} of insulating material on top of a semiconducting layer of thickness L sandwiched between two metals. If we neglect gate leakage currents, the Fermi energy level E_F is constant throughout the device, so we can set $E_F = 0$ without loss of generality. The electric potential $\varphi := -E_{LUMO}/q$ in the device can be computed by solving the equation

$$\begin{cases} -\text{div}(\epsilon \nabla \varphi) = -q n(\varphi) & \text{in } (-L, 0) \\ -\text{div}(\epsilon \nabla \varphi) = 0 & \text{in } (0, t_{ox}) \\ \varphi|_{-L} = \varphi_0; \quad \varphi|_{t_{ox}} = \varphi_{ox} + V \end{cases} \quad (1)$$

where ε denotes the electric permittivity, q the quantum of charge V the externally applied potential and the boundary condition values and are determined from the contact metal work function and the semiconductor material electron affinity as shown in Fig. 1. The accurate modeling of dependence of n on φ , which is crucial for understanding the impact of energetic disorder. If we assume the DOS to be a Gaussian centered at the LUMO, n may be expressed as

$$n = \int_{-\infty}^{\infty} g_{\sigma}(E - E_{LUMO}) f(E) dE \quad (2)$$

where

$$g_{\sigma}(x) = \frac{N_0}{\sigma\sqrt{2\pi}} \exp\left\{-\frac{x^2}{2\sigma^2}\right\} \quad (3)$$

and $F(E)$ is the Fermi distribution function. Although the ansatz (3) is very common, it has been shown in [6] that the energy level distribution may vary greatly near the insulator-semiconductor interface due to non-vanishing dipole density in the gate insulator material rendering (3) quite inaccurate. As the approach given by [6] for the modification of the DOS due to such effect has a very high computational cost, we take an alternative approach in order to account for this effect while retaining an acceptable level of model complexity. We introduce a modified density of state which we assume to take the following form

$$g_{\sigma,\lambda}(x) = g_{\sigma}(x) + \frac{\lambda N_{\lambda}}{2} \exp\{-\lambda|x|\} \quad (4)$$

and compute the parameters σ and λ in (4) via an automatic optimization procedure in order to fit the model of [6]. Fig. 2 shows a comparison of the simplified model (4) with that of [6].

3 Numerical algorithms and results

The CV characteristics are obtained from equations (1)-(4) via the numerical method, based on a Newton iteration, described in [2]. Suitable quadrature rules have been devised to compute the integrals appearing in (3) and (4) which need to be evaluated many times at each iteration step. The preliminary numerical results shown in Fig. 3 show a strong dependence of the CV curves (and of its derivative) on the disorder parameter σ . Ongoing research is directed towards the solution of the inverse problem of determining σ from measured CV characteristics.

References

1. Jenny Clark and Guglielmo Lanzani. Organic photonics for communications. *Nat Photon*, 4(7):438–446, 07 2010.
2. C. de Falco and E.O’Riordan. Interior layers in a reaction–diffusion equation with a discontinuous diffusion coefficient. *Int. J. Numer. Anal. Model.*, 7(4):444–461, 2010.

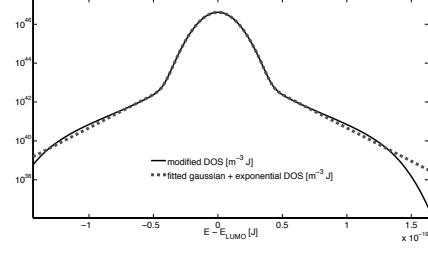


Fig. 2. Comparison of the simplified DOS model (5) with the model of [6]. The comparison is done one nanometer away from the interface.

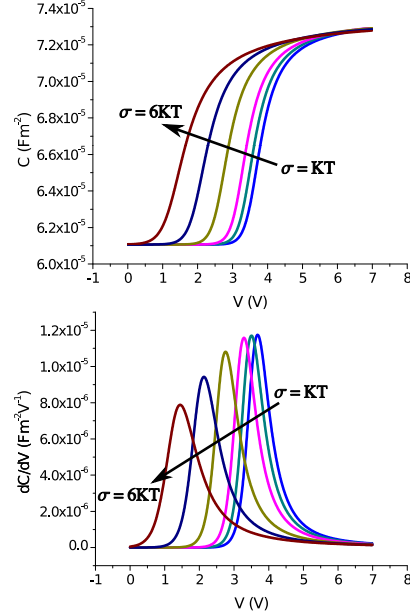


Fig. 3. Dependence of the CV curve (top) and of its derivative (bottom) on the DOS for a device with the following parameters: $T = 300K$, $N_0 = 4e27 \text{ m}^{-3}$, $L = 75e-9 \text{ m}$, $t_{ox} = 300e-9 \text{ m}$, $\varepsilon = 3 \varepsilon_0$ (semiconductor), $\varepsilon = 2.5 \varepsilon_0$ (insulator).

3. C. de Falco, R. Sacco, and M. Verri. Analytical and numerical study of photocurrent transients in organic polymer solar cells. *Comput. Methods Appl. Mech. Engrg.*, 199:1722–1732, 2010.
4. J. Nelson. Polymer:fullerene bulk heterojunction solar cells. *Materials Today*, 14(10):462–470, October 2011.
5. N.K. Patel, S. Cina, and J.H. Burroughes. High-efficiency organic light-emitting diodes. *Selected Topics in Quantum Electronics, IEEE Journal of*, 8(2):346–361, mar/apr 2002.
6. Tim Richards, Matthew Bird, and Henning Sirringhaus. A quantitative analytical model for static dipolar disorder broadening of the density of states at organic heterointerfaces. *J. Chem. Phys.*, 128, 2008.
7. H. Sirringhaus. Materials and applications for solution-processed organic field-effect transistors. *Proceedings of the IEEE*, 97(9):1570–1579, sept. 2009.
8. S. L. M. van Mensfoort and R. Coehoorn. Effect of gaussian disorder on the voltage dependence of the current density in sandwich-type devices based on organic semiconductors. *Phys. Rev. B*, 78, 2008.

Model order reduction for PDE constrained optimization in vibrations

Karl Meerbergen¹ and Yao Yue²

KU Leuven, Department of Computer Science, Karl.Meerbergen@cs.kuleuven.be,
Yao.Yue@cs.kuleuven.be

Summary. In PDE constrained optimization, physical parameters need to be determined so that some objective function is minimized. We assume here an objective function that depends on the output of a dynamical system, modeled by a discretized PDE. Krylov-Padé model reduction for computing the output can significantly decrease the computation time. In addition, gradients are well approximated, which allows using gradient based optimization on the reduced model. We show numerical results for different methods embedded in line search and trust region methods for benchmark problems from structural engineering.

1 Introduction

Given a dynamical system described by the following system of second order ordinary differential equations:

$$(K + sC + s^2M)x = fu(s) \quad (1)$$

$$y(s) = d^T x$$

where K , C , and M are respectively the stiffness, damping and mass matrices, are sparse, and have size $n \times n$ with n large. The vector f is input and d the output vector. Let the matrices depend on parameters $\gamma \in \mathbb{R}^p$, then we wish to determine the value of γ that minimizes one of the following functions

$$g_2(\gamma) = \int_{\omega_{\min}}^{\omega_{\max}} |y(i\omega)|^2 d\omega \quad (2)$$

$$g_\infty(\gamma) = \max_{\omega_{\min}}^{\omega_{\max}} |y(i\omega)| \quad (3)$$

The evaluation of g is expensive. We will therefore define a reduced model of (1) that approximates y well and is, because of its size, much cheaper to evaluate. The results of this paper are a summary of the full papers [4] [3]. In the remainder of the paper we use $A(s) = K + sC + s^2M$.

2 Krylov-Padé model reduction

One of the most popular model reduction techniques for vibrations are Krylov methods. For second order problems as (1), the SOAR method [1] is preferred. This method builds the matrices $V_k, W_k \in \mathbb{C}^{n \times k}$ with $k \ll n$. The columns of V_k span the derivatives of

orders $0, \dots, k-1$ of $A^{-1}(s)f$ around $s = s_0$. Similarly, the columns of W_k span the derivatives of orders $0, \dots, k-1$ of $A^{-*}(s)d$ around $s = s_0$. The reduced model is defined as

$$(\hat{K} + s\hat{C} + s^2\hat{M})\hat{x} = \hat{f}u(s) \quad (4)$$

$$\hat{y}(s) = \hat{d}^T \hat{x}$$

with $\hat{K} = W_k^* K V_k$, $\hat{C} = W_k^* C V_k$, and $\hat{M} = W_k^* M V_k$, and the vectors $\hat{f} = W_k^* f$ and $\hat{d} = V_k^* d$. It can be proven that the first $2k$ derivatives of y and \hat{y} evaluated at $s = s_0$ match. This property is also known as moment matching.

In order to evaluate g for a given $\gamma = \gamma_*$, we first build the corresponding reduced model \hat{y} using the two-sided SOAR method for the given value γ_* . The matrices \hat{K} , \hat{C} , and \hat{M} then also depend on γ . We hence have an interpolatory reduced model around the interpolation point γ_* . It can be shown [4] that $\nabla_\gamma y(\gamma_*)$ and $\nabla_\gamma \hat{y}(\gamma_*)$ match the first k derivatives around s_0 . We may thus conclude that two-sided SOAR models compute accurate approximations to y and its gradient s around s_0 and for fixed γ .

Then, g is computed using \hat{y} . For g_2 , we use a quadrature rule, and for g_{\max} we use a global optimization method consisting of a coarse grid search and local improvement by a quasi Newton method [4]. The gradient is computed accordingly.

Let us assume $p = 1$, i.e., γ is a single parameter. Another method that we will use for optimization is the PIMTAP method [2]. This is also a moment matching method for s , where in addition, also moments are matched for γ , as well as cross moments, i.e. the derivatives $\partial^{j+i} y / \partial s^j \partial \gamma^i$. The reduced model can then be used to efficiently evaluate y for all s near s_0 and γ near γ_* .

3 Line search optimization

In general, (2) is a nonconvex optimization problem. The default method for such problem is probably the damped BFGS method. In iteration j , the $j+1$ st iterate is computed as

$$\gamma_{j+1} = \gamma_j + \alpha_j p_j \quad , \quad H_j p_j = -\nabla_\gamma g(\gamma_j)$$

where H_j is the BFGS approximation of the true Hessian of g . For a nonconvex function, we determine α_j

so that the Armijo condition is satisfied. This is a condition that forces sufficient decrease of the objective function in order to achieve convergence. In general, a number of γ_{j+1} 's have to be computed for a sequence of values of α_j 's until the Armijo condition is satisfied. This is called backtracking. For each new value of γ , we build a new reduced model using the SOAR method.

Since γ_{j+1} lies on a line in the parameter space, $g(\gamma_{j+1})$ can be efficiently computed when we have a reduced model for both s and $\gamma_j + \alpha p_j$ for α in some interval. This can be achieved by a reduced model using the PIMTAP method.

We used damped BFGS accelerated by SOAR or PIMTAP for minimizing the vibrations in a concrete floor subjected to road noise by determining the best parameters of the floor damper [4]. In this case, there were two parameters: the stiffness and the damping of the floor damper. We see from Table 1 that for the optimization of g_2 , which is usually smooth and differentiable, the two-sided SOAR method reaches the best performance, while the minimization of g_∞ , which is not a smooth function and therefore requires many backtracking steps, is more efficient using PIMTAP. We also conclude that g_∞ op-

	g_2	g_∞
Direct	7,626	41,069
SOAR	179	1,104
PIMTAP	360	417

Table 1. Timings in seconds for the damped BFGS method for the optimization of a concrete floor damper

timization is harder than g_2 optimization, because g_∞ is a nonsmooth function.

4 Trust region based optimization

In [3], we discussed trust region approaches exploiting the effort done to build a reduced model. In the SOAR approach, we used the reduced model (4) for evaluating g for a fixed $\gamma = \gamma_j$. The idea here is simple: since $\nabla_\gamma g$ is well approximated at γ_j , the reduced model approximates g well for other values of γ , if g is Lipschitz continuous at γ_j . In contrast to the SOAR approach, we use (4) as a parametric model in s but also in γ , in a trust region setting. The difficulty is that this reduced model is an extrapolation and may therefore quickly lose its accuracy. Therefore, we developed a simple error estimation to control the quality of the reduced model. Since the Hessian is not necessarily well approximated, we rely again on a quasi-Newton method.

We then defined a trust region method, based on the error estimation of the reduced model. The trust

region contains the set of parameters γ where the reduced model is accurate. An error-based trust region approach is then used, relying on Cauchy points to guarantee convergence of the method. The solution of the trust region subproblem is cheap, since it fully relies on the reduced model. However, in order to have a provably convergent method, we may sometimes require additional reduced models to refine the trust region [3].

Table 2 compares the SOAR approach and the trust region approach for a model of a footbridge with four dampers. The eight parameters that model these dampers have to be determined so that the vibration in some point on the bridge is minimized. Note that only two reduced models are required, while 70 are needed for the SOAR approach. This leads to an important reduction of the computation time. However, it should be noted that the error estimation of g using the reduced model is much more expensive than evaluating the reduced model. This explains why there is no speed-up of a factor 35.

	Direct	SOAR	Trust region
Time (s)	70×540	897	194
iter.	70	70	2

Table 2. Results for the footbridge problem

Acknowledgement. This paper presents research results supported in part by the Belgian Network DYSCO, funded by the Interuniversity Attraction Poles Programme, initiated by the Belgian State Science Policy, and supported in part by the Research Council KU Leuven grants PFV/10/002 and OT/10/038.

References

1. Z. Bai and Y. Su. Dimension reduction of second-order dynamical systems via a second-order Arnoldi method. *SIAM J. Matrix Anal. and Applic.*, 26(5):1692–1709, 2005.
2. Y.-T. Li, Z. Bai, Y. Su, and X. Zeng. Model order reduction of parameterized interconnect networks via a Two-Directional Arnoldi process. *Computer-Aided Design of Integrated Circuits and Systems, IEEE Transactions on*, 27(9):1571–1582, 2008.
3. Y. Yue and K. Meerbergen. Accelerating pde-constrained optimization by model order reduction with error control. Technical report TW611, Department of Computer Science, K.U.Leuven, Celestijnenlaan 200A, 3001 Heverlee (Leuven), Belgium, 2012.
4. Y. Yue and K. Meerbergen. Using model order reduction for the design optimization of structures and vibrations. *International Journal of Numerical Methods in Engineering*, 2012. In press.

Stochastic Collocation Methods and Model Reduction for Maxwell's Equations

Peter Benner and Judith Schneider

Max Planck Institute for Dynamics of Complex Technical Systems, Sandtorstr. 1, 39106 Magdeburg, Germany
benner@mpi-magdeburg.mpg.de, will@mpi-magdeburg.mpg.de

Summary. We use a Stroud-based collocation method to analyze the parameter behavior of the time-harmonic Maxwell equations and reduce the computational costs by applying model order reduction to the system matrices.

1 Motivation

During the design process of semiconductor structures, simulations of new micro and nano scale systems are essential due to, e. g., the expensive production of prototypes. An important aspect is the ongoing miniaturization of the structures on the one hand and the increase in the working frequencies on the other hand. The high density of electric conductors induces parasitic effects, e. g., crosstalk, which have to be considered already in the design stage. Therefore, the exact knowledge of the semiconductor structures and the surrounding electromagnetic (EM) field is necessary.

Another effect, which plays a no longer negligible role, is the variation of the feature structure size caused by inaccuracies of the resolution during the lithography. To consider these variations in the simulation, models with parametric uncertainties are required. A variational analysis of the effect of these uncertainties on the EM field requires methods for uncertainty quantification (UQ) [4, 6]. For this purpose, we will employ non-intrusive approaches as they allow the use of EM field solvers for deterministic problems without accessing the source code. Possible choices are Monte Carlo and stochastic collocation. Here we will employ the latter due to their faster convergence. Still, UQ via stochastic collocation requires numerous full-order EM field solves which can be a time-consuming task for complicated 3D geometries. It is thus our goal to combine this approach with model order reduction methods (MOR) for the Maxwell equations to reduce the computational cost, where the reduced-order model needs to preserve the statistical properties of the full-order model. All these problems are addressed within the research network *Model Reduction for Fast Simulation of New Semiconductor Structures for Nanotechnology and Microsystems Technology (MoreSim4Nano)*, see [5]. Figure 1 shows a coplanar waveguide which serves as a benchmark

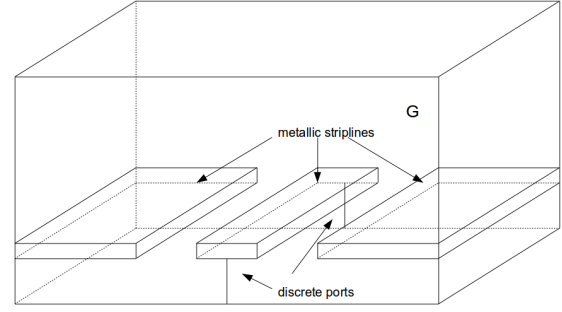


Fig. 1. Coplanar waveguide.

within MoreSim4Nano and for which we show some numerical results in Section 4.

2 Stochastic Collocation for EM Field Computations

The system of equations describing the EM field are Maxwell's equations

$$\begin{aligned}\partial_t(\epsilon \mathbf{E}) &= \nabla \times \mathbf{H} - \sigma \mathbf{E} - \mathbf{J} \\ \partial_t(\mu \mathbf{H}) &= -\nabla \times \mathbf{E} \\ \nabla \cdot (\epsilon \mathbf{E}) &= \rho \\ \nabla \cdot (\mu \mathbf{H}) &= 0,\end{aligned}$$

with the electric field intensity \mathbf{E} , the magnetic field intensity \mathbf{H} , the charge density ρ , the impressed current source \mathbf{J} , and material parameters $\epsilon = \epsilon_r \cdot \epsilon_0$ (permittivity), $\mu = \mu_r \cdot \mu_0$ (permeability), σ (electrical conductivity). For simplification, we work with the time-harmonic form

$$\nabla \times (\mu^{-1} \nabla \times \mathbf{E}) + i\omega \sigma \mathbf{E} - \omega^2 \epsilon \mathbf{E} = i\omega \mathbf{J}, \quad (1)$$

on the space $X = \{\mathbf{E} \in H_{curl}^0 \mid \nabla \cdot (\epsilon \mathbf{E}) = \rho\}$.

Up to now, we consider the material parameters ϵ_r , μ_r , and σ as uncertain. For the examination of their influence on the statistical behavior of the solution \mathbf{E} we use stochastic collocation [1] with Stroud interpolation points [2].

2.1 Stochastic Collocation

Collocation methods rely on interpolation. The idea is to approximate high-dimensional integrals, e. g., the

expectation value of our solution E , by an (efficient) quadrature rule

$$\mathbb{E}(E) = \int_{\Gamma} E(\xi) f(\xi) d\xi \approx \sum_{i=1}^n E(\xi_i) w_i.$$

Here Γ is the image of the probability space under the probability measure, f is the unknown probability density function of E , ξ_i are the n interpolation points and w_i are the associated weights.

2.2 Stroud Integration

The interpolation formula used in our algorithm was introduced in 1957 by A. H. Stroud [7] and yields either beta or normal distributed interpolation points which are weighted by $1/n$, where n is the number of interpolation points as in Sec. 2.1. Though we need $\varepsilon_r, \mu_r > 0$ and $\sigma \geq 0$, we suppose them to be log-normal distributed and use the exponential of the normal distributed Stroud points as interpolation points.

3 Model Order Reduction

The discretization of (1) leads to the following system

$$\begin{aligned} \mu_r A_{\mu_0} \mathbf{e} + \varepsilon_r A_{\varepsilon_0} \ddot{\mathbf{e}} + \sigma A \dot{\mathbf{e}} &= B u, \\ \mathbf{y} &= C \mathbf{e}, \end{aligned}$$

where \mathbf{e} is the discretized electric field, $A_{\mu_0}, A_{\varepsilon_0}$ and A are the parameter independent system matrices in $\mathbb{R}^{N \times N}$, u, y define the inputs/ outputs, and B, C specify the input/ output behavior. Here N is the number of grid points in G and large. This system is then reduced, e. g., by means of rational interpolation methods as in [3] and we achieve a reduced system of the form

$$\begin{aligned} \mu_r \hat{A}_{\mu_0} \hat{\mathbf{e}} + \varepsilon_r \hat{A}_{\varepsilon_0} \ddot{\hat{\mathbf{e}}} + \sigma \hat{A} \dot{\hat{\mathbf{e}}} &= \hat{B} u, \\ \hat{\mathbf{y}} &= \hat{C} \hat{\mathbf{e}}, \end{aligned}$$

where $\hat{A}_{\mu_0}, \hat{A}_{\varepsilon_0}, \hat{A} \in \mathbb{R}^{r \times r}$ with $r \ll N$ and $\|\mathbf{y} - \hat{\mathbf{y}}\|$ small.

4 Numerical Results Concerning the Stochastic Collocation Approach

As a benchmark we consider a coplanar waveguide with dielectric overlay, see Figure 1. The model consists of three perfectly conducting striplines situated at a height of 10mm in a shielded box with perfect electric conductor (PEC) boundary. The system is excited at one of the discrete ports and the output is taken at the other one.

Below a height of 15mm there is a substrate with $\varepsilon_r^1 \approx 4.4$ and $\sigma^1 \approx 0.02S/m$, above there is air with

$\varepsilon_r^2 \approx 1.07$ and $\sigma^2 \approx 0.01S/m$, while $\mu_r \approx 1$ within the whole box. The variance of each parameter is approximately 1% of the expected value.

The system is treated as a system with 5 uncertain parameters, which leads to the affine discretized form

$$\mu_r A_{\mu_0} \mathbf{e} + (\varepsilon_r^1 A_{\varepsilon_0}^1 + \varepsilon_r^2 A_{\varepsilon_0}^2) \ddot{\mathbf{e}} + (\sigma^1 A^1 + \sigma^2 A^2) \dot{\mathbf{e}} = B u, \\ \mathbf{y} = C \mathbf{e}.$$

The discretization is done in FEniCS by use of Nédélec finite elements and the Stroud-based collocation is implemented in MATLAB[®]. Since the used discretization has only 18755 degrees of freedom, there is no model order reduction used up to now.

The Stroud-based collocation uses only 10 supporting points and the computation requires less than a minute. To verify the accuracy, the results are compared with a Monte Carlo simulation which operates on 10000 interpolation points. This takes several hours. Using the frequency $\omega = 0.6 \cdot 10^9$ we achieve the following relative errors for the expected value of \mathbf{e} and \mathbf{y}

$$err_{rel, \mathbb{E}(\mathbf{e})} = 0.0038\% \quad \text{and} \quad err_{rel, \mathbb{E}(\mathbf{y})} = 0.0042\%.$$

Considering the fact that we use only 10 Stroud points the results are satisfactory. To achieve more accuracy one could use, e. g., a lot more sparse grid points, which would be much more expensive. For this reason and for systems of higher dimension we need MOR.

Acknowledgement. The work reported in this paper was supported by the German Federal Ministry of Education and Research (BMBF), grant no. 03MS613A. Responsibility for the contents of this publication rests with the authors.

References

1. I. Babuska, F. Nobile, and R. Tempone. A Stochastic Collocation Method for Elliptic Partial Differential Equations with Random Input Data. *SIAM Review*, 52(2):317–355, 2010.
2. H. Bagci, A. C. Yücel, J. S. Hesthaven, and E. Michielssen. A Fast Stroud-Based Collocation Method for Statistically Characterizing EMI/EMC Phenomena on Complex Platforms. *IEEE Transactions on Electromagnetic Compatibility*, 51(2):301–311, 2009.
3. U. Baur, C. A. Beattie, P. Benner, and S. Gugercin. Interpolatory projection methods for parameterized model reduction. 31(5):2489–2518, 2011.
4. H. G. Matthies. *Encyclopedia of Computational Mechanics*, volume 1, chapter Uncertainty Quantification with Stochastic Finite Elements. John Wiley and Sons, 2007.
5. <http://www.moresim4nano.org>.
6. C. Schwab and C. J. Gittelson. Sparse tensor discretizations of high-dimensional parametric and stochastic PDEs. *Acta Numerica*, 20:291–467, 2011.
7. A. H. Stroud. Remarks on the Disposition of Points in Numerical Integration Formulas. *Mathematical Tables and Other Aids to Computation*, 11(60):257–261, 1957.

Automatic model order reduction by moment-matching according to an efficient output error bound

Lihong Feng and Peter Benner

Max Planck Institute for Dynamics of Complex Technical Systems, Germany feng@mpi-magdeburg.mpg.de,
benner@mpi-magdeburg.mpg.de

Summary. An output error bound is proposed for model order reduction of linear time invariant (LTI) systems. According to the error bound, the model order reduction method based on moment-matching (moment-matching MOR) can be implemented by selecting the expansion points adaptively, such that the reduced model can be obtained automatically. The error bound is an estimation for the error between the transfer function of the original system and that of the reduced model. Simulation results show the efficiency of the error bound.

1 Introduction

Consider an LTI system

$$\begin{aligned} E \frac{dx}{dt} &= Ax + Bu(t), \\ y(t) &= Cx. \end{aligned} \quad (1)$$

If we use moment-matching MOR, usually we apply the Laplace transform to (1), and get

$$\begin{aligned} sEx(s) - Ax(s) &= Bu(s), \\ y(s) &= Cx(s). \end{aligned} \quad (2)$$

From the series expansion of $x(s)$,

$$x(s) = \sum_{i=0}^{\infty} [-(s_0E - A)^{-1}E]^i (s_0E - A)^{-1}BU(s)(s - s_0)^i, \quad (3)$$

the matrix V is computed as

$$\text{range}\{V\} = \text{span}\{\tilde{B}(s_0), \tilde{A}(s_0)\tilde{B}(s_0), \dots, (\tilde{A}(s_0))^q\tilde{B}(s_0)\}, \quad (4)$$

where $\tilde{A}(s_0) = (s_0E - A)^{-1}E$, $\tilde{B}(s_0) = (s_0E - A)^{-1}B$ and $q \ll n$. The reduced model is

$$\begin{aligned} V^T E V \frac{dz}{dt} &= V^T A V z + V^T B u(t), \\ y(t) &= C V z. \end{aligned} \quad (5)$$

Instead of using single-point expansion s_0 , one can use multi-point expansion to compute V . That is, choosing multiple expansion points s_i , $i = 0, 1, \dots, m$, we compute each matrix V_i corresponding to s_i according to (4). Finally, $V = \text{orthogonalize}\{V_1, \dots, V_m\}$.

By using multi-point expansion, the error of the reduced model can be kept small in a wider frequency range. At present, how to adaptively choose the expansion points s_i is under investigation using several

points of view. We aim to derive an error bound for the transfer function $\hat{H}(s)$ of the reduced model, such that the expansion points can be adaptively chosen according to the error bound. Since the transfer function can be considered as the impulse response of the LTI system in frequency domain, the error bound can be considered as the output error bound in frequency domain.

The error bound is motivated by the idea in [1], where an output error bound for the weak form of a parametrized Partial Differential Equation (PDE) is derived. The error bound in [1] is obtained in the function space for the weak form, where all the parameters in the PDE must be real variables. Since moment-matching MOR directly deal with the discretized system (2) in the vector space, it is best that an error bound is derived in the vector space rather than in the function space. Moreover, system (2) can be seen as a parametrized system with parameter s being a complex variable.

In summary, in order to obtain the error bound for $\hat{H}(s)$, the method in [1] is not valid due to the challenges below:

1. The error bound should be derived in the vector space C^n .
2. The error bound should be valid for complex parameters.

Method for deriving the output error bound must be adapted in order to meet the above two challenges.

2 Output Error Bound for an LTI System

We first present the analysis for single-input single-output (SISO) systems, then extend the result to multiple-input multiple-output (MIMO) systems.

We assume that the matrix $G(s) = sE - A$ satisfies

$$\text{Re}(x^* G(s) x) \geq \alpha(s) (x^* \tilde{A} x), \quad (6)$$

and

$$\text{Im}(x^* G(s) x) \geq \gamma(s) (x^* \tilde{A} x), \quad (7)$$

where $\text{Re}(\cdot)$ means the real part of $x^* G(s) x$, and $\text{Im}(\cdot)$ is the imaginary part. $\alpha(s), \gamma(s): C \rightarrow R_+$ may depend on the parameter s . The matrix $\tilde{A} = s_0E - A$ is

assumed to be symmetric, positive definite, which is satisfied by many engineering problems.

For systems with $C \neq B^T$, we need to define a dual system in frequency domain,

$$\begin{aligned} \bar{s}E^* \mathbf{x}^{du}(s) - A^* \mathbf{x}^{du}(s) &= -C^*, \\ y^{du} &= B^* \mathbf{x}^{du}(s). \end{aligned} \quad (8)$$

Let $r^{pr}(s) = B - G(s)\hat{\mathbf{x}}(s)$ be the residual for the primal system in (2), and $r^{du}(s) = -C^* - (\bar{s}E^* - A^*)\hat{\mathbf{x}}^{du}(s) = G^*(s)\hat{\mathbf{x}}^{du}(s)$ be the residual for the dual system. We will show that $r^{pr}(s)$ can be represented through a vector $\hat{\mathbf{e}}^{pr} \in \mathbb{C}^n$, and $r^{du}(s)$ can be represented through a vector $\hat{\mathbf{e}}^{du} \in \mathbb{C}^n$.

Define a function $f^{pr}(\xi) = \xi^* r^{pr}(s) : \mathbb{C}^n \rightarrow \mathbb{C}$ for the primal system. From the Riez representation theorem, there exists a unique vector $\hat{\mathbf{e}}^{pr} \in \mathbb{C}^n$, such that

$$f^{pr}(\xi) = \langle \hat{\mathbf{e}}^{pr}, \xi \rangle = \xi^* \tilde{A} \hat{\mathbf{e}}^{pr}. \quad (9)$$

We also define a function $f^{du}(\xi) = (r^{du}(s))^* \xi : \mathbb{C}^n \rightarrow \mathbb{C}$. Similarly, there exists a unique vector $\hat{\mathbf{e}}^{du} \in \mathbb{C}^n$, such that

$$f^{du}(\xi) = \langle \hat{\mathbf{e}}^{du}, \xi \rangle = \xi^* \tilde{A} \hat{\mathbf{e}}^{du}. \quad (10)$$

Theorem 1. *If the reduced model of the primal system (2) and that of the dual system (8) is computed by the same projection matrix V , the matrices E , A are symmetric, and $G(s)$ satisfies (6), and (7), then $-S_R - \beta_R \leq \text{Re}(H(s) - \hat{H}(s)) \leq S_R - \beta_R$ and $-S_I - \beta_I \leq \text{Im}(H(s) - \hat{H}(s)) \leq S_I - \beta_I$. Here, $\beta_R = \frac{1}{4\alpha(s)}(\hat{\mathbf{e}}^{pr})^* \tilde{A} \hat{\mathbf{e}}^{du} + \frac{1}{4\alpha(s)}(\hat{\mathbf{e}}^{du})^* \tilde{A} \hat{\mathbf{e}}^{pr}$, $\beta_I = \frac{\alpha(s)}{\gamma(s)}\beta_R$, $S_R = \frac{1}{2\alpha(s)}\sqrt{(\hat{\mathbf{e}}^{pr})^* \tilde{A} \hat{\mathbf{e}}^{pr} \sqrt{(\hat{\mathbf{e}}^{du})^* \tilde{A} \hat{\mathbf{e}}^{du}}}$, $S_I = \frac{\alpha(s)}{\gamma(s)}S_R$.*

From Theorem 1, we get the error bound,

$$|H(s) - \hat{H}(s)| \leq \sqrt{B_R^2 + B_I^2} := \Delta(s), \quad (11)$$

where $B_R = \max\{|S_R - \beta_R|, |S_R + \beta_R|\}$, $B_I = \max\{|S_I - \beta_I|, |S_I + \beta_I|\}$. The error bound $\Delta(s)$ can be computed cheaply though it is dependent on the parameter s , because the main computational part for $\Delta(s)$ is independent of s , which can be implemented off-line. If relative error is preferred, one should use $\Delta_{re}(s) = \Delta(s)/\hat{H}(s)$. For MIMO systems, assume $H_{ij}(s)$ is the transfer function corresponding to the i th input and j th output. For each pair of i, j , we can compute $\Delta_{ij}(s)$. The error bound $\Delta(s)$ can be defined as $\Delta(s) = \max_{ij} \Delta_{ij}(s)$.

3 Adaptively Choosing Expansion Points

From the construction of the error estimator $\Delta(s)$, the projection matrix V can be constructed by the algorithm as below,

Algorithm 1 $V = []$;

Choose initial s^* ;

$\varepsilon = 1$;

While $\varepsilon \geq \varepsilon_{tol}$ ($\varepsilon_{tol} < 1$ is the error tolerance.)

$\text{range}(V) = \text{range}(V) + \text{span}\{\tilde{B}(s^*), \tilde{A}(s^*)\tilde{B}, \dots, \tilde{A}^q(s^*)\tilde{B}\}$;

$s^* = \arg \max_{s \in \Xi_{train}} \Delta(s)$; (Ξ_{train} is the sample space for s .)

$\varepsilon = \Delta(s^*)$;

End While

4 Simulation Results

We take two examples to support the theoretical analysis above. One example is a spiral inductor, a SISO system; the other is an optical filter, a system with 5 outputs. Both examples are taken from the Oberwolfach Benchmark Collection (URL: <http://simulation.uni-freiburg.de/downloads/benchmark>).

Define $\varepsilon_{max} = \max_{ij} \max_k |H_{ij}(s_k) - \hat{H}_{ij}(s_k)| / |\hat{H}_{ij}(s_k)|$

as the maximal true error of the current $\hat{H}(s)$ over 2000 sample points, and it is used as the error of the current reduced model. Results of Algorithm 1 for the spiral inductor is listed in Table 1. r is the order of the reduced model. After 4 iterations, four expansion points have been selected, a reduced model with accuracy $O(10^{-8})$ is obtained. Figure 1 plots ε_{max} vs. the error bound $\Delta_{re}(s)$ for the multi-output system, showing $\Delta_{re}(s)$ performs well, especially at the latter iterations.

Table 1. Spiral inductor $q = 5$, $\varepsilon_{tol} = 10^{-3}$, $n = 1434$, $r = 24$

iteration	$s^*/(j\omega)$	ε_{max}	$\Delta_{re}(s^*)$
1	1×10^{10}	0.30	86.99
2	3.43×10^7	0.04	16.15
3	3.39×10^8	7×10^{-5}	6×10^{-3}
4	1.41×10^9	7.73×10^{-8}	7.50×10^{-6}

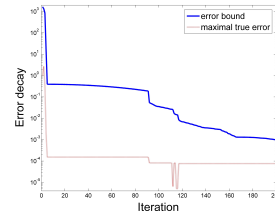


Fig. 1. Optical filter, $q = 1$, $\varepsilon_{tol} = 10^{-3}$, $n = 1668$, $r = 21$.

References

1. D. V. Rovas. *Reduced-Basis Output Bound Methods for Parametrized Partial Differential Equations*. PhD thesis, Massachusetts Institute of Technology, 2003.

Reduced order modeling of ODE-PDE networks

Michael Hinze¹ and Ulrich Matthes¹

Department of Mathematics, University of Hamburg, Bundesstr. 55, 20146 Hamburg, Germany,
michael.hinze@uni-hamburg.de, ulrich.matthes@math.uni-hamburg.de

Summary. We propose a model order reduction (MOR) approach for networks containing simple and complex components modeled by linear ODE and nonlinear PDE systems respectively. These systems are coupled through the network topology using the Kirchhoff laws. We consider as application MOR for electrical networks, where semiconductors form the complex components. POD combined with discrete empirical interpolation (DEIM) and passivity-preserving balanced truncation methods for electrical circuits (PABTEC) can be used to reduce the dimension of the whole model.

1 Introduction

We propose a simulation-based MOR approach for the reduction of networks consisting of (many) simple and (only few) complex components. We assume that the simple and complex components are modeled by systems of linear ODEs and nonlinear PDEs, respectively, which are coupled through the network topology using the Kirchhoff laws.

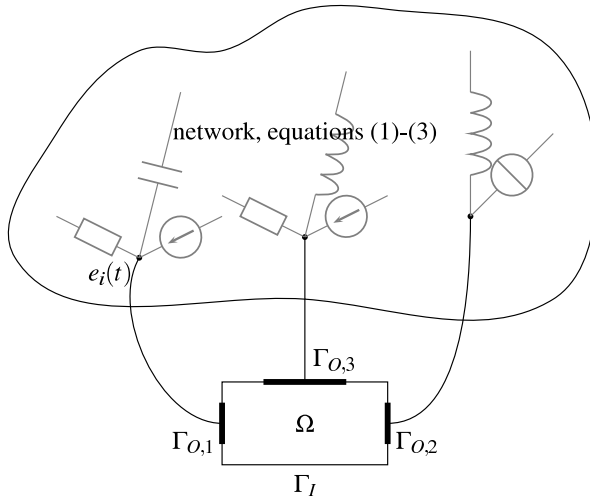


Fig. 1. Sketch of a coupled system with one semiconductor forming the complex component.

We consider electrical networks where the simple components consist of resistors, capacitors, voltage sources, current sources, and inductors, and the complex components are formed by e.g. semi-conductors, see Fig. 1. The overall system then is represented by

a nonlinear PDAE system, see e.g. [2, 5]. We address the following issues:

1. construction of reduced order models for the complex components
2. reduction of the complete network while retaining the structure of a network

2 Modeling of an electrical network

In electrical networks resistors, capacitors, and inductors form the simple components which in general are modeled by linear ODEs. Complex components are given by e.g. semiconductors which are modeled by PDE systems. Considering additional voltage and current sources the overall network can be modeled by a partial-differential algebraic equation (PDAE) which is obtained as follows. First the network containing only the simple components is modeled by a differential algebraic equation (DAE) which is obtained by a modified nodal analysis (MNA), including the Ohmic contacts Γ_O of the semiconductors as network nodes, see Fig. 1. Denoting by e the node potentials and by j_L , j_V , and j_S the currents of inductive, voltage source, and semiconductor branches, the DAE reads (see [5, 9, 12])

$$A_C \frac{d}{dt} q_C(A_C^\top e, t) + A_R g(A_R^\top e, t) + A_L j_L + A_V j_V + A_S j_S = -A_I i_s(t), \quad (1)$$

$$\frac{d}{dt} \phi_L(j_L, t) - A_L^\top e = 0, \quad (2)$$

$$A_V^\top e = v_s(t). \quad (3)$$

Here, the incidence matrix $A = [A_R, A_C, A_L, A_V, A_S, A_I]$ represents the network topology, e.g. at each non mass node i , $a_{ij} = 1$ if the branch j leaves node i and $a_{ij} = -1$ if the branch j enters node i and $a_{ij} = 0$ elsewhere. In particular the matrix A_S denotes the semiconductor incidence matrix. The functions q_C , g and ϕ_L are continuously differentiable defining the voltage-current relations of the network components. The continuous functions v_s and i_s are the voltage and current sources. For details we refer to [7].

In a second step the semiconductors are modeled by PDE systems, which are then coupled to the DAE of the network, see e.g. [1, 2] and the references cited

there. Further details of our approach are given in [7]. The analytical and numerical analysis of PDAE systems of the presented form is subject to current research, see [2, 4, 11, 12].

3 Reduced order models for complex components

We assume that every complex component is modeled by a time-dependent PDE system which is amenable to a numerical treatment with Galerkin methods. After appropriate spatial discretization the method of lines then yields a large, nonlinear ODE system representing the spatially discrete complex component. This nonlinear ODE system now represents the complex component in the network. The reduction of the complex components is based on simulation-based MOR with proper orthogonal decomposition (POD). In this approach time snapshots of the complex components are extracted from snapshots of the simulation of the complete network. POD for the complex component then is performed using the extracted parts of the snapshots. In combination with the direct empirical interpolation method (DEIM) this now delivers low dimensional, nonlinear surrogate models for the complex components, see [6] for details. It is an important feature of this reduction technique that it delivers distinct reduced order models for the same complex component at different locations in the network.

4 Reduction of the whole network

The overall network with simple and complex components is represented by a nonlinear DAE system, where the linear and nonlinear part stems from the simple and spatially-discrete complex components respectively. The reduction for the complex components is performed as in the previous section, whereas the linear part is approximated by a reduced order linear model of lower dimension. In the case of an electrical network the passivity preserving reduction method (MATLAB Toolbox) PABTEC [8, 10] is used for the reduction of the linear part of the network. Finally, the reduced order models obtained with the approaches sketched are recoupled appropriately. The obtained large and sparse nonlinear DAE system as well as the small and dense reduced-order model are integrated using the DASPK software package [3] based on a BDF method, where the nonlinear equations are solved using Newton's method.

The results obtained demonstrate that the recoupling of the PABTEC reduced order model with the POD-MOR model for the semiconductor delivers an overall reduced-order model for the circuit-device system which allows significantly faster simulations (the

speedup-factor is about 20) while keeping the relative errors below 10%.

Finally we sketch how our approach can be applied to parametrized MOR extending the techniques of [7].

Acknowledgement. The work reported in this paper was supported by the German Federal Ministry of Education and Research (BMBF), grant no. 03HIPAE5. Responsibility for the contents of this publication rests with the authors.

References

1. Anile, A., Mascali, G., Romano, V.: Mathematical problems in semiconductor physics. Lectures given at the C. I. M. E. summer school, Cetraro, Italy, July 15–22, 1998. Lecture Notes in Mathematics. Berlin: Springer (2003)
2. Bodestedt, M., Tischendorf, C.: PDAE models of integrated circuits and index analysis. *Math. Comput. Model. Dyn. Syst.* **13**(1), 1–17 (2007)
3. Brown, P., Hindmarsh, A., Petzold, A.: A description of DASPK: A solver for large-scale differential-algebraic systems. Tech. rep., *Lawrence Livermore National Report UCRL* (1992)
4. Günther, M.: Partielle differential-algebraische Systeme in der numerischen Zeitbereichsanalyse elektrischer Schaltungen. *VDI Fortschritts-Berichte, Reihe 20, Rechnerunterstützte Verfahren*, Nr. 343 (2001)
5. Günther, M., Feldmann, U., ter Maten, J.: Modelling and discretization of circuit problems. Schilders, W. H. A. (ed.) et al., *Handbook of numerical analysis. Vol XIII. Special volume: Numerical methods in electromagnetics*. Amsterdam: Elsevier/North Holland. *Handbook of Numerical Analysis* 13, 523–629 (2005)
6. Hinze, M., Kunkel, M.: Discrete empirical interpolation in pod model order reduction of drift-diffusion equations in electrical networks. *SCEE Proceedings 2010, Toulouse* (2010)
7. Hinze, M., Kunkel, M.: Residual based sampling in POD model order reduction of drift-diffusion equations in parametrized electrical networks. *ZAMM* 92:91–104 (2012)
8. Hinze, M., Kunkel, M., Steinbrecher, A., Stykel, T.: Model order reduction of coupled circuit-device systems. *Int. J. Numer. Model.* DOI: 10.1002/jnm.840 (2012)
9. Ho, C., Ruehli, A., Brennan, P.: The modified nodal approach to network analysis. *IEEE Trans. Circuits Syst.* **22**, 504–509 (1975)
10. Salih, H., Steinbrecher, A., Stykel, T.: MATLAB Toolbox PABTEC - A users guide. *Technical Report*. Tech. rep., Institut für Mathematik, Technische Universität Berlin, Germany (2011)
11. Selva Soto, M., Tischendorf, C.: Numerical analysis of DAEs from coupled circuit and semiconductor simulation. *Appl. Numer. Math.* **53**(2–4), 471–488 (2005)
12. Tischendorf, C.: Coupled Systems of Differential Algebraic and Partial Differential Equations in Circuit and Device Simulation. Habilitation thesis, Humboldt-University of Berlin (2003)

Index-aware model Order Reduction: LTI DAEs in electric networks

Nicodemus Banagaaya¹ and Wil Schilders¹

Dept. of Mathematics and Computer Science, Technische Universiteit Eindhoven, The Netherlands
n.banagaaya@tue.nl, w.h.a.schilders@tue.nl

Summary. Model order reduction (MOR) has been widely used in the electric networks but little has been done to reduce higher index differential algebraic equations (DAEs). Most methods first do an index reduction before reducing a higher DAEs but this can lead to loss of system physical properties. In this paper we present a new MOR method for DAEs called the index-aware MOR (IMOR) which can reduce higher index-2 system while preserving the index of the system.

1 Introduction

Consider a linear time invariant (LTI) DAE system:

$$Ex'(t) = Ax(t) + Bu, \quad x(0) = x_0, \quad (1a)$$

$$y(t) = C^T x(t), \quad (1b)$$

where $E, A \in \mathbb{R}^{n,n}$, $B \in \mathbb{R}^{n,m}$, $C \in \mathbb{R}^{n,\ell}$, $x(t) \in \mathbb{R}^n$ is the state vector, $u(t) \in \mathbb{R}^m$ is the input vector, $y(t) \in \mathbb{R}^\ell$ is the output vector and $x_0 \in \mathbb{R}^n$ must be a consistent initial value since E is singular. In many MOR methods [1] they always assume that $x_0 = 0$ which lead to a transfer function $H(s) = C^T(sE - A)^{-1}B$ if and only if matrix pencil $sE - A$ is regular. Unfortunately for the case of DAEs we cannot always have this freedom of choosing an arbitrary initial condition x_0 , in fact we cannot always obtain a transfer function especially for index greater than 1 as discussed in Sect. 2. This motivated us to propose a new MOR technique for DAEs called the IMOR method which takes care of this limitation [2, 3]. In this technique before we apply MOR we first decompose the DAE system into differential and algebraic parts using matrix and projector chains introduced by März [4] in 1996. We then use the existing MOR techniques such as the Krylov based methods on the differential part and develop new techniques for the algebraic part. This is done as follows: Assume (1a) is of tractability index μ , then it's projector and matrix chains can be written as, set $E_0 := E$, $A_0 := A$, then $E_{j+1} = E_j - A_j Q_j$, $A_{j+1} := A_j P_j$, $j \geq 0$, where $\text{Im} Q_j = \text{Ker} E_j$, $P_j = I_n - Q_j$. There exists μ such that E_μ is nonsingular while all E_j are singular for all $0 \leq j < \mu - 1$. Using these chains we can rewrite Equation (1a) as projected system of index- μ :

$$P_{\mu-1} \cdots P_0 x' + Q_0 x + \cdots + Q_{\mu-1} x = E_\mu^{-1} (A_\mu x + Bu) \quad (2)$$

In order to decompose higher index systems ($\mu > 1$), März [4] suggested an additional constraint $Q_j Q_i = 0$, $j > i$ on the projector construction. If this constraint holds then Equation (2) can be decomposed into differential and algebraic parts. However, the März decomposition leads to a decoupled system of dimension $(\mu + 1)n$. It does not even preserve the stability the DAE system. This motivated us to modify the März decomposition using special basis vectors as presented in papers [3] and [2] for the case of index-1 and index-2 respectively. Our decomposition leads to a decoupled system of the same dimension as that of the DAE system. Then we apply Krylov methods on the differential part and constructed subspaces to reduce the algebraic parts. In Sect. 2 we briefly discuss the IMOR method for index-2 systems (IMOR-2) more details can be found in [2].

2 Index-aware MOR for index-2 systems

Assume Equation (1a) is an index-2 system this implies $\mu = 2$. We observed that for higher index DAEs there is a possibility of obtaining a purely algebraic decoupled system depending on the nature of spectrum of the matrix pencil $\sigma(E, A) = \sigma_f(E, A) \cup \sigma_\infty(E, A)$, where $\sigma_f(E, A)$ and $\sigma_\infty(E, A)$ is the set of the finite and infinite eigenvalues respectively. This happens when matrix spectrum has only infinite eigenvalues, i.e. $\sigma_f(E, A) = \emptyset$. Thus higher index DAEs can be decomposed into two ways. Due to space we are going to only discuss the case when $\sigma_f(E, A) \neq \emptyset$ the other case can be found in our paper [2]. We now assume matrix pencil of Equation (1a) has atleast one finite eigenvalue. We then construct basis vectors (p, q) in \mathbb{R}^n with their inversion $(p_*, q_*)^T$ for the projectors P_0 and Q_0 respectively where $p \in \mathbb{R}^{n,n_0}$, $q \in \mathbb{R}^{n,k_0}$. This leads to a theorem below.

Theorem 1. Let $P_{01} = p_*^T P_1 p$, $Q_{01} = p_*^T Q_1 p$, then $P_{01}, Q_{01} \in \mathbb{R}^{n_0, n_0}$ are projectors in \mathbb{R}^{n_0} provided the constraint condition $Q_1 Q_0 = 0$ holds.

Next, we construct another basis matrix (p_{01}, q_{01}) in \mathbb{R}^{n_0} made of n_{01} independent columns of projector P_{01} and k_1 independent columns of its complementary projector Q_{01} such that $n_0 = n_{01} + k_1$ and it's inverse can be denoted by $(p_{01}^*, q_{01}^*)^T$. Then Equation (1) can be decomposed as:

$$\xi_p' = A_p \xi_p + B_p u, \quad (3a)$$

$$\xi_{q,1} = A_{q,1} \xi_p + B_{q,1} u, \quad (3b)$$

$$\xi_{q,0} = A_{q,0} \xi_p + B_{q,0} u + A_{q,01} \xi_{q,1}', \quad (3c)$$

$$y = C_p^T \xi_p + C_{q,1}^T \xi_{q,1} + C_{q,0}^T \xi_{q,0}, \quad (3d)$$

where

$$\begin{aligned} A_p &:= p_{01}^{*T} p_0^{*T} E_2^{-1} A_2 p_0 p_{01}, & B_p &:= p_{01}^{*T} p_0^{*T} E_2^{-1} B, \\ A_{q,1} &:= q_{01}^{*T} p_0^{*T} E_2^{-1} A_2 p_0 p_{01}, & B_{q,1} &:= q_{01}^{*T} p_0^{*T} E_2^{-1} B, \\ A_{q,0} &:= q_0^{*T} P_1 E_2^{-1} A_2 p_0 p_{01}, & B_{q,0} &:= q_0^{*T} P_1 E_2^{-1} B, \\ A_{q,01} &:= q_0^{*T} Q_1 p_0 q_{01}, & C_p &:= p_{01}^T p_0^T C \in \mathbb{R}^{n_{01}, \ell}, \\ C_{q,1} &:= q_{01}^T p_0^T C \in \mathbb{R}^{k_1, \ell}, & C_{q,0} &:= q_0^T C \in \mathbb{R}^{k_0, \ell}. \end{aligned}$$

Equations (3a), (3b) and (3c) are of dimension n_{01}, k_1 and k_0 respectively, where $n = n_{01} + k_1 + k_0$. System (3) preserves stability of the DAE system (1) since it can be proved that $\sigma(A_p) = \sigma_f(E, A)$. If we take the Laplace transform of (3) and set $\xi_p(0) = 0$ then we obtain

$$Y(s) = [H_p(s) + H_{q,1}(s) + H_{q,0}(s)] U(s) + H_{q,0}(0),$$

where $H_p(s) = C_p^T (sI_{n_0} - A_p)^{-1} B_p$, $H_{q,1}(s) = C_{q,1}^T [A_{q,1}(sI_{n_0} - A_p)^{-1} B_p + B_{q,1}]$, $H_{q,0}(s) = C_{q,0}^T [(A_{q,0} + sA_{q,01}A_{q,1})(sI_{n_0} - A_p)^{-1} B_p] + C_{q,0}^T [B_{q,0} + sA_{q,01}B_{q,1}]$, $H_{q,0}(0) = -C_{q,0}^T A_{q,01} B_{q,1} u(0)$. Thus not always we can obtain the transfer function of index 2 systems for arbitrary input vector u unless $H_{q,0}(0) = 0 \Rightarrow Y(s) = H(s)U(s)$. We can now apply IMOR-2 method as follows: If we choose the expansion point $s_0 \in \mathbb{C} \setminus \sigma(A_p)$, we construct a Krylov-subspace generated by $M_p := -(s_0 I_{n_0} - A_p)^{-1}$ and $R_p := (s_0 I_{n_0} - A_p)^{-1} B_p$. Then, $V_{p_r} := \text{orth}(\kappa_r(M_p, R_p))$, $r \leq n_{01}$. We then use V_{p_r} to construct the subspace $\mathcal{V}_{q,1} = \text{span}(B_{q,1}, A_{q,1} V_{p_r})$ and its orthonormal matrix is denoted by $V_{q_{\tau_1},1} = \text{orth}(\mathcal{V}_{q,1})$, $\tau_1 \leq \min((r+1)m, \dim(\mathcal{V}_{q_{\tau_1},1}))$. We finally construct subspace $\mathcal{V}_{q,0} = \text{Span}\{\mathcal{V}_{Q_1}, \mathcal{V}_{Q_2}, \mathcal{V}_{Q_3}\}$, where $\mathcal{V}_{Q_1} = A_{q,0} R_p + B_{q,0} + s_0(A_{q,01} A_{q,1} R_p + A_{q,01} B_{q,1})$, $\mathcal{V}_{Q_2} = A_{q,01} B_{q,1}$, $\mathcal{V}_{Q_3} = [(A_{q,0} + s_0 A_{q,01} A_{q,1}) M_p + A_{q,01} A_{q,1}] V_{p_r}$ and its orthonormal matrix is denoted by $V_{q_{\tau_0},0} = \text{orth}(\mathcal{V}_{q,0})$, where $\tau_0 \leq \min((r+2)m, \dim(\mathcal{V}_{q_{\tau_0},0}))$. We can now use the orthonormal matrices $V_{p_r}, V_{q_{\tau_1},1}$ and $V_{q_{\tau_0},0}$ to reduce the dimension of the subsystems (3a), (3b) and (3c) respectively as consequence the dimension of the decoupled system (3) is also reduced. Hence, if we substitute $\xi_p = V_{p_r} \xi_{p_r}$, $\xi_{q,1} = V_{q_{\tau_1},1} \xi_{q_{\tau_1},1}$, $\xi_{q,0} = V_{q_{\tau_0},0} \xi_{q_{\tau_0},0}$, into system (3) and simplifying we can obtain a reduced model of DAE system (1) which will call the IMOR-2 model.

3 Numerical results

We used an index -2 test system called S8OPI in [5] which is a large power system RLC model. It's a

single-input single-output (SISO) system of dimension 4182. We applied the IMOR-2 method using $s_0 = j10^3$. We obtained a reduced model of total dimension 219 as shown in Table 1. We observed that the magnitude of the transfer reduced model coincides with that of the original model at low frequencies with very small error as shown in Fig. 1. We have seen that

Table 1. Dimension of the Original and Reduced model

Models	Dimension		
	n_{01}	k_1	k_0
Original Model	4028	35	119
Reduced Model	170	1	48

the IMOR-2 method leads to good reduced model and can be used on any index-2 system.

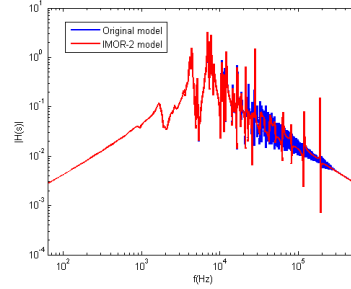


Fig. 1. Magnitude of the transfer functions

Acknowledgement. This work is funded by NWO.

References

1. W. Schilders, H. Van der Vorst and J. Rommes, *Model Order Reduction: Theory, Research Aspects and Applications*, Springer-Verlag, Berlin Heidelberg, 2008.
2. G. Ali, N. Banagaaya, W.H.T. Schilders and C. Tischendorf, *Index-aware model order reduction for index-2 differential-algebraic equations*, In preparation, 2012.
3. G. Ali, N. Banagaaya, W.H.T. Schilders and C. Tischendorf, *Index-aware model order reduction for differential-algebraic equations*. *Mathematics of Computation*, Submitted, 2011.
4. R. März, *Canonical Projectors for Linear Differential Algebraic Equations*, *Computers Math. Applic.* 31:121–135, 1996.
5. F.D. Freitas, N. Martins, S.L. Varrichio, J. Rommes and F.C. Véliz, *Reduced-Order Transfer Matrices From Network Descriptor Models of Electric Power Grids*, *Ieee transactions on power systems*, 26:1905–1919, 2011.

Adaptive-order rational Arnoldi method for Maxwell's equations

Matthias Bollhöfer¹ and André Bodendiek²

¹ TU Braunschweig, Institut Computational Mathematics, AG Numerik, Pockelsstraße 14, 38104 Braunschweig
m.bollhoefer@tu-bs.de

² TU Braunschweig, Institut Computational Mathematics, AG Numerik, Pockelsstraße 14, 38104 Braunschweig
a.bodendiek@tu-bs.de

Summary. We present some new results for model order reduction of Maxwell's equations using an adaptive-order rational Arnoldi method. In this context, we introduce a new adaptive choice of expansion points.

1 Introduction

In view of the increasing frequency range and the progressing miniaturization, the analysis of parasitic effects has become an important task for the development of integrated circuits. The appearing phenomena, e.g. crosstalk or signal delay, are usually modelled using Maxwell's equations.

Since high-dimensional model problems are often necessary for accurate simulations, model order reduction techniques are an important tool for the proper and fast analysis of these phenomena.

1.1 Model Order Reduction

We will apply model order reduction for linear time-invariant descriptor systems

$$\begin{aligned} \mathcal{E}\dot{x}(t) &= \mathcal{A}x(t) + \mathcal{B}u(t), \\ y(t) &= \mathcal{C}x(t), \end{aligned} \quad (1)$$

where $\mathcal{E}, \mathcal{A} \in \mathbb{R}^{N \times N}$, $\mathcal{B} \in \mathbb{R}^{N \times m}$ and $\mathcal{C} \in \mathbb{R}^{p \times N}$. Furthermore, $u(t) \in \mathbb{R}^m$ and $y(t) \in \mathbb{R}^p$ denote the input and the output of the descriptor system, respectively. In general, descriptor systems are associated with the transfer function

$$\mathcal{H}(s) = \mathcal{C}(s\mathcal{E} - \mathcal{A})^{-1}\mathcal{B}.$$

The reduced order model will be obtained from the projection of the original model (1) onto a proper subspace $V_n \in \mathbb{R}^{N \times n}$ with $n \ll N$, i.e.

$$\begin{aligned} V_n^T \mathcal{E} V_n \dot{\tilde{x}}(t) &= V_n^T \mathcal{A} V_n \tilde{x}(t) + V_n^T \mathcal{B} u(t), \\ y(t) &= \mathcal{C} V_n \tilde{x}(t). \end{aligned}$$

The computation of the subspace V_n should result in a small error

$$\|\mathcal{H}(s) - \tilde{\mathcal{H}}(s)\|$$

in terms of a proper norm, where $\tilde{\mathcal{H}}(s)$ denotes the transfer function of the reduced order model.

2 Adaptive Krylov subspace methods

The idea of Krylov subspace methods for model reduction, e.g. [4], results from the expansion of the transfer function

$$\mathcal{H}(s) = \sum_{j=0}^{\infty} Y^{(j)}(s_i)(s - s_i)^j,$$

where $S := \{s_1, \dots, s_k\}$ denotes a given set of expansion points and $Y^{(j)}(s_i) = \mathcal{C}^T X^{(j)}(s_i)$ with

$$X^{(j)}(s_i) = [-(s_i\mathcal{E} - \mathcal{A})^{-1}\mathcal{E}]^j (s_i\mathcal{E} - \mathcal{A})^{-1}\mathcal{B}.$$

The orthogonal columns of V_n span the same subspace as

$$[X^{(0)}(s_1), \dots, X^{(j_1)}(s_1), \dots, X^{(j_k)}(s_k)].$$

In [4], the authors present an adaptive choice for the size of the Krylov subspaces $X^{(j)}(s_i)$ applying the rational Arnoldi method. Assuming $Y^{(j)}(s_i) = \hat{Y}^{(j)}(s_i)$ for all $j = 0, \dots, \hat{j}_{i-1}$ and $s_i \in S$, the Krylov subspace of the expansion point $s_i \in S$ with

$$\max_{s_i \in S} |Y^{(\hat{j}_i)}(s_i) - \hat{Y}^{(\hat{j}_i)}(s_i)|$$

is increased by one additional vector in each iteration step. Here, $\hat{Y}^{(j)}(s_i)$ denotes the j -th output moment of the reduced order model.

The remaining problem of the adaptive-order rational Arnoldi method (AORA) consists of the adequate choice of the expansion points.

3 AORA with adaptive point selection

We will present a combination of the AORA method and an adaptive expansion point selection. In detail, from the subsequently computed reduced order models using the AORA method new expansion points are determined, until a certain tolerance is reached. The aim of the adaptive expansion point selection consists of the computation of a reduced order model, which offers a good approximation for the whole frequency range.

For the definition of an adequate measurement of the

error $\varepsilon_m = \|\mathcal{H}(s) - \hat{\mathcal{H}}_m(s)\|$, e.g. [3], we define the approximation

$$\hat{\varepsilon}_m = \sum_{l=1}^m 2^{l-m} \frac{\|\hat{\mathcal{H}}_l(s) - \hat{\mathcal{H}}_{l-1}(s)\|}{\|\hat{\mathcal{H}}_l(s)\|}, \quad (2)$$

where $\hat{\mathcal{H}}_{k-1}$ and $\hat{\mathcal{H}}_k$ denote transfer functions of reduced order models obtained from the AORA method. Since this definition does not give a hint, whether $\hat{\varepsilon}_m$ remains small due to convergence or stagnation, we will add one more expansion point in each iteration step.

3.1 Point selection for Maxwell's equations

Due to the high-frequency model problems with the frequency range $\mathcal{I} = [f_{\min}, f_{\max}]$ the first two expansion points are always defined via $s_1 = if_{\min}$ and $s_2 = if_{\max}$, where i denotes the imaginary unit. Furthermore, all expansion points are purely imaginary. Initially, we usually choose $s_1 = if_{\min}$, $s_2 = if_{\max}$ and $s_3 = i(f_{\min} + f_{\max})/2$ as the first set of expansion points S_0 .

In the $(k+1)$ -th iteration step, the expansion point $s_{k+1} = 2\pi if_{k+1}$ is determined, such that

$$s_{k+1} = \arg \max_s \frac{\|\hat{\mathcal{H}}_k(s) - \hat{\mathcal{H}}_{k-1}(s)\|}{\|\hat{\mathcal{H}}_k(s)\|}. \quad (3)$$

Specially, the error during the $(k+1)$ -th iteration step (3) is computed alternatingly on the intervals $\mathcal{I}_1 = [f_{\min}, (f_{\min} + f_{\max})/2]$ and $\mathcal{I}_2 = [(f_{\min} + f_{\max})/2, f_{\max}]$. If the error for the given interval \mathcal{I}_1 or \mathcal{I}_2 is less than a given tolerance $\delta > 0$, we switch back to the other interval and determine a new expansion point. This new expansion point should have a certain distance to previous expansion points from this interval. Finally, the algorithm terminates, if the global approximation error $\hat{\varepsilon}_k$ reached a given tolerance or the error during the $(k+1)$ -th iteration step (3) is less than $\delta > 0$ for both intervals \mathcal{I}_1 and \mathcal{I}_2 .

4 Numerical results

Some numerical results are presented for a coplanar waveguide with a dielectric overlay, where the transmission line is surrounded by two layers of multilayer board. The single input, single output model problem is enclosed in a metallic box and deals with the frequency range $[f_{\min}, f_{\max}] = [0.6, 3.0]$ GHz.

Here, the discretization of the model problem was carried out using the Finite Integration Technique, e.g. [5], with $N = 32924$ degrees of freedom.

Subsequently reduced order models $\hat{\mathcal{H}}_k(s)$ of dimension $n = 30$ have been computed until $\hat{\varepsilon}_m < 10^{-12}$ applying the tolerance $\delta = 7.0 \cdot 10^{-11}$. The expansion points in the i -th iteration step are denoted by S_i .

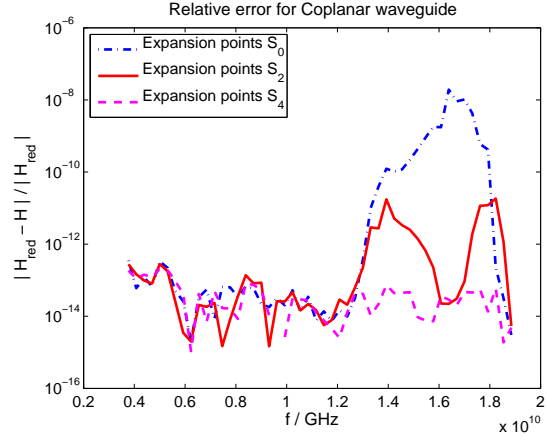


Fig. 1. Relative error for reduced order model with different sets of expansions points.

After four iteration steps the algorithm terminates due to the introduction of $\delta > 0$, where

$$\max_s \|\hat{\mathcal{H}}(s) - \mathcal{H}(s)\| \approx 1.5 \cdot 10^{-11}.$$

Future results will comprise of the application of incomplete multilevel factorizations for the computation of Krylov subspaces, e.g. [1], using previous preconditioning techniques for Helmholtz equations. Furthermore, existing adaptive expansion point selections, e.g. for machine tool simulations [2], will be applied to Maxwell's equations. In this context, a combination with the results from section 3 might be adopted.

Acknowledgement. The work is supported by the German Federal Ministry of Education and Research (BMBF), grant no. 03MS613B.

References

1. Matthias Bollhöfer and Yousef Saad. Multilevel Preconditioners Constructed From Inverse-Based ILUs. *SIAM Journal on Scientific Computing*, 27(5):1627–1650, 2006.
2. Heike Faßbender and Andreas Soppa. Machine Tool Simulation based on Reduced Order FE Models. In *Proceedings of the 2009 Conference of Mathematical Modelling*, pages 1266 – 1277, 2009.
3. E. Grimme and K. Gallivan. A Rational Lanczos Algorithm for Model Reduction II: Interpolation Point Selection. *Numerical Algorithms*, 12:33–63, 1998.
4. Heng-Jer Lee, Chia-Chi Chu, and Wu-Shiung Feng. An adaptive-order rational Arnoldi method for model-order reductions of linear time-invariant systems. *Linear Algebra and its Applications*, 415(23):235 – 261, 2006.
5. Thomas Weiland. A discretization method for the solution of Maxwell's equations for six-component fields. *Electronics and Communications*, 31(3):116–120, 1977.

Reduced Basis Modeling for Time-Harmonic Maxwell's Equations

Peter Benner and Martin Hess

Max Planck Institute for Dynamics of Complex Technical Systems, Sandtorstr. 1, 39106 Magdeburg, Germany
benner@mpi-magdeburg.mpg.de, hessm@mpi-magdeburg.mpg.de

Summary. The Reduced Basis Method generates low-order models of parametrized PDEs to allow for efficient evaluation of parametrized models in many-query and real-time contexts.

We show the theoretical framework in which the Reduced Basis Method is applied to Maxwell's equations and present first numerical results for model reduction in frequency domain.

1 Introduction

The Reduced Basis Method (RBM) generates low order models for the efficient solution of parametrized PDEs in real-time and many-query scenarios. The RBM employs rigorous error estimators to perform the model reduction and measure the quality of the reduced simulation. In recent years, the RBM has been developed to apply to a wide range of problems, of which [1] and the references therein, give an overview.

We address the use of the RBM in time-harmonic electromagnetic problems, which can exhibit parameter variations in geometry, material coefficients and frequency. We use the RBM in large 3D problems, that arise in the analysis of microscale semiconductor structures.

2 Model Problem

As an example model, we consider the coplanar waveguide, depicted in Fig. 1. The model setup is contained in a shielded box with perfect electric conducting (PEC) boundary. We consider three perfectly conducting striplines as shown in the geometry. The system is excited at a discrete port and the output is taken at a discrete port on the opposite end of the middle stripline. These discrete ports are used to model input and output currents/voltages.

2.1 Constitutive Equations

We consider the second order time-harmonic formulation of Maxwell's equations in the electric field E

$$\nabla \times \mu^{-1} \nabla \times E + i\omega \sigma E - \omega^2 \varepsilon E = i\omega J \quad \text{in } \Omega, \quad (1)$$

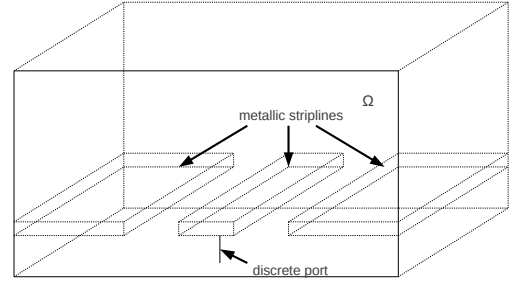


Fig. 1. Geometry of coplanar waveguide.

subject to zero boundary conditions

$$E \times n = 0 \quad \text{on } \Gamma_{\text{PEC}}. \quad (2)$$

We use the weak formulation to (1) with bilinear form $a(\cdot, \cdot; v)$ and linear form $f(\cdot; v)$ as

$$a(E(v), v; v) = f(v; v) \quad \forall v \in X, \quad (3)$$

where $v \in \mathcal{D} \subset \mathbb{R}^p$ denotes the parameter vector, $E(v)$ is the parameter-dependent electric field, v a test function and X the $H(\text{curl})$ -conforming finite element space, discretized with Nédélec finite elements.

All the model problems which are used in this work have been developed in the MoreSim4Nano project [3].

3 Reduced Basis Method for time-harmonic EM-problems

The aim of the RBM is to determine a low order space X_N of dimension N , which approximates the parametric manifold

$$M^v = \{E(v) | v \in \mathcal{D}\} \quad (4)$$

well. Given such a space X_N , it is possible to gain accurate approximations $E_N(v)$ to $E(v)$ by solving (3) in X_N

$$a(E_N(v), v_N; v) = f(v_N; v) \quad \forall v_N \in X_N, \quad (5)$$

i.e. projecting (3) onto X_N .

An integral part in the model reduction are error estimators $\Delta_N(\mathbf{v})$, which give rigorous bounds to the approximation error in the $H(\text{curl})$ norm

$$\|E(\mathbf{v}) - E_N(\mathbf{v})\|_X \leq \Delta_N(\mathbf{v}). \quad (6)$$

Additionally, the RBM requires to have fast evaluations of the error estimator in the sense that the complexity is $O(N)$, i.e. independent of the large discretisation of the full model. The necessary requirement is an affine decomposition of the forms as

$$a(E(\mathbf{v}), \mathbf{v}; \mathbf{v}) = \sum_{q=1}^Q \Theta^q(\mathbf{v}) a^q(E(\mathbf{v}), \mathbf{v}). \quad (7)$$

3.1 Error Estimation

The error estimator in the field is given by

$$\Delta_N(\mathbf{v}) = \frac{\|r(\cdot; \mathbf{v})\|_{X'}}{\beta_{LB}(\mathbf{v})}, \quad (8)$$

with $\|r(\cdot; \mathbf{v})\|_{X'}$ the dual norm of the residual and $\beta_{LB}(\mathbf{v})$ a lower bound to the inf-sup stability constant.

For error estimation in the output, the adjoint equation is solved to obtain the dual residual $r^{du}(\cdot; \mathbf{v})$, such that

$$\Delta_N^s(\mathbf{v}) = \frac{\|r^{pr}(\cdot; \mathbf{v})\|_{X'} \|r^{du}(\cdot; \mathbf{v})\|_{X'}}{(\beta_{LB}(\mathbf{v}))^{1/2} (\beta_{LB}(\mathbf{v}))^{1/2}}, \quad (9)$$

gives rigorous bounds in the output. Here, $r^{pr}(\cdot; \mathbf{v})$ denotes the original, primal residuum.

3.2 Geometric Parameters

To consider the linear combination of snapshots for different geometries, the PDE is transformed from the parameter-dependent domain $\Omega(\mathbf{v})$ to a parameter-independent reference domain $\Omega(\bar{\mathbf{v}})$.

Given a domain decomposition of $\Omega(\bar{\mathbf{v}})$, such that each domain under consideration can be found under affine transformations of the subdomains, the affine decomposition (7) is possible and therefore allows the Reduced Basis model reduction.

4 First Numerical Results

The full simulation has been performed with the finite element package FEniCS using a discretization with first order Nédélec finite elements. For our first numerical experiments, we used a coarse discretization of 2048 degrees of freedom. To work with geometric variations, a larger resolution is required.

Fig. 2 shows the transfer function of the coplanar waveguide. In our simulations, we applied the RBM

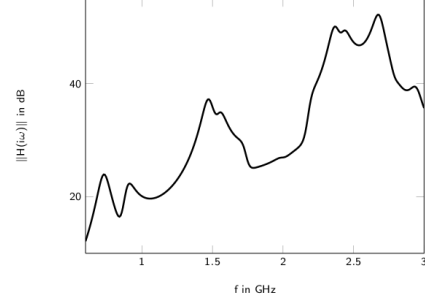


Fig. 2. Frequency response of coplanar waveguide.

over the frequency range $[0.6, 3.0]$ GHz. The time-harmonic equations are already stated in the affine form (7).

In Fig. 3, the relative approximation error for the order $N = 30$ and $N = 50$ are shown. In the case of $N = 50$, the relative error is already below 0.01%. Overall, the RBM achieves fast convergence in that the full model is approximated to machine precision with a space X_N of order 75 for the considered parameter range.

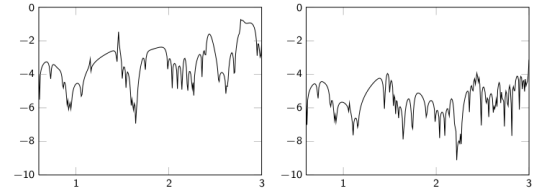


Fig. 3. Log-plot of relative error for $N = 30$ (left) and $N = 50$ (right).

References

1. G. Rozza, D.B.P. Huynh and A.T. Patera, Reduced Basis Approximation and a Posteriori Error Estimation for Affinely Parametrized Elliptic Coercive Partial Differential Equations, Arch. Comput. Methods Eng. (2008) 15:229-275.
2. R. Hiptmair, Finite Elements in computational electromagnetism, Acta Numerica (2002) 237 - 339.
3. MoreSim4Nano, Model reduction for fast simulation of new semiconductor structures for nanotechnology and microsystems technology, www.moresim4nano.org

Thursday, September 13

Electromagnetic Simulations in Power Electronic Converter Design

Didier Cottet¹, Stanislav Skibin¹, Ivica Stevanović¹, Bernhard Wunsch¹

¹ ABB Switzerland Ltd., Corporate Research, Segelhof 1K, 5405 Dättwil, Switzerland,
didier.cottet@ch.abb.com, stanislav.skibin@ch.abb.com,
ivica.stevanovic@ch.abb.com, Bernhard.wunsch@ch.abb.com

Summary The energy efficiency trends in power electronic converter design are leading to increasing demands for faster switching devices with minimal switching losses. Consequences are electromagnetic design challenges such as parasitic stray inductances and high frequency impedance characteristics of passive components. The only way to systematically approach these challenges are dedicated methods for efficient electromagnetic simulation.

1 Introduction

Nowadays, power electronics plays a central role in the discussions on energy efficiency and is therefore gaining high attention in academic and industrial research. With the objective of improving the converter performance in terms of power quality, efficiency and cost, large progress is achieved in power semiconductors research. The consequences are that increasing blocking voltages, current switching capabilities and switching speeds, thus leading to very high dI/dt and dU/dt , and consequently to an increased complexity of EMI problems to be solved [1]. With the introduction of fast switching wide bandgap semiconductors (i.e. SiC and GaN), this trend will be even more significant [2].

In order to systematically address above EMI problems, dedicated simulation methodologies for power electronic converter design have been developed. Even though the basic power converter circuit topologies are very similar for the various applications, the components used and the electromagnetic effects observed are very different, thus demanding for dedicated numerical methods.

The methods discussed here include 3D field simulations, circuit simulations, semiconductors and passive components macro modeling and model simplification and acceleration methods.

2 Methodologies

One of the most relevant electrical design parameter in a power converter is the stray inductance in the power commutation loops [1].

3D field simulations magnetic field patterns (Fig. 1), and current density distributions (Fig. 2), are therefore used to characterize and optimize the layouts of power modules [3] bus bars [4, 5] and PCBs for minimal stray inductance.

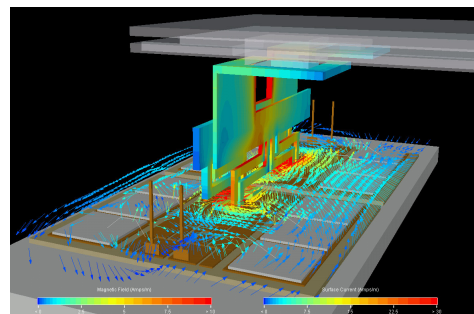


Fig. 1 Magnetic field patterns inside an IGBT power module.

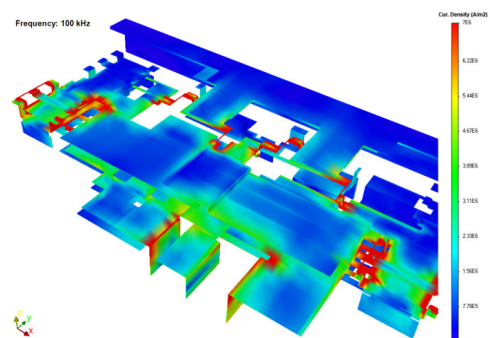


Fig. 2 Current density distribution in planar multi-layer bus bar.

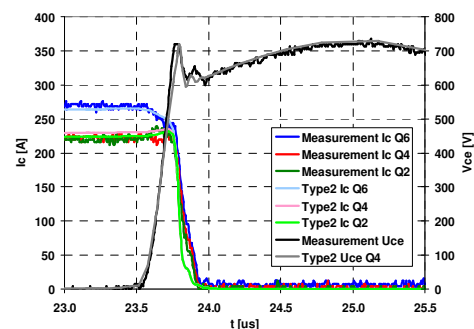


Fig. 3 Comparison of simulated and measured turn-off waveforms.

Extracted bus bar and PCB impedances are then used in circuit simulations to analyze the system switching behavior (Fig. 3) in the time and frequency domain [6, 7]. For that purpose, other system components also need to be modeled and added to the circuit. Most important components are the power semiconductors (IGBTs, diodes) [8] and passive components such as capacitors, chokes (Fig. 4) [9] or cables [10].

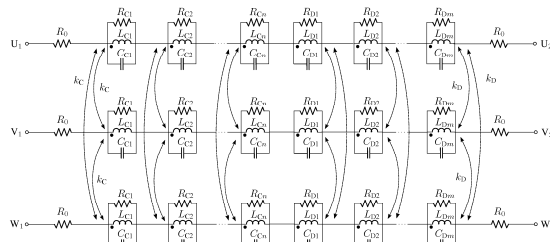


Fig. 4 Equivalent circuit of 3-phase choke.

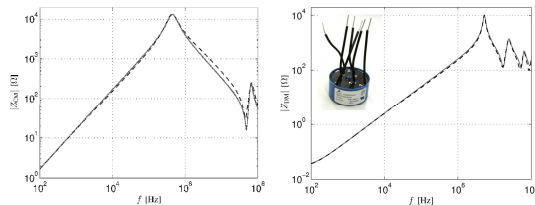


Fig. 5 Comparison of measured and modeled common- and differential mode impedance of a 3-phase choke.

With increasing number and complexity of component models, the computation effort can become prohibitively large and memory demanding. Different acceleration methods have therefore been developed at system model level with divide-and-conquer approaches [7], at component model level with model order reduction [4] and at solver level using reluctance matrix methods [4].

3 Summary

In recent years, electromagnetic simulations have become a powerful tool for power electronic converter design. Major challenges have been to identify the appropriate numerical methods and to develop or adopt efficient simulation platforms and tools for the specific demands of power electronics. Today, the usage of simulations in actual product design is about to become standard, especially for IGBT power modules design, bus bar design and circuit simulation including electromagnetic macro models of active and passive components.

References

1. R. Bayerer, D. Daniel Domes, "Power circuit design for clean switching," In *Proc. 6th International Conference on Integrated Power Electronics Systems (CIPS)*, Nuremberg, Germany, 16-18 March, 2010.
2. I. Josifović, J. Popović-Gerber, J.A. Ferreira, "Improving SiC JFET switching behaviour under influence of circuit parasitics", to appear on *IEEE Transactions on Power Electronics*, 2012.
3. D. Cottet, S. Hartmann, U. Schlapbach, "Numerical simulations for electromagnetic power module design," in *Proc. IEEE Int. Symposium on Power Semiconductor Devices and ICs, ISPSD 2006*, Naples, Italy, pp 1-4, June 4-8, 2006.
4. D. Cottet, I. Stevanović, B. Wunsch, D. Daroui, J. Ekman, G. Antonini, "EM simulation of planar bus bars in multi-level power converters," to appear in *Proc. IEEE EMC Europe Conference*, Rom, Italy, Sept. 17-21, 2012.
5. D. Cottet, I. Stevanović, "Electromagnetic simulation and design of complex, planar bus bars for multi-level, high power converters," to appear in *Proc. 13th IEEE Control and Modeling for Power Electronics (COMPEL)*, Conference, Kyoto, Japan, June, 10-13, 2012.
6. M. Paakkinen, D. Cottet, "Simulation of the non-idealities in current sharing in parallel IGBT subsystems," in *Proc. IEEE Applied Power Electronics Conference and Exposition*, Austin, TX, USA, Feb. 24-28, 2008, pp. 211-215.
7. I. Stevanović, D. Cottet, B. Wider, D. Daroui, and J. Ekman, "Modeling of large bus bars using PEEC method and circuit level simulators," in *Proc. 12th IEEE Control and Modeling for Power Electronics (COMPEL)*, Conference, Boulder, USA, 28-30 June, 2010, pp.1-7.
8. F. Chimento, N. Mora, M. Bellini, I. Stevanović, S. Tomarchio, "A simplified spice based IGBT model for power electronics modules evaluation," in *Proc. 37th Annual Conference of the IEEE Industrial Electronics Society IECON 2011*, pp. 1096-1101, Melbourne, Australia, Nov. 7-10, 2011.
9. I. Stevanović, S. Skibin, "Behavioral circuit modeling of single- and three-phase chokes with multi-resonances," in *Proc. International Conference on Power Electronics, ECCE Asia*, Jeju, Korea, May 30 – June 3, 2011.
10. I. Stevanović, B. Wunsch, G.-L. Madonna, M.-F. Vancu, S. Skibin, "Multiconductor cable modeling for EMI simulations in power electronics," to appear in *Proc. 38th Annual Conference of the IEEE Industrial Electronics Society*, Montréal, Canada, Oct. 25-28, 2012.

Numerical Simulations for Power and Distribution Transformers

Thorsten Steinmetz¹, Bernardo Galletti¹, Jasmin Smajic², and Andreas Blaszczyk¹

¹ ABB Switzerland Ltd, Corporate Research, CH-5405 Baden, Switzerland thorsten.steinmetz@ch.abb.com, bernardo.galletti@ch.abb.com, andreas.blaszczyk@ch.abb.com

² HSR- Hochschule für Technik Rapperswil, CH-8640 Rapperswil, Switzerland jsmajic@hsr.ch

Summary. Numerical simulations of different physical design aspects of ABB distribution and power transformers are presented. The design aspects include stray loss assessment, dielectric insulation and thermal management. The simulations contribute to a better understanding of the operation of transformers, which allows to improve the transformer product development.

1 Introduction

In the present days, energy-efficiency is a paramount requirement in the life-cycle of power products, as it is mandatory for an ecological and economical operation of transmission and distribution networks. Important components of these networks are distribution and power transformers. Hence, a high energy-efficiency has to be targeted in the development and design of modern transformers.

Evidently, low power losses during operation are of particular importance to achieve a high energy-efficiency. However, according to life-cycle-assessment, low material usage for the production of transformers contributes further to highly energy-efficient devices. As a consequence, competitive transformer designs have to be as compact as possible, thus approaching the physical limits.

Power losses and compactness are mainly determined by the electric and the magnetic design of a transformer. A part of this is the dielectric insulation which clearly limits the compactness, because certain insulation distances have to be maintained to prevent failures by electric discharges. Moreover, the dissipated power losses heat up the transformer components during operation. The temperature rise within the device, which affects the power losses and limits the expected lifetime of the insulation, needs thus to be controlled by a thermal management.

To achieve competitive transformer designs considering the aforementioned aspects, numerical simulations have become a very significant tool in product development and optimization.

2 Electromagnetic Simulations

For magneto-quasistatic simulations in transformers, the commercial field solver MagNet is applied [1]. Its

Finite-Element-Method formulation is based on hierarchical elements which allow to use shape functions of various polynomial orders in the same mesh [4]. In the frequency-domain, the magnetic vector-field \mathbf{H} in conductive domains,

$$\text{curl} \left((\sigma + i\omega\epsilon)^{-1} \text{curl}(\mathbf{H}) \right) + i\omega\mu\mathbf{H} = 0, \quad (1)$$

and the scalar magnetic potential Ψ in non-conductive domains,

$$\text{div}(\mu(\mathbf{H}_s - \text{grad}(\Psi))) = 0, \quad (2)$$

are the solved for. The angular frequency is denoted by ω , while μ and ϵ denote the permeability and the permittivity. In non-conductive domains, the magnetic field is computed by $\mathbf{H} = \mathbf{H}_s - \text{grad}\Psi$ with \mathbf{H}_s being a known source field. The resulting (non)-linear systems of equations are solved by standard methods, e.g. a Newton-Raphson scheme for linearization and a preconditioned Conjugate Gradient solver for the linear systems.

2.1 Stray Loss Assessment

Three-dimensional magneto-quasistatic simulations are applied e.g. for stray loss assessment of ABB transformers. For example, Fig. 1 shows the distribution of the stray losses on a dry-type transformer.

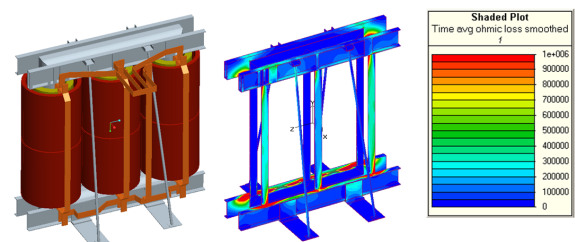


Fig. 1. CAD model of a dry-type transformer (left), and the stray loss distribution on its structural components(right).

The accuracy of the simulated stray losses reached here is about 7% [3]. Furthermore, the stray field emission of transformers are subject to legal regulations in some countries. An analysis of the magnetic stray field of this unit will be shown.

Beyond this assessment, electromagnetic simulations are used to evaluate objective functions in the frame of multi-objective optimization schemes. An application of these schemes based on an evolutionary algorithm will be presented.

2.2 Dielectric Insulation

Standardized tests have to be passed in order to verify the dielectric insulation of real transformers, for instance the applied voltage (AC) test or the lightning impulse (LI) test. The prediction of test results for dry-type transformers requires an evaluation of the dielectric design criteria that are based on stages of the electric discharge in air, i.e. streamer inception, streamer propagation and leader transition [2].

Under the AC and LI tests, for example, streamer inception can be tolerated in small regions at sharp edges of the core or terminals as long as the streamer propagation criterion (based on clearances) is fulfilled [2]. But streamer inception cannot be tolerated in the weakly inhomogeneous field of the main duct between low- and high-voltage windings, unless complex barrier systems are used. To avoid inception, the following criterion must be evaluated using electrostatic field computations:

$$\int_S \alpha_{\text{eff}}(E) dx < \ln(N_c) \quad (3)$$

Here, α_{eff} denotes the effective ionization coefficient w.r.t. the electric field magnitude E . Inception does not occur if the integral along the discharge path S (typically computed as a field line) is smaller than the logarithm of the limit for electron generations N_c . Applications of the dielectric criteria to transformer design will be presented in the extended version of the paper.

3 Thermal Simulations

One significant duty of the thermal management is to control the temperature rise of the windings, which originates from dissipated power losses. The higher the average temperature of the windings, the higher is their electric resistance, and thus the poorer is the energy-efficiency in operation. Furthermore, the lifetime of the transformer depends on the highest temperature in the windings.

The heat generated in the windings is transferred by conduction through the solid winding insulation. The heat is then taken away from the surfaces of the solid insulation by the insulation fluid (e.g. oil or air) via convection. The latter can be either forced or natural depending on whether the flow is driven by an externally imposed pressure gradient or by buoyancy effects, respectively.

Numerical simulations are applied to solve the physical models that govern the heat transfer mechanisms described above. The numerical thermal problem involves the solution of the Navier-Stokes equations in the fluid, the heat conduction equation in the solid parts and the radiation model for describing the radiating energy exchanged between mutually facing surfaces. As a result of the simulations, the spatial temperature distribution inside the transformer is determined. This simulation procedure has become possible recently for full three-dimensional transformer configurations by using state-of-the-art computational tools along with modern high-performance computers.

The simulation procedure was validated by comparing numerical results against measurements for a dry-type transformer winding prototype, where the conductors of the winding turns are casted in epoxy. The maximum deviation between simulation and measurements at the 31 sensor locations was less than 5%. The simulated temperature distribution is shown in Fig. 2.

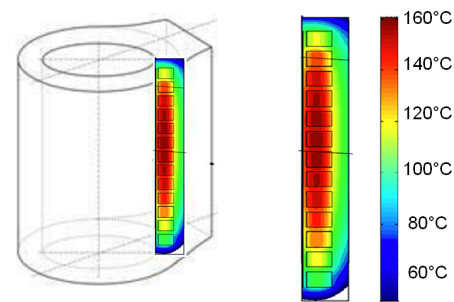


Fig. 2. Simulated temperature distribution of a dry-type transformer winding prototype cooled by natural convection.

This validated procedure was applied to compute the temperature distribution of many transformer designs. Details on the application to a particular dry-type transformer will be presented.

References

1. Infolytica Corporation. Infolytica MagNet <http://www.infolytica.com>
2. A. Pederson, T. Christen, A. Blaszczyk, and H. Boehme. Streamer inception and propagation models for designing air insulated power devices. *Proc. IEEE Conf. on Elec. Ins. and Dielec. Phenom.*, Virginia Beach, USA, 19 - 21 Oct 2009
3. J. Smajic, T. Steinmetz, B. Cranganu-Cretu, A. Nogues, R. Murillo, J. Tepper. Analysis of near and far stray magnetic fields of dry-type transformers: 3-D simulations versus measurements. *IEEE Trans. Mag.*, Vol. 47, Issue 5, 2011
4. J.P. Webb, B. Forghani. A T-Omega method using hierarchical edge elements. *IEE Proceedings, Sci. Meas. Technol.*, Vol. 142, No. 2, 1995

Uncertainty Quantification from an Industrial Perspective

Albert Gilg¹, Meinhard Paffrath¹, and Utz Wever¹

Siemens Corporate Technology, D-81739 Munich, Germany Albert.Gilg@siemens.com,
Meinhard.Paffrath@siemens.com, Utz.Weaver@siemens.com

Summary. This presentation considers uncertainty quantification from an industrial perspective. Some successful methods in the field of stochastic optimization and reliability analysis as well as industrial applications are presented.

1 Content

Deterministic design optimization approaches are no longer adequate for the development of industrial high technology products. Product and process designs often push to the envelope of physical limits to improve performance. In this regime uncertainty originating from fluctuations during fabrication and small disturbances in system operations severely impacts product performance and quality. Design robustness becomes a key issue in optimizing industrial designs.

The design phase of a product or system is characterized by having no direct interaction with data. Here, the methods of uncertainty quantification try to predict confidence intervals for the behavior in the phase of operation. Also optimization and keeping quality limits for products and systems plays an important role in the design phase. Here, special stochastic optimization schemes and reliability analysis must be developed. For an industrial application they have to be designed such that as less function evaluations as possible are needed. The phase of operation is characterized by the interaction with data. For this phase a main task is the calibration of models with incomplete and noisy data. Here, the Bayesian concepts come into play.

We present challenges and solution approaches implemented in our robust design tool RoDeO applied to turbo charger design. In contrast to electricity generating turbines, turbo chargers have to work efficiently not only for one operating point, but for a wide range of rotation frequencies. High computation times for 3D aerodynamic (CFD) and mechanical (FEM) computations, for large sets of frequencies, are a severe limiting factor even for deterministic optimization procedures. Furthermore constrained deterministic optimization cannot guarantee critical design limits under impact of uncertainty during fabrication. Especially, the treatment of design constraints in terms of thresholds for von Mises stress or modal frequencies become crucial. We introduce an efficient approach for the numerical treatment of such absolute

reliability constraints that even do not need additional CFD and FEM calculations in our robust design tool set.

A second application concerns the wheel set of a train. For this component (which is the most sensitive part of a train) a life cycle analysis is performed. In real life, such a component is faced by scattering outer impact and abrasion and thus, with a certain probability, the design leads to finite time fatigue resistance in spite it has been designed for infinite time. The underlying physics are the laws of fracture mechanics and crack growth. The failure criteria is the crack size exceeding a given length. The proposed stochastic method is in particular suited for CPU time intensive and large scale physical models. Based on these life time computations also inspection planning can be considered. In doing so we assume that all components are replaced if a crack is detected. The probability of detecting a crack during inspection is itself a random number. Knowing the costs for replacement of components, loss due to the outage during inspection etc., optimal inspection schemes can be derived.

An outlook for further design challenges concludes the presentation.

Uncertainty Quantification of Inrush Currents in Electric Machines with Respect to Measured Material Data

Sebastian Schöps^{1,2}, Roland Pulch¹, Andreas Bartel¹, and Herbert De Gersem³

¹ Chair of Applied Mathematics and Numerical Analysis, Bergische Universität Wuppertal, Gaußstraße 20, D-42119 Wuppertal, Germany {schoeps,bartel,pulch}@math.uni-wuppertal.de,

² Chair of Electromagnetic Theory, Bergische Universität Wuppertal, Gaußstraße 20, D-42119 Wuppertal, Germany

³ Wave Propagation and Signal Processing Research Group, KU Leuven, 8500 Kortrijk, Belgium
herbert.degersem@kuleuven-kulak.be

Summary. The startup of most electrical machines exhibits a strong nonlinear behavior due to saturation. In practice, the underlying nonlinear saturation curve is modeled according to measurement data that typically contain errors. The electromagnetic fields and in particular the inrush currents inherit this uncertainty. In this paper, we propose a specific stochastic model (BH-curve) to describe uncertainties and we demonstrate the use of generalized polynomial chaos for the uncertainty quantification of these inrush currents. This requires time stepping of systems of nonlinear partial differential algebraic equations that result from the coupling of field and circuit systems.

1 Introduction

Efficient design of electric machines (transformers, actuators, generators etc.) requires insight into the device's electromagnetic field distribution. Often, the available inputs, e.g. material data, include unknown errors for example due to measurements. The influence of these errors can be characterized by uncertainty quantification. In the mathematical models, the corresponding parameters are substituted by random variables to describe the uncertainties.

In this paper a transformer, modeled by the magnetoquasistatic approximation to Maxwell's partial differential equations (PDEs), is considered. This system is coupled to a network model of an electric circuit given by a system of differential algebraic equations (DAEs). The coupling is necessary in order to simulate the startup phase where the highest inrush currents can be observed. To account for the measurement errors, the material curves include (random) parameters, such that the time-dependent solution of the PDAEs becomes a random process.

Uncertainties in the material parameters of magnetoquasistatic problems have been studied before but only considering linear material laws in frequency domain, e.g., [2, 3, 11]. In this paper we do not propose to model the material laws as uncertain, but the underlying measurement data. This allows for a natural choice of the probability distribution.

The stochastic model can be solved by a quasi Monte-Carlo simulation, for example. We use the gen-

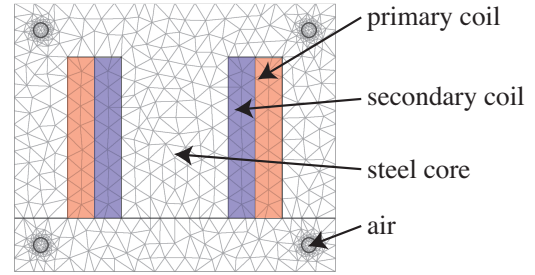


Fig. 1: 2D model of a transformer, taken from [9].

eralized polynomial chaos (gPC), see [1, 6, 12], in the numerical simulation to investigate how this approach behaves. A stochastic Galerkin method results in a larger coupled system of DAEs, cf. [10]. To illustrate the modeling and the simulation, we discuss a 2D finite element discretization of a transformer.

2 Field Model

In the low-frequency regime the electromagnetic field, i.e., the eddy current problem, is typically described in terms of the magnetic vector potential \mathbf{A} (MVP), with magnetic flux density $\mathbf{B} = \nabla \times \mathbf{A}$, on a computational domain by the curl-curl equation

$$\kappa \frac{\partial \mathbf{A}}{\partial t} + \nabla \times (\mathbf{v} \nabla \times \mathbf{A}) = \mathbf{J}_{\text{src}} \quad (1)$$

with conductivity κ and nonlinear reluctivity \mathbf{v} . In our model, $\mathbf{v} = \mathbf{v}(\nabla \times \mathbf{A}, \mathbf{Y})$ may depend on random variables \mathbf{Y} to account for measurement errors. The system is equipped with boundary and initial conditions for \mathbf{A} . The material parameters are piecewise constant in all subdomains, only for ferromagnetic materials (e.g. the steel core in Fig. 1) the Brauer model, [4], is chosen to account for nonlinear saturation

$$\mathbf{v}(\mathbf{B}, \mathbf{Y}) = k_1(\mathbf{Y}) \cdot \exp(k_2(\mathbf{Y}) \cdot |\mathbf{B}|^2) + k_3(\mathbf{Y}), \quad (2)$$

where the model parameters k_i are fitted from measurement data and thus depend on the errors described by \mathbf{Y} .

The circuit coupling is established by identifying parts of the computational domain as branches in the circuit. Typically for coils the stranded conductor model is used and for massive bars the solid conductor model is feasible, [5]. In the case of a number of N_{str} stranded conductor models (i.e., spatially resolved field elements), the excitation from the circuit is imposed on the field by the source term

$$\mathbf{J}_{\text{src}} = \sum_{k=1}^{N_{\text{str}}} \chi_k \mathbf{i}_k, \quad (3)$$

where the winding functions χ spatially distributes the corresponding currents \mathbf{i} . To obtain current/voltage relations for each field element, additional coupling equations are needed, e.g.

$$\int_{\Omega} \chi_k \cdot \frac{\partial \mathbf{A}}{\partial t} dV = v_k - R_k i_k \quad (k=1, \dots, N_{\text{str}}) \quad (4)$$

with the DC resistances \mathbf{R} for the windings. Hence, given voltage drops \mathbf{v} , the system (1-4) defines \mathbf{A}, \mathbf{i} .

3 Uncertainties in the Measurement

The material parameter ν is implicitly given by measurements of the BH-curve (B_i, H_i) , for $i = 1, \dots, N$. The Brauer material model (2) can be fitted either by a nonlinear least squares algorithm, as e.g. in [8], or less elegantly by selecting 3 measurement points and computing the reluctivity function that fulfills

$$H_i = \nu(B_i) B_i$$

exactly where we choose the points $i = 1, 2, 3$ without loss of generality, e.g. [7]. We follow the second approach to keep the parameter space small.

The field strength H is assumed to be affected by a measurement error:

$$(B_i, H_i \cdot Y_i) \quad \text{for } i = 1, 2, 3$$

where Y_i is normally distributed with mean $\mu = 1$ and standard deviation $\sigma = 0.1$.

We propose to quantify the impact of the perturbations above on the currents \mathbf{i} in (4) by the generalized polynomial chaos.

The transformer model as depicted in Fig. 1 has been simulated for 100 realization of the above introduced normally distributed random variables. The results are shown in Fig.2. The uncertainties cause deviations of up to 20A in the primary inrush current.

In the full paper the computation of the expected values and the variance of the currents are discussed in more detail and using different uncertainty quantification techniques.

Acknowledgement. The work is partially funded by the BMBF Verbundprojekt SOFA (03MS648E). Also the Post-Doc funding of the Fachgruppe Mathematik at the Bergische Universität Wuppertal is acknowledged.

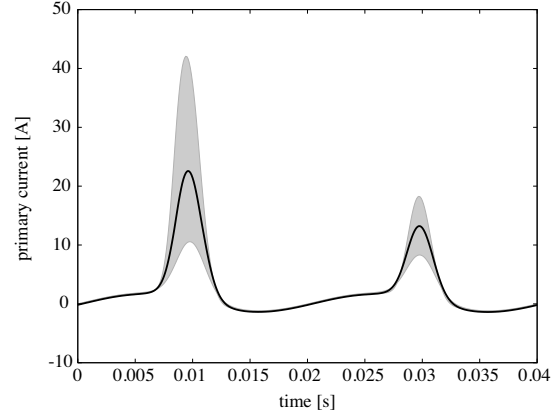


Fig. 2: Impact of random parameters on the primary current. The black line denotes the mean of the 100 random walks, the grey neighborhood is given by the maxima and minima.

References

1. F. Augustin, A. Gilg, M. Paffrath, P. Rentrop, and U. Wever. Polynomial chaos for the approximation of uncertainties: Chances and limits. *Eur. J. Appl. Math.*, 19:149–190, 2008.
2. K. Beddek, S. Clenet, O. Moreau, V. Costan, Y. Le Menach, and A. Benabou. Adaptive method for non-intrusive spectral projection – application on a stochastic eddy current NDT problem. *IEEE Trans. Magn.*, 48(2):759–762, 2012.
3. K. Beddek, Y. Le Menach, S. Clenet, and O. Moreau. 3-D stochastic spectral finite-element method in static electromagnetism using vector potential formulation. *IEEE Trans. Magn.*, 47(5):1250–1253, 2011.
4. J. R. Brauer. Simple equations for the magnetization and reluctivity curves of steel. *IEEE Trans. Magn.*, 11(1):81, 1975.
5. H. De Gersem and T. Weiland. Field-circuit coupling for time-harmonic models discretized by the Finite Integration Technique. *IEEE Trans. Magn.*, 40(2):1334–1337, 2004.
6. R. G. Ghanem and P. D. Spanos. *Stochastic finite elements: a spectral approach*. Civil, Mechanical and Other Engineering Series. Dover Publications, rev. edition, 2003.
7. S. Hoole and N. Hoole. Reluctivity characteristics in nonlinear finite element analysis of magnetostatic fields. *IEEE Trans. Magn.*, 22(5):1352–1353, 1986.
8. T. Hülsmann. Nonlinear material curve modeling and sensitivity analysis for MQS-problems. Master's thesis, Bergische Universität Wuppertal, 2012.
9. D. Meeker. *Finite Element Method Magnetism User's Manual*, 2010. Version 4.2 (09Nov2010 Build).
10. R. Pulch. Polynomial chaos for the computation of failure probabilities in periodic problems. In Janne Roos and Luis R. J. Costa, editors, *SCEE 2008*, pages 191–198, Berlin, 2010. Springer.
11. E. Rosseel, H. De Gersem, and S. Vandewalle. Spectral stochastic simulation of a ferromagnetic cylinder rotating at high speed. *IEEE Trans. Magn.*, 47(5):1182–1185, 5 2011.
12. D. Xiu and J.S. Hesthaven. High order collocation methods for differential equations with random inputs. *SIAM J. Sci. Comput.*, 27(3):1118–1139, 2005.

Dielectric Breakdown Simulations of an On-Load Tap-Changer in a Transformer Considering the Influence of Tap Leads and Windings

M. Wiesmüller^{1,2}, B. Glaser¹, F. Fuchs¹, and O. Sterz¹

¹ Maschinenfabrik Reinhausen GmbH (MR), Falkensteinstr. 8, 93059 Regensburg, Germany

² University of Applied Sciences Deggendorf, Edlmaistr. 6 and 8, 94469 Deggendorf, Germany

Summary. This paper reports on the simulation of an on-load tap-changer in a power transformer. The electric fields are computed and resulting breakdown voltages are estimated by using the streamer criterion. The environment of the on-load tap changer is taken into account by modeling tap leads in detail as well as transformer windings. The goal of the investigations is to justify standard design and test-procedures which assume a low dependency of the interior dielectric properties of the on-load tap-changer on the surrounding.

1 Introduction

On-Load Tap-Changers (OLTCs) are devices which permit the change of the turn ratios of transformers, allowing voltage regulation or phase shifting under load without interruption.

Power transformers equipped with OLTCs have been main components of electrical networks and industrial applications for nearly 80 years [2, 4].

One crucial criterion for the selection of an adequate OLTC for a certain transformer or application is its insulation level. Generally, the dielectric strength depends on the whole system, i.e. the transformer, as well as the connection-leads and the OLTC. However, usual test-procedures by OLTC manufacturers are not done within a transformer but on a separate OLTC. Also during design the influence of leads and windings on the internal OLTC insulation is usually neglected. This gives rise to further investigations justifying this approach. Therefore, a typical system is simulated by computing the electric field and breakdown voltages with and without windings and tap-leads.

2 Finite Element Simulation

For simulation half of the core and the tap windings of the transformer phase nearest to the OLTC are modeled. The OLTC itself is represented by its lower part—the tap selector. After several simplifications the CAD-data of the tap selector are directly imported into the simulation software [1]. The leads are created manually. Finally the transformer tank is built as a surrounding box.

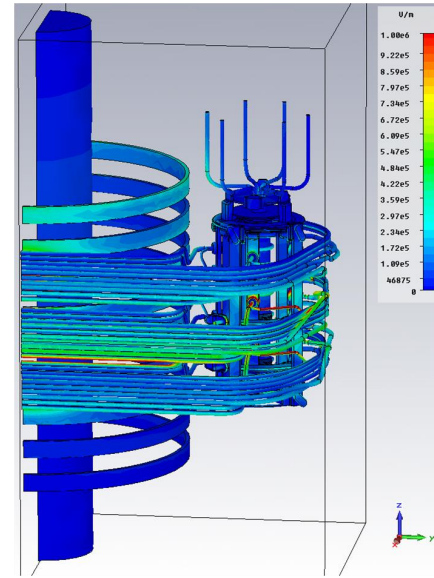


Fig. 1. Magnitude of the electric field of the total arrangement. Red colored parts of the plot are above 1 kV/mm.

Here, we consider AC stresses. Hence, the electric field is computed for the electrostatic case, i.e. we solve

$$\nabla \cdot (\epsilon \nabla \phi) = 0 \quad \text{in } \Omega, \quad (1)$$

where Ω is the non-conductive domain, applying constant potentials $\phi = \phi_0$ on Dirichlet boundaries representing grounded and stressed electrodes and the transformer tank.

For the calculation 2nd order, isoparametric finite elements are used. The result of a computation with 22.6 million unknowns is shown in Fig.1.

3 Dielectric Breakdown Calculation

Breakdown in oil cannot be described by one coherent theory as in gas. To explain the main mechanisms two basic approaches are used: one is an extension of gaseous breakdown, the other one assumes that breakdown is caused by bridges of fibrous impurities.

To calculate the breakdown voltage in inhomogeneous electric fields different methods can be used, see e.g. [3,5]. The calculation method we use is based

on the streamer criterion along a critical path C

$$\int_C \alpha(|\mathbf{E}(\mathbf{x})|) dl_x \geq k, \quad (2)$$

where α is the effective ionization coefficient, \mathbf{E} the electric field and k defines the number of electrons necessary for breakdown. With an exponential equation for α and the introduction of a normalized electric field $e(x) := |\mathbf{E}(\mathbf{x})|/U$, (2) can be solved as in [3] for the breakdown voltage

$$U_b = (1\text{mm})^{1/z} \cdot \left(\int_C \left(\frac{e(x)}{E_0} \right)^z dl_x \right)^{-1/z} \quad (3)$$

with constants $E_0 = 15\text{ kV/mm}$ and $z = 4.2$. These constants are derived from measured breakdown data of uniform fields.

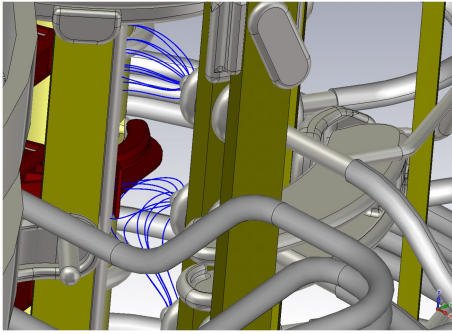


Fig. 2. A subset of evaluated critical lines in the tap selector

The streamer criterion (2) has to be evaluated along critical paths, which for breakdown in oil gaps are fieldlines starting at electrodes with high electric field stresses. Since the most critical fieldline does not necessarily start at a local field maximum many fieldlines have to be evaluated, some of them are shown in Fig. 2. The most critical path and the associated U_b is determined by finding the minimum over all calculated voltages.

4 Influence of the Tap Leads and Windings

To investigate the influence of the transformer and the leads on the dielectric strength of the OLTC three different systems are simulated, see Fig. 3. Field values along several lines parallel to the tap selector axis are compared. In Fig. 4 field values along two of these lines are shown. One line represents a region with low, the other one a region with high electric stresses.

In regions with low fields there is a significant influence of the transformer and the leads, but in regions with high field stresses, which are critical concerning dielectric strength, the differences are maximum 10%. Regarding the calculated breakdown voltages the deviation is even less than 1%.

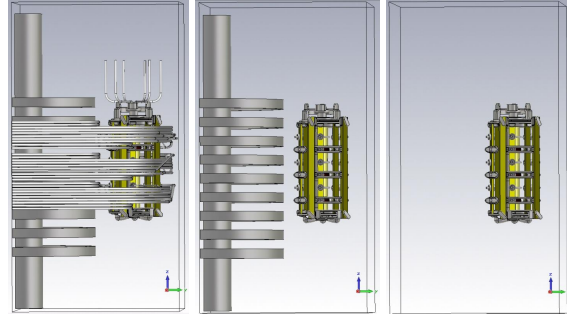


Fig. 3. Different geometries. Left: Tap selector with leads and transformer windings. Middle: Tap selector and windings. Right: Only tap selector

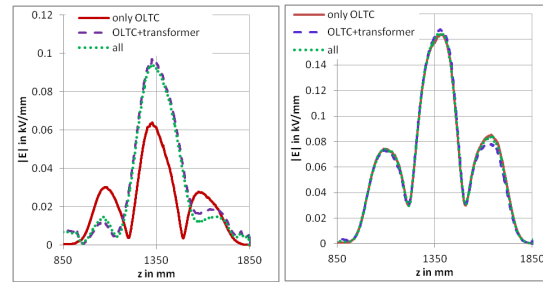


Fig. 4. $|E|$ comparing all geometric arrangements, region with low fields (left), region with high fields (right)

5 Conclusion

It has been shown that for the investigated typical example the influence of the transformer and the tap leads on the internal OLTC insulation is small enough to neglect them during design optimization and test-procedures.

Acknowledgement. The authors acknowledge discussions with D. Breitfelder and B. Bakija, Siemens AG, and thank for support of T. Strof, T. Manthe, J. Niesner, and B. Visser, MR GmbH.

References

1. CST EM STUDIO®, www.cst.com.
2. D. Dohnal. *On-Load Tap-Changers in Power Transformers. A Technical Digest*. MR-Publication PB252/04 EN 06/09, Regensburg, 2009.
3. W. Knorr and D. Breitfelder. Breakdown in transformer oil with AC and impulse voltage stress. *IEEE Int. Symp. on Electrical Insulation.*, 291–296, 1984.
4. A. Krämer. *On-Load Tap-Changers for Power Transformers. Operation, Principles, Applications and Selection*. MR-Publication, Regensburg, 2000.
5. A. Küchler. *Hochspannungstechnik (in German)*. Springer, Berlin-Heidelberg, 2009.
6. M. Wiesmüller. Evaluation of the dielectric strength of an OLTC in a transformer using electrical field simulations (in German). Master's thesis, University of Applied Sciences Deggendorf, Deggendorf, 2012.

Nonlocal hydrodynamic Drude model of nano-plasmonic optical devices

Lin Zschiedrich¹, Kirankumar R. Hiremath², and Frank Schmidt^{1,2}

¹ JCMwave GmbH, Berlin, Germany lin.zschiedrich@jcmwave.com

² Zuse Institute Berlin (ZIB), Germany

Summary. As optical devices get much smaller than the wavelength of the operating light, local material models for metallic structures like the Drude model and the Lorentz model become inadequate to describe accurately the light-matter interactions. To overcome this, a sophisticated non-local hydrodynamic Drude model has been proposed. We discuss a weak formulation of the nonlocal hydrodynamic Drude model in the frequency domain and apply the finite element method for scattering and propagating mode problems to demonstrate the dramatic impact of non-local effects on the device characteristics.

1 Introduction

The dispersive material properties of plasmonic structures are usually described by the Drude model and the Lorentz model. These material models take into account spatially *purely local* interactions between electrons and the light. Recent investigations have shown that these local models are inadequate as the size of the plasmonic structure becomes much smaller than the wavelength of the exciting light [1, 2]. To overcome this, a sophisticated *nonlocal* material model is required, such as the hydrodynamic model of the electron gas [3].

The hydrodynamic model is formulated by coupling macroscopic Maxwell's equations with the equations of motion of the electron gas. This gives rise to a hydrodynamic polarization current. Considering only the kinetic energy of the free electrons, it yields the nonlocal hydrodynamic Drude model, which is given in frequency domain by a coupled system of equations

$$\nabla \times \mu_0^{-1}(\nabla \times \mathbf{E}) - \omega^2 \epsilon_0 \epsilon_{\text{loc}} \mathbf{E} = i\omega \mathbf{J}_{\text{HD}}, \quad (1)$$

$$\beta^2 \nabla(\nabla \cdot \mathbf{J}_{\text{HD}}) + \omega(\omega + i\gamma) \mathbf{J}_{\text{HD}} = i\omega \omega_p^2 \epsilon_0 \mathbf{E}, \quad (2)$$

where \mathbf{E} is the electric field, \mathbf{J}_{HD} is the hydrodynamic current, ϵ_{loc} is the relative permittivity due to the local-response, β^2 is a term proportional to the Fermi velocity, γ is the damping constant, and $\omega_p^2 = \frac{e^2 n_0}{\epsilon_0 m_e}$ is the plasma frequency of the free electron gas, c.f. [6, 7].

The hydrodynamic current is non-zero only in a region Ω_m filled with metal. We assume that Ω_m is bounded and contained in the computational domain Ω . *Transparent boundary conditions* such as PML (Perfectly Matched Layers) are required to model the coupling of the light field with the exterior domain [9].

2 Weak formulation

Appropriate Sobolev spaces for the electric field \mathbf{E} and the hydrodynamic current \mathbf{J}_{HD} are $H(\text{curl}, \Omega)$ and

$$H_0(\text{div}, \Omega_m) = \{ \mathbf{J}_{\text{HD}} \in (L^2(\Omega_m))^3 \mid \nabla \cdot \mathbf{J}_{\text{HD}} \in (L^2(\Omega_m))^3, \mathbf{n} \cdot \mathbf{J}_{\text{HD}} = 0 \text{ on } \partial\Omega_m \},$$

respectively. This restricts the hydrodynamic current to the metallic domain, and imposes a zero normal component on the boundary of the metal.

One can use textbook Nédélec finite element spaces to discretize $H(\text{curl}, \Omega)$ and $H_0(\text{div}, \Omega_m)$, leading to a consistent discretization of the problem, fulfilling the required boundary and material interface conditions [8, Ch. 5].

Special geometries such as z -invariant structures or with a rotational symmetry, can be treated as in the standard Maxwell case. This allows for the computation of plasmon-polariton waveguide modes of a z -invariant structure on a 2D cross-section domain. In this case it is assumed that the electric field and the hydrodynamic current depend harmonically on z :

$$\begin{aligned} \mathbf{E}(x, y, z) &= \mathbf{E}(x, y) e^{ik_z z}, \\ \mathbf{J}_{\text{HD}}(x, y, z) &= \mathbf{J}_{\text{HD}}(x, y) e^{ik_z z} \end{aligned}$$

Replacing all z -derivatives in the coupled system (1), (2) with ik_z yields a quadratic eigenvalue problem for the propagation constant k_z .

3 Numerical examples

3.1 Cylindrical plasmonic nanowires

We validate the present approach by simulating a test case of cylindrical nanowire as in [1], for which an analytical solution based on Mie theory is available.

Consistent with the observations in [1], peaks due to nonlocal interactions are present *only* beyond the bulk plasma frequency, c.f. Fig. 1. The positions of the surface plasmon resonance and the nonlocal hydrodynamic Drude resonances agree very good with the analytical Mie results.

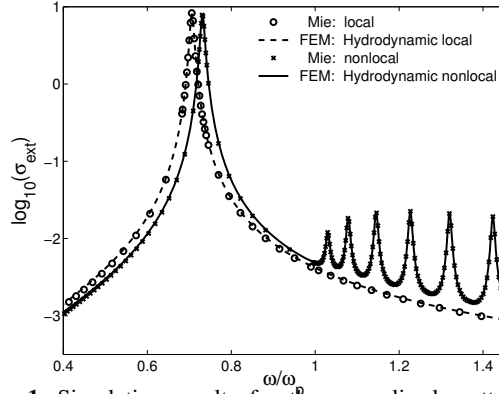


Fig. 1. Simulation results for the normalized scattering cross section σ_{ext} of the cylindrical nanowire in [1]. The curves show comparison of the numerical finite element solutions for the nonlocal and the local hydrodynamic model with the corresponding analytical solutions based on Mie theory.

3.2 V groove channel plasmon-polariton resonances

To demonstrate capability of the method to handle an arbitrary shaped geometry, we simulate a channel plasmon-polariton (CPP) waveguide with a V groove.

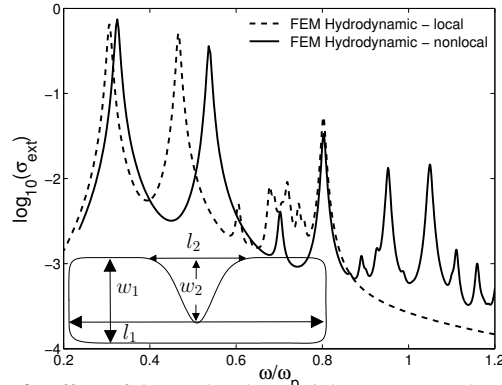


Fig. 2. Effect of the nonlocal material response on the resonance modes of V groove CPP waveguide. The waveguide parameters are: $l_1 = 7$ nm, $w_1 = 1$ nm, a groove of length $l_2 = 0.7$ nm, width $w_2 = 0.7$ nm is placed in the center. The material and the hydrodynamic parameters are taken as in the case of cylindrical nanowires in [1]. The sharp corners of the waveguide are rounded with corner radius of 0.1 nm. Resonances are excited by a unit amplitude, x -polarized plane wave propagating in the direction of minus y -axis.

We consider a V groove configuration as shown in clip of Fig. 2. First we simulated it for the local Drude model. As seen from the dashed curve in Fig. 2, several resonance modes are excited. When this setting is simulated with the nonlocal Drude model, the mode spectrum changes significantly (solid-line curve). Some of the local Drude model modes such as at $\omega/\omega_p = 0.306332$ and $\omega/\omega_p = 0.80262$ experience small shifts towards high frequency, whereas others

like at $\omega/\omega_p = 0.466485$ and $\omega/\omega_p = 0.605087$ undergo noticeable shifts towards high frequency. As in the case of the cylindrical nanowires, also for the V groove waveguide a completely new set of resonances appear at the frequencies beyond the plasma frequency. For the present simulation setting, some of these hydrodynamic resonance modes are more prominent than the higher order waveguide resonance modes. It gives the indication that the modal properties of the CPP waveguides change significantly with the inclusion of nonlocal effects.

Acknowledgement. This work is partially funded by the DFG (German Research Foundation) priority program 1391 “Ultrafast Nanooptics”.

References

1. R. Rupp. Extinction properties of thin metallic nanowires. *Optics Communications*, 190(1-6):205–209, 2001.
2. S. Palomba, L. Novotnyb, and R. E. Palmer. Blue-shifted plasmon resonance of individual size-selected gold nanoparticles. *Optics Communications*, 281(3):480–483, 2008.
3. A. D. Boardman. *Electromagnetic surface modes*, chapter Hydrodynamic theory of plasmon-polaritons on plane surfaces, pages 1–76. John Wiley and Sons Ltd., 1982.
4. J. M. McMahon, S. K. Gray, and G. C. Schatz. Calculating nonlocal optical properties of structures with arbitrary shape. *Physical Review B*, 82:035423, 2010.
5. S. Raza, G. Toscano, A. P. Jauho, M. Wubs, and N. A. Mortensen. Unusual resonances in nanoplasmonic structures due to nonlocal response. *Physical Review B*, 84:121412, 2011.
6. G. Toscano, S. Raza, A.-P. Jauho, N. A. Mortensen, M. Wubs, Modified field enhancement and extinction by plasmonic nanowire dimers due to nonlocal response, *Opt. Express* 20 (4) (2012) 4176–4188.
7. K. R. Hiremath, L. Zschiedrich, and F. Schmidt. Numerical solution of nonlocal hydrodynamic Drude model for arbitrary shaped nano-plasmonic structures using Nédélec finite elements. arXiv:1201.1527v2 (submitted to J. Comp. Phys.), 2012.
8. P. Monk. *Finite Element Methods for Maxwell’s equations*. Oxford Science Publications, 2003.
9. L. Zschiedrich. Transparent boundary conditions for Maxwell’s equations: Numerical concepts beyond the PML method, Ph.D. thesis, Freie Universität Berlin (2009). http://www.diss.fu-berlin.de/diss/receive/FUDISS_thesis_000000013994

Model order reduction for efficient battery electro-thermal simulation

Lucas Kostetzer¹ and Evgeny Rudnyi¹

CADFEM (Suisse) AG, Wittenwilerstrasse 25, CH 8355 Aadorf, Switzerland lkostetzer@cadfem.de, erudnyi@cadfem.de

Summary. Battery finite element thermal model is reduced using moment matching method and coupled with electrical cell models at the system level in order to have accurate and fast simulation for designing management systems. A switching method between reduced order models is presented to evaluate different cooling conditions of the battery pack.

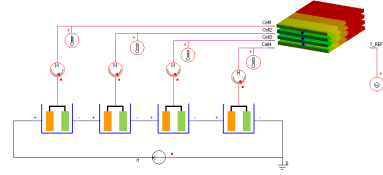


Fig. 1. Electro-thermal coupling at the system level applied to a battery pack

1 Introduction

Battery performance is directly related to operating temperature [1] due to influences in the electrochemical behavior, specially for Lithium ion types. High temperature can initiate exothermic side reactions that cause self heating, and a potential damage. At low temperatures slow diffusion of Lithium ions can cause saturations at the electrodes that results in higher internal electrical resistances [2], in other words power is influenced. Battery life is also affected by temperature. For calendar life (only storage), internal resistances can increase 30% more if temperatures are raised from 30°C to 55°C [3]. Hence an efficient and accurate thermal management is necessary.

For an electro-thermal battery model first we need a temperature dependent electrical battery model which is also capable to describe heat losses. Heat losses from a battery enter into the thermal subsystem where temperature distribution is evaluated. Temperature influences electrical properties of the battery as well as its power dissipation. The joint simulation of an electrical and a thermal subsystem can therefore be referred as electro-thermal simulation, Fig. 1. A practical problem is related to the fact that finite elements are usually employed to develop a thermal model of the battery pack. Such models are high dimensional and incompatible with system simulation as its transient simulation takes too much time. The development of a compact thermal model based on a finite element model is therefore necessary as an intermediate step.

2 Model Order Reduction

After the discretization of a finite element transient thermal model one gets a system of ordinary differential equations in the following form:

$$E\dot{\mathbf{x}} + K\mathbf{x} = \mathbf{f} \quad (1)$$

Where E is the heat capacity matrix, K is the heat conductivity matrix, and the state vector \mathbf{x} contains the degrees of freedom, DOF, which for thermal problems are the node temperatures. For model order reduction, MOR, the concept of input/output is introduced. The load vector $\mathbf{f}(t)$ is divided in constant vectors \mathbf{b}_i and in time functions $u(t)$. Constant vectors transfer the time functions to specific degrees of freedom.

$$\mathbf{f}(t) = \sum \mathbf{b}_i u(t) \quad (2)$$

At the system level there is no need of the complete state vector \mathbf{x} but just a part of that, named \mathbf{y} . The relation between them is defined by the output matrix C :

$$\mathbf{y} = C\mathbf{x} \quad (3)$$

The idea of model order reduction is to reduce the dimension of the state vector and preserve the dynamical behavior of the input/output relations [4]. Mathematicians and engineers developed [5] different techniques for model reduction and some of them use the projection idea

$$\mathbf{x} = V\mathbf{z} + \boldsymbol{\varepsilon} \quad (4)$$

The projection matrix V approximates the state vector \mathbf{x} with a few of degrees of freedom \mathbf{z} . Neglecting the approximation error $\boldsymbol{\varepsilon}$ the original state vector is described in the sub-space defined by matrix V . The reduced order model is found by projecting the eq. 1 into the lower sub-space:

$$V^T E V \dot{\mathbf{z}} + V^T K V \mathbf{z} = V^T B V u \quad (5)$$

$$\mathbf{y} = C V \mathbf{z} \quad (6)$$

Among existing methods, the present work focuses in the moment matching via Krylov subspace. The moment matching means after transforming the dynamic

system into Laplace domain, in such that lower-order system have the same first derivatives in the Taylor expansion around expansion points. A particular Krylov subspace finds the projection and the reduced order model matches the first moments automatically.

In this work first we show how a thermal battery pack finite element model is reduced to system level and coupled with electrical battery cell model. Second we explore a model order reduction switching between two reduced models applied to the battery pack model.

3 Electro-thermal coupling at the system level

The battery pack thermal model contains four battery cells that are cooled by air flow. The model is 3D and build in ANSYS. Fluid channels are modeled with 1D elements (FLUID116) and coupled with the thermal elements by a convection boundary condition. For the reduced order model, ROM, inputs are defined as the heat generation per battery cell and outputs are the temperature at cell center. Fluid operation conditions are constant.

The model reduction is done with the tool MOR for ANSYS with 10 DOF's per input resulting a dimension of 40 in the reduced model. The coupling is done with electrical cell model in a system level environment, ANSYS Simplorer [6], according to fig. 1. The electro-thermal coupled model is then used to evaluate the battery thermal management in a more accurate way since more realistic temperatures are predicted by using the ROM. In the other side better heat generation loads can be calculated at the system level.

4 Switching reduced order models

One limitation of the battery pack reduced model in section 3 is a fixed fluid cooling velocity. In an active cooling a control system is necessary, and for that the ROM should have fluid velocity as input. One can solve this in two ways, by using parametric model reduction or by switching different reduced order models. We studied the second methodology.

The fluid velocity has two contributions in the model: convection transport of heat by the fluid (mass flow) and the heat transfer coefficient (convection BC). Both quantities after discretization are in the K matrix from eq. (1). In this context we generate one reduced model for each desired velocity (we assume all channels have the same velocity) and switch between the ROM's at the system level.

At every switch event the reduced state variables \mathbf{z} must be initialized and this is done based on the last value of the previous reduced model assuming the

equality of the full state vector \mathbf{x} from eq. (4) as the following:

$$V_I \mathbf{z}_I + \varepsilon_I = V_{II} \mathbf{z}_{II} + \varepsilon_{II} \quad (7)$$

$$\mathbf{z}_{II} = V_{II}^T V_I \mathbf{z}_I \quad (8)$$

Results show that switch from a non-zero fluid velocity to a case with zero velocity is not successful since state variables from the two ROM's at switching event have differences in the order of 30%. Behavior that may be explained by a too different K matrix, what makes the projection from eq. (8) not accurate enough.

When the change of fluid velocity is not to zero, but a value up 1000 times, the switching transition is successfully smooth with differences in the states vectors in the order of 0.05%. Absolute values are also good by comparing with the full solution obtained from ANSYS, see fig.2. Differences are smaller than line thickness.

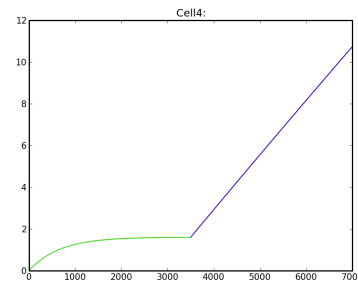


Fig. 2. Temperature rise values from a heat generation step response with a ROM switch at instant 3600s, fluid velocity is reduced by a factor of 1000.

References

1. A. Pesaran. Battery thermal management in evs and hev's: Issues and solutions, 2001.
2. K. Smith, T. Markel, G.H. Kim, and A. Pesaran. Design of electric drive vehicle batteries for long life and low cost, 2010.
3. E.V. Thomas, I. Bloom, J.P. Christophersen, and V.S. Battaglia. Statistical methodology for predicting the life of lithium-ion cells via accelerated degradation testing. *Journal of Power Sources*, 184(1):312 – 317, 2008.
4. T. Bechtold and E.B. Rudnyi. Introduction into model order reduction. *CAD/FEM Journal - Infoplaner*, N1:53–55, 2012.
5. T. Bechtold, J.G. Korvink, and E.B. Rudnyi. *Fast simulation of electro-thermal MEMS: efficient dynamic compact models*. Microtechnology and MEMS. Springer, 2007.
6. L. Kostetzer. Battery pack electro-thermal simulation. Master's thesis, University of Applied Sciences of Landshut and University of Applied Sciences of Ingolstadt, 2012.

Metamaterial design for magnetic field shielding

Mustafa Boyvat¹, Christian Hafner²

^{1,2} Electromagnetic Fields and Microwave Electronics Laboratory
Gloriastrasse 35
CH-8092 Zurich
Switzerland

¹ mustafa.boyvat@ifh.ee.ethz.ch

² Christian.Hafner@ifh.ee.ethz.ch

Summary. Metamaterials, usually composed of large arrays of coupled resonators, have been studied mostly for high frequency applications. However, they provide an alternative to conventional shielding techniques at very low frequencies, i.e. 50-60 Hz. In this work, we show how to analyze and design such metamaterials and we evaluate the effect of the polarizabilities, the geometric arrangement and the number of resonators using quasi-static approximation to shield magnetic field.

1 Introduction

Metamaterials are artificial structures, which enable naturally unavailable electromagnetic properties and engineering of them. Metamaterials have been studied for years extensively, mostly aiming for optical frequency applications. However, metamaterials also have the potential to be used at very low frequencies, such as the shielding of magnetic field at power frequencies.

A metamaterial is usually composed of coupled resonators and shows complex behaviour. This complication brings the need for simulation and optimization tools. At very low frequencies, the resonators, which are the basic unit of metamaterials, are simple LC resonators formed by lumped circuit elements, i.e. inductors and capacitors. Shielding may be obtained mainly by the following mechanism: The incident magnetic field induces currents in the inductors which then loads the connected capacitors. In [1], it has been shown that it is possible to use metamaterials to shield magnetic field at very low frequencies.

In this paper, the effects of the polarizabilities and the geometric arrangement of resonators are analyzed for the shielding application whereas the number of LC resonators is considered as a parameter to be kept low, because of high costs.

2 Design

As shown in [1], metamaterials are naturally anisotropic materials and this gives the possibility to obtain high shielding factors. Electromagnetic properties of metamaterials such as effective permeability can be obtained by effective medium approximations. To be able to use effective medium approximations, there must be a high density of LC resonators in the metamaterial block. One of the discussed points in this work is that although decreasing the number of LC resonators prevents us from using these approximations, it is still possible to obtain high shielding factors. In this case, the metamaterial becomes a set of 'meta-sheets', as illustrated in Figure 1. The shielding of a meta-sheet of which the coil axes are oriented in the direction of the source magnetic field (i.e. x direction in Figure 1) is realized by opposing magnetic field produced by LC resonators. The shielding of such a sheet is shown in Figure 2. The LC resonators are ideal (no resistance) and the meta-sheet is inhomogeneous.

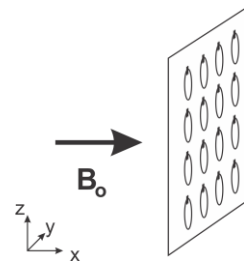


Figure 1: A meta-sheet, which is composed of LC resonators. B_0 shows the source magnetic flux density vector and is in x- direction where as the meta-sheet is in y-z plane.

3 Numerical Method

The LC resonators are modelled by current loops. The magnetic field of a current loop is given in [2]. The currents in LC resonators are obtained by equating the magnetic flux density to zero at some test points in the region to be shielded and this results in a linear matrix equation (see Equation (1)) [1]. $B'_{ji,k}$ is the k component of the magnetic flux density produced by the j^{th} current loop with unit current at the i^{th} test point. $B_{oi,k}$ is the source magnetic flux density and I_j is the current in the j^{th} loop.

$$\underbrace{\begin{pmatrix} B'_{11,x} & B'_{21,x} & \cdots & B'_{N1,x} \\ B'_{11,y} & B'_{21,y} & \cdots & B'_{N1,y} \\ B'_{11,z} & B'_{21,z} & \cdots & B'_{N1,z} \\ \vdots & \vdots & \vdots & \vdots \\ B'_{1M,y} & \cdots & \cdots & B'_{NM,y} \\ B'_{1M,z} & \cdots & \cdots & B'_{NM,z} \end{pmatrix}}_B \underbrace{\begin{pmatrix} I_1 \\ I_2 \\ \vdots \\ I_N \end{pmatrix}}_C = \underbrace{\begin{pmatrix} -B_{o1,x} \\ -B_{o1,y} \\ \vdots \\ -B_{oM,y} \end{pmatrix}}_D \quad (1)$$

By using more test points than necessary for the linear matrix equation, the problem turns into the optimization of vector C, which is formed by the currents in the loops (See Equation (1) and (2)) [1], [3].

$$\min_C \frac{1}{2} \|BC - D\|_2^2 \quad (2)$$

Putting additional coils with axes are oriented in y and z directions, the shielding can be improved by also trapping the magnetic field, similar to the shielding by high permeability materials.

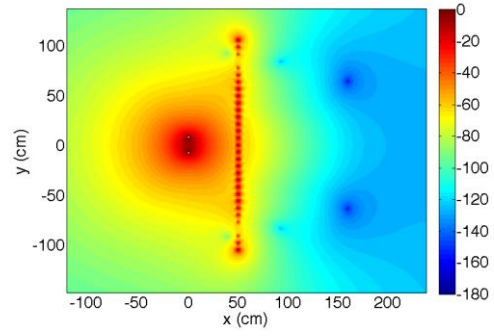


Figure 2: Shielding of an inhomogeneous meta-sheet. The color map shows the magnetic flux density in dB scale at $z=0$. The magnetic field source is a coil located at $(0,0,0)$ and the meta-sheet is located at $x=50$ cm.

4 Conclusions

Metamaterials can be used to shield magnetic field at very low frequencies. The number of LC resonators can be decreased by using meta-sheets and the shielding characteristic can be improved by modifying polarizabilities and the geometric arrangement of resonators. A numerical method for the design of meta-sheets has been presented. Since this method is based on a linear matrix equation, it is efficient and fast.

Acknowledgement: We acknowledge the support of EWZ.

References

1. M. Boyvat and C. V. Hafner, "Molding the flow of magnetic field with metamaterials: magnetic field shielding", *Progress In Electromagnetics Research*, Vol. 126, 303-316, 2012
2. W.R. Smythe, *Static and Dynamic Electricity*, p. 266, McGraw-Hill, New York, 1950
3. <http://www.mathworks.com>, The MathWorks, Inc.

Friday, September 14

The Discontinuous Galerkin Method on Dynamical hp -Meshes

Sascha M. Schnepf¹ and Thomas Weiland²

¹ Graduate School Computational Engineering, Technische Universität Darmstadt, Dolivostrasse 15, 64293 Darmstadt, Germany schnepf@gsc.tu-darmstadt.de,

² Institut fuer Theorie Elektromagnetischer Felder, Technische Universität Darmstadt, Schlossgartenstrasse 8, 64289 Darmstadt, Germany thomas.weiland@temf.tu-darmstadt.de

Summary. An hp -adaptive Discontinuous Galerkin method for time-domain electromagnetics problems is proposed. The method allows for arbitrary anisotropic refinements in the approximation order p and the mesh step size h regardless of the resulting level of hanging nodes. The adaptation process is guided by so-called reference solutions [14, 15], which are employed for estimating the solution error and finding the best type of refinement.

1 Introduction

In this article, we are concerned with solving the Maxwell equations for electromagnetic fields with arbitrary time dependence in a three-dimensional domain $\Omega \subset \mathbb{R}^3$. They read

$$\nabla \times \mathbf{E}(\mathbf{x}, t) = -\frac{\partial}{\partial t} \mu(\mathbf{x}) \mathbf{H}(\mathbf{x}, t), \quad (1a)$$

$$\nabla \times \mathbf{H}(\mathbf{x}, t) = \frac{\partial}{\partial t} \varepsilon(\mathbf{x}) \mathbf{E}(\mathbf{x}, t) + \mathbf{J}(\mathbf{x}, t), \quad (1b)$$

with the spatial variable $\mathbf{x} \in \Omega$ and the temporal variable $t \in [t_0, T] \subset \mathbb{R}$ subject to boundary conditions specified at the domain boundary $\partial\Omega$ and initial conditions specified at time t_0 . The electric and magnetic field vectors are denoted by \mathbf{E} and \mathbf{H} , \mathbf{J} denotes the electric current density. In (1), we assumed resting heterogeneous, linear, isotropic, non-dispersive and time-independent materials. The magnetic permeability and dielectric permittivity μ and ε for this case are scalar values depending on the spatial position only.

For discretizing (1), we employ the discontinuous Galerkin (DG) method [1, 2]. Nowadays, the DG method has gained wide acceptance as a numerical method, which combines the key features of accuracy and flexibility. Its flexibility stems from the highly localized character of the numerical approximation. This renders the method specially suited for time-domain problems as well as for applying adaptive mesh refinement. In particular, the method can easily deal with meshes with hanging nodes as stated in [3], which makes it particularly well suited for hp -adaptivity, i.e., the adaptation of the computational mesh regarding the local mesh step size h and the local approximation order p .

There is a well established body of literature on the DG method for various types of problems avail-

able. It has been thoroughly investigated by several research groups (see e.g. [3–5] and references therein). Concerning Maxwell's equations in time-domain, the DGM has been studied in particular in [5–8].

This paper focuses on error controlled dynamic hp -adaptation. In parts, it is a continuation of our work in [13], where a general formulation of the DGM on non-regular hexahedral meshes was introduced. The first published work on h -, p - and hp -adaptivity within the DG framework is presumably [9], where the authors consider linear scalar hyperbolic conservation laws in two dimensional space. For a selection of other publications see [10–12] and the references therein. Our formulation allows for arbitrary anisotropic h - and p -refinements with very relaxed demands on the level of hanging nodes.

2 Automatic and dynamic mesh adaptation with the DG method

The space and time continuous electromagnetic fields are approximated on a tessellation \mathcal{T} of the domain of interest Ω . The approximation of the electric field local to the element with index i reads

$$\mathbf{E}_i(\mathbf{x}, t) = \sum_p \mathbf{e}_i^p(t) \varphi_i^p(\mathbf{x}), \quad \mathbf{x} \in \mathcal{T}_i \quad (2)$$

with the polynomial basis functions $\varphi(\mathbf{x})$ of order $p \in \mathcal{P} = \{0, \dots, P\}$ and the time-dependent vector of coefficients \mathbf{e} . The magnetic field is approximated respectively.

It is specific to the DG method that the basis functions are defined with element-wise compact support. As a consequence the individual element-local approximations are not trivially connected, which inherently leads to a globally discontinuous approximation. Element communication is established via the so-called numerical interface fluxes only, which appear in the form of element surface integrals in the weak formulation of (1) (see e.g. [13] for details). This high degree of localization turns mesh adaptation into a purely element-local operation.

By defining proper finite element spaces associated with refined or reduced elements of h -, p - and hp -type the best approximation in the L^2 -sense, f^* , of

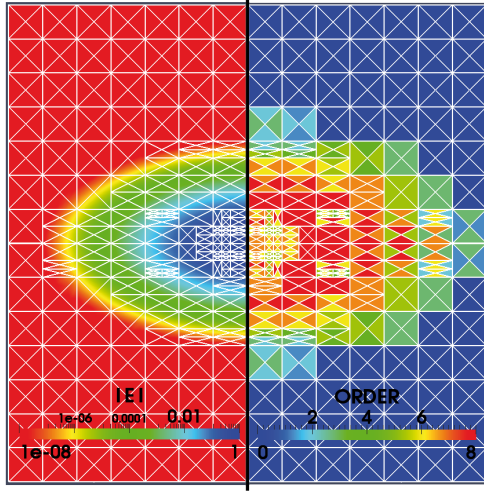


Fig. 1. Cut view of the electric field magnitude having a 3D Gaussian distribution (left) and corresponding anisotropically refined hp -mesh for an error tolerance of 10^{-9} in the L^2 norm. The mesh view makes use of the common tensor product order visualization technique [14].

a DG approximation f given on an existing hp -mesh is obtained by the orthogonal projection operator Π^p

$$f^* = \sum_p \Pi^p(f) \varphi_i^p = \sum_p \frac{(\varphi_i^p, f)_{\mathcal{T}_i}}{(\varphi_i^p, \varphi_i^p)_{\mathcal{T}_i}} \varphi_i^p, \quad (3)$$

where $(u, v)_{\mathcal{T}_i}$ denotes the inner product $\int_{\mathcal{T}_i} uv d\mathbf{x}$ on the element \mathcal{T}_i . In [13] it is shown that this projection can be performed very efficiently, and that it guarantees stability by respecting the electromagnetic energy of the current field solution as a strict upper limit.

In order to perform automatic mesh adaptation, the approximation error has to be estimated in an element-wise fashion in a first step. In [13] an error estimator based the size of the interelement jumps of the DG solution was proposed. In a second step the best type of adaptation, i.e., h -, p - and hp -refinement and/or reduction, has to be determined. This information is inferred from a local regularity estimation.

In this contribution, we apply the concept of *reference solutions* [14, 15]. A reference solution is a numerically computed approximation, which is assumed to be significant more accurate than the present approximation. This can be achieved by performing one isotropic h -refinement combined with increasing the approximation order by one on the element under consideration. The error of the present solution is computed with respect to the reference solution, which is also employed for finding the best refinement out of a list of candidates. Figure 1 shows an example of an anisotropically refined hp -mesh yielding an approximation error below 10^{-9} in the L^2 -norm. We adopted the common tensor product order visualization technique of [14, 15], where the color of a triangle including, e.g., an x -directed edge visualizes the order P_x .

Acknowledgement. The work of S.M. Schnepf is supported by the 'Initiative for Excellence' of the German Federal and State Governments and the Graduate School of Computational Engineering at Technische Universität Darmstadt.

References

1. W. Reed and T. Hill, Triangular mesh methods for the neutron transport equation. *Tech. rep., Los Alamos Scientific Laboratory Report*, 1973.
2. P. LeSaint and P.-A. Raviart. On a finite element method for solving the neutron transport equation. In C. de Boor, editor, *Mathematical Aspects of Finite Elements in Partial Differential Equations* Academic Press, New York, 1974, pp. 89–123.
3. B. Cockburn, C. Shu. Runge-kutta discontinuous galerkin methods for convection-dominated problems. *J. Sci. Comput.* 16(3):173–261, 2001.
4. J. S. Hesthaven, T. Warburton. *Nodal Discontinuous Galerkin Methods*. Springer, Berlin Heidelberg New York, 2008.
5. L. Fezoui, S. Lanteri, S. Lohrengel, S. Piperno. Convergence and stability of a discontinuous galerkin time-domain method for the 3d heterogeneous maxwell equations on unstructured meshes. *ESAIM-Math. Model. Num.* 39(6):1149–1176, 2005.
6. J. S. Hesthaven, T. Warburton. Nodal high-order methods on unstructured grids i. time-domain solution of maxwell's equations. *J. Comput. Phys.* 181(1):186–221, 2002.
7. G. Cohen, X. Ferrieres, S. Pernet. A spatial high-order hexahedral discontinuous Galerkin method to solve Maxwell's equations in time domain. *J. Comput. Phys.* 217(2):340–363, 2006.
8. E. Gjonaj, T. Lau, S. Schnepf, F. Wolfheimer, T. Weiland. Accurate modelling of charged particle beams in linear accelerators. *New. J. Phys.* 8:1–21, 2006.
9. K. Bey, J. Oden. hp-version discontinuous galerkin methods for hyperbolic conservation laws. *Comput. Method. Appl. M.* 133:259–286, 1996.
10. P. Houston, E. Süli. hp-adaptive discontinuous galerkin finite element methods for first-order hyperbolic problems. *SIAM J. Sci. Comput.* 23:1226–1252, 2001.
11. I. Perugia, D. Schötzau. The hp-local discontinuous galerkin method for low-frequency time-harmonic maxwell equations. *Math. Comput.* 72(243):1179–1214, 2003.
12. P. Houston, I. Perugia, D. Schötzau. Energy norm a posteriori error estimation for mixed discontinuous galerkin approximations of the maxwell operator. *Comput. Method. Appl. M.* 194(2-5):499–510, 2005.
13. S. Schnepf and T. Weiland. Efficient Large Scale Electromagnetics Simulations Using Dynamically Adapted Meshes with the Discontinuous Galerkin Method. *J. Comput. Appl. Math.*, Article in Press.
14. L. Demkowicz. *Computing with HP-Adaptive Finite Elements: Volume 1: One and Two Dimensional Elliptic and Maxwell Problems*. Chapman & Hall/CRC, 2007.
15. P. Solin, J. Cerveny, I. Dolezel. Arbitrary-level hanging nodes and automatic adaptivity in the hp-fem. *Math. Comput. Simulat.* 77(1):117 – 132, 2008.

Optimal design of reflecting photonic structures for space applications

Nikolay Komarevskiy¹, Valery Shklover¹, Leonid Braginsky¹, Christian Hafner¹, and John Lawson²

¹ Swiss Federal Institute of Technology (ETH) Zürich, 8092 Zürich, Switzerland

n.komarevskiy@ifh.ee.ethz.ch, V.SHKLOVER@mat.ethz.ch, leonid.braginsky@mat.ethz.ch, christian.hafner@ifh.ee.ethz.ch

² MS-234-1, NASA Ames Research Center, Moffett Field, 94035 California, USA john.w.lawson@nasa.gov

Summary. During atmospheric entries, vehicles can be exposed to strong electromagnetic radiation from gas in the shock layer. We propose and analyze silicon carbide and glassy carbon structures to increase the reflection of radiation. We performed numerical optimizations of photonic structures using an evolutionary strategy. Among the considered structures are layered, woodpile, porous and guided-mode resonance structures. The role of structural imperfections on the reflectivity is analyzed.

1 Introduction

Practical applications of photonic crystals (PhCs) are diverse [1, 2]. An interesting, but not yet practically realized, application of PhCs is as radiation shields for atmospheric re-entry of space vehicles. Electromagnetic radiation from ionized gas in the shock layer can constitute up to 30-50% [3] of the overall heat flux for lunar return trajectories, although for relatively short times. For Jupiter entries, on the other hand, most of the heating is radiative [4]. Therefore, in addition to protection against convective heating, a reentry thermal protection systems (TPS) should also be designed for radiation shielding. Ideally, the design should be tuned to the radiative spectra of a specific planet and specific entry conditions.

One of the easiest way to design radiation shields for atmospheric re-entry is with layered media [5]. Provided the two constituent materials possess a sufficient dielectric contrast and low absorption, broadband radiation shields with high omnidirectional reflection can be designed [6]. However, applications such as atmospheric re-entry impose many additional constraints on the material properties (thermal, mechanical, etc.). Therefore, finding a suitable pair of materials can be very demanding.

Currently, TPS for the most demanding atmospheric re-entries are made of highly porous carbon based materials. These materials, for example, PICA (phenolic-impregnated carbon ablators), possess many of the required thermal and mechanical properties. However, these materials are strong absorbers of radiation and therefore currently offer no protection at all from radiative heating. On the other hand, if these materials could be structured in such way that high

reflection is obtained, radiative heating of the vehicle during re-entry could be reduced. We analyze the potential of glassy carbon and silicon carbide as radiation shields for Earth atmospheric re-entry. The effects of structural imperfections on reflectivity are also analyzed.

1.1 Optimization goal

The goal is to design a radiation shield that maximizes the total reflection of normally incident *unpolarized* radiation u_v , shown in Fig. 1.

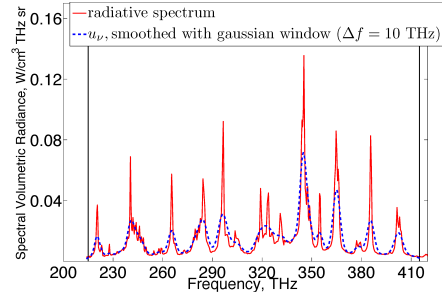


Fig. 1. (Red curve - experimental data of spectral radiation distribution, obtained at atmospheric re-entry relevant conditions [7] blue dashed curve - spectrum smoothed with Gaussian window function of full width $\Delta f = 10$ THz.

Therefore, the function to be maximized is:

$$\langle R_{u_v} \rangle = \frac{\int R_{\Sigma} u_v dv}{u_{\text{tot}}}, \quad u_{\text{tot}} = \int u_v dv, \quad (1)$$

where R_{Σ} is the total reflection of the incident unpolarized radiation:

$$R_{\Sigma} = 0.5(R^s + R^p), \quad (2)$$

where R^s and R^p are the sum of reflection efficiencies for the s- and p-polarization, respectively:

$$R^{s,p} = R_0^{s,p} + \sum_i D_i^{s,p}, \quad i = \pm 1, \pm 2, \dots \quad (3)$$

here the summation is performed over the propagating diffraction orders in the upper air half space.

For numerical optimization, we used evolutionary strategy (ES) algorithms. Based on previous experience [8], it is very powerful for real parameter optimization problems and outperforms genetic algorithm, particle swarm optimization, and other methods in most cases. We used an $(m+n)$ evolutionary strategy with adaptive mutation for the optimization. Here m is the initial number of parents and n is the number of children created in each generation.

Some of the structures to be optimized are shown in Fig. 2.

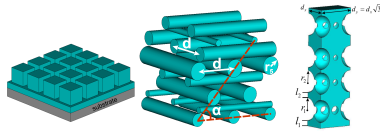


Fig. 2. (From left to right: guided mode resonance structure, woodpile, porous-reflector

Acknowledgement. This work was supported by ETH project 0-20590-09, Materials for Infra Red Protection.

References

1. J. Joannopoulos, S. Johnson, J. Winn, and R. Meade, *Photonic crystals: molding the flow of light* (Princeton Univ Pr, 2008).
2. V. Shklover, L. Braginsky, G. Witz, M. Mishrikey, and C. Hafner, "High-Temperature Photonic Structures. Thermal Barrier Coatings, Infrared Sources and Other Applications," *Journal of Computational and Theoretical Nanoscience* **5**, 862 (2008).
3. J. Grinstead, M. Wilder, J. Olejniczak, D. Bogdanoff, G. Allen, K. Dang, and M. Forrest, "Shock-heated Air Radiation Measurements at Lunar Return Conditions," *AIAA Paper* **1244**, 2008 (2008).
4. C. Park, "Stagnation-region heating environment of the galileo probe," *Journal of thermophysics and heat transfer* **23**, 417–424 (2009).
5. N. Komarevskiy, L. Braginsky, V. Shklover, C. Hafner, and J. Lawson, "Fast numerical methods for the design of layered photonic structures with rough interfaces," *Optics Express* **19**, 5489–5499 (2011).
6. N. Komarevskiy, V. Shklover, L. Braginsky, C. Hafner, O. Fabrichnaya, S. White, and J. Lawson, "Design of reflective, photonic shields for atmospheric reentry," *Journal of Electromagnetic Analysis and Applications* **3**, 228–237 (2011).
7. A. Brandis, C. Johnston, B. Cruden, D. Prabhu, and D. Bose, "Uncertainty analysis of neqair and hara predictions of air radiation measurements obtained in the east facility," in "42nd AIAA Thermophysics Conference," (American Institute of Aeronautics & Astronautics (AIAA), 2011).
8. J. Fröhlich, "Evolutionary optimization for computational electromagnetics," Ph.D. thesis, ETH Zurich, IFH Laboratory (1997).

Back-reflector optimization in thin-film silicon solar cells using 3D finite element simulations

Mark Blome¹, Kevin McPeak², Sven Burger¹, Frank Schmidt¹, and David Norris²

¹ Zuse Institute Berlin, Germany blome@zib.de, burger@zib.de, frank.schmidt@zib.de

² Optical Materials Engineering Laboratory, ETH Zürich, Switzerland kmcpeak@ethz.ch, dnorris@ethz.ch

Summary. We numerically optimize the light trapping efficiency of a periodic, pyramid structured back metal contact in thin-film amorphous silicon solar cells. Light propagation simulations are carried out by rigorously solving Maxwell's equations in 3D space for a wide range of model geometry parameters. In using our optimization approach we have identified nanostructure back reflector geometries that display a significant increase in short circuit current density over flat back reflectors.

1 Introduction

Thin-film amorphous silicon based solar cells are an attractive design for providing cost-effective and efficient solar energy. Amorphous hydrogenated silicon (a-Si:H) can be deposited in thin layers on cheap substrate materials such as glass or plastic offering low fabrication costs suitable for mass production.

One of the major barriers to the widespread use of a-Si:H solar cells is their increased defect density under light exposure the Staebler-Wronski (SW) effect. To mitigate (SW) effects, low thickness absorber layers (in the range of a few hundred nanometers) that exhibit a high electric field are typically employed. Considering the large absorption length of amorphous silicon near its bandgap, these thicknesses necessitate light-trapping concepts for realizing efficient thin-film silicon solar cells [1].

2 Methodologies

Within this work we optimize geometry parameters of a periodic, pyramid structured back metal contact in a model (p-i-n type) thin-film solar cell. Our goal is to find optimal model parameters that considerably increase the solar cells light trapping efficiency compared to flat designs.

2.1 Finite element light propagation modeling

To judge the efficiency of different solar cell models we compute short circuit current densities

$$I_{sc} = \frac{q}{hc} \int_{\lambda_{min}}^{\lambda_{max}} \lambda QE(\lambda) S(\lambda) d\lambda \quad (1)$$

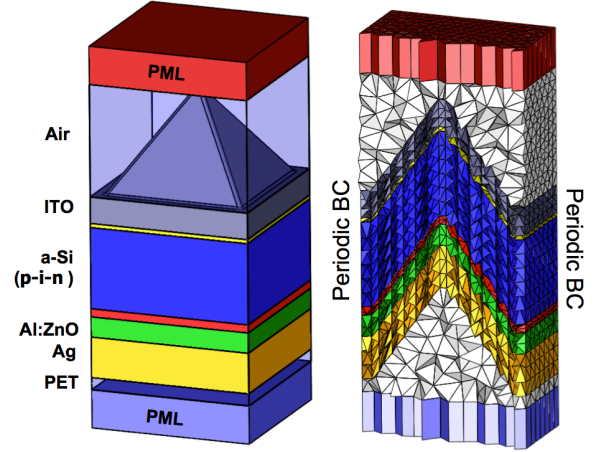


Fig. 1. Sample CAD representation of the model (p-i-n type) solar cell used (left) and vertical cut through a corresponding volume mesh (right). The computational domain is periodic in x,y directions; transparent boundary conditions are realized by adaptive perfectly matched layers (PML).

for the solar cell models under consideration. In (1) λ denotes the wavelength, q the elementary charge, h is Planck's constant, c is the speed of light and $S(\lambda)$ is the weighted sun spectrum (air mass 1.5 solar spectral irradiance). For each solar cell model short circuit current densities are computed over a wavelength range of 350 to 900 nanometers.

Estimating I_{sc} requires knowledge about the solar cells quantum efficiency $QE(\lambda)$ defined as the ratio of the number of generated charge carriers to the number of total incident photons:

$$QE(\lambda) = \frac{1}{P_o} \int \frac{1}{2cn} \frac{4\pi k}{\lambda} |E(\lambda, \mathbf{r})|^2 d\mathbf{r}. \quad (2)$$

Here P_o is the optical input power, n and k are the real and imaginary parts of the complex refractive index and integration is carried out in the intrinsic a-Si solar cell layer.

$E(\lambda)$ in (2) is the electric field in the solar cells absorber layer, which, considering the involved length scales, needs to be computed by rigorously solving Maxwell's equations. For this purpose we employ a frequency domain finite element method. To assure

a high solution accuracy we use higher order shape functions and adaptive perfectly matched layers for realizing transparent boundary conditions [4].

2.2 Model discretization using CAD techniques

To avoid discretization errors that would pollute the finite element solutions, investigated solar cell geometries need to be modeled and discretized with high accuracies. Furthermore, to be able to apply optimization algorithms for finding optimal back reflector geometries, it is essential that solar cell geometry models can be fully parameterized. For this purpose we have developed computer-aided design (CAD) techniques specifically tailored for the construction of parameterized nano-photonic device models.

A sample CAD representation of our model (p-i-n type) solar cell is displayed in Fig. 1. It consists of a nano-structured silver back contact deposited on a plastic substrate, followed by 50 nm of Al:ZnO, 200 nm of a-Si:H and a final layer of tin doped indium oxide. Edge rounding (fillet) is applied on sharp edges of the model geometry to avoid spurious reflections. The CAD model is parameterized by the period of the structure (in x,y directions) and the base width of the pyramids. In addition to these parameters other geometry parameters are currently being investigated.

A hybrid meshing scheme is used to discretize the model geometries with high quality structured/unstructured tetrahedral cells. The periodicity of the computational domain is automatically enforced during volume meshing and prismatic cells are added for realizing transparent boundary conditions with perfectly matched layers (Fig. 1).

So far material interface layers within the solar cell stacks are modeled by extrusion of the pyramid structured PET-Ag interface layer in positive Z-direction (as displayed in Fig. 1). To achieve a more accurate representation of the topography of the individual material layers, a level-set based topography simulation method is currently being developed. The method relies on the ballistic transport and reaction model developed by [2] and employs the level-set method to evolve interface layers [3].

3 Results

Our simulation results reveal that the employed pyramid structured back-reflectors effectively increase the light path in the absorber by (i) exciting photonic waveguide modes in the absorber and (ii) coupling incident photons to surface plasmon polaritons (SPPs). Using our optimization approach, we have identified nanostructure back reflector geometries that display a significant increase in short circuit current densities compared to a flat solar cell design with identical material layer thicknesses.

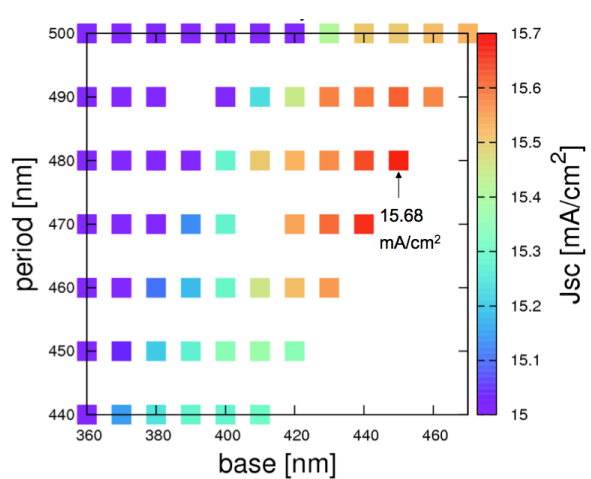


Fig. 2. Short circuit current densities I_{sc} computed for a series of solar cell models with varying cell periodicities and pyramid base widths. Displayed I_{sc} values are considerably larger than the value obtained for a flat back-reflector ($I_{sc} = 10.2 \text{ mA/cm}^2$).

Fig. 2 shows a map of computed short circuit current densities I_{sc} for a series of solar cell models with varying cell periodicities and pyramid base widths. A maximum value of $I_{sc} = 15.68 \text{ mA/cm}^2$ was identified for a solar cell model with a periodicity of 480 nm and a pyramid base width of 450 nm, which is considerably larger than the value obtained for a flat back-reflector ($I_{sc} = 10.2 \text{ mA/cm}^2$). Additional model parameters are currently being investigated. Furthermore, other type of back-reflector geometries are going to be analyzed in the framework of this ongoing research project.

Acknowledgement. The research presented here is the result of a multi-disciplinary, collaborative project headed by K. McPeak (OMEL, ETH Zürich). In addition to the authors of this abstract, the project relies on the work and contributions of: T. S. Cale (Process Evolution Ltd.), N. Wyrsh (EPFL, Lausanne) and M. Hojeij, Y. Ekinici (Paul Scherrer Institut).

References

1. H. A. Atwater and A. Polman. Plasmonics for improved photovoltaic devices. *Nature Materials*, 9:205–213, 2010.
2. T. S. Cale and V. Mahadev. *Thin Films: Modeling of Film Deposition for Microelectronic Applications*, volume 22, pages 176–277. Academic Press, 1996.
3. J. A. Sethian. *Level Set Methods and Fast Marching Methods*. Cambridge University Press, 2 edition, 1999.
4. L. Zschiedrich, R. Klose, A. Schädle, and F. Schmidt. A new finite element realization of the perfectly matched layer method for helmholtz scattering problems on polygonal domains in 2d. *J. Comput. Appl. Math.*, 188:12–32, 2006.

Derivation and test of high order fluid model for streamer discharges

Aram Markosyan¹, Saša Dujko^{1,2}, and Ute Ebert^{1,3}

¹ CWI, P.O. Box 94079, NL-1090 GB Amsterdam, Netherlands Aram.Markosyan@cwi.nl

² Institute of Physics, P.O.Box 68, 11080 Zemun Belgrade, Serbia sasha@phy.bg.ac.yu, S.Dujko@cwi.nl

³ Eindhoven University of Technology, P.O. Box 513, 5600 MB Eindhoven, Netherlands Ebert@cwi.nl

Summary. A high order fluid model for streamer dynamics is developed by closing the system after the 4th moment of the Boltzmann equation in local mean energy approximation. This is done by approximating the high order pressure tensor in the heat flux equation through the previous moments. Mathematical characteristics of the system is studied. Then planar ionization fronts for negative streamers in N₂ are simulated with the classical streamer model, MC-PIC particle model, and with the present higher order model.

1 High order fluid model

Streamer discharges occur in nature and as well in many industrial applications such as the treatment of exhaust gasses, polluted water or biogas. They appear when non-ionized or lowly ionized matter is exposed to high electric fields. Here we present a high order fluid model for streamer discharges, and we use it to simulate planar ionization fronts for negative streamers in nitrogen under normal conditions; and we compare the results with those of the classical fluid model.

1.1 Model description

The high order model is derived by taking the first 4 moments of the Boltzmann equation, i.e., by multiplying the Boltzmann equation with the k th power of velocity ($k = 0, 1, 2, 3$) and integrating over velocity space. In principle, the set of moment equations is infinite, but we consider only electron density ($k = 0$), momentum ($k = 1$), energy ($k = 2$) and energy flux ($k = 3$). The system is truncated in the energy flux equation (4) by approximating the high order pressure tensor by the product of lower order moments and by introducing factor of parametrization β . As a result the hydrodynamical formalization of the streamer dynamics in 1D is described by the nonlinear system of equations

$$\partial_t \mathbf{u} + \mathbf{A}(\mathbf{u}) \partial_x \mathbf{u} = \mathbf{F}(\mathbf{u}), \quad (1)$$

where the primitive variables are

$$\mathbf{u} = (n, nv, n\varepsilon, n\xi)^T, \quad (2)$$

the matrix $\mathbf{A}(\mathbf{u})$ is defined in following way

$$\mathbf{A}(\mathbf{u}) = \begin{pmatrix} 0 & 1 & 0 & 0 \\ 0 & 0 & \frac{2}{3m} & 0 \\ 0 & 0 & 0 & 1 \\ -\beta \frac{2\varepsilon^2}{3m} & 0 & \beta \frac{4\varepsilon}{3m} & 0 \end{pmatrix}, \quad (3)$$

and the source term is

$$\mathbf{F}(\mathbf{u}) = \begin{pmatrix} nvI \\ \frac{nqE}{m} - nvv_m \\ qEnv - n\{v_e[\varepsilon - \frac{3}{2}kT_0] + \sum_{\alpha} v_{e\alpha}\varepsilon_{e\alpha} + v_I\varepsilon_I\} \\ \frac{5qE}{3m}n\varepsilon - n\xi v_m \end{pmatrix}. \quad (4)$$

Here n , v , ε and ξ are electron number density, average electron velocity, average electron energy and electron energy flux, correspondingly. E is the electric field and T_0 is room temperature. $v_m(\varepsilon)$ and $v_e(\varepsilon)$ are the momentum and elastic energy transfer collision frequencies, $v_I(\varepsilon)$ is the ionization frequency and $v_{e\alpha}(\varepsilon)$ are the collision frequencies for inelastic processes. As charge is conserved, the continuity equation for the ion density n_{ion} is

$$\partial_t n_{ion} = nvI, \quad (5)$$

when the ions are approximated as immobile. Space charge effects are taken into account through the Poisson equation

$$\partial_x E = \frac{e}{\varepsilon_0}(n_{ion} - n), \quad (6)$$

where ε_0 is the dielectric constant and e is the elementary charge.

Mathematical characteristics and numerical solution of the system

Lemma 1. *The system (1) is hyperbolic if and only if*

$$\beta = 0 \quad \text{or} \quad \beta \geq 1. \quad (7)$$

In the case of $\beta > 1$, the system (1) is strictly hyperbolic.

Although the eigenvalues of (1) have a simple form, the corresponding right and left eigenvectors are very complicated, which makes it impossible to work with them.

The finite volume method is used to spatially discretize the system (1),(5),(6) on uniform control volumes or cells V_j as follows:

$$V_j := [j\Delta x, (j+1)\Delta x), \quad x_j := \left(j + \frac{1}{2}\right) \Delta x, \quad (8)$$

where $j = 0, 1, \dots, M-1$, $\Delta x = L/M$ is the spatial grid size and L is the length of the simulation domain. To approximate the spatial derivative in (1) we use the second-order central difference discretization [1]. In our numerical experiments we saw that this spatial discretization approximates quite well the analytically predicted front velocity for the minimal model [2]. The time derivatives are approximated with the Runge-Kutta 4 method [1]. This is an explicit method, which always has a bounded stability domain. In our case the stability condition or CFL restriction is

$$\beta \sqrt{\frac{2}{3m}} \sqrt{\max \varepsilon} \frac{\Delta t}{2\Delta x} \leq C, \quad (9)$$

where C depends on the particular method and space discretization. In our simulations we use the value $C = 0.1$.

1.2 Particle model and classical fluid model

In essentially all numerical fluid models for streamers in the past 30 years, except for [3, 4], the electron density is approximated by a reaction drift diffusion approximation

$$\partial_t n - \partial_x (\mu E n + D \partial_x n) = n \nu_I, \quad (10)$$

This model is called the minimal model; it implies a local field approximation of reaction and transport coefficients.

As a second reference model we use the MC-PIC particle model from [5].

2 Results and discussion

Fig. 1 compares the results of the high order model, the particle model and of the minimal model for the same initial and boundary conditions and for the same electric field ahead of the ionization front. A multi term theory for solving the Boltzmann equation [6] is used to calculate flux transport coefficients and mean-energy dependent collisional rates required as an input in fluid equations.

The following main conclusions can be drawn:

1) The overall front structure is the same, but the particle model is much better approximated by the high order model than by the minimal model.

2) That the mean electron energy ahead of the front increases while the electric field is constant, was also seen in Monte Carlo simulations before [2], but

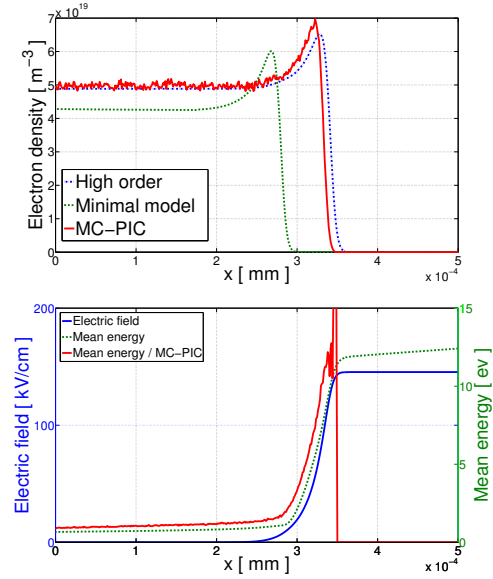


Fig. 1. Top: Electron density profile for the high order model (dashed dotted line, blue), the particle model (solid line, red) and for the minimal model (dashed line, green), bottom: mean electron energy (dashed line, green) and electric field (solid line, blue) profiles in the high order model, mean electron energy in the particle method (solid line, red). The plots show the simulation for instant 0.7 ns for identical initial conditions. The electric field ahead of the ionization front is 145 kV/cm at standard temperature and pressure, which corresponds to 590 Td.

not yet included in fluid models. The mean electron energy behind the front where the electric field vanishes, is close to 1 eV, because energy relaxation is slow in this region. This feature was not included in fluid models before.

In summary, the new high order fluid model captures effects in streamer simulations that up to now were only inherent in the more microscopic Monte Carlo simulations. This is a step forward for long time calculations.

Acknowledgement. Aram Markosyan acknowledges support by STW-project 10751.

References

1. W. Hundsdorfer, J. Verwer. *Numerical Solution of Time-Dependent Advection-Diffusion-Reaction Equations*. Springer, Berlin Heidelberg New York, 2003.
2. C. Li et al. *J. Appl. Phys.* 101, 123305 (2007).
3. C. Li et al. *J. Phys. D: Appl. Phys.* 42, 202003 (5p) (2009).
4. Z. Kanzari et al. *J. Appl. Phys.* 84, 4161 (1998).
5. C. Li et al. *J. Phys. D: Appl. Phys.* 41, 032005 (2008).
6. R. D. White et al. *J. Phys. D: Appl. Phys.* 42 (2009) 194001.

Electro-hydrodynamic numerical modelling of corona discharge

D. Cagnoni^{1,2}, F. Agostini¹, T. Christen¹, C. de Falco², N. Parolini², and I. Stevanović¹

¹ ABB Switzerland Ltd., Corporate Research, CH-5405 Baden-Dättwil, Switzerland
ivica.stevanovic@ch.abb.com

² Dipartimento di Matematica “F. Brioschi”, Politecnico di Milano, via Bonardi 9, 20133 Milano, Italy

Summary. Prediction of cooling by forced convection due to corona-induced ion flow in an electro-hydrodynamic (or EHD) simulation requires a reliable corona electrode model, which has to be formulated as a boundary condition (BC) to the EHD partial differential equations. We discuss and compare four different BCs in the context of finite-volume methods (FVM). It turns out that the optimum choice depends on the given physical information.

1 EHD differential and numerical model

Corona discharge refers to field induced gas ionization near an electrode, e.g., a thin wire (*emitter*), in series with the dark discharge associated with the ion drift towards counter electrodes (*collector*). The ion motion induces a drag of the neutral gas, and can be used to convection cool a heat source, which may be the collector at the same time. The associated equations consist of the Poisson equation for the electric potential ϕ , and the balance equations for the densities for ion number N_p , mass ρ , momentum $\rho \mathbf{v}$, and energy (written in terms of the temperature T). In the Boussinesq approximation, they read

$$-\nabla \cdot (\varepsilon \nabla \phi) = q N_p \quad (1)$$

$$\frac{\partial N_p}{\partial t} = -\nabla \cdot \left(\frac{\mathbf{j}}{q} \right) = -\nabla \cdot ((b\mathbf{E} + \mathbf{v})N_p + a\nabla N_p) \quad (2)$$

$$\nabla \cdot \mathbf{v} = 0 \quad (3)$$

$$\frac{D\mathbf{v}}{Dt} = \nu \Delta \mathbf{v} - \nabla \left(\frac{p}{\rho} - \mathbf{g} \cdot \mathbf{x} \right) + \mathbf{f}_B + \mathbf{f}_{\text{EHD}} \quad (4)$$

$$\rho C_V \frac{DT}{Dt} = k \Delta T + \mathbf{j} \cdot \mathbf{E} - \mathbf{f}_{\text{EHD}} \cdot \mathbf{v} \quad (5)$$

where ε is the electric permittivity, q the ion charge, $\mathbf{E} = -\nabla \phi$ the electric field, b the ion mobility, a the diffusion constant, $\frac{D\bullet}{Dt} = \frac{\partial \bullet}{\partial t} + \mathbf{v} \cdot \nabla \bullet$ the material derivative for the velocity field \mathbf{v} , ν the viscosity, p the pressure, \mathbf{g} the gravitational acceleration, $\mathbf{f}_B = \beta(T_{\text{ref}} - T)$ the buoyancy force, and $\mathbf{f}_{\text{EHD}} = qN_p \mathbf{E}$ the Coulomb force, assumed to be distributed over all gas particles via scattering. The electric current density \mathbf{j} consists of drift, convection, and diffusion currents.

The system of coupled, nonlinear PDEs has to be solved for given initial and boundary conditions. Prior to discussing the latter, we summarize the global solution procedure. First, in a Gauss-Seidel-like approach, the solution is determined progressively for the block

$\phi - N_p$, then for the block $p - \mathbf{v}$ and finally for T . Because of the weak influence of each block to the preceding ones, only one iteration per time step is performed. Electrostatics equations are solved with nonlinear formulation to reach convergence (for details, see [2]) while Navier-Stokes block is solved via a SIMPLE-like projection method ($\lambda(\mathbf{v})$ being a coefficient depending on both the estimated velocity and the grid). Here we sketch how this iteration is built:

- until $\int_{\Omega} (N_p^{(k-1)} e^{\phi^{(k,0)} - \phi^{(k,n)}} - N_p^{(k)}) < \text{tol}$.
 - until $\|\phi^{(k,n-1)} - \phi^{(k,n)}\|_{\infty} < \text{tol}$.
 - ▲ solve $-\nabla \cdot (\varepsilon \nabla \phi^{(k,n)}) = q N_p^{(k-1)} e^{\phi^{(k,0)} - \phi^{(k,n)}}$, linearized around $\phi^{(k,n-1)}$
 - solve $q \frac{\partial N_p^{(k)}}{\partial t} = -\nabla \cdot (\mathbf{j}(\phi^{(k,n)}, N_p^{(k)}))$
- solve momentum equation (4) for $\mathbf{v}^{(0)}$
- until $\int_{\Omega} \nabla \cdot \mathbf{v}^{(j)} < \text{tol}$.
 - solve $-\nabla \cdot (\lambda(\mathbf{v}^{(j-1)}) \nabla p^{(j)}) = \nabla \cdot \mathbf{v}^{(j-1)}$
 - correct $\mathbf{v}^{(j)} = \mathbf{v}^{(j-1)} - \lambda(\mathbf{v}^{(j-1)}) \nabla p^{(j)}$
- solve temperature equation (5)

2 Corona discharge boundary conditions

We restrict our discussion to the BC for N_p at the *corona* electrode, comparing four different BC types. For the rest of the boundaries, instantaneous recombination BC ($\mathbf{n} \cdot \nabla N_p = 0$) is applied at counter electrodes, while in all other cases well-known standard BCs can be used.

The first approach we present is the *natural condition*, namely imposing the normal flux j_n associated to (2) to be uniform; this approach is very accurate when geometry is symmetric and one knows the actual current from measurements, but has the drawback of being totally unresponsive. Nonetheless, this approach is sometimes used with arbitrary geometries, defining an *active surface* that emits the necessary current density. The generally accepted *Kaptsov's hypothesis* (see [5]) states that $E_n := \mathbf{E} \cdot \mathbf{n} = E_{\text{on}}$, namely the field remains constant at the (virtual) electrode once the corona discharge is triggered. A value for E_{on} can be computed from *Peek's law* (see e.g. [6], ch. 4) and allows to define the active region as the part of the boundary where $E_n > E_{\text{on}}$ holds.

For having a predictive condition, instead, one needs to somehow enforce a *constitutive law* linking

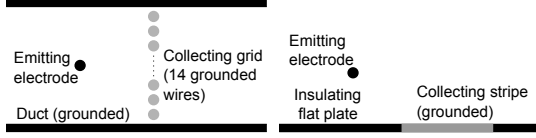


Fig. 1. Gometries from [4] (left) and from [3] (right).

j_n or N_p with E_n . We choose to adopt the second, simpler formulation, namely to impose $F_i(E_n, N_p) = 0$ to be satisfied on the boundary. Our first approach, given in [1], is based on a simplified physical model of the virtual contact which takes into account charge carriers injected solely from the active surface (with a saturation current density $j_{\text{sat}}H(E_n - E_{\text{on}})$, where $H(\bullet)$ is the Heaviside step function), and backscattered carriers (with current density given by $-qN_p w$ at the contact, where w is a characteristic velocity). Neglecting diffusion current at the electrode, this approach can be interpreted as imposing the relation

$$F_1(E_n, N_p) = qN_p(bE_n - w) - j_{\text{sat}}H(E_n - E_{\text{on}}) = 0 \quad (6)$$

Choice for the parameters j_{sat} and w needs to guarantee that the injected charge can naturally force $E_n = E_{\text{on}}$, otherwise current density saturates to $j_n = j_{\text{sat}}$ and *space charge controlled current* (SCCC) regime is not reached anymore.

Our second approach is to model the boundary as an ideal *rectifying diode*, in which no ion density is flowing under the E_{on} threshold, while every N_p value is possible when $E_n = E_{\text{on}}$. Explicitly, this approach is equivalent to enforce the following:

$$F_2(E_n, N_p) = N_p \left(1 - \left(\frac{E_n}{E_{\text{ons}}} \right)^\beta \right) = 0 \quad (7)$$

$\beta \in [0, 1]$ being a smoothing factor. This relation strongly enforces both N_p to vanish in the other non active portion of the electrode, and E_n to match E_{on} in the active portion.

Our last approach assumes a constitutive relation which is a more regular version for the former one:

$$F_3(E_n, N_p) = N_p - N_{\text{ref}} \left(\exp \left(\frac{E_n}{E_{\text{ref}}} \right) + 1 \right) = 0 \quad (8)$$

where N_{ref} and E_{ref} are a device-off ion density and a reference electric field. The choice of these two values can thus be made independently from the particular case (using e.g. air conductivity for N_{ref}).

3 Results and conclusions

As examples, a wire-to-grid geometry [4] and a wire-to-plate geometry [3] have been investigated (Fig. 1).

The former consists of a duct with a grounded grid in the middle (both collectors), and an emitter placed upstream. The E_{on} value is determined from the experimental onset voltage (4 kV). Simulations

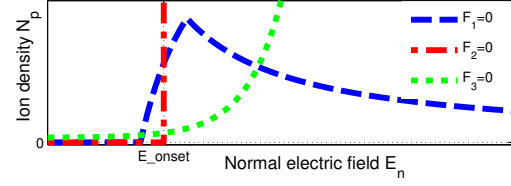


Fig. 2. Comparison of the graphs on the $N_p - E_n$ plane defined by the constitutive relations $F_i(E_n, N_p) = 0$.

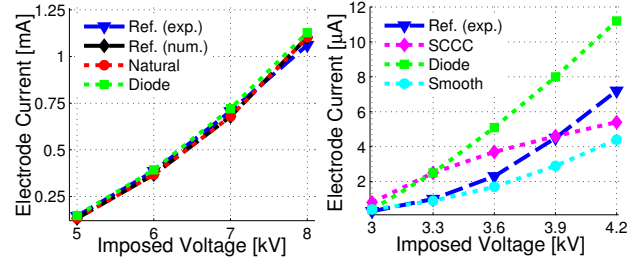


Fig. 3. IV-characteristic for the wire to grid (left) and wire to plate (right) geometries.

show how the natural condition matches exactly the experimental value, and the iterative condition as in (7) still captures well the electrical behavior. One may thus consider that in cases like this, even when lacking measured currents, the ideal diode model is still appropriate.

The latter geometry has a heated plate with a collecting stripe and the emitter is lifted from the plate. As shown in Fig 3, this case is not as well reproduced as the former, due to the highly nonuniform E_n on the electrode. This issue may be solved with a parameter optimization, which has not yet been undertaken in the present study. The current, being the most influential parameter for the fluid dynamics and thermal computing, was predicted with acceptable accuracy.

References

1. T. Christen and M. Seeger. Simulation of unipolar space charge controlled electric fields. *J. Electrostatics*, 65:11–20, 2007.
2. C. de Falco, J. W. Jerome, and R. Sacco. Quantum-corrected drift-diffusion models: Solution fixed point map and finite element approximation. *J. Comp. Phys.*, 228:1770–1789, 2009.
3. D. B. Go et al. Enhancement of external forced convection by ionic wind. *I.J. Heat Mass Transfer*, 51:6047–6053, 2008.
4. N. E. Jewell-Larsen et al. Modeling of corona-induced electrohydrodynamic flow with comsol multiphysics. In *Proc. of ESA Annual Meeting on Electrostatics*, 2008.
5. N. A. Kaptsov. *Elektricheskie Yavleniya v Gazakh i Vakuume*. OGIZ, Moskva, 1947.
6. H. J. White. *Industrial electrostatic precipitation*. Addison-Wesley, New York, 1963.

Efficient Simulation of Frequency-Transient Mixed Co-Simulation of Coupled Heat-Electromagnetic Problems

Christof Kaufmann¹, Michael Günther¹, Daniel Klagges², Jan ter Maten¹, Matthias Richwin², Sebastian Schöps¹

¹ Bergische Universität Wuppertal, Wicküler Park, Gaußstraße 20, D-42119 Wuppertal
 {kaufmann,schoeps,guenther,termaten}@math.uni-wuppertal.de

² Leopold Kostal GmbH & Co. KG, Hauert 11, 44227 Dortmund, {d.klagges,m.richwin}@kostal.com

Summary. This paper discusses an efficient mixed mode simulation method for induction heating problems. For time-harmonic inputs the electromagnetic part can be considered in the frequency domain. This avoids the inefficient time integration of high frequency signals. By leaving the heat problem in time domain this approach leads to a frequency-transient simulation with low computational costs. The coupling is established by an average power transfer model.

1 Introduction

Inductive power transfer problems deal with electromagnetic fields that transport large amounts of energy. Even small power losses can result in considerable heating up [3, 5, 6]. The skin effect causes most heat generation at material boundaries. Hence the temperature considerably influences the material parameters, e.g. the electric conductivity, and thus the electromagnetic fields. This underlines the need for a mutual coupling of the heat and electromagnetic field models.

A transient simulation of the coupled problem often suffers from relative small time steps due to high frequencies in the electromagnetic part. However, heating up is a comparatively slow effect. Therefore simulations of large time intervals are necessary. The small time steps in combination with long time intervals induce high computational cost or make a simulation even infeasible (multirate behaviour).

It is beneficial to reduce the computational effort for solving the electromagnetic problem. In this paper we discuss an adapted model that allows for a mixed formulation: frequency domain analysis of the EM problem and time domain for the heat problem, [2]. This approach is similarly implemented in COMSOL Multiphysics, [4]. We focus on numerical analysis in the framework of dynamic iteration, e.g. [1].

An model example from industry is used for numeric results. KOSTAL describes with that the power transfer by induction for an inductive charging station. It will be used to charge batteries of electric cars.

2 Modelling

Electromagnetic fields are mathematically described by a system of time-dependent partial-differential equations on a domain Ω . It reads in curl-curl formulation:

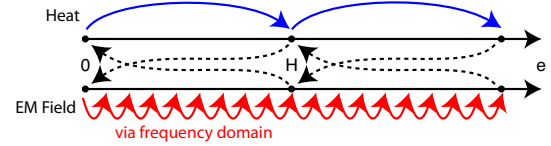


Fig. 1. Time windows τ_i , time steps due to dynamics (red and blue arrows) and coupling scheme (black arrows). Small time steps (red) are avoided in frequency domain.

$$\varepsilon \frac{\partial^2 \mathbf{A}}{\partial t^2} + \sigma(T) \frac{\partial \mathbf{A}}{\partial t} + \nabla \times (\nu \nabla \times \mathbf{A}) = \mathbf{J}_e, \quad (1)$$

where the reluctivity ν and the permittivity ε depend only on space $\mathbf{r} \in \Omega$, the electrical conductivity σ also on temperature T , the external current density \mathbf{J}_e is a given sinusoidal source and the magnetic vector potential $\mathbf{A}(t)$ is unknown on $t \in [t_0, t_e]$. For brevity the space dependency \mathbf{r} is always neglected. On the other hand we have the heat equation

$$\rho c \frac{\partial T}{\partial t} = \nabla \cdot (\mathbf{k} \nabla T) + Q, \quad (2)$$

where the temperature T is an unknown function and the mass density ρ , the heat capacity c and the heat conductivity \mathbf{k} depends on space and temperature. The term Q is a source term. It is given by the power loss of the electromagnetic field and couples (1) and (2). If we neglect hysteresis losses, Q is described by

$$Q(\mathbf{A}, T) = \sigma(T) \frac{\partial \mathbf{A}}{\partial t} \cdot \frac{\partial \mathbf{A}}{\partial t} - \frac{\partial \mathbf{A}}{\partial t} \cdot \mathbf{J}_e. \quad (3)$$

We equip (1)-(3) with boundary and initial conditions at t_0 and discretise it. However (1) requires very small time steps for the fast varying signal \mathbf{J}_e . This problem is addressed in the next section.

3 Averaging Power and Temperature

We split the time interval of interest $[t_0, t_e]$ in time windows $[\tau_i, \tau_{i+1}]$ according to the time scale of the heat transfer, see Fig. 1. Since heat transfer is a rather slow process, it is sufficient to consider only the averaged power per time window that is generated:

$$\bar{Q}_i = \frac{1}{\tau_{i+1} - \tau_i} \int_{\tau_i}^{\tau_{i+1}} Q(\mathbf{A}(t), T(t)) dt \quad (4)$$

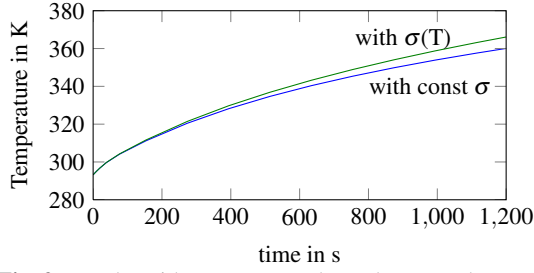


Fig. 2. Results with temperature dependent σ and const. σ

and similarly the temperature is averaged:

$$\bar{T}_i = \frac{1}{\tau_{i+1} - \tau_i} \int_{\tau_i}^{\tau_{i+1}} T(t) dt. \quad (5)$$

It follows for time-harmonic input signals \mathbf{J}_e

$$\bar{Q}_i = \sigma(\bar{T}_i) \frac{\omega^2}{2} \|\hat{\mathbf{A}}_c\|_c^2 + \frac{\omega}{2} \text{Im}(\hat{\mathbf{A}}_c) \cdot \hat{\mathbf{J}}_e, \quad (6)$$

where ω is the angular frequency and $\hat{\mathbf{J}}_e$ the amplitude of \mathbf{J}_e and $\hat{\mathbf{A}}_c$ is the complex fourier coefficient of the solution for $\mathbf{A} = \hat{\mathbf{A}}_c e^{j\omega t}$ of (1) with $\mathbf{J}_e = \hat{\mathbf{J}}_e e^{j\omega t}$.

We derive a simplified system consisting of a (1) in frequency domain and a (2) in time domain:

$$(j\omega\sigma(\bar{T}_i) - \omega^2\epsilon)\hat{\mathbf{A}}_c + \nabla \times (\mathbf{v} \nabla \times \hat{\mathbf{A}}_c) = \hat{\mathbf{J}}_e \quad (7)$$

$$\rho c \frac{\partial T}{\partial t} - \nabla \cdot (\mathbf{k} \nabla T) = \bar{Q}_i, \quad (8)$$

where \bar{Q}_i is defined in (6) and \bar{T}_i in (5). Equation (7) is equivalent to an average power transfer model of (1). However, in frequency domain only a linear system has to be solved instead of many time steps. This approach exploits efficiently different time scales.

4 Co-simulation

We solve the system (6)-(8) iteratively, [1]. In the following the subscript index i belongs to time step t_i and the superscript index (l) denotes the iteration step l .

$$(j\omega\sigma(\bar{T}_{i+1}^{(l)}) - \omega^2\epsilon)\hat{\mathbf{A}}_{i+1}^{(l+1)} + \nabla \times (\mathbf{v} \nabla \times \hat{\mathbf{A}}_{i+1}^{(l+1)}) = \hat{\mathbf{J}}_e$$

$$\bar{Q}_{i+1}^{(l+1)} = \sigma(\bar{T}_{i+1}^{(l+1)}) \frac{\omega^2}{2} \|\hat{\mathbf{A}}_{i+1}^{(l+1)}\|_c^2 + \frac{\omega}{2} \text{Im}(\hat{\mathbf{A}}_{i+1}^{(l+1)}) \cdot \hat{\mathbf{J}}_e$$

$$\bar{T}_{i+1}^{(l+1)} - \frac{h_i}{\rho c} \nabla \cdot (\mathbf{k} \nabla \bar{T}_{i+1}^{(l+1)}) = \bar{T}_i + \frac{h_i}{\rho c} \bar{Q}_{i+1}^{(l+1)}$$

The co-simulation can be organized as shown in Fig. 3 for the special case where time step and time window sizes agree, i.e., $h_i = \tau_{i+1} - \tau_i$.

In the full paper this algorithm is numerically analysed and convergence of the inner loop is shown. This converges to the *average power and temperature model* from Sec. 3. In a second step it will be shown, that this model converges to the original model from Sec. 2 when the time steps turn to zero. In addition the computational sequence of the subsystem will be discussed. The results are verified by a 2D model of the industry example, see Fig. 2.

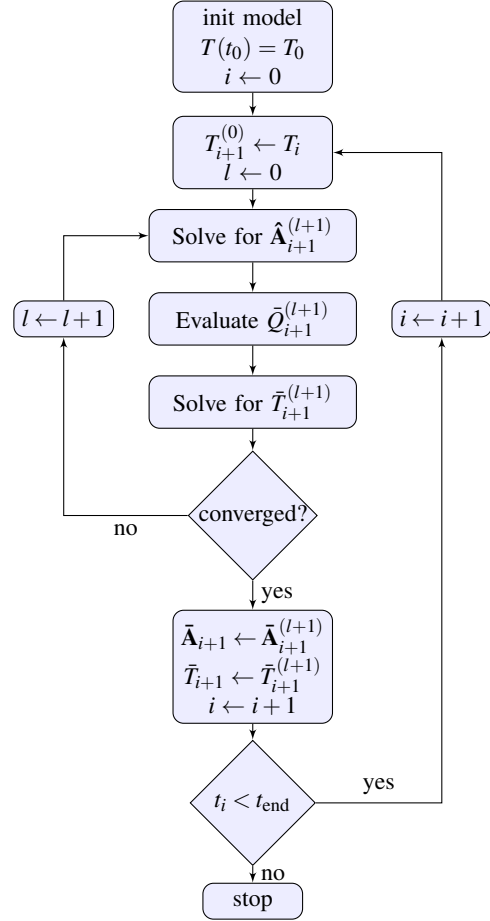


Fig. 3. Co-Simulation

Acknowledgement. This work is supported by the German BMBF in the context of the SOFA project (grant number 03MS648E).

References

1. A. Bartel, M. Brunk, M. Günther, and S. Schöps. Dynamic iteration for coupled problems of electric circuits and distributed devices. Preprint 11/16, 2011.
2. J. Driesen and K. Hameyer. The simulation of magnetic problems with combined fast and slow dynamics using a transient time-harmonic method. *Eur Phys J Appl Phys*, 14:165–169, 2001.
3. H.H.J.M. Janssen, E.J.W. ter Maten, and D. van Houwelingen. Simulation of coupled electromagnetic and heat dissipation problems. *IEEE Trans Magn*, 30(5):3331–3334, sep 1994.
4. COMSOL Multiphysics. *Command Reference*. Comsol AB, 2007.
5. E.J.W. ter Maten and J.B.M. Melissen. Simulation of inductive heating. *IEEE Trans Magn*, 28(2):1287–1290, mar 1992.
6. J. Will. An optimal control problem in electromagnetic induction heating. Master's thesis, Chemnitz University of Technology, Department of Mathematics, Germany, 2010.

Designing High Performance Electronic Devices, Circuits and Systems

Giuseppe Nicosia¹

Dept. of Mathematics and Computer Science University of Catania - Italy
nicosia@dmf.unict.it
<http://www.dmf.unict.it/nicosia>

The increasing complexity of electronic design needs to be managed with effective optimization algorithms and accurate statistical description of models in order to maximize the performances and the reliability of the electronic systems and minimize the tight time-to-market constraints. New optimization algorithms have to balance accuracy, robustness and computational effort. Typical electronic design problems are computationally hard and require the handling of multiple, conflicting, and non-commensurate objective functions having strong nonlinear interdependence. In this talk we present a simulation-based multi-scenario and multi-objective optimization algorithm for designing devices, analog mixed-signal circuits, and systems-on-chip. We express the design problems as large-scale constrained multi-objective optimization problems (defined in a mixed integer-discrete-continuous domain) for which a class of efficient algorithms has been designed and implemented. The algorithm scales gracefully with systems size and type; the framework has been tested on several real-world devices, circuits and systems. This framework satisfies the constraints, optimizes the performances while minimizes plastic/silicon area, power consumption, energy and delay maximizing the overall yield. We report on several applications of electronic system design:

- 1) at the device-level, we tackle the design of MESFETs, MOSFETs and Power MOSFETs;
- 2) at the circuit-level, we face the design of RF Low Noise Amplifier, Leapfrog Filter, Ultra Wideband Low Noise Amplifier, and Fully Differential Folded-Cascode Operational Amplifiers;
- 3) while at the system-level, we present the results for a pipeline A/D Converter, a Receiver front-ends for UMTS and UWB Communications and a Multi Processor Systems-on-Chip.

The effectiveness and robustness of the proposed approach, as compared with the state-of-art of academic and commercial methods, are demonstrated. The results show a significant improvement in all the tackled electronic design problems.

Acknowledgement. This work is supported by the ERG - Energy for a Green Society (ENIAC-JTI) - WP on Optimal Solar Cell Design, May 2011 - May 2014.

References

1. A. M. Anile, V. Cutello, G. Nicosia, R. Rascuna, and S. Spinella. Comparison among evolutionary algorithms and classical optimization methods for circuit design problems. In IEEE Congress on Evolutionary Computation, CEC - Sept. 2-5, 2005, Edinburgh, UK, volume 1, pages 765772, 2005.
2. A. Ciccazzo, T. Halfmann, A. Marotta, G. Nicosia, S. Rinaudo, G. Stracquadanio, and A. Venturi. New coupled em and circuit simulation for integrated spiral inductor by introducing symbolic simplified expressions. In IEEE Industrial Electronics Society Press, editor, IEEE Int. Symp. on Industrial Electronics - ISIE 2008, June 30 - July 2, 2008, Cambridge, UK, pages 12031208, 2008.
3. P. Conca, G. Nicosia, G. Stracquadanio, and J. Timmis. Nominal-yield-area tradeoff in automatic synthesis of analog circuits: A genetic programming approach using immune-inspired operators. In IEEE Computer Society Press, editor, NASA/ESA Conf. on Adaptive Hardware and Systems (AHS-2009) - 46th Design Automation Conference (DAC 2009), July 29 - August 1, 2009, San Francisco, CA, USA, pages 399406, 2009.
4. C. Drago, G. Nicosia, V. Romano, and G. Stracquadanio. Multi-objective optimization of doping profile in semiconductor design. In ACM Genetic and Evolutionary Computation Conference - GECCO 2010, July 7-11, 2010, Portland, Oregon, USA, pages 12431250.
5. F. Fiorante, G. Greco, G. Nicosia, S. Rinaudo, and G. Stracquadanio. Automatic layout optimization of power mosfets using an effective population-based algorithm. In SIAM Optimization Conf. - OP08, Boston - MA, USA, May 10-13, 2008, 2008.
6. G. Nicosia, C. M. Palano, N. E. Porto, F. D Amico, and G. Morelli. Smtps interactive design simulator - efficient power-supply designs. In Cadence CDNLive! EMEA, May 4-6, 2010, Munich, Germany, 2010.
7. G. Nicosia, S. Rinaudo, and E. Sciacca. An evolutionary algorithm-based approach to robust analog circuit design using constrained multi-objective optimization. Knowledge-Based Systems J., 21(3):175183, 2008.

8. G. Nicosia and G. Stracquadanio. Robust device and circuit design using effective constrained multi-objective optimization. In Cadence CDNLive! EMEA, May 4-6, 2010, Munich, Germany, 2010.
9. G. Stracquadanio, C. Drago, V. Romano, and G. Nicosia. Evolutionary design of semiconductor devices. In IEEE World Congress on Computational Intelligence - WCCI 2010, Barcelona, Spain, July 18-23, 2010.

Abstracts for Poster Sessions

Tuesday Regular Poster Session 14:50 - 16:20

Page	Title	Author(s)
119	Swarm-based algorithms for the Minimization of the Magnetic Field of Underground Power Cables	D. Altomonte, A. Laudani, G. Pulcini, A. Salvini, F. Riganti Fulginei
121	Numerical modeling of standard lightning impulse on overhead lines	S. Antonescu, C. Munteanu
129	Fast Solution of a Magnetostatic Problem with Parallel ILU	M. Bollhoefer, R. Bianchetti, J. Ostrowski, and D. Pusch
131	Efficient Shooting Method Based on Leading Dynamics Determination by QR Decomposition	Federico Bizzarri, Angelo Brambilla, Giambattista Gruosso, and Giancarlo Storti Gajani
135	On an integral equation method for the electromagnetic scattering of biperiodic structures	Beatrice Bugert and Gunther Schmidt
145	Advanced Computer Methods for Grounding Analysis	Ignasi Colominas, Jose Paris, Xesus Nogueira, Fermin Navarrina, and Manuel Casteleiro
149	Transmission line parameters computed by NURBS-based impedance boundary conditions: the case of different conductivities	Rafael Vazquez, Annalisa Buffa, and Luca Di Rienzo
153	Time Domain Models for Lossless Multiport Waveguide Structures in Impedance and Admittance Formulation based on Real Eigenmodes	Thomas Flisgen and Ursula van Rienen
155	Field of values analysis of Laplace preconditioners for the Helmholtz equation	Antti Hannukainen
159	Validation of the Potential Method; comparing measurements of a dihedral with calculations	Magnus Herberthson
169	Efficient solvers for optimal control of eddy current problems with regularized state constraints	Michael Kolmbauer and Ulrich Langer
173	The (1+1)D Space-Time Discontinuous Galerkin Trefftz Method	Fritz Kretzschmar, Sascha M. Schnepp, Igor Tsukerman, and Thomas Weiland
181	On the autocorrelation of environment induced noise	B.L. Michielsen
187	Grating profile optimization for reflection 1st order Littrow mounting	Andrey A. Petukhov, Michael K. Trubetskov, and Alexander N. Bogolyubov
191	Modeling and Analysis of the Performance Improvement Techniques for EMI Filters	Adina Racasan, Calin Munteanu, Vasile Topa, Dan Micu, Claudia Pacurar, Ema Adam
195	Coupling of FEM and Fourier-mode expansion for the scattering by perfectly conducting gratings	Guanghai Hu and Andreas Rathsfeld
197	A new indicator to assess the quality of a Pareto approximation set applied to improve the optimization of a magnetic shield	E. Dilettoso, S.A. Rizzo, N. Salerno
199	Accurate and efficient FEM simulations of circular spiral planar inductors	S.A. Rizzo, N. Salerno and S. Sindoni
203	An Embarrassingly Parallel Algorithm for Finite Element Formulations	Eike Scholz, Sebastian Schoeps, and Markus Clemens
205	The Reconstruction of Shape with 3-Step Modeling Strategy	Murat Simsek
207	A High-Order Discontinuous Galerkin-Approach-Based Particle-In-Cell Method for the Simulation of Large Scale Plasma Devices	A. Stock, J. Neudorfer, M. Pfeiffer, R. Schneider, S. Fasoulas, and C.-D. Munz

Wednesday Regular Poster Session 14:50 - 16:20

Page	Title	Author(s)
143	Frequency Parameterized Models for Planar On-Chip Inductors	Gabriela Ciuprina, Daniel Ioan, Cosmin-Bogdan Dita, and Mihai-Iulian Andrei
151	Dynamical analysis and control of chaos in Vilnius chaotic oscillator circuit	Selcuk Emiroglu, Yilmaz Uyaroglu
157	Optimization of Planar Structures by Means of Shifted Winding	Claudia Hebedean, Calin Munteanu, Adina Racasan
165	Eddy current analysis of a PWM controlled induction machine	Hai Van Jorks, Erion Gjonaj, Thomas Weiland
175	Novel alternate mixed-mode chaotic circuit models for secure communication	Umesh Kumar
179	Simulation of a double-gate MOSFET by a non parabolic energy-transport subband model based on MEP including surface roughness scattering	V. D. Camiola, G. Mascali, and V. Romano
183	CIBSOC Program - Spiral Inductor Inductance Calculation and Layout Optimization	Claudia Pacurar, Vasile Topa, Adina Racasan, Calin Munteanu
185	Circuit Modelling, Simulation and Realization of the new Sundarapandian-Pehlivan Chaotic System	Ihsan Pehlivan, Ismail Koyuncu, Vaidyanathan Sundarapandian, Yilmaz Uyaroglu
193	Analyzing Distortion Contributions in a Complex Device Model	Timo Rahkonen, Janne P. Aikio
209	Realization Of Sprott Case C Attractor With CCIIs	Yilmaz Uyaroglu, Ihsan Pehlivan

Thursday Regular Poster Session 12:30 - 13:30

Page	Title	Author(s)
123	Optimization of the efficiency of a photovoltaic cell by means of a genetic algorithm	Giuseppe Ali , Francesco Butera, and Nella Rotundo
125	Convergence behaviour of coupled pressure and thermal networks	Andreas Blaszczyk, Reto Flückiger, Thomas Müller, Carl-Olof Olsson
127	Thermal Design of VSD Dry-Type Transformer	Marcos Bockholt, Wolfgang Mönig, Benjamin Weber, Bhavesh Patel, B. Cranganu-Cretu
141	Streamer Inception and Propagation from Electric Field Simulations	Thomas Christen

Optimization of the efficiency of a photovoltaic cell by means of a genetic algorithm

Giuseppe Ali^{1,2}, Francesco Butera¹, and Nella Rotundo¹

¹ Dipartimento di Matematica, Università della Calabria, Arcavacata di Rende I-87036, Cosenza, Italy
giuseppe.ali@unical.it, francesco.butera@unical.it, nella.rotundo@unical.it

² INFN, Gruppo collegato di Cosenza, Arcavacata di Rende I-87036, Cosenza, Italy

Summary. We consider an optimization problem for a photovoltaic cell, modeled by the drift diffusion equations, modified to include optical effects. In order to optimize the efficiency of the cell, first we determine the most relevant parameters, such as the number of fingers in a channel or the initial concentration. Then we use a genetic algorithm to determine the sets of parameters which optimize the efficiency of the cell.

1 Introduction

The current efficiency of photovoltaic cell panels is around 20% [1]. Higher values of efficiency (around 23%) can be achieved by selecting more expensive types of silicon crystals [2], but their use is limited to those cases in which cost is not an issue.

By contrast, commercial panels often fail to reach even the 20% limit of accuracy, falling closer to a value around 15% [3]. Raising the efficiency of commercial panels to values higher than 20% would be an important goal, both scientifically and technologically. An immediate increase of the efficiency of solar panels is possible by following two distinct paths: selecting materials with higher Energy gaps and increasing the area of the exposed solar cells.

In most commercial solar cells, the soldering contacts and the connections between the wafers that compose the cells themselves are on the same side of the surface which is exposed to the sun. Moving the contacts and the soldering connection on the back of the wafers offers is one of the possible way to increase the surface exposed to the sun. Solar cells constructed using this technique are usually referred to as "Back-contact silicon solar cells" [4].

2 The photovoltaic cell model

We consider a simplified test model of a photovoltaic cell, corresponding to a transversal section of a solar panel. In order to include the effect of the number of fingers in a channel, that is, the distance between two fingers, we consider a block comprising two cells, as in figure.

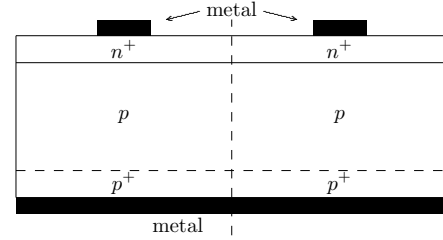


Fig. 1. Geometry of the test photovoltaic cell

The cell is modeled by the drift-diffusion equations, implemented in the commercial simulator Sentaurus Device. Thus, we neglect all thermal effects, and assume that two carriers are responsible for the diode's output current, that is, electrons with negative charge $-q$, and holes with positive charge q . The behavior of the device in the test cell, denoted by Ω , is described in terms of number densities of electrons and holes, denoted by $n(x, t)$, $p(x, t)$, quasi-Fermi potentials for electron and holes, denoted by $\phi_n(x, t)$, $\phi_p(x, t)$, current densities for electrons and holes, denoted by $j_n(x, t)$, $j_p(x, t)$, and electrostatic potential, denoted by $\phi(x, t)$. These variables satisfy the following drift-diffusion system [5],

$$-\nabla \cdot (\epsilon \nabla \phi) = q(N + p - n), \quad (1)$$

$$-q \frac{\partial n}{\partial t} + \nabla \cdot j_n = qR, \quad j_n = -q\mu_n n \nabla \phi_n, \quad (2)$$

$$q \frac{\partial p}{\partial t} + \nabla \cdot j_p = -qR, \quad j_p = -q\mu_p p \nabla \phi_p, \quad (3)$$

where $(x, t) \in \Omega \times [t_0, t_1]$. The densities n , p , are related to the quasi-Fermi potentials by relations derived from the Fermi statistics,

$$n = n_i \gamma_n \exp\left(\frac{\phi - \phi_n}{U_T}\right), \quad p = n_i \gamma_p \exp\left(-\frac{\phi - \phi_p}{U_T}\right),$$

where n_i is the intrinsic concentration, and γ_n , γ_p are complicated functions of the unknowns, which reduce to 1 for Maxwell-Boltzmann statistics. In (2), (3), $N(x)$ is the doping profile, μ_n , μ_p are the mobilities for electrons and holes, respectively, and R is the recombination-generation term. For the mobilities we use the PHUMOB model present in Sentaurus. We consider Shockley-Read-Hall and Auger

recombination-generation terms, combined with a radiative model. The system (1)–(3) is supplemented with appropriate boundary conditions.

3 Optimization

Our goal was to maximize the efficiency of Back-contact silicon solar cells. We used an optimization strategy based on a genetic algorithm applied to some physical parameters of the solar cell. In particular we focused on optimizing the doping concentrations of the bulk and of the emitter.

The Sentaurus device simulator was interfaced with a genetic algorithm written in C, via a wrapper capable of restarting Sentaurus with given physical parameters.

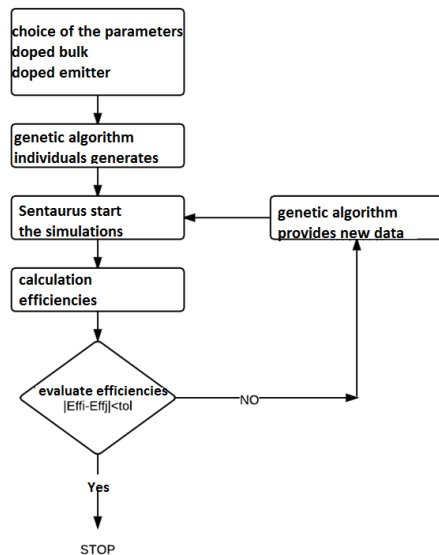


Fig. 2. flow chart simulator device and genetic algorithm

The coupling between Sentaurus and the genetic algorithm was controlled via an heuristic algorithm, in which the difference between the computed efficiency in two consecutive steps was used to determine whether the entire optimization process could be stopped.

A wrapper written in C supervises the communication between Sentaurus and the genetic algorithm. The entire process was run under Linux, which provides an ideal platform for these kinds of algorithms.

References

1. M.A. Green, *Solar cells: operating principles, technology and system applications*. 1986, Kensington: UNSW.
2. P. Würfel, *Physics of Solar Cells*. 2005, Weinheim: Wiley.
3. A. Luque and S. Hegedus, *Handbook of Photovoltaic Science and Engineering*. 2003, West Sussex: John Wiley and Sons Ltd.

4. F. Granek, M. Hermle, C. Reichel, O. Schultz-Wittmann, and S.W. Glunz, *High-efficiency back-contact back-junction silicon solar cell research at Fraunhofer ISE*, in Proceedings of the 23rd European Photovoltaic Solar Energy Conference, Valencia, Spain, 991-5 (2008).
5. P. A. Markowich, *The Stationary Semiconductor Device Equations* (Springer, 1986).

Swarm-based algorithms for the Minimization of the Magnetic Field of Underground Power Cables

D. Altomonte, A. Laudani, G. Pulcini, A. Salvini, F. Riganti Fulginei

DEA, University of RomaTre, Via della Vasca Navale 84, I-00146, Rome, Italy, e-mail: daltomonte@uniroma3.it, alaudani@uniroma3.it, gpulcini@uniroma3.it, asalvini@uniroma3.it, riganti@uniroma3.it

Summary. In this paper a Swarm-Based algorithm approach for detecting an optimal geometrical and electrical connection of underground cables is presented, in order to minimize the magnetic field strength on the ground surface. Since the problem is a Mixed-Integer and Constraint Programming, a Discrete version of Flock-of-Starlings Optimization has been developed. A death penalty method has been used in the optimization process for evaluate the constraints. A comparative analysis is presented for different configurations, with the aim to evaluate the performance.

1 Introduction

In the last years the electric companies has revisited the design method of the underground power cables in order to address the problem of an optimal displacement of them. On the other hand, it is widely acknowledged that the current (50-60 Hz) of transmission and distribution lines, including electrical substations, generates magnetic fields that are the basis of electromagnetic pollution. Indeed the underground power lines were identified as major sources of magnetic fields, since they can produce a significant magnetic field on the ground surface, especially in cases where there are more than four three phase circuits. From an economic point of view, shielding the entire path of a transmission line is impractical. For these reason there needs of optimization techniques at design concerning both the geometrical and circuit assignation of each bundle [1, 2]. From the computational prospective this kind of problems belongs to the Mixed-Integer and Constraint Programming (MICP), in which discrete variables appear. The algorithms usually employed for these problems operate as a string generator, where the string is the individual, which codifies a possible solution. Being the solution a string of numbers the first inconvenient is that some solutions are incompatible with the physical problem.

In this paper a new kind of binary algorithm derived from the Flock of Starlings Optimization algorithm is presented and its performance over MICP problems are analyzed. In the work

particular attention is given to the optimization of a system of power lines that generates the magnetic field of lower intensity without sacrificing efficacy, stability and availability of power systems.

2 Discrete Flock-of-Starlings Optimization

FSO is a bio-inspired algorithm, swarm-based, which has been employed successfully in several others electromagnetic optimization problems, thanks to its high capability of exploration and to escape from local minima [4]. As FSO can be considered an extension of PSO, so Discrete FSO (DFSO) is an extension of the Discrete Particle Swarm Optimization. In these model the trajectories of particles/birds have a probabilistic mean. In particular the velocity of a single particle must be interpreted as the probability that the current position may change from current state to another. Being the algorithm binary, also each coordinate of the position of k-th bird $x_k(t)$ can be 0 or 1. In addition the various component of the personal best and the global best are integer in $\{0,1\}$. The velocity of k-th bird $v_k(t)$ is a probability and it must be constrained. A logistic transformation is introduced by using a sigmoid function in order to do this:

$$S(v_k) = (1 + e^{-v_k})^{-1}$$

The resulting change in the j-th component of position then is defined by the following rule:

$$x_k^j(t) = \begin{cases} 1 & \text{if } S(v_k^j) > \text{random}(0,1) \\ 0 & \text{otherwise} \end{cases}$$

Starting from these equations we can obtain the DFSO model. Indeed, in the FSO each individual chooses the direction in accord to the velocity of other members arbitrary chosen in the swarm. But now the velocity is the probability that an individual will change its status. Therefore, the choice of an individual is influenced from the mean probability of changing of the other member followed by it. The updating velocity equation for the DFSO becomes:

$$v_k = M_k \cdot [\omega v_k + \lambda(p_{best_k} - x_k) + \gamma^j(g_{best} - x_k)]$$

where M_k is the average velocity among controlled birds, expressing the probability of changing a digit from 0 to 1 of the members followed by the generic individuals in the swarm. The value of the M_k is constrained in $[0.0, 1.0]$, in order to underestimate the influence of other members on the generic individual: this choice is extremely important since linking in a strong way the individuals can produce a stagnation and saturation in 1 or 0 direction. In figure 1 the pseudo code of DFSO is presented.

```

Initialization;
Building of the Interconnection Matrix;
For i = 1 : Nstep
    For each bird
        Fitness evaluation;
        Personal and Global best evaluation;
        Mccb computation;
        Update the Velocity;
        Update Position;
    End
End

```

Fig. 1. Pseudo code of DFSO

3 Codification of the problem and results

The simulation performed in this section takes as reference the analysis done in [1]. In [1] the design of cables displacement in a tunnel is trefoil configuration with the aim to minimize the effects of capacitive and inductive currents and support by racks. In the example hereafter presented, we use a simplified version of the circuit used in [1], by changing the number of circuits employed. The data are reported in Table 1, whereas in the fig. 2 are depicted the displacement of cables in the rack with relative position of the bundles. The combination of the cables are 6 and they can be explicitly expressed, 123;132; 213; 231; 312; 321, for instance if there is a string such as 6345, it means that the first circuit is arranged as 321, second as 213 and etc. Set N_C as the number of circuit and with N_B the number of bundles, then any element is codified as an array of 0 and 1 of assigned length.

We have implemented the algorithm in the MATLAB© environment and all the tests has been performed starting from a random initialization. In order to take into account the constraints we divided the array in 2 parts: the first part of the array represents an individual and must consist of integer value in the range 1-6;

whilst the second portion of array represents the connections. Then we use a death penalty, which consists of assigning a huge value to the “bad” solution that doesn’t meet the constraints. The fitness function, that is the magnetic field intensity, is computed by using Biot-Savart formula and the result of a statistical analysis performed on 50 BFSO launches is reported in Table 2, showing the good performance reached.

Table 1. Data of the power circuit employed in the test

N.circuit	P(Mw)	Q(MVAr)	Im (A)	θ (deg)
A	180	60	680	18
B	155	43	577	16
C	-100	-25	370	194
D	125	-30	461	193

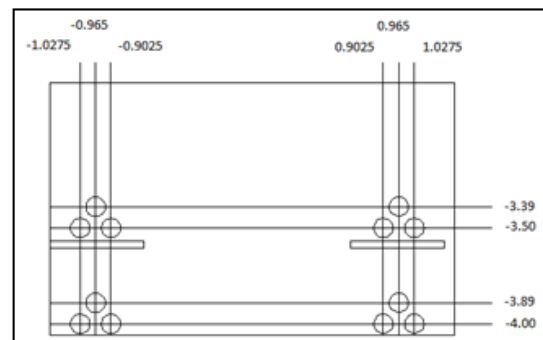


Fig. 2. Displacement of bundles in the underground rack, all values is expressed in meter.

Table 2. Results of BFSO

Mean	Variance	Best Configuration	Best Fitness Value
6.4005e-007	3.262e-016	56533124	6.2566e-007

References

1. G.G. Lai et al. Optimal Connection of Power Transmission Lines With Underground Power Cables to Minimize Magnetic Flux Density Using Genetic Algorithms. *IEEE Trans on Power Delivery*, v. 23, 3, pp. 1553-1560, 2008.
2. A. Pavic and Z. Stih. The Influence of Cables on the Electromagnetic Fields Around the Power System Substation., *IEEE MELECON 2004*, Dubrovnik, Croatia, 2004.
3. Ö. Yeniay. Penalty function methods for constrained optimization with genetic algorithms. *Mathematical and Computational Applications*, Vol. 10, No. 1, pp. 45-56, 2005.
4. F.Riganti Fulginei and A. Salvini, Hysteresis model identification by the Flock-of-Starlings Optimization, *International Journal of Applied Electromagnetics And Mechanics* 30, pp. 321-331, 2009.

Numerical modeling of standard lightning impulse on overhead lines

Phd. Eng. Oana Simona ANTONESCU¹, Prof. Dr. Eng. Calin MUNTEANU²

¹Technical University of Cluj Napoca, oana.antonescu@et.utcluj.ro

²Technical University of Cluj Napoca, calin.munteanu@et.utcluj.ro

Summary: The paper approaches the topic of the numerical modelling of the electromagnetic disturbances that occurs on HV lines. Being broadband signals, an accurate evaluation of the disturbances propagation on HV lines requires that the transmission lines model to be taken into consideration. Therefore, in the first part of the paper the principles of modelling using non-uniform transmission lines are emphasized. Then the per-unit-length parameters computation is detailed, with the terms which take account of the influence of a lossy ground. In the second part of the paper the numerical computation algorithm implemented is presented. In the last part of the paper there are presented several examples using a concrete HV line to which several standard test signals have been applied.

1 Introduction

The principle of modeling the non-uniform transmission lines is based on the idea of dividing the line into multiple pieces of uniform lines with the length very small in comparison with the wavelength.

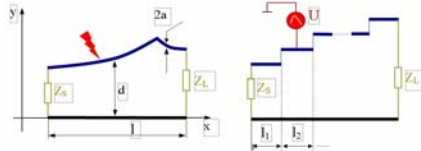


Fig. 1. Modelling using non-uniform transmission lines

The numerical modelling of the electromagnetic disturbances propagation on HV lines can be achieved using professional software packages designed for circuits' numerical analysis. In this paper the PSPICE software that is included in the ORCAD 9.2 package was used. The general flowchart of the numerical algorithm implemented in accordance with the details outlined in the above paragraphs is presented in Fig. 2.

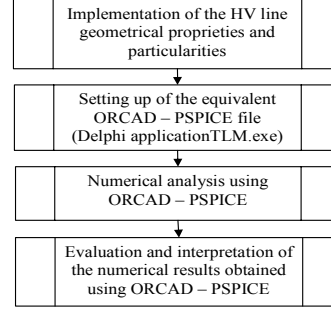


Fig. 2. General flowchart structure of the numerical analysis algorithm implemented

2 The per-unit-length parameter

The HV line per-unit-length parameters are computed according to Carson's theory and approximations for wave propagation above loss ground.

Self impedance includes three components:

$$Z_{ii} = j\omega L_{ii} + Z_c + Z_g \quad (1)$$

The loop inductance is:

$$L_{ii} = \frac{\mu_0}{2\pi} \ln \frac{2h_i}{r_i} \quad (2)$$

The internal impedance:

$$Z_c = R_c + jX_c = \frac{\rho\gamma}{2\pi r} \frac{I_0(\gamma r)}{I_1(\gamma r)} \quad (3)$$

in which the material constants μ and σ respectively the propagation constant $\gamma = \sqrt{j\omega\mu(\sigma + j\omega\epsilon)}$

The mutual impedance Z_{ij} of two conductors i and j , both parallel to the ground, with their respective heights above the ground being h_i and h_j have two components:

$$Z_{ij} = j\omega L_{ij} + Z_{gm} \quad (4)$$

The mutual inductance L_{ij} is:

$$L_{ij} = \frac{\mu_0}{2\pi} \ln \frac{D'_{ij}}{D_{ij}} \quad (5)$$

The impedance of the ground return path Z_{gm} is:

$$Z_{gm} = R_{gm} + jX_{gm} \quad (6)$$

In the computation of the capacitance of transmission line accepts two factors: the length is larger than the dimensions of the circuits, the environment is uniform (air), the conductors have a cylindrical configuration.

The impedance of the earth return path is represented by Carson's correction terms for the self and mutual impedances.

3 Numeric simulation results

This paper presents several numerical applications of the developed algorithm. The examples focus on a 110 kV LEA. For the LEA parameters modeling, existing towers in the National Energetic System are used. Consider the case of an overhead power transmission line, at the left end one apply the lightning pulse voltage $1.2/50 \mu\text{s}$. The line parameters are computed at frequency 50Hz and the ground is characterized by $\rho=100 \Omega\text{m}$. The response wave presented in Fig. 3 is the signal at the open load end of the high voltage line obtained with the proposed software module.

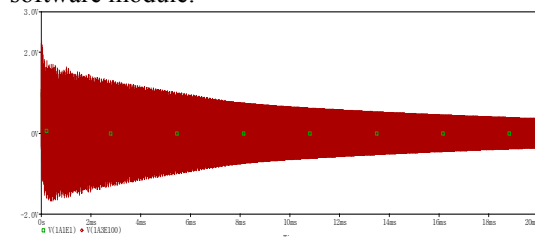


Fig. 3. Lightning pulse voltage, signal on load– proposed software

To validate the results obtained with the modul software proposed, in Fig. 4 is presented the result obtained with ATP.

In case when the parameters are evaluation at 500 KHz frequency, we can see the wave shape of signal in Fig.5 and when the ground is characterized by $\rho=1000 \Omega\text{m}$ the result is in Fig.6.

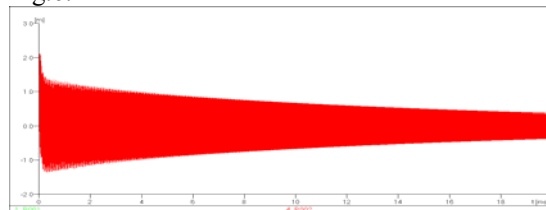


Fig. 4. Lightning pulse voltage, signal on load-phase 1 with defect –ATP

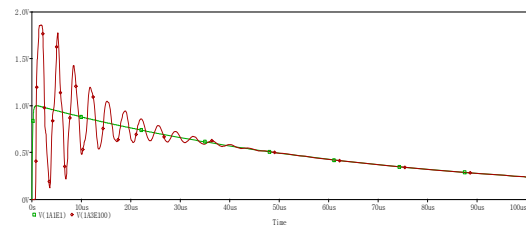


Fig. 5. Lightning pulse voltage, signal on load – proposed software

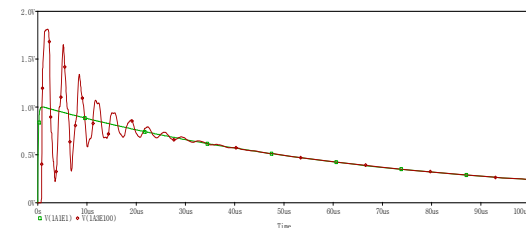


Fig. 6. Lightning pulse voltage, signal on load – proposed software

The conclusion of analyses performed is that the appearance of a lightning pulse on one phase of the HV line conductors generates significant over-voltages and over-currents, while the waves shape is essentially influenced by the geometrical properties of the line.

References

- [1] **F. Rachidi, C. A. Nucci, M. Ianoz**, *Transient Analysis of Multiconductor Lines Above a Lossy Ground*, IEEE Transactions on Power Delivery, Vol. 14, No. 1, pp. 294-302.
- [2] **F. M. Tesche, M. Ianoz, T. Karlsson**, *EMC Analysis Methods and Computational Models*, J. Wiley&Sons, New York, 1996.
- [3] *** Canadian/ American EMTP User Group, *Alternative Transients Program (ATP) - Rule Book*, 1992.
- [4] *** CIGRE WG 33-01: *Guide to procedures for estimating the lightning performance of transmission lines*.
- [5] *** *Guide for improving the lightning performance of transmission lines*, IEEE standard 1243-1997.
- [6] **Vermesan Claudiu, Munteanu Calin, Oana ANTONESCU, Pop T. Ioan**, *The Influence Of Lossy Ground In Numerical Modeling Of Perturbations On High Voltage Lines Using Tlm*, WEC Regional Energy Forum – FOREN 2006, Neptun, 11-15 June 2006
- [7] **Oana Simona ANTONESCU, Călin MUNTEANU, Adina RĂCĂȘAN, Claudia RĂCĂȘAN**, *Numerical Analysis Of $1 \mu\text{s}$ Unit Pulse And $1.2/50 \mu\text{s}$ Waves Propagation On High Voltage Lines*, EUROCON 2007, Varșovia, Polonia, 9-12 septembrie 2007

Index-aware model Order Reduction: LTI DAEs in electric networks

Nicodemus Banagaaya¹ and Wil Schilders¹

Dept. of Mathematics and Computer Science, Technische Universiteit Eindhoven, The Netherlands
n.banagaaya@tue.nl, w.h.a.schilders@tue.nl

Summary. Model order reduction (MOR) has been widely used in the electric networks but little has been done to reduce higher index differential algebraic equations (DAEs). Most methods first do an index reduction before reducing a higher DAEs but this can lead to loss of system physical properties. In this paper we present a new MOR method for DAEs called the index-aware MOR (IMOR) which can reduce higher index-2 system while preserving the index of the system.

1 Introduction

Consider a linear time invariant (LTI) DAE system:

$$Ex'(t) = Ax(t) + Bu, \quad x(0) = x_0, \quad (1a)$$

$$y(t) = C^T x(t), \quad (1b)$$

where $E, A \in \mathbb{R}^{n,n}$, $B \in \mathbb{R}^{n,m}$, $C \in \mathbb{R}^{n,\ell}$, $x(t) \in \mathbb{R}^n$ is the state vector, $u(t) \in \mathbb{R}^m$ is the input vector, $y(t) \in \mathbb{R}^\ell$ is the output vector and $x_0 \in \mathbb{R}^n$ must be a consistent initial value since E is singular. In many MOR methods [1] they always assume that $x_0 = 0$ which lead to a transfer function $H(s) = C^T(sE - A)^{-1}B$ if and only if matrix pencil $sE - A$ is regular. Unfortunately for the case of DAEs we cannot always have this freedom of choosing an arbitrary initial condition x_0 , in fact we cannot always obtain a transfer function especially for index greater than 1 as discussed in Sect. 2. This motivated us to propose a new MOR technique for DAEs called the IMOR method which takes care of this limitation [2, 3]. In this technique before we apply MOR we first decompose the DAE system into differential and algebraic parts using matrix and projector chains introduced by März [4] in 1996. We then use the existing MOR techniques such as the Krylov based methods on the differential part and develop new techniques for the algebraic part. This is done as follows: Assume (1a) is of tractability index μ , then its projector and matrix chains can be written as, set $E_0 := E, A_0 := A$, then $E_{j+1} = E_j - A_j Q_j$, $A_{j+1} := A_j P_j$, $j \geq 0$, where $\text{Im} Q_j = \text{Ker} E_j$, $P_j = I_n - Q_j$. There exists μ such that E_μ is nonsingular while all E_j are singular for all $0 \leq j < \mu - 1$. Using these chains we can rewrite Equation (1a) as projected system of index- μ :

$$P_{\mu-1} \cdots P_0 x' + Q_0 x + \cdots + Q_{\mu-1} x = E_\mu^{-1} (A_\mu x + Bu) \quad (2)$$

In order to decompose higher index systems ($\mu > 1$), März [4] suggested an additional constraint $Q_j Q_i = 0$, $j > i$ on the projector construction. If this constraint holds then Equation (2) can be decomposed into differential and algebraic parts. However, the März decomposition leads to a decoupled system of dimension $(\mu + 1)n$. It does not even preserve the stability the DAE system. This motivated us to modify the März decomposition using special basis vectors as presented in papers [3] and [2] for the case of index-1 and index-2 respectively. Our decomposition leads to a decoupled system of the same dimension as that of the DAE system. Then we apply Krylov methods on the differential part and constructed subspaces to reduce the algebraic parts. In Sect. 2 we briefly discuss the IMOR method for index-2 systems (IMOR-2) more details can be found in [2].

2 Index-aware MOR for index-2 systems

Assume Equation (1a) is an index-2 system this implies $\mu = 2$. We observed that for higher index DAEs there is a possibility of obtaining a purely algebraic decoupled system depending on the nature of spectrum of the matrix pencil $\sigma(E, A) = \sigma_f(E, A) \cup \sigma_\infty(E, A)$, where $\sigma_f(E, A)$ and $\sigma_\infty(E, A)$ is the set of the finite and infinite eigenvalues respectively. This happens when matrix spectrum has only infinite eigenvalues, i.e. $\sigma_f(E, A) = \emptyset$. Thus higher index DAEs can be decomposed into two ways. Due to space we are going to only discuss the case when $\sigma_f(E, A) \neq \emptyset$ the other case can be found in our paper [2]. We now assume matrix pencil of Equation (1a) has atleast one finite eigenvalue. We then construct basis vectors (p, q) in \mathbb{R}^n with their inversion $(p_*, q_*)^T$ for the projectors P_0 and Q_0 respectively where $p \in \mathbb{R}^{n,n_0}$, $q \in \mathbb{R}^{n,k_0}$. This leads to a theorem below.

Theorem 1. Let $P_{01} = p_*^T P_1 p$, $Q_{01} = p_*^T Q_1 p$, then $P_{01}, Q_{01} \in \mathbb{R}^{n_0, n_0}$ are projectors in \mathbb{R}^{n_0} provided the constraint condition $Q_1 Q_0 = 0$ holds.

Next, we construct another basis matrix (p_{01}, q_{01}) in \mathbb{R}^{n_0} made of n_{01} independent columns of projector P_{01} and k_1 independent columns of its complementary projector Q_{01} such that $n_0 = n_{01} + k_1$ and its inverse can be denoted by $(p_{01}^*, q_{01}^*)^T$. Then Equation (1) can be decomposed as:

$$\xi_p' = A_p \xi_p + B_p u, \quad (3a)$$

$$\xi_{q,1} = A_{q,1} \xi_p + B_{q,1} u, \quad (3b)$$

$$\xi_{q,0} = A_{q,0} \xi_p + B_{q,0} u + A_{q,01} \xi_{q,1}', \quad (3c)$$

$$y = C_p^T \xi_p + C_{q,1}^T \xi_{q,1} + C_{q,0}^T \xi_{q,0}, \quad (3d)$$

where

$$\begin{aligned} A_p &:= p_{01}^{*T} p_0^{*T} E_2^{-1} A_2 p_0 p_{01}, & B_p &:= p_{01}^{*T} p_0^{*T} E_2^{-1} B, \\ A_{q,1} &:= q_{01}^{*T} p_0^{*T} E_2^{-1} A_2 p_0 p_{01}, & B_{q,1} &:= q_{01}^{*T} p_0^{*T} E_2^{-1} B, \\ A_{q,0} &:= q_{01}^{*T} P_1 E_2^{-1} A_2 p_0 p_{01}, & B_{q,0} &:= q_{01}^{*T} P_1 E_2^{-1} B, \\ A_{q,01} &:= q_{01}^{*T} Q_1 p_0 q_{01}, & C_p &:= p_{01}^T p_0^T C \in \mathbb{R}^{n_{01}, \ell}, \\ C_{q,1} &:= q_{01}^T p_0^T C \in \mathbb{R}^{k_1, \ell}, & C_{q,0} &:= q_0^T C \in \mathbb{R}^{k_0, \ell}. \end{aligned}$$

Equations (3a), (3b) and (3c) are of dimension n_{01}, k_1 and k_0 respectively, where $n = n_{01} + k_1 + k_0$. System (3) preserves stability of the DAE system (1) since it can be proved that $\sigma(A_p) = \sigma_f(E, A)$. If we take the Laplace transform of (3) and set $\xi_p(0) = 0$ then we obtain

$$Y(s) = [H_p(s) + H_{q,1}(s) + H_{q,0}(s)] U(s) + H_{q,0}(0),$$

where $H_p(s) = C_p^T (sI_{n_0} - A_p)^{-1} B_p$, $H_{q,1}(s) = C_{q,1}^T [A_{q,1}(sI_{n_0} - A_p)^{-1} B_p + B_{q,1}]$, $H_{q,0}(s) = C_{q,0}^T [(A_{q,0} + sA_{q,01}A_{q,1})(sI_{n_0} - A_p)^{-1} B_p] + C_{q,0}^T [B_{q,0} + sA_{q,01}B_{q,1}]$, $H_{q,0}(0) = -C_{q,0}^T A_{q,01} B_{q,1} u(0)$. Thus not always we can obtain the transfer function of index 2 systems for arbitrary input vector u unless $H_{q,0}(0) = 0 \Rightarrow Y(s) = H(s)U(s)$. We can now apply IMOR-2 method as follows: If we choose the expansion point $s_0 \in \mathbb{C} \setminus \sigma(A_p)$, we construct a Krylov-subspace generated by $M_p := -(s_0 I_{n_0} - A_p)^{-1}$ and $R_p := (s_0 I_{n_0} - A_p)^{-1} B_p$. Then, $V_{p_r} := \text{orth}(\kappa_r(M_p, R_p))$, $r \leq n_{01}$. We then use V_{p_r} to construct the subspace $\mathcal{V}_{q,1} = \text{span}(B_{q,1}, A_{q,1} V_{p_r})$ and its orthonormal matrix is denoted by $V_{q_{\tau_1},1} = \text{orth}(\mathcal{V}_{q,1})$, $\tau_1 \leq \min((r+1)m, \dim(\mathcal{V}_{q_{\tau_1},1}))$. We finally construct subspace $\mathcal{V}_{q,0} = \text{Span}\{\mathcal{V}_{Q_1}, \mathcal{V}_{Q_2}, \mathcal{V}_{Q_3}\}$, where $\mathcal{V}_{Q_1} = A_{q,0} R_p + B_{q,0} + s_0(A_{q,01} A_{q,1} R_p + A_{q,01} B_{q,1})$, $\mathcal{V}_{Q_2} = A_{q,01} B_{q,1}$, $\mathcal{V}_{Q_3} = [(A_{q,0} + s_0 A_{q,01} A_{q,1}) M_p + A_{q,01} A_{q,1}] V_{p_r}$ and its orthonormal matrix is denoted by $V_{q_{\tau_0},0} = \text{orth}(\mathcal{V}_{q,0})$, where $\tau_0 \leq \min((r+2)m, \dim(\mathcal{V}_{q,0}))$. We can now use the orthonormal matrices $V_{p_r}, V_{q_{\tau_1},1}$ and $V_{q_{\tau_0},0}$ to reduce the dimension of the subsystems (3a), (3b) and (3c) respectively as consequence the dimension of the decoupled system (3) is also reduced. Hence, if we substitute $\xi_p = V_{p_r} \xi_{p_r}$, $\xi_{q,1} = V_{q_{\tau_1},1} \xi_{q_{\tau_1},1}$, $\xi_{q,0} = V_{q_{\tau_0},0} \xi_{q_{\tau_0},0}$, into system (3) and simplifying we can obtain a reduced model of DAE system (1) which will call the IMOR-2 model.

3 Numerical results

We used an index -2 test system called S8OPI in [5] which is a large power system RLC model. It's a

single-input single-output (SISO) system of dimension 4182. We applied the IMOR-2 method using $s_0 = j10^3$. We obtained a reduced model of total dimension 219 as shown in Table 1. We observed that the magnitude of the transfer reduced model coincides with that of the original model at low frequencies with very small error as shown in Fig. 1. We have seen that

Table 1. Dimension of the Original and Reduced model

Models	Dimension		
	n_{01}	k_1	k_0
Original Model	4028	35	119
Reduced Model	170	1	48

the IMOR-2 method leads to good reduced model and can be used on any index-2 system.

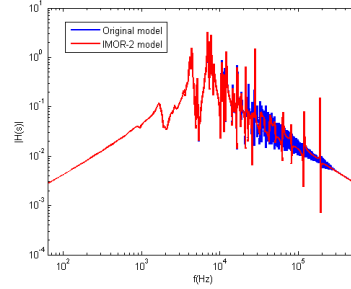


Fig. 1. Magnitude of the transfer functions

Acknowledgement. This work is funded by NWO.

References

1. W. Schilders, H. Van der Vorst and J. Rommes, *Model Order Reduction: Theory, Research Aspects and Applications*, Springer-Verlag, Berlin Heidelberg, 2008.
2. G. Ali, N. Banagaaya, W.H.T. Schilders and C. Tischendorf, *Index-aware model order reduction for index-2 differential-algebraic equations*, In preparation, 2012.
3. G. Ali, N. Banagaaya, W.H.T. Schilders and C. Tischendorf, *Index-aware model order reduction for differential-algebraic equations*. *Mathematics of Computation*, Submitted, 2011.
4. R. März, *Canonical Projectors for Linear Differential Algebraic Equations*, *Computers Math. Applic.* 31:121–135, 1996.
5. F.D. Freitas, N. Martins, S.L. Varrichio, J. Rommes and F.C. Véliz, *Reduced-Order Transfer Matrices From Network Descriptor Models of Electric Power Grids*, *Ieee transactions on power systems*, 26:1905–1919, 2011.

Convergence behaviour of coupled pressure and thermal networks

Andreas Blaszczyk¹, Reto Flückiger¹, Thomas Müller², Carl-Olof Olsson³

¹ABB Corporate Research Switzerland, Andreas.Blaszczyk@ch.abb.com, Reto.Flueckiger@ch.abb.com

²LRR Institute for Computer Science, Technical University Munich, Germany, Thomas.Mueller@in.tum.de

³ABB Corporate Research Sweden, Carl-Olof.Olsson@se.abb.com

Summary: A new concept of the coupling between pressure and thermal networks for thermal simulations of power devices is presented. The solution method and the convergence behaviour are discussed.

1 Introduction

The network approach is traditionally used for thermal simulations of electric power devices. In particular the coupling between thermal and pressure network seems to offer a good alternative to the mesh based methods like CFD thanks to an acceptable accuracy and a moderate computational effort. However, the first attempts to couple both network types have shown that the convergence behaviour is a limiting factor [1]. In this paper we present a new concept of the coupling between thermal and pressure networks as well as results of our investigations to mitigate the convergence problems.

2 Network concept

Let us consider a power transformer represented as a simple thermal model, Fig 1a. It consists of a coil submerged in a fluid as a heating device and a radiator as a cooling device dissipating heat to the ambient air. The circulation of the fluid through the coil and the radiator keeps the temperature of the coil within the required limit. The flow of the fluid determines the topology of the extended pressure network shown in Fig. 1b. Each “fluid flow” branch (red, thick line in the middle) is assisted by two “temperature” branches (thin, green lines) that enable propagation of the fluid temperature along the network according to the computed direction of the flow. The mixing of the fluid at different temperatures is performed by the “mixing nodes”. The coupling to the thermal network is realized by the “thermal junction” element. This element creates a temperature jump $\Delta\theta$ in the corresponding temperature branch, which is determined by the mass flow rate \dot{m} in this branch and the power P flowing from/to the thermal network via the “fluid node”:

$$P = \dot{m} c_p \Delta\theta \quad (1)$$

where c_p is the specific heat of the fluid. The formula (1) is also used as a basic equation in implementation of the “mixing nodes”.

The “fluid nodes” provide a galvanic connection to the thermal network, which is partially shown in Fig. 1c. The resistors used in the network schemes (Fig. 1bc) are formulated according to thermodynamic similarity theory [2] and will be explained in the extended version of this paper.

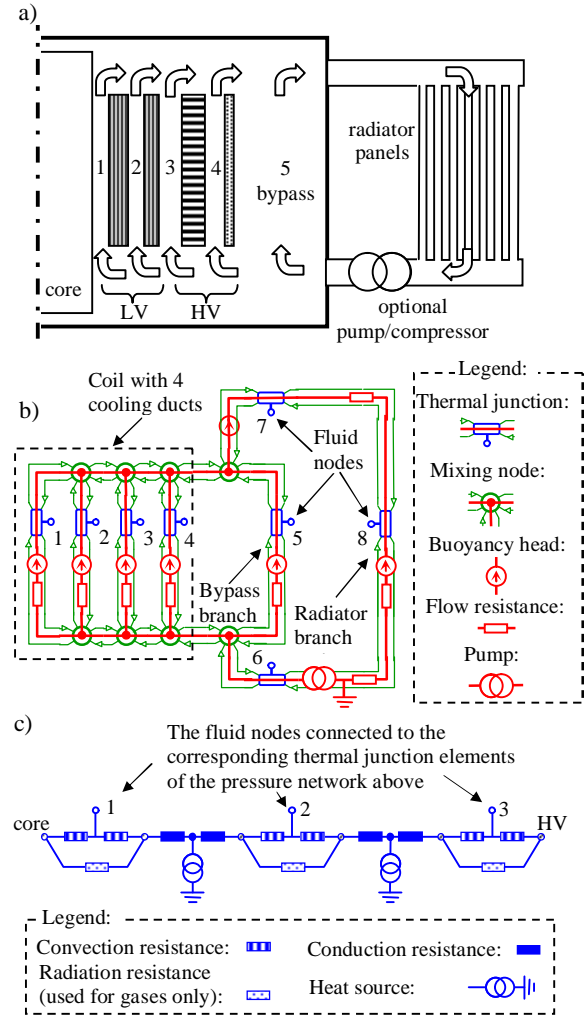


Fig. 1 a) Transformer coil and radiator as a thermal model, b) the corresponding extended pressure network, c) part of the thermal network (for 2 inner LV solid segments of the coil and adjacent ducts)

Table 1 Analogy between quantities and units of electric, thermal and pressure networks.

Electric network	Thermal network	Extended pressure network	
		Temperature branches	Fluid flow branches
Current [A]	Power [W]	- *)	Mass flow rate [kg/s]
Voltage U [V]	Temperature [°C]	Temperature [°C]	Pressure [Pa]
Electric resistance [Ohm]	Thermal resistance [K/W]	- *)	Flow resistance [1/(m*s)]

*) There is no “current” in the temperature branches of the pressure network. These branches transfer the “temperature signal” only. The direction of this transfer is the same as the direction of the fluid flow.

3 Solution method

In order to obtain a stable solution of the coupled networks we applied 3 following techniques:

- Separation of fluid flow branches from thermal/temperature branches
- Adaptive relaxation
- Control of the flow direction change

Ad a): The coupled network problems are difficult to solve using the Newton-Raphson method implemented by Spice. Therefore, we have split the coupled network into 2 separate networks and solve them iteratively. The first network, pure pressure one, consists of the fluid flow branches including all flow resistances, buoyancy heads and pumps. The second one consists of the whole thermal network and the temperature branches of the extended pressure network. The “thermal junction” and the “mixing node” elements are the only network components that have a separate representation dedicated for each of the both networks. The separated networks can be solved using Spice by assuming boundary conditions in form of interface variables that are iteratively delivered by the solution of the other network. These interface variables include mass flow rates and velocities as a solution of the pure pressure network as well as temperatures as a solution of the thermal/temperature network.

Ad b): A relaxation technique is needed to ensure the convergence. The actual values of the interface variables are modified in such a way that the difference between subsequent iterations is adaptively reduced from 80 % (for the first iteration) up to 1 % (for higher iteration counts).

Ad c): The network branches with a small mass flow rate show a tendency to change the flow direction during the iterative solution. Due to the significant temperature difference between the top and bottom fluid the direction changes may lead to non-convergence. For the vertical coil ducts this problem can be mitigated by disabling the flow from the top to the bottom by means of “blocking” resistors. In case of branches for which the flow can be bidirectional an enhanced relaxation technique has to be applied.

4 Result

An example of the convergence behaviour has been presented in Fig. 2. It shows the mass flow rate within a coil duct of a liquid type power transformer. We selected a duct transporting a relatively small fraction of the total heat power (<0.5 %). Consequently we need 49 iterations to achieve the convergence criterion (≤ 0.001 relative change). Other load cases of the same transformer with larger or zero heat power transported through the same duct converge within 10-20 iterations. The typical solution time on a standard computer is in the range of 0.5 s.

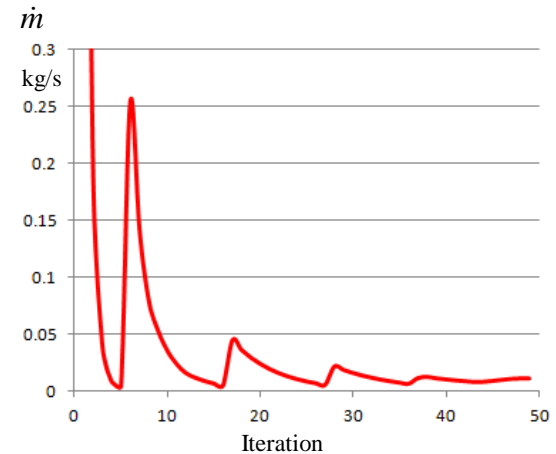


Fig. 2 Example of a convergence curve for mass flow rate in a transformer coil duct

References

- [1] Gramsch C., Blaszczyk A., Löbl H., and Grossmann S., *Thermal Network Method in the Design of Power Equipment*. Springer Verlag, Heidelberg, SCEE Conference Book 2007 (ISBN 978-3-540-71979-3).
- [2] Rohsenow W. M., Hartnett J. P., and Cho, Y. I. (Eds.), 1998, *Handbook of Heat Transfer*, McGraw-Hill, New York.

Thermal Design of VSD Dry-Type Transformer

Marcos Bockholt¹, Wolfgang Mönig¹, Benjamin Weber¹
Bhavesh Patel¹, B. Cranganu-Cretu²

¹ ABB AG, DEDC / CoE Dry Type Converter Transformers, Keffelkerstr. 66, 59929, Brilon, Germany.
Contact: marcos.bockholt@de.abb.com, wolfgang.moenig@de.abb.com, benjamin.weber@de.abb.com,
bhavesh.k1.patel@de.abb.com.

² ABB Schweiz AG, Corporate Research, Segelhofstrasse 1K, 5405, Baden-Dättwil, Switzerland.
Contact: bogdan.cranganu-cretu@ch.abb.com

Summary Design of variable speed drive (VSD) dry-type transformers requires accurate electromagnetic and thermal modelling of the transformer. The models should be able to explain the behaviour of the transformer under normal and short circuit conditions. If not appropriately taken into consideration, load losses can generate local overheating in the transformer and hence cause the transformer failure due to increased winding temperature. A thermal network model to be used with a finite element model of the unit is described. This method is shown to deliver a good compromise between time-consuming simulations and a semi-empirical thermal model for reliable designs of complex dry-type VSD transformers.

1 Introduction

Variable speed drives are used to control the speed of rotation of electronic motors in many industrial applications. These are pumps, ventilators, compressors, belt conveyors, rolling mills, paper machines and an innumerable amount of different machines used in manufacturing and other industries. ABB Dry Type Converter Transformers have an extensive experience with VSD transformers since more than 20 years. Especially the harmonic frequencies content in the transformer current increases the mechanical, dielectrical and thermal stresses. Therefore the transformers must be specially designed for this duty, fulfilling the IEC [3] requirements and beyond.

2 Electromagnetic Simulation of VSD-Transformers

Analytic formulations for the losses in the windings which are governed by skin and proximity effects are limited because of the complex arrangement of the windings in typical VSD transformers. As a result, the use of computational electromagnetic is vital in order to predict these losses at the normal operating conditions. In this paper, we consider the case of a 12-pulse transformer consisting of the two secondary low voltage (LV) windings.

3 Thermal Network Model

The main focus of this work relies on the thermal

model to be used with the losses computed by the electromagnetic simulations [4] and predict local overheating of the windings. The model proposed uses physics-based formulation of mass, energy and momentum balance equations which enables a large validity range of the method in opposite to purely empirical models.

3.1 Physics-based Thermal Model

The physics of the thermal model is described in three basic structures. The simplified generic structures show to be very efficient for modelling and simulating advanced thermal systems [1,2,5].

3.1.1. Solid Structure

The winding losses from the electromagnetic simulation (ohmic and eddy-current) are applied in the solid structure. In this structure, the conductors and insulation material are described. The energy balance is stated as follows

$$0 = P_k - \dot{Q}_{cond}, \quad (1)$$

where P_k are the transformer losses and \dot{Q}_{cond} is the (axial and radial) heat diffusion inside the windings.

3.1.2. Surface Structure

The surface structure is used to map the interface between a solid potential and a fluid potential. The energy balance equation is stated as follows:

$$0 = \dot{Q}_{cond} - \dot{Q}_{conv} - \dot{Q}_{rad}, \quad (2)$$

where \dot{Q}_{conv} , \dot{Q}_{rad} are convective and radiation heat transfer, respectively.

3.1.3. Fluid Structure

The fluid structure is used to map the cooling duct between winding blocks.

$$0 = \dot{Q}_{conv} + \dot{m}_in \cdot \left(h_{in} + \frac{v_{in}^2}{2} + gz_{in} \right) - \dots \quad (3)$$

$$\dots - \dot{m}_{out} \cdot \left(h_{out} + \frac{v_{out}^2}{2} + gz_{out} \right)$$

where \dot{m}_{in} , \dot{m}_{out} are the inlet and mass flow rate of the cooling medium inside the transformer cooling duct, respectively. h_{in} and h_{out} are the inlet and outlet enthalpy of the cooling medium, respectively. v_{in} and v_{out} are the inlet and outlet velocity of the cooling medium, respectively.

The non-linear algebraic system of equations described in the structures is represented in Eq. 4 and is solved by a standard algebraic equations solver.

$$F(x) = 0, \quad (4)$$

where X is the vector of temperatures of all structures of the transformer model.

Figure 1 shows an overview of the thermal model. The solid structures are connected with each other via heat conduction axially. The solid and surface structures are connected radially via conduction. The surface structures are connected to each other via radiation resistance. The connection between a surface and a fluid is done by convective resistance. Both the convective and the radiation resistance are non-linear, temperature dependent resistances.

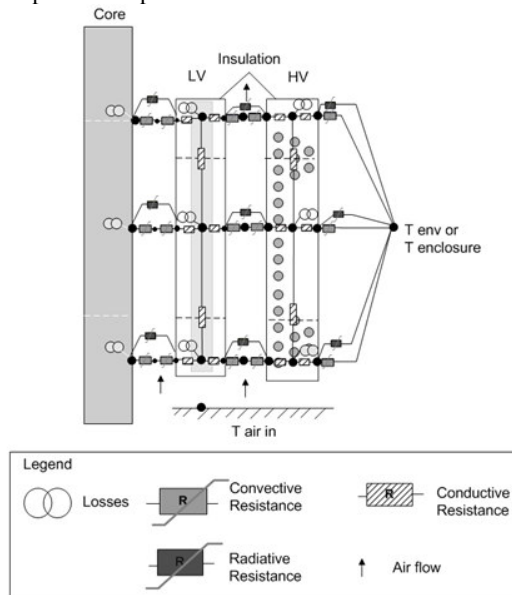


Fig. 1: Network representation of the thermal model with a vertical discretization of 3 structures (In this example: 1 low voltage and 1 high voltage winding package)

3.2 Object-Oriented Structure

Figure 2 shows the object oriented structure of the transformer. The structure of the model is fixed, i.e. one coil, one core and an open number of low voltage (NLV) and high voltage (NHV) winding packages. The geometry is fully parametrized which allows high freedom during design process.

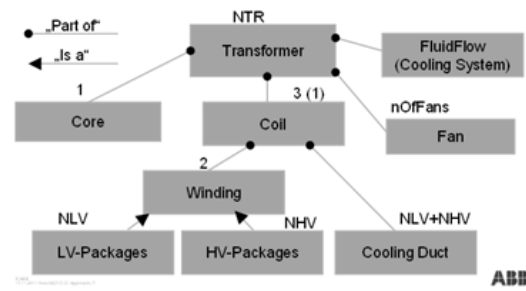


Fig. 2: Object-oriented structure of the sub-models of the transformer thermal model

3.3. Thermal Management of Windings

As part of the design optimization, it is possible to visualize the thermal management of each winding block. The thermal management gives information about the heat transfer by convection at the winding surroundings. The designers are able to choose more effective cooling ducts by comparing thermal characteristic number as the Rayleigh number.

4 Weak Coupling of Electromagnetic Simulation with Thermal Network Model

A weak coupling of the thermal network model is conducted by using the same axial discretization (number of structures in axial direction) of the thermal model and the post-processed losses of the electromagnetic simulation [4]. The losses computed during the electromagnetic simulations are used as input for the thermal model.

5 Conclusion

The method shown in the present work speeds up the design process of complex VSD-transformers. Overheated areas are localized before production of the unit. This method has been proven to be a good compromise between time-consuming simulation and a semi-empirical thermal model for production of complex dry-type transformer designs.

References

1. Bockholt, M *Transient Modelling of a Controllable Low Pressure Accumulator in CO₂ Refrigeration Cycles*, 6th International Modelica Conference, March 3rd-4th, 2008 www.modelica.org
2. Bockholt, M. *Dynamische Optimierung von mobilen CO₂-Klimaanlagen mit innovativen Komponenten* PhD-Thesis, TU-Braunschweig, 2009.
3. IEC 60076-11. *Dry-Type Transformers*, CEI/IEC 60076-11:2004.
4. MagNET v.7, Infolytica Corporation, www.infolytica.com, Last access: 30.09.2011.
5. Tegethoff, W. *Eine Objekt-orientierte Simulationsplattform für Kälte-, Klima- und Wärmepumpensysteme*. PhD-Thesis, TU-Braunschweig, 1999.

Fast Solution of a Magnetostatic Problem with Parallel ILU

M. Bollhoefer¹, R. Bianchetti², J. Ostrowski², and D. Pusch²

¹ Institute of Computational Mathematics, TU Braunschweig, D-38106 Braunschweig, Germany
m.bollhoefer@tu-bs.de

² ABB Switzerland, Corporate Research, 5405 Baden-Dättwil, Segelhofstrasse, Switzerland
Romeo.Bianchetti@ch.abb.com, Joerg.Ostrowski@ch.abb.com, David.Pusch@ch.abb.com

Summary. In this contribution we investigate the performance of a parallel ILU preconditioner for the iterative solution of a magnetostatic model problem. Using the magnetic vector potential \mathbf{A} and conformal FEM-discretization results in a singular system matrix. We construct the preconditioner for the CG-solver by applying a shift for regularization, see [2, 3, 6]. The resulting regular matrix is then decomposed by the ILUPACK¹ library and is used for preconditioning. ILUPACK is a MPI-parallelized implementation of the inverse-based multilevel block ILU, see [4].

1 Introduction

The magnetostatic problem under consideration writes

$$\operatorname{curl} \frac{1}{\mu} \operatorname{curl} \mathbf{A} = \mathbf{j}. \quad (1)$$

Herein \mathbf{A} is the magnetic vector potential, \mathbf{j} is a prescribed divergence free current density, and μ is the possibly nonlinear magnetic permeability. Using conformal finite elements for the discretization leads to the following problem that is to be solved in weak formulation

$$\left(\frac{1}{\mu} \operatorname{curl} \mathbf{A}, \operatorname{curl} \mathbf{A}' \right) = (\mathbf{j}, \mathbf{A}'). \quad (2)$$

The solution of magnetostatic problems in presence of nonlinear magnetic material can be time consuming. The change in the material parameters during the nonlinear iteration results in a change in the system matrix $\mathbf{M} := (\frac{1}{\mu} \operatorname{curl} \mathbf{A}, \operatorname{curl} \mathbf{A}')$. Magnetostatic problems are typically solved by preconditioned iterative solvers [2, 5, 7]. Jumps in the magnetic permeability deteriorate the condition of the problem, and preconditioning is mandatory. The preconditioner \mathbf{P}^{-1} has to be updated many times if \mathbf{M} changes too much during the outer nonlinear iteration, see Fig. 1. Therefore it is essential to provide a fast way of updating the preconditioner.

The system matrix \mathbf{M} is singular. In this paper we regularize \mathbf{M} by using a small shift $\beta \in \mathbb{R}$. This yields the preconditioner

$$\mathbf{P} := \left(\frac{1}{\mu} \operatorname{curl} \mathbf{A}, \operatorname{curl} \mathbf{A}' \right) + \left(\frac{\beta}{\mu} \mathbf{A}, \mathbf{A}' \right). \quad (3)$$

¹ <http://ilupack.tu-bs.de>

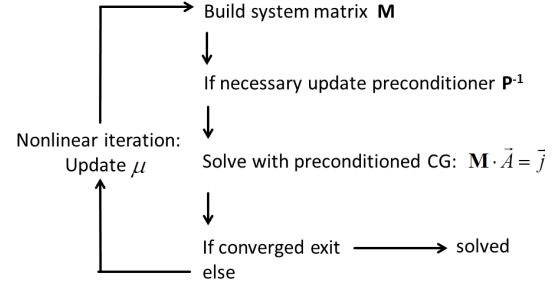


Fig. 1. Algorithm to solve a nonlinear magnetostatic problem.

The decomposition of \mathbf{P} is then accomplished by using the mentioned MPI-parallelized ILUPACK library. In the next Section 2 we introduce the theoretical background of ILUPACK. In the numerical experiments of the final Section 3 we show the parallel scaling performance of the ILU-preconditioner as well as the preconditioning behavior itself.

2 Inverse-Based Multilevel Block ILU

For preconditioning the conjugate gradient method, ILUPACK computes an incomplete Cholesky-like factorization $\mathbf{P} \approx \mathbf{L} \mathbf{D} \mathbf{L}^T$, where \mathbf{L} is unit lower triangular and entries of small modulus are dropped. ILUPACK's hallmark is to keep $\|\mathbf{L}^{-1}\|$ below a given bound κ during the factorization [4]. To do so, at each step l of the decomposition we either pursue the factorization whenever $\|\mathbf{L}^{-1}\| \leq \kappa$, or we postpone a step, otherwise (cf. Figure 2). The block of postponed updates S_C (known as Schur complement) becomes the starting matrix of the next level. Using this inverse-based strategy and a moderate value of κ (e.g. $\kappa = 5$) it can be shown that small eigenvalues of \mathbf{P} are revealed by S_C . Thus S_C serves as some kind of coarse grid system.

The parallelization of ILUPACK mainly consists of a nested dissection partitioning of the graph of \mathbf{P} . This yields a hierarchy of subsystems which can be represented by an incomplete binary task tree. Starting with the leaves, the multilevel ILU is applied to all subsystems concurrently until these join the same parent task. Separators are factorized at last [1].

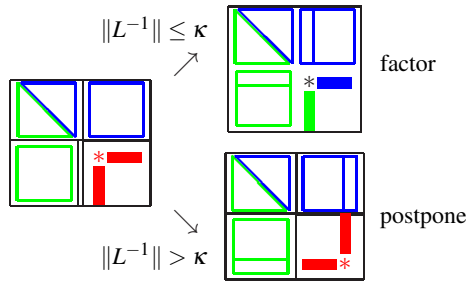


Fig. 2. ILUPACK pivoting strategy.

3 Numerical Experiments

Numerical experiments were made on the model problem of Fig. 3. It consists of a copper coil, and a non-conductive high permeable core. The tests were

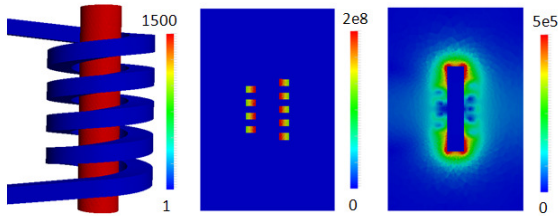


Fig. 3. Results of the magnetostatic field computations. The left picture shows the setting and the relative magnetic permeability, the central picture shows the exciting current density (1kA total current), and the right picture shows the resulting magnetic field $\mathbf{H} = \frac{1}{\mu_r \cdot \mu_0} \cdot \text{curl} \mathbf{A}$.

carried out on a 12-core INTEL-Westmere workstation with 3.06GHz and activated hyper-threading. We chose $\beta = 0.01$ for the regularization parameter in (3). In our experiments we are testing the parallel performance up to 8 cores. The results of the CPU times of the solver are shown in Fig. 4. Therein, the key values of two different meshes for 1.2E+6 unknowns and for 1.02E+7 unknowns are drawn. One can observe a perfectly parallel scaling for the pure ILU factorization part. A slightly worse behavior can be seen for the preconditioned conjugate gradient (PCG) solver. Moreover, the PCG needs more time than the factorization for greater problem dimensions. This is due to the fact, that the number of iterations is also increasing with the number of unknowns, see Fig. 5.

Finally, it can be concluded that ILUPACK seems to be a very promising library for the fast parallel solution of magnetostatic problems. This needs to be confirmed for more complex geometries.

References

1. J.I. Aliaga, M. Bollhöfer, A.F. Martín, and E.S. Quintana-Ortí. Exploiting thread-level parallelism in

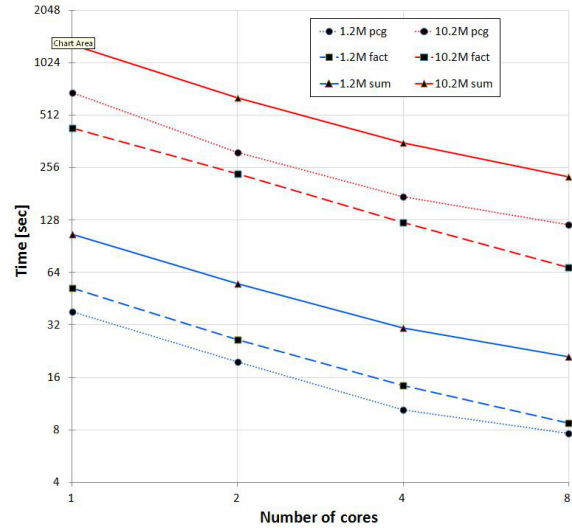


Fig. 4. CPU times for ILUPACK.

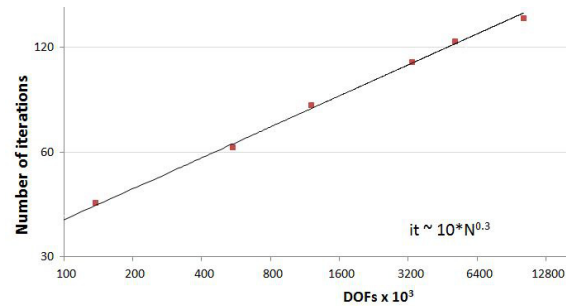


Fig. 5. Number of iteration steps.

the iterative solution of sparse linear systems. *Parallel Comput.*, 37(3):183–202, 2011.

2. M. Bebendorf and J. Ostrowski. Parallel hierarchical matrix preconditioners for the curl-curl operator. *Journal of Computational Mathematics*, 2009, Volume 27, No. 5, pp. 624-641.
3. M. Bollhöfer und S. Lanteri. Block Preconditioning Strategies for High Order Finite Element Discretization of the Time-Harmonic Maxwell Equations *Springer Book, SCEE 2010 Mathematics in Industry*, 2012, Volume 16,
4. M. Bollhöfer and Y. Saad. Multilevel preconditioners constructed from inverse-based ILUs. *SIAM J. Sci. Comput.*, 27(5), 2006.
5. R. Hiptmair and J. Xu. Nodal auxiliary space preconditioning in $H(\text{curl})$ and $H(\text{div})$ spaces. *SIAM J. Numer. Anal.*, 45(6):2483-2509 (electronic), 2007.
6. J. Ostrowski, M. Bebendorf, F. Kraemer and R. Hiptmair. H-Matrix based operator preconditioning for full Maxwell at low frequencies. *IEEE Transactions on Magnetics*, Volume 46, Number 8, pp. 3193-3196, Aug 2010, ISSN 0018-9464
7. S. Reitzinger and J. Schoeberl. An algebraic multigrid method for finite element discretizations with edge elements. *Numer. Linear Algebra Appl.*, 9(3):223-238, 2002.

Efficient Shooting Method Based on Leading Dynamics Determination by QR Decomposition

Federico Bizzarri¹, Angelo Brambilla¹, Giambattista Gruosso¹, and Giancarlo Storti Gajani¹

Politecnico di Milano, DEI, p.za Leonardo da Vinci, 32, 26013 Milano, Italy
bizzarri,brambilla,gruosso,storti@elet.polimi.it

Abstract In this paper an improved version of the conventional shooting method based on the Newton iterative algorithm is presented. One of the main drawbacks of the shooting method is due to the determination of the fundamental matrix by means of a product of partial matrices that limits its application to medium size circuits. Fundamental matrix free approaches have been presented in literature, they are based on the use of the GMRES method that lowers the computational effort from that of matrix by matrix product to that of matrix by vector product. In this paper a different approach is presented that exploits the properties of the QR decomposition to determine the leading dynamics of the circuit, i.e. the working modes represented by the eigenvectors of the circuit fundamental matrix associated to the Floquet exponents with the smaller negative real part. This can drastically reduce the number of matrix by vector products as in the GMRES method, but still makes available the main and most useful portion of the fundamental matrix, which is a key element, for example, in the determination of the stability of circuits working in a steady state condition.

1 Introduction

The shooting method, in contrast to harmonic balance, is well suited to compute the steady state behaviour of strong non-linear circuits and its importance has been recently strengthened to the reliable extension of this approach to mixed-signal problems [2]. Its “engine” is based on a time domain analysis that solves the DAE modeling the circuit with a variable time step integration method [1, 5]. Time domain analyses computes the residue, i.e. the difference among state variable values at the beginning and at the end of the integration time interval, and the sensitivity matrix, also known as the fundamental matrix \mathbf{M} , that relates variations of state variables at the end of the integration period to those at the beginning. One of the main drawbacks of the shooting method is that its application is limited to medium size circuits. This is due to the fact that \mathbf{M} is derived as a product of partial matrices each computed at each integration time step of the time domain analysis. If we assume that the circuit is characterised by N state variables and that the integration is performed on S time points, the effort to compute \mathbf{M} , which in general is full, is proportional to $S \times N^3$ [7]. The introduction of the “matrix free” shooting methods

based on GMRES sensibly reduces the computational effort [6]. The GMRES method builds the Krylov base $\mathcal{B} = [\mathbf{M}\mathbf{p}, \mathbf{M}^2\mathbf{p}, \dots, \mathbf{M}^n\mathbf{p}]$ where $\mathbf{M} \in \mathbb{R}^{N \times N}$ and $\mathbf{p} \in \mathbb{R}^N$ is a “tentative” vector. If \mathcal{B} spans the solution of the steady state problem with respect to a given error threshold, the solution is found in n matrix by vector products with a total cost $S \times n \times N^2$. The gain is thus proportional to a factor $(N - n)$. Consider now

$$\begin{cases} \frac{d\mathbf{x}}{dt} + G(\mathbf{x}, t) = 0 \\ \mathbf{x}(t + T) - \mathbf{x}(t) = 0 \end{cases} \quad (1)$$

where $G(\mathbf{x}, t) : \mathbb{R}^{N+1} \rightarrow \mathbb{R}^N$, models the vector field, $\mathbf{x} \in \mathbb{R}^N$ is the solution, $t \in \mathbb{R}^+$ represents time and $T \in \mathbb{R}^+$ is the working period. Assume to solve Eq. (1) in the time domain with the simple Implicit Euler integration method and consider one integration time step of length $h \in \mathbb{R}^+$, from t_n to $t_{n+1} = t_n + h$, we have

$$\mathbf{x}(t_{n+1}) - \mathbf{x}(t_n) + hG(\mathbf{x}(t_{n+1}), t_{n+1}) = 0.$$

By deriving this equation with respect to the $\mathbf{x}(t_0)$ initial condition we obtain

$$\frac{d\mathbf{x}(t_{n+1})}{d\mathbf{x}(t_0)} - \frac{d\mathbf{x}(t_n)}{d\mathbf{x}(t_0)} + h \frac{G(\mathbf{x}(t_{n+1}), t_{n+1})}{d\mathbf{x}(t_{n+1})} \frac{d\mathbf{x}(t_{n+1})}{d\mathbf{x}(t_0)} = 0$$

from which the sensitivity of $\mathbf{x}(t_{n+1})$ with respect to $\mathbf{x}(t_0)$ can be immediately computed as

$$\frac{d\mathbf{x}_{n+1}}{d\mathbf{x}_0} = \overbrace{\left(\mathbb{I}_N + h \frac{dG(\mathbf{x}_{n+1}, t_{n+1})}{d\mathbf{x}_{n+1}} \right)^{-1}}^{\mathbf{M}_{n+1}} \frac{d\mathbf{x}_n}{d\mathbf{x}_0} \quad (2)$$

where \mathbb{I}_N is the order N identity matrix and subscript n refers to time instant t_n . To compute product $\mathbf{M}\mathbf{p}$, either the \mathbf{M}_n matrices with $n = [1, \dots, S]$ in Eq. (2) or the \mathbf{x}_n solution vectors must be stored and this can be problematic when dealing with large circuits. The implementation chosen in our simulator PAN² follows the second solution to minimise memory usage. Therefore, to compute $\mathbf{M}\mathbf{p}$, $G(\mathbf{x}_{n+1}, t_{n+1})$ is reevaluated at each time point, the \mathbf{M}_{n+1} matrix is recomputed (at the cost of one LU factorisation) and the

² Our simulator PAN is available at the URL: <http://brambilla.ws.dei.polimi.it>.

$$\mathbf{M}_{n+1} \prod_{k=1}^n \mathbf{M}_k \mathbf{p} \quad (3)$$

left matrix by vector product is performed.

2 The proposed approach

According to Floquet theory, matrix \mathbf{M} can be decomposed as

$$\mathbf{M} = \sum_{k=1}^N e^{\lambda_k T} \mathbf{v}_k \mathbf{u}_k^T \quad (4)$$

where λ_k are the Floquet exponents of \mathbf{M} and $\mathbf{u}_k, \mathbf{v}_k$ are the corresponding right and left eigenvectors [3]. The boundary value problem defined in Eq. (1) can be solved with the Newton iterative method

$$\mathbf{x}_0^{p+1} = \mathbf{x}_0^p - \left(\sum_{k=1}^N e^{\lambda_k T} \mathbf{v}_k \mathbf{u}_k^T - \mathbb{I}_N \right)^{-1} (\mathbf{x}_S^p - \mathbf{x}_0^p)$$

where p is the iteration index and \mathbf{x}_0^p is an approximation of the initial condition. If we sort in decreasing order the Floquet exponents and set to 0 those having a real part considerably less than $\Re(\lambda_1)$ we have

$$\tilde{\mathbf{x}}_0^{p+1} = \mathbf{x}_0^p - (\tilde{\mathbf{M}} - \mathbb{I}_N)^{-1} (\mathbf{x}_S^p - \mathbf{x}_0^p)$$

where $\tilde{\mathbf{M}} = \sum_{k=1}^{N-L} e^{\lambda_k T} \mathbf{v}_k \mathbf{u}_k^T \in \mathbb{R}^{N \times N}$ is a rank L matrix that represents the *leading dynamics* of the system modeled by Eq. (1) and $\tilde{\mathbf{x}}_0^{p+1}$ is the approximated new tentative solution computed by the Newton method.

Apparently, the “truncated” matrix $\tilde{\mathbf{M}}$ can be derived only after having performed the complete matrix product (3). On the other hand the leading dynamics of the circuit can be computed by exploiting properties of the QR decomposition as shown in the sequel. Consider the product shown in Eq. (3) performed using only the first $S_1 < S$ time samples. Consider the $\mathbf{Q}_{1,S_1} \mathbf{R}_{1,S_1} = \mathbf{M}_{1,S_1} \mathbf{P}_{1,S_1}$ QR decomposition where $\mathbf{R}_{1,S_1} \in \mathbb{R}^{N \times N}$ is upper triangular and \mathbf{P}_{1,S_1} is a permutation matrix sorting the diagonal of \mathbf{R}_{1,S_1} in decreasing order. We set to 0 the $r_{i,j}$ entries of \mathbf{R} such that $r_{i,i} < \alpha |r_{1,1}|$. It can be shown that $|r_{i,i}| > |r_{i,j}|$ with $j > i$ so that $N - L$ last columns of \mathbf{Q}_{1,S_1} can be *dropped* in the subsequent left matrix product performed to compute the fundamental matrix. A QR decomposition can be performed after a predefined number of integration time steps. The structure of \mathbf{R} can be thus checked to see if other columns of the related \mathbf{Q} matrix can be dropped. At the end of this process, i.e. at the end of the integration process along the T working period, we have performed no more than $S \times (N - M) \times N^2$ matrix by vector products (as with GMRES), with the advantage of having computed a version of $\tilde{\mathbf{M}}$ representing the leading dynamics of the system, i.e. that has the same $(N - L)$ eigenvalues and eigenvectors of the \mathbf{M} fundamental matrix and, finally, with the advantage of avoiding the storage of partial matrices or solutions.

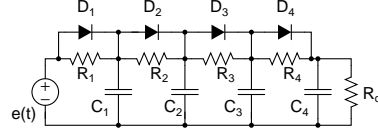


Figure 1. The schematic of the fourth order nonlinear ladder circuit. $C_x = 1 \mu\text{F}$, $R_x = 1 \text{ k}\Omega$, $e(t) = 10 \sin(200\pi t)$.

3 Simple simulation example

The schematic of a simple example circuit is shown in Fig. 1. It is a nonlinear ladder circuit with 4 state variables. The working period of the circuit is $T = 10 \text{ ms}$. After $T/4$, a QR decomposition of \mathbf{M}_{1,S_1} gives

$$\mathbf{R}_{1,S_1} = \begin{bmatrix} -0.1 & 0 & -0.1 & -0.1 \\ 0 & 9.7 \times 10^{-4} & -7.0 \times 10^{-4} & 9.2 \times 10^{-4} \\ 0 & 0 & -2.0 \times 10^{-6} & 8.6 \times 10^{-7} \\ 0 & 0 & 0 & 1.8 \times 10^{-9} \end{bmatrix}$$

Setting $\alpha = 10^{-3}$, the last two rows of \mathbf{R}_{1,S_1} can be set to 0, i.e. the leading dynamics is adequately spanned by the first two columns of \mathbf{Q}_{1,S_1} . The maximum relative error in computing the Floquet multipliers of \mathbf{M} is less than 6×10^{-4} showing the effectiveness of the proposed method. This approach has been applied also to the oscillator described in [4] characterized by about 500 state variables. With the proposed approach, choosing $\alpha = 10^{-7}$, the leading dynamics is spanned by only 41 columns of \mathbf{Q} just after $T/10$.

References

1. Brambilla A., Gruosso G., and Storti Gajani G. Fssa: Fast steady-state algorithm for the analysis of mixed analog/digital circuits. *IEEE Trans. on CAD*, 29(4):528–537, Apr 2010.
2. F. Bizzarri, A. Brambilla, and G.S. Gajani. Phase noise simulation in analog mixed signal circuits: An application to pulse energy oscillators. *Circuits and Systems II: Express Briefs, IEEE Transactions on*, 58(3):154–158, March 2011.
3. Miklós Farkas. *Periodic motions*. Springer-Verlag New York, Inc., New York, NY, USA, 1994.
4. S. Gagliolo, G. Pruzzo, and D. D. Caviglia. Phase noise performances of a cross-coupled cmos vco with resistor tail biasing. In *SBCCI05, 18th Annual Symposium on Integrated Circuits and System Design. Florianopolis, Brazil.*, pages 149–153, NEW YORK, NY, September 4-7 2005. ACM Press.
5. K. Kundert. *The Designer's Guide To Spice And Spectre*. Kluwer Academic Publishers, New York, NY, USA, 1995.
6. Y. Saad and H. Schultz. Gmres: A generalized minimal residual algorithm for solving non symmetric linear systems. *SIAM Journal on Scientific and Statistical Computing*, 7:pp. 856–869, July 1986.
7. J. Stoer. *Einführung in die Numerische Mathematik*. Springer Verlag, Berlin - Heidelberg - New York, 1972.

On an integral equation method for the electromagnetic scattering of biperiodic structures

Beatrice Bugert and Gunther Schmidt

Weierstrass Institute, Mohrenstr. 39, 10117 Berlin, Germany bugert@wias-berlin.de,
schmidt@wias-berlin.de

Summary. In this note we study an integral formulation for electromagnetic scattering by a biperiodic structure. It is derived from the time-harmonic Maxwell equations via potential methods by the combined use of a Stratton-Chu integral representation and an electric potential ansatz. We obtain results on existence and uniqueness for the solutions of this singular integral equation and give an outlook on the equation's numerical treatment via the fast multipole Boundary Element Method.

1 Introduction

Studying an integral formulation for electromagnetic scattering by a biperiodic structure generalizes the results from [5] where the equivalent problem for one-periodic structures was treated. Up to now, both in the one- and the biperiodic case several integral formulations have been proposed and implemented (e.g. [4]). We derive a new formulation by adapting the approach of [2], in which instead of a periodic structure a bounded obstacle was focussed on.

2 The electromagnetic scattering problem

Let Σ be a smooth non-selfintersecting surface which is 2π -periodic in both x_1 - and in x_2 -direction and separates two regions $G_{\pm} \subset \mathbb{R}^3$ filled with materials of constant electric permittivity ε_{\pm} and magnetic permeability μ_{\pm} . The surface is illuminated from G_+ by an electromagnetic plane wave at oblique incidence

$$(\mathbf{E}^i, \mathbf{H}^i) = (\mathbf{p}, \mathbf{s}) e^{i(\alpha_1 x_1 + \alpha_2 x_2 - \alpha_3 x_3)} e^{-i\omega t}, \quad (1)$$

which is $\tilde{\alpha}$ -quasiperiodic¹ in x_1 and in x_2 of period 2π , i.e. satisfies the relation

$$\mathbf{u}(\tilde{x} + 2\pi, x_3) = e^{i2\pi(\alpha_1 + \alpha_2)} \mathbf{u}(x). \quad (2)$$

The total fields are given by

$$\mathbf{E}_+ = \mathbf{E}^i + \mathbf{E}^{\text{refl}}, \quad \mathbf{H}_+ = \mathbf{H}^i + \mathbf{H}^{\text{refl}}, \quad (3)$$

$$\mathbf{E}_- = \mathbf{E}^{\text{tran}}, \quad \mathbf{H}_- = \mathbf{H}^{\text{tran}} \quad (4)$$

¹ In the following the tilde indicates the orthogonal projection of a three-dimensional vector on the (x_1, x_2) -plane.

and - after dropping the factor $e^{-i\omega t}$ - satisfy the time-harmonic Maxwell equations

$$\text{curl} \mathbf{E} = i\omega \mu \mathbf{H} \quad \text{and} \quad \text{curl} \mathbf{H} = -i\omega \varepsilon \mathbf{E}, \quad (5)$$

just like the incident and the scattered fields. When crossing the surface the tangential components of the total fields are continuous

$$\mathbf{n} \times (\mathbf{E}_+ - \mathbf{E}_-) = 0, \quad \text{on } \Sigma, \quad (6)$$

$$\mathbf{n} \times (\mathbf{H}_+ - \mathbf{H}_-) = 0, \quad \text{on } \Sigma, \quad (7)$$

where \mathbf{n} is the unit normal to the interface Σ . As the domain is unbounded, we must additionally impose the so called outgoing wave condition at infinity

$$(\mathbf{E}^{\text{refl}}, \mathbf{H}^{\text{refl}}) = \sum_{n \in \mathbb{Z}^2} (\mathbf{E}_n^+, \mathbf{H}_n^+) e^{i(\alpha_n \cdot \tilde{x} + \beta_n^+ x_3)}, \quad (8)$$

$$(\mathbf{E}^{\text{tran}}, \mathbf{H}^{\text{tran}}) = \sum_{n \in \mathbb{Z}^2} (\mathbf{E}_n^-, \mathbf{H}_n^-) e^{i(\alpha_n \cdot \tilde{x} - \beta_n^- x_3)}, \quad (9)$$

where $n = (n_1, n_2)^T$, $\tilde{x} = (x_1, x_2)^T$, $\alpha_n = (\alpha_1 + n_1, \alpha_2 + n_2)$ and $\beta_n^{\pm} = \sqrt{\kappa_{\pm}^2 - |\alpha_n|^2}$ with $\kappa_{\pm}^2 = \omega^2 \varepsilon_{\pm} \mu_{\pm}$. We shall assume $\kappa_+ > 0$, $\text{Re } \kappa_- > 0$, $\text{Im } \kappa_- \geq 0$. As we can easily derive the magnetic field in dependence of the electric field \mathbf{E} as $\mathbf{H} = -\frac{i}{\omega \mu} \text{curl} \mathbf{E}$, we are now interested in finding vector fields \mathbf{E} satisfying (5)-(8) such that

$$\mathbf{E}, \text{curl} \mathbf{E} \in (L_{loc}^2(\mathbb{R}^3))^3. \quad (10)$$

The $\tilde{\alpha}$ -quasiperiodicity of the incident waves motivates these two fields to be $\tilde{\alpha}$ -quasiperiodic themselves.

3 Boundary integral formulation

In order to solve the electromagnetic scattering problem introduced in section 2, we derive an equivalent integral equation via potential methods. For this, we combine a direct with an indirect method: in the domain G_+ above the grating surface Σ , we work with the quasiperiodic version of the Stratton-Chu integral representation and in the domain G_- below the grating surface, we make use of an electric potential ansatz. As it is common when working with periodic structures, we restrict our calculations to one period $\Gamma = \{\tilde{x} \mid 0 < x_1, x_2 < 2\pi\}$ of the surface. Its one-sided limit from G_{\pm} will be denoted by Γ_{\pm} .

3.1 Derivation of the boundary integral equation

The potentials which provide $\tilde{\alpha}$ -quasiperiodic solutions of the time-harmonic Maxwell equations are based on the $\tilde{\alpha}$ -quasiperiodic fundamental solution

$$G_{\kappa, \tilde{\alpha}}(x) = \frac{i}{8\pi^2} \sum_{n \in \mathbb{Z}^2} \frac{e^{i\alpha_n \cdot \tilde{x} + i\beta_n |x|}}{\beta_n}. \quad (11)$$

The single layer potential $\mathbf{S}_{\kappa, \tilde{\alpha}}$ is then given by

$$(\mathbf{S}_{\kappa, \tilde{\alpha}} \mathbf{u})(x) = \int_{\Gamma} G_{\kappa, \tilde{\alpha}}(x-y) \mathbf{u}(y) d\sigma(y), \quad (12)$$

for $x \in \mathbb{R}^3 \setminus \Gamma$. We define the electric potential $\Psi_{E_{\kappa}}^{\tilde{\alpha}}$ generated by $\mathbf{j} \in \mathbf{H}_{\times, \tilde{\alpha}}^{-\frac{1}{2}}(\text{div}_{\Gamma}, \Gamma)$ as

$$\Psi_{E_{\kappa}}^{\tilde{\alpha}} \mathbf{j} = \kappa^{-1} \text{curl curl } \mathbf{S}_{\kappa, \tilde{\alpha}} \mathbf{j} \quad (13)$$

and the magnetic potential $\Psi_{M_{\kappa}}^{\tilde{\alpha}}$ generated by $\mathbf{m} \in \mathbf{H}_{\times, \tilde{\alpha}}^{-\frac{1}{2}}(\text{div}_{\Gamma}, \Gamma)$ as

$$\Psi_{M_{\kappa}}^{\tilde{\alpha}} \mathbf{m} = \text{curl } \mathbf{S}_{\kappa, \tilde{\alpha}} \mathbf{m}. \quad (14)$$

Defining the Dirichlet traces $\gamma_{\mathcal{D}}$ and the Neumann traces $\gamma_{\mathcal{N}_{\kappa}}$

$$\gamma_{\mathcal{D}}^{\pm} \mathbf{u} = (\mathbf{n} \times \mathbf{u})|_{\Gamma_{\pm}}, \gamma_{\mathcal{N}_{\kappa}}^{\pm} \mathbf{u} = \kappa^{-1} (\mathbf{n} \times \text{curl } \mathbf{u})|_{\Gamma_{\pm}} \quad (15)$$

as well as

$$[\gamma_{\mathcal{D}}] = \gamma_{\mathcal{D}}^{-} - \gamma_{\mathcal{D}}^{+}, \{\gamma_{\mathcal{D}}\} = -\frac{1}{2} (\gamma_{\mathcal{D}}^{-} + \gamma_{\mathcal{D}}^{+}), \quad (16)$$

$$[\gamma_{\mathcal{N}_{\kappa}}] = \gamma_{\mathcal{N}_{\kappa}}^{-} - \gamma_{\mathcal{N}_{\kappa}}^{+}, \{\gamma_{\mathcal{N}_{\kappa}}\} = -\frac{1}{2} (\gamma_{\mathcal{N}_{\kappa}}^{-} + \gamma_{\mathcal{N}_{\kappa}}^{+}), \quad (17)$$

we have the following jump relations for the electric and magnetic potential:

$$[\gamma_{\mathcal{D}}] \Psi_{E_{\kappa}}^{\tilde{\alpha}} = 0, [\gamma_{\mathcal{N}_{\kappa}}] \Psi_{E_{\kappa}}^{\tilde{\alpha}} = -I, \quad (18)$$

$$[\gamma_{\mathcal{N}_{\kappa}}] \Psi_{M_{\kappa}}^{\tilde{\alpha}} = 0, [\gamma_{\mathcal{D}}] \Psi_{M_{\kappa}}^{\tilde{\alpha}} = -I. \quad (19)$$

With the Stratton-Chu ansatz

$$\mathbf{E}^{\text{refl}} = \Psi_{E_{\kappa+}}^{\tilde{\alpha}} \gamma_{\mathcal{N}_{\kappa+}}^{\tilde{\alpha}} \mathbf{E}^{\text{refl}} + \Psi_{M_{\kappa+}}^{\tilde{\alpha}} \gamma_{\mathcal{D}}^{\tilde{\alpha}} \mathbf{E}^{\text{refl}} \quad (20)$$

in G_{+} and the ansatz

$$\mathbf{E}^{\text{tran}} = \Psi_{E_{\kappa+}}^{\tilde{\alpha}} \mathbf{j} \quad (21)$$

in G_{-} , the use of the transmission conditions (6),(7) as well as the use of the jump relations (18),(19) for the electric and magnetic potential lead to the singular integral equation

$$\begin{aligned} \mathbf{A}_{\tilde{\alpha}} \mathbf{j} &= \left[\rho_1 C_{\tilde{\alpha}}^{+} \left(M_{\tilde{\alpha}}^{-} + \frac{1}{2} I \right) + \left(M_{\tilde{\alpha}}^{+} + \frac{1}{2} I \right) C_{\tilde{\alpha}}^{-} \right] \mathbf{j} \\ &= -\gamma_{\mathcal{D}}^{-} \mathbf{E}^{\text{i}}, \end{aligned} \quad (22)$$

where $\rho_1 = \frac{\mu_{+} \kappa_{-}}{\mu_{-} \kappa_{+}}$ and

$$C_{\tilde{\alpha}}^{\pm} = \{\gamma_{\mathcal{D}}\} \Psi_{E_{\kappa\pm}}^{\tilde{\alpha}} = \{\gamma_{\mathcal{N}_{\kappa\pm}}\} \Psi_{M_{\kappa\pm}}^{\tilde{\alpha}}, \quad (23)$$

$$M_{\tilde{\alpha}}^{\pm} = \{\gamma_{\mathcal{D}}\} \Psi_{M_{\kappa\pm}}^{\tilde{\alpha}} = \{\gamma_{\mathcal{N}_{\kappa\pm}}\} \Psi_{E_{\kappa\pm}}^{\tilde{\alpha}}. \quad (24)$$

3.2 Properties of the boundary integral equation

We can show that the singular integral operator $\mathbf{A}_{\tilde{\alpha}}$ is Fredholm with index 0 and that under certain conditions there exists a unique solution of the integral equation (22). The proofs are based on techniques used in [3], [2] and [5].

Theorem 1 (Fredholmness). *Assume that the electric permittivity ε_{\pm} and the magnetic permeability μ_{\pm} satisfy $\left(1 + \frac{\mu_{-}}{\mu_{+}}\right) \neq 0$ and $\left(1 + \frac{\varepsilon_{+}}{\varepsilon_{-}}\right) \neq 0$. Then $\mathbf{A}_{\tilde{\alpha}}$ is a Fredholm operator of index zero on $\mathbf{H}_{\times, \tilde{\alpha}}^{-\frac{1}{2}}(\text{div}_{\Gamma}, \Gamma)$.*

Theorem 2 (uniqueness). *Assume $\text{Im } \varepsilon_{-}, \text{Im } \mu_{-} \geq 0$ with $\text{Im}(\varepsilon_{+} + \mu_{+}) \geq 0$. Then (22) has at most one solution if $\ker\{\Psi_{E_{\kappa+}}^{\tilde{\alpha}}\} = \{0\}$.*

Theorem 3 (existence). *Let $\varepsilon_{-}, \mu_{-} \in \mathbb{R}_{+}$ and suppose the conditions of Theorem 1 are satisfied. If the electric potential $\Psi_{E_{\kappa-}}^{\tilde{\alpha}}$ is invertible, then there exists a solution $\mathbf{j} \in \mathbf{H}_{\times, \tilde{\alpha}}^{-\frac{1}{2}}(\text{div}_{\Gamma}, \Gamma)$ of (22).*

4 Numerical treatment and prospects

Considering the future implementation of the integral equation (22) we will use the Boundary Element Method which reduces the spatial dimensionality by one compared to the Finite Element Method. Furthermore, we want to accelerate occurring multiplications via a fast multipole method. A crucial issue is the evaluation of the $\tilde{\alpha}$ -quasiperiodic Green's function (11). The use of Ewald's method seems to be promising in this context (cp. [1]).

So far we have only studied the electromagnetic scattering problem for smooth surfaces Σ , but want to extend our results to Lipschitz surfaces with edges and corners.

References

1. T. Arens. Scattering by biperiodic layered media: the integral equation approach. Habilitation treatise, KIT, Karlsruhe, 2010.
2. M. Costabel and F. Le Louer. On the Kleinman-Martin integral equation method for electromagnetic scattering by a dielectric body. *SIAM J. Appl. Math.*, 71:635–656, 2011.
3. W. McLean. Periodic pseudodifferential operators and periodic function spaces. *Applied Mathematics Preprint*, 10:1–54, 1989.
4. J.-C. Nedelec and F. Starling. Integral equation methods in a quasi-periodic diffraction problem for the time-harmonic Maxwell's equations. *SIAM J. Math. Anal.*, 22(6):1679–1701, 1991.
5. G. Schmidt. Integral methods for conical diffraction. *WIAS preprint*, No. 1435, 2009.

Electro-hydrodynamic numerical modelling of corona discharge

D. Cagnoni^{1,2}, F. Agostini¹, T. Christen¹, C. de Falco², N. Parolini², and I. Stevanović¹

¹ ABB Switzerland Ltd., Corporate Research, CH-5405 Baden-Dättwil, Switzerland
ivica.stevanovic@ch.abb.com

² Dipartimento di Matematica “F. Brioschi”, Politecnico di Milano, via Bonardi 9, 20133 Milano, Italy

Summary. Prediction of cooling by forced convection due to corona-induced ion flow in an electro-hydrodynamic (or EHD) simulation requires a reliable corona electrode model, which has to be formulated as a boundary condition (BC) to the EHD partial differential equations. We discuss and compare four different BCs in the context of finite-volume methods (FVM). It turns out that the optimum choice depends on the given physical information.

1 EHD differential and numerical model

Corona discharge refers to field induced gas ionization near an electrode, e.g., a thin wire (*emitter*), in series with the dark discharge associated with the ion drift towards counter electrodes (*collector*). The ion motion induces a drag of the neutral gas, and can be used to convection cool a heat source, which may be the collector at the same time. The associated equations consist of the Poisson equation for the electric potential ϕ , and the balance equations for the densities for ion number N_p , mass ρ , momentum $\rho \mathbf{v}$, and energy (written in terms of the temperature T). In the Boussinesq approximation, they read

$$-\nabla \cdot (\varepsilon \nabla \phi) = q N_p \quad (1)$$

$$\frac{\partial N_p}{\partial t} = -\nabla \cdot \left(\frac{\mathbf{j}}{q} \right) = -\nabla \cdot ((b\mathbf{E} + \mathbf{v})N_p + a\nabla N_p) \quad (2)$$

$$\nabla \cdot \mathbf{v} = 0 \quad (3)$$

$$\frac{D\mathbf{v}}{Dt} = \nu \Delta \mathbf{v} - \nabla \left(\frac{p}{\rho} - \mathbf{g} \cdot \mathbf{x} \right) + \mathbf{f}_B + \mathbf{f}_{\text{EHD}} \quad (4)$$

$$\rho C_V \frac{DT}{Dt} = k \Delta T + \mathbf{j} \cdot \mathbf{E} - \mathbf{f}_{\text{EHD}} \cdot \mathbf{v} \quad (5)$$

where ε is the electric permittivity, q the ion charge, $\mathbf{E} = -\nabla \phi$ the electric field, b the ion mobility, a the diffusion constant, $\frac{D\bullet}{Dt} = \frac{\partial \bullet}{\partial t} + \mathbf{v} \cdot \nabla \bullet$ the material derivative for the velocity field \mathbf{v} , ν the viscosity, p the pressure, \mathbf{g} the gravitational acceleration, $\mathbf{f}_B = \beta(T_{\text{ref}} - T)$ the buoyancy force, and $\mathbf{f}_{\text{EHD}} = qN_p\mathbf{E}$ the Coulomb force, assumed to be distributed over all gas particles via scattering. The electric current density \mathbf{j} consists of drift, convection, and diffusion currents.

The system of coupled, nonlinear PDEs has to be solved for given initial and boundary conditions. Prior to discussing the latter, we summarize the global solution procedure. First, in a Gauss-Seidel-like approach, the solution is determined progressively for the block

$\phi - N_p$, then for the block $p - \mathbf{v}$ and finally for T . Because of the weak influence of each block to the preceding ones, only one iteration per time step is performed. Electrostatics equations are solved with nonlinear formulation to reach convergence (for details, see [2]) while Navier-Stokes block is solved via a SIMPLE-like projection method ($\lambda(\mathbf{v})$ being a coefficient depending on both the estimated velocity and the grid). Here we sketch how this iteration is built:

- until $\int_{\Omega} (N_p^{(k-1)} e^{\phi^{(k,0)} - \phi^{(k,n)}} - N_p^{(k)}) < \text{tol}$.
 - until $\|\phi^{(k,n-1)} - \phi^{(k,n)}\|_{\infty} < \text{tol}$.
 - ▲ solve $-\nabla \cdot (\varepsilon \nabla \phi^{(k,n)}) = q N_p^{(k-1)} e^{\phi^{(k,0)} - \phi^{(k,n)}}$, linearized around $\phi^{(k,n-1)}$
 - solve $q \frac{\partial N_p^{(k)}}{\partial t} = -\nabla \cdot (\mathbf{j}(\phi^{(k,n)}, N_p^{(k)}))$
- solve momentum equation (4) for $\mathbf{v}^{(0)}$
- until $\int_{\Omega} \nabla \cdot \mathbf{v}^{(j)} < \text{tol}$.
 - solve $-\nabla \cdot (\lambda(\mathbf{v}^{(j-1)}) \nabla p^{(j)}) = \nabla \cdot \mathbf{v}^{(j-1)}$
 - correct $\mathbf{v}^{(j)} = \mathbf{v}^{(j-1)} - \lambda(\mathbf{v}^{(j-1)}) \nabla p^{(j)}$
- solve temperature equation (5)

2 Corona discharge boundary conditions

We restrict our discussion to the BC for N_p at the *corona* electrode, comparing four different BC types. For the rest of the boundaries, instantaneous recombination BC ($\mathbf{n} \cdot \nabla N_p = 0$) is applied at counter electrodes, while in all other cases well-known standard BCs can be used.

The first approach we present is the *natural condition*, namely imposing the normal flux j_n associated to (2) to be uniform; this approach is very accurate when geometry is symmetric and one knows the actual current from measurements, but has the drawback of being totally unresponsive. Nonetheless, this approach is sometimes used with arbitrary geometries, defining an *active surface* that emits the necessary current density. The generally accepted *Kaptsov's hypothesis* (see [5]) states that $E_n := \mathbf{E} \cdot \mathbf{n} = E_{\text{on}}$, namely the field remains constant at the (virtual) electrode once the corona discharge is triggered. A value for E_{on} can be computed from *Peek's law* (see e.g. [6], ch. 4) and allows to define the active region as the part of the boundary where $E_n > E_{\text{on}}$ holds.

For having a predictive condition, instead, one needs to somehow enforce a *constitutive law* linking

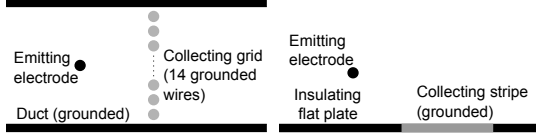


Fig. 1. Gometries from [4] (left) and from [3] (right).

j_n or N_p with E_n . We choose to adopt the second, simpler formulation, namely to impose $F_i(E_n, N_p) = 0$ to be satisfied on the boundary. Our first approach, given in [1], is based on a simplified physical model of the virtual contact which takes into account charge carriers injected solely from the active surface (with a saturation current density $j_{\text{sat}}H(E_n - E_{\text{on}})$, where $H(\bullet)$ is the Heaviside step function), and backscattered carriers (with current density given by $-qN_p w$ at the contact, where w is a characteristic velocity). Neglecting diffusion current at the electrode, this approach can be interpreted as imposing the relation

$$F_1(E_n, N_p) = qN_p(bE_n - w) - j_{\text{sat}}H(E_n - E_{\text{on}}) = 0 \quad (6)$$

Choice for the parameters j_{sat} and w needs to guarantee that the injected charge can naturally force $E_n = E_{\text{on}}$, otherwise current density saturates to $j_n = j_{\text{sat}}$ and *space charge controlled current* (SCCC) regime is not reached anymore.

Our second approach is to model the boundary as an ideal *rectifying diode*, in which no ion density is flowing under the E_{on} threshold, while every N_p value is possible when $E_n = E_{\text{on}}$. Explicitly, this approach is equivalent to enforce the following:

$$F_2(E_n, N_p) = N_p \left(1 - \left(\frac{E_n}{E_{\text{ons}}} \right)^\beta \right) = 0 \quad (7)$$

$\beta \in [0, 1]$ being a smoothing factor. This relation strongly enforces both N_p to vanish in the other non active portion of the electrode, and E_n to match E_{on} in the active portion.

Our last approach assumes a constitutive relation which is a more regular version for the former one:

$$F_3(E_n, N_p) = N_p - N_{\text{ref}} \left(\exp \left(\frac{E_n}{E_{\text{ref}}} \right) + 1 \right) = 0 \quad (8)$$

where N_{ref} and E_{ref} are a device-off ion density and a reference electric field. The choice of these two values can thus be made independently from the particular case (using e.g. air conductivity for N_{ref}).

3 Results and conclusions

As examples, a wire-to-grid geometry [4] and a wire-to-plate geometry [3] have been investigated (Fig. 1).

The former consists of a duct with a grounded grid in the middle (both collectors), and an emitter placed upstream. The E_{on} value is determined from the experimental onset voltage (4 kV). Simulations

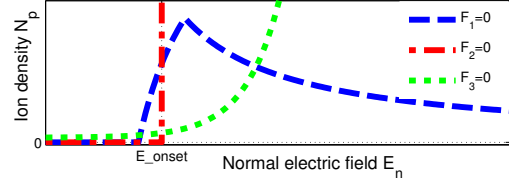


Fig. 2. Comparison of the graphs on the $N_p - E_n$ plane defined by the constitutive relations $F_i(E_n, N_p) = 0$.

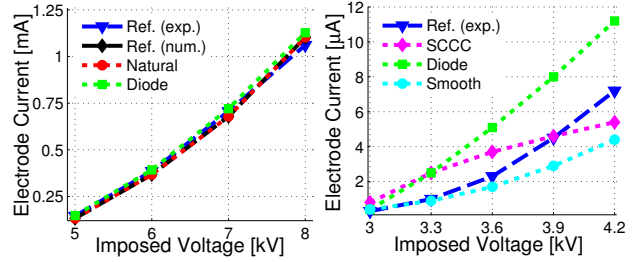


Fig. 3. IV-characteristic for the wire to grid (left) and wire to plate (right) geometries.

show how the natural condition matches exactly the experimental value, and the iterative condition as in (7) still captures well the electrical behavior. One may thus consider that in cases like this, even when lacking measured currents, the ideal diode model is still appropriate.

The latter geometry has a heated plate with a collecting stripe and the emitter is lifted from the plate. As shown in Fig 3, this case is not as well reproduced as the former, due to the highly nonuniform E_n on the electrode. This issue may be solved with a parameter optimization, which has not yet been undertaken in the present study. The current, being the most influential parameter for the fluid dynamics and thermal computing, was predicted with acceptable accuracy.

References

1. T. Christen and M. Seeger. Simulation of unipolar space charge controlled electric fields. *J. Electrostatics*, 65:11–20, 2007.
2. C. de Falco, J. W. Jerome, and R. Sacco. Quantum-corrected drift-diffusion models: Solution fixed point map and finite element approximation. *J. Comp. Phys.*, 228:1770–1789, 2009.
3. D. B. Go et al. Enhancement of external forced convection by ionic wind. *I.J. Heat Mass Transfer*, 51:6047–6053, 2008.
4. N. E. Jewell-Larsen et al. Modeling of corona-induced electrohydrodynamic flow with comsol multiphysics. In *Proc. of ESA Annual Meeting on Electrostatics*, 2008.
5. N. A. Kaptsov. *Elektricheskie Yavleniya v Gazakh i Vakuume*. OGIZ, Moskva, 1947.
6. H. J. White. *Industrial electrostatic precipitation*. Addison-Wesley, New York, 1963.

Simulation of a double-gate MOSFET by a non parabolic energy-transport subband model based on MEP including crystal heating

V. D. Camiola¹, G. Mascali², and V. Romano¹

¹ University of Catania, Italy camiola@dmi.unict.it, romano@dmi.unict.it

² University of Calabria, and INFN-Gruppo collegato di Cosenza, Italy mascali@unical.it

Summary. A nanoscale double-gate MOSFET is simulated by using a model based on the maximum entropy principle (MEP) by including the heating of the crystal lattice. The influence of this latter on the electrical performance of the device is discussed.

1 Mathematical model and simulations

The main aim of the paper is to simulate the nanoscale silicon double gate MOSFET (hereafter DG-MOSFET) reported in Fig. 1, by including also the crystal heating which can influence the electrical properties of the device and pose severe restrictions on its performance. In fact the phonons emitted by hot electrons create a phonon hot spot which increases the generated power density of the integrated circuits. This effect is becoming crucial by shrinking the dimension of the devices which is now below 100 nm, a length comparable with the wavelength of acoustic phonons [1, 2].

We consider a DG-MOSFET with length $L_x = 40$ nm, the width of the silicon layer $L_z = 8$ nm and the oxide thickness $t_{ox} = 1$ nm. The n^+ regions are 10 nm long. The doping in the n^+ regions is $N_D(x) = N_D^+ = 10^{20} \text{ cm}^{-3}$ and in the n region is $N_D(x) = N_D^- = 10^{15} \text{ cm}^{-3}$, with a regularization at the two junctions by a hyperbolic tangent profile.

Due to the symmetries and the dimensions of the device, the transport is, within a good approximation, one dimensional and along the longitudinal direction with respect the two oxide layers, while the electrons are quantized in the transversal direction. Six equivalent valleys are considered with a single effective mass $m^* = 0.32m_e$, m_e being the free electron mass.

Since the longitudinal length is of the order of a few tens of nanometers, the electrons as waves achieve equilibrium along the confining direction in a time which is much shorter than the typical transport time. Therefore we adopt a quasi-static description along the confining direction by a coupled Schrödinger-Poisson system which leads to a subband decomposition, while the transport along the longitudinal direction is described by a semiclassical Boltzmann equation for each subband.

Numerical integration of the Boltzmann-Schrödinger-Poisson system is very expensive from a computational point of view, for computer aided design (CAD) purposes (see references quoted in [3, 4]) In [3] we have formulated an energy transport model for the charge transport in the subbands by including the non parabolicity effects through the Kane dispersion relation. The model has been obtained, under a suitable diffusion scaling, from the Boltzmann equations by using the moment method and closing the moment equations with the Maximum Entropy Principle (MEP). Scatterings of electrons with acoustic and non polar optical phonons are taken into account. The parabolic subband case has been treated and simulated in [4].

The crystal heating is included adding a further equation for the lattice temperature T_L in the same spirit as in ref.s [5, 6]

$$\rho_{cV} \frac{\partial T_L}{\partial t} - \text{div} [K(T_L) \nabla T_L] = H, \quad (1)$$

with ρ and c_V silicon density and specific heat respectively. H is the phonon energy production given by

$$H = -(1 + P_S) n C_W + P_S \mathbf{J} \cdot \mathbf{E}, \quad (2)$$

where P_S plays the role of a thermopower coefficient, $n C_W$ is the electron energy production term with n electron density, and \mathbf{J} is the current. The electron density is related to the surface density in each subband by the relation

$$n = \sum_v \rho_v |\phi_v|^2$$

where ϕ_v are the envelope functions obtained solving the Schrödinger-Poisson system. In [5] a more general model for H has been proposed.

We stress that the lattice temperature enters into the electron-phonon scattering and in turn in the production terms of the balance equations for the electron variables. The main aim of the present paper is to address the importance of the crystal heating on the electric performance of the device.

A suitable modification of the numerical scheme for the MEP energy transport-Schrödinger-Poisson

system developed in [4] is proposed which includes also the discretization of the lattice temperature balance equation via an ADI approach. Since the characteristic time of the crystal temperature is about one or two orders of magnitude longer than that of electrons, a multirate time step method is employed as in [6].

In the figures we report some preliminary results. It is possible to see a tremendous raise of the crystal energy $k_B T_L$, which at room temperature is about 0.0259 eV, near the drain where the electron energy has its maximum values due to the high electric field present there. It is likely that the lattice temperature reaches the silicon melting temperature. This poses severe restrictions on the source/drain and source/gate voltages with stringent design constraints.

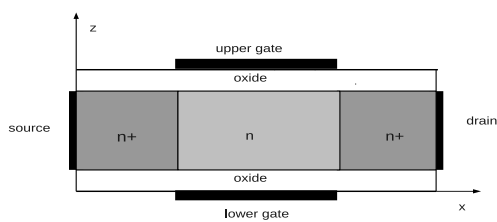


Fig. 1. Schematics representation of the simulated DG-MOSFET

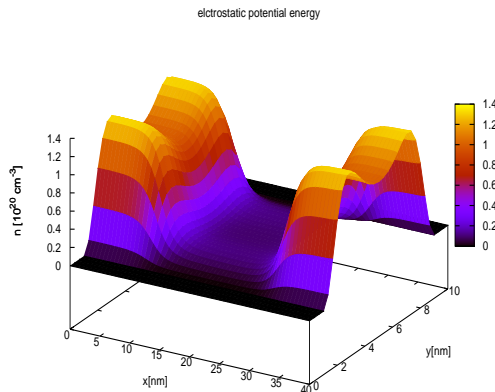


Fig. 2. Electron density when the applied potential between source and drain is $V_{SD} = 0.1$ V and source and gate are equipotential

Acknowledgement. V.D.C. and V. R. acknowledge the financial support by the P.R.I.N. project 2010 Kinetic and macroscopic models for particle transport in gases and semiconductors: analytical and computational aspects and by P.R.A. University of Catania. G. M. acknowledges the financial support by P.R.A., University of Calabria.

References

1. S. Sinha and K.E. Goodson. Thermal conduction in sub-100 nm transistors. *Microelectronics Journal*, 37: 1148–

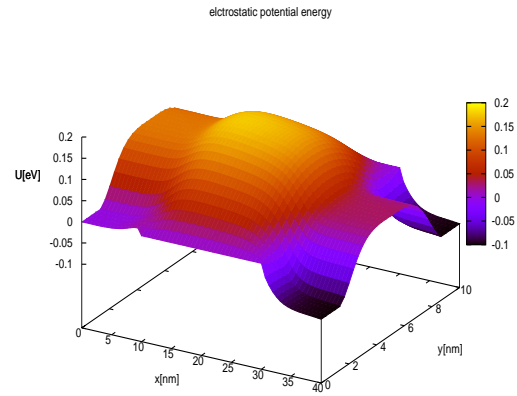


Fig. 3. Electrostatic energy when the applied potential between source and drain is $V_{SD} = 0.1$ V and source and gate are equipotential

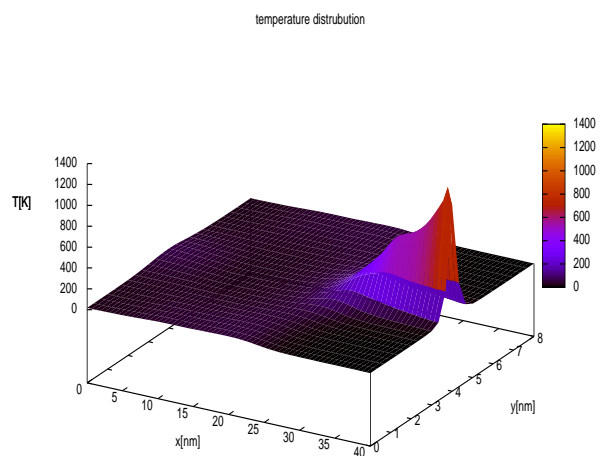


Fig. 4. Electrostatic energy when the applied potential between source and drain is $V_{SD} = 0.1$ V and source and gate are equipotential

- 1157, 2006.
2. J. A. Rowlette and K. E. Goodson. Fully coupled nonequilibrium electron-phonon transport in nanometer-scale silicon FETs *IEEE trans. on electron device*, 55: 220–232, 2008
3. G. Mascali and V. Romano. A non parabolic hydrodynamical subband model for semiconductors based on the maximum entropy principle. *Mathematical and Computer Modelling*, 55:1003–1020, 2012.
4. V.D. Camiola, G. Mascali and V. Romano. Numerical simulation of a double-gate MOSFET with a subband model for semiconductors based on the maximum entropy principle. *Continuum Mech. Thermodyn.*, 2012 (available online).
5. V. Romano and M. Zwierz. Electron-phonon hydrodynamical model for semiconductors. *Z. Angew. Math. Phys.*, 61:1111–1131, 2010.
6. V. Romano and A. Rusakov, 2d numerical simulations of an electronphonon hydrodynamical model based on the maximum entropy principle. *Comput. Methods Appl. Mech. Engrg.*, 199: 274–2751, 2010.

Streamer Inception and Propagation from Electric Field Simulations

Thomas Christen

ABB Switzerland Ltd., Corporate Research, CH-5405 Baden-Dättwil, Switzerland

Summary. A recipe is introduced for the determination of streamer inception regions and streamer propagation paths from the electric background field. The method is based on the equivalence of the streamer inception integral with a first order partial differential equation (PDE). It can be easily used in modern commercial multi-physics simulation tools, and circumvents the cumbersome search for critical field lines and their postprocessing.

Introduction

Streamer inception (SI) at an electrode and subsequent streamer propagation (SP) towards the counter electrode are initial steps of dielectric gas breakdown in nonuniform high electric fields [1]. Often, the aim of electric field calculations is to identify the locations where SI can occur and to determine how far streamers can propagate. This note introduces a simple procedure to calculate SI and SP from quasi-static electric background fields using common SI and SP criteria [1, 2].

We thus assume that the solution of the Laplace equation for the electric potential $U(\mathbf{x})$ in the compact spatial region of interest, $\Omega \subset \mathbf{R}^3$, is given for appropriate boundary conditions. The boundary of Ω is denoted by $\partial\Omega$. Let the potential be positive at the electrode under consideration, $\partial\Omega_0 \subset \partial\Omega$, i.e., $U_0 = U(\mathbf{x}) > 0$ for $\mathbf{x} \in \partial\Omega_0$ (Dirichlet boundary condition). Assume further that the potential at the counter electrode(s) is smaller, for instance grounded, such that the field lines of the electric field, $\mathbf{E} = -\nabla U$, point away from $\partial\Omega_0$. The *SI criterion* is associated with the critical electron avalanche size and is formulated as an integral condition to the effective ionization coefficient $\alpha(E)$ along a field-line path γ where α is positive and which ends at $\partial\Omega_0$ [1, 2],¹

$$\int_{\gamma} \alpha(E) ds \geq C_{\text{crit}} \quad (1)$$

with field strength $E(\mathbf{x}) = |\mathbf{E}|$. For a field distribution $\mathbf{E}(\mathbf{x})$ in an arbitrary geometry, it is not a priori obvious which are the critical field lines satisfying Eq. (1); they are not necessarily related to electrode locations with maximum field.

¹ The integral (1) gives $\ln N/N_0$, where N is the number of electrons in an avalanche, and N_0 is the number of starting electrons. For negative α , electrons recombine or are attached.

The required search for and extraction of information on field lines from electric simulations for realistic geometries, as it is needed for (1), is usually not a feature provided by typical commercial E-field simulation tools. But we will show that there is a simple way to determine the critical SI region $\Gamma \subset \Omega$, and thus the critical electrode region, $\partial\Gamma_0 = \Gamma \cap \partial\Omega_0$, without cumbersome postprocessing.

Streamer Inception (SI)

We introduce the scalar field variable $\phi(\mathbf{x})$, which satisfies the 1st order PDE

$$-\mathbf{v} \cdot \nabla \phi = \alpha(E) \Theta(\alpha) \quad (2)$$

where Θ is the Heaviside theta-function such that the right side vanishes for negative α , and

$$\mathbf{v}(\mathbf{x}) = \frac{\mathbf{E}}{E} \quad (3)$$

is the normalized vector field along the field lines. Equation (2) means that the derivative of ϕ along the backward direction of the field lines (i.e., towards the electrode $\partial\Omega_0$), equals α . Hence the solution of Eq. (2) is the integral of α along field lines and equal to the streamer integral (1), provided $\phi = 0$ in regions where $\alpha \leq 0$. The latter condition is ensured by using a homogeneous Dirichlet boundary condition, $\phi = 0$, at the counter electrode(s), where the flow lines of \mathbf{v} end. The theta-function in Eq. (2) ensures integration only for $\alpha \geq 0$. The SI region Γ , where streamers will emerge, is then obtained from $\phi(\mathbf{x}) \geq C_{\text{crit}}$. Note that because $\Gamma \subset \Omega$ is a volume region, the procedure allows also the determination of electrodeless SI.

Steamer Propagation (SP)

A SP model has to predict where and how far the emerging streamers will go. If they reach the counter electrode, dielectric breakdown may occur. Streamer-to-leader transition is not discussed here [4]. A simple SP model makes use of the observation that a streamer length increase requires a roughly constant voltage drop, which can be associated with a field E_s along

the streamer path. The potential drop along a streamer of length s is then [4]

$$U_s(s) = U_{s,0} + E_s s \quad (4)$$

where $U_{s,0}$ can be interpreted as the streamer head voltage. If it is assumed that streamers follow field lines, the path can be found by solving the ordinary differential equation (ODE) for the location $\mathbf{x}(t)$ of, say, the streamer head

$$\frac{d\mathbf{x}}{dt} = \mathbf{v}(\mathbf{x}) h(\Delta U, t) \quad (5)$$

with initial condition $\mathbf{x}(0) \in \partial\Gamma$ (or, here, Γ_0) for $t = 0$, and $\Delta U = U_0 - U(\mathbf{x})$ is the voltage drop along the streamer line. Note that t is equal to the streamer length s because $|\mathbf{v}| = 1$ (\mathbf{v} is not the true streamer velocity but its direction vector; the true speed, which is typically of the order of mm/ns [3] is not needed for determining the streamer length for many practical cases). The prefactor $h(\Delta U, t)$ is either 1 or 0, depending on whether the SP criteria is satisfied or not. The prefactor h ensures that the streamer stops if the local potential drop is insufficient for further propagation. For brevity, the considerations are here restricted to $U_{s,0} = 0$, where $h = \Theta(\Delta U - E_s s)$.

The assumption that streamers follow field lines may not always be valid, as was critically discussed in Refs. [4, 5]. Nevertheless, generalized models might be taken into account in our simple propagation model by a redefinition of $\mathbf{v}(\mathbf{x})$ in Eq. (5) [4].

Results

The incorporation of our SI approach in typical commercial multi-physics simulation tools, which usually solve 2nd order PDEs, requires a mimicry of the 1st order PDE (2) with a 2nd order PDE of the form $D\Delta\phi - \mathbf{v} \cdot \nabla\phi = \alpha(E)$. The structural difference between them leads to a singularly perturbed problem (i.e., the limit $D \rightarrow 0$ is not equivalent to $D = 0$). However, the solution of Eq. (2) can be approximated with sufficient accuracy for practical purposes, if D is small enough and the boundary conditions to ϕ are appropriately chosen. In particular, the disturbance of the solution by the boundary condition at $\partial\Omega_0$ should be negligibly small. Because for $D = 0$ one has $\partial_s\phi = \alpha$ at $\partial\Omega_0$, one must have $D \ll 1/|\partial_E \ln(\alpha)\partial_s E|$, and the boundary condition must be $\mathbf{n} \cdot \nabla\phi = -\alpha$, where \mathbf{n} denotes the surface normal vector at $\partial\Omega_0$.

As an example, we consider a tip-plate geometry in normal air, where [6] $\alpha = p[k(\frac{E}{p} - \Lambda)^2 - A]$ with $k = 1.6 \text{ mm bar/kV}^2$, $\Lambda = 2.2 \text{ kV/(mm bar)}$, $A = 0.3 \text{ 1/(mm bar)}$, $p = 1 \text{ bar}$, tip-plate distance 19 cm, tip radius 1 cm, and $E_s = 0.5 \text{ kV/mm}$. A result for $U_0 = 80 \text{ kV}$ is shown in Fig. 1; the SI voltage, when the first streamer appears is ca. 67 kV. The SI region is visible

as the small dark area in front of the tip. The voltage when the first streamer crosses the gap is for this case $U_{bd} = 95 \text{ kV}$.

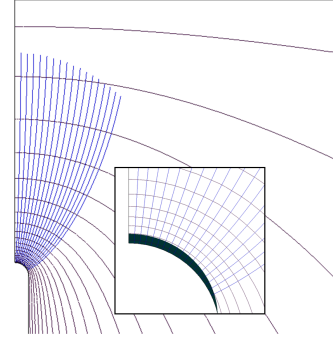


Fig. 1. Tip-plate geometry with simulated equipotential curves, SI region in front of the tip (insert), and streamer lines (simulation tool: Comsol; streamer lines with "particle tracing" feature).

Conclusion

Streamer lines associated with the common SI and SP criteria used in electrical engineering, can be calculated directly from standard multi-physics simulation tools without cumbersome postprocessing of electric field line data, provided the tool exhibits at solvers for an additional linear PDE (for SI) and an ODE (for SP).

References

1. Boeck W. and Pfeiffer W., *Conduction and Breakdown in Gases*, in "Wiley encyclopedia of electrical and electronics engineering", Vol 4, J. G. Webster (editor), J. Wiley & Sons Inc., New York, 1999, pp. 123-172.
2. Gallimberti I., *The mechanism of the long spark formation*, Colloque de physique 40, 1979, pp. 193-250.
3. T. Briels et al. *Positive and negative streamers in ambient air: measuring diameter, velocity and dissipated energy*, J. Phys. D: Appl. Phys 41, 234004 (2008).
4. T. Christen et al, *Streamer line modeling*, Scientific computing in electrical engineering SCEE 2010, Eds. B Michielsen and J-R. Poirier, Springer (2012), pp. 173.
5. A. Pedersen et al, *Streamer inception and propagation models for designing air insulated power devices*, CEIDP Conference Material, Virginia Beach (Oct. 2009).
6. K. Petcharaks, *Applicability of the streamer breakdown criterion to inhomogeneous gas gaps*, ETH Thesis No. 11192 (1995).

Frequency Parameterized Models for Planar On-Chip Inductors

Gabriela Ciuprina, Daniel Ioan, Cosmin-Bogdan Diță, and Mihai-Iulian Andrei

"Politehnica" University of Bucharest, Electrical Engineering Department, Numerical Methods Lab.,
Spl. Independentei 313, Bucharest, Romania, lmn@lmn.pub.ro,

Summary. The paper proposes an efficient method for the modeling of high frequency electromagnetic field effects, such as skin or proximity effects, inside on-chip metallic conductors. Compact sub-models obtained by using an electromagnetic field discretization approach based on the Finite Integration Technique in which frequency dependent Hodge operators are used, are connected to magnetic circuits that describe inductive couplings.

1 Frequency Dependence

Designers of integrated circuits require models of passive components which describe all relevant electromagnetic field effects at high frequency. These effects are quantified by the Maxwell equations of the electromagnetic field. In the Finite Integration Technique (FIT), by applying the global form of electromagnetic field equations on the mesh elements (elementary faces and their borders), a system of differential algebraic equations, called Maxwell Grid Equations (MGE) is obtained [2]. Due to high conductivity ($\sigma \gg \omega\epsilon$), the electromagnetic field inside metallic conductors can be considered a magneto-quasi-static (MQS) one. MGE for MQS regime are combined with the Hodges operators, which describe the material behavior

$$\begin{aligned} \mathbf{B} &= \mu \mathbf{H}, & \mathbf{J} &= \sigma \mathbf{E} & \Rightarrow \\ \Rightarrow \quad \varphi &= \mathbf{M}_\mu \mathbf{u}_m = \mathbf{M}_v^{-1} \mathbf{u}_m, & \mathbf{i} &= \mathbf{M}_\sigma \mathbf{u}_e, \end{aligned} \quad (1)$$

where the following global variables have been used: electric and magnetic voltages \mathbf{u}_e , \mathbf{u}_m , and magnetic fluxes φ and conduction currents \mathbf{i} , that are associated to the grids elements in a coherent manner.

In the classical FIT approach, the discrete Hodge operators \mathbf{M}_v and \mathbf{M}_σ are constant diagonal matrices, which can be built by independent averaging of material constants $v = 1/\mu$ and σ over each cell. In order to describe field effects at high frequency such as skin and proximity effects, the cell dimensions have to be much less than the skin depth $\delta = \sqrt{2/(\omega\mu\sigma)}$, which is $6.7\mu\text{m}$ for Cu at 100 GHz and $15\mu\text{m}$ at 20 GHz. In order to keep the number of cells at a reasonable level, non-uniform grids could be used, with peripheral cells smaller than internal ones. Even so, the number of cells required by a reasonable accuracy can be relatively high. To avoid this drawback, it was proposed to replace the Hodge operators

used in classical FIT with others appropriate for the description of high field effects in conductors [3].

By solving the complex Helmholtz equation for the electric field in a rectangular homogeneous cell having the conductivity σ and the permeability μ , of dimensions: a (along the Ox axis), $2b$ and $2c$ (along Oy and Oz, respectively), we found that the complex admittance of the cell along the Ox direction is

$$\mathbf{Y} = \frac{8}{\pi^2 R_0} \sum_{k=1}^{\infty} \frac{1}{(2k-1)^2} \left[\frac{\tanh(\lambda_k b)}{\lambda_k b} + \frac{\tanh(\mu_k c)}{\mu_k c} \right], \quad (2)$$

where $R_0 = a/(4\sigma bc)$ is the D.C. resistance of the analyzed cell along the Ox direction, and the complex numbers λ_k and μ_k are given by

$$\lambda_k = \sqrt{\gamma^2 + \left[\frac{(2k-1)\pi}{2c} \right]^2}, \quad (3)$$

$$\mu_k = \sqrt{\gamma^2 + \left[\frac{(2k-1)\pi}{2b} \right]^2}, \quad (4)$$

where $\gamma^2 = i\omega\mu\sigma$ is the complex diffusion constant in the conductor. Relation (2) does a smooth connection between the D.C. value R_0 and the value given by a strong skin depth formula $a/(4(b+c)\delta)$ (Fig. 1).

The first results carried out in FIT with FredHO on a simple test case having an analytical solution taken as reference, are given in Table 1 and Fig. 1 and show its efficiency both with respect to the computational effort and error. FredHO is able to catch not only the dependence of the A.C. resistance with respect to the frequency, but also the frequency dependence of the conductor inner inductivity.

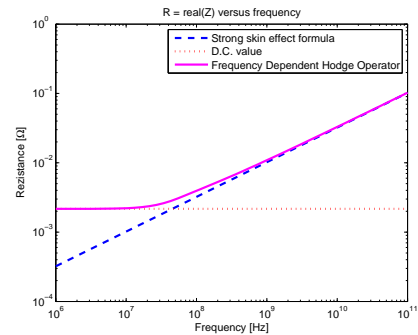
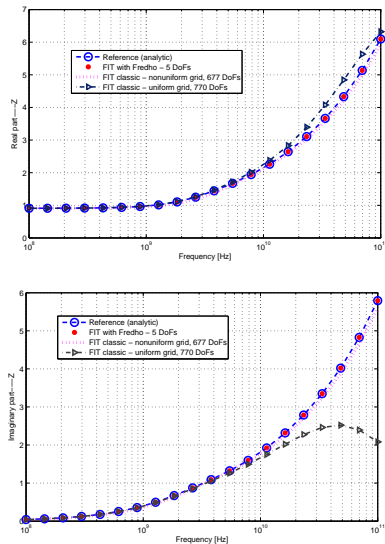


Fig. 1. Dependence of the A.C. resistance $R_{AC} = \text{real}(1/Y)$ with respect to the frequency.

Table 1. Validation of FIT with FredHO

	No. DoFs.	Relative error [%]
Analytic	-	0
Classical FIT, uniform grid	770	31
Classical FIT, non-uniform grid	667	3
FIT with FredHO	5	0.0006

**Fig. 2.** Frequency characteristic - with or without FredHO.

2 Inductive Effects

Our models of the inductors consist of two coupled circuits: an electric and a magnetic one. The electric circuit includes frequency dependent reactances inside conductors and RC sub-circuits outside, whereas the the magnetic circuit describes inductive (magnetic) couplings. Magnetic hooks are placed in the holes of each fundamental loop of the electric circuit.

The magnetic circuit is driven by "voltage" sources (actually magnetic voltage sources), controlled by the independent loop currents of the electric circuit (co-tree currents). The electric induced voltages are modeled by voltage sources placed in the co-tree branches of the electric circuit, which are controlled by the time derivative of the magnetic circuit "currents" (actually magnetic fluxes). The magnetic reluctances are associated to fundamental current loops and they are extracted directly from the field solution. The controlling by time derivatives of magnetic fluxes is obtained by means of a third "derivative" subcircuit. Thus, the model extracted becomes compatible with any circuit simulator, including standard Spice. Contrary to VPEC or other partial-inductance/reluctance approaches [5, 6] our reluctances are associated to fundamental current loops and they are extracted directly from the field solution. By using the loop-reluctance matrix instead of partial reluctances/inductances ("K elements"), the sparsification is very effective and robust (the passivity is not lost), which is an essential request [1, 4].

3 Conclusion

In frequency domain simulation, high frequency field effects can be taken into consideration in a very effective manner, if the Hodge operators depend on the frequency. From the computational resources point of view, this is more efficient than using a fine discretization grid inside the conductors, even if this implies some matrix re-assembling at every frequency sample. In this paper this technique is combined with the use of magnetic circuits describing inductive effects in order to obtain compact models for planar inductors. Our presentation will describe in detail this technique and will show results for real benchmarks.

Acknowledgement. The work has been co-funded by the Sectoral Operational Programme Human Resources Development 2007-2013 of the Romanian Ministry of Labour, Family and Social Protection through the Financial Agreements POSDRU/89/1.5/S/62557, POSDRU/88/1.5/S/61178, POSDRU/107/1.5/S/76813, and by UPB/CIEAC research funds.

References

1. S. Bantas, S. Stefanou, K. Karouzakis, F. Toufexis, A. Liapis, and P. Papadopoulos. Rapid rclk modeling of on-chip passives and interconnects with efficient k reduction and passivity enforcement. *International Journal of RF and Microwave Computer-Aided Engineering*, 22:41–48, 2012.
2. D. Ioan and G. Ciuprina. Reduced order models of on-chip passive components and interconnects, workbench and test structures. In W.H.A. Schilders, H.A. van der Vorst, and J. Rommes, editors, *Model Order Reduction: Theory, Research Aspects and Applications*, volume 13, pages 447–467. Springer-Verlag, Heidelberg, 2008.
3. D. Ioan and M. Piper. FIT models with frequency dependent hodge operators for hf effects in metallic conductors. In *in Progress In Electromagnetics Research - book of abstracts*. Pisa, Italy, 2004.
4. Y. Tanji, T. Watanabe, and H. Asai. Generating stable and sparse reluctance/ inductance matrix under insufficient conditions. In *ASP-DAC '08 Proc. Asia and South Pacific Design Automation Conference*. 2008.
5. Hao Yu and Lei He. Vector potential equivalent circuit based on peec inversion. In *DAC '03 Proc. of the 40th annual Design Automation Conference*. 2003.
6. Mengsheng Zhang, Wenjian Yu, Zeyi Wang, and Yu Du. An efficient algorithm for 3-d reluctance extraction considering high frequency effect. In *ASP-DAC '06 Proc. of the Asia and South Pacific Design Automation Conference*. 2006.

Advanced Computer Methods for Grounding Analysis

Ignasi Colominas¹, José París¹, Xesús Nogueira¹, Fermín Navarrina¹, and Manuel Casteleiro¹

Group of Numerical Methods in Engineering-GMNI, Civil Engineering School, Universidade da Coruña, SPAIN
icolominas@udc.es

Summary. In this work we present the foundations of a numerical formulation based on the Boundary Element Method for grounding analysis developed for the authors in last years. Furthermore, a revision of main applications of this numerical approach to some problems in electrical engineering practice is shown.

Main goals of an earthing system are to safeguard that persons working or walking in the surroundings of the grounded installation are not exposed to dangerous electrical shocks and to guarantee the integrity of equipment and the continuity of the power supply under fault conditions. Thus, the equivalent resistance of the electrode should be low enough to assure the current dissipation mainly into the earth, while maximum potential differences between close points on the earth surface must be kept under certain maximum values defined by the safety regulations [1–3].

Although the electric current dissipation is a well-known phenomenon, the computing of grounding grids of large electrical substations in practical cases present some difficulties mainly due to the specific geometry of these grids [4, 5].

In the last years, the authors have proposed a numerical approach based on the transformation of the Maxwell's differential equations onto an equivalent boundary integral equation. This integral approach is the starting point for the development of a general numerical formulation based on the Boundary Element Method which allows to derive specific numerical algorithms of high accuracy for grounding analysis embedded in uniform soils models [6]. On the other hand, the anomalous asymptotic behaviour of the classical computer methods proposed for earthing analysis can be rigorously explained identifying different sources of error [4]. Besides, the Boundary Element formulation has been extended for grounding grids embedded in stratified soils [7, 8].

This methodology has been implemented in a CAD tool for grounding systems comprising all stages of the analysis: the preprocessing, the computing and the postprocessing, including the calculation of the characteristic safety parameters [9]. Furthermore, high-efficient convergence acceleration techniques have been also derived improving the earthing analysis for the case of layered soil models [10].

In 2005, the authors proposed a methodology for the analysis of a common and very important en-

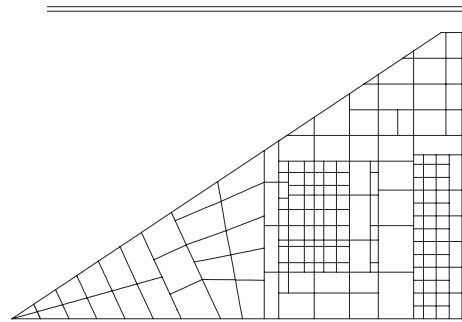


Fig. 1. Grounding grid plan and situation of the two railway tracks in the surroundings of the electrode.

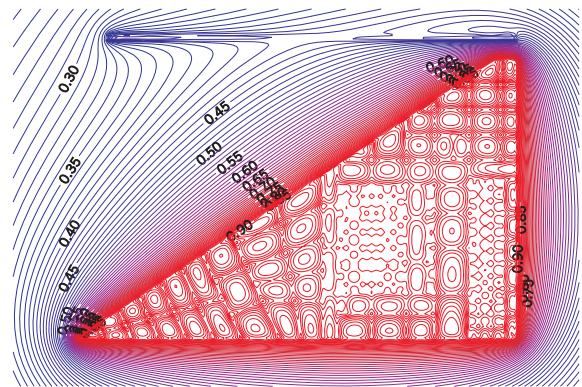


Fig. 2. Potential distribution ($\times 10$ kV) on the earth surface due to the energization of the grounding grid considering the phenomena of the transferred potentials by the tracks.

gineering problem in the grounding field: the problem of transferred earth potentials by grounding grids [11]. “Transferred earth potentials” refer to the phenomenon of the earth potential of one location appearing at another location with a contrasting earth potential. This transference occurs, for example, when a grounding grid is energized up to a certain voltage (typically, the Ground Potential Rise) during a fault condition, and this voltage—or a fraction of it—appears (or it is “transferred”) out to a non-fault site by a buried or semiburied conductors: communication or signal circuits, neutral wires, metal pipes, rails, metallic fences, etc., leaving the substation area.

The danger that can imply this potential transference to people, animals or the equipment is evident, especially because in some cases it is produced in un-

expected and non-protected areas [2]. While the prevention of these hazardous voltages has been traditionally carried out by combining a good engineering expertise, some crude calculations and even field measurements, an accurate determination of the transferred earth potentials by grounding grids can be currently performed by using computer methods: in [12], the authors proposed a numerical methodology for the case of uniform soil models, and the generalization for stratified soil models was published in [13].

Figure 1 shows the plan of the grounding grid of an electrical substation and the situation of two tracks in the surroundings of the electrode, as an application example of transferred earth potential analysis. The grounding grid has 408 cylindrical electrodes (diameter: 12.85 mm), it is buried 0.80 m. and its maximum dimensions are $145 \times 90 \text{ m}^2$. The resistivity of the soil is $60 \Omega\text{m}$ and the GPR considered is 10 kV. There are also two tracks—with a length of 130 m (diameter: 94 mm)—buried 0.10 m. Figures 2 and 3 show the potential distribution on the earth surface computed by using a Boundary Element formulation for transferred earth grounding voltages in uniform soil models. In both graphs, it can be observed the modification of the potential mapping on the earth surface due to the presence of the tracks and the voltage level induced on them.

Finally, most recently the authors have proposed a methodology for the analysis of grounding grids buried in soils which present some finite volumes with very different conductivities. In our opinion, these kinds of numerical models should allow for example the computational modeling of earthing systems of underground compact substations [14].

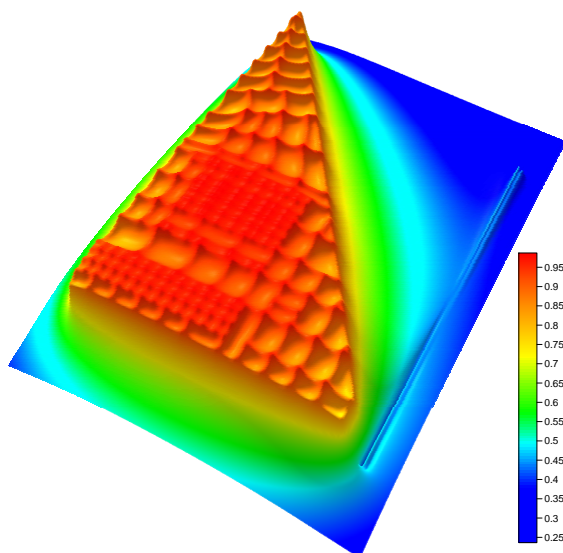


Fig. 3. TOTBEM Postprocessing module: 3D visualization of the potential distribution on the earth surface.

Acknowledgement. This work has been partially supported by the “Ministerio de Educación y Ciencia” (grants DPI2009 14546-C02-01 and DPI2010-16496), and by R&D projects of the Xunta de Galicia (grants CN2011/002, PGDIT09 MDS00718PR and PGDIT09 REM005118PR), cofinanced with FEDER funds.

References

1. IEEE Std. 80, *IEEE Guide for safety in AC substation grounding*. New York, 2000.
2. IEEE Std. 142, *IEEE Recommended practice for grounding of industrial and commercial power systems*. New York, 2007.
3. J. G. Sverak, “Progress in step and touch voltage equations of ANSI/IEEE Std 80. Historical perspective”, *IEEE Trans. Power Del.*, **13**, (3), 762-767, July 1998.
4. F. Navarrina, I. Colominas, and M. Casteleiro, “Why do computer methods for grounding produce anomalous results?”, *IEEE Trans. Power Del.*, **18**, (4), 1192-1202, Oct. 2003.
5. D. L. Garrett and J. G. Pruitt, “Problems encountered with the average potential method of analyzing substation grounding systems”, *IEEE Trans. Power App. Syst.*, **104**, (12), 3586-3596, Dec. 1985.
6. I. Colominas, F. Navarrina, and M. Casteleiro, “A boundary element numerical approach for grounding grid computation”, *Comput. Meth. Appl. Mech. Eng.*, **174**, 73-90, 1999.
7. I. Colominas, J. Gómez-Calviño, F. Navarrina, and M. Casteleiro, “Computer analysis of earthing systems in horizontally and vertically layered soils”, *Elect. Power Syst. Res.*, **59**, 149-156, 2001.
8. I. Colominas, F. Navarrina, and M. Casteleiro, “A numerical formulation for grounding analysis in stratified soils”, *IEEE Trans. Power Del.*, **17**, (2), 587-595, Apr. 2002.
9. J. París, I. Colominas, X. Nogueira, F. Navarrina, and M. Casteleiro, “Numerical simulation of multilayer grounding grids in a user-friendly open-source CAD interface”, *Proceedings of the ICETCE-2012*, IEEE Pub., New York, 2012.
10. I. Colominas, J. París, F. Navarrina, and M. Casteleiro, “Improvement of the computer methods for grounding analysis in layered soils by using high-efficient convergence acceleration techniques”, *Adv. Engrg. Soft.*, **44**, 80-91, 2012.
11. Nichols N., Shipp D.D., “Designing to avoid hazardous transferred earth potentials”, *IEEE Trans. Ind. Appl.*, **1A-18**, 340-347, July 1982.
12. I. Colominas, F. Navarrina, and M. Casteleiro, “Analysis of transferred earth potentials in grounding systems: A BEM numerical approach”, *IEEE Trans. Power Del.*, **20**, (1), 339-345, Jan. 2005.
13. I. Colominas, F. Navarrina, and M. Casteleiro, “Numerical Simulation of Transferred Potentials in Earthing Grids Considering Layered Soil Models”, *IEEE Trans. Power Del.*, **22**, (3), 1514-1522, July 2007.
14. I. Colominas, J. París, X. Nogueira, F. Navarrina, and M. Casteleiro, “Grounding Analysis in Heterogeneous Soil Models: Application to Underground Substations”, *Proceedings of the ICETCE-2012*, IEEE Pub., New York, 2012.

Body-fitting meshes for the Discontinuous Galerkin Method

J. Cui¹, S. M. Schnepf¹, and T. Weiland^{1,2}

¹ Graduate School of Computational Engineering, Technische Universitaet Darmstadt, Dolivostrasse 15, 64293 Darmstadt, Germany, cui@gsc.tu-darmstadt.de, schnepf@gsc.tu-darmstadt.de

² Institut fuer Theorie Elektromagnetischer Felder, Technische Universitaet Darmstadt, Schlossgartenstrasse 8, 64289 Darmstadt, Germany, thomas.weiland@temf.tu-darmstadt.de

Summary. A mesh scheme is developed to deal with curved boundaries of the geometry using quadrilateral elements for the Discontinuous Galerkin Method (DGM). To achieve this, we first generate the inner part of the mesh in a structured manner and connect it to the curved boundary with a so-called buffer layer. Elements in the buffer layer employ a high order mapping to fit the boundary. We demonstrate high order convergence rates with an electromagnetic problem in a cylindrical cavity. Furthermore, we show that the frequency spectrum, which is extracted from the time-domain signal is clean, i.e., no spurious modes are observed in any of the examples considered.

1 Introduction

The DGM is a high order numerical method. In order to maintain its high order accuracy in the presence of curved objects, boundaries (surfaces) of the geometries have to be described with high order accuracy as well. The study in [1] shows that meaningful high order accurate results can be obtained only if the curved boundaries are considered with high order geometric approximations. In [2] problems in a cylindrical cavity are solved by pushing the straight edges of elements onto the exact circular boundary.

Both implementations [1, 2] employ triangular meshes for the DGM and achieve high order convergence. We propose an alternative mesh scheme based on Cartesian grids. It generates quadrilateral meshes in a simple process for both, exact geometries and objects represented by Non-Uniform Rational B-Splines (NURBS). The scheme enjoys many advantages due to the ability of applying tensor product bases within quadrilateral elements (see e.g. [3, 4]).

2 Body-fitting mesh scheme

We generate a set of buffer elements in the gap between the exact curved boundary and the interior structured mesh as demonstrated in Fig. 1. Figure 2 (left) shows that if no buffer layer is applied, degenerated elements (marked with arrows) are likely to occur, which is guaranteed not to happen with the insertion of a buffer layer [5] (right). Figure 3 gives an example, where a

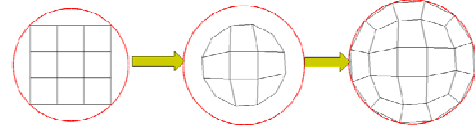


Fig. 1: Buffer layer mesh scheme based on a 3-by-3 regular mesh.

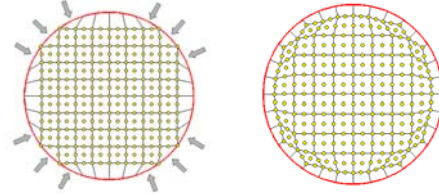


Fig. 2: Curved elements of 2nd order without (left) and with (right) buffer layer scheme based on a 9-by-9 regular mesh.

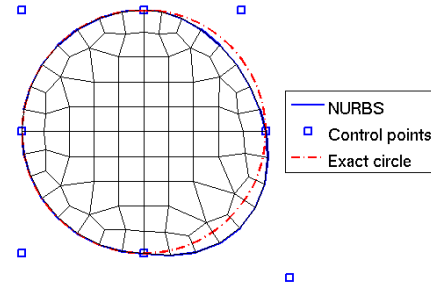


Fig. 3: Buffer layer mesh with NURBS. The approximation can be exact for both a circle (left half) and an arbitrary curve (right half) using control points.

mesh is generated fitting a geometry described by NURBS. For performing the local element deformation in the buffer layer we apply Transfinite Interpolation (TFI) [6].

3 Solving electromagnetic problems

We consider transverse magnetic (TM) problems in a two-dimensional circular domain Ω with the boundary $\partial\Omega$. The Maxwell's equations read as follows:

$$\mu \frac{\partial H_x}{\partial t} = -\frac{\partial E_z}{\partial y}, \quad \mu \frac{\partial H_y}{\partial t} = \frac{\partial E_z}{\partial x}, \quad (1)$$

$$\varepsilon \frac{\partial E_z}{\partial t} = \frac{\partial H_y}{\partial x} - \frac{\partial H_x}{\partial y}, \quad (2)$$

where H_x and H_y are the x- and y-components of the magnetic field vector, and E_z the z-component of the electric field vector. The parameters ε and μ are the electric permittivity and the magnetic permeability, respectively.

In this DGM approach, Legendre polynomials are applied as basis functions and the explicit leap-frog scheme is used for the time discretization [4]. The TM31 mode in a cylindrical cavity is chosen for a convergence study. The errors are measured in the L^2 norm at the end of one periodic oscillation.

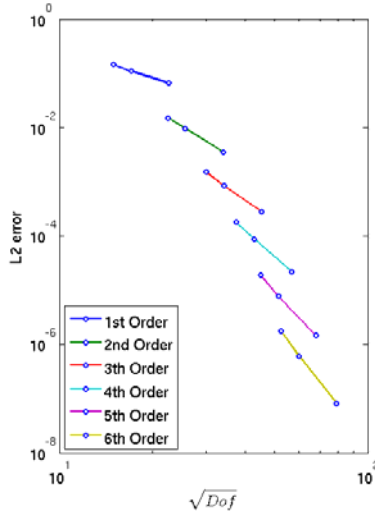


Fig. 4: For a resonant mode in the cylindrical cavity, DGM with upwind flux shows $(p+1)$ convergence using body-fitting meshes.

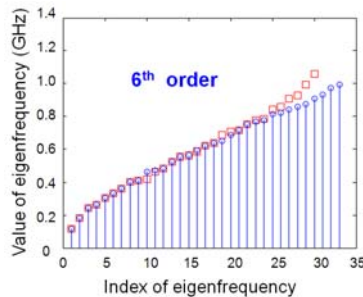


Fig. 5: Analytical values (red squares) and captured numerical eigen-modes (blue stems)

Figure 4 shows that the optimal convergence of $(p+1)$ is achieved where p is the polynomial order. We also extracted eigenfrequencies via a Fourier Transform. The results in Fig. 5 were obtained using central fluxes and 32 elements of 6th order. The eigenfrequencies obtained from the time-domain solution agree with the analytical ones for frequencies up to 0.8 GHz. Above this frequency the spatial resolution is insufficient leading to errors.

4 Conclusions

A body-fitting mesh scheme employing high order curved elements with the DG method is proposed. High order convergence rates in the presence of curved objects are observed. Furthermore, we extracted frequency spectra from simulations of a cylindrical cavity and found the agreement between the numerical results and the respective analytical solutions, i.e., clean spectra are obtained.

Acknowledgement. The work of J. Cui and S. M. Schnepf is supported by the 'Initiative for Excellence' of the German Federal and State Governments and the Graduate School of Computational Engineering at Technische Universitaet Darmstadt.

References

1. F. Bassi and S. Rebay, "High-Order Accurate Discontinuous Finite Element Solution of the 2D Euler Equations* 1", *J. Comput. Phys.* 138(2), 251–285, 1997.
2. J. S. Hesthaven and T. Warburton, *Nodal discontinuous Galerkin methods: algorithms, analysis, and applications*. Springer Verlag, 2007.
3. D. Wirasaet, S. Tanaka, E. J. Kubatko, J. J. Westerink, and C. Dawson, "A performance comparison of nodal discontinuous Galerkin methods on triangles and quadrilaterals", *Int. J. Numer. Math. Fl.* 64(10–12), 1336–1362, 2010.
4. Schnepf and Weiland, "Efficient Large Scale Electromagnetics Simulations Using Dynamically Adapted Meshes with the Discontinuous Galerkin Method", *J. Comput. Appl. Math. (Article in Press)*, 2011
5. S. J. Owen and J. F. Shepherd, "Embedding Features in a Cartesian Grid", *Proceedings of the 18th International Meshing Roundtable*, pp. 117–138, 2009.
6. W. J. Gordon and C. A. Hall, "Transfinite element methods: blending-function interpolation over arbitrary curved element domains", *Numerische Mathematik*, 21(2), 109–129, 1973.

Transmission line parameters computed by NURBS-based impedance boundary conditions: the case of different conductivities

Rafael Vázquez¹, Annalisa Buffa¹, and Luca Di Rienzo²

¹ Istituto di Matematica Applicata e Tecnologie Informatiche - CNR, via Ferrata 1 - 27100, Pavia, Italy
vazquez@imati.cnr.it, annalisa@imati.cnr.it

² Dipartimento di Elettrotecnica, Politecnico di Milano, Piazza L. da Vinci, 32 - 20133, Milano, Italy
luca.dirienzo@polimi.it

Summary. High order surface impedance boundary conditions (SIBCs) have been coupled with the Boundary Element Method (BEM) to produce an integral formulation for the computation of the impedance matrix of multiconductor transmission lines of arbitrary cross-section [1, 2]. The method extends the use of SIBCs into lower frequencies and does so efficiently in that the solution of the integral equations need only be computed once whereas the solution may be obtained over the whole applicable frequency domain. In the case of different conductivities of the parallel conductors, care must be taken in the perturbation expansion when the formulation is derived. The use of NURBS gives a better representation of complex geometries and helps in the computation of the radius of curvature and of the tangential derivatives of the unknowns. As a realistic application, the per-unit-length parameters of sector shaped cables are computed, showing the accuracy of the method.

1 Non-uniform rational B-splines

Recently, the so-called Isogeometric Analysis method was introduced in the context of mechanical engineering [3], with the aim of improving the communication between Computer Aided Design (CAD) software and numerical solvers. The method can be understood as a generalization of finite elements, where the standard polynomial shape functions are replaced by the functions used by CAD to describe the geometry.

The most widespread functions in CAD are probably non-uniform rational B-splines (NURBS), due to their flexibility and their capability to design smooth geometries. To define a NURBS curve first it is necessary to introduce a partition of a reference interval. NURBS basis functions are defined on this partition as a set of piecewise rational polynomials. The curve is then created as a linear combination of these basis functions, by associating a control point to each one of them [4].

The method we propose is based on NURBS to represent the contour of the cross section of the conductors, whereas the discrete solution is sought as a non-rational spline. The use of NURBS not only gives a good representation of complex geometries, but it also allows an exact computation of the radius of cur-

vature, as required by high order SIBCs. Moreover, a discretization based on high order B-splines is necessary to compute the tangential derivatives appearing in high order SIBCs, which can not be accurately computed with low order BEM.

2 Integral formulation of the problem

We work on a two-dimensional geometry. Assume that we have N different conductors, where electric currents of intensity I_j , $j = 1, \dots, N$ flow. We denote by Γ_j the boundary of their cross sections. We choose an eddy-current model written in terms of the magnetic vector potential \mathbf{A} . In the 2D case this vector is parallel to the conductors axis, for which $\mathbf{A} = A\mathbf{e}_z$.

Splitting the potential into “source” and “eddy” components, $A = A^s + A^e$, our continuous problem becomes

$$\Delta A^e = i\omega\mu\sigma A^e, \quad \int_{\Gamma_j} \frac{1}{\mu} \frac{\partial A^e}{\partial n} = I_j, \quad (1)$$

$$[A^e]_{\Gamma_j} = -A^s, \quad \left[\frac{\partial A^e}{\partial n} \right]_{\Gamma_j} = 0, \quad A^e = O\left(\frac{1}{|\mathbf{r}|}\right), \quad |\mathbf{r}| \rightarrow +\infty,$$

where A^s is an unknown, and is constant for each conductor.

Denoting by $G(\mathbf{r}, \mathbf{r}')$ the fundamental solution of the 2D Laplace equation, we define the integral operators associated to the single and double layer potentials

$$S_j u(\mathbf{r}) = \oint_{\Gamma_j} G(\mathbf{r}, \mathbf{r}') u(\mathbf{r}') d\gamma(\mathbf{r}'), \quad (2)$$

$$D_j u(\mathbf{r}) = \oint_{\Gamma_j} \frac{\partial G(\mathbf{r}, \mathbf{r}')}{\partial n_{\mathbf{r}'}} u(\mathbf{r}') d\gamma(\mathbf{r}'), \quad (3)$$

and denoting by $K = \frac{\partial A^e_{\text{ext}}}{\partial n}$, the solution of our problem satisfies the integral equation

$$A^s(\mathbf{r}) + \sum_{j=1}^N S_j K(\mathbf{r}) = \left(\frac{-I}{2} + \sum_{j=1}^N D_j \right) A^e_{\text{int}}(\mathbf{r}). \quad (4)$$

3 Approximation by SIBCs

SIBCs can be applied whenever the skin depth

$$\delta = \sqrt{\frac{2}{\omega\mu\sigma}}, \quad (5)$$

is “small enough”. Following [1,5], the fields are written as asymptotic expansions in terms of δ , in the form:

$$A_{\text{int}}^e(\mathbf{r}, \delta) \simeq \sum_{i=0}^3 A_{\text{int}}^{e,i}(\mathbf{r}) \delta^i, \quad (6)$$

$$A^s(\mathbf{r}, \delta) \simeq \sum_{i=0}^3 A^{s,i}(\mathbf{r}) \delta^i, \quad K(\mathbf{r}, \delta) \simeq \sum_{i=0}^3 K^i(\mathbf{r}) \delta^i, \quad (7)$$

and denoting the curvature of Γ by \mathcal{C} , and by $\frac{\partial^2 u}{\partial \tau^2}$ the second tangential partial derivative, it holds:

$$A_{\text{int}}^{e,i} = \sum_{l=1}^i \psi_l(K^{i-l}), \quad \text{with} \quad \psi_1[u] = u, \quad (8)$$

$$\psi_2[u] = \frac{\mathcal{C}}{2}u, \quad \psi_3[u] = \frac{3\mathcal{C}^2}{8}u + \frac{1}{2}\frac{\partial^2 u}{\partial \tau^2}.$$

We then solve sequentially the problem, for $i = 0, \dots, 3$

$$A^{s,i}(\mathbf{r}) + \sum_{j=1}^N S_j K^i(\mathbf{r}) = \left(\frac{-I}{2} + \sum_{j=1}^N D_j \right) \left(\sum_{l=1}^i \psi_l(K^{i-l}(\mathbf{r})) \right), \quad (9)$$

together with the intensity conditions: $\int_{\Gamma_j} \frac{1}{\mu} K^0 = I_j$,

and $\int_{\Gamma_j} \frac{1}{\mu} K^l = 0$, for $l = 1, 2, 3$.

4 The case of different conductivities

Let us assume that the electrical conductivity of each conductor is σ_j , $j = 1, \dots, N$, and define the small parameter for each conductor, δ_j , as in (5). It is also necessary to define a small parameter for the exterior domain, that we can take, for instance, $\delta_0 = \delta_N$. With this choice of small parameters, we rewrite the asymptotic expansions (7) based on δ_0 , whereas the expansion (6) is written with a different δ_j in each conductor. Since the small parameters are different for the conductors and the insulator, when considering the continuity conditions on the interface, it is not possible just to equate the terms with the same coefficients, but we must adjust the equations multiplying and dividing some terms by powers of δ_0 .

5 Three sector-shaped cable

We have applied the method to the simulation of a three sector-shaped cable with a shield, as the one shown in Fig. 1. Each sector is made of copper, with

$\sigma = 5.8 \times 10^7$ S/m, and for the shield the electrical conductivity is $\sigma = 1.1 \times 10^6$ S/m. We notice that the corners of each sector have been rounded, because the SIBC can only be applied in smooth geometries.

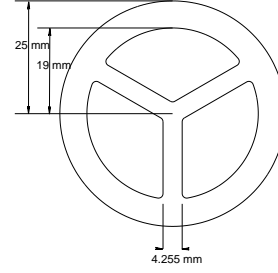


Fig. 1. Geometry of the three sector-shaped cable

The contour of each sector is parametrized with a quadratic NURBS with 9 elements, and the shield with a quadratic NURBS formed by 4 elements. Then, the problem is solved in a refined mesh formed by 45 elements on each conductor, and 20 elements on the shield. Our results are compared in Fig. 2 with the ones given by a commercial FEM software, in a mesh formed by 187607 elements

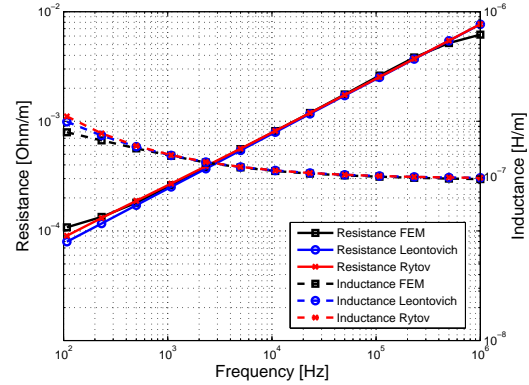


Fig. 2. P.u.l. self-resistance and self-inductance for one sector of the three sector cable

References

1. L. Di Rienzo, S. Yuferev, and N. Ida. Computation of the impedance matrix of multiconductor transmission lines using high-order surface impedance boundary conditions. *Electromagnetic Compatibility, IEEE Transactions on*, 50(4):974–984, nov. 2008.
2. S. Yuferev and L. Di Rienzo. Surface impedance boundary conditions in terms of various formalisms. *Magnetics, IEEE Transactions on*, 46(9):3617–3628, sept. 2010.
3. J. A. Cottrell, T. J. R. Hughes, and Y. Bazilevs. *Isogeometric Analysis: toward integration of CAD and FEA*. John Wiley & Sons, 2009.
4. L.A. Piegl and W. Tiller. *The Nurbs Book*. Springer-Verlag, New York, 1997.
5. H. Haddar, P. Joly, and H.-M. Nguyen. Generalized impedance boundary conditions for scattering by strongly absorbing obstacles: the scalar case. *Math. Models Methods Appl. Sci.*, 15(8):1273–1300, 2005.

Dynamical analysis and control of chaos in Vilnius chaotic oscillator circuit

Selçuk Emiroğlu¹, Yılmaz Uyaroglu¹

¹Sakarya University, Eng. Faculty, Electrical Electronics Engineering Department, 54187, Esentepe Campus, Sakarya, Turkey, selcukemiroglu@sakarya.edu.tr, uyaroglu@sakarya.edu.tr

Summary. In this paper, Vilnius chaotic oscillator circuit is realized. Electronic circuit implementation of the Vilnius chaotic oscillator was realized using Multisim®. Also, the state equations of Vilnius chaotic oscillator are obtained by circuit theory. Dynamical analysis of Vilnius chaotic circuit is investigated by using dynamic state equations. The mathematical model of oscillator is constructed using MATLAB®. In addition, control of chaos in Vilnius chaotic oscillator is determined by using time delay feedback theory. Time delay feedback controllers are designed to eliminate chaos from system trajectories and stabilize the system at its equilibrium point. Numerical simulations results confirming the analytical analysis are shown and MATLAB® simulations are also performed to confirm the efficiency of the proposed control scheme.

1 Introduction

Chaos has not a general definition in literature but there are some properties of chaotic systems. The chaotic systems are very sensitivity to initial conditions. In order that any nonlinear system is able to behave chaotic, the system must be at least three dimensional for an autonomous system or two dimensional for non-autonomous system in the continuous system [1]. In chaos, Lyapunov exponents must be determined to identify whether the system behaves chaotic or not [2]. In the 3D system, one of the lyapunov exponents of the system must be positive, the second one negative and third one zero, respectively. So, in a third order dynamical system, the sign of the Lyapunov exponent could be positive, negative and zero for chaotic behavior [3]. In oscillator circuit, in order to can show chaotic behavior, autonomous circuit designed by resistor, capacitor and inductor elements must contain:

- one or more nonlinear elements
- one or more locally active resistors
- three or more energy storage elements [4].

Many chaotic oscillator circuits are developed. Vilnius oscillator which has a simple circuit scheme is developed for educational purpose by A. Tamasevicius in 2005 [5].

2 Vilnius chaotic oscillator and its dynamical analysis

In this section, Vilnius chaotic oscillator circuit is shown in Fig. 1.

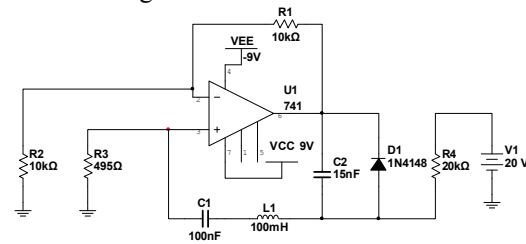


Fig. 1 Vilnius chaotic oscillator circuit

This circuit is constructed in Multisim program. By changing the R_3 resistor, dynamic analysis of circuit is analyzed using Multisim and simulation results are given in Fig. 2

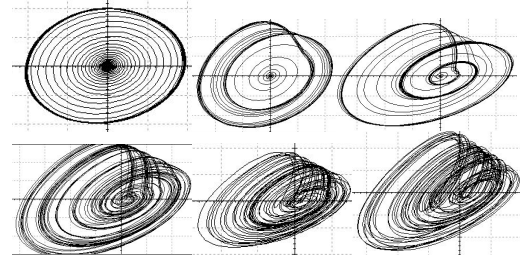


Fig. 2 Phase portraits of Vilnius circuit $R=100, 220, 350, 400, 495, 600 \text{ ohm}$

Using KCL and KVL circuit theory, state equations of Vilnius chaotic oscillator circuit are obtained as shown in Eq. 1.

$$\begin{aligned} C_1 \frac{dV_{C1}(t)}{dt} &= I_L \\ L_1 \frac{dI_{L1}(t)}{dt} &= (k-1)R_3 I_{L1} - V_{C2} - V_{C1} \\ C_2 \frac{dV_{C2}(t)}{dt} &= I_{R4} + I_{L1} - I_D \end{aligned} \quad (1)$$

By using some transformations, dimensionless state equations may be obtained in Eq. 2.

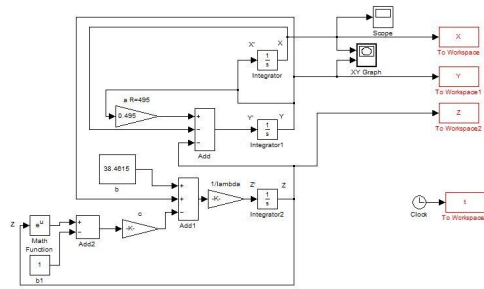


Fig. 3 Matlab-Simulink model of circuit via state equations

$$\begin{aligned}\dot{x} &= y \\ \dot{y} &= \frac{(k-1)R_3}{\rho} y - x - z \\ \dot{z} &= \frac{1}{\varepsilon} (b + y - c(e^z - 1))\end{aligned}\quad (2)$$

$$\text{where, } \rho = \sqrt{\frac{L_1}{C_1}}, \quad \varepsilon = \frac{C_2}{C_1}, \quad k = 1 + \frac{R_1}{R_2}, \quad b = \frac{\rho I_{R4}}{V_T},$$

$$c = \frac{\rho I_S}{V_T}$$

Using Simulink model, phase portraits of circuit are obtained as shown in Fig. 4.

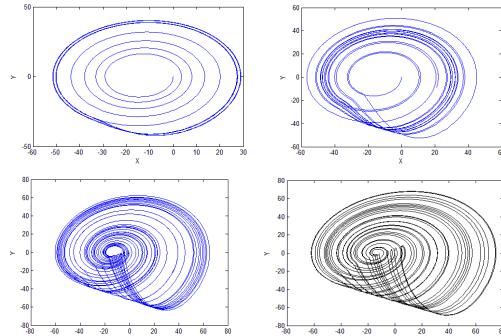


Fig. 4 Phase portraits of circuit $R=100, 220, 350, 600$ ohm using Matlab

Also, electronic circuit implementation of vilnius chaotic oscillator is realized and phase portrait of circuit are obtained by oscilloscope.

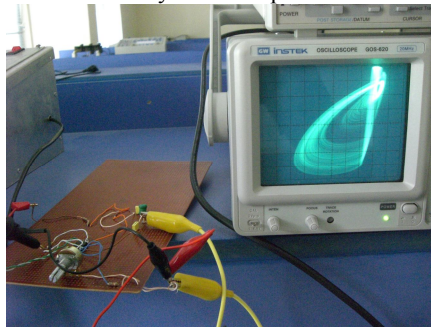


Fig.5 Electronic circuit experiment



Fig.6. Phase portrait of system $R=100$ ohm- Limit cycle

3 Time delay feedback control of chaos in Vilnius chaotic oscillator

In this section, control of chaos in Vilnius oscillator is realized by using time delay feedback control theory. The controller [6] is designed based on time delay feedback control scheme in Eq 3.

$$u = K(x(t) - x(t - \tau)) \quad (3)$$

Time delay feedback controller is applied to the Vilnius system as shown in Eq. 4

$$\begin{aligned}\dot{x} &= y + K(x(t) - x(t - \tau)) \\ \dot{y} &= \frac{(k-1)R_3}{\rho} y - x - z \\ \dot{z} &= \frac{1}{\varepsilon} (b + y - c(e^z - 1))\end{aligned}\quad (4)$$

Finally, phase portraits of controlled Vilnius circuit will be obtained.

References

1. N. Noroozi, B.Khaki, A.Seifi, *Chaotic Oscillations Damping in Power System by Finite Time Control Theory*, I.R.E.E., Vol. 3, N. 6 (2008).
2. Kinsner W. *Characterizing chaos through Lyapunov metrics*. IEEE Trans Syst Man Cybernet C;36(2):141–51(2003).
3. M. Zribi, A. Oteafy, N. Smaoui, *Controlling chaos in the permanent magnet synchronous motor*, Chaos, Solitons and Fractals 41 1266–1276 (2009).
4. Chua, Leon O.; Matsumoto, T., and Komuro, M. *The Double Scroll*. IEEE Tran. on Circ and Systems CAS-32 (8): 798–818, August 1985.
5. A. Tamasevicius et al, *A simple chaotic oscillator for educational purposes*, Eur. J. Phys. 26 (2005)61-63..
6. Pyragas, K., *Continuous Control Of Chaos By Self-Controlling Feedback*, Phys. Lett. A, Vol. 170, Pp.421 - 428 , 1992

Time Domain Models for Lossless Multiport Waveguide Structures in Impedance and Admittance Formulation based on Real Eigenmodes

Thomas Flisgen¹ and Ursula van Rienen¹

Institut for General Electrical Engineering, University of Rostock, Albert-Einstein-Str. 2, 18059 Rostock, Germany.
thomas.flisgen@uni-rostock.de, ursula.van-rienen@uni-rostock.de

Summary. The creation of equivalent models of waveguide structures is a challenging task. This contribution revisits a method to establish systems of ordinary differential equations to model the transient dependency between port voltages and currents of the structure based on real eigenmodes. These equations can be derived either in an impedance or admittance formulation. The method is illustrated by the transfer properties of a rectangular waveguide. It is shown that the frequency domain impedance parameters of this waveguide, obtained by an eigenmode expansion, converge to the parameters which are commonly known from literature.

1 Introduction

The computation of transfer functions of lossless radio frequency (RF) multiport structures is a common issue related to scientific computing in electrical engineering. A large variety of methods is discussed in the literature to determine these transfer functions in frequency domain. However, frequency domain approaches fail, if field filling and defilling processes in RF structures [2, 4] or the response of these structures due to transient port stimuli are of interest. In this contribution a modal expansion is employed to transfer the electrodynamic wave equation with excitation to a coupled first order ordinary differential equation (ODE). This differential equation approximates the dependency of port quantities like voltages and currents in an explicit time domain formulation and is therefore referred to as lumped equivalent model of the structure. In this context it is remarkable that eigenmodes of the closed structure are suitable to expand the fields in a device with waveguide ports.

However, in contrast to previous publications on eigenmode expansions for multiport systems (see e.g. [1, 3, 5, 6]) this contribution performs the expansion using continuous fields and focusses on the creation of structure's equivalent ODE systems. In addition to theoretical derivations, the procedure is exemplified by means of a rectangular waveguide to obtain a time domain equivalent ODE model for this waveguide in an impedance formulation. It is shown that the frequency domain transfer function of the equivalent model converges to the well-known impedance parameters of the waveguide, if an infinite number of real eigenmodes is considered in the expansion.

2 Mathematical Modeling

For the derivation of waveguide structure's equivalent models Faraday's law of induction

$$\nabla \times \mathbf{E}(\mathbf{r}, t) = -\mu \frac{\partial}{\partial t} \mathbf{H}(\mathbf{r}, t) - \mathbf{J}_m(\mathbf{r}, t) \quad (1)$$

and Ampere's law

$$\nabla \times \mathbf{H}(\mathbf{r}, t) = \varepsilon \frac{\partial}{\partial t} \mathbf{E}(\mathbf{r}, t) + \mathbf{J}_e(\mathbf{r}, t) \quad (2)$$

are taken as a starting point. There, $\mathbf{E}(\mathbf{r}, t)$ denotes the electric field strength, $\mathbf{H}(\mathbf{r}, t)$ the magnetic field strength, ε a constant permittivity, μ a constant permeability, $\mathbf{J}_m(\mathbf{r}, t)$ the magnetic and $\mathbf{J}_e(\mathbf{r}, t)$ the electric current density.

2.1 Impedance Formulation

The impedance formulation describes the transient port voltages as a function of electric port currents. Therefore, the magnetic currents are set to zero in (1). Taking the curl of the resulting equation, using the electric fields to be free of any sources and replacing the curl of the magnetic fields by the r.h.s. of (2) leads to the wave equation with electric current excitation:

$$\Delta \mathbf{E}(\mathbf{r}, t) - \varepsilon \mu \frac{\partial^2}{\partial t^2} \mathbf{E}(\mathbf{r}, t) = \mu \frac{\partial}{\partial t} \mathbf{J}_e(\mathbf{r}, t). \quad (3)$$

The electric fields are expanded in terms of real eigenmodes $\tilde{\mathbf{E}}_v(\mathbf{r})$ and a transient weighting factor $x_v(t)$:

$$\mathbf{E}(\mathbf{r}, t) = \sum_{v=1}^N \tilde{\mathbf{E}}_v(\mathbf{r}) x_v(t). \quad (4)$$

Note, that the eigenmodes $\tilde{\mathbf{E}}_v(\mathbf{r})$ satisfy

$$\Delta \tilde{\mathbf{E}}_v(\mathbf{r}) + \varepsilon \mu \tilde{\omega}_v^2 \tilde{\mathbf{E}}_v(\mathbf{r}) = \mathbf{0} \text{ on } \Omega, \quad (5)$$

$$\mathbf{n} \times \tilde{\mathbf{E}}_v(\mathbf{r}) = \mathbf{0} \text{ on } \partial\Omega_{\text{wall}}, \quad (6)$$

$$\mathbf{n} \cdot \tilde{\mathbf{E}}_v(\mathbf{r}) = \mathbf{0} \text{ on } \partial\Omega_{\text{ports}}, \quad (7)$$

with the resonant angular frequency $\tilde{\omega}_v$ of the v -th mode. Condition (6) corresponds to perfect electric material on the boundary of the waveguide, whereas

(7) corresponds to perfect magnetic conducting material on the cross section of the waveguide ports. Replacing the transient electric fields in (3) by (4), exploiting the orthogonality of the eigenmodes

$$\iiint_{\Omega} \tilde{\mathbf{E}}_v(\mathbf{r}) \cdot \tilde{\mathbf{E}}_n(\mathbf{r}) d\mathbf{r} = \begin{cases} 2W_v/\epsilon, & \text{if } v = n, \\ 0, & \text{if } v \neq n, \end{cases} \quad (8)$$

and utilizing the fact that the excitation current density can be expressed as a superposition of impressed excitation current densities $\tilde{\mathbf{J}}_{port,m}(\mathbf{r}) i_m(t)$ on the cross sections of all M waveguide ports

$$\mathbf{J}_e(\mathbf{r}, t) = \sum_{m=1}^M \tilde{\mathbf{J}}_{port,m}(\mathbf{r}) i_m(t) \quad (9)$$

leads to the ordinary differential equation

$$2W_v \left(\tilde{\omega}_v^2 x_v(t) + \frac{\partial^2 x_v(t)}{\partial t^2} \right) = \frac{\partial}{\partial t} \sum_{m=1}^M f_{v,m} i_m(t). \quad (10)$$

Here W_v is defined as the energy stored in the v -th mode, $i_m(t)$ the modal current of the m -th port and

$$f_{v,m} = \iiint_{\Omega} \tilde{\mathbf{E}}_v(\mathbf{r}) \cdot \tilde{\mathbf{J}}_{port,m}(\mathbf{r}) d\mathbf{r}. \quad (11)$$

Equation (10) can be expressed for all N considered eigenmodes and all M ports as the state equation

$$\begin{aligned} \underbrace{\frac{\partial}{\partial t} \begin{pmatrix} \hat{x}_1(t) \\ x_1(t) \\ \vdots \\ \hat{x}_N(t) \\ x_N(t) \end{pmatrix}}_{\mathbf{x}(t)} &= \underbrace{\begin{pmatrix} 0 & 1 & \dots & 0 & 0 \\ -\tilde{\omega}_1^2 & 0 & \dots & 0 & 0 \\ \vdots & \vdots & \ddots & \vdots & \vdots \\ 0 & 0 & \dots & 0 & 1 \\ 0 & 0 & \dots & -\tilde{\omega}_N^2 & 0 \end{pmatrix}}_{\mathbf{A}_z} \underbrace{\begin{pmatrix} \hat{x}_1(t) \\ x_1(t) \\ \vdots \\ \hat{x}_N(t) \\ x_N(t) \end{pmatrix}}_{\mathbf{x}(t)} \\ &+ \underbrace{\frac{1}{2} \begin{pmatrix} 0 & 0 & \dots & 0 \\ \frac{f_{1,1}}{W_1} & \frac{f_{1,2}}{W_1} & \dots & \frac{f_{1,M}}{W_1} \\ \vdots & \vdots & \ddots & \vdots \\ 0 & 0 & \dots & 0 \\ \frac{f_{N,1}}{W_N} & \frac{f_{N,2}}{W_N} & \dots & \frac{f_{N,M}}{W_N} \end{pmatrix}}_{\mathbf{B}_z} \underbrace{\begin{pmatrix} i_1(t) \\ i_2(t) \\ \vdots \\ i_M(t) \end{pmatrix}}_{\mathbf{i}(t)}. \end{aligned} \quad (12)$$

The dependency of the voltages at the ports and the inner states is described via the output equation

$$\underbrace{\begin{pmatrix} v_1(t) \\ v_2(t) \\ \vdots \\ v_M(t) \end{pmatrix}}_{\mathbf{v}(t)} = \underbrace{\begin{pmatrix} 0 & f_{1,1} & \dots & 0 & f_{N,1} \\ 0 & f_{1,2} & \dots & 0 & f_{N,2} \\ \vdots & \vdots & \ddots & \vdots & \vdots \\ 0 & f_{1,M} & \dots & 0 & f_{N,M} \end{pmatrix}}_{\mathbf{C}_z} \underbrace{\begin{pmatrix} \hat{x}_1(t) \\ x_1(t) \\ \vdots \\ \hat{x}_N(t) \\ x_N(t) \end{pmatrix}}_{\mathbf{x}(t)}. \quad (13)$$

Note that the state space system (12) and (13) with the matrices $\{\mathbf{A}_z, \mathbf{B}_z, \mathbf{C}_z\}$ is an equivalent ODE model of the multiport waveguide structure in an impedance formulation, since it describes the transient port voltages as a function of transient port currents.

2.2 Admittance Formulation

The derivation of the state space systems in an admittance formulation is similar to the procedure proposed in section 2.1. However, for the admittance formulation magnetic currents are used to excite the structure, the expansion is performed using magnetic fields and perfect electric conducting boundary conditions are chosen on the port cross sections for the eigenmodes.

3 Application Example and Convergence

A homogeneously filled rectangular waveguide with constant cross section carrying a TE₁₀ mode is chosen as an example. This structure is well suited for validation and demonstration purposes as the eigenvalue problem (5) - (7) can be solved analytically for this geometry. As a central result of this contribution it is shown, that the frequency domain transfer function of the state space system (12) and (13) converges to the analytically known impedance matrix $\mathbf{Z}(i\omega)$ of the waveguide, if an infinite number of eigenmodes is considered in the modal expansion:

$$\lim_{N \rightarrow \infty} \mathbf{C}_z \left(i\omega \mathbf{I} - \mathbf{A}_z \right)^{-1} \mathbf{B}_z = \mathbf{Z}(i\omega). \quad (14)$$

Here $\mathbf{I} \in \mathbb{R}^{N \times N}$ denotes the identity matrix.

4 Summary and Conclusions

This work illustrates the derivation of ODE models in an impedance and admittance formulation for lossless RF structures based on real eigenmodes. The method is exemplified by employing a simple waveguide. Furthermore, the convergence of the method is discussed for this test example.

References

1. J.R. Brauer and G.C. Brauer. Microwave filter analysis using a new 3-D finite-element modal frequency method. *IEEE Trans. Microw. Theory Tech.*, 45(5):810 – 818, May 1997.
2. M. Dohlus, H.-W. Glock, D. Hecht, and U. van Rienen. Filling and beam loading in TESLA superstructures. TESLA-REPORT 98-14, 1998.
3. M. Dohlus, R. Schuhmann, and T. Weiland. Calculation of frequency domain parameters using 3D eigen-solutions. *International Journal of Numerical Modelling*, 12:41 – 48, Januar 1999.
4. H.-W. Glock, M. Kurz, P. Hülsmann, and H. Klein. Rise time of the amplitudes of time harmonic fields in multicell cavities. In *Proc. of the Particle Accelerator Conference 1993*, volume 1, pages 623 – 625, May 1993.
5. J. C. Slater. Microwave electronics. *Rev. Mod. Phys.*, 18:441–512, Oct 1946.
6. T. Wittig, R. Schuhmann, and T. Weiland. Model order reduction for large systems in computational electromagnetics. *LinAlgApp*, 415(2 - 3):499 – 530, 2006.

Field of values analysis of Laplace preconditioners for the Helmholtz equation.

Antti Hannukainen¹

Aalto University, Department of Mathematics and Systems Analysis, P.O. Box 11100, FI-00076 Aalto, Finland
antti.hannukainen@aalto.fi

Summary. In this talk, we analyze the convergence of the preconditioned GMRES method for the first order finite element discretizations of the Helmholtz equation in media with losses. We consider a Laplace preconditioner and an inexact Laplace preconditioner. Our analysis is based on bounding the field of values of the preconditioned matrix in the complex plane. The obtained results are illustrated by numerical examples.

1 Introduction

Finite element discretizations of wave propagation problems lead to very large, indefinite, non-hermitian, and complex valued linear systems. One strategy to solve these systems is to use a suitable Krylov subspace solver such as GMRES, CGN, BiCGStab (see [6]) together with a preconditioner.

Finding good preconditioners for wave propagation problems has proven to be very difficult. The number of iterations required to solve the linear system depends strongly on the mesh density h and on the wave-number κ . For Helmholtz equation, the dependency between mesh density and the required number of iterations is due to the Laplace-operator part. Several preconditioners are capable of eliminating this dependency, see e.g. [3, 4]. The κ -dependency is related to the indefiniteness of the problem. Eliminating it has proven to be considerably more difficult.

Preconditioners for the Helmholtz equation can be divided roughly into shifted-Laplace (see e.g [3, 4]) and two-level methods (see e.g. [1, 5]). The shifted-Laplace preconditioners are successful in cutting the growth in the condition number due to the Laplace operator part. However, a κ -dependency in the required number of iterations still remains in the preconditioned system. The two-level preconditioners can eliminate this dependency, but are very expensive to evaluate.

In this talk, we consider the problem

$$\begin{aligned} -\Delta u - (\kappa^2 - i\sigma)u &= f & \text{in } \Omega \\ u &= 0 & \text{on } \partial\Omega \end{aligned} \quad (1)$$

where $\kappa, \sigma \in \mathbb{R}$, $\kappa > 0, \sigma > 0$. The domain $\Omega \subset \mathbb{R}^d$, $d = 2, 3$ and the load function $f \in L^2(\Omega)$. We assume that this problem is discretized using first order finite elements on triangular or tetrahedral quasi-

regular mesh. The mesh density parameter is denoted as h .

We present a field of values (FOV) based analysis for the convergence of the preconditioned GMRES method. We consider the Laplace and the inexact Laplace preconditioner, in which the Laplace problem is solved approximately by using a suitable iterative method.

A FOV analysis has been given in [8] for Hermitian positive definite split preconditioners and for shifted-Laplace preconditioner in [7]. The main difference compared to this work is that we estimate the FOV by using methods similar to the ones applied in the analysis of additive Schwarz preconditioners for elliptic problems. The novelty of our approach is that it allows us to analyze the inexact Laplace preconditioners in detail and it can also be applied to analyze two-level preconditioners.

The presented approach also takes the non-normal nature of the linear system automatically into account. This is especially important for inexact Laplace preconditioners, as their non-normality is not solely related to the mass matrix. We can analyze these preconditioners via a perturbation argument.

2 Field of values

The convergence of the GMRES method (see [6]) for the linear system $A\mathbf{x} = \mathbf{b}$ is related to the minimization problem

$$|\mathbf{r}_i| = \min_{\substack{p \in P_i \\ p(0)=1}} |p(A)\mathbf{r}_0|, \quad (2)$$

in which \mathbf{r}_i is the residual on step i and P_i the space of polynomials of order i . Based on this minimization problem, different convergence estimates can be derived, see e.g. [2]. When the matrix A is non-normal, the convergence can be related to the properties of the pseudospectrum or the field of values (FOV).

The FOV is defined as the set

$$\mathcal{F}(A) = \left\{ \frac{\mathbf{x}^* A \mathbf{x}}{\mathbf{x}^* \mathbf{x}} \mid \mathbf{x} \in \mathbb{C}^n, \mathbf{x} \neq 0 \right\}. \quad (3)$$

The convergence of GMRES is related to the dimensions and the location of the FOV in the complex plane. A simple estimate is given as

$$|\mathbf{r}_i| \leq \left(\frac{s}{|c|} \right)^i |\mathbf{r}_0|. \quad (4)$$

In which s and c are related to the disk

$$D = \{ z \in \mathbb{C} \mid |z - c| \leq s \}$$

containing the FOV, but not the origin.

3 Laplace preconditioner

The Laplace preconditioner $P: V_h \rightarrow V_h$ is defined as: For each $u \in V_h$ find $Pu \in V_h$ such that

$$(\nabla Pu, \nabla v) = (u, v) \quad \forall v \in V_h. \quad (5)$$

The matrix form of the operator P is $K^{-1}M$, where K is the stiffness matrix and M the mass matrix. The right preconditioned linear system is

$$AK^{-1}M\tilde{\mathbf{x}} = \mathbf{b}. \quad (6)$$

The FOV for this system is characterized by two following Theorems.

Theorem 1. *There exists a constant $C > 0$, independent of h , σ , and κ , such that*

$$\mathcal{F}(AK^{-1}M) \subset [C(1 - \kappa^2)h^d, Ch^d] \times [0, C\sigma h^d],$$

in which d is the spatial dimension.

Theorem 2. *There exists a constant $C > 0$, independent of h , σ and κ , such that $\mathcal{F}(AK^{-1}M) \subset S$,*

$$S = \left\{ z \in \mathbb{C} \mid ch^d - \frac{\kappa^2}{\sigma} \Im z \leq \Re z \leq Ch^d - \frac{\kappa^2}{\sigma} \Im z \right\},$$

in which d is the spatial dimension.

4 Inexact Laplace preconditioned

In practical computations, the solution to the Laplace problem $K\mathbf{x} = \mathbf{b}$ would be replaced with some approximation $\mathbf{x} \approx K_N^{-1}\mathbf{b}$.

We assume that such an approximation is obtained with a symmetric iterative method convergent in the $\|\cdot\|_{L^2(\Omega)}$ and $\|\cdot\|_{H^1(\Omega)}$ norms. This is, there exists constants $\gamma_i, 0 < \gamma_i < 1, i = 1, 2$ and $C > 0$, independent on γ_0 and γ_1 , such that for any $u \in V_h$ there holds

$$\|E_N u\|_{H^1(\Omega)} \leq C\gamma_1^N \|u\|_{H^1(\Omega)}$$

and

$$\|E_N u\|_{L^2(\Omega)} \leq C\gamma_0^N \|u\|_{L^2(\Omega)}$$

In which, E_N is the error propagation operator relating e_0 to e_N , i.e., error on step 0 to error on step N . A suitable approximation can be obtained for example with the multigrid method.

The FOV for the preconditioned system satisfies

$$\mathcal{F}(AK_N^{-1}M) \subseteq \mathcal{F}(AK^{-1}M) \oplus \mathcal{F}(A(K_N^{-1} - K^{-1})M).$$

Bound for the FOV is obtained by combining an estimate for the size of the perturbation set

$$\mathcal{F}(A(K_N^{-1} - K^{-1})M). \quad (7)$$

with an estimate for the FOV for the Laplace preconditioned system.

Theorem 1. *There exists a constant $C > 0$, independent of γ_0 , γ_1 , κ , h , and σ , such that*

$$\Re \mathcal{F}(A(K_N^{-1} - K^{-1})M) \subset U_R$$

and

$$\Im \mathcal{F}(A(K_N^{-1} - K^{-1})M) \subset U_I$$

in which

$$U_R = \left[-Ch^d(\gamma_0^N + \kappa^2 \gamma_1^N), Ch^d(\gamma_0^N + \kappa^2 \gamma_1^N) \right]$$

and

$$U_I = \left[-Ch^d(\gamma_0^N + \sigma \gamma_1^N), Ch^d(\gamma_0^N + \sigma \gamma_1^N) \right].$$

where d is the spatial dimension and N the number of iterations used to compute the preconditioned.

From theoretical point of view, the implication of this theorem is that the number of iterations should be increased when the parameter κ grows to keep the size of the perturbation set small and the origin outside the FOV.

Acknowledgement. The author was supported by the grant 133174 from the Academy of Finland

References

1. X-C. Cai and O. Widlund. Multiplicative schwarz algorithms for some nonsymmetric and indefinite problems. *SIAM J. Numer. Anal.*, 30(4):936–952, 1993.
2. M. Embree. How descriptive are GMRES convergence bounds? Technical report, Oxford University Computing Laboratory, 1999.
3. Y. A. Erlangga. Advances in iterative methods and preconditioners for the Helmholtz equation. *Arch. Comput. Methods Eng.*, 15(1):37–66, 2008.
4. Y. A. Erlangga, C. Vuik, and C. W. Oosterlee. On a class of preconditioners for solving the Helmholtz equation. *Appl. Numer. Math.*, 50(3-4):409–425, 2004.
5. Z. Leyk, J. E. Pasciak, and J. Bramble. Iterative schemes for non-symmetric and indefinite elliptic boundary value problems. *Math. Comp.*, 60:1–22, 1993.
6. Y. Saad. *Iterative Methods for Sparse Linear Systems*. SIAM, 2003.
7. M. B. van Gijzen, Y. A. Erlangga, and C. Vuik. Spectral analysis of the discrete Helmholtz operator preconditioned with a shifted Laplacian. *SIAM J. Sci. Comput.*, 29(5):1942–1958, 2007.
8. M.B. van Gijzen and Y. A. Erlangga. Convergence bounds for preconditioned GMRES using element-by-element estimates of the field of values. In *Proceedings of the ECCOMAS-CFD 2006 conference*, 2006.

Optimization of Planar Structures by Means of Shifted Winding

Claudia Hebedean¹, Calin Munteanu¹, Adina Racasan¹

¹Technical University of Cluj-Napoca, Claudia.Hebedean@ethm.utcluj.ro, Calin.Munteanu@ethm.utcluj.ro, Adina.Racasan@ethm.utcluj.ro

Summary. Planar structures are often used recently due to their many advantages. Transformers, power inductors and EMI filters are only a few components that are constructed using this technique. In order to increase their efficiency, parasitic capacitance (EPC) must be decreases and HF losses must be appropriate to their utilisation. In previous studies it was discovered that a shifted winding of the planar structures decreases EPC. This paper represents a study which aims at finding an optimum shifting of the windings, wich will decrease EPC and increase HF losses.

1 Introduction in planar structures

Planar technology has many advantages such as improving high frequency (HF) characteristics, reducing size, lowering profile, achieving structural and functional integration, lowering manufacturing time and cost [1].

A planar integrated structure is composed of alternating layers of conductors, dielectrics, insulation and ferrite materials [2].

The difference between conventional and planar magnetic components is in terms of orientation of winding layers. Windings in a planar magnetic component have flat, wide and rectangular cross sections, and the core of a planar structure has a lower profile than that of a conventional structure. A comparison between planar and conventional structures is shown in Fig. 1.

Planar structures also have disadvantaged like large footprint area, increased parasitic capacitance and low window utilization factor. Depending on the analyzed structure and its mode of operation, different parameters must be optimized.

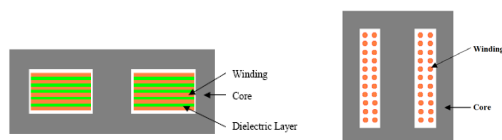


Fig. 1. Comparison between planar and conventional structure

EMI filters can also be constructed as planar structures. In order to optimize their behavior, equivalent parasitic capacitance (EPC) and equivalent series inductance (ESL) must be reduced and because the role of EMI filters is to attenuate unwanted noise, a higher loss factor at high frequency is needed.

Because the aim of this study is to improve planar structures with the same parameters and role as EMI filters, the EPC needs to be decreased and the HF losses of the planar structure increased.

2 Presentation and validation of the technique used to increase HF losses

In previous studies, the shifting of the winding was demonstrated to be the best method to decrease EPC [4], but it was not considered to be a factor that influences the HF losses. The authors considered this as an alternative to the nickel plating of the copper conductors, which is also a method to increase HF losses, and researched the way that shifted windings affect the loss values.

The original structure from Fig. 2 was the

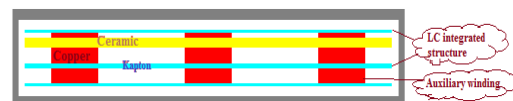


Fig. 2. Model to be studied [3].

object of this study. In previous researches, the conductors of winding3 were placed so as to decrease EPC. A study of the loss variations depending on the shifted windings was conducted. Winding3 was shifted to eight different positions and the losses were calculated with the help of a 2D numerical modeling program of the electromagnetic field.

The notation SO from Fig. 3 represents the original structure and the other notations are referring to structures with different shifting of winding3, for example bd1.1 represents a

structure with winding3 shifted to the right with 1.1mm from its original position.

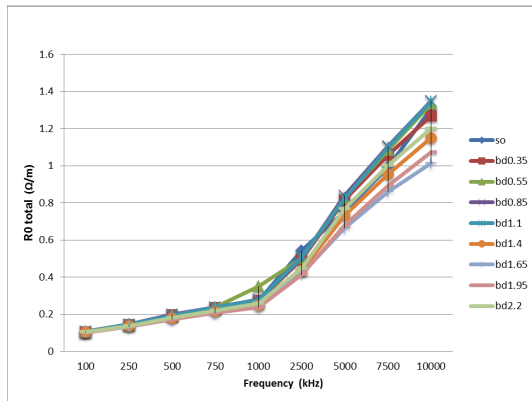


Fig.3. Structure losses depending on winding3 shifting for the original structure

The conclusions of this study are that the shifted winding affects the high frequency losses. From further investigations, the results show that for the structures with pure copper conductors, the optimum or maximum value of the losses is present for the structure with winding3 shifted with 1.1 mm as shown in Fig. 4.

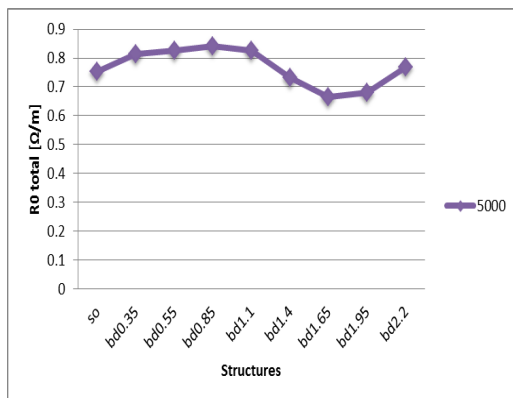


Fig. 4. Variation of losses with the shifting of winding3 for the original structure

3 Study of the optimal positioning of the conductors

In this chapter, the optimum structure from the HF losses point of view is presented. As for the EMI filters, the value for the losses must be increased at HF. The results were obtained using an software program previously tested.

The problem of determining the optimal location of the conductors is considered to be a

magnetostatic problem, so for the numerical analysis module of the field the boundary element method (BEM) was chosen. BEM is a semi-analytical method, which leads to accurate results using a small number of mesh elements and is fast in terms of computing time.

Because the number of “mobile” elements is relatively small, the algorithm of optimal design is based on conjugate gradient method (CG) with an optimum step in the search direction.

The paper presents the optimum structure starting from simple structures with one or two mobile conductors, reaching more complex ones. The results are compared with the optimal results for the EPC reduction.

Finally, is attempted to be obtained an optimum result considering the losses and also the parasitic capacitance.

Acknowledgement This paper was supported by the project "Doctoral studies in engineering sciences for developing the knowledge based society-SIDOC" contract no. POSDRU/88/1.5/S/60078, project co-funded from European Social Fund through Sectorial Operational Program Human Resources 2007-2013

References

1. R.Chen, J.D.van Wyk, Shuo Wang, W.G. Odendaal, “Technologies and characteristics of integrated EMI Filters for switching mode power supplies”, *35th Annual IEEE Power Electronics Specialists Conference*,Aachen Germany,2004, pp 4873-4880
2. Adina Racasan, C. Munteanu, V. Topa, Claudia Racasan, Oana Antonescu, “Technologies to improve high frequency characteristics of integrated EMI filters”, *6th International Conference on Electromechanical and Power Systems*, Chisinau, Rep.Moldova,October 2007
3. R. Chen, J. D. van Wyk, S. Wang, W.G. Odendaal, “Improving the characteristics of integrated EMI Filters by embedded conductive layer”, *IEEE Transactions on Power Electronics*, vol.20,no3,May 2005, pp 611-619
4. Adina Racasan, C. Munteanu, V. Topa, Claudia Pacurar, Claudia Hebedean, Sorin Lup,”Advances on parasitic capacitance reduction of EMI filters”,*10th International Conference on Applied and Theoretical Electricity-ICATE2010*, Craiova, October 8-9, 2010, pp.220-223
5. S. Wang, Fred C., J. D. van Wyk, “Design of Inductor Winding Capacitance Cancellation for EMI Suppresion”, *IEEE Transaction on Power Electronics*, vol.21,no. 6, November 2006

Validation of the Potential Method; comparing measurements of a dihedral with calculations

Magnus Herberthson^{1,2}

¹ Sensor and EW Systems, FOI, Swedish Defence Research Agency, magnus.herberthson@foi.se,

² Department of Mathematics, Linköping University, magnus.herberthson@liu.se

Summary. Earlier reported is the potential method, which addresses the EFIE (Electric Field Integral Equation) or MFIE/CFIE by applying the Hodge decomposition theorem to a one-form related to the physical current \mathbf{J} . In this approach, one solves for two unknown scalar potentials, Φ and Ψ , which carries the same information as \mathbf{J} . Here we compare calculations on a 100° dihedral with measurements. The calculations are made on meshes with different triangle sizes, which give a simple convergence study. The computational burden is also compared with other methods.

1 Introduction

We look at the electromagnetic scattering problem in frequency domain. More precisely, we first address the Electric Field Integral Equation, EFIE, [1]. In the standard formulation using the method of moments (MoM), objects which are large compared to the wavelength will produce linear systems which easily becomes too large to solve with direct solvers. This problem can be tackled in various way, and one option is to use the potential method, [2].

This method has been reported earlier, [3], [4], demonstrating proof of concept under various circumstances. In this work, we will make more quantitative evaluations, comparing measurements on a 100° dihedral (see Fig. 1) with calculations using the potential method. We will make a simple convergence study, i.e., compare calculations using different meshes, and also compare the number of unknowns with other approaches.

2 Formulation

In standard notation, with a plane wave illuminating a PEC surface S and in an adapted ON-basis, the EFIE (electric field integral equation) reads

$$\forall \mathbf{r} \in S : -E_0 e^{-ikz} \hat{\mathbf{x}} \hat{=} ikc\mu_0 \left(\mathbf{I} + \frac{1}{k^2} \nabla \nabla \cdot \right) \int_S g(\mathbf{r}, \mathbf{r}') \mathbf{J}(\mathbf{r}') dS'. \quad (1)$$

Here \mathbf{J} is the unknown current, g is the standard Green's function and $\hat{=}$ means tangential equality. By the replacement

$$h(\mathbf{r}, \mathbf{r}') = g(\mathbf{r}, \mathbf{r}') e^{ik(z-z')}, \quad \mathbf{K}(\mathbf{r}') = e^{ikz'} \mathbf{J}(\mathbf{r}') \quad (2)$$

and by the application of Hodge decomposition to \mathbf{K} (under the assumption that S is homeomorphic to a sphere), so that, in vector calculus notation,

$$\mathbf{K} = \nabla_S \Phi + \hat{\mathbf{n}} \times \nabla_S \Psi,$$

we can express the EFIE in terms of the complex scalar functions Φ and Ψ , which serve as potentials for \mathbf{K} . $\hat{\mathbf{n}}$ is normal to S . ∇_S is the intrinsic (to S) gradient operator.

The resulting equation is obtained by multiplying (1) with e^{ikz} , and then use (2) to express everything in terms of Φ and Ψ . The resulting equation is not given here, see for instance [3]. Rather, we focus on possible advantages and results. Two major advantages are the facts that 1) After multiplication with e^{ikz} , the left hand side of (1) becomes an exact one-form (and this is true whether on regards $-E_0 \hat{\mathbf{x}}$ as a one-form in \mathbf{R}^3 or as a one-form on S), and 2) The replacement $\mathbf{K}(\mathbf{r}') = e^{ikz'} \mathbf{J}(\mathbf{r}')$ allows for potentially sparser sampling, and hence reduced numerics. (C.f. [5].)

3 Numerical results

We have performed calculations on a 100° dihedral with dimensions as in Fig. 1. The calculations have

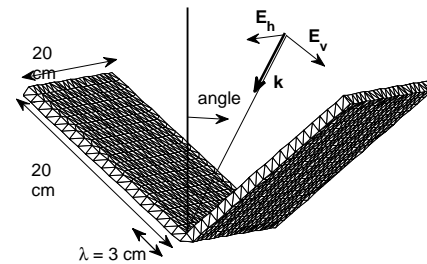


Fig. 1. The dihedral with its dimensions. The opening angle of the dihedral is 100° , and the dihedral is illuminated with a plane wave with $f=10$ GHz from above at different angles. The convention for horizontal and vertical polarization is indicated in the figure.

been performed with different meshes, resulting in a simple convergence study. The calculations are also compared with measurements and finally the number of unknown are compared to the number of unknown suggested by a commercial software. In Fig. 2, calcu-

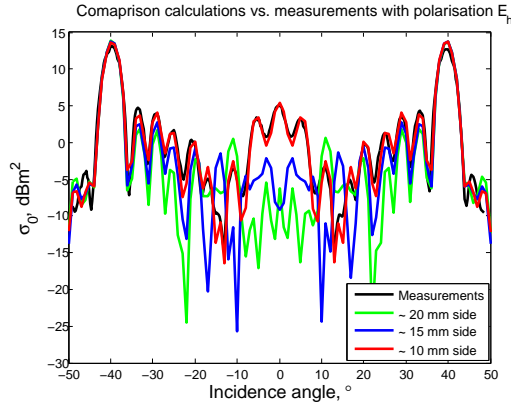


Fig. 2. Measurements vs. calculations for different mesh sizes, horizontal polarization (see Fig. 1). Numbers in the legend indicate typical side length in the mesh.

lations are compared with measurement for horizontal polarization (see Fig. 1). A reasonable agreement with measurements and calculations are obtained with a mesh size with a typical side length of 10 mm. Compared with the wavelength λ , this is only \sim three triangles/wavelength which is well below the rule of thumb which is typically eight or ten triangles/wavelength. With our mesh, we have 3406 triangles and a total number of unknown which is 3410. Using the commercial software FEKO, (in standard MoM setting), it is for the given geometry and frequency suggested a mesh which gives 127000 unknowns. Al-

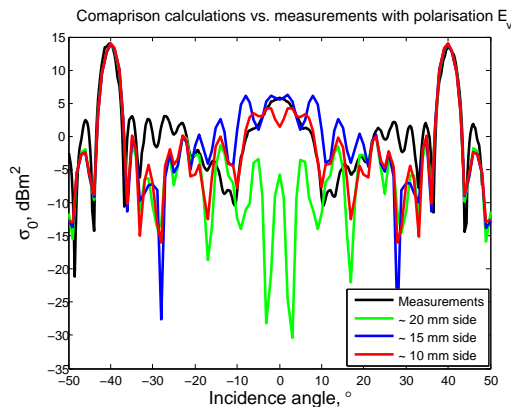


Fig. 3. Measurements vs. calculations for different mesh sizes, vertical polarization (see Fig. 1). Numbers in the legend indicate typical side length in the mesh.

though we do not claim our results to be as accurate as with FEKO, the reduction of unknowns is substantial. On the other hand, using the same meshes for calculations of the scattering from vertical polarization, the results are less satisfactory, see Fig. 3. By refining the mesh, clear improvements are noticed for the mesh with a side length of \sim 5 mm, especially around incidence angle around 0° , although the agreement is worse around incidence angles around 25° . It might

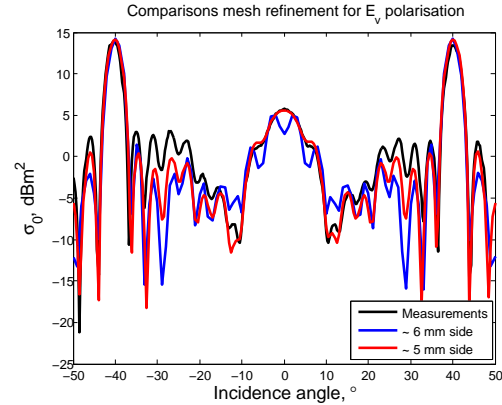


Fig. 4. Measurements vs. calculations for mesh refinements, vertical polarization (see Fig. 1). Numbers in the legend indicate typical side length in the mesh.

be claimed that this mesh size is close to the rule of thumb, but the mesh is only refined at the illuminated part, with parts in the shadow having a coarser mesh. As a result, the number of unknown N is 16872, which is still a good factor less than 127000. As the cost for solving the resulting linear equation scales as N^3 , there is a noticeable difference.

4 Conclusions

We have applied the potential method for calculations on a dihedral with opening angle of 100° . It is indicated that the non-convexity of the dihedral requires different mesh sizes in different polarizations. However, in both cases, reasonable results are produced when the number of unknowns are well below the number of unknown given by meshes following the rule of thumb, saying that the side lengths should be $\sim \lambda/10$. This decreases the memory requirements as well as the time for solving the produced linear system, as compared to standard MoM.

References

1. C.A. Balanis *Advanced engineering electromagnetics*. Wiley, 1989.
2. M. Herberthson The potential method for calculations of scattering from metallic bodies *Submitted for publication*.
3. M. Herberthson EM Scattering Calculations Using Potentials In J. Roos, L.R.J. Costa, editors, *Scientific Computing in Electrical Engineering SCEE 2008*. Springer, Berlin Heidelberg 2010.
4. M. Herberthson Application of the potential method to the magnetic field integral equation *Applied Computational Electromagnetics Society*, Tammerfors, Finland, 2010, pp. 120-123.
5. O. Bruno, C. Geuzaine. *A high-order, high-frequency method for surface scattering by convex obstacles* In *14th Conference on the Computation of Electromagnetic Fields*. pp. 132-133, 2003

Broad Band Surface Impedance Boundary Conditions for Higher Order Time Domain Discontinuous Galerkin Method

Irene Hiltunen^{1,2}, Erion Gjonaj², and Thomas Weiland²

¹Graduate School of Computational Engineering, Technische Universität Darmstadt, Dolivostr. 8, D-64293 Darmstadt

²Institut für Theorie Elektromagnetische Felder, Technische Universität Darmstadt, Schloßgartenstr. 8, D-64289 Darmstadt
hiltunen@temf.tu-darmstadt.de, gjonaj@temf.tu-darmstadt.de,
weiland@temf.tu-darmstadt.de

Summary. An implementation of the broad band Surface Impedance Boundary Condition (SIBC) for the high order Discontinuous Galerkin (DG) method in the time domain is presented. In order to treat the frequency dependent impedance function a set of auxiliary differential equations is introduced. The effect of the DG approximation order on the accuracy will be studied, and the results will be compared with the conventional time domain Finite Element Method.

1 Introduction

Time domain modeling is very attractive for wide band electromagnetic problems, since it allows to compute for a large range of frequencies in a single simulation. However, when the frequency band of interest is wide, the dispersive nature of material parameters, i.e. their variation with respect to frequency, needs to be considered. In order to model dispersive electromagnetic materials in time domain simulations, one generally needs to evaluate one or more convolution integrals. Clearly a direct computation of convolution terms is too expensive for every practical computation. For this purpose, several numerically efficient approaches have been proposed. One approach is a recursive convolution [7]. Another technique which is particularly suited for explicit time domain simulations is the Auxiliary Differential Equation (ADE) method. In the following, ADE is applied in the context of SIBC for arbitrary frequency dependent electric conductivities. Finite Difference Time Domain method (FDTD) [11] is widely used for time domain simulations. It leads to explicit time stepping and it is straightforward to implement. However, FDTD has a two important disadvantages: First, the method loses substantial accuracy at curved geometrical boundaries. Second, FDTD is at most 2nd order accurate, thus, it suffers under large numerical dispersion errors at high frequencies. Finite Element Method (FEM) [12] is very accurate as far as the modeling of arbitrary geometries is concerned. However, the time domain FEM leads to implicit time stepping [5], and is therefore numerically extremely expensive. The Time Domain Discontinuous Galerkin Method (DG) [3] combines the advantages of the

mentioned methods: it is free of numerical dispersion, modeling of arbitrary geometries is straightforward, and due to the global discontinuity of the basis functions, the resulting time stepping scheme is explicit. However, due to the discontinuity of basis functions at cell interfaces, unphysical spurious modes will occur. A possible cure to the problem of spurious modes is the application of various penalization methods as proposed, e.g., in [3], [1].

In this study, we will describe the implementation of a wide band SIBC for higher order DG by means of the ADE method. Furthermore, the effect of discretization order, rational approximation order for the impedance function as well as the impact of penalization on the accuracy of DG simulations with SIBC will be investigated.

2 DG Method

In this study, we will consider the Maxwellian initial value problem. The three-dimensional computational domain Ω is discretized into N non-overlapping elements, and on the boundary $\partial\Omega$, the SIBC is applied. Within an element, the electric field \mathbf{E} and the magnetic flux density \mathbf{B} are approximated by a linear combination of vectorial basis functions ϕ_E and ϕ_B , respectively. As both of the basis functions, ϕ_E and ϕ_B , are defined cell-wise without global continuity, in the DG method, a numerical flux approach is applied in order to impose the necessary continuity at the interfaces between mesh cells in the weak sense. A detailed description of the method as well as of the approximation functions, ϕ_E and ϕ_B , used in the present implementation is given in [1].

3 The SIBC Approach

Modeling of media with large but finite electrical conductivities typically leads to very dense meshes and thus to small time steps as required for stability in explicit time domain simulations. Therefore, it is desirable to exclude the lossy media from the computational domain. This can be done by introducing at the boundary surface of the conductive do-

main impedance-like conditions, which provide a relationship between the tangential electric field to the tangential magnetic field components. The classical SIBC was introduced by Leontovich (cf. [10]). It assumes the lossy surface to be planar and ignores the tangential variation of the field quantities. The error of the Leontovich SIBC is order of $O(\delta^2)$, where δ is skin depth, which makes it especially suitable for high frequencies. [4]. The second order SIBC [6] takes into account also the curvature of the surface. It is, furthermore, possible to construct higher order, thus, more accurate SIBC by taking into account, in addition, the tangential variation of the field components along the lossy surface [8]. When the thickness of the conductive medium is of the order of skin depth, the electromagnetic fields on the different sides of lossy medium interact with each other. Also this type of problems can be modeled by means of SIBC, using e.g. Sarto's [9] approach.

4 Approximation of Impedance Function

In order to transform the dispersive impedance function into the time domain, it is first approximated in the frequency domain as a series of rational functions [2]. The rational approximation for the tangential magnetic field can be written as:

$$Y(\omega)\mathbf{E}_t \approx Y_0\mathbf{E}_t + \sum_{i=1}^P \frac{Y_i\mathbf{E}_t}{j\omega - \omega_i}, \quad (1)$$

where \mathbf{E}_t is tangential electric field on the surface, P is the order of the rational approximation, Y_0 free space admittance, Y_i and ω_i are approximation parameters. Let us rewrite the rational approximation given in (1) as $Y(\omega)\mathbf{E}_t \approx \mathbf{Y}_0 + \sum_{i=1}^P \mathbf{Y}_i$. The the SIBC condition transforms in the time domain to

$$\mathbf{Y}_0 = Y_0\mathbf{E}_t \quad \text{and} \quad \frac{d}{dt}\mathbf{Y}_i - \omega_i\mathbf{Y}_i = Y_i\mathbf{E}_t. \quad (2)$$

Equation (2) represent the auxiliary differential equations of the ADE method which need to be solved for in the time domain together with the full set of Maxwell's equations.

5 System of Equations

The system of discrete equations to be solved in the time domain can be written as:

$$\begin{cases} \mathbf{C}_E\mathbf{e} + \frac{d}{dt}\mathbf{M}_\mu\mathbf{h} = 0 \\ \mathbf{C}_H\mathbf{h} - \frac{d}{dt}\mathbf{M}_\epsilon\mathbf{e} = \mathbf{C}_Y\sum_{i=0}^P \mathbf{Y}_i \\ \mathbf{Y}_0 = Y_0\mathbf{e}_t \\ \frac{d}{dt}\mathbf{Y}_i - \omega_i\mathbf{Y}_i = Y_i\mathbf{e} \quad \text{for } i = 1 \dots P, \end{cases} \quad (3)$$

where \mathbf{C}_E and \mathbf{C}_B are curl-matrices obtained by high order DG discretization, \mathbf{C}_Y is so called "admittance flux" matrix, and \mathbf{M}_μ and \mathbf{M}_ϵ are block-diagonal

mass matrices. In the full paper, the numerical accuracy and efficiency of this approach with respect to discretization order for different rational function approximations (1) will be discussed.

6 Summary

Dispersive SIBC will be implemented for time domain DG method in order to model a wide frequency band at a single simulation. The frequency dependent conductivity of lossy surfaces is considered in time domain by auxiliary differential equations. We will study the accuracy of the solution for different DG discretization orders and impedance function approximations, and compare our results with the standard SIBC-FDTD method.

Acknowledgement. This work is supported by the Graduate School of Computational Engineering at Technische Universität Darmstadt.

References

1. E. Gjonaj and T. Weiland. A projection penalization approach for the high-order dg-fem in the time domain. *Radio Science*, 46(10), 2011.
2. B. Gustavsen and A. Semlyen. Rational approximation of frequency domain responses by vector fitting. *Power Delivery, IEEE Transactions on*, 14(3):1052 – 1061, jul 1999.
3. J.S. Hesthaven and T. Warburton. *Nodal Discontinuous Galerkin Methods: Algorithms, Analysis, and Applications*. Springer Verlag, New York., 2008.
4. N. Ida, Lemenach Y., and Henneron T. High order surface impedance boundary conditions with the a- ϕ formulation. *Facta Univ. Ser.: Elec. Energ.*, 24(2):147 – 155, Aug. 2011.
5. J.M. Jin. *The Finite Element Method in Electromagnetics*. New York: John Wiley & Sons, 1993.
6. K.M. Mitzner. An integral equation approach to scattering from a body of finite conductivity. *Radio Science*, 2(12):1459–1470, 1967.
7. K.S. Oh and J.E. Schutt-Aine. An efficient implementation of surface impedance boundary conditions for the finite-difference time-domain method. *Antennas and Propagation, IEEE Transactions on*, 43(7):660 – 666, jul 1995.
8. S.M. Rytov. Calcul du skin-effet par la methode des perturbations. *Journal of Physics*, II(3), 1940.
9. M.S. Sarto. A new model for the fdtd analysis of the shielding performances of thin composite structures. *Electromagnetic Compatibility, IEEE Transactions on*, 41(4):298 – 306, nov 1999.
10. T. Senior. Impedance boundary conditions for imperfectly conducting surfaces. *Applied Scientific Research, Section B*, 8:418–436, 1960. 10.1007/BF02920074.
11. K. Yee. Numerical solution of initial boundary value problems involving maxwell's equations in isotropic media. *Antennas and Propagation, IEEE Transactions on*, 14(3):302–307, 1966.
12. O.C. Zienkiewicz. *The Finite Element Method*. London; New York : McGraw-Hill, 1977.

Computation of Optimal Model Parameters of an Extended Brauer Model for Ferromagnetic Material Behaviour

Timo Hülsmann¹, Andreas Bartel¹, Sebastian Schöps¹, and Herbert De Gersem²

¹ Bergische Universität Wuppertal {huelmann,bartel,schoeps}@math.uni-wuppertal.de,

² Katholieke Universiteit Leuven Herbert.DeGersem@kuleuven-kulak.be

Summary. Simulation of low-frequency magnetic fields in electric machines demands for implicit time integration. For the nonlinear reluctivity of the ferromagnetic yoke, a smooth material curve is needed to avoid convergence problems in Newton's method. In this paper the Brauer model is extended to fit the material behavior at low fields more accurately and to guarantee physically correctness for high fields. Furthermore, a procedure to obtain optimal parameters is developed and discussed using a numerical example.

1 Introduction

Typically Finite Element (FE) based simulations of eddy currents use the magnetic vector potential \mathbf{A} and the curl-curl equation

$$\sigma \frac{d\mathbf{A}}{dt} + \nabla \times (\nu \nabla \times \mathbf{A}) = \mathbf{J}_s, \quad (1)$$

with conductivity σ , reluctivity ν and source current density \mathbf{J}_s . For iron parts the material relation $\mathbf{H}(\mathbf{B}) = \nu \mathbf{B}$ becomes nonlinear, where $\mathbf{B} = \nabla \times \mathbf{A}$ is the magnetic flux density and \mathbf{H} the magnetic field strength. We neglect anisotropy and hysteresis. Hence, we can apply $H = \nu B$ in terms of $H := \|\mathbf{H}\|_2$ and $B := \|\mathbf{B}\|_2$. Typical models are spline interpolations of measurements, [3], and Brauer's model, [1]:

$$H_{br}(B) = \nu_{br}(B^2)B = (k_1 e^{k_2 B^2} + k_3)B.$$

Both allow a simple calculation of the reluctivity $\nu = \nu(B^2)$ and its derivative $\frac{d}{dB^2} \nu$, needed in the computation of material matrices occurring in the space discretization of (1), see e.g. [2]. Brauer's model is well understood, e.g., a sensitivity analysis shows that currents and fluxes through machines are most sensitive w.r.t. to perturbations in k_2 followed by k_1 and k_3 . The model is sufficiently accurate for medium fields but the behavior for low fields (Rayleigh region) and high fields (full saturation, i.e., $\frac{dH}{dB} = \nu_0$ as for vacuum) cannot be represented accurately.

2 Extended Brauer model

For high fields the material behaves like vacuum

$$H_{sat}(B) = \nu_0(B - B_s) + H_s.$$

For low fields the dependence of B on H is quadratic:

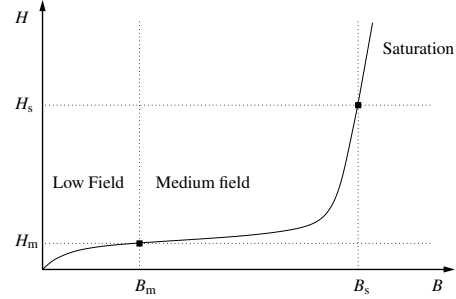


Fig. 1. Regions of the $H(B)$ -curve.

$$H_{ray}(B) = \sqrt{\frac{1}{4\alpha^2 \nu_{init}^2} + \frac{B}{\alpha}} - \frac{1}{2\alpha \nu_{init}}$$

with initial reluctivity ν_{init} and Rayleigh constant α . In combination we obtain a $H(B)$ -curve as shown in Fig. 1, with interface points (B_m, H_m) and (B_s, H_s) .

Let us determine the coefficients of an extended Brauer model s.t. the global model is continuous differentiable. The classical model does not simply allow to replace low field and high field parts. A shift of the Brauer model enables to fulfill the continuity and differentiability conditions at B_m :

$$H_{ebr}(B) = (k_1(e^{k_2(B-B_m)^2} - 1) + \nu_{d,m})(B - B_m) + H_m$$

with $\nu_{d,m} := \frac{dH}{dB} H_{ray}(B_m)$ the differential reluctivity at the end of the Rayleigh region. We define the function

$$H(B) := \begin{cases} H_{ray}(B) & \text{if } 0 \leq B < B_m, \\ H_{ebr}(B) & \text{if } B_m \leq B < B_s, \\ H_{sat}(B) & \text{if } B_s \leq B. \end{cases} \quad (2)$$

To fix the model parameters k_1 and k_2 , we use the continuity conditions $H_{ebr}(B_s) = H_s$ and $\frac{dH}{dB} H_{ebr}(B_s) = \nu_0$, and solve each equation for k_1 :

$$k_1 = \frac{\frac{H_s - H_m}{B_s - B_m} - \nu_{d,m}}{e^{k_2(B_s - B_m)^2} - 1}, \quad (3)$$

$$k_1 = \frac{\nu_0 - \nu_{d,m}}{(2k_2(B_s - B_m)^2 + 1)e^{k_2(B_s - B_m)^2} - 1}. \quad (4)$$

From (3) and (4) we find a nonlinear equation for $k_2 > 0$, which is solvable under the conditions $\nu_0 > \nu_{d,m}$

$$0 < \frac{\frac{H_s - H_m}{B_s - B_m} - \nu_{d,m}}{\nu_0 - \nu_{d,m}} < \frac{1}{3}$$

and $B_s > B_m > 0$, $H_s > H_m > 0$, $\nu_0 > \nu_{d,m}$.

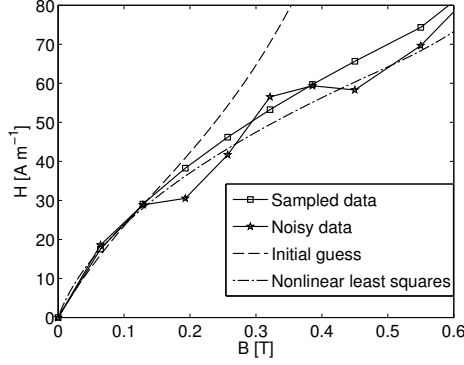


Fig. 2. Low field region.

The Rayleigh constant can be obtained by $\alpha := (B_m/H_m - 1/v_{\text{init}})/H_m$. Therefore the model (2) can be fixed from the data $\mathbf{p} := (v_{\text{init}}, B_m, H_m, B_s, H_s)$.

3 Optimal Model Parameters

Let us consider measurement points (B_j, H_j) , $j = 1, \dots, N$, of a ferromagnetic material. We assume monotonicity of the data and a distinctive Rayleigh region.

To find optimal model parameters we solve a nonlinear least squares (NLS) problem, i.e.,

$$\min_{\mathbf{p}} \sum_{j=1}^N \frac{(H(B_j; \mathbf{p}) - H_j)^2}{H_j^2}. \quad (5)$$

Proper initial guesses are important because of the nonliterary. A procedure for this purpose is given by:

- The fraction of first non-zero measurement points approximates v_{init} . Then find index r that minimizes $(H_{r+1} - H_r)/(B_{r+1} - B_r)$. (B_r, H_r) . It is an approximation to (B_m, H_m) . Compute α and $v_{d,m}$.
- Approximate the beginning of the saturation region with the last measurement points. Solve (3) and (4) for k_1 and k_2 by replacing v_0 with the secant slope v_N of the last two measurement points.
- If $v_N \approx v_0$, use the last point as approximation of (B_s, H_s) . Otherwise solve $\frac{dH}{dB} H_{\text{ebr}}(B_s) = v_0$ for B_s and compute $H_s = H_{\text{ebr}}(B_s)$.
- Solve the NLS problem (5).

4 Example

For validation we created test data from (2) using $v_{\text{init}} = 400 \text{ mH}^{-1}$, $(B_m, H_m) = (0.5 \text{ T}, 70 \text{ A m}^{-1})$ and $(B_s, H_s) = (2 \text{ T}, 100 \text{ kA m}^{-1})$. We sample the first two regions with 8 equidistant points. We incorporate Gaussian measurement noise by $\tilde{H}_i = \max(0, H_i \cdot (1 + \sigma X_i))$, where $X_i \sim \mathcal{N}(0, 1)$ and $\sigma = 0.1$. Fig. 2 and 3 show the fitted results. The proposed initial guess is sufficient to achieve convergence of the NLS problem. We obtain a curve close to the original curve.

The extended Brauer model is tested in a 2-D FE simulation of a transformer at no-load. Simulation results with the extended Brauer model with parameters

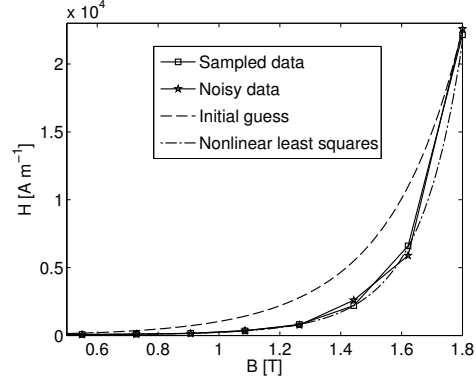


Fig. 3. Medium field region.

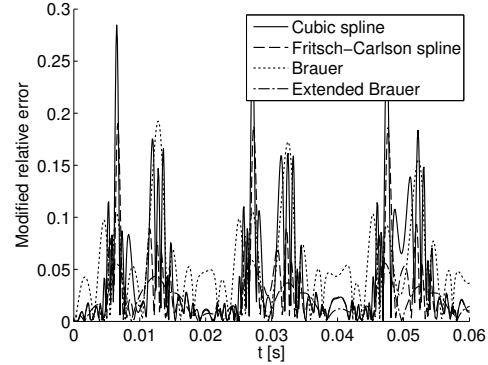


Fig. 4. Errors $|i - \hat{i}|/(|i| + 0.1)$ of no-load current. The current peaks are at 0.01, 0.03 and 0.05.

from above are used as a reference. For the spline interpolation (cubic and Fritsch-Carlson spline) we smoothened the noisy samples in the Rayleigh region with a moving average filter. Errors of the no-load current i through the device are depicted in Fig. 4.

The original Brauer model is the computationally least expensive but yields large errors in comparison to the reference solution. It cannot match the shape of the material curve for low and high fields. Spline interpolated measurements yield medium errors but need a high number of Newton steps to converge, cf. [4]. The extended Brauer model is only slightly more expensive than the original Brauer model but is the most accurate also in Fig. 4. It also recovers the reference curve.

References

- J. R. Brauer. Simple Equations for the Magnetization and Reluctivity Curves of Steel. *IEEE Trans. Magn.*, 11(1):81, 1975.
- H. De Gersem, I. Munteanu, and T. Weiland. Construction of Differential Material Matrices for the Orthogonal Finite-Integration Technique With Nonlinear Materials. *IEEE Trans. Magn.*, 44(6):710–713, 2008.
- B. Heise. Analysis of a fully discrete finite element method for a nonlinear magnetic field problem. *SIAM J. Num. Ana.*, 31(3):745–759, 1994.
- H. Vande Sande, F. Henrotte, and K. Hameyer. The Newton-Raphson method for solving non-linear and anisotropic time-harmonic problems. *COMPEL*, 23(4):950–958, 2004.

Eddy current analysis of a PWM controlled induction machine

Hai Van Jorks¹, Erion Gjonaj², Thomas Weiland³

Technische Universität Darmstadt, Institute of Computational Electromagnetics
Schloßgartenstraße 8, 64289 Darmstadt, Germany,

¹jorks@temf.tu-darmstadt.de

²gjonaj@temf.tu-darmstadt.de

³weiland@temf.tu-darmstadt.de

Summary We investigate the high frequency eddy currents and compute the Common Mode Impedance of a PWM controlled induction motor by Finite Element simulations. It is shown that in order to determine machine parameters accurately, three-dimensional analysis taking into account explicitly the eddy currents induced in the iron core laminations is necessary.

1 Introduction

Modern induction machines are most often powered by Pulse Width Modulation (PWM) voltage source inverters. Although PWM switching clearly improves the overall performance and efficiency of the drive system, it also promotes the formation of common mode voltages which may evoke harmful high frequency bearing currents [1]. While the PWM switching frequency is usually in the order of 20 kHz, the short rise time of the pulses may induce higher frequency currents of several MHz in the housing, laminated core as well as in the shaft bearings of the machine. Therefore, when analysing PWM controlled induction machines, a broad frequency range has to be considered.

An essential parameter in the equivalent circuit representation of electric drives is the Common Mode Impedance (Z_{com}). This quantity allows to compute among others the bearing currents for different machine operation conditions. In the following, Z_{com} will be determined exclusively from Finite Element (FE) simulations. Using this approach substantial information can be obtained already in the design stage without necessitating on-machine measurement data.

In the FE analysis of induction machines, several symmetries can be exploited. Usually, for the middle part a two-dimensional (2D) projection of the motor cross section is considered [2]. In this paper, however, a fully three-dimensional (3D) analysis is proposed which allows to take into account explicitly the eddy currents induced in the core laminations. The end-windings, which in general do additionally contribute to Z_{com} , are not considered in the present analysis. The Common

Mode calculation is completed by assembling the parameter matrices extracted from the middle and eventually the end parts of the machine using transmission line theory [3].

2 Lamination Modelling

Eddy currents in core laminations have been found to have a large impact on the transmission line parameters and, thus, on the Common Mode Impedance of PWM driven induction machines [3,4]. Magnetic machine cores are specifically designed to suppress eddy currents at supply frequency. However, higher frequency voltage harmonics arising from PWM switching may lead to pronounced eddy currents loops in the core. This is because the skin depth in the iron at PWM frequencies becomes comparable or even smaller than the thickness of lamination sheets.

When employing laminated materials in FE analysis it is often not possible to model every single iron sheet because this would lead to enormous computational costs. Instead, the lamination is treated as a homogeneous material adopting equivalent electromagnetic properties. A well-known homogenisation model utilizes a frequency dependent equivalent permeability for the iron core given by,

$$\mu_{eq} = \frac{\mu_0 \mu_r \sinh(\alpha b)}{\alpha b \cosh(\alpha b)}, \quad \alpha = \frac{(1+j)}{\delta}, \quad (1)$$

where $\mu_0 \mu_r$ is the permeability of iron, $2b$ the thickness of the plate and δ the skin depth at a given frequency [5]. The magnetic field problem for the homogenised core in the middle part of the motor reduces to a planar 2D problem. While this approach allows for very efficient 2D-FE analysis, certain inaccuracies can be expected. First, the equivalent model (1) assumes a uniform primary magnetic field with no variation in the cross-sectional plane of the motor (cf. [5]). Second, possible edge effects in the eddy current distribution arising at the winding yoke transitions are not considered. Finally, in the

equivalent permeability model the iron core is considered to be non-conductive. Hence, the field reaction to the eddy current loops is neglected. The conductivity of iron is only introduced in post-processing for calculating electric losses. Thus, in particular in the high frequency range, it may be necessary to perform a more detailed eddy current analysis which takes into account all of these effects in core laminations.

3 Fully 3D-FE Approach

For testing purposes, a circular conductor model is considered (see Fig. 1). The copper conductor is surrounded by a laminated iron core. The lamination layers consist of oxide insulation sheets with a thickness of 0.65 mm. The width of the air gap between conductor and core is 0.1 mm.

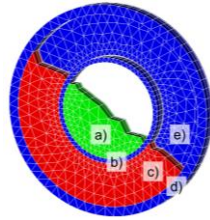


Fig. 1: Single conductor model with 5 material blocks: a) copper, b) air gap, c) iron, d) air and e) oxide layer.

In the homogenized equivalent permeability model (1), the eddy current problem can be solved analytically. For comparison, the geometry is discretized with a 3D mesh and analysed by means of FE simulations. In the first set of simulations the equivalent permeability is employed while in the second fully 3D-FE analysis including the iron and oxide layers is applied. Resulting electric losses and stored magnetic energy in the conducting parts of the arrangement are shown in Fig. 2. While the homogenized model gives quite accurate results in the copper conductor at lower frequencies (< 1 kHz), electric losses in the iron are subject to major errors (46% in this model), independent of frequency. However, at low frequencies, copper losses are much greater than iron losses. At higher frequencies, the field solution in the copper conductor is increasingly influenced by the lamination and large deviations occur for both electric losses and magnetic energy. Considering the present analysis, the homogenization approach (1) might not be valid for high frequency simulations of induction motors.

Therefore, the fully 3D approach will be applied to calculate the Common Mode Impedance of an existing 240 kW motor and will be presented in the full paper.

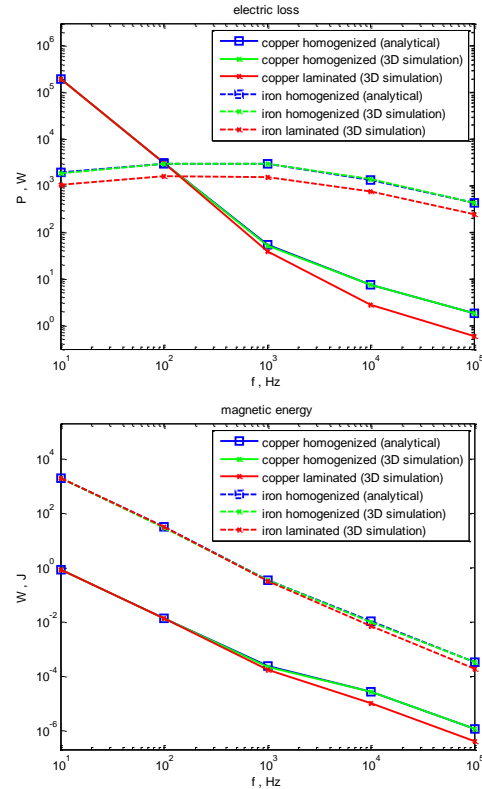


Fig. 2: Electric loss (top) and stored magnetic energy (bottom) for the single conductor model.

Acknowledgement This work is funded by the Deutsche Forschungsgemeinschaft (DFG) under the collaborative research group grant FOR 575.

References

1. S. Chen, et al. *Source of induction motor bearing currents caused by PWM inverters*. IEEE Trans. on Energy Conv., vol. 11, no.1. 1996, pp. 25–32.
2. I. Boldea, S. A. Nasar. *The induction machine handbook*. CRC Press, 2002.
3. H. De Gersem, A. Muetze. *Finite-Element Supported Transmission-Line Models for Calculating High-Frequency Effects in Machine Windings*. IEEE Trans. on Mag., vol. 48, no. 2. 2012, pp. 787-790.
4. H. Jorke, et al. *Three-dimensional simulations of an induction motor including eddy current effects in core laminations*. IET Science, Measurement & Technology, 2012 (accepted for publication).
5. R.L. Stoll. *The analysis of eddy currents*. Oxford University Press. 1974.

Electrical Modelling of Large-area Organic Light-emitting Devices

Evelyne Knapp and Beat Ruhstaller

Institute of Computational Physics, Zurich University of Applied Sciences, Wildbachstr. 21, 8401 Winterthur, Switzerland
evelyne.knapp@zhaw.ch, beat.ruhstaller@zhaw.ch

Summary. Systematic improvement of the performance and lifetime of organic light-emitting devices (OLEDs) are facilitated by electrical characterization through experiments and simulations. We model charge transport in organic disordered materials with the aid of a numerical 1D model for different experimental setups such as current-voltage curves, current transients and electrical impedance spectroscopy. For large-area OLEDs we couple the anode and cathode with the 1D model leading to an efficient 1+2D approach.

1 Introduction

Although the commercial success of organic light-emitting devices (OLEDs) in displays and lighting proceeds rapidly, further research is necessary to improve the efficiency and lifetime. Numerical simulations help to reduce the number of prototype iterations. Electrical characterization of devices and materials is crucial as it sheds light on the physical models of charge carrier transport in disordered, organic semiconductors. Charge transport and recombination models have been introduced several years ago for organic LEDs [1–5]. However, organic semiconductors differ considerably from their inorganic counterparts, not only by low carrier mobilities and long recombination times but also by the disorder. Taking the disordered nature of organic materials into account leads to a description in terms of a Gaussian density of states (DOS) which affects the mobility of charge carriers and the diffusion coefficient. The Gaussian DOS enhances the nonlinearities and the coupling between the equations. These circumstances prevent the use of classical drift-diffusion solvers. With the aid of a one-dimensional numerical OLED model we are able to simulate different operating conditions such as current-voltage curves [6], dark-injection measurements and impedance spectroscopy. We conduct steady-state, transient and small-signal analysis for the 1D OLED model and compare them with experiments. For lighting applications OLED panels are used that need to be as homogeneous as possible. To take this requirement into account we couple the 1D model to two 2D domains.

2 Physical Model

The drift-diffusion model (1) and (2) with the organic model ingredients (such as a Gaussian density of states and the use of the Fermi-Dirac statistics) are discretized with the finite volume method, the current expression (3) with the Scharfetter-Gummel discretization [7]. The resulting system of discretized equations is then solved in a coupled manner with Newton's algorithm for the transient as well as the steady-state case [8].

$$\nabla \cdot (\epsilon \nabla \psi) = q(n_f + n_t - p_f - p_t), \quad (1)$$

$$\begin{aligned} \nabla \cdot J_n - q \left(\frac{\partial n}{\partial t} \right) &= qR(n_f, p_f), \\ \nabla \cdot J_p + q \left(\frac{\partial p}{\partial t} \right) &= -qR(n_f, p_f), \end{aligned} \quad (2)$$

$$\begin{aligned} J_n &= -qn_f\mu_n\nabla\psi + qD_n\nabla n_f, \\ J_p &= -qp_f\mu_p\nabla\psi - qD_p\nabla p_f. \end{aligned} \quad (3)$$

For the small-signal analysis, the steady-state voltage V_0 is modulated with a sinusoidal voltage with the amplitude V^{ac} and with the angular frequency ω : $V = V_0 + V^{ac}e^{i\omega t}$. The potential ψ and the charge densities p and n can be expanded into a steady-state and harmonic term, e.g. $\psi(x, t) = \psi_0(x) + \psi^{ac}(x)e^{i\omega t}$ where the ac components are complex-valued. To solve the small-signal equations, the solution of the dc problem for $V = V_0$ is required. After inserting the expansions into the linearized drift-diffusion model we obtain a linear system of equations for the unknown ac components and thus for the ac current J^{ac} . From the complex admittance $Y = J^{ac}/V^{ac}$, the small-signal capacitance C and conductance G can be obtained. Charge traps originate in impurities or material degradation and affect the transport. In Fig. 1 we show the effect of different charge trap types on the normalized capacitance at different frequencies. Fast traps are in quasi-equilibrium with free carriers, the transit time is longer than the trapping time whereas for slow traps the transit time is shorter than the trapping time. Slow traps enhance the capacitance at low frequencies while fast traps follow the dynamics of the trap-free case [9]. Similarly, charge traps affect current transients and current-voltage curves.

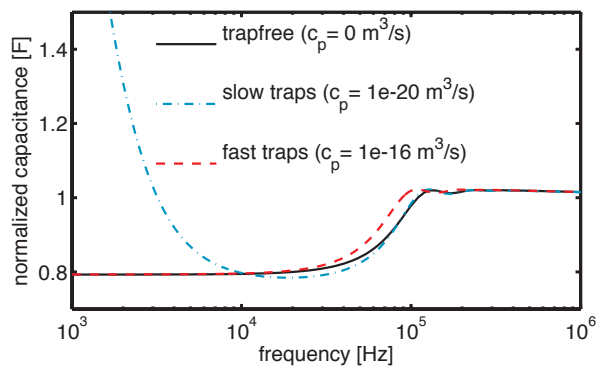


Fig. 1. Normalized capacitance of different trap types at various frequencies.

3 2+1D Approach for Large-area OLEDs

Aiming for a fast PC model for large-area OLEDs we have to take into account that realistic OLED structures consist of transparent anodes with a relatively low electrical conductivity. This affects the homogeneity of the OLED. Metal grid structures are applied to large-area OLEDs to improve the situation. To quantify the potential and temperature drop in large-area OLEDs we extend the 1D modelling of the organic material to higher dimensions. The 2+1D approach captures the important features of the transport process, and accounts for the high aspect ratio between the in-plane and the through-plane dimensions of OLEDs. In comparison to full 3D models, the 2+1D approach requires a reduced number of degrees of freedom, but still provides the lateral potential and temperature distribution. We make use of our in-house FEM tool (SESES) that allows the nonlinear coupling of 2D domains with the aid of the 1D model as shown in Fig. 2. The connection between the anode and cathode can either be:

- a parameterized experimental curve
- an analytical formula
- or a numerical model.

In Fig. 2 we show an OLED panel before optimizing the metal grid layout. No metal structure is present to improve the homogeneity of the OLED.

4 Conclusions

In this paper, we present a 1D model for organic LEDs that is applied to different operating conditions such as steady-state, transient and ac response. We investigate different charge trap types and their influence on the frequency-dependent capacitance. Further, we propose a 2+1D modeling approach for large-area OLEDs.

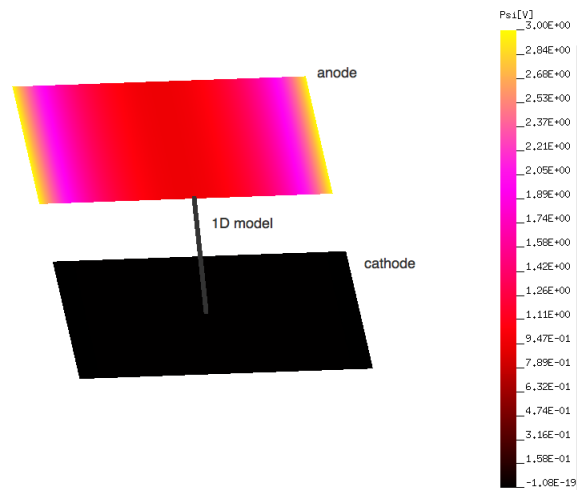


Fig. 2. Coupling of the 1D and 2D domains in an organic LED model. We display the potential drop before a metal grid structure is added.

Acknowledgement. We acknowledge financial support from the European Communitys Seventh Framework program under grant agreement no. 213708 (AEVIOM.eu) and NMP4-SL-2011-295368 (im3oled.eu).

References

1. J.C. Scott and G.G. Malliaras. Charge injection and recombination at the metalorganic interface. *Chem. Phys. Lett.*, 299:115, 1999.
2. B.K. Crone, P.S. Davids, I.H. Campbell, D.L. Smith. Device model investigation of bilayer organic light emitting diodes. *J. Appl. Phys.*, 87(4):1974, 2000.
3. P.W.M. Blom, M.J.M. de Jong, J.J.M. Vleggaar. Electron and hole transport in poly(p-phenylene vinylene) devices. *Appl. Phys. Lett.*, 68(23):3308, 1996.
4. B. Ruhstaller, S.A. Carter, S. Barth, H. Riel, W. Riess, J.C. Scott. Transient and steady-state behavior of space charges in multilayer organic light-emitting diodes. *J. Appl. Phys.*, 89(8):4575, 2001.
5. B. Ruhstaller, T. Beierlein, H. Riel, S. Karg, J.C. Scott, W. Riess. Simulating electronic and optical processes in multilayer organic light-emitting devices. *IEEE J. Sel. Top. Quantum Electron.*, 9(3):723, 2003.
6. S.L.M. van Mensfoort, S.I.E. Vulto, R.A.J. Janssen, R. Coehoorn. Hole transport in polyfluorenebased sandwich-type devices: quantitative analysis of the role of energetic disorder. *Phys. Rev. B*, 78(8):085208, 2008.
7. D.L. Scharfetter and H.K. Gummel. Large-signal analysis of a silicon read diode oscillator. *IEEE Trans. Electr. Dev.*, 16(28):64, 1969.
8. E. Knapp, R. Häusermann, H. Schwarzenbach, B. Ruhstaller. Numerical simulation of charge transport in disordered organic semiconductor devices. *J. Appl. Phys.*, 99(9):093304, 2011.
9. E. Knapp and B. Ruhstaller. Numerical impedance analysis for organic semiconductors with exponential density of localized states. *Appl. Phys. Lett.*, 108(5):054504, 2010.

Efficient solvers for optimal control of eddy current problems with regularized state constraints

Michael Kolmbauer¹ and Ulrich Langer^{1,2}

¹ Institute of Computational Mathematics, Johannes Kepler University, Altenbergerstr. 69, A-4040 Linz, Austria.
kolmbauer@numa.uni-linz.ac.at, ulanger@numa.uni-linz.ac.at

² RICAM, Johann Radon Institute for Computational and Applied Mathematics, Austrian Academy of Sciences,
Altenbergerstr. 69, A-4040 Linz, Austria. ulrich.langer@assoc.oeaw.ac.at

Summary. This work is devoted to the robust and efficient solution of an optimal control problems for time-harmonic or time-periodic eddy current problems in the presence of pointwise state constraints imposed on the Fourier coefficients. For the discrete version of the linearized and reduced optimality systems of the Moreau-Yosida penalized minimization problems, condition number estimates of the preconditioned systems are provided. We show, that block-diagonal preconditioners can lead to parameter-robust and efficient solution strategies for these kind of problems.

1 Introduction

During recent years, the importance of solving optimization problems with constraints in form of partial differential equations has been growing. Usually, the partial differential equation is treated as a constraint, and the minimizing solution is determined by solving the corresponding optimality system. Typically, this approach leads to very bad condition systems of linear equations, and therefore the iterative solution of these kind of equations is a delicate issue.

In [2, 3] an optimal control problem with a simple time-periodic parabolic partial differential equation as the state equation is considered. The optimality system is discretized in terms of the harmonic balance finite element method, and parameter robust solvers are constructed for the resulting frequency domain equations. The aim of this work is to extend these ideas also to the eddy current optimal control problem, cf. [4, 5]. Therefore, we consider optimal control problems, where the partial differential equations is given by time-harmonic or time-periodic eddy current problems. Indeed, in the time-periodic setting, we establish the harmonic balance finite element method, in combination with efficient and robust solvers for the resulting frequency domain equations, as a powerful tool for solving optimal control problems in computational electromagnetics.

Furthermore, we include pointwise state constraints in our model, since they may be important to filter out undesired singularities in the solution of the eddy current problem.

2 Optimal control problem

We concentrate on the solution of the following optimal control problem:

$$\min_{(\mathbf{y}^c, \mathbf{y}^s, \mathbf{u}^c, \mathbf{u}^s) \in \mathbf{H}_0(\mathbf{curl})^2 \times \mathbf{L}_2(\Omega)^2} J(\mathbf{y}^c, \mathbf{y}^s, \mathbf{u}^c, \mathbf{u}^s), \quad (1)$$

subject to

$$\begin{cases} \mathbf{curl}(\nu \mathbf{curl} \mathbf{y}^c) + \omega \sigma \mathbf{y}^s = \mathbf{u}^c, & \text{in } \Omega, \\ \mathbf{curl}(\nu \mathbf{curl} \mathbf{y}^s) - \omega \sigma \mathbf{y}^c = \mathbf{u}^s, & \text{in } \Omega, \\ \mathbf{y}^c \times \mathbf{n} = \mathbf{y}^s \times \mathbf{n} = \mathbf{0}, & \text{on } \partial\Omega, \end{cases} \quad (2)$$

and to the pointwise state constraints

$$\mathbf{y}_a^j(\mathbf{x}) \leq \mathbf{y}^j(\mathbf{x}) \leq \mathbf{y}_b^j(\mathbf{x}), \quad \text{a.e. in } \Omega, j \in \{c, s\}. \quad (3)$$

The quadratic cost functional is given by

$$J(\mathbf{y}^c, \mathbf{y}^s, \mathbf{u}^c, \mathbf{u}^s) := \frac{1}{2} \sum_{j \in \{c, s\}} \left[\|\mathbf{y}^j - \mathbf{y}_d^j\|_0^2 + \lambda \|\mathbf{u}^j\|_0^2 \right].$$

The regularization parameter $\lambda > 0$, the model parameters σ, ν and ω , and $\mathbf{y}_d^c, \mathbf{y}_d^s, \mathbf{y}_a^c, \mathbf{y}_b^c, \mathbf{y}_a^s, \mathbf{y}_b^s \in \mathbf{L}_2(\Omega)$ are given data.

Following [6], we use a Moreau-Yosida regularization, that penalizes the pointwise state constraints, i.e., we add the penalty term

$$\frac{1}{2\varepsilon} \sum_{j \in \{c, s\}} \left[\|\max(\mathbf{0}, \mathbf{y}^j - \mathbf{y}_b^j)\|_0^2 + \|\min(\mathbf{0}, \mathbf{y}^j - \mathbf{y}_a^j)\|_0^2 \right],$$

$\varepsilon > 0$, to the cost functional J . The resulting minimization can be solved by deriving the (reduced) optimality system. Due to the penalized state constraints, the optimality system becomes nonlinear. The nonlinearity can be dealt with in terms of a primal dual active set strategy, that is known to be equivalent to the semi-smooth Newton method [1]. At each Newton step, a two-fold saddle point problem has to be solved. Typically, the model parameters σ, ν and ω , the regularization parameters λ and ε , as well as the discretization parameter h , coming from the finite element approximation, impinge on the convergence of any iterative method applied to the unpreconditioned problem. Therefore, the aim of this paper is to present a preconditioning technique for the robust and efficient solution of the saddle point system at each Newton step.

3 Block-diagonal preconditioner

The finite element discretization of the penalized, linearized and reduced optimality system of (1)-(3), yields the linear system of equations

$$\mathcal{A} \mathbf{x} = \mathbf{b}, \quad (4)$$

where the system matrix \mathcal{A} is given by

$$\mathcal{A} = \begin{pmatrix} \mathbf{M} + \frac{1}{\varepsilon} \mathbf{M}_{\mathcal{E}^c} & \mathbf{0} & \mathbf{K}_v & -\mathbf{M}_{\omega, \sigma} \\ \mathbf{0} & \mathbf{M} + \frac{1}{\varepsilon} \mathbf{M}_{\mathcal{E}^s} & \mathbf{M}_{\omega, \sigma} & \mathbf{K}_v \\ \mathbf{K}_v & \mathbf{M}_{\omega, \sigma} & -\frac{1}{\lambda} \mathbf{M} & \mathbf{0} \\ -\mathbf{M}_{\omega, \sigma} & \mathbf{K}_v & \mathbf{0} & -\frac{1}{\lambda} \mathbf{M} \end{pmatrix}.$$

Here \mathbf{K}_v corresponds to the stiffness matrix, \mathbf{M} to the mass matrix, $\mathbf{M}_{\omega, \sigma}$ to a weighted mass matrix, and $\mathbf{M}_{\mathcal{E}^c}$ and $\mathbf{M}_{\mathcal{E}^s}$ to the mass matrices on the active sets \mathcal{E}^c and \mathcal{E}^s , respectively. In order to solve (4), we follow the strategy used in [5] and construct a preconditioned MinRes solver. We propose and analyze the block-diagonal preconditioner

$$\mathcal{C} = \text{diag}(\sqrt{\lambda} \mathbf{E}, \sqrt{\lambda} \mathbf{E}, \frac{1}{\sqrt{\lambda}} \mathbf{E}, \frac{1}{\sqrt{\lambda}} \mathbf{E}), \quad (5)$$

where $\mathbf{E} = \mathbf{K}_v + \mathbf{M}_{\omega, \sigma} + \frac{1}{\sqrt{\lambda}} \mathbf{M}$. We show, that the condition number of the preconditioned system can be estimated by a constant, that is independent of the mesh size h , the regularization parameter λ , the model parameters σ , v , and ω , as well as the active sets \mathcal{E}^c and \mathcal{E}^s from the primal dual active set strategy, i.e.,

$$\kappa(\mathcal{C}^{-1} \mathcal{A}) \leq c \neq c(\omega, \sigma, h, \lambda, \mathcal{E}^c, \mathcal{E}^s).$$

Therefore, the number of MinRes iterations required for reducing the initial error by some fixed factor $\delta \in (0, 1)$ is independent of ω , σ , h , λ , \mathcal{E}^c , and \mathcal{E}^s . In practice, the diagonal blocks \mathbf{E} of (5) are replaced by appropriate efficient and parameter robust preconditioners.

4 Time-periodic optimization

The presented solving technique provides a robust tool for solving optimal control problems with a time-harmonic eddy current problem as the state equation. Indeed, the theory can be extended to time-periodic optimal control problems of the form:

$$\min J(\mathbf{u}, \mathbf{y}) = \frac{1}{2} \int_0^T \|\mathbf{y} - \mathbf{y}_a\|_0^2 dt + \frac{\lambda}{2} \int_0^T \|\mathbf{u}\|_0^2 dt,$$

subject to

$$\begin{cases} \sigma \frac{\partial \mathbf{y}}{\partial t} + \text{curl}(v \text{curl} \mathbf{y}) = \mathbf{u}, & \text{in } \Omega \times (0, T), \\ \mathbf{y} \times \mathbf{n} = \mathbf{0}, & \text{on } \partial \Omega \times (0, T), \\ \mathbf{y}(0) = \mathbf{y}(T), & \text{in } \Omega, \end{cases} \quad (6)$$

with state constraints associated to the Fourier coefficients of \mathbf{y} . Due to the periodic structure, a time approximation of the state \mathbf{y} and the control \mathbf{u} in terms of a truncated Fourier series can be used, i.e.,

$$\mathbf{y}(\mathbf{x}, t) = \sum_{k=0}^N \mathbf{y}_k^c \cos(k\omega t) + \mathbf{y}_k^s \sin(k\omega t).$$

Due to the linearity of (6), we obtain a decoupling of the frequency domain equations with respect to the individual modes $k = 0, \dots, N$. For each mode, a linear system of equations, that obtains high structural similarities to (4) has to be solved. Hence, an efficient and parameter robust solver can be constructed in the same manner as done in the previous section. Indeed, this approach is an extension the harmonic balance finite element method to optimal control problems.

5 Conclusion

The method developed in this work shows great potential for solving both time-harmonic and time-periodic eddy current optimal control problems in an efficient and robust way.

Acknowledgement. The research was funded by the Austrian Science Fund (FWF) under the grants P19255-N18 and W1214-N15, project DK04. Furthermore, the authors thank the Austria Center of Competence in Mechatronics (ACCM), which is part of the COMET K2 program of the Austrian Government, for supporting their work on eddy current problems.

References

1. K. Ito and K. Kunisch. Semi-smooth Newton methods for state-constrained optimal control problems. *Systems Control Lett.*, 50(3):221–228, 2003.
2. M. Kollmann and M. Kolmbauer. A preconditioned minres solver for time-periodic parabolic optimal control problems. *Numer. Linear Algebra Appl.*, August 2011. accepted for publication in NLA.
3. M. Kollmann, M. Kolmbauer, U. Langer, M. Wolfram, and W. Zulehner. A finite element solver for a multiharmonic parabolic optimal control problem. NuMa-Report 2011-10, Institute of Computational Mathematics, Linz, December 2011.
4. M. Kolmbauer. Efficient solvers for multiharmonic eddy current optimal control problems with various constraints. NuMa-Report 2011-09, Institute of Computational Mathematics, Linz, November 2011.
5. M. Kolmbauer and U. Langer. A robust preconditioned MinRes solver for distributed time-periodic eddy current optimal control problems. NuMa-Report 2011-04, Institute of Computational Mathematics, Linz, May 2011.
6. I. Yousept. Optimal control of Maxwell's equations with regularized state constraints. *Computational Optimization and Applications*, pages 1–23, 2011.

Optimal design of reflecting photonic structures for space applications

Nikolay Komarevskiy¹, Valery Shklover¹, Leonid Braginsky¹, Christian Hafner¹, and John Lawson²

¹ Swiss Federal Institute of Technology (ETH) Zürich, 8092 Zürich, Switzerland

n.komarevskiy@ifh.ee.ethz.ch, V.SHKLOVER@mat.ethz.ch, leonid.braginsky@mat.ethz.ch, christian.hafner@ifh.ee.ethz.ch

² MS-234-1, NASA Ames Research Center, Moffett Field, 94035 California, USA john.w.lawson@nasa.gov

Summary. During atmospheric entries, vehicles can be exposed to strong electromagnetic radiation from gas in the shock layer. We propose and analyze silicon carbide and glassy carbon structures to increase the reflection of radiation. We performed numerical optimizations of photonic structures using an evolutionary strategy. Among the considered structures are layered, woodpile, porous and guided-mode resonance structures. The role of structural imperfections on the reflectivity is analyzed.

1 Introduction

Practical applications of photonic crystals (PhCs) are diverse [1, 2]. An interesting, but not yet practically realized, application of PhCs is as radiation shields for atmospheric re-entry of space vehicles. Electromagnetic radiation from ionized gas in the shock layer can constitute up to 30-50% [3] of the overall heat flux for lunar return trajectories, although for relatively short times. For Jupiter entries, on the other hand, most of the heating is radiative [4]. Therefore, in addition to protection against convective heating, a reentry thermal protection systems (TPS) should also be designed for radiation shielding. Ideally, the design should be tuned to the radiative spectra of a specific planet and specific entry conditions.

One of the easiest way to design radiation shields for atmospheric re-entry is with layered media [5]. Provided the two constituent materials possess a sufficient dielectric contrast and low absorption, broadband radiation shields with high omnidirectional reflection can be designed [6]. However, applications such as atmospheric re-entry impose many additional constraints on the material properties (thermal, mechanical, etc.). Therefore, finding a suitable pair of materials can be very demanding.

Currently, TPS for the most demanding atmospheric re-entries are made of highly porous carbon based materials. These materials, for example, PICA (phenolic-impregnated carbon ablators), possess many of the required thermal and mechanical properties. However, these materials are strong absorbers of radiation and therefore currently offer no protection at all from radiative heating. On the other hand, if these materials could be structured in such way that high

reflection is obtained, radiative heating of the vehicle during re-entry could be reduced. We analyze the potential of glassy carbon and silicon carbide as radiation shields for Earth atmospheric re-entry. The effects of structural imperfections on reflectivity are also analyzed.

1.1 Optimization goal

The goal is to design a radiation shield that maximizes the total reflection of normally incident *unpolarized* radiation u_v , shown in Fig. 1.

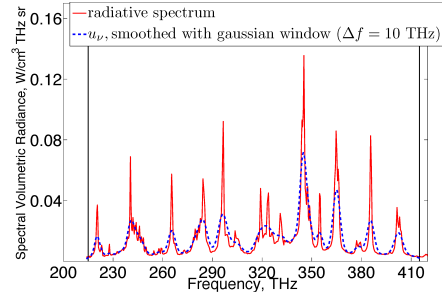


Fig. 1. (Red curve - experimental data of spectral radiation distribution, obtained at atmospheric re-entry relevant conditions [7] blue dashed curve - spectrum smoothed with Gaussian window function of full width $\Delta f = 10$ THz.

Therefore, the function to be maximized is:

$$\langle R_{u_v} \rangle = \frac{\int R_{\Sigma} u_v dv}{u_{\text{tot}}}, \quad u_{\text{tot}} = \int u_v dv, \quad (1)$$

where R_{Σ} is the total reflection of the incident unpolarized radiation:

$$R_{\Sigma} = 0.5(R^s + R^p), \quad (2)$$

where R^s and R^p are the sum of reflection efficiencies for the s- and p-polarization, respectively:

$$R^{s,p} = R_0^{s,p} + \sum_i D_i^{s,p}, \quad i = \pm 1, \pm 2, \dots \quad (3)$$

here the summation is performed over the propagating diffraction orders in the upper air half space.

For numerical optimization, we used evolutionary strategy (ES) algorithms. Based on previous experience [8], it is very powerful for real parameter optimization problems and outperforms genetic algorithm, particle swarm optimization, and other methods in most cases. We used an $(m+n)$ evolutionary strategy with adaptive mutation for the optimization. Here m is the initial number of parents and n is the number of children created in each generation.

Some of the structures to be optimized are shown in Fig. 2.

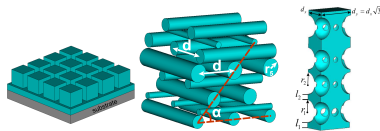


Fig. 2. (From left to right: guided mode resonance structure, woodpile, porous-reflector

Acknowledgement. This work was supported by ETH project 0-20590-09, Materials for Infra Red Protection.

References

1. J. Joannopoulos, S. Johnson, J. Winn, and R. Meade, *Photonic crystals: molding the flow of light* (Princeton Univ Pr, 2008).
2. V. Shklover, L. Braginsky, G. Witz, M. Mishrikey, and C. Hafner, "High-Temperature Photonic Structures. Thermal Barrier Coatings, Infrared Sources and Other Applications," *Journal of Computational and Theoretical Nanoscience* **5**, 862 (2008).
3. J. Grinstead, M. Wilder, J. Olejniczak, D. Bogdanoff, G. Allen, K. Dang, and M. Forrest, "Shock-heated Air Radiation Measurements at Lunar Return Conditions," *AIAA Paper* **1244**, 2008 (2008).
4. C. Park, "Stagnation-region heating environment of the galileo probe," *Journal of thermophysics and heat transfer* **23**, 417–424 (2009).
5. N. Komarevskiy, L. Braginsky, V. Shklover, C. Hafner, and J. Lawson, "Fast numerical methods for the design of layered photonic structures with rough interfaces," *Optics Express* **19**, 5489–5499 (2011).
6. N. Komarevskiy, V. Shklover, L. Braginsky, C. Hafner, O. Fabrichnaya, S. White, and J. Lawson, "Design of reflective, photonic shields for atmospheric reentry," *Journal of Electromagnetic Analysis and Applications* **3**, 228–237 (2011).
7. A. Brandis, C. Johnston, B. Cruden, D. Prabhu, and D. Bose, "Uncertainty analysis of neqair and hara predictions of air radiation measurements obtained in the east facility," in "42nd AIAA Thermophysics Conference," (American Institute of Aeronautics & Astronautics (AIAA), 2011).
8. J. Fröhlich, "Evolutionary optimization for computational electromagnetics," Ph.D. thesis, ETH Zurich, IFH Laboratory (1997).

The (1+1)D Space-Time Discontinuous Galerkin Trefftz Method

Fritz Kretzschmar¹, Sascha M. Schnepf¹, Igor Tsukerman², and Thomas Weiland³

¹ Graduate School of Computational Engineering, Technische Universität Darmstadt, Dolivostraße 15, 64293 Darmstadt, Germany kretzschmar@gsc.tu-darmstadt.de, schnepf@gsc.tu-darmstadt.de

² Department of Electrical & Computer Engineering, The University of Akron, Akron, Ohio 44325-3904, USA itsukerman@uakron.edu

³ Institut für Theorie Elektromagnetischer Felder, Technische Universität Darmstadt, Schloßgartenstraße 8, 64289 Darmstadt, Germany thomas.weiland@temf.tu-darmstadt.de

Summary. A novel Discontinuous Galerkin Finite Element Method for space-time electrodynamic problems is presented. The method employs space-time Trefftz basis functions that satisfy the underlying partial differential equations exactly in an element-wise fashion. A major advantage of Trefftz approximations is their high accuracy that in many cases leads to spectral convergence. First computational results are presented.

1 Introduction

Discontinuous Galerkin Finite Element Methods (DG-FEM) [1–4] are a major class of tools to numerically simulate complicated Electro-Magnetic (EM) systems. Here we present a highly accurate type of DG-FEM. A distinguishing new feature of the method is the use of Trefftz basis functions instead of the traditional generic polynomials. By definition space-time Trefftz basis functions satisfy Maxwell's equations exactly in an element-wise fashion. The method is, hence, a Discontinuous Galerkin Trefftz Finite Element Method (DGT-FEM) [5]

2 Development of the Method

This section consists of three parts. First, we state Maxwell's equations in (1+1)D. Second, we derive a weak formulation of Maxwell's equations and finally introduce Trefftz-type basis functions.

2.1 Maxwell's Equations in 1D

For a wave traveling in the x -direction, with electric and magnetic fields polarized as $E := E_y$ and $H := H_z$, we can write Maxwell's equations in the one dimensional form

$$\begin{aligned} \begin{pmatrix} \partial_t \\ \partial_x \end{pmatrix}^T \cdot \begin{pmatrix} \varepsilon & 0 \\ 0 & 1 \end{pmatrix} \cdot \begin{pmatrix} E \\ H \end{pmatrix} &= 0, \\ \begin{pmatrix} \partial_t \\ \partial_x \end{pmatrix}^T \cdot \begin{pmatrix} 0 & \mu \\ 1 & 0 \end{pmatrix} \cdot \begin{pmatrix} E \\ H \end{pmatrix} &= 0. \end{aligned} \quad (1)$$

Here μ is the magnetic permeability and ε is the dielectric permittivity. We assume the space-time domain of interest Ω to be free of any sources. With the abbreviations

$$\eta_\varepsilon := \begin{pmatrix} \varepsilon & 0 \\ 0 & 1 \end{pmatrix}, \quad \eta_\mu := \begin{pmatrix} 0 & \mu \\ 1 & 0 \end{pmatrix} \quad \text{and} \quad \nabla := \begin{pmatrix} \partial_t \\ \partial_x \end{pmatrix},$$

we cast Maxwell's equations into the form

$$\nabla^T \cdot \eta_\varepsilon \cdot \mathbf{F} = 0 \quad \text{and} \quad \nabla^T \cdot \eta_\mu \cdot \mathbf{F} = 0. \quad (2)$$

Here the EM field vector \mathbf{F} reads

$$\mathbf{F} := \begin{pmatrix} E \\ H \end{pmatrix}.$$

2.2 Weak DG-Form of Maxwell's Equations

We obtain the weak form of (2) by multiplying (2) with a vectorial test function

$$\mathbf{v} := \begin{pmatrix} v^E \\ v^H \end{pmatrix}.$$

and integrating over the domain of interest. This leads to the following form

$$\int_{\Omega} (\nabla^T \cdot \eta_\varepsilon \cdot \mathbf{F}) v^H dA + \int_{\Omega} (\nabla^T \cdot \eta_\mu \cdot \mathbf{F}) v^E dA = 0,$$

After integration by parts and a subsequent application of the Gauss Theorem the weak form of Maxwell's equations reads

$$\begin{aligned} \int_{\partial\Omega} v^H (\eta_\varepsilon \cdot \mathbf{F}) \cdot \mathbf{n} d\Gamma - \int_{\Omega} (\nabla^T v^H) \cdot \eta_\varepsilon \cdot \mathbf{F} dA \\ + \int_{\partial\Omega} v^E (\eta_\mu \cdot \mathbf{F}) \cdot \mathbf{n} d\Gamma - \int_{\Omega} (\nabla^T v^E) \cdot \eta_\mu \cdot \mathbf{F} dA = 0. \end{aligned} \quad (3)$$

where \mathbf{n} is the unit normal on the space-time domain boundary $\Gamma := \partial\Omega$.

2.3 The Trefftz Basis

Standard FEM uses generic polynomials as basis functions. However, problem-specific basis functions, especially Trefftz-type functions [6] can provide much

better accuracy. Here, we use vectorial basis functions whose components are transport polynomials (see Fig. 1) of the form

$$\mathbf{u}^{p,\pm} = \begin{pmatrix} u^{E,p,\pm} = \pm(x \pm vt)^p \\ u^{H,p,\pm} = Z(x \pm vt)^p \end{pmatrix}, \quad (4)$$

where $Z = \sqrt{\frac{\mu}{\epsilon}}$ is the intrinsic impedance and v the speed of light in the medium. The basis function $\mathbf{u}^{p,+}$ corresponds to a wave traveling leftward whereas $\mathbf{u}^{p,-}$ corresponds to a wave traveling rightward; p is the order of the basis function. The field vector is a linear combination of the Trefftz waves

$$\mathbf{F} = \sum_{p=0}^P f^p (\mathbf{u}^{p,+} + \mathbf{u}^{p,-}), \quad (5)$$

where P is the maximum order of approximation and f^p is the field coefficient of order p . Therefore the total number of coefficients f^p is $2(1+P)$, each corresponding to a vectorial basis function \mathbf{u}^p .

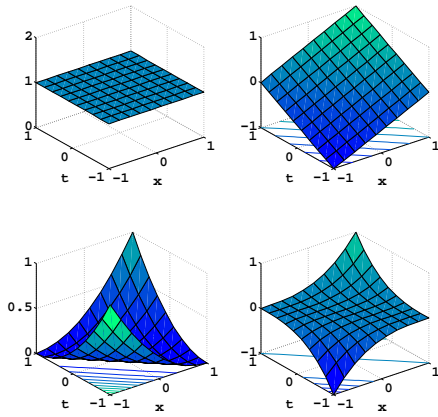


Fig. 1. The first four transport polynomials of order $p = 0, p = 1, p = 2$ and $p = 3$ plotted in a computational space-time domain $(x, t) \in [-1, 1] \times [-1, 1]$

3 Results

As a first test of the new method, we simulate a Gaussian wave in a domain with an interface between two media at $x = -5$. For obtaining Fig. 2 we set $P = 10$, $N_s = 30$ and $N_t = 60$. The medium left of $x = -5$ is a medium with $\mu = 1$ and $\epsilon_r = 16$. The space-time solution shows the right behavior in each medium. At the interface a partial reflexion occurs with the right amplitudes of the reflected and transmitted waves. Also the speed-of-light in the medium changes (by a factor of four) resulting in a different trace-angles. In Fig. 3 the relative error of the vacuum simulation is plotted against the number of the Degrees of Freedom (DoF). We obtain exponential convergence of the relative error measured in the \mathcal{L}^2 norm.

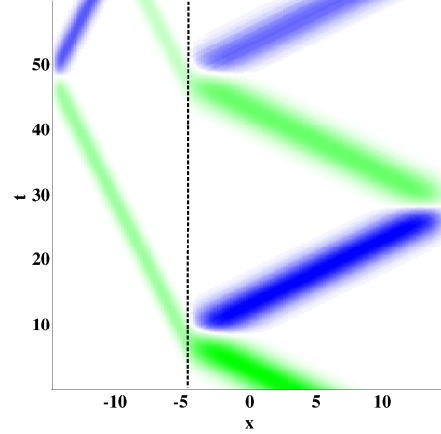


Fig. 2. The electric field of a 1D Gaussian wave, simulated with the DGT-FEM. The solution in the whole space-time domain of interest $(x, t) \in [-15, 15] \times [0, 60]$ is displayed. A medium interface is set at $x = -5$.

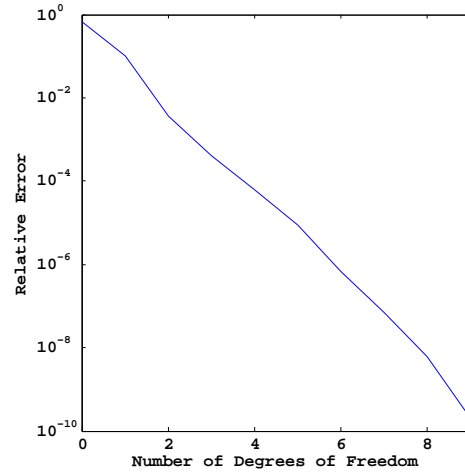


Fig. 3. The relative error of the vacuum simulation plotted against the number of the Degrees of Freedom.

References

1. W. Reed, T. Hill, Triangular mesh methods for the neutron transport equation, *Tech. rep., Los Alamos Scientific Laboratory Report*, 1973.
2. P. LeSaint, P.-A. Raviart, *On a finite element method for solving the neutron transport equation*, Academic Press, 89–123, 1974.
3. B. Cockburn, C. Shu, Runge–Kutta discontinuous Galerkin methods for convection-dominated problems, *J Sci Comput* 16 (3), 173–261, 2001.
4. S.M. Schnepp, Thomas Weiland Efficient large scale electromagnetic simulations using dynamically adapted meshes with the discontinuous Galerkin method *J. of Comput. Appl. Math. (Article in Press)*, 2011.
5. J. Jirousek, A.P. Zielinski Survey of Trefftz-type element formulations. *Comput. Struct.* 63, 1997.
6. I. Tsukerman Electromagnetic applications of a new finite-difference calculus. *IEEE Trans. Magn.* 41 (7) 22062225, 2005.

Novel alternate mixed-mode chaotic circuit models for secure communication

Umesh Kumar

Department of Electrical Engineering

IIT, New Delhi, India

E.mail:drumeshkumar98@rediffmail.com

Abstract---In this paper we explore alternative models to implement the nonautonomous as well as autonomous chaotic dynamics in mixed-mode chaotic circuits. The parallel LC circuit based MMCC model and Wien bridge oscillator based MMCC model are presented alongwith their Pspice simulations to verify their mixed mode chaotic behaviour. Virtual simulations of alternative implementations of mixed-mode chaotic circuit were found satisfactory and successful.

Keywords:- Chaos, chaotic oscillator, mixed-mode chaotic circuit, Parallel LC circuit, Wien bridge circuit, secure communication.

I. INTRODUCTION

The first mixed-mode chaotic circuit was proposed by Recai Kilic et al in 2000 [1] which is a combination of both an autonomous chaotic Chua's circuit and a nonautonomous chaotic MLC circuit developed by Murali et al in 1994 [9]. It is able to provide greater reliability in the form of a wide range of parameter variations and extra security keys. Since then various improved realisations of MMCC have been presented [2,3,4] including circuits using CFOA's. Senani R and Gupta S S [8] have reported implementation of Chua's chaotic circuit using current feedback Op amps in 1998. Robust Op amp realisations of Chua's circuit was reported by Kenndy M P [10] in the year 1992. Recently MMCC circuits using quadrature core oscillators and blocks were reported by Klomkarn K and Sooraksa P [5,11] in the years 2010 -2011. Work on impulsive synchronization between two MMCC have also been

reported by Recai Kilic [6, 7] in the years 2005 and 2006.

II. ALTERNATE REALISATIONS

(a)The parallel LC autonomous model

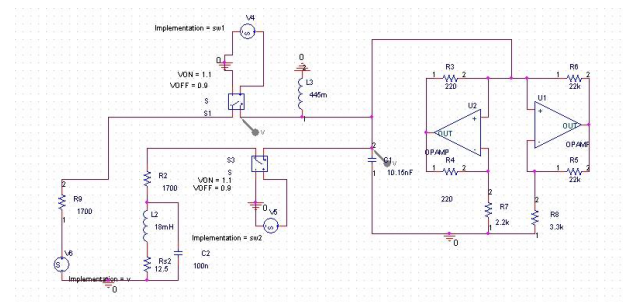


Figure 1 Parallel LC circuit based MMCC circuit

In this model, we have replaced the series LC combination in the non-autonomous mode with a parallel LC circuit as shown above in figure 1.

(b) Wien bridge oscillator based MMCC model

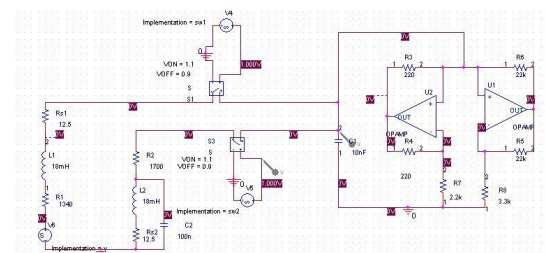


Fig. 2 Wien bridge oscillator based MMC Model.

In this model, we have replaced the original autonomous part with a Wien Bridge Oscillator based implementation. Theoretically a gain of 3 would be required to start the oscillations. In our

circuit, we have implemented a slightly higher gain, that is, a gain of 3.1.

III CONCLUSIONS

Virtual simulations of alternative implementations of the mixed-mode circuit were successful and satisfactory. As can be seen from the transient analysis of capacitor voltage, we see how the circuits jump to and fro the non-autonomous and the autonomous mode of operation. The first model clearly exhibits the characteristics of a parallel LC circuit along with the dynamics due to the autonomous mode. The resultant chaos was satisfactory. The Wien Bridge Oscillator based model was simulated and the resulting plot showed double scroll attractor characteristic.

REFERENCES

1. Kilic R., Alci M. & Tokmakci M., "Mixed-mode chaotic circuit", *Electron. Lett.* 36(2), 2000, pp 103-104.
2. Kilic R., Alci M., Ugur Cam & Hakan Kuntman, "Improved Realisation of Mixed-mode chaotic circuit", *International Journal of Bifurcation and chaos*, Vol. 12, No. 6, 2002, pp 1429-1435.
3. Cam U., "A new high performance realization of mixed-mode chaotic circuit using current-feedback operational amplifiers", *Computers and Electrical Engineering*, Elsevier 30, 2004, PP 281-290.
4. Kilic R., Yildirim F., "Current-feedback operational amplifier based inductorless mixed-mode Chua's circuits", *International Journal of Bifurcation and chaos*, Vol. 16, No. 3, 2006, pp 709-714.
5. Klomkarn K., Sooraksa P. & Chen G., "New construction of mixed-mode chaotic circuits", *International Journal of bifurcation and chaos*, Vol. 20, No. 5, 2010, pp 1485-1497.
6. Kilic R., "Impulsive synchronization between two mixed-mode chaotic circuits", *Journal of circuits, systems and computers*, World Scientific, Vol. 14, No. 2, 2005, pp 1-14.
7. Kilic R., "Experimental investigation of Impulsive synchronization between two mixed-mode chaotic circuits", *International Journal of Bifurcation and chaos*, Vol. 16, No. 5, 2006, pp 1527-1536.
8. Senani R. and Gupta S.S., "Implementation of Chua's chaotic circuit using current feedback op-amps, *Electron. Lett.* 34, 1998, pp 829-830.
9. Murali K., Lakshmanan, M. & Chua L. O., "Bifurcation and chaos in the simplest dissipative non-autonomous circuit", *International journal of Bifurcation and chaos*, Vol. 6, 1994, pp 1511-1524.
10. Kennedy M.P., "Robust op-amp realization of Chua's circuit", *Frequenz*, 1992, 46, pp 66-80.
11. Sergio F., "Design with operational amplifiers and analog integrated circuits, 3rd edition, 2002, McGraw-Hill, NY.
12. Klomkarn K., Sooraksa P. & Chen G., "Simple self instructional modules based on chaotic oscillators: Few blocks generating many patterns", *International Journal of bifurcation and chaos*, Vol.21, No.5, 2011 pp. 1469-1491.

Derivation and test of high order fluid model for streamer discharges

Aram Markosyan¹, Saša Dujko^{1,2}, and Ute Ebert^{1,3}

¹ CWI, P.O. Box 94079, NL-1090 GB Amsterdam, Netherlands Aram.Markosyan@cwi.nl

² Institute of Physics, P.O.Box 68, 11080 Zemun Belgrade, Serbia sasha@phy.bg.ac.yu, S.Dujko@cwi.nl

³ Eindhoven University of Technology, P.O. Box 513, 5600 MB Eindhoven, Netherlands Ebert@cwi.nl

Summary. A high order fluid model for streamer dynamics is developed by closing the system after the 4th moment of the Boltzmann equation in local mean energy approximation. This is done by approximating the high order pressure tensor in the heat flux equation through the previous moments. Mathematical characteristics of the system is studied. Then planar ionization fronts for negative streamers in N₂ are simulated with the classical streamer model, MC-PIC particle model, and with the present higher order model.

1 High order fluid model

Streamer discharges occur in nature and as well in many industrial applications such as the treatment of exhaust gasses, polluted water or biogas. They appear when non-ionized or lowly ionized matter is exposed to high electric fields. Here we present a high order fluid model for streamer discharges, and we use it to simulate planar ionization fronts for negative streamers in nitrogen under normal conditions; and we compare the results with those of the classical fluid model.

1.1 Model description

The high order model is derived by taking the first 4 moments of the Boltzmann equation, i.e., by multiplying the Boltzmann equation with the k th power of velocity ($k = 0, 1, 2, 3$) and integrating over velocity space. In principle, the set of moment equations is infinite, but we consider only electron density ($k = 0$), momentum ($k = 1$), energy ($k = 2$) and energy flux ($k = 3$). The system is truncated in the energy flux equation (4) by approximating the high order pressure tensor by the product of lower order moments and by introducing factor of parametrization β . As a result the hydrodynamical formalization of the streamer dynamics in 1D is described by the nonlinear system of equations

$$\partial_t \mathbf{u} + \mathbf{A}(\mathbf{u}) \partial_x \mathbf{u} = \mathbf{F}(\mathbf{u}), \quad (1)$$

where the primitive variables are

$$\mathbf{u} = (n, nv, n\mathcal{E}, n\xi)^T, \quad (2)$$

the matrix $\mathbf{A}(\mathbf{u})$ is defined in following way

$$\mathbf{A}(\mathbf{u}) = \begin{pmatrix} 0 & 1 & 0 & 0 \\ 0 & 0 & \frac{2}{3m} & 0 \\ 0 & 0 & 0 & 1 \\ -\beta \frac{2\mathcal{E}^2}{3m} & 0 & \beta \frac{4\mathcal{E}}{3m} & 0 \end{pmatrix}, \quad (3)$$

and the source term is

$$\mathbf{F}(\mathbf{u}) = \begin{pmatrix} nvI \\ \frac{nqE}{m} - nvv_m \\ qEnv - n\{v_e[\mathcal{E} - \frac{3}{2}kT_0] + \sum_{\alpha} v_{e\alpha}\mathcal{E}_{e\alpha} + v_I\mathcal{E}_I\} \\ \frac{5qE}{3m}n\mathcal{E} - n\xi v_m \end{pmatrix}. \quad (4)$$

Here n , v , \mathcal{E} and ξ are electron number density, average electron velocity, average electron energy and electron energy flux, correspondingly. E is the electric field and T_0 is room temperature. $v_m(\mathcal{E})$ and $v_e(\mathcal{E})$ are the momentum and elastic energy transfer collision frequencies, $v_I(\mathcal{E})$ is the ionization frequency and $v_{e\alpha}(\mathcal{E})$ are the collision frequencies for inelastic processes. As charge is conserved, the continuity equation for the ion density n_{ion} is

$$\partial_t n_{ion} = nvI, \quad (5)$$

when the ions are approximated as immobile. Space charge effects are taken into account through the Poisson equation

$$\partial_x E = \frac{e}{\epsilon_0}(n_{ion} - n), \quad (6)$$

where ϵ_0 is the dielectric constant and e is the elementary charge.

Mathematical characteristics and numerical solution of the system

Lemma 1. *The system (1) is hyperbolic if and only if*

$$\beta = 0 \quad \text{or} \quad \beta \geq 1. \quad (7)$$

In the case of $\beta > 1$, the system (1) is strictly hyperbolic.

Although the eigenvalues of (1) have a simple form, the corresponding right and left eigenvectors are very complicated, which makes it impossible to work with them.

The finite volume method is used to spatially discretize the system (1),(5),(6) on uniform control volumes or cells V_j as follows:

$$V_j := [j\Delta x, (j+1)\Delta x), \quad x_j := \left(j + \frac{1}{2}\right) \Delta x, \quad (8)$$

where $j = 0, 1, \dots, M-1$, $\Delta x = L/M$ is the spatial grid size and L is the length of the simulation domain. To approximate the spatial derivative in (1) we use the second-order central difference discretization [1]. In our numerical experiments we saw that this spatial discretization approximates quite well the analytically predicted front velocity for the minimal model [2]. The time derivatives are approximated with the Runge-Kutta 4 method [1]. This is an explicit method, which always has a bounded stability domain. In our case the stability condition or CFL restriction is

$$\beta \sqrt{\frac{2}{3m}} \sqrt{\max \epsilon} \frac{\Delta t}{2\Delta x} \leq C, \quad (9)$$

where C depends on the particular method and space discretization. In our simulations we use the value $C = 0.1$.

1.2 Particle model and classical fluid model

In essentially all numerical fluid models for streamers in the past 30 years, except for [3, 4], the electron density is approximated by a reaction drift diffusion approximation

$$\partial_t n - \partial_x (\mu E n + D \partial_x n) = n \nu_I, \quad (10)$$

This model is called the minimal model; it implies a local field approximation of reaction and transport coefficients.

As a second reference model we use the MC-PIC particle model from [5].

2 Results and discussion

Fig. 1 compares the results of the high order model, the particle model and of the minimal model for the same initial and boundary conditions and for the same electric field ahead of the ionization front. A multi term theory for solving the Boltzmann equation [6] is used to calculate flux transport coefficients and mean-energy dependent collisional rates required as an input in fluid equations.

The following main conclusions can be drawn:

1) The overall front structure is the same, but the particle model is much better approximated by the high order model than by the minimal model.

2) That the mean electron energy ahead of the front increases while the electric field is constant, was also seen in Monte Carlo simulations before [2], but

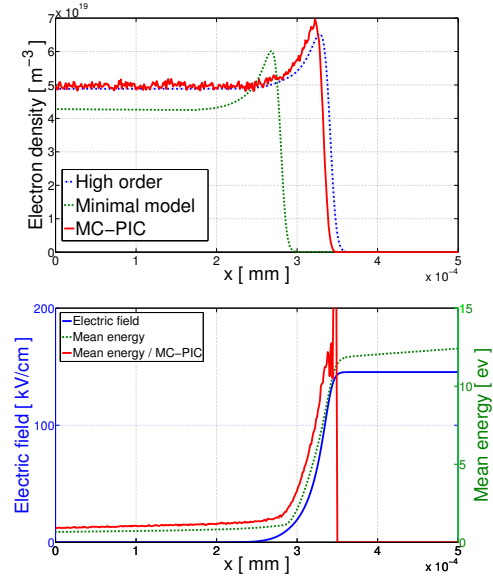


Fig. 1. Top: Electron density profile for the high order model (dashed dotted line, blue), the particle model (solid line, red) and for the minimal model (dashed line, green), bottom: mean electron energy (dashed line, green) and electric field (solid line, blue) profiles in the high order model, mean electron energy in the particle method (solid line, red). The plots show the simulation for instant 0.7 ns for identical initial conditions. The electric field ahead of the ionization front is 145 kV/cm at standard temperature and pressure, which corresponds to 590 Td.

not yet included in fluid models. The mean electron energy behind the front where the electric field vanishes, is close to 1 eV, because energy relaxation is slow in this region. This feature was not included in fluid models before.

In summary, the new high order fluid model captures effects in streamer simulations that up to now were only inherent in the more microscopic Monte Carlo simulations. This is a step forward for long time calculations.

Acknowledgement. Aram Markosyan acknowledges support by STW-project 10751.

References

1. W. Hundsdorfer, J. Verwer. *Numerical Solution of Time-Dependent Advection-Diffusion-Reaction Equations*. Springer, Berlin Heidelberg New York, 2003.
2. C. Li et al. *J. Appl. Phys.* 101, 123305 (2007).
3. C. Li et al. *J. Phys. D: Appl. Phys.* 42, 202003 (5p) (2009).
4. Z. Kanzari et al. *J. Appl. Phys.* 84, 4161 (1998).
5. C. Li et al. *J. Phys. D: Appl. Phys.* 41, 032005 (2008).
6. R. D. White et al. *J. Phys. D: Appl. Phys.* 42 (2009) 194001.

Simulation of a double-gate MOSFET by a non parabolic energy-transport subband model based on MEP including surface roughness scattering

V. D. Camiola¹, G. Mascali², and V. Romano¹

¹ University of Catania, Italy camiola@dmi.unict.it, romano@dmi.unict.it

² University of Calabria, and INFN-Gruppo collegato di Cosenza, Italy mascali@unical.it

Summary. A nanoscale double-gate MOSFET is simulated by using a model based on the maximum entropy principle (MEP) by including the surface scattering roughness. The influence of this latter on the electrical performance of the device is discussed.

1 Mathematical model and simulations

The main aim of the paper is to simulate the nanoscale silicon double gate MOSFET (hereafter DG-MOSFET) shown in Fig. 1. The length of the diode is $L_x = 40$ nm, the width of the silicon layer is $L_z = 8$ nm and the oxide thickness is $t_{ox} = 1$ nm. The n^+ regions are 10 nm long. The doping in the n^+ regions is $N_D(x) = N_D^+ = 10^{20} \text{ cm}^{-3}$ and in the n region is $N_D(x) = N_D^- = 10^{15} \text{ cm}^{-3}$, with a regularization at the two junctions by a hyperbolic tangent profile.

Due to the symmetries and dimensions of the device, the transport is, within a good approximation, one dimensional and along the longitudinal direction with respect the two oxide layers, while the electrons are quantized in the transversal direction. Six equivalent valleys are considered with a single effective mass $m^* = 0.32m_e$, m_e being the free electron mass.

Since the longitudinal length is of the order of a few tents of nanometer, the electrons as waves achieve equilibrium along the confining direction in a time which is much shorter than the typical transport time. Therefore we adopt a quasi-static description along the confining direction by a coupled Schrödinger-Poisson system which leads to a subband decomposition, while the transport along the longitudinal direction is described by a semiclassical Boltzmann equation for each subband.

Numerical integration of the Boltzmann-Schrödinger-Poisson system is very expensive, from a computational point of view, for computer aided design (CAD) purposes (see references quoted in [1, 2]) In [1] we have formulated an energy transport model for the charge transport in the subbands by including the non parabolicity effect through the Kane dispersion relation. The model has been obtained, under a suitable diffusion scaling, from the Boltzmann equations by using the moment method and closing the mo-

ment equations with the Maximum Entropy Principle (MEP). Scatterings of electrons with acoustic and non polar optical phonons are taken into account. The parabolic subband case has been treated and simulated in [2].

The main aim of the present paper is to include also the surface roughness scattering in which electrons scatter off the boundaries of the confining potential. The rate of this scattering is higher when the gate voltage increases and the width of the silicon layer is below ten nm and therefore comparable with the fluctuations in the oxide thickness. We want to assess the relevance of this scattering on the electric performance of the device after proposing an appropriate numerical scheme for the MEP energy transport-Schrödinger-Poisson system. In the Figures we report the results obtained by including the nonparabolicity effects but without surface roughness scattering. These preliminary simulations are rather encouraging and we are currently working upon the inclusion of the scattering at the surface.

Acknowledgement. V.D.C. and V. R. acknowledge the financial support by the P.R.I.N. project 2010 Kinetic and macroscopic models for particle transport in gases and semiconductors: analytical and computational aspects and by P.R.A. University of Catania. G. M. acknowledges the financial support by P.R.A., University of Calabria.

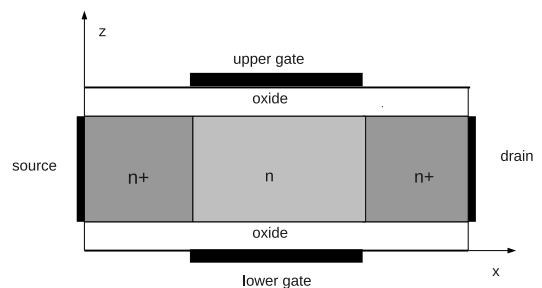


Fig. 1. Simulated DG-MOSFET

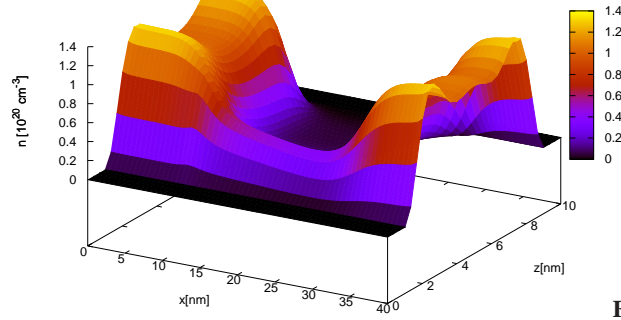


Fig. 2. Density in the case source-drain voltage $V_D = 0.5$ V and both gate voltages equal to -3 V

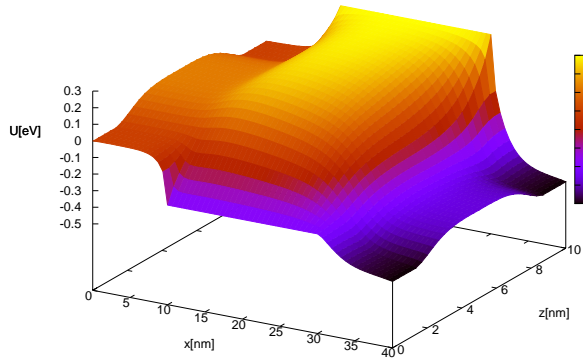


Fig. 3. Electrostatic potential energy in the same case as in Fig. 2

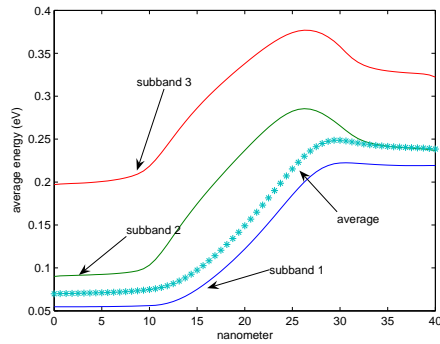


Fig. 4. Energies in the first three subbands in the case $V_D = 0.5$ V and lower gate voltage $V_{gl} = -3$ V, upper gate voltage $V_{gu} = 3$ V

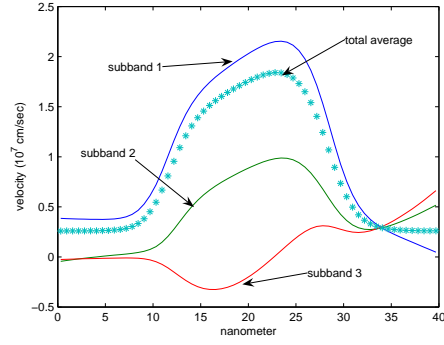


Fig. 5. Velocities in the first three subbands in the same case as in Fig. 4

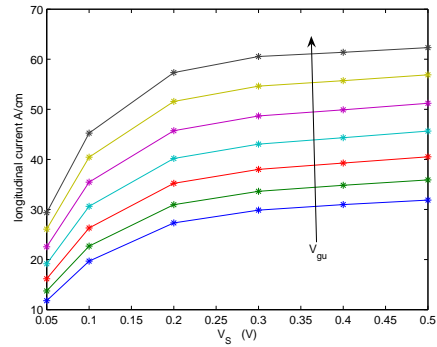


Fig. 6. Longitudinal mean current (A/cm) versus the source-drain voltage V_D with $V_{gl} = -3$ V and V_{gu} ranging from -3 V to +3 V according to the arrow

References

1. G. Mascali, and V. Romano, A non parabolic hydrodynamical subband model for semiconductors based on the maximum entropy principle. *Mathematical and Computer Modelling* 55: 1003, 2012
2. V. D. Camiola, G. Mascali, and V. Romano, Numerical simulation of a double-gate MOSFET with a subband model for semiconductors based on the maximum entropy principle. *Continuum Mech. Thermodyn.* (2012) (already available online).

On the autocorrelation of environment induced noise

B.L. Michielsen

Onera, Toulouse, France Bastiaan.Michielsen@Onera.fr

Summary. A fundamental relation between energy loss in electromagnetic engineering models leads to the definition of canonical stochastic fields. This canonical stochastic electromagnetic field model, which has been established in previous work (see [2–4]), is here used to construct stochastic processes weakly equivalent to the induced processes according to the canonical field model. Such processes can be used to test electronic systems, in particular communication links which are sensitive to specific correlation distances in induced noise.

1 Introduction

Because the environment in which an electronic system has to operate is not deterministically known, stochastic fields play an important role in electronic system testing. In this contribution, we elaborate on a fundamental relation between “energy loss” and stochastics generalising the well-known concept of noise temperature in electronics. The fundamental observation is that if a system’s model shows loss of electromagnetic energy into some environment, it is implied that this environment works as a stochastic source of electromagnetic energy on the system in question.

We shall first recall the definition of a canonical stochastic electromagnetic field having a good space-time covariance operator. Having available this “a priori” model for the stochastic fields in the environment we can try to compute directly those characteristics of the signals which are decisive for our purpose. An example of this is the auto-covariance function of induced noise sources, which gives essential information on the internal structure this noise. In this contribution, we show a rather simple way to compute this auto-covariance function for a large class of problems. We also show how to generate noise realisations, functions of time, and compute the appropriate statistics from simulation results. This may be a practical strategy for essentially non-linear problems or when a direct method is not known.

2 Basic field theory

The energy emission operator of time-domain electromagnetic field theory is given by $C(J) = E(J) - \overline{E(\bar{J})}$ (\bar{X} is the time reversal of X). This is the electric field

propagator anti-symmetrised with respect to time reversal, i.e., $C(\bar{J}) = -C(J)$. The following integral relation justifies the name.

$$\int_{D \times \{t_1\}} (\mu_0 H^a \cdot H^b + \epsilon_0 E^a \cdot E^b) = - \int_{D \times (t_0, t_1)} C(J^b) \cdot J^a \quad (1)$$

Here (t_0, t_1) is a time interval and the current distributions J^a and J^b have their spatial support in D and vanish outside the given time interval.

It has been shown in [4] that this energy emission operator is also the covariance operator, C_E , of a stochastic field defined by a probability measure on the space of initial values, $\mathcal{S}'(\mathbb{R}^3 \times \{t_0\})$, (\mathcal{S}' , here, denotes the vector-valued tempered distributions), i.e., by a stochastic distribution $\psi_0 = (e_0, h_0)$, such that

$$\forall f, g \in \mathcal{S} \quad \mathbb{E}(\langle \psi_0, f \rangle \langle \psi_0, g \rangle) = \sigma^2 \langle f, g \rangle_{\mathcal{H}}$$

where \mathcal{S} is Schwartz’ space of infinitely smooth test fields, \mathcal{H} is the direct sum Hilbert space with the inner product given by the LHS of (1) and $\mathcal{S} \subset \mathcal{H} \subset \mathcal{S}'$ are dense inclusions (see [1]). We obtain for any two distributions J^a and J^b ,

$$\int_{D \times (t_0, t_1)} C_{E_0}(J^a) \cdot J^b = \sigma^2 \int_{D \times (t_0, t_1)} C(J^a) \cdot J^b \quad (2)$$

where E_0 is the electric field corresponding to the stochastic distribution ψ_0 on $D \times \{t_0\}$ and σ^2 a variance parameter of this stochastic initial value distribution.

3 Observables on stochastic fields

We now concentrate on Thévenin sources representing the action of electromagnetic fields, in some environment, on an electronic system placed in it. Thévenin sources are “observables” defined through distributions on electromagnetic fields. For example, $\mathcal{V} = \langle J_P, E \rangle = \int_P E$, where P is a curve defining an electronic port and E is the total electric field in the port region. If the electric field is a stochastic field, the given formula defines the Thévenin source as a generalised stochastic process.

An important characteristic is the auto-covariance of the Thévenin sources as function of time. Supposing that the average field is zero, we get,

$$\begin{aligned} \mathbb{E}(V(t_1)V(t_2)) &= \mathbb{E}(\langle J_{P,t_1}, E \rangle \langle J_{P,t_2}, E \rangle) \\ &= \langle J_{P,t_1}, C_E(J_{P,t_2}) \rangle \end{aligned} \quad (3)$$

where C_E is the covariance operator of the stochastic field E . Thévenin sources have alternative integral representations in terms of a time reversed current distribution, $\overline{j(t)}$, on the conductors of the electronic system and only the incident part of the total electric field. The current distribution, $j(t)$, appearing in such a representation is the one appearing by applying a Dirac current source to the electronic port considered. This current distribution corresponds to the scattering of an elementary dipole field by the conductors of the system. The electric field, $e = C_E(j)$, appearing in (3), is the opposite of the trace of the elementary dipole field on the conductors. This simplifies (3) to $\mathbb{E}(V(t_1)V(t_2)) = \langle j(t_1), e(t_2) \rangle$, which is more easily computed than the general expression.

4 Statistically equivalent stochastic processes and the radiation resistance

The analysis presented thus-far, allows for estimating a priori covariances of interference sources to be applied to system models accounting for uncertain environments in a way consistent with the mechanisms of electromagnetic energy loss to this environment. In order to actually test a system by simulations using the stochastic environment model, we may want to generate time functions for the noise sources and compute statistics on the essential properties of the system. The question arises, then, whether the generated time functions are representative for those one will obtain in the actual situation. However, such a question has no answer, the only thing we can find out is whether a set of generated time functions is statistically equivalent to the actual processes we try to model. That means if we create sufficiently many functions with our algorithm, we want that the statistics we are interested in converge to the statistics we would obtain in the situation we model. In our case, we want the sample functions we generate to have an autocorrelation function with a good convergence to the autocorrelation function obtained in the actual situation.

We will obtain the desired result in two steps. The first step is to show how we can compute the spectral representation of the autocovariance function of an observable on a canonical stochastic field. The second step is to apply a standard Fourier integral representation trick to generate a stochastic process which has this auto covariance function.

The autocovariance of the observable Thévenin source V is given by

$$\begin{aligned} C_V(s, t) &= \mathbb{E} \left[\int_{\omega \in \mathbb{R}} V_{\omega}(s) \int_{\nu \in \mathbb{R}} V_{\nu}(t) \right] \\ &= \int_{\omega, \nu \in \mathbb{R}^2} \langle j_{\omega}(s), C_E j_{\nu}(t) \rangle \\ &= \int_{\omega, \nu \in \mathbb{R}^2} \langle \widehat{j_{\omega}} \exp(j\omega s), C_E \widehat{j_{\nu}} \exp(j\omega t) \rangle \end{aligned}$$

where $\widehat{j_{\omega}}$ is the spectral component of the current distribution defining the observable.

Using the stationarity of the processes, i.e. invariance under time translations, we can reduce the double integral over the frequencies to a single one and we get

$$\begin{aligned} \forall t \in \mathbb{R} \quad C_V(t, t + \tau) &= \int_{\omega \in \mathbb{R}} \langle j_{\omega}, E(j_{\omega}) \rangle \exp(j\omega \tau) \\ &= \int_{\omega \in \mathbb{R}} R_j(\omega) \exp(j\omega \tau) \end{aligned}$$

and $R_j(\omega)$ is the frequency domain radiation resistance of the current distribution j_{ω} .

For the second step, we use a well-known relation

$$\mathbb{E}[f(t)f(s)] = \int_{\omega \in \mathbb{R}} \text{var}(\widehat{f}(\omega)) \exp(j\omega(s-t))$$

valid for spectral amplitudes $\widehat{f}(\omega)$ and $\widehat{f}(\nu)$ statistically independent if $\nu \neq \pm\omega$, and, in addition satisfying $\mathbb{E}[\text{Re}(\widehat{f}(\omega))\text{Im}(\widehat{f}(\omega))] = 0$ and $\mathbb{E}[\text{Re}(\widehat{f}(\omega))^2] = \mathbb{E}[\text{Im}(\widehat{f}(\omega))^2]$. This result implies that a stochastic process which has spectral amplitudes satisfying the said constraints and have a variance equal to the frequency domain radiation resistance has the correct autocovariance function.

5 Conclusion

We obtain explicitly computable time functions which are realisations of a stochastic process statistically equivalent (with respect to the autocorrelation function) to an observable on a canonical stochastic field. This process includes the geometrical properties of the system, by means of the traversal times and the evaluation of the defining current distributions on the material configuration, but it also accounts for resonances in the configuration and between the configuration and the environment through the environment's Green function which defines the space-time covariance operator of the canonical stochastic field.

References

1. Gel'fand, I.M. and Vilenkin, N.Ya., "Generalised Functions" vol. 4, Academic Press, New York and London, 1964
2. Michielsen, B.L. and Fiachetti, C., "Covariance operators, green functions and canonical stochastic fields", *Radio Science*, 40(5):1–12, 2005.
3. B.L. Michielsen "Canonic Stochastic Electromagnetic Fields", Scientific Computing in Electrical Engineering, SCEE 2008, Helsinki, Finland
4. Michielsen, B., "Stochastic Processes Induced by Electromagnetic Waves with White Noise Initial Values", WAVES 2009, Pau, France

CIBSOC Program – Spiral Inductor Inductance Calculation and Layout Optimization

Claudia Pacurar¹, Vasile Topa¹, Adina Racasan¹, Calin Munteanu¹

¹Technical University of Cluj-Napoca, 26-28 Baritiu Street, Romania, Claudia.Pacurar@et.utcluj.ro; Vasile.Topa@et.utcluj.ro; Adina.Racasan@et.utcluj.ro; Calin.Munteanu@et.utcluj.ro

Summary Spiral inductors are very often used in integrated circuits for many applications. To design spiral inductors or to improve the spiral inductors performances is absolutely necessary to calculate their inductances and/or to optimize their layouts. In this effect we create a software program, named CIBSOC (Spiral Inductors Inductance Calculation and Layout Optimization). The program is dedicated to calculate dc inductances and to optimize layouts for spiral inductors. We use a wide range of inductors in the applications made with our program. We compare the results of our applications with the measurements results existing in the literature and also with the results that we have obtained using a commercial field solver in order to validate our program. Our program is accurate enough, has a very friendly interface, is very easy to use and it calculates the problems in a very sort running time compared with other similar programs. Since spiral inductors tolerance is generally on the order of several percent, a more accurate program is not needed in practice. The program is very useful for the spiral inductors design, because it calculates the inductance of spiral inductors with a very good accuracy. It is also useful for the spiral inductors optimization, because it affords optimal solutions for spiral inductor layouts in terms of the technological limitations and/or of the users' needs.

1. Introduction

The passive components parameters extraction from radio frequency integrated circuits such as inductance, capacitance and resistance extraction are research topics of great interest and also very provocative. This fact is motivate by the continual technological progress thanks to it is now possible to implement integrated circuit at microns dimensions. The minimization of the integrated circuit dimensions at this extreme level lead in an implicit way to the significant rise of parameters extraction importance. These parameters must be calculated with a very good accuracy. We focus on inductance calculation. The inductance value extraction was and is intense studied in the literature. At this moment exists many expressions and methods used for integrated circuits inductance extraction [1]-[5],

but as is mentioned in the literature, there are limits in their application.

2. CIBSOC Software Program

To design and to optimize the spiral inductors from integrated circuits is first necessary to find the exact parameters values, such as inductance value. So the fast and accurate inductance extractions become more and more important for design, optimization and design verification of the spiral inductors and for their performances improvement. The exact inductance calculation for spiral inductors; the spiral inductors optimization by finding their optimal layout for a given maximal inductance or for any given inductance value keeping a constant area for the inductor implementation in the integrated circuits are still needed to improve the spiral inductors performances. To this aim we implement a software program that allow fast and accurate inductance calculation and spiral inductor layout optimization. The program is composed of four modules. The first and the second one are create to calculate the spiral inductor inductance. The third and the fourth one are created to optimize the spiral inductor layout.

3. Applications in CIBSCO Program

We create a set of spiral inductors and we implement them in our program to find their inductances and to optimize their layouts. We present in this paper only the spiral inductors with square shape, even if the program allows also the calculation for hexagonal, octagonal and circular shapes of spiral inductors. We use CIBSOC program to calculate the total inductance for each of the square spiral inductor that we create and to optimize their layouts. All the dimensions used in the paper are in [μm] and the inductance values in [nH].

4. Comparison with Measurements

We calculate the inductance for some square spiral inductors that exist in the literature with measurements results (Table I) and we compare these results with the results obtained with our program. We demonstrate the accuracy of our CIBSOC program results.

Table I
Comparison of our results with measurements results

N (turn)	Ref.	d _c (μm)	w (μm)	s (μm)	t (μm)	L _{me} (nH)	L _{CIBSOC} (nH)	ε _r (%)
2.75	[6]	279	18.3	1.9	0.9	3.1	3.009	2.93
7.50	[6]	166	3.2	1.9	0.9	12.4	11.987	3.33
9.50	[6]	153	1.8	1.9	0.9	18.2	17.842	1.96
2.75	[6]	277	18.3	0.8	0.9	3.1	3.055	1.45
5.00	[6]	171	5.4	1.9	0.9	6.10	5.859	3.95
3.75	[6]	321	16.5	1.9	0.9	6.1	6.026	1.21
3.00	[7]	300	19	4	0.9	3.3	3.4977	5.99
5.00	[7]	300	24	4	0.9	3.5	3.7736	7.81
9.00	[7]	230	6.5	5.5	0.9	9.7	9.6791	0.21
8.00	[8]	226	6	6	0.9	9.00	9.143	1.58
16.00	[8]	300	5	4	0.9	34	36.544	7.48
6.00	[7]	300	9	4	0.9	11.7	12.444	6.36

5. Comparison with Commercial Field Solver

To validate our CIBSOC program we consider a very good opportunity to use a demo version of a commercial field solver dedicate to the parameters extraction from different types of complex integrated circuits. We implement in this program a wide range of square spiral inductors starting with the one that we create. The results of inductance variation in terms of the number of turns are presented in Table II.

Table II
Comparison of Results. Inductance vs. number of turns.

Number of turns	L _{CIBSOC} (nH)	L _{commercial program} (nH)
1	1.808	1.7309
2	5.582	5.4228
3	10.527	10.285
4	16.15	15.833
6	28.081	27.637
8	39.347	38.794
12	55.315	54.704
16	60.064	59.646

The inductance variation in terms of the number of turns is plotted in Fig. 1. We observe close agreement between the results. With dotted line

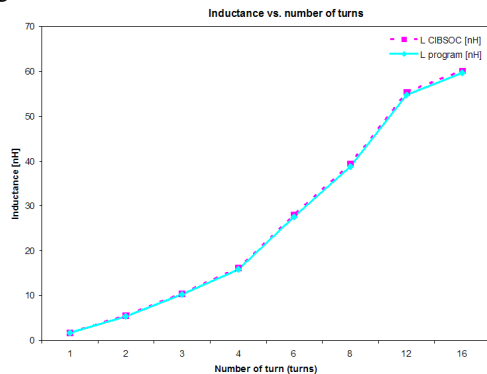


Fig. 1. The comparison of the results obtained with CIBSOC program, and respectively with the parameters extraction program.

are plot the results obtained with our CIBSOC program, and with continuous line the results obtained with the commercial program.

6. Conclusions

The main aim of this paper was to present the inductance calculation and layout optimization for spiral inductors CIBSOC software program implemented by the authors. The program validation was done by comparison of the results obtained with our CIBSOC program, with the measurements results taken form literature and respectively with the results obtained by modeling the square spiral inductors also with a commercial field solver create especially for parameters extraction. Analyzing the results obtain on these three different ways we ascertain the results similitude, the small errors that prove the accuracy of our program. We consider our program very useful for design and for optimization of spiral inductors. It is easy to use and the running times are small compared with other similar programs. We want to extent our program also for ac parameters calculation, at high frequency.

References

1. C. P. Yue, C. Ryu, J. Lau, T. H. Lee, and S. S. Wong, *A physical model for planar spiral inductors on silicon*, in Proceedings IEEE IEDM'96, 1996.
2. J. Crols, P. Kinget, J. Craninckx, and M. Steyeart, *An analytical model of planar inductors on lowly doped silicon substrates for analog design up to 3GHz*, in Symposium on VLSI Circuits, Digest of Technical Papers, 1996, pp. 28-29.
3. H. M. Greenhouse, *Design of planar rectangular microelectronic inductors*, IEEE Transactions on parts, hybrids, and packaging, vol. PHP-10, no. 2, pp. 101-109, 1974.
4. H. A. Wheeler, *Simple inductance formulas for radio coils*, Proceedings of the IRE, vol. 16, no. 10, pp. 1398-1400, October 1928.
5. H. E. Bryan, *Printed inductors and capacitors*, Teletech and electronic industries, 1955.
6. J. J. Zhou and D. J. Allstot, *Monolithic transformers and their application in a differential CMOS RF low-noise amplifier*, IEEE Journal of Solid-State Circuits, vol. 33, no. 12, pp. 2020-2027, 1998.
7. K. B. Ashby, I. A. Koullias, W. C. Finley, J. J. Bastek, and S. Moinian, *High Q inductors for wireless applications in a complementary silicon bipolar process*, IEEE Journal of Solid-State Circuits, vol. 31, no. 1, pp. 4-9, 1996.
8. J. N. Burghartz, K. A. Jenkins, and M. Soyuer, *Multilevel-spiral inductors using VLSI interconnect technology*, IEEE Electron device letters, vol. 17, no. 9, pp. 428-430, 1996.

Circuit Modelling, Simulation and Realization of the new Sundarapandian-Pehlivan Chaotic System

İhsan Pehlivan¹, İsmail Koyuncu², Vaidyanathan Sundarapandian³,
Yılmaz Uyaroglu⁴

¹Electronics and Computer Education Department, Sakarya University, 54187, Esentepe Campus, Sakarya, Turkey, ipehlivan@sakarya.edu.tr

²Department of Control and Automation, Duzce, Vocational High School, Duzce University, Uzun Mustafa Mah. 81010, Duzce, Turkey, ismailkoyuncu@duzce.edu.tr

³Research and Development Centre, Vel Tech Dr. RR & Dr. SR Technical University, Avadi, Chennai-600 062, Tamil Nadu, India, sundarvtu@gmail.com

⁴Sakarya University, Eng. Faculty, Electrical Electronics Engineering Department, 54187, Esentepe Campus, Sakarya, Turkey, uyaroglu@sakarya.edu.tr

Summary

Sundarapandian and Pehlivan discovered a novel chaotic attractor. Basic dynamical properties of the new attractor system were analyzed by means of equilibrium points, eigenvalue structures, Lyapunov exponents and parameters regions [1]. This paper introduces the electronic circuit modelling, simulation and realization of the newly discovered chaotic attractor. Our investigation was completed using a combination of theoretical analysis, simulations and real experimental implementation. To implement as electronics of this new chaotic system is very easy due to having zero initial conditions.

1 Introduction

The Lorenz system displays very complex dynamical behaviour, especially the well-known two-scroll butterfly-shaped chaotic attractor [2]. Chen constructed another chaotic system [3], which is, nevertheless, not topologically equivalent to the Lorenz's system [3]-[4]. The Chen's system is dual to the Lorenz system and similarly has a simple structure [4]. Lü and Chen found the critical chaotic system [5], which represents the transition between the Lorenz and Chen attractors. Recently, Yang et al. [6] and Pehlivan et al. [7] introduced and analyzed the new 3D chaotic systems with six terms including only two quadratic terms in a form very similar to the Lorenz, Chen, Lü and Yang-Chen systems, but they have two very different fixed points: two stable node-foci.

There has been increasing interest in exploiting chaotic dynamics in engineering applications, where some attention has been focused on effectively creating chaos via simple physical systems, such as electronic circuits [8-12].

Motivated by such previous work Sundarapandian and Pehlivan discovered a novel chaotic attractor [1].

In this paper, Section I introduces the Sundarapandian chaotic system. Section 2 presents the electronic circuit modelling and OrCad-PSpice® simulation results. The real circuit implementation oscilloscope outputs are given in Section 3. Finally, conclusions and discussions are given.

2 Circuit Modelling of the Chaotic System

The simple electronic circuit is modelled that can be used to study chaotic phenomena. The circuit employs simple electronic elements such as resistors, and operational amplifiers, and is easy to construct.

Figure 1 and 2 show Orcad-PSpice simulation result and circuit schematic of the 1new chaotic circuit. In this simulation, parameters and initial conditions are taken as $a=1.5$, $b=0.4$, $c=0.4$, $x_1(0)=0$, $x_2(0)=0$, $x_3(0)=0.1$ respectively.

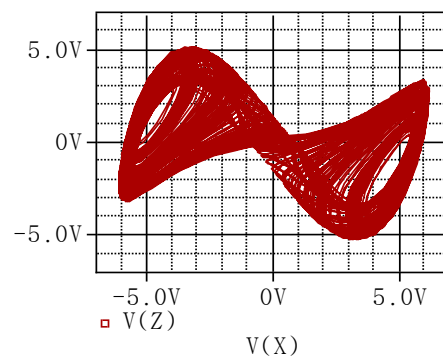


Fig. 1. Pspice Simulation Result of the New Chaotic Circuit (xz-attractor)

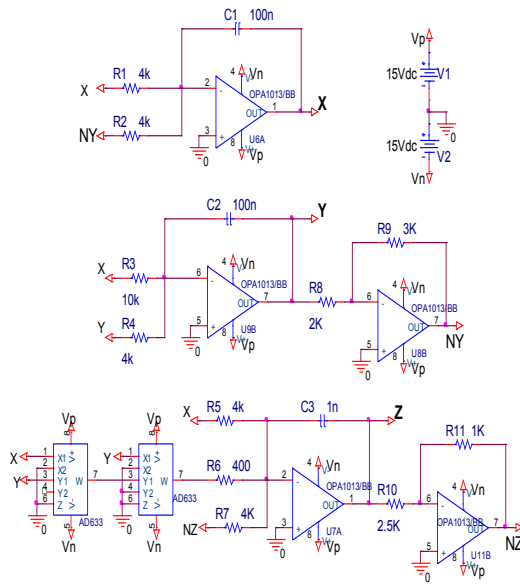


Fig. 2. Circuit Schematic of the New Chaotic Attractor

3 Electronic Circuit Design and Implementation of The New Attractor

Figure 3 shows oscilloscope outputs of the real circuit implementation.

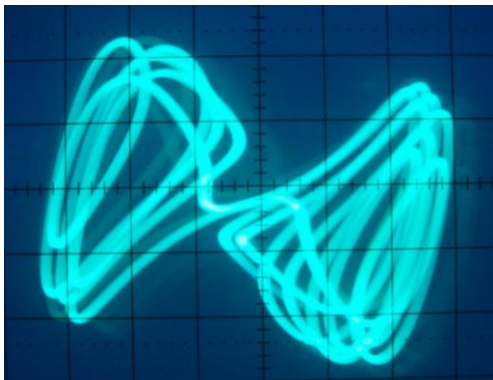


Fig. 3. Oscilloscope output of the real circuit implementation (xz-attractor)

Acknowledgement

This work was supported by the Sakarya University Scientific Research Projects Commission Presidency (No. 2010-01-00-002).

References

1. V. Sundarapandian and I. Pehlivan. *Analysis, Control, Synchronization and Circuit Design of a Novel Chaotic System*. Mathematical and Computer Modelling, (Accepted 2011., doi:10.1016/j.mcm.2011.11.048)
2. E.N. Lorenz. Deterministic Nonperiodic Flow, *Journal of the Atmospheric Sciences*, vol. 20, March 1963, pp. 130-141.
3. G. Chen and T. Ueta. Yet Another Chaotic Attractor, *International Journal of Bifurcation and Chaos*, vol. 9, no. 7, 1999, pp. 1465-1466.
4. T. Ueta and G. Chen. Bifurcation Analysis of Chen's Attractor, *International Journal of Bifurcation and Chaos*, vol. 10, no.8, 2000, pp. 1917-1931.
5. J. Lü and G. Chen. A New Chaotic Attractor Coined, *International Journal of Bifurcation and Chaos*, vol. 12, no. 3, 2002, pp. 659-661.
6. Q.G. Yang, Z.C. Wei and G.R. Chen. An Unusual 3D Autonomous Quadratic Chaotic System with Two Stable Node-Foci, *International Journal of Bifurcation and Chaos*, vol. 20, no. 4, 2010, pp. 1061-1083.
7. I. Pehlivan and Y. Uyaroglu. A New Chaotic Attractor from General Lorenz System Family and its Electronic Experimental Implementation, *Turkish Journal of Electrical Engineering and Computer Science*, vol. 18, no. 2, 2010, pp. 171-184.
8. K.M. Cuomo and A.V. Oppenheim. Circuit Implementation of Synchronized Chaos with Applications to Communications, *Physical Review Letters*, vol. 71, no. 1, July 1993, pp. 65-68.
9. J.C. Sprott. Simple Chaotic Systems and Circuits, *American Journal of Physics*, vol. 68, no. 8, August 2000, pp. 758-763.
10. S. Ozoğuz, A. Elwakil and M.P. Kennedy. Experimental Verification of the Butterfly Attractor in a Modified Lorenz System, *International Journal of Bifurcation and Chaos*, vol. 12, no. 7, 2002, pp. 1627-1632.
11. A. Elwakil and M. Kennedy. Construction of Classes of Circuit-Independent Chaotic Oscillators using Passive-Only Nonlinear Devices, *IEEE Transactions on Circuits and Systems I: Fundamental Theory and Applications*, vol. 48, 2001, pp. 289-307.
12. I. Pehlivan, Y. Uyaroglu and M. Yogun. Chaotic Oscillator Design and Realizations of the Rucklidge Attractor and its Synchronization and Masking Simulations, *Scientific Research and Essays*, vol. 5, no. 16, 2010, pp. 2210-2219.

Grating profile optimization for reflection 1st order Littrow mounting

Andrey A. Petukhov¹, Michael K. Trubetskov², and Alexander N. Bogolyubov¹

¹ Moscow State University, Faculty of Physics, Moscow, Russia petukhov@physics.msu.ru, bogan7@yandex.ru

² Moscow State University, Research Computing Center, Moscow, Russia trub@srcc.msu.ru

Summary. One-dimensional multilayer reflection gratings with different groove shapes are considered and optimized for maximum diffraction efficiency in the first order in Littrow conditions. A rigorous formulation for the design optimization problem based on merit function minimization is presented. Nelder-Mead (simplex) method is applied for minimizing the merit function. At each step the direct problem is solved by means of a combination of the incomplete Galerkin's method and matrix techniques.

1 Introduction

Due to its selective special properties and capability of spacial decomposition of waves with different frequencies as well as spacial redistribution of the wave energy, diffraction gratings are extensively applied in modern optical devices, especially in laser systems [1]. Diffraction gratings are widely applied in semiconductor diode lasers for wavelength stabilization as mirrors in external resonators [2] as well as for laser tuning [3]. Another application of diffraction gratings in laser physics is connected with pulse compression in ultrashort high-power lasers that are based on chirped pulse amplifications [4]. In all cases it is crucial to use gratings which are capable of reflecting the incident light at a desired frequency (or wavelength) into one diffraction order with an efficiency as close to 100% as possible and special grating configurations are used, such as Littrow configuration (i.e. the geometry in which the light of a specific wavelength diffracted from a grating into a given diffraction order travels back along the direction of the incident light [1]). In such systems the gratings are traditionally covered with metallic films, or purely metallic gratings are implemented. Being fragile the gratings can be easily damaged, especially by high-intensity laser pulses [5]. To minimize the damage and to ensure reflection into one diffraction order it is desirable to implement entirely dielectric diffraction gratings [6, 7]. This gives rise to a specific problem of grating design and optimization. This problem, with respect to the applications described above has been widely discussed in the literature. However in many cases no optimization problem is solved but only some heuristic considerations are presented. Only several papers (for example [6]) contain rigorous formulation of the design problem in terms of a merit function which is

minimized for obtaining the optimized structure. Thus it is very important to provide a rigorous formulation for the grating design problem and apply rigorous non-heuristic methods for obtaining the solution.

2 Problem statement

Within this paper we consider entirely dielectric one-dimensional multilayer reflection gratings with different groove shapes such as binary (Fig.1) and triangular (Fig.2) gratings. As the dielectric grating itself provides only good redistribution of incident wave energy between several diffraction orders, a multilayer dielectric mirror should be used for ensuring good reflectance (schematically presented as green and light green layers in Figs.1,2). The grating is placed on the top of the multilayer dielectric mirror deposited on a substrate (represented as a light brown area in Figs.1,2). The wave is considered to be incident (direction $< i >$) at a grating at some given angle θ . Our goal is to optimize the grating parameters via maximizing the diffraction into the first order for a given wavelength in case of first order Littrow conditions, i.e for the case when the $< i >$ and $< 1 >$ directions in Figs.1,2 are coincident.

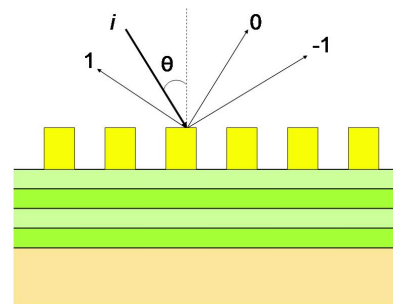


Fig. 1. Binary multilayer grating

3 Optimization algorithm

In each case (binary and triangular gratings) the multilayer grating structure is parametrized. A binary grating is determined by its period, groove depth and

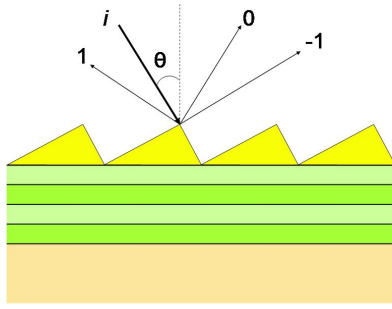


Fig. 2. Multilayer grating with triangular grooves

groove width, a triangular grating is determined by its period and blaze angle. There can be some restrictions on these parameters, apart from trivial physical ones (non-negative values of the parameters), resulting from the following requirements:

- only two diffraction orders (0, 1) should be propagating in both the incident medium and the substrate, all higher orders being evanescent;
- there should be no waveguide modes in the multilayer stack at a given wavelength and at a given angle of incidence [6].

We provide a grating optimization algorithm based on a merit function minimization (or maximization) in terms of the variable grating parameters given above under the described constraints. The merit function represents the first order diffraction efficiency and should be maximized. Another formulation is also used, such as minimizing of the zero-order diffraction efficiency in case of only two propagating orders (0, 1). The multilayer mirror parameters are optimized independently, providing almost 100% reflectance for a given wavelength and for a given angle of incidence and as a starting point a quarter-wave stack is taken. The merit function minimization algorithm is based on the Nelder-Mead (simplex) optimization [8]. At each step the merit function is evaluated by obtaining the solution of a full-vectorial diffraction problem for Maxwell equations, which is obtained by means of a combination of the incomplete Galerkin's method [9, 10] and matrix techniques such as transfer matrix and scattering matrix methods [11]. These methods provide efficient solution of the problem of wave diffraction on a multilayer grating.

Within this paper we provide multilayer diffraction grating optimization for maximizing first-order reflection in Littrow conditions. Different polarization states (TE and TM polarizations) are considered. The results for gratings with different groove shapes, such as binary and triangular gratings, are obtained and compared with each other.

References

1. Ch. Palmer and E. Loewen. *Diffraction Grating Handbook*. Newport Corporation, sixth edition, 2005.
2. M. Fleming and A. Mooradian. Spectral characteristics of external-cavity controlled semiconductor lasers. *IEEE J. Quantum Electron.*, 17(1):44–59, 1981.
3. K. Liu and M. G. Littman. Novel geometry for single-mode scanning of tunable lasers. *Opt. Lett.*, 6(3):117–118, 1981.
4. E. B. Treacy. Optical pulse compression with diffraction gratings. *IEEE J. Quantum Electron.*, 5(9):454–458, 1969.
5. R. D. Boyd and J. A. Britten et al. High-efficiency metallic diffraction gratings for laser applications. *Appl. Opt.*, 34(10):1697–1706, 1995.
6. K. Hehl and J. Bischoff et al. High-efficiency dielectric reflection gratings: design, fabrication and analysis. *Appl. Opt.*, 38(30):6257–6271, 1999.
7. Patrick P. Lu and Ke-Xun Sun et al. Precise diffraction efficiency measurements of large-area greater-than-99 percent-efficient dielectric gratings at the littrow angle. *Opt. Lett.*, 34(11):1708–1710, 2009.
8. D.M. Himmelblau. *Applied Nonlinear Programming*. The McGraw-Hill Companies, 1972.
9. A.G. Sveshnikov. Incomplete galerkin's method. *RAS USSR*, 236(5):1076–1079, 1977.
10. A.N. Bogolyubov, A.A. Petukhov, and N.E. Shapkina. Mathematical modeling of waveguides with fractal insets. *Moscow University Physics Bulletin*, 66(2):122–125, 2011.
11. L. Li. Formulation and comparison of two recursive matrix algorithms for modeling layered diffraction gratings. *J. Opt. Soc. Am. A*, 13:1024–1035, 1996.

Bulk and Interface Balance Equations for Organic Solar Cell Simulation

Matteo Porro^{1,2}, Carlo de Falco^{1,3}, Riccardo Sacco¹, and Maurizio Verri¹

¹ Dipartimento di Matematica “F. Brioschi”, Politecnico di Milano, Piazza L. da Vinci 32, 20133 Milano, Italy

² Center for Nano Science and Technology @PoliMi, Istituto Italiano di Tecnologia, via Pascoli 70/3, 20133 Milano, Italy

³ MOX Modeling and Scientific Computing

matteo.porro@mail.polimi.it, carlo.defalco@polimi.it, riccardo.sacco@polimi.it, maurizio.verri@polimi.it

Summary. In this communication, we present a computational model for heterojunction Organic Solar Cells (OSCs) consisting of a system of semilinear PDEs and ODEs. The mathematical model is discussed, focusing on the transmission conditions at material interfaces, together with the numerical method used for its solution. Steady-state and transient simulations are performed on realistic devices with various interface morphologies.

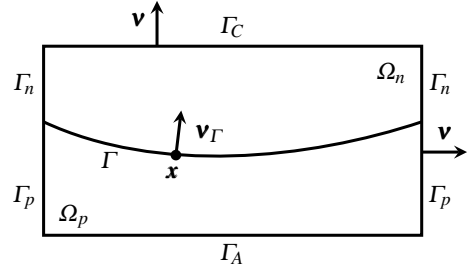


Fig. 1. OSC cell geometry.

1 Introduction and Motivation

In the design of efficient OSCs the impact of material interface morphology on performance is currently considered to be of paramount importance. For this reason, material scientists are putting much of their research effort into techniques for controlling interfaces down to the nanoscale, for example by studying materials that have the ability to self-assemble into ordered nanostructures during the deposition process. For the same reason, computational models that allow to estimate device performance carefully accounting for the material interface geometry and the phenomena occurring on it are in high demand. Previous approaches in this direction can be found in [1] (for biplanar devices) and [7]. In this communication we present our work aimed at extending the model of [1] to treat arbitrary multidimensional morphologies.

2 Mathematical Model

Let Ω be an open subset of \mathbb{R}^d , $d = 1, 2, 3$, representing the geometrical model of an OSC and \mathbf{v} be the unit outward normal vector over the boundary $\partial\Omega$. The device structure is divided into two open disjoint subregions, Ω_n (acceptor) and Ω_p (donor), separated by a regular surface Γ on which \mathbf{v}_Γ is the unit normal vector oriented from Ω_p into Ω_n . The cell electrodes, cathode and anode, are denoted as Γ_C and Γ_A , respectively (see Fig. 1 for the 2D case). Let e, n and p denote the volumetric densities of excitons, electrons and holes in the cell, respectively, P be the areal density of polaron pairs and ϕ be the electric potential. For any function $f : \Omega \rightarrow \mathbb{R}$, let $\llbracket f \rrbracket := f_n - f_p$, f_n and f_p being the traces of f on Γ from Ω_n and Ω_p ,

respectively. Excitation phenomena occurring in the bulk are described by the parabolic problem:

$$\begin{cases} \frac{\partial e}{\partial t} - \nabla \cdot (D_e \nabla e) = Q - \frac{e}{\tau_e} & \text{in } \Omega \setminus \Gamma, \\ \llbracket e \rrbracket = 0, & \text{on } \Gamma, \\ \llbracket -\mathbf{v}_\Gamma \cdot D_e \nabla e \rrbracket = \eta k_{\text{rec}} P - \frac{2H}{\tau_{\text{diss}}} e & \text{on } \Gamma, \\ e = 0 & \text{on } \Gamma_C \cup \Gamma_A, \\ e(\mathbf{x}, 0) = 0, & \forall \mathbf{x} \in \Omega. \end{cases} \quad (1a)$$

Dissociation/recombination of excitons, electrons and holes into polaron pairs at the material interface is described by the ODE:

$$\begin{cases} \frac{\partial P}{\partial t} = \frac{2H}{\tau_{\text{diss}}} e + 2H\gamma n p - (k_{\text{diss}} + k_{\text{rec}}) P & \text{on } \Gamma, \\ P(\mathbf{x}, 0) = 0, & \forall \mathbf{x} \in \Gamma. \end{cases} \quad (1b)$$

Transport of photogenerated electrons in the acceptor domain Ω_n is described by the parabolic problem:

$$\begin{cases} \frac{\partial n}{\partial t} + \nabla \cdot \mathbf{J}_n = 0 & \text{in } \Omega_n, \\ \mathbf{J}_n = -D_n \nabla n + \mu_n n \nabla \phi & \text{in } \Omega_n, \\ -\mathbf{v}_\Gamma \cdot \mathbf{J}_n = -k_{\text{diss}} P + 2H\gamma n p & \text{on } \Gamma, \\ -\kappa_n \mathbf{v} \cdot \mathbf{J}_n + \alpha_n n = \beta_n & \text{on } \Gamma_C, \\ n(\mathbf{x}, 0) = 0, & \forall \mathbf{x} \in \Omega. \end{cases} \quad (1c)$$

A parabolic problem completely similar to (1c) describes hole transport in the donor domain Ω_p . The dependence of the electric potential and field on the space charge density in the cell is described by the Poisson equation:

$$\begin{cases} \nabla \cdot (-\epsilon \nabla \phi) = -qn & \text{in } \Omega_n, \\ \nabla \cdot (-\epsilon \nabla \phi) = +qp & \text{in } \Omega_p, \\ \llbracket \phi \rrbracket = \llbracket -\mathbf{v}_T \cdot \epsilon \nabla \phi \rrbracket = 0 & \text{on } \Gamma, \\ \phi = 0 & \text{on } \Gamma_C, \\ \phi = V_{\text{appl}} + V_{\text{bi}} & \text{on } \Gamma_A. \end{cases} \quad (1d)$$

A list of the model parameters with their corresponding physical meaning is reported in Table 1. The PDE/ODE model (1) has been introduced in [2] and represents a multi-dimensional generalization of the 1D formulation proposed in [1]. System (1) is completed by periodic boundary conditions on $\Gamma_n \cup \Gamma_p$. We notice that the dissociation and recombination processes occurring at the donor-acceptor interface Γ are dealt with by the nonlinear transmission conditions (1a)₃ and (1c)₂, whose dependence on the local electric field magnitude and orientation is contained in the polaron dissociation rate constant k_{diss} [2].

Table 1. Model parameters.

Symbol	Parameter
μ_i, D_i	Mobility and diffusivity of species i , $i = e, n, p$
Q	Exciton generation rate
$\tau_e, \tau_{\text{diss}}$	Exciton decay and dissociation times
$k_{\text{rec}}, k_{\text{diss}}$	Polaron recombination and dissociation rates
γ	Electron-hole recombination rate constant
η	Singlet exciton fraction
H	Active layer thickness

3 Algorithms and Simulation Results

System linearization (by a quasi-Newton method) and approximation are carried out by adapting the approach used in [3]. Time advancing is treated using Rothe's method and adaptive BDF formulas, while the exponentially fitted Galerkin finite element method studied in [5] is used for spatial discretization. The interface conditions at the donor-acceptor interface are taken care of by means of the substructuring techniques described in [6].

Model (1) is here validated in both stationary and transient regimes. In a first set of simulations, we study the finger-shaped heterostructure considered in [7]. Fig. 2 shows the output current-voltage characteristics predicted by our model, which is in excellent agreement with that computed in [7]. In a second set

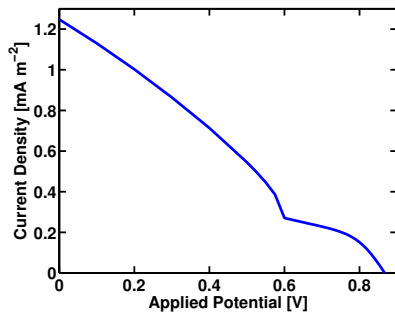


Fig. 2. Current-voltage characteristics for the finger-shaped heterostructure investigated in [7].

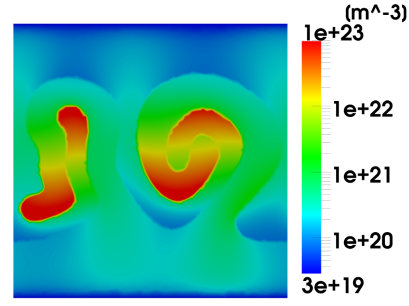


Fig. 3. Free carrier densities for a device with complex morphology

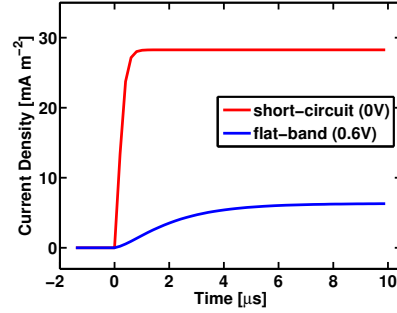


Fig. 4. Contact current density transient at two different voltage regimes.

of simulations, we test the ability of the model to describe the behaviour of a cell characterized by a complex interface morphology. Fig. 3 shows the free carrier densities computed for a “curly-shaped” geometry at short circuit working conditions. In a third set of simulations, we test the model in the time-dependent case. Fig. 4 shows the cell current response under two different biasing conditions for a planar device geometry similar to that studied in [1]. Ongoing activity is devoted to the investigation of the working principles of the light-harvesting device described in [4].

References

1. J.A. Barker, C.M. Ramsdale, and N.C. Greenham. Modeling the current-voltage characteristics of bilayer polymer photovoltaic devices. *Phys. Rev. B*, 67:075205, 2003.
2. C. de Falco, M. Porro, R. Sacco, and M. Verri. Multiscale modeling and simulation of organic solar cells. Under review, 2012.
3. C. de Falco, R. Sacco, and M. Verri. Analytical and numerical study of photocurrent transients in organic polymer solar cells. *Comput. Meth. Appl. Mech. Engrg.*, 199(25-28):1722 – 1732, 2010.
4. M. Garbugli, M. Porro, V. Roiati, A. Rizzo, G. Gigli, A. Petrozza, and G. Lanzani. Light energy harvesting with nano-dipoles. *Nanoscale*, 4:1728–1733, 2012.
5. E. Gatti, S. Micheletti, and R. Sacco. A new Galerkin framework for the drift-diffusion equation in semiconductors. *East-West J. Numer. Math.*, 6:101–136, 1998.
6. T.J.R. Hughes, G. Engel, L. Mazzei, and M.G. Larson. The continuous Galerkin method is locally conservative. *J. Comp. Phys.*, 163:467–488, 2000.
7. J. Williams and A.B. Walker. Two-dimensional simulations of bulk heterojunction solar cell characteristics. *Nanotechnology*, 19:424011, 2008.

Modeling and Analysis of the Performance Improvement Techniques for EMI Filters

Adina Racasan¹, Calin Munteanu¹, Vasile Topa¹, Dan Micu¹, Claudia Pacurar¹, Ema Adam²

¹Department of Electrotechnics, The Technical University of Cluj-Napoca, Baritiu 26-28, 400027 Cluj – Napoca, Romania, Adina.Racasan@et.utcluj.ro, Calin.Munteanu@et.utcluj.ro, Vasile.Topa@et.utcluj.ro, Dan.Micu@et.utcluj.ro, Claudia.Pacurar@et.utcluj.ro

²Department of Foreign Languages and Communication, The Technical University of Cluj-Napoca, Baritiu 26-28, 400027 Cluj – Napoca, Romania, Ema.Adam@lang.utcluj.ro

Summary Improving the characteristics of a filter presupposes two major directions of action: the first direction refers to the increase of attenuation (by means of the increase of losses) in high frequency, while the second direction refers to the suppression of the parasitic effects in the constitutive devices. Thus, in this light, the paper presents the authors' contribution to the two major directions of actions mentioned above; in the first part, techniques of loss increase are presented, while in the second part techniques of minimizing the parallel equivalent capacity are shown, techniques proposed by the authors. In part three of the paper these techniques are applied simultaneously to an EMI filter made by use of planary magnetic technology in order to study its performance through 2D and 3D numerical modelling. The final conclusions will close the present paper.

1 Introduction

The main technological challenge for the integrated EMI filters, as it appears from the speciality literature, is that of improving its performance for high frequencies by reducing the equivalent parallel capacity (EPC) and the equivalent series inductance (ESL) of the integrated capacitor coils, by the increase of losses at high frequency, respectively [1], [2]. The fundamental element of any integrated magnetic planar device is represented by its LC integrated structure. For the construction of the EMI filters, an LC integrated structure with three coils per layer has been chosen, an attractive structure which is also often mentioned in the literature for the manufacturing of different planary integrated magnetic devices; it is presented in Fig. 1.

2 Techniques for improving the performance of the integrated EMI filters

In order to achieve the integrated EMI filters big

losses at high frequency are desired, that is small losses at low frequencies, respectively. Aiming at that, the authors propose the *technique of nickel coating conductors*, a technique to be described in detail in the final work.

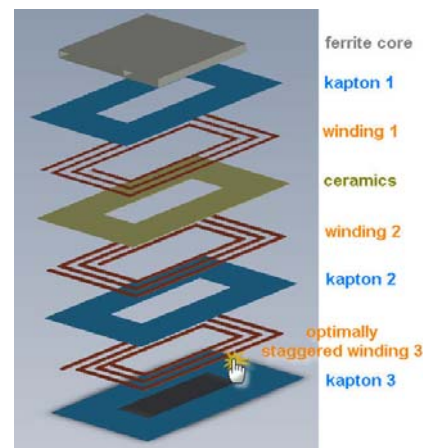


Fig. 1. Explanatory_ LC integrated structure with 3 coils –3D detailed image.

As far as the parallel equivalent capacity is concerned, since great geometrical complexity structures are involved, it cannot be defined by means of direct calculus relationships nor can it be localized in a certain device, since it is practically distributed within the space between the coil windings constituting the filter. A new technique for reducing the parallel equivalent capacity is proposed within the paper, that is applying a geometrical staggering among the coil windings. The structure of the optimum placing of the staggered coiling constitutes the subject of a study for optimal planning with specific numeric optimization algorithms created by the authors. These techniques of increasing loss at high frequency and of minimizing the EPC respectively are applied in the case of EMI integrated filters in order to improve their performance.

The equivalent principle scheme for an EMI filter achieved by means of planary magnetic technology is given in Fig. 2 [3].

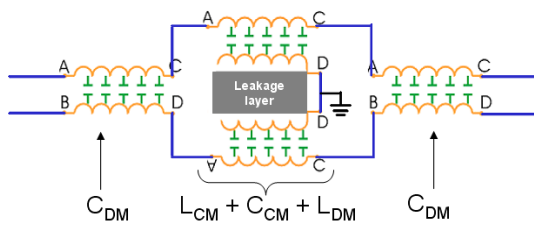


Fig. 2. The equivalent principle scheme for an EMI filter [3]

In order to highlight the performance introduced by means of applying the techniques proposed by the authors, a comparative study has been carried out, having as a starting point an initial structure achieved in the classical variant, the so called "original structure" and an "optimized structure" in the afore mentioned sense, respectively. The two structures are presented in Fig. 3, the constituting elements being mentioned alongside their functional role within the EMI filter.

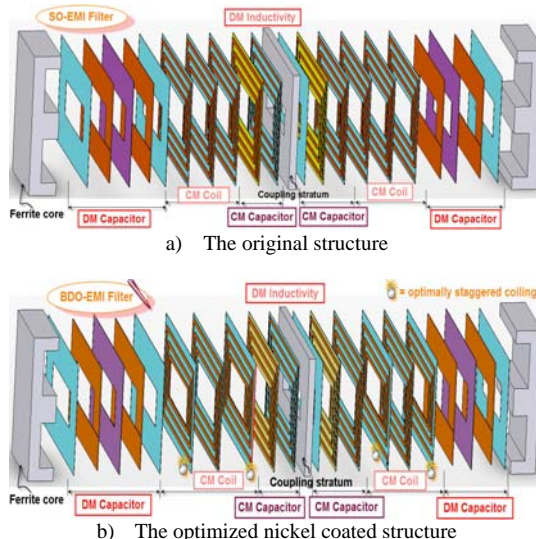


Fig. 3. Explanatory 3D EMI Filters – unfolded representations.

Comparing the capacity matrixes obtained following the numeric modeling of the two proposed filters, it can be noticed that the parasitic capacity corresponding to the CM_1 coil decreases from 219.4 pF, the value obtained in the matrix corresponding to the EMI filter based on the original structure, to 102.32 pF in the case of the EMI filter based on the coiling structure optimally staggered, the parasitic capacity corresponding to the CM_2 coil decreases from 219.16 pF to 101.61 pF respectively. The impedance variation with frequency at the inlet of the closed filter for a 50 Ω charge in the case of the two proposed structures is shown in Fig. 4.

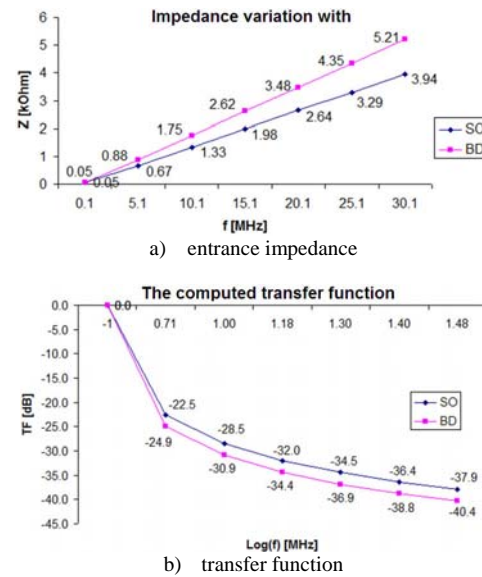


Fig. 4. The results of the comparative analysis of the variation with the frequency in case of EMI filters: SO – the original structure; BD – nickel plated, staggered coiling.

3 Conclusions

Following the analysis of the results obtained which have been detailed in the present paper, it can be stated that the techniques proposed by the authors for the improvement of the EMI filter performance prove to be efficient. Thus, the EMI filters which have applied these techniques have a parallel equivalent capacity reduced to approximately 47% of the initial value while the HF losses are increased with approximately 32% with respect to the initial value respectively.

Acknowledgement This paper was supported by the TE_253/2010_CNCSIS project – "Modeling, Prediction and Design Solutions, with Maximum Effectiveness, for Reducing the Impact of Stray Currents on Underground Metallic Gas Pipelines", No. 34/2010.

References

1. J.D. van Wyk, F.C. Lee, Z. Liang, R. Chen, S. Wang and B. Lu. *Integration Active, Passive and EMI-Filter Functions in Power Electronics System: A Case Study of Some Technologies*. IEEE Transactions on Power Electronics, vol. 20, 2005.
2. R. Chen, S. Wang, J.D. van Wyk and W.G. Odendaal. *Integration of EMI Filter for Distributed Power System (DPS) Front-end Converter*. IEEE, 2003.

Analyzing Distortion Contributions in a Complex Device Model

Timo Rahkonen, Janne P. Aikio

Department of Electrical Engineering, Electronics Laboratory, P.O. Box 4500 90014 University of Oulu, Finland

Summary. This paper studies how distortion contribution analysis is affected by the internal structure of the device models. It is shown that to keep the distortion contributions tractable and physically meaningful we need to lump the contributions so that they resemble the contributions of a classical transistor pi-model. The technical challenges related to this are also discussed.

1 Introduction

Until now, distortion contributions have been analyzed mostly fully analytically, using symbolic Volterra analysis and simplified schematics[1,2]. The authors have proposed a fully numerical distortion contribution analysis method called Volterra-on-Harmonic-Balance (VoHB) [3,4], that both builds the polynomial models needed for Volterra analysis, and propagates the distortion contributions to any chosen node. VoHB proceeds in the following steps: HB is run to obtain voltage and current spectra in all nodes and branches. Using these, a polynomial model is built for each non-linear VCCS and VCQS. Then, a linearized network is built (using the linear terms of the fitted polynomials), and - using the direct current method - the response of the injected distortion currents is calculated in a given node.

VoHB operates at VCCS level and does not need modifications into the device models. However, the output contains the response of all non-linear VCCS and VCQS found inside the device model, so that in addition to the dominant sources it includes reverse biased pn junctions, or parasitic devices of BJTs, for example. Many of these insignificant terms can be masked away simply based on their low magnitude, but another problem has emerged.

Many new device models are distributed as an executable Verilog-A code, which is automatically converted into a model structure. The syntax of verilog-A makes it possible to write models whose structure differs notably from traditional device models and is not necessarily optimal for Spice-like simulators, or distortion contribution analysis in particular. For example, Fig. 1 shows a rather typical example where the transistor's I_{ds} source is split into two by generating an intermediate node in the middle of the source. From terminal current

point of view this modification is absolutely ok, but it scrambles the distortion contribution analysis. VoHB calculates the contributions of all the sources, and adding an equivalent (and equal) distortion current sources parallel to I_{ds} and I_{dsx} as in Fig 2a generates two large distortion contributions that cancel each other. The net current sum for example in the collector terminal is still correct, but the physical meaning and intuition is lost: the names of the sources do not mean anything to the engineer, any more, and the mutually cancelling contributions have no physical meaning.

For the above reasons, there is a clear interest to reduce the entire internal structure of a complex device model (Fig. 2a) into something resembling a classic transistor pi-model (Fig. 1a) to keep the distortion contribution analysis results tractable. The idea is to lump all the input and output-related non-linear currents together, as shown in Fig.2b. Now the designer can again clearly recognize the effects of input and output related conductive or capacitive non-linearities.

Building the equivalent distortion current model is straight-forward. HB simulation is run, and terminal distortion current spectra I_d , I_s and I_g are recorded. Then equivalent current sources are fitted so that the terminal distortion currents are correctly modeled by these imaginary distortion sources. These sources are fitted using the spectra of terminal currents and intrinsic node voltages.

Even in a lumped model the terminal distortion currents consist of distortion generated in several sources. For example, the current in the drain terminal comes from the gm-element $I_{ds}(v_{gs}, v_{ds})$, and drain charge $Q_{ds}(v_{gs}, v_{ds})$, both of which are controlled by intrinsic v_{gs} and v_{ds} voltages. Moreover, the current from Q_{ds} is proportional to the tone frequency Ω , while I_{ds} has a transit delay τ that rotates the phases of the tones by $\exp(-j\omega\tau)$. Hence, i_d would be described as

$$\begin{aligned} i_d &= i_{gm} + i_{qds} \\ &= \text{diag}(e^{-j\Omega\tau}) \cdot \text{gmpoly}(v_{gs}, v_{ds}) \cdot \\ &\quad + \text{diag}(j\Omega) \cdot \text{qdspoly}(v_{gs}, v_{ds}) \end{aligned} \quad (1)$$

where $\text{diag}()$ is a diagonal matrix, Ω is the frequency of a given tone, and $\text{gmpoly}()$ and $\text{qdspoly}()$ are model function matrices. In the model function matrices each row corresponds to one frequency in the spectrum, and each column corresponds to one $v_{gs}^i \cdot v_{ds}^j$ product term in the polynomial model.

Similar equation can be written for the gate current i_g :

$$\begin{aligned} i_g &= i_{gpi} + i_{qgs} \\ &= \text{gpipoly}(v_{gs}, v_{ds}) \\ &\quad + \text{diag}(j\Omega) \cdot \text{qgspoly}(v_{gs}, v_{ds}) \end{aligned} \quad (2)$$

where $\text{gpipoly}()$ corresponds to the possible conductive part of the input current (needed in BJTs) and $\text{qgspoly}()$ models the current caused by the input charge.

Solving the polynomial coefficients from (1) has some technical challenges. Currently, VoHB has i_{gm} and i_{qds} available separately, and can fit the two polynomials independently. This keeps the number of unknowns in some bounds. In a lumped model we must fit (1) simultaneously, which increases the number of unknown coefficients. As we can fit only as many coefficients as there are equations this approach may not be possible using a 1-tone spectrum, but we must use 2- or 3-tone excitations. The $j\Omega$ emphasis also means that the effect of capacitive lower harmonics is attenuated, and more easily buried underneath the effect of conductive non-linearities. Second, the frequency response $\text{diag}(j\Omega)$ of capacitive current is known a priori, but the transit delay τ of the i_{ds} source is not necessarily known, if we want to keep the analysis independent of the device models. Hence, τ needs to be found by iterating (1). Third, the above only gives the equivalent polynomials that can be used to calculate the nonlinear distortion currents i_{NL} . Addition to this, we need to build the linearized circuit model to propagate the currents to a given node. For this reason we also need to find linear models for all VCCS elements in the original model.

As an example, we took the MET model [5] of Freescale's LDMOS power transistor MRF21030. Its output drain current consists of currents from three sources: the g_m source $i_{ds}(V_{gs}, V_{ds})$, drain charge $Q_{ds}(V_{ds})$, and gate-drain charge $Q_{gd}(V_{gd})$. i_{ds} strongly dominates the total drain current, and Q_{gd} is insignificant. In a simple example, we tried to model total drain current i_d as a sum of i_{ds} +

i_{Qds} . The combined model matrix is very badly ill-conditioned ($\text{cond} \sim 3e13$), and Q_{ds} fits poorly. Much better results was obtained by iterating a couple of times in a loop, where i_{ds} was first estimated, and subtracted from i_d before fitting i_{Qds} . This reduces the order of the fitted system and improves especially the fitting of the capacitive currents that are buried underneath the dominating i_{ds} current. The condition number of the i_{ds} fitting matrix drops to $\sim 1e7$, which is mostly set by the heavy correlation between V_{gs} and V_{ds} signals.

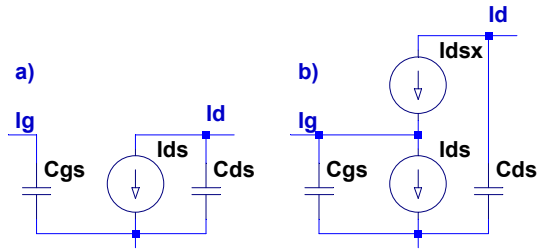


Fig. 1 a) Transistor pi-model, b) example structure that may result when automatically generated from a Verilog-A source.

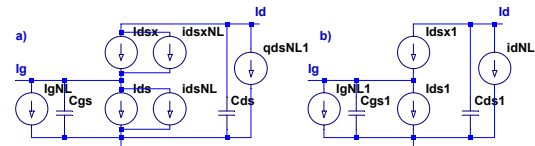


Fig. 2 a) Distortion current sources next to each VCCS, b) lumped distortion current sources.

Acknowledgement. This work is funded by the Academy of Finland

References

- [1] P. Wambacq & W. M. C. Sansen. *Distortion Analysis of Analog Integrated Circuits*. Kluwer Academic Publisher, 1998
- [2] J. Vuolevi & T. Rahkonen, *Distortion in power amplifiers*. Artech House, 2003
- [3] J. P. Aikio, T. Rahkonen, "Detailed distortion analysis technique based on large-signal voltage and current spectra." *IEEE Trans. Microw. Theory Tech.*, vol 53, no. 10, pp. 3057-3066, Oct. 2005.
- [4] J. Aikio, T. Rahkonen. Utilization of distortion contribution analysis. In proc. Europ. Conf on Circuit Theory and Design (ECCTD) 2011, pp. 701-704.
- [5] Motorola's Electrothermal (MET) LDMOS model. <http://www.freedra.org/doc/elements/mosnld-met.pdf>

Coupling of FEM and Fourier-mode expansion for the scattering by perfectly conducting gratings

Guanghui Hu¹ and Andreas Rathsfeld¹

Weierstrass Institute for Applied Analysis and Stochastics, Mohrenstr. 39, 10117 Berlin, Germany
Guanghui.Hu@wias-berlin.de, Andreas.Rathsfeld@wias-berlin.de

Summary. To simulate the diffraction of planar waves by periodic surface structures, Huber et al. [2] have proposed to combine a Fourier-mode expansion over the half space with a finite element approximation of the electric field close to the surface. We analyze a slight modification of this mortar method and discuss an application to an inverse problem in scatterometry. In particular, we present a shape derivative formula for the derivative with respect to geometry parameters.

1 Boundary Value Problem for Gratings

Suppose the space \mathbb{R}^3 is filled with two materials separated by an interface Γ , which is a small perturbation of the $x_3 = 0$ plane and which is 2π -periodic in the x_l directions for $l = 1, 2$. Furthermore, suppose the material below Γ is perfectly conducting and that in the domain Ω above Γ is lossless. To compute the diffraction of a time-harmonic plane wave \mathbf{E}^{in} incident on Γ from above, we have to solve

$$\nabla \times \nabla \times \mathbf{E} - k^2 \mathbf{E} = 0 \quad \text{on } \Omega, \quad (1)$$

$$\mathbf{v} \times \mathbf{E} = 0 \quad \text{on } \Gamma, \quad (2)$$

$$\mathbf{E}(\mathbf{x}) - \mathbf{E}^{\text{in}}(\mathbf{x}) = \sum_{n \in \mathbb{Z}^2} \mathbf{E}_n e^{i\mathbf{v}_n \cdot \mathbf{x}} \quad \text{for } x_3 > b. \quad (3)$$

Here \mathbf{v} is the unit normal vector on Γ , b is a fixed x_3 coordinate greater than those of Γ , and \mathbf{v}_n are the vectors of the upward radiating (plane wave and evanescent) Fourier modes.

2 Mortar Method

It is natural, to approximate \mathbf{E} for $x_3 > b$ by \mathbf{E}^{in} plus a Fourier-mode expansion \mathbf{E}^+ like that on the right-hand side of (3). In the domain between the artificial surface $\Gamma'_b := \{\mathbf{x} \in \mathbb{R}^3 : x_3 = b\}$ and Γ , an FE approximation with quasi-periodic edge elements is possible. Clearly, the FEM can be restricted to the cell of periodicity $\Omega_b := \{\mathbf{x} \in \Omega : x_3 < b, 0 \leq x_l \leq 2\pi, l = 1, 2\}$ and the mode expansion to the bounded upper domain $\Omega_b^+ := \{\mathbf{x} \in \mathbb{R}^3 : b \leq x_3 \leq b+1, 0 \leq x_l \leq 2\pi, l = 1, 2\}$ or even to $\Gamma_b := \{\mathbf{x} \in \Gamma_b : 0 \leq x_l \leq 2\pi, l = 1, 2\}$. Following the idea of Huber et al. [2], we couple the two approximations by a mortar technique. More precisely, we

replace the boundary value problem by the following variational equation

$$a\left((\mathbf{E}, \mathbf{E}^+), (\mathbf{V}, \mathbf{V}^+)\right) = -a\left((0, \mathbf{E}^{\text{in}}), (\mathbf{V}, \mathbf{V}^+)\right),$$

required for all $\mathbf{V} \in H(\text{curl}, \Omega_b)$ and $\mathbf{V}^+ \in H(\text{curl}, \Omega_b^+)$, where the sesquilinear form a is defined as the sum of

$$\int_{\Omega_b} \{\nabla \times \mathbf{E} \cdot \nabla \times \bar{\mathbf{V}} + \mathbf{E} \cdot \bar{\mathbf{V}}\} \\ - \int_{\Gamma_b} \nabla \times \mathbf{E}^+ \cdot \mathbf{v} \times \bar{\mathbf{V}} + \int_{\Gamma_b} \mathbf{v} \times (\mathbf{E} - \mathbf{E}^+) \cdot \nabla \times \bar{\mathbf{V}}^+$$

plus a certain sesquilinear form corresponding to a finite rank operator. We get (cf. [4])

Theorem 1. *The operator corresponding to the variational equation is Fredholm of index zero. The solution of the sesquilinear form is equivalent to the boundary value problem (1)-(3).*

Unfortunately, there are examples of gratings such that the solution of the boundary value problem is non-unique. However, the scattered (non-evanescent) plane wave modes are always unique (cf. [4]).

Using Theorem 1, the justification of a coupled Fourier-mode-FE method should be possible (compare [1]). Simply, the E and V are to be replaced by edge finite elements and the E^+ and V^+ by truncated Fourier-mode expansions. Of course, the variational form is to be modified slightly. Frequently, in practical computations, only a small number of the Rayleigh coefficients \mathbf{E}_n (cf. (3)) differ essentially from zero. Thus only a few terms in the Fourier-mode expansions are needed.

3 Inverse Problem in Scatterometry

To evaluation the fabrication process of lithographic masks, simple periodic or biperiodic structures must be measured. Using scatterometric techniques, the corresponding part of the surface is illuminated by a ray of laser light. The efficiencies (intensities) of the scattered plane wave modes are measured. Finally, a biperiodic surface structure is sought, the efficiencies of which coincide with the measured data, i.e., an inverse problem is to be solved.

Though this problem is severely ill-posed, we are looking for small deviations of the surface structure

from the fabrication standard, i.e., for surfaces described by a small number of geometry parameters. The reduction to these parameters is like a regularization of the inverse problem, and the determination of the parameters with high accuracy should be possible. Note that we do not discuss the effect of modeling errors or random perturbations.

The numerical solution of the inverse problem can be realized minimizing a functional $\mathcal{F}(\mathbf{E})$, where $\mathcal{F}(\mathbf{E})$ is some measure for the deviation of the measured efficiencies and the efficiencies of the scattered field \mathbf{E} corresponding to a grating structure with given parameters. Although the gratings are not perfectly conducting anymore, the scattered field \mathbf{E} can be computed by an FEM similar to that of Sect. 3. Optimization schemes like the Gauß-Newton method or the Levenberg-Marquardt algorithm can be applied. However these local optimization routines require the Jacobian of the operator, mapping the set of geometry parameters to the vector of efficiency values. In other words, we need formulas for the derivatives of \mathbf{E} with respect to the geometry parameters.

4 Shape Derivative

In the case of periodic gratings, i.e., for the two-dimensional Helmholtz equation, the classical methods for shape calculus apply. Unfortunately, for the time-harmonic Maxwell equation (1), an analogous procedure is not possible. Indeed, the underlying energy space $H(\text{curl}, \Omega_b)$ is not invariant under the transformations corresponding to a change of the geometry parameter.

On the other hand, in our optical applications the magnetic permeability μ is constant. For this case, it is known that the magnetic vector \mathbf{H} is piecewise in the Sobolev space H^1 . Using this fact, the shape calculus applies to the derivative of \mathbf{H} . Switching now from the magnetic vector to the electric field, we can derive a formula for the derivative w.r.t. a geometry parameter p (cf. [3])

$$\partial_p \mathcal{F}(E) = \text{Re } a_1(E, E_{\text{adj}}). \quad (4)$$

Here $a_1(E, F)$ is a special sesquilinear form depending on the L^2 functions $E, F, \nabla \times E$, and $\nabla \times F$. The field E in (4) is the actual electric solution of the time-harmonic Maxwell equation. The field E_{adj} is the solution of the adjoint equation. In other words, E_{adj} is the solution of an equation with the adjoint FEM matrix and with a right-hand side depending on the functional \mathcal{F} .

In a numerical experiment, we have implemented a version of (4) discretized by FEM. The numerical algorithm for the inverse problem mentioned in Sect. 3, including the shape derivative based on (4), converges well.

Acknowledgement. The first author gratefully acknowledges the support by the German Research Foundation (DFG) under Grant No. EL 584/1-2.

References

1. P. Monk. *Finite Element Method for Maxwell's Equations*. Oxford, Oxford Univ Press, 2003.
2. M. Huber, J. Schoeberl, A. Sinwel, and S. Zaglmayr. Simulation of diffraction in periodic media with a coupled finite element and plane wave approach. *SIAM J. Math. Anal.*, 43:1205–1231, 2009.
3. A. Rathsfeld. Shape derivatives for the scattering by bi-periodic gratings. WIAS Preprint No. 1640, Berlin, 2011.
4. G. Hu and A. Rathsfeld. Scattering of time-harmonic electromagnetic plane waves by perfectly conducting diffraction gratings. WIAS Preprint No. 1694, Berlin, 2012.

A new indicator to assess the quality of a Pareto approximation set applied to improve the optimization of a magnetic shield.

E. Dilettoso, S.A. Rizzo, N. Salerno

Dipartimento di Ingegneria Elettrica, Elettronica ed Informatica - Università di Catania, Catania 95125, Italy,
{emanuele.dilettoso; santi.rizzo; nunzio.salerno}@dieei.unict.it

Summary Evaluating the performances of an optimization algorithm is more complex in the case of multi-objective optimization problems than single-objective ones. In the former case, the optimization aims to obtain a set of non-dominated solutions close to the Pareto-optimal front, well-distributed, maximally extended and full filled. This paper presents a new quality indicator encompassing the aforementioned goals. The quality indicator is then used to select a suitable algorithm for the multi-objective optimization of a magnetic shield in an induction heating system.

1 Introduction

The optimization results provided by a multi-objective algorithm are, usually, a set of non-dominated solutions (called approximation set in the decision space and Pareto approximation front in the objective functions space).

The main goal of such algorithms is to provide an approximation set matching the Pareto-optimal set.

The notion of performance of an optimization algorithm involves the quality of the solutions that it is able to produce and the computational effort required to provide such solutions.

The definition of quality is a complex topic to deal with in the case of multi-objective optimization problems. A good optimization algorithm should [1]:

- minimize the distance from the Pareto approximation front to the Pareto-optimal front;
- obtain a good (usually uniform) distribution of the solutions found;
- maximize the extension of the Pareto approximation front, i.e., for each objective, a wide range of values should be covered by the non-dominated solutions;
- maximize the “density” of the Pareto approximation front, i.e. is desirable a high cardinality for the approximation set.

In literature, there are different methods that assign a quality indicator or a set of quality indicators that are a measure of the

aforementioned goals and, usually, a combination of them is used in order to evaluate the goodness of a multi-objectives optimization algorithm [2].

In this paper, a new unary quality indicator, called *Degree of Approximation (DOA)*, is presented. It takes into account all the goals listed before. DOA was then helpful for the choice of the optimization algorithm more suitable to perform the multi-objective optimization of a magnetic shield.

2 Degree of Approximation indicator

DOA is a distance-based unary quality indicator that also encompasses the distribution, the extension and the cardinality of a Pareto approximation front.

In detail, for a Pareto front approximation set A , *DOA* is computed as described in the following.

First, given a solution i belonging to the Pareto-optimal front (POF), the sub-set of A containing the solutions dominated by i , $D_{i,A}$, is determined. Hence, if the number of elements belonging to $D_{i,A}$ is not null ($|D_{i,A}| > 0$), for each approximated solution $a \in D_{i,A}$ is computed the Euclidean distance $df_{i,a}$ (see Fig.2) between a and i as:

$$df_{i,a} = \sqrt{\sum_{k=1}^n [f_{k,a} - f_{k,i}]^2} \quad (1)$$

where n is the number of objective functions, $f_{k,a}$ is the value of the k -th objective function of approximated solution a , $f_{k,i}$ is the value of the k -th objective function of optimal solution i .

Then the parameter $d_{i,A}$ is computed: it is the Euclidean distance between i and the nearest approximated solution belonging to $D_{i,A}$:

$$d_{i,A} = \begin{cases} \min(df_{i,a}) & a \in D_{i,A} \text{ if } |D_{i,A}| > 0 \\ \infty & \text{if } |D_{i,A}| = 0 \end{cases} \quad (2)$$

Another quantity, $rf_{i,a}$ is computed as:

$$rf_{i,a} = \sqrt{\sum_{k=1}^n [\max(0, f_{k,a} - f_{k,i})]^2} \quad (3)$$

it is a ‘reduced’ distance between i and a not dominated solution a of A .

Then considering the solutions of A not dominated by i . the parameter $r_{i,A}$, is computed similarly to $d_{i,A}$:

$$r_{i,A} = \begin{cases} \min(rf_{i,a}) & a \in A \setminus D_{i,A} \text{ if } |A \setminus D_{i,A}| > 0 \\ \infty & \text{if } |A \setminus D_{i,A}| = 0 \end{cases} \quad (4)$$

Finally, defining, for each $i \in \text{POF}$, the value $s_{i,A}$ as the minimum between $d_{i,A}$ and $r_{i,A}$, the new unary quality indicator, DOA , is computed as:

$$DOA(A) = \frac{1}{|POF|} \sum_{i=1}^{|POF|} s_{i,A} \quad (5)$$

The smaller is DOA the better is the Pareto approximation front.

3 Optimization of a magnetic shield

The DOA quality indicator was used to compare the Pareto approximation fronts given by two different multi-objective optimization algorithms NPAEP [3] and NSGA II [4] applied to mathematical benchmark problems for which the true POF was known. In particular, Table 1 shows the results obtained by NPAEP and NSGA II for the Fonseca and Fleming problem [5] (FON) using only 1000 and 2500 objective function evaluations. The results are the DOA mean values (over one hundred trials): the lower the index is the better the algorithm works.

Table 1. Results for the FON problem.

n_v	NPAEP	NSGA II
1000	0.006427	0.018121
2500	0.003008	0.006400

NPAEP works better than NSGA II, it is worth pointing out that NSGA II needs 2500 fitness evaluations to reach results comparable to those of NPAEP. For all the mathematical benchmark problems with few design variables and for which the true POF was regular, NPAEP shown the same behaviour. NSGA II outperforms NPAEP when the number of design parameters increases.

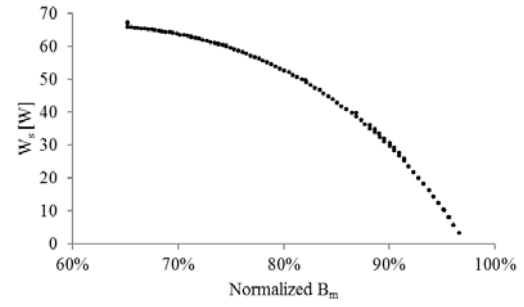


Fig. 1. POF provided by NPAEP.

Hence NPAEP was chosen for the optimization of the shielding of the axisymmetric induction heating system optimized in [6] in which the different objectives were combined in a single objective function. Two design parameters are used: the semi-height and the outer radius of the steel shield; while the two optimization targets to minimize, i.e. the mean magnetic induction B_m in the target area and the power losses W_s in the shield, are kept distinct. Here are reported the results of the passive shield optimization only. Figure 1 shows the POF obtained by NPAEP after 2000 numerical simulations carried out by means of FEM-DBCI [6]. The POF is well-distributed and full filled thus the decision maker has several solutions to choose from.

More details and results will be given in the full contribution.

References

1. E. Zitzler, K. Deb, L. Thiele, “Comparison of multiobjective evolutionary algorithms: empirical results”, *Evol. Comp.*, vol. 8, n.2, pp.173-195, 2000.
2. D. A. Van Veldhuizen, G. B. Lamont, A. Zalazala, R. Eberhart, “On measuring multiobjective evolutionary algorithm performance”, *IEEE CEC2000*, vol. 1, pp.204-211, 2000.
3. E. Dilettoso, S. A. Rizzo, N. Salerno, “Niche Pareto-Archived Evolutionary Programming for Multi-Objective Electromagnetic Optimization”, *17th IEEE COMPUMAG, Florianopolis (BR)*, 2009.
4. K. Deb, S. Agrawal, A. Pratap, T. Meyarivan, “A fast and elitist multiobjective genetic algorithm: NSGA-II”, *IEEE Trans. Evolutionary Computation*, vol. 6, no. 2, pp. 182-197, 2002.
5. C. M. Fonseca, P. J. Fleming, “Multiobjective genetic algorithms made easy: Selection, sharing and mating restriction,” *IEE Genetic Alg. in Eng. Syst.: Innovat. and Appl.*, pp. 45–52, Sep. 1995.
6. S. Alfonzetti, E. Dilettoso, S. A. Rizzo, N. Salerno, “Stochastic Optimization of Magnetic Shields in Induction Heating Applications by means of FEM-DBCI”, *IEEE Tr.Mag.*, vol.45, pp.1752-1755, 2009.

Accurate and efficient FEM simulations of circular spiral planar inductors

S.A. Rizzo¹, N. Salerno¹ and S. Sindoni¹

¹Dipartimento di Ingegneria Elettrica, Elettronica e Informatica - Università di Catania - Catania, Italy
sarizzo@dieei.unict.it, nsalerno@dieei.unict.it and ssindoni@dieei.unict.it

Summary. In this paper an efficient methodology to simulate electromagnetic devices involving circular spiral planar windings is illustrated. The numerical simulations are carried out by means of 2D axisymmetric finite element (FE) analyses to solve electrostatic and magneto quasi-stationary (MQS) field problems taking into account all parasitic effects, in order to obtain accurate results with a reduced computational effort.

1 Introduction

One of the more pressing objective of technology is to improve performances of electrical and electronic devices reducing their dimensions, weight, power consumption and cost. To achieve this goal miniaturization of devices components, increase of signals frequency and easy manufacturing are mandatory.

Integrated planar electromagnetic devices are widely applied and, in particular, spiral planar windings can be used as integrated inductors for RF systems [1], as antennas for wireless transmissions, in RFID applications, as HF transformers [2], for contactless energy transmission systems or as EMI filters [3].

In this paper, the performances of coreless planar spiral windings (CPSW) used as integrated planar EMI filter for limiting conducted emissions are investigated by means of numerical simulations. The simulations were carried out by means of FE analyses following an efficient strategy, described in section 2, that allows to obtain accurate results with a reduced computational effort. A prototype was realized and comparison between simulated and measured results were made as shown in section 3.

2 Finite element strategy

Electromagnetic planar devices are affected by several parasitic effects that influence their operation and performances. The increase of signal frequency produce an increase of the windings resistance due to the skin effect and to

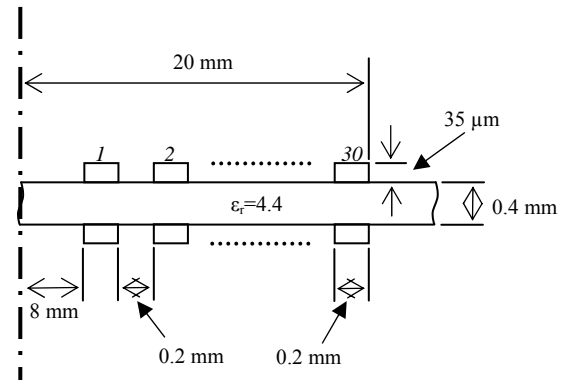


Fig. 1. Axisymmetric section of the prototype and geometric parameters.

the proximity of other conductors; the capacitive effects, that are negligible at low frequency, must be considered and they determines the frequency response of the device and its resonances.

In this work, a coreless EMI filter made by two circular spiral planar inductors drawn on a double face printed circuit board (PCB) is analyzed. To simulate the planar EMI filter, FE analyses were preferred to analytical models: since these models are often too simple and inaccurate especially to determine distributed turn-to-turn capacitances and the resistance in presence of skin and proximity effects. In order to consider all these effects, a full wave 3D FE analysis should be necessary but it requires a huge computational effort particularly if conductors must be discretized by means of a fine mesh.

In this work, authors present a strategy to carry out accurate FE simulations with an acceptable computational cost in terms of memory usage and CPU time.

This strategy consists in the following steps:

- 1) the real 3D geometry of the filter is approximated with an axisymmetrical one as shown in Fig. 1;
- 2) an electrostatic FE analysis is carried out by mean of FEM-DBCI [4] in order to calculate the matrix of capacitances [5] among all turns;

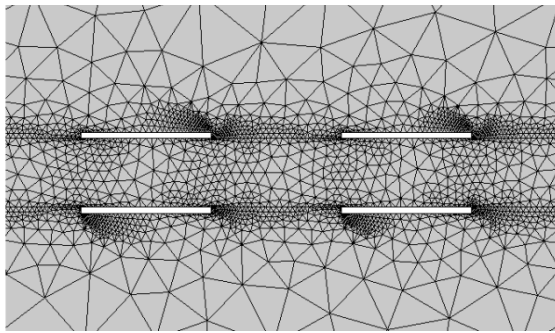


Fig. 2. FE mesh near conductors.

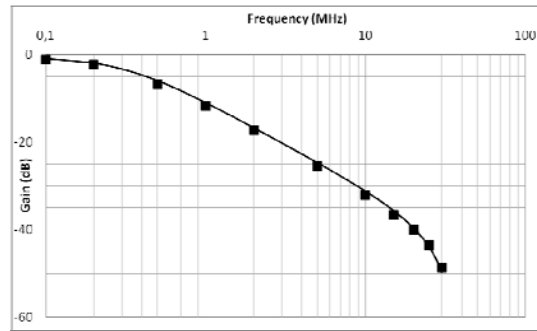


Fig. 3. Simulated (continuous line) and measured (marks) transfer gain for the CM filter.

3) MQS analyses [6] are then performed in the range 1÷30 MHz and the capacitive contribution is taken into account by means of concentrated capacitors connected between each couple of turns (circuit elements interface with finite elements).

Steps 2 and 3 were performed by means of a script that launched the FE analyses consecutively: first the electrostatic solution and then the MQS analyses in which all the capacitors are automatically inserted between each pair of turns.

3 Simulation results

Figure 2 shows a detail of the FE mesh for electrostatic analysis: in this case conductors are not discretized and a total of about 13,500 second order finite elements were used. In the MQS analyses conductors should be discretized according with penetration dept in order to have accurate results: to avoid the use of an adaptive meshing, the mesh with the right accuracy at 30 MHz was used for all the frequencies (a total of about 75,000 second order finite elements were employed).

All the computations were performed by means of ELFIN, an FE code developed by the authors [7]. The simulations runs on a PC (Pentium IV, 3,2 GHz, 4Gb RAM): they take about one hundred minutes. On the same machine it was impossible to complete a full wave 3D FE analysis of the real device, also using a coarse mesh inside conductors.

A prototype was realized on which several measures were performed.

Figure 3 shows a comparison between simulated and measured transfer gain for the CM filter: numerical results are in good agreement with measures.

Similar results were obtained for the DM filter.

More details and results will be given in the full contribution.

References

1. J. N. Burghartz and B. Rejaei. On the Design of RF Spiral Inductors on Silicon. *IEEE Transactions on Electron Devices*, 50: 718-729, 2003.
2. S. C. Tang, S. Y. (Ron) Hui and H. Shu-Hung Chung. Coreless Planar Printed-Circuit-Board (PCB) Transformers - A Fundamental Concept for Signal and Energy Transfer. *IEEE Transactions on Power Electronics*, 15: 931-941, 2000.
3. Xun Liu, C.K. Lee and S.Y. Hui. An Integrated Planar EMI Filter for Ultra-high Frequency Power Converters. *IEEE Power Electronics Specialists Conference (PESC)*, 1528 – 1534, 2007.
4. G. Aiello, S. Alfonzetti, S. Coco and N. Salerno. Axisymmetric Unbounded Electrical Field Computation by Charge Iteration. *IEEE Transactions on Magnetics*, 29: 2043-2046, 1993.
5. G. Aiello, S. Alfonzetti and S. Coco. Capacitance Computation in Symmetric Multiconductor Systems. *IEEE Transactions on Magnetics*, 30: 2952-2955, 1994.
6. G. Aiello, S. Alfonzetti, S. Coco and N. Salerno. Current Iteration for Unbounded Skin-Effect Problems. *International Journal for Computation and Mathematics in Electrical and Electronic Engineering (COMPEL)*, 13: 299-304, 1994.
7. G. Aiello, S. Alfonzetti, G. Borzi and N. Salerno. An Overview of the ELFIN Code for Finite Element Research in Electrical Engineering. *Software for Electrical Engineering Analysis and Design IV*, Wessex Institute of Technology Press, 143-152, 1999.

Stochastic Collocation Methods and Model Reduction for Maxwell's Equations

Peter Benner and Judith Schneider

Max Planck Institute for Dynamics of Complex Technical Systems, Sandtorstr. 1, 39106 Magdeburg, Germany
benner@mpi-magdeburg.mpg.de, will@mpi-magdeburg.mpg.de

Summary. We use a Stroud-based collocation method to analyze the parameter behavior of the time-harmonic Maxwell equations and reduce the computational costs by applying model order reduction to the system matrices.

1 Motivation

During the design process of semiconductor structures, simulations of new micro and nano scale systems are essential due to, e. g., the expensive production of prototypes. An important aspect is the ongoing miniaturization of the structures on the one hand and the increase in the working frequencies on the other hand. The high density of electric conductors induces parasitic effects, e. g., crosstalk, which have to be considered already in the design stage. Therefore, the exact knowledge of the semiconductor structures and the surrounding electromagnetic (EM) field is necessary.

Another effect, which plays a no longer negligible role, is the variation of the feature structure size caused by inaccuracies of the resolution during the lithography. To consider these variations in the simulation, models with parametric uncertainties are required. A variational analysis of the effect of these uncertainties on the EM field requires methods for uncertainty quantification (UQ) [4, 6]. For this purpose, we will employ non-intrusive approaches as they allow the use of EM field solvers for deterministic problems without accessing the source code. Possible choices are Monte Carlo and stochastic collocation. Here we will employ the latter due to their faster convergence. Still, UQ via stochastic collocation requires numerous full-order EM field solves which can be a time-consuming task for complicated 3D geometries. It is thus our goal to combine this approach with model order reduction methods (MOR) for the Maxwell equations to reduce the computational cost, where the reduced-order model needs to preserve the statistical properties of the full-order model. All these problems are addressed within the research network *Model Reduction for Fast Simulation of New Semiconductor Structures for Nanotechnology and Microsystems Technology (MoreSim4Nano)*, see [5]. Figure 1 shows a coplanar waveguide which serves as a benchmark

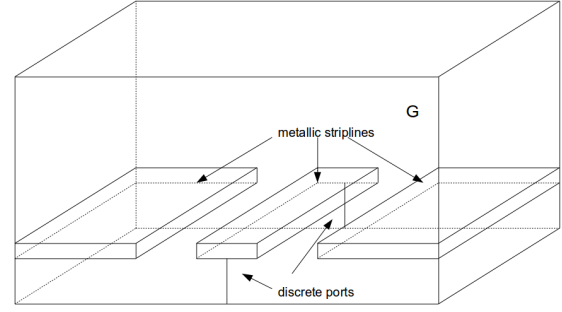


Fig. 1. Coplanar waveguide.

within MoreSim4Nano and for which we show some numerical results in Section 4.

2 Stochastic Collocation for EM Field Computations

The system of equations describing the EM field are Maxwell's equations

$$\begin{aligned}\partial_t(\epsilon \mathbf{E}) &= \nabla \times \mathbf{H} - \sigma \mathbf{E} - \mathbf{J} \\ \partial_t(\mu \mathbf{H}) &= -\nabla \times \mathbf{E} \\ \nabla \cdot (\epsilon \mathbf{E}) &= \rho \\ \nabla \cdot (\mu \mathbf{H}) &= 0,\end{aligned}$$

with the electric field intensity \mathbf{E} , the magnetic field intensity \mathbf{H} , the charge density ρ , the impressed current source \mathbf{J} , and material parameters $\epsilon = \epsilon_r \cdot \epsilon_0$ (permittivity), $\mu = \mu_r \cdot \mu_0$ (permeability), σ (electrical conductivity). For simplification, we work with the time-harmonic form

$$\nabla \times (\mu^{-1} \nabla \times \mathbf{E}) + i\omega \sigma \mathbf{E} - \omega^2 \epsilon \mathbf{E} = i\omega \mathbf{J}, \quad (1)$$

on the space $X = \{\mathbf{E} \in H_{curl}^0 \mid \nabla \cdot (\epsilon \mathbf{E}) = \rho\}$.

Up to now, we consider the material parameters ϵ_r , μ_r , and σ as uncertain. For the examination of their influence on the statistical behavior of the solution \mathbf{E} we use stochastic collocation [1] with Stroud interpolation points [2].

2.1 Stochastic Collocation

Collocation methods rely on interpolation. The idea is to approximate high-dimensional integrals, e. g., the

expectation value of our solution E , by an (efficient) quadrature rule

$$\mathbb{E}(E) = \int_{\Gamma} E(\xi) f(\xi) d\xi \approx \sum_{i=1}^n E(\xi_i) w_i.$$

Here Γ is the image of the probability space under the probability measure, f is the unknown probability density function of E , ξ_i are the n interpolation points and w_i are the associated weights.

2.2 Stroud Integration

The interpolation formula used in our algorithm was introduced in 1957 by A. H. Stroud [7] and yields either beta or normal distributed interpolation points which are weighted by $1/n$, where n is the number of interpolation points as in Sec. 2.1. Though we need $\varepsilon_r, \mu_r > 0$ and $\sigma \geq 0$, we suppose them to be log-normal distributed and use the exponential of the normal distributed Stroud points as interpolation points.

3 Model Order Reduction

The discretization of (1) leads to the following system

$$\begin{aligned} \mu_r A_{\mu_0} \mathbf{e} + \varepsilon_r A_{\varepsilon_0} \ddot{\mathbf{e}} + \sigma A \dot{\mathbf{e}} &= B u, \\ y &= C \mathbf{e}, \end{aligned}$$

where \mathbf{e} is the discretized electric field, $A_{\mu_0}, A_{\varepsilon_0}$ and A are the parameter independent system matrices in $\mathbb{R}^{N \times N}$, u, y define the inputs/ outputs, and B, C specify the input/ output behavior. Here N is the number of grid points in G and large. This system is then reduced, e. g., by means of rational interpolation methods as in [3] and we achieve a reduced system of the form

$$\begin{aligned} \mu_r \hat{A}_{\mu_0} \hat{\mathbf{e}} + \varepsilon_r \hat{A}_{\varepsilon_0} \ddot{\hat{\mathbf{e}}} + \sigma \hat{A} \dot{\hat{\mathbf{e}}} &= \hat{B} u, \\ \hat{y} &= \hat{C} \hat{\mathbf{e}}, \end{aligned}$$

where $\hat{A}_{\mu_0}, \hat{A}_{\varepsilon_0}, \hat{A} \in \mathbb{R}^{r \times r}$ with $r \ll N$ and $\|y - \hat{y}\|$ small.

4 Numerical Results Concerning the Stochastic Collocation Approach

As a benchmark we consider a coplanar waveguide with dielectric overlay, see Figure 1. The model consists of three perfectly conducting striplines situated at a height of 10mm in a shielded box with perfect electric conductor (PEC) boundary. The system is excited at one of the discrete ports and the output is taken at the other one.

Below a height of 15mm there is a substrate with $\varepsilon_r^1 \approx 4.4$ and $\sigma^1 \approx 0.02S/m$, above there is air with

$\varepsilon_r^2 \approx 1.07$ and $\sigma^2 \approx 0.01S/m$, while $\mu_r \approx 1$ within the whole box. The variance of each parameter is approximately 1% of the expected value.

The system is treated as a system with 5 uncertain parameters, which leads to the affine discretized form

$$\mu_r A_{\mu_0} \mathbf{e} + (\varepsilon_r^1 A_{\varepsilon_0}^1 + \varepsilon_r^2 A_{\varepsilon_0}^2) \ddot{\mathbf{e}} + (\sigma^1 A^1 + \sigma^2 A^2) \dot{\mathbf{e}} = B u, \\ y = C \mathbf{e}.$$

The discretization is done in FEniCS by use of Nédélec finite elements and the Stroud-based collocation is implemented in MATLAB[®]. Since the used discretization has only 18755 degrees of freedom, there is no model order reduction used up to now.

The Stroud-based collocation uses only 10 supporting points and the computation requires less than a minute. To verify the accuracy, the results are compared with a Monte Carlo simulation which operates on 10000 interpolation points. This takes several hours. Using the frequency $\omega = 0.6 \cdot 10^9$ we achieve the following relative errors for the expected value of \mathbf{e} and y

$$err_{rel, \mathbb{E}(\mathbf{e})} = 0.0038\% \quad \text{and} \quad err_{rel, \mathbb{E}(y)} = 0.0042\%.$$

Considering the fact that we use only 10 Stroud points the results are satisfactory. To achieve more accuracy one could use, e. g., a lot more sparse grid points, which would be much more expensive. For this reason and for systems of higher dimension we need MOR.

Acknowledgement. The work reported in this paper was supported by the German Federal Ministry of Education and Research (BMBF), grant no. 03MS613A. Responsibility for the contents of this publication rests with the authors.

References

1. I. Babuska, F. Nobile, and R. Tempone. A Stochastic Collocation Method for Elliptic Partial Differential Equations with Random Input Data. *SIAM Review*, 52(2):317–355, 2010.
2. H. Bagci, A. C. Yücel, J. S. Hesthaven, and E. Michielssen. A Fast Stroud-Based Collocation Method for Statistically Characterizing EMI/EMC Phenomena on Complex Platforms. *IEEE Transactions on Electromagnetic Compatibility*, 51(2):301–311, 2009.
3. U. Baur, C. A. Beattie, P. Benner, and S. Gugercin. Interpolatory projection methods for parameterized model reduction. 31(5):2489–2518, 2011.
4. H. G. Matthies. *Encyclopedia of Computational Mechanics*, volume 1, chapter Uncertainty Quantification with Stochastic Finite Elements. John Wiley and Sons, 2007.
5. <http://www.moresim4nano.org>.
6. C. Schwab and C. J. Gittelsohn. Sparse tensor discretizations of high-dimensional parametric and stochastic PDEs. *Acta Numerica*, 20:291–467, 2011.
7. A. H. Stroud. Remarks on the Disposition of Points in Numerical Integration Formulas. *Mathematical Tables and Other Aids to Computation*, 11(60):257–261, 1957.

An Embarrassingly Parallel Algorithm for Finite Element Formulations

Eike Scholz, Sebastian Schöps, and Markus Clemens

Chair of Electromagnetic Theory, Bergische Universität Wuppertal
 {scholz,sschoeps,clemens}@uni-wuppertal.de

Summary. In this paper we derive a new stepwise embarrassingly parallel, globally convergent algorithm for linear and non-linear electrostatic problems. It is based on a new interpretation of the classical finite element formulation. We show problems with cellwise linear materials and prove convergence of the proposed method.

1 Overview

Nodal search finite element methods have been derived in [1] using a non-Galerkin approach. It allows a natural decoupling of finite elements similarly to discontinuous Galerkin approaches [2]. This paper will lay out this algorithm using a variation of the usual variational Galerkin method based finite element approach (see e.g. [3]) for equation 1.

$$\operatorname{div}(\varepsilon \operatorname{grad}(\phi)) = \rho \quad (1)$$

Using the Galerkin finite element approach (see e.g. [3]) has the advantage that it is easier to apply, broadly known, and seems to yield better conditioned systems, although it is less general than the initial approach in [1].

1.1 A Special Finite Element Representation

The proposed algorithm is based on a Lagrange finite element formulation, in which the resulting problem, after using the Galerkin approach, has the form

$$\mathbf{P}^T \mathbf{A} \mathbf{P} \alpha = -\mathbf{P}^T \mathbf{A} \lambda_0, \quad (2)$$

where \mathbf{A} is a block diagonal matrix, whose sub-matrices describe the local finite element stiffness matrices for associated single mesh cells, λ_0 is a vector containing boundary data, α is the vector of global degrees of freedom (dof), and \mathbf{P} is a very sparse incidence matrix mapping global to local degrees of freedom. The mathematical details of this are discussed in the full paper. Since \mathbf{A} is positive definite and symmetric, solving equation 2 is equivalent to solving

$$(\lambda_0 + \mathbf{P} \alpha)^T \mathbf{A} (\lambda_0 + \mathbf{P} \alpha) \stackrel{!}{=} \min. \quad (3)$$

Equation 3 is solved directly, using a direct search optimization algorithm, that changes only one global degree of freedom in each step. The used algorithm is

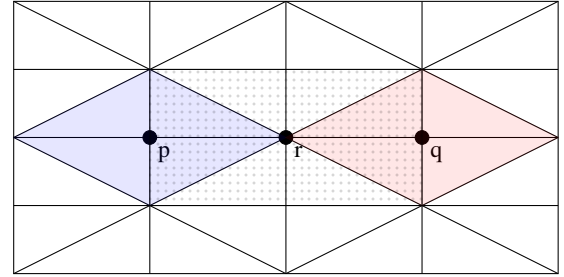


Fig. 1. Schematic sketch of a 2D Lagrange FEM mesh with affected cells and independent degrees of freedom. The affected cells of the dof associated with node p are blue, the ones associated with node q are red, and the ones associated with the node r are dotted. The set $\{p, q\}$ is a set of independent degrees of freedom, while the set $\{p, r, q\}$ is not.

a simple generating set search method as discussed in [4]. Further in the nonlinear case \mathbf{A} depends on α which requires some additional care. This approach results in an algorithm with global convergence, even in many non-linear cases. The mathematical details and constraints are discussed in the full paper.

2 Nodal Search

The nodal search algorithms exploits the fact, that a change in a global degree of freedom only affects a very local area of an approximation function build from finite elements. The basic idea is to find first, for every degree of freedom, the area where a change in the degree of freedom actually has an effect on the associated approximation function. This is done by finding the affected cells, as shown in Fig. 1, of every global degree of freedom.

Next, the algorithm determines a decomposition of all global degrees of freedom into a set of sets of independent degrees of freedom. Where independent means that the degrees of freedom have no affected cells in common, as shown in Fig. 1. A rigorous mathematical analysis of this decomposition approach is provided in the full paper. Last, an iteration over nodal search steps is done which terminates when the step-length becomes lower than a given threshold.

A nodal search step tries to improve the value of one node's dof. This leads to a formulation that is similar to a multiplicative Schwarz method and in

fact is, for first order finite elements, a multiplicative Schwarz method, which is shown in the full paper. Further in the first order case it is similar to the algorithm in [5] as well. The computation of a nodal search step obviously depends only on a few degrees of freedom. A nodal search step on node l improves an existing approximation described by α to a new better approximation α^{new} via $\alpha^{new} = \alpha + \theta_l \mathbf{e}_l$ where the nodal search step length θ_l can, for cellwise linear isotropic materials, be computed by

$$\theta_l = -\frac{\xi_l + \mathbf{v}_l^T \alpha}{\chi_l}, \quad (4)$$

where ξ_l, χ_l are real numbers and \mathbf{v}_l is a sparse vector for all l . All values i.e. ξ_l, χ_l and \mathbf{v}_l^T can be computed in parallel using λ_0, \mathbf{P} and \mathbf{A} .

Further, the computation of all θ_l in a set of independent degrees of freedom is embarrassingly parallel, which is proven in the full paper. Thus, iterating through all sets of a decomposition into sets of independent degrees of freedom, yields a stepwise embarrassingly parallel algorithm.

3 Test Implementation and Results

The algorithm has been implemented with OpenMP parallelization. This test implementation uses second order tetrahedral elements, and an ad-hoc iterative mark and sweep algorithm to create the required decomposition of degrees of freedom into sets of independent degrees of freedom. The algorithm has been tested using the real world problem shown in Fig.2. The details of the model are described in [6].

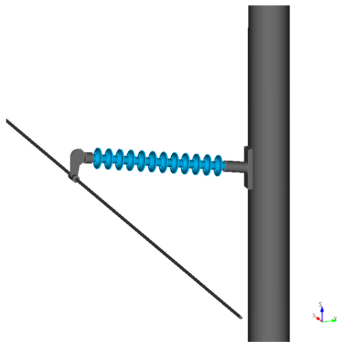


Fig. 2. A real world insulator model for testing, meshed using second order tetrahedrons with about 4.8 million nodes.

These results show, that the algorithm does not only work in theory, but in practice as well. The results show that the convergence is slow but secure even without preconditioning on ill conditioned systems. Its speed, of course, depends on the size of the problem and the amount of parallel processors. Thus a variant of this algorithm, e.g. extended by a multi-grid scheme, might become a good default algorithm, on GPGPU systems, similarly to the approach in [7].

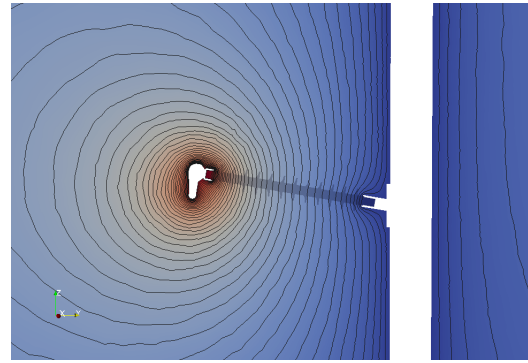


Fig. 3. A result for the geometry in Fig. 2 visualizing the electric potential by color and equipotential surfaces by black lines. Computation took about 10h on a 48core (2.8GHz AMD Opteron) machine.

4 Outlook

We have presented a new massively parallel algorithm for solving electrostatic problems. The full paper provides a rigorous mathematical treatment of the algorithm derivation and convergence with a lot more references. Further, the above and additions numerical results are discussed in detail, regarding convergence, speed and stability.

References

1. Eike Scholz, Principles of Optimal Residual Formulations and Optimal Residual Finite Element Methods for Solving Partial Differential Equations. Mathematics Diploma Thesis, University Hamburg 2012.
2. Tim Warburton, Jan S. Hesthaven Nodal Discontinuous Galerkin Methods Texts in Applied Mathematics 54, Springer Science+Buisines Media 2008
3. Alexandre Ern, Jean-Luc Guermond Theory and Practice of Finite Elements Applied Mathematical Sciences 159, Springer-Verlag New York 2004
4. Tamara G. Kolda, Robert M. Lewis, Virginia Torczon Optimization By Direct Search: New Perspectives on Some Classical and Modern Methods In Siam Review, Vol. 45, No. 3, pp. 385-482, Society for Industrial and Applied Mathematics
5. Joao Pedro A. Bastos, Nelson Sadowski A New Method to Solve 3-D Magnetodynamic Problems Without Assembling an $Ax = b$ System IEEE Transactions on Magnetics, Vol. 46, No. 8, August 2010
6. D. Stefanini, M. Clemens, J.M. Seifert Three Dimensional FEM Electric Field Calculations for EHV Composite Insulator Strings International Power Modulators and High Voltage Conference (IPMHVC 2010), 23.-27.05.2010, Atlanta, USA, pp. 238-242
7. David M. Fernandes, Maryam Mehri Dehnavi, Warren J. Gross, Dennis Giannacopoulos Alternate Parallel Processing Approach for FEM IEEE Transactions on Magnetics, Vol. 48, No 2 February 2012

The Reconstruction of Shape with 3-Step Modeling Strategy

Murat Simsek¹

Electronics and Communication Department, Istanbul Technical University, Turkey simsekmu@itu.edu.tr

Summary. Three step modeling strategy is newly developed to improve the performance of Artificial Neural Network through Knowledge Based Techniques. This strategy provides not only more accurate results but also time efficiency especially in complex modeling problems. In this study the reconstruction of shape obtained from measurements of scattered electromagnetic fields is considered. Multi Layer Perceptron is chosen for realization of Artificial Neural Networks. In order to demonstrate the efficiency of three step modeling, the reconstruction of shape for two different geometries are considered.

1 Introduction

Artificial Neural Network (ANN) is a well known approach in modeling problems where only input-output data is available. Data generation, number of neurons and number of iterations are important features that effect the accuracy of ANN. Since for complex modeling problems it is difficult to have input-output necessary data, modeling is hardly applicable for such problems.

Knowledge Based Techniques were developed to reduce complexity of modeling problem by using the knowledge about the considered problem [2,4]. Three step modeling strategy further improves the efficiency of knowledge based techniques. This strategy uses same training data and same number of neurons, but generates more accurate results and less time consuming than the conventional ANN modeling.

In this work, the main contribution over [1] is to use MLP as ANN structure. MLP, Prior Knowledge Input (PKI) [4] and Prior Knowledge Input with Difference (PKI-D) [2] are used in first (M-1), second (M-2) and third (M-3) steps of 3-step modeling strategy [1], respectively. In order to show the efficiency of the method inverse scattering problem is considered.

2 3-Step Modeling Strategy

3-step modeling strategy provides gradual improvements during modeling. For this purpose, it firstly utilizes ANN structure. After training process is completed, this model is named model-1 (M-1). M-1 generates prior knowledge for PKI model. PKI utilizes response of M-1 and complexity of modeling problem is reduced via this prior knowledge. After training

process is completed, this model named model-2 (M-2). Finally PKI-D utilizes M-2 response both at input and output. Therefore M-2 is used to reduce complexity and it narrows the output range using difference between original response and M-2 response.

Each step uses same number of iterations and total number of iterations and neurons are the same as in conventional ANN model. This strategy gradually improves accuracy during three steps and total time consumption is always less than using conventional ANN model.

Modeling steps and necessary formulations of 3-step modeling strategy are given as follows:

- **Step-1:**

Training ANN and calculate training response

$$x_{M-1} = f_{ANN}(Y_f)$$

- **Step-2:**

Training ANN using extra knowledge Y_{M-1} and calculate training response

$$x_{M-2} = x_{PKI} = f_{ANN}(Y_f, x_{M-1})$$

- **Step-3:**

Training ANN using extra knowledge Y_{M-2}

$$x_{M-3} = x_{PKI-D} = f_{ANN}(Y_f, x_{M-2}) + x_{M-2}$$

- **Test error:**

Calculate test data using $M-1$, $M-2$ and $M-3$ and find test error for 3-step modeling

$$Mean\ Error = \frac{1}{N} \times \sum_{i=1}^N \frac{|X_{original,i} - X_{method,i}|}{X_{original,i}}$$

$$Max\ Error = \max_i \left\{ \frac{|X_{original,i} - X_{method,i}|}{X_{original,i}} \right\}$$

After training process is completed for 3-step modeling as shown in Fig.1, each model is used to calculate test error. This error performance is useful to compare this strategy with conventional modeling technique.

3 Inverse Scattering Problem

The direct scattering problems investigate the scattering fields for a given object. On the other hand, the aim of inverse scattering problems is to find out the properties of an object, such as shape, electromagnetic parameters, position for given scattered fields. Five Fourier coefficients (one of them is real others are complex) are used as inputs and 10 complex values obtained by measurement points in Fig.2 are used as outputs of the original model [3]. In this

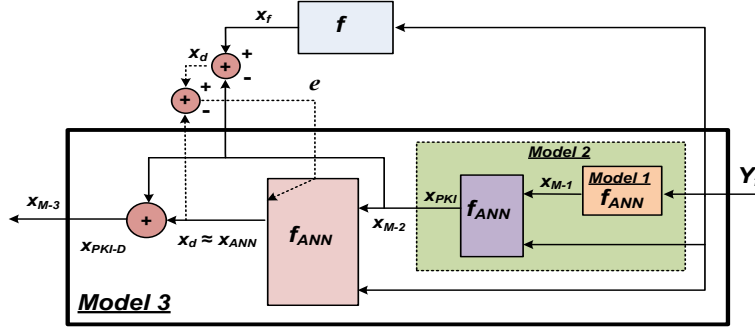


Fig. 1. 3-step modeling of inverse scattering problem.

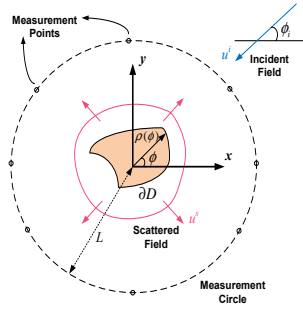


Fig. 2. Geometry of scattering problem.

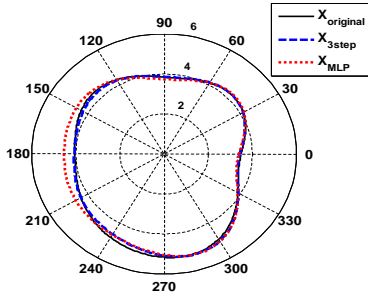


Fig. 3. The comparing original shape with the shape reconstruction of 3-step model and MLP-ANN model for geometry-1.

work, number of neurons and number of iterations are chosen 60×60 for conventional ANN modeling and 15×15 , 20×20 , 25×25 for the first, second and third step of 3-step modeling strategy. In total conventional ANN and 3-step modeling use same number of iterations and neurons. The geometry of inverse scattering problem is shown in Fig.2. Time consumption is 1.95 sec in M-1, 2.215 sec in M-2 and 2.231 sec in M-3. Total time consumption of 3-step modeling (6.396 sec) is less than conventional ANN's (20.187 sec). To compare test results of 3-step modeling and conventional ANN, 5 randomly generated geometry are obtained. Original shape, the reconstruction of shape obtained from 3-step modeling and conventional ANN are given together in Fig.3 for geometry – 1 and Fig.4 for geometry – 2.

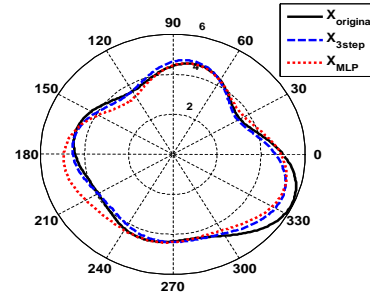


Fig. 4. The comparing original shape with the shape reconstruction of 3-step model and MLP-ANN model for geometry-2.

4 Conclusion

Although 3-step model utilizes same number of iterations and number of neurons as conventional ANN, it generates more accurate results (mean error: %3.7) in less time than conventional structure (mean error: %4.2). This efficiency is based on knowledge based strategy in 3-step modeling. This work demonstrates the efficiency of this strategy for inverse scattering problem as well.

References

1. M. Simsek. Developing 3-step modeling strategy exploiting knowledge based techniques. In *The European Conference on Circuit Theory and Design*, pages 616–619, Linköping, Sweden, August 29 to 31 2011.
2. M. Simsek and N. S. Sengor. A knowledge-based neuromodeling using space mapping technique: compound space mapping-based neuromodeling. *Int. J. Numer. Model: Electronic Networks, Devices And Fields*, 21(1-2):133–149, 2008.
3. M. Simsek and N. S. Tezel. The reconstruction of shape and impedance exploiting space mapping with inverse difference method. *IEEE Transactions on Antennas and Propagation*, 60(4):1868–1877, Apr. 2010.
4. Q. J. Zhang and K. C. Gupta. *Neural Networks for RF and Microwave Design*. Artech House, Boston, 2000.

A High-Order Discontinuous Galerkin-Approach-Based Particle-In-Cell Method for the Simulation of Large Scale Plasma Devices

A. Stock¹, J. Neudorfer¹, M. Pfeiffer², R. Schneider³, S. Fasoulas², and C.-D. Munz¹

¹ Institut für Aerodynamik und Gasdynamik, Universität Stuttgart, Germany stock@iag.uni-stuttgart.de, iagneudo@iag.uni-stuttgart.de, munz@iag.uni-stuttgart.de

² Institut für Raumfahrtssysteme, Universität Stuttgart, Germany mpfeiffer@irs.uni-stuttgart.de, fasoulas@irs.uni-stuttgart.de

³ Institut für Hochleistungsimpuls- und Mikrowellentechnik, Karlsruher Institut für Technologie, Germany rudolf.schneider@kit.edu

Growing computational capabilities and simulation tools based on high-order methods allow for complex shaped plasma devices to simulate the entire nonlinear dynamics of the Vlasov-Maxwell system modelling the particle-field-interactions of a non-neutral plasma without significant simplifications [4]. Thereby, new insights into physics on a level of detail that has never been available before provides new design implications and a better understanding of the overall physics.

In the field of gyrotron design state-of-the-art fast codes play a crucial role [2, 6]. While procuring their rapidity by making strong physical simplifications and approximations, the correctness of these assumptions is not known to be valid for all considered variations of the geometry and operation setup. Solving the nonlinear Vlasov-Maxwell system without significant physical reductions, the self-consistent transient 3D electromagnetic Particle-In-Cell (PIC) method [1, 3] can provide better insights into these setups and beyond that can serve as validation tool for a fast design code.

We present a high-order discontinuous Galerkin method based PIC code with high-order coupling techniques on unstructured grids in a parallelization framework allowing for large scale applications on high performance computing clusters [7, 10]. We simulate the geometrically complex gyrotron resonant cavity and the quasi-optical mode converter of the 170 GHz gyrotron aimed for plasma resonance heating of the fusion reactor ITER [5, 9]. A result of our high-order transient resonator simulations is shown in Figure 1.

Currently we enhance the range of applications of our PIC-code to rarefied plasma flows in which particles interaction has to be taken into account, i.e. collisional phenomena of the Boltzmann integral. According to the nature of these interactions, the Boltzmann collision integral has to be approximated with different appropriate approaches which require their own numerical model and method. The Direct Simulation Monte Carlo (DSMC) method which has been adopted and coded is the state-of-the-art approach for the numerical modeling of short-range elastic elec-

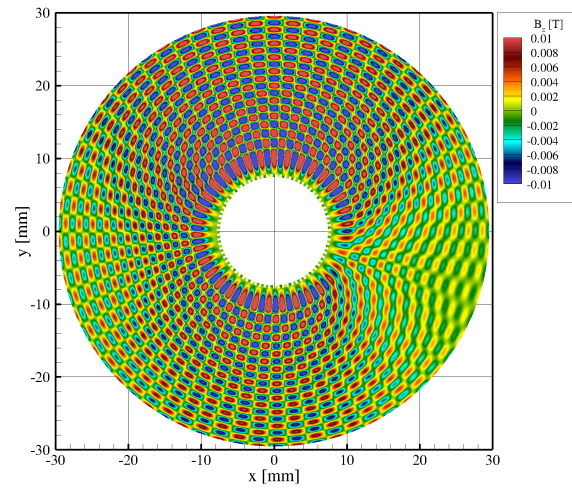


Fig. 1. B_z -field of a 170 GHz gyrotron resonator simulated with the PIC method on 512 processes.

tron neutral collisions and binary inelastic reactions like excitation, ionization, dissociation, recombination, etc. .

The coupling of the DSMC module with the DG-PIC solver has been carried out and the coupled code is applied to a variety of discharge problems for validation purposes. Besides collective phenomena from computations in gyrotrons, we will here further present and discuss results from plasma streamer simulations (see Fig. 2). Especially, we will focus our attention to the avalanche-streamer transition, the streamer formation and the subsequent streamer evolution which are key mechanisms in the early stage of the discharge phenomenology.

So far, scientific demonstration calculations for gyrotron devices and streamers have been performed [7, 10]. We expect that the growing potential of the code will enable us to simulate a broad range of applications also on industrial scale. Besides streamers and micro and millimeter wave sources, also applications with electromagnetic vulnerability background, such as the impact of space weather on satellites, and

new space propulsion concepts such as the *Mini Magnetospheric Plasma Propulsion* can be considered [8].

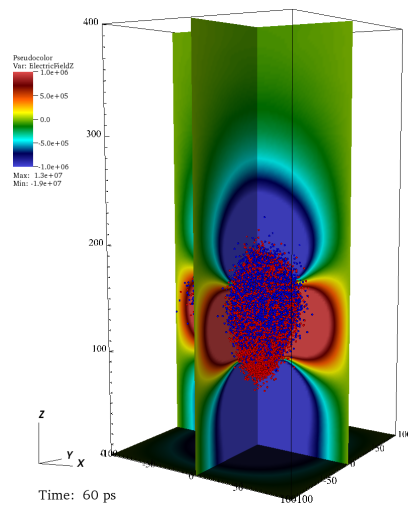


Fig. 2. Field and particle distribution from the streamer simulation on 500 MPI processes with the DG-PIC solver coupled with the DSMC module.

Acknowledgement. Work supported by the Deutsche Forschungsgemeinschaft (DFG) grant “Numerical Modeling and Simulation of Highly Rarefied Plasma Flows”.

References

1. C.K. Birdsall and A.B. Langdon. *Plasma Physics via Computer Simulation*. Adam Hilger, Bristol, Philadelphia, New York, 1991.
2. M. Botton, T. M. Antonsen, B. Levush, K. T. Nguyen, and A. N. Vlasov. MAGY: a time-dependent code for simulation of slow and fast microwave sources. *IEEE Transactions on Plasma Science*, 26:882–892, June 1998.
3. R. Hockney and J. Eastwood. *Computer Simulation using Particles*. McGraw-Hill, New York, 1981.
4. G.B. Jacobs and J.S. Hesthaven. High-order nodal discontinuous Galerkin particle-in-cell method on unstructured grids. *J. Comput. Phys.*, 214:96 – 121, 2006.
5. J. Jin, M. Thumm, B. Piosczyk, and T. Rzesnicki. Theoretical Investigation of an Advanced Launcher for a 2-MW 170-GHz TE_{34,19} Coaxial Cavity Gyrotron. *IEEE Transactions on Microwave Theory and Techniques*, 54(3):1139–1145, 2006.
6. S. Kern. *Numerische Simulation der Gyrotron-Wechselwirkung in koaxialen Resonatoren*. PhD thesis, Forschungszentrum Karlsruhe GmbH, FZKA 5837, 1996.
7. J. Neudorfer, A. Stock, J. Flamm, F. Hindenlang, G. Gassner, C.-D. Munz, R. Schneider, and S. Roller. Numerical investigation of high-order gyrotron mode propagation in launchers at 170 GHz. accepted for publication in: *IEEE Transaction on Plasma Science*, XX:yyy–yyy, 2012.
8. M. Pfeiffer, D. Petkow, G. Herdrich, and S. Fasoulas. Assessment of a numerical approach suitable for the m2p2 problem. *The Open Plasma Physics Journal*, 4:24–33, 2011.
9. B. Piosczyk, G. Dammertz, O. Dumbrajs, O. Drumm, S. Illy, J. Jin, and M. Thumm. A 2-MW, 170-GHz coaxial cavity gyrotron. *IEEE Transactions on Plasma Science*, 32(2):413– 417, April 2004.
10. A. Stock, J. Neudorfer, M. Riedlinger, G. Pirrung, G. Gassner, R. Schneider, S. Roller, and C.-D. Munz. Three-dimensional numerical simulation of a 30 GHz gyrotron resonator with an explicit high-order discontinuous galerkin based particle-in-cell method. accepted for publication in: *IEEE Transaction on Plasma Science*, XX:yyy–yyy, 2012.

Realization Of Sprott Case C Attractor With CCII's

Yılmaz Uyaroglu¹, İhsan Pehlivan²

¹Sakarya University, Eng. Faculty, Electrical Electronics Engineering Department, 54187, Esentepe Campus, Sakarya, Turkey, uyaroglu@sakarya.edu.tr

²Electronics and Computer Education Department, Sakarya University, 54187, Esentepe Campus, Sakarya, Turkey, ipehlivan@sakarya.edu.tr

Summary

The nonlinear autonomous Sprott Case C chaotic equations are algebraically simple but can generate a complex chaotic attractor. In this paper, we propose to realize Sprott Case C Equation known well by using CCII's. Chaotic electronic implementation of the Sprott Case C attractor was realized using OrCad-PSpice® with CCII's. We gathered a new design which advocates a wide band of frequencies and prosperously gives the simulation results of Sprott Case C Equation. Chaotic graphics were just the same as other realizations devised before.

1 Introduction

Up to now, various chaotic systems are introduced in [1,7]. Sprott embarked upon an extensive search for autonomous three dimensional chaotic systems with fewer than seven terms in the right hand side of the model equations [8]. Several thousands of chaotic cases were found by using computer programs. Only 33 cases are distinct in the point that their functional forms are different and not related by a trivial transposition of variables. By performing various algebraic transformations on these cases, 15 additional cases were found satisfying for the criterions of simplicity that mentioned above. Of these total 48 (33+15) cases only 19 (Labeled by 'A' to 'S') appear to be distinct in the sense that there is no obvious transformation from one to another. In these 19 ('A' to 'S') cases, 'A' to 'E' (five) have five terms and two nonlinearities while cases 'F' to 'S' (fourteen) have six terms and one nonlinearity in the right hand side. In this search, no case was found fewer than five terms and any number of quadratic nonlinearity, which shows chaotic behavior. Among these nineteen cases, only Case 'A' is conservative (volume preserving) while others are dissipative flows (volume contracting) and shows strange attractors.

This paper focuses on realization of Sprott Case C Attractor with CCII's. Section II presents the dynamical analyses of Sprott Case C attractor. In

Section III, electronic circuit design and PSpice® Simulations of chaotic Sprott Case C system. Finally, conclusions and discussions are given.

2 Dynamical analyses of Sprott Case C attractor

Following Sprott Case C chaotic system was used for realizing the chaotic circuit.

$$\begin{aligned}\dot{x} &= y \cdot z \\ \dot{y} &= x - y \\ \dot{z} &= 1 - x^2\end{aligned}\quad (1)$$

Using Matlab-Simulink modeling, xy phase portrait of the Sprott Case C system are achieved in Figure 1.

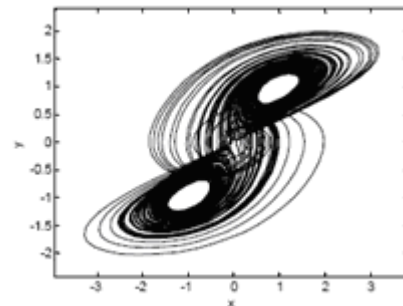


Fig. 1. x-y phase portrait of Sprott Case C Attractor

3 Electronic circuit design and simulation of the Sprott Case C attractor with CCII's

Chaotic differential equations of the Sprott Case C chaotic circuit are given below.

$$\begin{aligned}\dot{x} &= \frac{1}{R_1 C_1} y.z \\ \dot{y} &= \frac{R_4}{R_2 R_5 C_2} x - \frac{R_4}{R_3 R_5 C_2} y \\ \dot{z} &= \frac{R_8 V_p}{R_7 R_9 C_3} - \frac{R_8}{R_6 R_9 C_3} x^2\end{aligned}\quad (2)$$

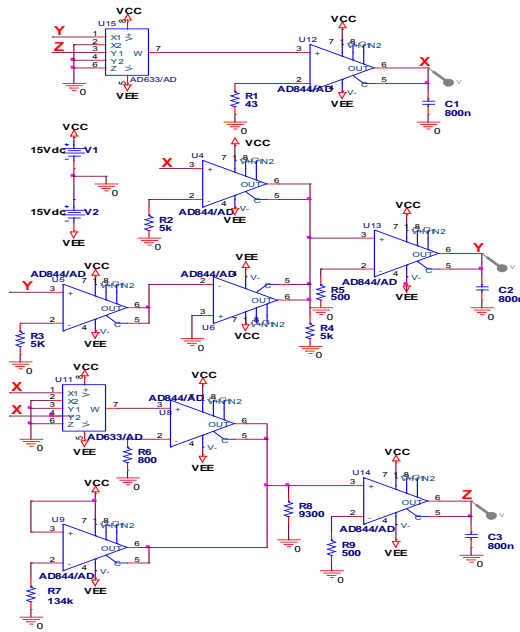


Fig. 2. Circuit Schematic of the Sprott Case C attractor with CCIIIs

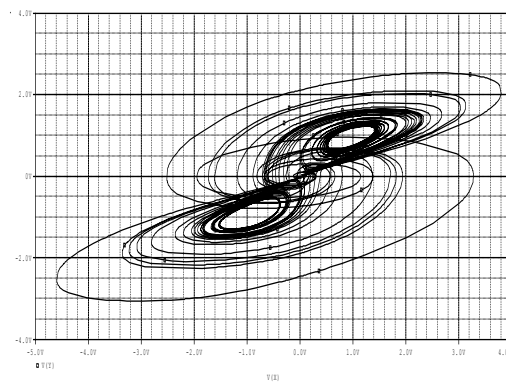


Fig. 3. Pspice Simulation Result of the Sprott Case C attractor with CCIIIs (xy-attractor)

References

1. G. Chen and T. Ueta. Yet Another Chaotic Attractor, *International Journal of Bifurcation and Chaos*, vol. 9, no. 7, 1999, pp. 1465-1466.
2. T. Ueta and G. Chen. Bifurcation Analysis of Chen's Attractor, *International Journal of Bifurcation and Chaos*, vol. 10, no.8, 2000, pp. 1917-1931.
3. J. Lü and G. Chen. A New Chaotic Attractor Coined, *International Journal of Bifurcation and Chaos*, vol. 12, no. 3, 2002, pp. 659-661.
4. Q.G. Yang, Z.C. Wei and G.R. Chen. An Unusual 3D Autonomous Quadratic Chaotic System with Two Stable Node-Foci, *International Journal of Bifurcation and Chaos*, vol. 20, no. 4, 2010, pp. 1061-1083.
5. I. Pehlivan and Y. Uyaroglu. A New Chaotic Attractor from General Lorenz System Family and its Electronic Experimental Implementation, *Turkish Journal of Electrical Engineering and Computer Science*, vol. 18, no. 2, 2010, pp. 171-184.
6. K.M. Cuomo and A.V. Oppenheim. Circuit Implementation of Synchronized Chaos with Applications to Communications, *Physical Review Letters*, vol. 71, no. 1, July 1993, pp. 65-68.
7. V. Sundarapandian and I. Pehlivan. *Analysis, Control, Synchronization and Circuit Design of a Novel Chaotic System*. Mathematical and Computer Modelling, (Accepted 2011., doi:10.1016/j.mcm.2011.11.048)
8. J.C. Sprott. Simple Chaotic Systems and Circuits, *American Journal of Physics*, vol. 68, no. 8, August 2000, pp. 758-763.

Acknowledgement

This work was supported by the Sakarya University Scientific Research Projects Commission Presidency (No. 2010-01-00-002).

Dielectric Breakdown Simulations of an On-Load Tap-Changer in a Transformer Considering the Influence of Tap Leads and Windings

M. Wiesmüller^{1,2}, B. Glaser¹, F. Fuchs¹, and O. Sterz¹

¹ Maschinenfabrik Reinhausen GmbH (MR), Falkensteinstr. 8, 93059 Regensburg, Germany

² University of Applied Sciences Deggendorf, Edlmaistr. 6 and 8, 94469 Deggendorf, Germany

Summary. This paper reports on the simulation of an on-load tap-changer in a power transformer. The electric fields are computed and resulting breakdown voltages are estimated by using the streamer criterion. The environment of the on-load tap changer is taken into account by modeling tap leads in detail as well as transformer windings. The goal of the investigations is to justify standard design and test-procedures which assume a low dependency of the interior dielectric properties of the on-load tap-changer on the surrounding.

1 Introduction

On-Load Tap-Changers (OLTCs) are devices which permit the change of the turn ratios of transformers, allowing voltage regulation or phase shifting under load without interruption.

Power transformers equipped with OLTCs have been main components of electrical networks and industrial applications for nearly 80 years [2, 4].

One crucial criterion for the selection of an adequate OLTC for a certain transformer or application is its insulation level. Generally, the dielectric strength depends on the whole system, i.e. the transformer, as well as the connection-leads and the OLTC. However, usual test-procedures by OLTC manufacturers are not done within a transformer but on a separate OLTC. Also during design the influence of leads and windings on the internal OLTC insulation is usually neglected. This gives rise to further investigations justifying this approach. Therefore, a typical system is simulated by computing the electric field and breakdown voltages with and without windings and tap-leads.

2 Finite Element Simulation

For simulation half of the core and the tap windings of the transformer phase nearest to the OLTC are modeled. The OLTC itself is represented by its lower part—the tap selector. After several simplifications the CAD-data of the tap selector are directly imported into the simulation software [1]. The leads are created manually. Finally the transformer tank is built as a surrounding box.

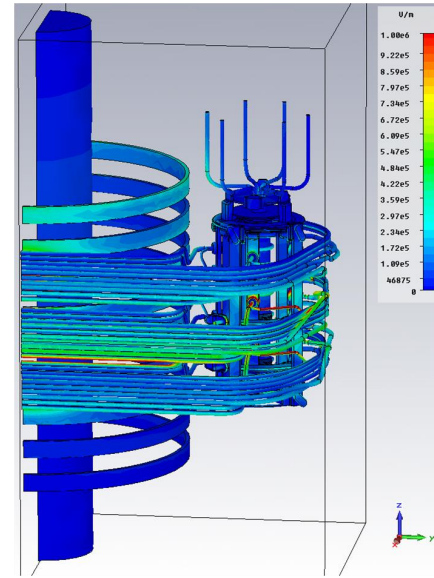


Fig. 1. Magnitude of the electric field of the total arrangement. Red colored parts of the plot are above 1 kV/mm.

Here, we consider AC stresses. Hence, the electric field is computed for the electrostatic case, i.e. we solve

$$\nabla \cdot (\epsilon \nabla \phi) = 0 \quad \text{in } \Omega, \quad (1)$$

where Ω is the non-conductive domain, applying constant potentials $\phi = \phi_0$ on Dirichlet boundaries representing grounded and stressed electrodes and the transformer tank.

For the calculation 2nd order, isoparametric finite elements are used. The result of a computation with 22.6 million unknowns is shown in Fig.1.

3 Dielectric Breakdown Calculation

Breakdown in oil cannot be described by one coherent theory as in gas. To explain the main mechanisms two basic approaches are used: one is an extension of gaseous breakdown, the other one assumes that breakdown is caused by bridges of fibrous impurities.

To calculate the breakdown voltage in inhomogeneous electric fields different methods can be used, see e.g. [3,5]. The calculation method we use is based

on the streamer criterion along a critical path C

$$\int_C \alpha(|\mathbf{E}(\mathbf{x})|) dl_x \geq k, \quad (2)$$

where α is the effective ionization coefficient, \mathbf{E} the electric field and k defines the number of electrons necessary for breakdown. With an exponential equation for α and the introduction of a normalized electric field $e(x) := |\mathbf{E}(\mathbf{x})|/U$, (2) can be solved as in [3] for the breakdown voltage

$$U_b = (1\text{mm})^{1/z} \cdot \left(\int_C \left(\frac{e(x)}{E_0} \right)^z dl_x \right)^{-1/z} \quad (3)$$

with constants $E_0 = 15\text{ kV/mm}$ and $z = 4.2$. These constants are derived from measured breakdown data of uniform fields.

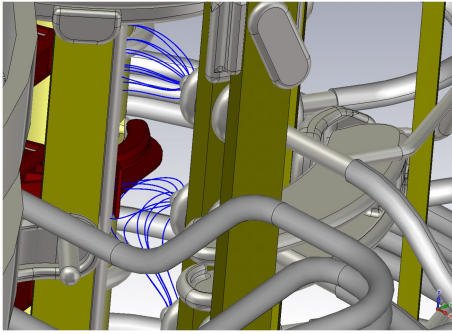


Fig. 2. A subset of evaluated critical lines in the tap selector

The streamer criterion (2) has to be evaluated along critical paths, which for breakdown in oil gaps are fieldlines starting at electrodes with high electric field stresses. Since the most critical fieldline does not necessarily start at a local field maximum many fieldlines have to be evaluated, some of them are shown in Fig. 2. The most critical path and the associated U_b is determined by finding the minimum over all calculated voltages.

4 Influence of the Tap Leads and Windings

To investigate the influence of the transformer and the leads on the dielectric strength of the OLTC three different systems are simulated, see Fig. 3. Field values along several lines parallel to the tap selector axis are compared. In Fig. 4 field values along two of these lines are shown. One line represents a region with low, the other one a region with high electric stresses.

In regions with low fields there is a significant influence of the transformer and the leads, but in regions with high field stresses, which are critical concerning dielectric strength, the differences are maximum 10%. Regarding the calculated breakdown voltages the deviation is even less than 1%.

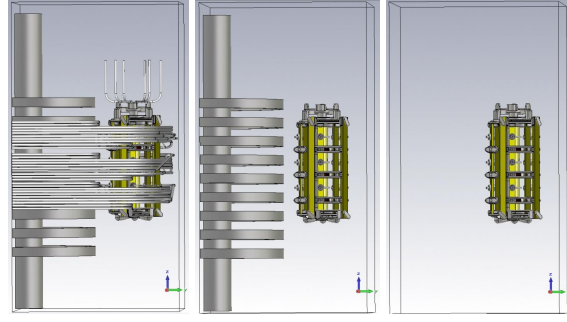


Fig. 3. Different geometries. Left: Tap selector with leads and transformer windings. Middle: Tap selector and windings. Right: Only tap selector

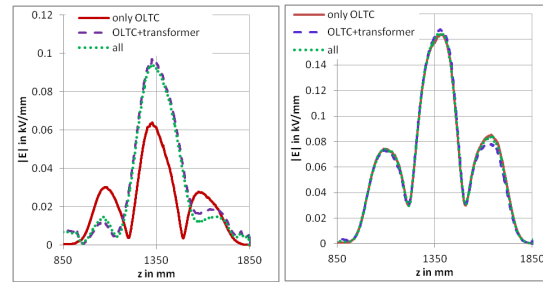


Fig. 4. $|\mathbf{E}|$ comparing all geometric arrangements, region with low fields (left), region with high fields (right)

5 Conclusion

It has been shown that for the investigated typical example the influence of the transformer and the tap leads on the internal OLTC insulation is small enough to neglect them during design optimization and test-procedures.

Acknowledgement. The authors acknowledge discussions with D. Breitfelder and B. Bakija, Siemens AG, and thank for support of T. Strof, T. Manthe, J. Niesner, and B. Visser, MR GmbH.

References

1. CST EM STUDIO®, www.cst.com.
2. D. Dohnal. *On-Load Tap-Changers in Power Transformers. A Technical Digest*. MR-Publication PB252/04 EN 06/09, Regensburg, 2009.
3. W. Knorr and D. Breitfelder. Breakdown in transformer oil with AC and impulse voltage stress. *IEEE Int. Symp. on Electrical Insulation.*, 291–296, 1984.
4. A. Krämer. *On-Load Tap-Changers for Power Transformers. Operation, Principles, Applications and Selection*. MR-Publication, Regensburg, 2000.
5. A. Küchler. *Hochspannungstechnik (in German)*. Springer, Berlin-Heidelberg, 2009.
6. M. Wiesmüller. Evaluation of the dielectric strength of an OLTC in a transformer using electrical field simulations (in German). Master's thesis, University of Applied Sciences Deggendorf, Deggendorf, 2012.

Participant	Affiliation	email
Adeyemo, Oluwaseun	Toltim Electrical Engineering, Ormande/South Africa	aytaca@ifh.ee.ethz.ch
Ali, Giuseppe	Dip. di Matematica, Università della Calabria, Cosenza, Italy	giuseppe.ali@unical.it
Alparslan, Aytac	IFH, ETH Zurich, Switzerland	aytaca@ifh.ee.ethz.ch
Altomonte, Daniele	DEA, University of Roma 3, Italy	daltomonte@uniroma3.it
Antonescu, Oana Simona	Technical University of Cluj Napoca, Romania	oana.antonescu@et.utcluj.ro
Banagaaya, Nicodemus	Dept. of Math. and Comp. Science, TU Eindhoven, The Netherlands	n.banagaaya@tue.nl
Bandlow, Bastian	FG Theoretische Elektrotechnik, EN 2, TU Berlin, Germany	bandlow@tet.tu-berlin.de
Bittner, Kai	University of Applied Sciences Upper Austria, Hagenberg, Austria	Kai.Bittner@fh-hagenberg.at
Blaszczyk, Andreas	ABB Switzerland Ltd., Corporate Research, Baden-Dättwil, Switzerland	Andreas.Blaszczyk@ch.abb.com
Blome, Mark	Zuse Institute Berlin, Germany	blome@zib.de, burger@zib.de
Bockholt, Marcos	ABB AG, DEDC / CoE Dry Type Converter Transformers, Brilon, Germany	marcos.bockholt@de.abb.com
Bodendiek, André	Institut Computational Mathematics, TU Braunschweig, Germany	a.bodendiek@tu-bs.de
Bollhöfer, Matthias	Institut Computational Mathematics, TU Braunschweig, Germany	m.bollhoefer@tu-bs.de
Boyvat, Mustafa	D-ITET, ETH Zurich, Switzerland	mustafa.boyvat@ifh.ee.ethz.ch
Brambilla, Angelo	DEI, Politecnico di Milano, Italy	brambill@elet.polimi.it
Bugert, Beatrice	Weierstrass Institute, Berlin, Germany	bugert@wias-berlin.de
Cagnoni, Davide	Politecnico di Milano, Dipartimento di Matematica/Italy	davidecagnoni@alice.it
Camiola, Vito Dario	University of Catania, Italy	camiola@dmi.unict.it
Christen, Thomas	ABB Switzerland Ltd., Corporate Research, Baden-Dättwil, Switzerland	thomas.christen@ch.abb.com
Ciuprina, Gabriela	Electrical Eng. Dept., "Politehnica" University of Bucharest, Romania	gabriela@lmn.pub.ro
Colominas, Ignasi	Civil Engineering School, Universidade da Coruña, Spain	icolominas@udc.es
Cottet, Didier	ABB Switzerland Ltd., Corporate Research, Baden-Dättwil, Switzerland	didier.cottet@ch.abb.com
Cui, Jian	Graduate School of Computational Engineering, TU Darmstadt, Germany	cui@gsc.tu-darmstadt.de
De Falco, Carlo	MOX-Modeling and Scientific Computing, Politecnico di Milano, Italy	carlo.defalco@polimi.it
Demir, Alper	Koç University, Istanbul, Turkey	aldemir@ku.edu.tr
Denk, Georg	Infineon Technologies AG München/Germany	georg.denk@infineon.com
Di Rienzo, Luca	Politecnico di Milano/Italy	luca.dirienzo@polimi.it
Emiroglu, Selçuk	Eng. Faculty, Sakarya University, Turkey	selcukemiroglu@sakarya.edu.tr
Emson, Cris	Infolytica Europe/UK	Cris.Emson@infolytica.co.uk
Feng, Lihong	Dynamics of Complex Technical Systems, MPI, Magdeburg, Germany	feng@mpi-magdeburg.mpg.de
Flisgen, Thomas	Inst. for General Electrical Engineering, University of Rostock, Germany	thomas.flisgen@uni-rostock.de
Grognuz, Joel	CADFEM AG, Switzerland	joel.grognuz@cadfem.ch

Günther, Michael	University of Wuppertal, Germany	guenther@math.uni-wuppertal.de
Hanke, Martin	CADFEM GmbH, Berlin, Germany	MHanke@cadfem.de
Hannukainen, Antti	Dept. of Mathematics and Systems Analysis, Aalto University, Finland	antti.hannukainen@aalto.fi
Hebedean, Claudia	Technical University of Cluj-Napoca	Claudia.Hebedean@ethm.utcluj.ro
Herberthson, Magnus	Department of Mathematics, Linköping University, Sweden	magnus.herberthson@liu.se
Hess, Martin	Dynamics of Complex Technical Systems, MPI, Magdeburg, Germany	hessm@mpi-magdeburg.mpg.de
Hiltunen, Irene	Graduate School of Computational Engineering, TU Darmstadt, Germany	hiltunen@temf.tu-darmstadt.de
Hiptmair, Ralf	Seminar for Applied Mathematics, ETH Zurich, Switzerland	ralf.hiptmair@sam.math.ethz.ch
Hülsmann, Timo	Bergische Universität Wuppertal, Germany	huelsmann@math.uni-wuppertal.de
Ioan, Daniel	Polytechnic University of Bucharest/Romania	lmn@lmn.pub.ro
Jorks, Hai Van	Inst. of Comp. Electromagnetics, TU Darmstadt, Germany	jorks@temf.tu-darmstadt.de
Kaufmann, Christof	Bergische Universität Wuppertal, Germany	kaufmann@math.uni-wuppertal.de
Klöckner, Andreas	Courant Institute of Mathematical Sciences, New York, USA	kloekner@cims.nyu.edu
Knapp, Evelyne	Inst. of Comp. Physics, Zurich University of Applied Sciences, Switzerland	evelyne.knapp@zhaw.ch
Kolmbauer, Michael	Inst. of Comp. Mathematics, Johannes Kepler University, Linz, Austria	kolmbauer@numa.uni-linz.ac.at
Komarevskiy, Nikolay	Laboratorium für Kristallographie, ETH Zurich, Switzerland	n.komarevskiy@ifh.ee.ethz.ch
Kostetzer, Lucas	CADFEM (Suisse) AG, Aadorf, Switzerland	lkostetzer@cadfem.de
Kräck, Veronika	Friedrich-Alexander University Erlangen/Nürnberg, Germany	Kraeck@eam.eei.uni-erlangen.de
Kretschmar, Fritz	Graduate School of Computational Engineering, TU Darmstadt, Germany	kretschmar@gsc.tu-darmstadt.de
Kumar, Umesch	Dept. of Electrical Engineering, IIT, New Delhi, India	drumeshkumar98@rediffmail.com
Kurz, Stefan	Electromagnetics, TU Tampere, Finland	stefan.kurz@tut.fi
Lavesson, Nils	ABB Corporate Research, Vasteras, Sweden	nils.lavesson@se.abb.com
Le Maître, Olivier	LIMSI-CNRS, Orsay, France	olm@limsi.fr
Leuchtmann, Pascal	Lab. El.magn.Fields and Microwave El., ETH Zurich, Switzerland	leuchtmann@ifh.ee.ethz.ch
Markosyan, Aram	CWI, Amsterdam, The Netherlands	Aram.Markosyan@cw.nl
Mascali, Giovanni	Dip. di Matematica, Università della Calabria, Cosenza, Italy	mascali@unical.it
Matthes, Ulrich	Dept. of Math.s, University of Hamburg, Germany	ulrich.matthes@math.uni-hamburg.de
Meerbergen, Karl	Department of Computer Science, KU Leuven, Belgium	Karl.Meerbergen@cs.kuleuven.be
Mehlin, Michaela	Institute of Mathematics, University of Basel, Switzerland	michaela.mehlin@unibas.ch
Michielsen, Bastiaan	Onera, Toulouse, France	Bastiaan.Michielsen@Onera.fr
Muscato, Orazio	Dip. di Matematica e Informatica, Università di Catania, Italy	muscato@dmi.unict.it
Nicosia, Giuseppe	Dept. of Math and Comp. Science, University of Catania, Italy	nicosia@dmi.unict.it
Ostrowski, Jörg	ABB Baden-Dättwil, Switzerland	joerg.ostrowski@ch.abb.com
Pacurar, Claudia	Technical University of Cluj-Napoca, Romania	Claudia.Pacurar@et.utcluj.ro
Paganini, Alberto	Seminar for Applied Mathematics, ETH Zurich, Switzerland	alberto.paganini@sam.math.ethz.ch

Pehlivan, Ihsan	Electronic and Comp. Education Dept., Sakarya University, Turkey	ipehlivan@sakarya.edu.tr
Petukhov, Andrey	Faculty of Physics, Moscow State University, Russia	petukhov@physics.msu.ru
Porro, Matteo	Dip. di Matematica, Politecnico di Milano, Italy	matteo.porro@mail.polimi.it,
Racasan, Nicoleta-Adina	Technical University of Cluj-Napoca, Romania	Adina.Racasan@et.utcluj.ro
Rahkonen, Timo	Dept. of Electrical Engineering, University of Oulu, Finland	timor@ee.oulu.fi
Rathsfeld, Andreas	Weierstrass Institute for Applied Analysis and Stochastics, Berlin, Germany	Andreas.Rathsfeld@wias-berlin.de
Rizzo, Santi	Dip. di Ingegneria Elettrica, Università di Catania, Italy	rizzo@dieei.unict.it
Romano, Vittorio	University of Catania, Italy	romano@dmi.unict.it
Salerno, Nunzio	Dip. di Ingegneria Elettrica, Università di Catania, Italy	salerno@dieei.unict.it
Schilders, Wil	TU Eindhoven, The Netherlands	w.h.a.schilders@TUE.nl
Schmidt, Kersten	DFG Research Center MATHEON, TU Berlin, Germany	kersten.schmidt@math.tu-berlin.de
Schmithusen, Bernhard	Synopsys Switzerland	schmithu@synopsys.com
Schneider, André	Dynamics of Complex Technical Systems, MPI, Magdeburg, Germany	andre.schneider@mpi-magdeburg.mpg.de
Schneider, Judith	Dynamics of Complex Technical Systems, MPI, Magdeburg, Germany	will@mpi-magdeburg.mpg.de
Schnepp, Sascha	Graduate School of Computational Engineering, TU Darmstadt, Germany	schnepp@gsc.tu-darmstadt.de
Scholz, Eike	Bergische Universität Wuppertal, Germany	scholz@uni-wuppertal.de
Schöps, Sebastian	TU Darmstadt, Germany	schoeps@math.uni-wuppertal.de,
Simsek, Murat	Electronics and Communication Dept., Istanbul Technical University, Turkey	simsekmu@itu.edu.tr
Steinmetz, Thorsten	ABB Switzerland Ltd., Corporate Research, Baden-Dättwil, Switzerland	thorsten.steinmetz@ch.abb.com
Sterz, Oliver	Maschinenfabrik Reinhausen GmbH (MR), Regensburg, Germany	o.sterz@reinhausen.com
Stevanovic, Ivica	ABB Switzerland Ltd., Corporate Research, Baden-Dättwil, Switzerland	ivica.stevanovic@ch.abb.com
Stock, Andreas	Inst. für Aerodynamik und Gasdynamik, Universität Stuttgart, Germany	stock@iag.uni-stuttgart.de
ter Maten E. Jan W.	Bergische Universität Wuppertal/Germany	E.J.W.ter.Maten@tue.nl
Uyaroglu, Yilmaz	Electronic and Comp. Education Dept., Sakarya University, Turkey	uyaroglu@sakarya.edu.tr
van Rienen, Ursula	University Rostock, Germany	ursula.van-rienen@uni-rostock.de
Weiland, Thomas	TU Darmstadt, Germany	Thomas.Weiland@TEMF365.onmicrosoft.com
Wever, Utz	Siemens Corporate Technology, Munich, Germany	Utz.Weber@siemens.com
Wiesmüller, Maximilian	Maschinenfabrik Reinhausen GmbH (MR), Regensburg, Germany	maximilian.wiesmueller@gmx.de
Zaglmayr, Sabine	CST AG, Darmstadt, Germany	sabine.zaglmayr@cst.com
Zschiedrich, Lin	JCMwave GmbH, Berlin, Germany	lin.zschiedrich@jcmwave.com

SCEE2012 Local Organizers

[Dr. Andreas Blaszczyk](#)

ABB Corporate Research
Switzerland

[Prof. Ralf Hiptmair](#)

Seminar for Applied Mathematics
Raemistrasse 101
CH-8092 Zurich
Switzerland

[Dr. Pascal Leuchtmann](#)

Electromagnetic Fields and Microwave Electronics Laboratory
Gloriastrasse 35
CH-8092 Zurich
Switzerland

[Dr. Jörg Ostrowski](#)

ABB Switzerland Ltd.
Corporate Research
Baden-Dättwil
Switzerland

Local staff

Dominique Ballarin (ETH)
Christina Buchmann (ETH)
Marianne Pfister (ETH)
Eva Sigrist (ETH)
Irene Stepanek (ETH)
Rosmarie Weber (ABB Baden-Dättwil)

SCEE2012 Programme Committee

[Prof. Gabriela Ciuprina](#)

Politehnica University of Bucharest
Romania

[Dr. Georg Denk](#)

Infineon
Germany

[Prof. Michael Günther](#)

University of Wuppertal
Germany

[Dr. Jan ter Maten](#)

University of Wuppertal
The Netherlands

[Ir. Bastiaan Michielsen](#)

ONERA
France

[Prof. Ursula van Rienen](#)

University of Rostock
Germany

[Prof. Vittorio Romano](#)

University of Catania
Italy

[Prof. Wil Schilders](#)

TU Eindhoven
The Netherlands

[Prof. Thomas Weiland](#)

TU Darmstadt & CST
Germany